UNIVERSIDAD AUTÓNOMA DE MADRID

DOCTORAL THESIS

# A Systematic Search of Dark Matter Subhalos in Gamma Rays among Unidentified Sources and Constraints on Dark Matter Properties

*Author:*
Javier Coronado Blázquez

*Supervisors:*
Dr. Miguel A. Sánchez-Conde
Prof. Carlos Muñoz

*Thesis submitted in partial fulfillment of the requirements for the degree of Doctor of Philosophy*

*at the*

Instituto de Física Teórica y Departamento de Física Teórica

Madrid, July 2021

*A mi madre, por traerme al mundo*
*Y a Irene, por hacer de él un lugar mejor*

*"Behind every beautiful thing there's been some kind of pain"*

Bob Dylan, *Not Dark Yet* (1997)

*"Think before you speak. Read before you think"*

Fran Lebowitz, *Social Studies* (1981)

*"I don't know where I'm going from here, but I promise it won't be boring"*

David Bowie

*"There is a crack in everything – that's how the light gets in"*

Leonard Cohen, *Anthem* (1992)

*"Jesus died for somebody's sins but not mine"*

Patti Smith, *Gloria* (1975)

*"Sic parvis magna"*

Sir Francis Drake

*"In fondo, è solo un trucco"*

Jep Gambardella, *La Grande Bellezza* (2013)

*"...But life is just a party, and parties weren't meant to last"*

Prince, *1999* (1982)

# *Agradecimientos*

Aquí estamos, al final del camino.

Mi mayor agradecimiento deber ser para Miguel Ángel Sánchez-Conde, masc. Nunca podré llegar a comprender cómo mi vida ha cambiado gracias a ti. Gracias, ante todo, por haber creído en mí cuando nadie más lo hizo. De no haber sido así, hoy no estaría escribiendo estas palabras, y nunca habría llegado a poner un "PhD" tras mi nombre. Las ramificaciones de todas las vidas posibles son infinitas; no sé qué me habría encontrado de haber transitado por ellas, pero es difícil que superen a esta. Por eso quiero que sepas lo mucho que te debo y que nunca podré pagarte más que con la promesa de atesorar incontables recuerdos. Y mis sinceras disculpas por haberte estafado con alevosía y premeditación durante 4 años llevándote a creer que sabía algo de lo que estaba haciendo.

Mi máximo agradecimiento, admiración y cariño al grupo DAMASCO, que he tenido el privilegio de ver crecer desde su mismo nacimiento. Aunque en un futuro no forme parte de él, estoy seguro de que seguirá su imparable desarrollo y nos regalará no pocas alegrías en este campo aún joven de la física de astropartículas. Siempre recordaré nuestros míticos "DAMASCO meetings" llenos de ideas, discusión y risas. Gracias a Ale y Angie por nuestros N-body coffees (y esos ensayos al piano que nos evadían de la cruel realidad de python), a Bryan, Daniele, Francesca, Judit, Thomas y Vivy. También a aquellos que dejaron una profunda huella en DAMASCO a pesar de ser visitantes — Christian, Ottavio, Pedro y Sergio. Y mi especial recuerdo a Mathieu; ojalá hubiéramos tenido más tiempo.

Por el camino me he encontrado con muchísima gente. Gracias sobre todo a la colaboración Fermi-LAT, donde tantísimo he aprendido. Desde aquella primera charla en Pisa, cuando apenas llevaba 5 meses en esto; me encontré en una sala rodeado de expertos en materia oscura, rayos gamma o ambas, y ahí iba yo, con mi Powerpoint pocho sin saber muy bien de qué estaba hablando. Pero donde esperaba encontrar dolor o, en el mejor escenario, humillación, sólo encontré una excepcional calidad humana y científica. Mi especial agradecimiento a Jean Ballet, Regina Caputo, Eric Charles, Seth Digel, Mattia di Mauro, Christopher Eckner, Chris Karwin, Elizabeth Ferrara, Michael Gustafsson, Benoît Lott, Manuel Meyer, Néstor Mirabal, Pablo Saz-Parkinson, David Smith y Gabrijela Zaharijas. De la misma forma, ha sido fantástico formar parte del futuro telescopio CTA (que sin duda será una revolución), y agradezco especialmente a Michele Doro, Moritz Hütten, Fabio Iocco, Reshmi Mukherjee y todo el grupo DMEP. También a Alba Fernández-Barral, con la que he tenido el inmenso placer de trabajar como representante de divulgación en España. Gracias también a todo el personal del IFT, tanto científico como de apoyo y administración, especialmente a Carlos Muñoz y la 5ª planta, y a los colaboradores de la UCM, Jose Luis Contreras, Alberto Domínguez, Marcos López y Dani Nieto.

Y por supuesto, nada de esto habría sido posible sin el apoyo de Irene. No me queda vida para agradecerte todas las alegrías (y rants) compartidas, todos los momentos en los que me hacías ver la realidad de forma más objetiva, y en general por estar a mi lado y hacer del mundo un lugar menos hostil. Igualmente, infinita gratitud a mi familia materna, especialmente a mis abuelos Mari Paz y Ricardo, Benito, mi hermana Laura y ante todo mi madre, Carmen, que siempre consiguió vencer los infinitos obstáculos puestos por otros para que pudiera dedicarme a esto. Gracias también a todas por haber estado ahí cuando mi salud no fue la mejor.

Por último, quiero dedicar esta Tesis a todas aquellas personas que han estado en primera línea contra la pandemia de la COVID-19. El mundo nunca os lo podrá agradecer lo suficiente, ni parece estar muy interesado en hacerlo. Ojalá algún día aquellos que sabemos lo que ha sido estemos en la posición de agradecerlo de verdad.

En resumen, muchas gracias por vuestro tiempo. Ha sido divertido.

Mis mejores deseos,
Javier

# *Resumen*

A lo largo de esta Tesis Doctoral, la línea de investigación se centra en el entendimiento de la naturaleza última de la Materia Oscura (DM, del inglés *Dark Matter*). Para ello, he seguido un enfoque basado en búsquedas indirectas con rayos gamma. A continuación, resumo las principales contribuciones de este trabajo al campo.

Desde el comienzo de la Tesis, se identificaron a los subhalos de materia oscura como los principales objetos a estudiar. Estos subhalos son las mínimas estructuras que la materia oscura puede formar, predichos por el paradigma cosmológico actual, $\Lambda$CDM. En este marco de referencia, la formación de estructuras sigue un modelo jerárquico "bottom-up", en el cual las estructuras más pequeñas aparecen y se viri-alizan primero, mientras que mayores estructuras surgen de procesos de fusión y acreción de las primeras. Por debajo de una cierta masa, los subhalos no logran retener gas o contenido bariónico, por lo que permanecen invisibles en cualquier longitud de onda del espectro electromagnético, es decir, siendo "subhalos oscuros". Pese a ello, asumiendo que la DM está compuesta de partículas tipo WIMP (acrónimo de partícula masiva débilmente interactuante) en una escala de masas GeV–TeV, estos subhalos podrían brillar en rayos gamma, producto de la co-aniquilación de los WIMPs que los forman. El flujo de fotones de este proceso es proporcional al cuadrado de la densidad de DM y, siendo los subhalos objetos extremadamente compactos, constituyen excelentes objetos donde buscar DM de forma indirecta, mediante rayos gamma.

En el primer Capítulo, introduzco el problema de la DM en la física moderna, comenzando por las evidencias observacionales y su formulación matemática, para centrarnos después en sus propiedades y distribución, sus mecanismos de producción y búsquedas actuales. Siendo nuestro interés la detección indirecta de DM, dedico el Capítulo 2 a la astronomía de rayos gamma, presentando el pasado, presente y futuro de los telescopios gamma, así como las diferentes componentes del cielo en altas energías.

En un primer trabajo, presentado en el Capítulo 3, se desarrolla la metodología general a emplear para buscar subhalos con el instrumento *Fermi*-LAT, a bordo del satélite Fermi de la NASA. Al emitir sólo en rayos gamma, estos subhalos aparecerían como fuentes no identificadas (unIDs, del inglés *unIDentified source*) en los catálogos de fuentes gamma, sin asociación de ningún tipo. El primer paso es obtener una estimación realista de la población de subhalos en nuestra galaxia, la Vía Láctea (MW, *Milky Way*). Para ello se suele recurrir a simulaciones cosmológicas de N-cuerpos; sin embargo, éstas no logran reproducir todo el rango de masas de los subhalos, por falta de resolución numérica. Para superar esta limitación, desarrollamos un algoritmo de repoblación, que incluye los subhalos de baja masa por debajo del límite de resolución, pudiendo entonces caracterizar las propiedades estadísticas de los subhalos y sus luminosidades de aniquilación (codificadas en el llamado "J-factor"). Desde el punto de vista observacional, definimos una serie de filtros según las características que debería tener la emisión en rayos gamma de subhalos. Esto nos permite reducir el número de potenciales candidatos. Además, calculamos la sensibilidad instrumental de *Fermi*-LAT para DM, teniendo en cuenta la configuración del catálogo, las coordenadas de la fuente, el canal de aniquilación y la masa del WIMP. Al no poder dirimir el origen de estas fuentes no asociadas, sólo podemos restringir el espacio de parámetros sección eficaz de aniquilación vs. masa del

WIMP, obteniendo límites competitivos que son capaces de descartar WIMPs de baja masa producidos térmicamente. Estas cotas son independientes de otras obtenidas con objetos como las galaxias esferoidales enanas (dSph, de su acrónimo inglés *dwarf Spheroidal*), actualmente considerados los más robustos y competitivos en el campo.

Una vez se ha establecido la metodología general, continuamos explotando los datos de *Fermi*-LAT en una continuación de este trabajo, presentada en el Capítulo 4. Al lograr reducir el número de candidatos a subhalo (de unos 1500 a 44), podemos realizar un análisis espectral usando más datos, para así reforzar o descartar la hipótesis DM en estas fuentes. Esto permite reducir aún más el número de candidatos supervivientes, además de destacar un par de fuentes con una moderada preferencia estadística a DM. Además, realizamos un análisis de extensión espacial, puesto que los subhalos más brillantes deberían aparecer como fuentes gamma extensas, afirmación respaldada por nuestras simulaciones. Sin embargo, todos nuestros candidatos resultan ser fuentes puntuales en el análisis espacial. Esto, no obstante, no es un resultado concluyente, como se discute en el siguiente Capítulo, ya que la respuesta instrumental debe tenerse en cuenta para obtener una respuesta definitiva. En este trabajo empleamos dos herramientas más para intentar dirimir la naturaleza de los unIDs: i) un espacio de parámetros privilegiado en el cual la separación entre DM y las clases astrofísicas es clara bajo ciertas condiciones, herramienta presentada en un contexto DM aquí por primera vez con posible aplicación futura en un contexto de algoritmos de clasificación de machine learning, y ii) una búsqueda de *stellar streams* en las coordenadas de las fuentes con datos del telescopio *Gaia*, lo que indicaría la disrupción de una dSph o un cúmulo globular debido al potencial de la MW. Un candidato resulta coincidente con la stream de Sagittarius, pero no es posible establecer una asociación inequívoca, y es necesario trabajo adicional para explorar esta excitante posibilidad.

En el Capítulo 5, exploramos más en detalle la información espacial de los subhalos. Para dirimir si *Fermi*-LAT es capaz de detectar extensión angular de subhalos, generamos miles de simulaciones de estos objetos con datos gamma reales. El principal ingrediente aquí es el perfil espacial de aniquilación, que podemos construir a partir de las propiedades estructurales de los subhalos en las simulaciones de N-cuerpos. Usando dos modelos extremos –un subhalo masivo y lejano, y otro ligero y cercano–, que resultan ser notablemente similares en sus propiedades espaciales, podemos recalcular la sensibilidad instrumental, ahora para fuentes extensas, así como estudiar el rendimiento de *Fermi*-LAT en una variedad de configuraciones como diferentes masas de WIMP y secciones eficaces de aniquilación. La conclusión general es que *Fermi*-LAT debería detectar al menos indicios de extensión espacial para WIMPs ligeros, independientemente de la sección eficaz de aniquilación. Para WIMPs más pesados, por encima de unos 500 GeV, *Fermi*-LAT es aún capaz de recuperar una cierta información espacial para secciones eficaces suficientemente grandes. Estas conclusiones tienen un impacto muy relevante en las cotas que se pueden poner, que son degradadas al integrar la señal de rayos gamma hasta un cierto ángulo en lugar de hasta el un radio físico característico, como se hacía previamente.

Esto, junto a la publicación del catálogo de rayos gamma más completo, el 4FGL, motiva un nuevo análisis espectral y espacial con toda la información obtenida de estos trabajos, como hacemos en el Capítulo 6. Este nuevo catálogo tiene un gran número de fuentes individuales, por lo que el número de candidatos a subhalo sube ahora hasta un centenar; pese a ello, la mayoría pueden descartarse con el análisis espectral. Resulta interesante que, aún aplicando correcciones a la significancia estadística por el llamado "*trials factor*", un puñado de fuentes aún muestran una

cierta preferencia hacia la hipótesis DM, con extensión espacial en algunos casos. Aunque se necesitarían más datos, este constituye el indicio más fuerte de detección de subhalos de DM hasta la fecha.

Además del telescopio espacial *Fermi*-LAT, también podemos emplear observatorios Cherenkov terrestres para buscar subhalos en rayos gamma. La principal ventaja de estos es una mejora en la resolución angular y sensibilidad a mayores energías, a costa de una menor área del cielo observado. En el Capítulo 7 empleamos HAWC para este estudio. HAWC resulta ser el observatorio más apropiado, ya que cubre 2/3 del cielo diariamente. Los datos en bruto de HAWC no están públicamente disponibles, y sólo proveen información limitada; no obstante, ésta resulta suficiente para estimar el número de posibles subhalos en sus catálogos. Aplicando los mismos filtros del primer trabajo (Capítulo 3), sólo encontramos un unID compatible, que además resulta ser espacialmente extenso. Sin embargo, al no poder realizar un análisis espectral detallado, sólo podemos poner las cotas habituales a la sección eficaz de aniquilación de DM, las cuales son muy competitivas para WIMPs pesados, $\mathcal{O}(10)$ TeV.

El futuro de la astronomía de rayos gamma, el Cherenkov Telescope Array (CTA), actualmente en fase de construcción, será también un excelente instrumento para búsquedas de subhalos, como exploramos en el Capítulo 8. En este caso, sólo podemos recurrir a datos simulados por el momento, que empleamos para calcular la sensibilidad instrumental a subhalos, de forma análoga al trabajo de *Fermi*-LAT. Identificamos tres estrategias observacionales, basadas en los *Key Science Projects* (KSPs) de CTA. Determinamos que no es necesario dedicar tiempo específico a búsqueda de subhalos, sino que se acumula de forma natural simplemente sumando exposiciones de los KSPs y otras observaciones programadas – al ser las coordenadas de los subhalos desconocidas, sólo se puede esperar a encontrarlos de forma serendípica en el campo de visión de otros apuntados. Estimamos la estrategia observacional de CTA en 10 años de operaciones, extrapolando el programa observacional de MAGIC, un telescopio Cherenkov actualmente en operación en las Islas Canarias. Con esta información, podemos calcular la probabilidad de encontrar un subhalo por encima de cierto J-factor de aniquilación, y poner cotas que se encuentran a un orden de magnitud del valor de la sección eficaz térmica.

En el Capítulo 9, exploramos un candidato alternativo para DM, que ha ganado mucha atención en los últimos años gracias a la incipiente astronomía de ondas gravitacionales: los agujeros negros primordiales (PBHs, del inglés *Primordial Black Holes*). Estos son agujeros negros producidos no por el colapso de estrellas masivas al final de sus vidas, sino por sobredensidades en el Universo primitivo. De acuerdo a la radiación de Hawking, los agujeros negros deberían evaporarse en un tiempo inversamente proporcional a su masa, emitiendo (entre otras partículas) fotones de cada vez más alta energía. En las últimas etapas de su existencia, deberían emitir en energías de rayos X y gamma. Al ser la DM estable (al menos hasta nuestros días), podemos buscar una posible contribución de PBHs en el fondo isotrópico de rayos X y gamma, estimando así la fracción máxima de DM que podría estar compuesta de PBHs. Nuestros resultados mejoran trabajos previos (entre un factor 2–50 dependiendo de la masa del PBH) y somos capaces de descartar PBHs muy ligeros, $\mathcal{O}(10^{16-17})$ g, en una de las ventanas de masa actualmente abiertas para este tipo de candidatos.

Finalmente, en el Capítulo 10 presento las conclusiones principales del trabajo realizado, así como posible trabajo futuro para continuar esta línea de investigación.

Para concluir, es natural motivar estas búsquedas de DM. Aunque los rayos gamma como herramienta para detectar WIMPs han suscitado un gran interés en

las últimas dos décadas, no se ha encontrado aún una señal concluyente. Por otra parte, el modelo WIMP está lejos de ser explorado en su totalidad al nivel de la sección eficaz térmica – es decir, todavía hay lugar más que suficiente para los WIMPs como explicación a la DM. Al realizar estas búsquedas, no pocos descubrimientos científicos, muchos de ellos completamente inesperados, han sido realizados, y no hay razón para pensar que esto será distinto en el futuro, con observatorios como CTA. Los próximos años serán tiempos muy excitantes tanto para las búsquedas de DM como para la astronomía de rayos gamma. Este es el camino.

# *Summary*

Through this Thesis, the main research activities are devoted to the understanding of the ultimate nature of Dark Matter (DM). To do so, an approach based on indirect detection with gamma rays is employed. Below I summarize the contribution of the work I realized to this field.

Since the beginning of this Thesis, DM subhalos were identified as the central targets. These are the smallest structures DM can form in the Universe, predicted by the current ΛCDM cosmological paradigm. Within this framework, structure formation follows a bottom-up hierarchical model, in which smallest structures appear and virialize first, and larger ones arise from merging and accretion of the former. Below a certain mass, these subhalos are unable to retain any gas or baryonic content, therefore being completely invisible at any wavelength, i.e., "dark subhalos". Nevertheless, under the assumption of DM being composed by *Weakly Interacting Massive Particles* (WIMPs) in the GeV–TeV scale, subhalos may shine in gamma rays, product of the co-annihilation of WIMPs. The photon flux of this process is proportional to the squared density of DM and, being subhalos extremely compact objects, they become excellent targets for indirect DM detection.

In the first Chapter, I introduce the DM problem in modern physics, starting from the observational evidence and mathematical formulation, and then focusing on DM properties and distribution, production mechanisms and current searches. Being our interest indirect searches with gamma rays, I devote Chapter 2 to gamma-ray astronomy, presenting the past, current and future generation of gamma-ray observatories, as well as the different components of the high-energy sky.

In the first work, which is presented in Chapter 3, a general methodology is developed to search for DM subhalos with the *Fermi*-LAT instrument on board the NASA Fermi satellite. As they would only shine in gamma rays, they would appear as unidentified sources (unIDs) in gamma-ray catalogs, with no association whatsoever. The first step is to obtain a realistic estimation of the subhalo population in the Milky Way (MW). This is usually characterized with N-body simulations, yet they fail to reproduce the entire mass range of subhalos due to numerical resolution. To overcome this limitation, we develop a repopulation algorithm to include the low-mass subhalos below the original mass resolution limit, this way making it possible to characterize the statistical properties of dark subhalos as well as their annihilation luminosities (codified in the so-called J-factor). From the observational point of view, by defining a series of "filters" according to the expected subhalo gamma-ray emission properties, we are able to reduce the initial pool of potential candidates. Additionally, the precise instrumental sensitivity to DM annihilation is computed for the *Fermi*-LAT, taking into account the catalog setup, source coordinates, annihilation channel and WIMP mass. Having inconclusive candidates, we cannot trust them to be actual DM subhalos, and therefore we proceed to set constraints to the annihilation cross section vs. WIMP mass parameter space, which are competitive limits able to rule light thermal WIMPs, and are independent to other probes such as the dwarf spheroidal satellite galaxies (dSphs), considered to be the most robust and competitive ones in the field at present.

Once the methodology is established, in a follow-up work presented in Chapter 4 we further exploit *Fermi*-LAT data. As the pool of candidates is reduced (from roughly 1500 to 44), we perform a dedicated spectral analysis with more gamma-ray data, in order to enforce or reject the DM hypothesis. This allows a further reduction of the number of surviving subhalo candidates, as well as highlighting a couple of sources with moderate statistical preference for DM. In addition, a spatial analysis is

performed, as the brightest subhalos should appear as spatially extended, which is supported by our repopulated simulations. However, every surviving candidate appears as point-like in our spatial analysis. Nevertheless, this result is not conclusive yet, as detailed in the next Chapter 5, as the instrumental response has to be properly taken into account in order to make firm statements. Two additional tools are used to shed light on the nature of the unIDs: i) a privileged parameter space where separation from DM and astrophysical classes is clearer under some conditions, a tool here presented for the first time in a DM context which can serve as application for classification machine learning algorithms, and ii) a search for so-called stellar streams in the sources coordinates with *Gaia* data, which would indicate a disruption of a dSph or globular cluster by the MW potential. One candidate is found to be coincident with the Sagittarius stream, yet no unequivocal association is possible, and further work would be needed to explore this exciting possibility.

In Chapter 5, the spatial information of subhalos is further explored. To determine whether *Fermi*-LAT is able to detect angular extension from subhalos, we perform thousands of simulations of DM subhalos with real gamma-ray data. The key ingredient is the spatial annihilation profile, which we computed starting from typical inner structural properties of subhalos in the N-body simulations. By using two extreme models –a massive and far subhalo, and a light and near one–, which turn out to be remarkably similar in terms of their spatial properties, we are able to derive the instrumental sensitivity, now for extended DM sources, as well as studying the performance of *Fermi*-LAT in a variety of configurations such as different WIMP masses and annihilation cross sections. The general conclusion is that *Fermi*-LAT should detect at least hints of subhalo spatial extension for light WIMPs, regardless of the annihilation cross section value. For heavy WIMPs –above 500 GeV– *Fermi*-LAT is still able to recover some spatial information for sufficiently large annihilation cross sections. These conclusions have great impact on the derived constraints, which are now degraded when integrating the gamma-ray signal up to a certain angle instead of a characteristic physical radius, as done before.

This, together with the publication of the most complete gamma-ray catalog, the 4FGL, motivates a new spectral and spatial analysis with all the knowledge gathered from these works, as done in Chapter 6. Being the new catalog composed of a larger number of individual sources, the subhalo candidate number is raised to a hundred, yet the vast majority are discarded after performing an spectral analysis. Interestingly, even when applying the corresponding trials factor correction to the statistical significances, a handful of sources still show a slight preference for a DM hypothesis, and exhibit spatial extension in some cases. Although more data is needed, this is the strongest hint for DM subhalo detection to this date.

In addition to the space-borne *Fermi*-LAT, ground-based Cherenkov gamma-ray telescopes can also be used to search for DM subhalos. The main advantage is the improved angular resolution and sensitivity at higher energies, at the cost of smaller sky coverage. In Chapter 7 we use HAWC for such study. HAWC turns out to be the most suitable observatory, as it daily covers almost $2/3$ of the sky. HAWC raw data are not publicly available, and only limited information is provided, yet the latter can be used to estimate the number of DM subhalo candidates. By applying the same filters of the first work (Chapter 3), we are able to keep just one unID as subhalo candidate, which also turns out to be spatially extended. Nevertheless, as no spectral analysis is feasible, we just set upper limits to the DM annihilation cross section, that are particularly competitive for heavy WIMPs, $\mathcal{O}(10)$ TeV.

The future of gamma-ray astronomy, the Cherenkov Telescope Array (CTA), currently in construction phase, will also be an excellent instrument for DM subhalo

searches, as explored in Chapter 8. In this case, we can only rely on simulated data for the time being, which we use to estimate the instrumental sensitivity to DM subhalos, similarly to what we did for the *Fermi*-LAT work. We identify three different observational strategies for subhalo searches, based on the planned Key Science Projects (KSPs) of CTA. We find that the best strategy requires no dedicated time at all, and is reached naturally by simply accumulating exposures from KSPs and other targeted observations – as the actual coordinates of subhalos are unknown, we can only hope for a serendipitous discovery on the field of view of different pointings. We estimate the observational strategy of CTA in 10 years of operations, by extrapolating the actual observation program developed by MAGIC along the years, a Cherenkov telescope currently in operation in Canary Islands. With this information, we are able to estimate the probability of spotting a subhalo above certain annihilation J-factor values, as well as to set DM constraints, which in this case are an order of magnitude above the thermal value at best.

In Chapter 9, we explore an alternative candidate for DM, which has gained a lot of attention in the last years thanks to the dawn of gravitational wave astronomy: Primordial Black Holes (PBHs). These are black holes produced not by the collapse of massive stars at the end of their lives, but by overdensities in the very early Universe. According to the Hawking radiation, black holes should evaporate in a time inversely proportional to their mass, emitting increasingly more energetic photons (as well as other particles). In the last part of their existence, they should be able to reach X-ray and gamma-ray energies. As DM is expected to be stable up to our days, by searching for a contribution of PBHs in the gamma- and X-ray isotropic background we can estimate the maximum fraction of DM made of PBHs. Our results improve previous constraints (a factor 2–50 depending on the PBH mass) and are able to rule out very light PBHs, $\mathcal{O}(10^{16-17})$ g, which is one of the currently open windows for such candidates.

Finally, in Chapter 10 I draw the main conclusions of the presented work, and discuss some ideas for possible future work on this same research line.

To conclude, it is natural to motivate these DM searches. Although gamma rays as probes of WIMPs have aroused a big deal of interest in the last two decades, no conclusive signal has been found yet. Nevertheless, the whole WIMP paradigm is far from being explored at the level of thermal relics, meaning there is still plenty of room for WIMPs. While performing these searches, many scientific unexpected discoveries and breakthroughs have been made, and there is no reason to think that this will cease in the future with new observatories such as CTA. The coming years will be thrilling times both for DM searches and gamma-ray astronomy. This is the way.

# Contents

**Agradecimientos** iii

**Resumen** v

**Summary** ix

**Contents** xiii

**1 Introduction: The Dark Matter problem in fundamental physics** 1
1.1 Observational evidence for dark matter . . . 1
1.1.1 First signs of dark matter . . . 2
1.1.2 Dark matter evidence on galactic scales . . . 2
1.1.3 Dark matter evidence on intermediate scales . . . 4
1.1.4 Dark matter evidence on cosmological scales . . . 6
1.2 The ΛCDM cosmological model . . . 7
1.2.1 Historical notes and mathematical formulation . . . 7
1.2.2 Production mechanisms of dark matter . . . 16
Thermal production of dark matter . . . 16
Non-thermal production of dark matter . . . 18
1.3 Dark matter distribution in the Universe . . . 19
1.3.1 Structure formation in ΛCDM . . . 19
1.3.2 N-body cosmological simulations as probes of dark matter substructure . . . 20
1.3.3 Challenges in ΛCDM halos . . . 25
1.4 The nature of dark matter: from WIMPs to primordial black holes . . . 28
1.4.1 Particle dark matter models . . . 28
1.4.2 Macroscopic dark matter models . . . 30
1.5 The quest for dark matter . . . 32
1.5.1 Production at colliders . . . 33
1.5.2 Direct detection . . . 34
Nuclear recoil experiments . . . 36
Primakoff effect axion searches . . . 37
Annual modulation experiments . . . 38
1.5.3 Indirect detection . . . 39
Neutrinos . . . 40
Cosmic rays . . . 42
Gamma rays . . . 46

**2 Gamma-ray Astronomy: detection techniques and current state** 91
2.1 Observation of gamma rays: a historical perspective . . . 91
2.2 Gamma-ray observatories . . . 93
2.2.1 Space-borne telescopes . . . 93
2.2.2 Ground-based observatories . . . 95

2.3 Composition of the gamma-ray sky . . . 102
2.3.1 Galactic diffuse gamma-ray emission . . . 103
2.3.2 Isotropic gamma-ray background . . . 105
2.3.3 Point and extended gamma-ray sources . . . 105

**3 Unidentified Gamma-ray sources as targets for indirect dark matter detection with the *Fermi* Large Area Telescope 119**
3.1 Introduction . . . 119
3.2 Predictions of the gamma-ray annihilation flux from subhalos . . . 121
3.2.1 Annihilation spectra . . . 122
3.2.2 Subhalo J-factors . . . 123
3.3 Search of DM subhalo candidates in *Fermi*-LAT source catalogs . . . 127
3.4 *Fermi*-LAT sensitivity to DM subhalos . . . 135
3.5 DM Constraints . . . 136
3.5.1 Procedure to set DM limits . . . 138
3.5.2 Current DM limits . . . 141
3.5.3 Sensitivity reach of the method . . . 141
3.6 Discussion and conclusions . . . 143
3.7 Appendix . . . 145
3.7.1 Impact of uncertainties . . . 145
3.7.2 Impact of the low-mass subhalo repopulation on DM limits . . . 147
3.7.3 Full set of DM constraints . . . 149

**4 Spectral and spatial analysis of the dark matter subhalo candidates among *Fermi* Large Area Telescope unidentified sources 161**
4.1 Introduction . . . 161
4.2 Spectral analysis of DM candidates . . . 163
4.2.1 Technical setup and analysis pipeline . . . 163
4.2.2 Analysis results and DM hypothesis test . . . 165
4.3 Limits on the DM annihilation cross section . . . 168
4.4 The $\beta$ plot: a technique to address DM/pulsar confusion . . . 171
4.5 Spatial analysis of remaining DM candidates . . . 176
4.5.1 Technical setup and data analysis results . . . 176
4.5.2 $\Lambda$CDM predictions of subhalo angular sizes . . . 176
4.6 Search for Stellar Counterparts with *Gaia* DR2 . . . 179
4.7 Conclusions and prospects . . . 181
4.8 Rejection criteria for the unIDs . . . 183

**5 Spatial extension as a "smoking gun" for dark subhalo detection with *Fermi*-LAT and implications for WIMP constraints 191**
5.1 Introduction . . . 191
5.2 Gamma-ray signal from Milky Way subhalos . . . 194
5.2.1 Building of the subhalo DM density profile . . . 194
5.2.2 Gamma-ray flux from subhalos . . . 197
5.3 LAT sensitivity to extended dark matter subhalos . . . 199
5.3.1 Threshold flux for extended subhalo detection . . . 200
5.3.2 Recovery of spatial information from dark subhalos . . . 204
5.4 Implications for WIMP dark matter constraints . . . 207
5.5 Discussion and conclusions . . . 210
5.6 Precision of recovered signal . . . 212
5.6.1 DM spectrum . . . 212

5.6.2 Evolution of the signal with the normalization . . . 213

**6 Hints of dark subhalo detection with the *Fermi*-LAT 223**
6.1 Introduction . . . 223
6.2 Sample selection . . . 224
6.3 Dark subhalo candidates analysis . . . 225
6.4 Discussion and conclusions . . . 227

**7 Constraints to dark matter annihilation from high-latitude HAWC unidentified sources 233**
7.1 Introduction . . . 233
7.2 HAWC unidentified sources . . . 234
7.2.1 HAWC and the TeV sky . . . 235
7.2.2 Target selection . . . 236
7.2.3 2HWC J1040+308 as a DM subhalo candidate . . . 237
7.3 DM constraints . . . 238
7.3.1 Minimum detection flux . . . 239
7.3.2 J-factor . . . 240
7.3.3 Results . . . 242
7.4 Summary and conclusions . . . 245

**8 Sensitivity of the Cherenkov Telescope Array to dark subhalos 253**
8.1 Introduction . . . 253
8.2 Dark subhalo search scenarios . . . 255
8.2.1 EGAL . . . 256
8.2.2 DEEP . . . 257
8.2.3 EXPO . . . 257
8.3 Dark subhalo detectability . . . 258
8.3.1 CTA sensitivity to DM spectra . . . 258
8.3.2 Subhalo annihilation flux . . . 263
8.4 Results . . . 264
8.4.1 Expected number of dark subhalos . . . 264
8.4.2 Exclusion curve for the no-detection case . . . 266
8.5 Discussion . . . 268
8.6 Summary and conclusions . . . 270
8.7 Appendix . . . 272
8.7.1 Normal vs. divergent pointing . . . 272
8.7.2 Building up the CTA EXPO scenario from MAGIC observation records . . . 273
8.7.3 Impact of the subhalo mass cut in the dark matter constraints . 274

**9 X-ray and gamma-ray limits on the primordial black hole abundance from Hawking radiation 285**
9.1 Introduction . . . 285
9.2 Hawking radiation from PBHs . . . 286
9.3 The X-ray and gamma-ray AGN background . . . 287
9.4 Constraints and prospects on $f$ . . . 289
9.5 Discussion and Conclusions . . . 292

**10 Conclusions and future work 299**

**A List of Publications 305**

**List of Figures** **307**

**List of Tables** **321**

**List of Abbreviations** **323**

# Chapter 1

# Introduction: The Dark Matter problem in fundamental physics

Dark matter (DM) is nowadays one of the most pressing challenges in Cosmology. The fact that most of the matter in the Universe is invisible, and does not interact with the known matter but gravitationally took decades to become widely recognized by the scientific community, after overwhelming evidence at different scales. Indeed, the observed Universe is not possible without this mysterious component, yet its ultimate nature is still unknown. Through this Chapter, we non-exhaustively review the key measurements which supported the existence of DM. Then, we introduce selected DM historical cosmological breakthroughs, both theoretical and observational, and study its possible production mechanisms. Later on, we detail its distribution in the Universe as well as possible candidates in and beyond the Standard Model. Finally, we review the different search strategies for DM, as well as the current constraints on its micro-physics properties.

## 1.1 Observational evidence for dark matter

Through the last century, mounting evidence at different scales has been found for the existence of non-luminous matter. This unknown component of the Universe is known as "dark matter" (DM). Different experimental approaches have failed to detect DM in a laboratory, despite observing its gravitational effects on scales ranging from a few kpc (i.e., inside our own galaxy) to Mpc and Gpc (i.e., cosmological scales). Indeed, the first evidence for DM came from astrophysical probes as a violation of the expected behaviour from Newton's gravitation. This mismatch at different scales suggested the existence of a non-baryonic form of matter which neither emits nor reflects light, i.e., dark. Although it does not interact via electromagnetism (EM), it does with gravitational forces, affecting the dynamics of surrounding bodies. Traditional, well-established gravity fails to reproduce the observed celestial dynamics in objects such as galaxies or galaxy clusters.

Although the first robust evidence of DM comes from the dynamics of these systems, nowadays there are precise measurements by different probes, such as the cosmic microwave background (CMB), strong and weak gravitational lensing, light element abundances, Lyman-$\alpha$ forest and the large scale structure (LSS) of the Universe. Despite these strong observational indications of DM, its ultimate nature, i.e.,

what is the DM made of, is still unknown. In this Section we will briefly review different observational evidence for DM at all scales. This list is far from being an exhaustive collection of all possible evidence of DM; we defer the interested reader to, e.g., Bertone et al. (2005).

### 1.1.1 First signs of dark matter

A population of "dark objects" in the Milky Way (MW) was already proposed by Lord Kelvin in 1904 Thomson (2010), who suggested there might exist a large number of dark stars, which affected the kinematics of the system via the velocity dispersion. Some years later, in 1922, Jeans determined the local (near the Sun) matter density by measuring vertical kinematics of stars and gas around the Galactic plane Einasto (2010). The observed motion was quite different from the expected according to gravitation laws, and Jeans proposed a non-visible population of stars ("dark stars"), which exceeded by a factor 2 the number of visible stars. This way, the potential generated by the total mass could account for the measured dynamics. Jeans estimations were refined years later (see e.g. Bahcall (1984)), but they were roughly correct, and supposed the first theory of DM.

Although historically is regarded as the original "father" of DM, Zwicky actually proposed it 11 years later. Indeed, in 1933 he measured the redshift of individual galaxies in the Coma cluster Zwicky (1933), and found that the velocity dispersion of the galaxies was much larger than expected from Newton's dynamics. As Jeans, the way Zwicky tackled this problem was by assuming there was a much larger gravitational potential, generated by a dark component of matter. His calculations yielded a mass-to-light ratio of about $M/L \sim 400$, which translates into $\sim$10 times more DM than visible matter. Current estimates are consistent with this value Kubo et al. (2007), ranging from 200–300 for galaxy clusters Bahcall and Fan (1998); Kashlinsky (1998); Carlberg et al. (2001). Similarly to Jeans, Zwicky's proposal did not receive attention until decades later.

### 1.1.2 Dark matter evidence on galactic scales

In this Section we will review the main DM evidence on galactic scales, i.e., $z \simeq 0$[1], which are galaxy rotation curves and dwarf galaxies.

- **Galaxy rotation curves:** One of the most convincing evidence of DM was the measurement of the anomalous galactic rotation curves – the circular velocities of stars and gas vs. the distance to the center of the galaxy. In the decade of 1970, different groups, most notably Rubin & Ford Rubin and Ford (1970); Rubin et al. (1980) and Freeman Freeman (1970) measured the rotation curves of spiral galaxies by combining 21cm line[2] spectroscopy with optical surface photometry. By Newton's second law, one can compute the expected galactic rotation curve assuming circular orbits,

$$F = ma \Rightarrow \frac{GM(r)m}{r^2} = m\frac{v^2}{r} \Rightarrow v = \sqrt{\frac{GM(r)}{r}} \tag{1.1}$$

[1] $z$ refers to the redshift, which is a usual distance measurement in Cosmology, as explained in Section 1.2.1.

[2] This is produced by the hyperfine structure transition of H in its $S_2$ ground state due to the electron flipping its spin orientation.

This is, the expected behaviour of the galactic rotation curve is a decreasing velocity as we go further away from the galactic center. Surprisingly, Rubin and Ford found that all measured rotation curves were flat towards the outskirts of the galaxies. At this point, and attending Eq. 1.1, three different scenarios are possible:

- There is an unknown perturber which makes the orbits not to be circular.
- There is a component of invisible matter, which outnumbers the visible matter and increases towards large radii.
- Newtonian gravity, which is formally obtained under some conditions from General Relativity (GR, see Section 1.2.1) fails to explain the dynamics of these bodies, and a revision is necessary.

We refer the reader to Faber and Gallagher (1979) and references therein for a review of different alternatives as proposed in the same decade as the measurements. While the first scenario is not very appealing, as the same perturber would have to be present in every galaxy of the sample (which, in a way, would lead to the second scenario), the modification of Newtonian laws is nowadays an still explored scenario, under the family of MOND (Modification Of Newton Dynamics) theories Milgrom (2020) or, more recently, the relativistic version of MOND, TeVeS (TEnsor, VEctor, Scalar) Mavromatos et al. (2009). Although these were first proposed to explain precisely the dynamics of spiral galaxies Milgrom and Sanders (2005, 2007), they fail to give a satisfactory explanation to every DM evidence, and, in the end, some of them even require a small amount of DM Sanders (2003).

The principal limitation of galactic rotation curves is that they the measurements can only me done up to distances of $\mathcal{O}(10)$ kpc, as they are based on the distribution of light or neutral hydrogen (21 cm line), while DM is expected to be dominant precisely where baryonic matter is not. Therefore, we can just obtain information about the innermost parts of these galaxies. This makes the total amount of DM and its radial distribution profile difficult to quantify (see Section 1.3).

Further evidence can be obtained in our own galaxy, by performing an analysis of the MW rotation curve, combining the actual star velocities with proxies for baryonic matter, such as microlensing optical depth or local surface density. These studies prove that, regardless of the actual DM distribution (see Section 1.3), baryonic matter cannot solely account for the observed MW dynamics Iocco et al. (2015).

- **Dwarf galaxies:** Our galaxy, the MW, possess a population of satellite galaxies. The two most notable members, which can be spotted with the naked eye on the Southern hemisphere, are the Large and Small Magellanic Clouds (LMC and SMC), which are known since the X$^{\text{th}}$ century Bertone et al. (2005). Many centuries later, well inside the XX$^{\text{th}}$ century, Shapley discovered another satellite galaxy, named Sculptor after the constellation which coordinates was in Shapley (1938). As the astronomy instrumentation advanced, a handful of new satellites were discovered. The breakthrough came with the birth of the new century and the Sloan Digital Sky Survey (SDSS) SDSS Collaboration (2000), a survey which lowered the luminosity threshold of detected sources, identifying groups of stars which were grouped as faint satellite galaxies. More

recently, the Dark Energy Survey (DES) DES Collaboration (2015a,b), which began operations in 2013, increased even more the satellite population with ultra-faint galaxies. Currently, more than 50 satellites are known within 300kpc of the MW Simon (2019); Nadler et al. (2019).

These satellites are pressure-supported dwarf spheroidals galaxies (dSphs) with low or null star formation and low metallicities Mateo (1998). They share some similarities to globular clusters, e.g., their total luminosity and velocity dispersion Arca-Sedda and Capuzzo-Dolcetta (2016). Yet, the measured dispersion in globular clusters prove no DM is required to virialize the system, while dSphs are highly DM-dominated objects, with mass-to-light ratios $M/L \gtrsim 100$ Simon and Geha (2007). In fact, there are significant differences which make them a distinct class of objects. Globular clusters have a half-light radius –the radius at which 50% of the total luminosity is reached– $\mathcal{O}(10)$ pc, while dSphs may extend up to 1 kpc Burkert (2015); globular clusters also present higher metallicities, with $[Fe/H] \sim -2$ Pritzl et al. (2005), as opposed to the metal-poor dSphs Hughes and Wallerstein (2011).

As mentioned, dSphs are pressure-supported objects, i.e., by the velocity dispersion of the star members. Measuring this dispersion allows to determine the mass profile of the dSphs; unfortunately, the kinematics of these stars come with big uncertainties, as the typical number of stars can be as low as $20 - 30$ Kalirai et al. (2010); Walker (2013); Chiappo et al. (2016); Brownsberger and Randall (2020). Nevertheless, the state-of-the-art *Gaia* telescope, launched in 2013, has improved the situation, by obtaining 3D velocities of over a million individual stars Prusti et al. (2016); Brown et al. (2018).

- **Gaps in stellar streams:** When the potential of the MW disrupts a dSph or globular cluster, its star content may be drawn in a 1-D distribution around the MW Malhan and Ibata (2019); Malhan et al. (2019). These linear aggrupations of stars are known as stellar streams. *Gaia* has allowed the discovery of several of these structures Malhan and Ibata (2018).

  Nevertheless, as these structures orbit the MW, they may encounter light DM subhalos (see Section 1.3) in their trajectory. These will affect its dynamics, creating underdensities of stars through the stream, which are known as "stellar gaps" Carlberg (2012a,b). This phenomenon can be used to infer the population of DM subhalos, which is a strong evidence of the existence of DM. This has been recently claimed by Banik et al. (2021), although other groups disregard these possible subhalos as observational inhomogeneities Thomas et al. (2016); Ibata et al. (2020).

### 1.1.3 Dark matter evidence on intermediate scales

On scales larger than galactic distances, in the typical galaxy cluster scale ($z \sim 0.1 - 1$), we can find evidence for DM coming from weak and strong gravitational lensing effect and from galaxy clusters themselves, as pointed out in Section 1.1.1.

- **Gravitational lensing:** One of the consequences of Einstein's GR (see Section 1.2.1) is the deflection of light in the presence of strong gravitational fields. This will make the observed radiation to be bent, magnified, and/or distorted with respect to the original, emitted light. This phenomenon is known as gravitational lensing, and, being DM precisely a huge amount of invisible mass, it will act as a lens when background light travels through it. Indeed, from the

distortion of observed light it is possible to infer the DM mass and its distribution (see, e.g., Bartelmann and Maturi (2016); Nadler et al. (2021) and references therein). According to the magnitude of the distortion, we distinguish between strong and weak lensing:

- Strong lensing is produced by the most massive objects in the Universe: galaxy clusters. When light emitted by farther galaxies in the background travels through the clusters' huge DM content is heavily deflected, resulting in multiple images of the galaxies. A rich casuistic is found depending on parameters such as the lens spatial distribution of light and the position of the lensed object(s) with respect to the lens and the observer. We can differentiate between closed rings (so-called "Einstein rings") or elongated arcs. A detailed analysis of the lensed image can be used to reconstruct the DM distribution in the cluster. For a comprehensive review of strong lensing see, e.g., Barnacka (2018); Cunha and Herdeiro (2018) and references therein.
- Weak lensing, on the other hand, is referred to the distortion produced by mild gravitational fields, either due to not very massive objects or to the deflection happening far from them. It is the most frequent form of lensing, yet the DM mass distribution is more difficult to determine than in the strong case, as only statistical analysis of background galaxies can be performed via the cosmic shear, i.e., the average number of elongated galaxies on a portion of the sky compared to a random field. See, e.g., Mandelbaum (2018); Umetsu (2020) and references therein for a full review of weak lensing.

There is another lensing phenomenon which has received great attention from the DM community recently: microlensing. This refers to gravitational lensing produced by small and compact objects Gaudi (2021), such as exoplanets Tsapras (2018) and primordial black holes (PBHs) Fleury and García-Bellido (2020), which is still a viable DM candidate (see Section 1.4.2 for more details).

- **Galaxy clusters:** As already mentioned, Zwicky found evidence than the kinematics (velocity dispersion) of individual galaxies within the Coma cluster pointed to a gravitational potential generated by a mass much larger than inferred from observations Zwicky (1933). Nowadays, the same trend has been observed in different clusters, by more precise measurements using weak lensing (see, e.g., Schindler (1996); Mantz and Allen (2011); Foëx et al. (2012); Fong et al. (2018)).

  Nevertheless, one of the most famous DM evidence is the source 1E 0657–558, commonly known as the "Bullet cluster"Hayashi and White (2006); Clowe et al. (2006). Despite its name, it is actually a pair of two galaxy clusters in collision. According to Figure 1.1, there is an offset between the observations of X-ray emission by hot material in each of the clusters and the DM distribution as inferred from weak lensing. Indeed, as visible matter interacts via EM forces in the collision, it is slowed down, while the DM component seems to freely travel, effectively decoupling visible and invisible matter. This supposes an overwhelming proof of the existence of dark matter Clowe et al. (2006). Furthermore, no MOND theory (see Section 1.1.2) can successfully explain the dynamics of the Bullet cluster. Indeed, in a MOND scenario the gravitational lensing would be stronger in the vicinity of the X-ray emission, tracing the

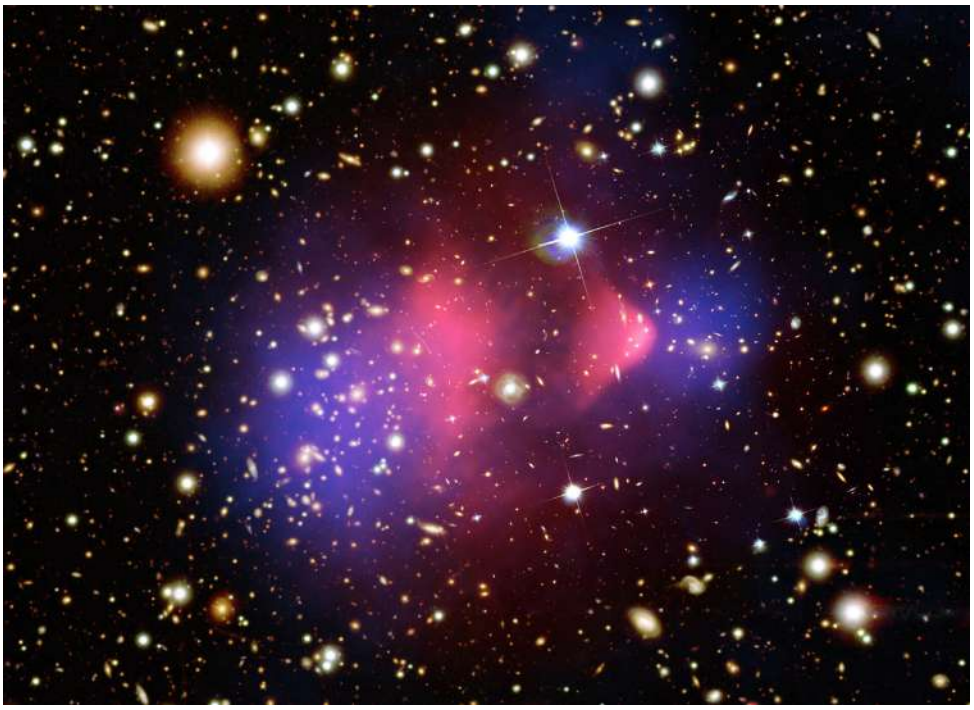

FIGURE 1.1: Composite image of the merging cluster 1E 0657–558, commonly known as the "Bullet cluster", with optical emission from the individual galaxies (orange), X-ray emission from the hot gas (pink/red) and DM halos inferred from gravitational lensing (blue) European Space Agency (2007).

hot material, yet measurements place the strongest lensing well outside this region. More recently, simulations of the Bullet cluster further confirmed the DM hypothesis naturally explaining the observed dynamics without any special parameter tuning Lage and Farrar (2014).

### 1.1.4 Dark matter evidence on cosmological scales

At scales much larger than the galaxy clusters ($z \gg 1$), we can find DM evidence coming from the CMB anisotropies, the baryonic acoustic oscillations (BAO), the Sunyaez-Zel'dovich (SZ) effect, and the Lyman-$\alpha$ forest.

- **Cosmic Microwave Background anisotropies:** The main cosmological evidence for DM, and one of the strongest, is the temperature anisotropy of the CMB. Given its paramount relevance in the current cosmological model, we will review it with detail in Section 1.2.1. As a summary, the small anisotropies in the almost homogeneous background of infra-red (IR) radiation that permeates the Universe nowadays can be used to infer the total amount of DM in the Universe, among other cosmological parameters.

- **Sunyaev-Zel'dovich effect:** Further evidence for DM can be obtained form the CMB, but this time by using the spectral distortion of CMB radiation when travelling cosmological distances, due to inverse Compton (IC) scattering with hot electrons in galaxy clusters ($\gamma + e^- \rightarrow \gamma + e^-$), known as the Sunyaev–Zel'dovich effect Sunyaev and Zeldovich (1972); Desert (2000). The number of CMB photons is conserved in this process, but they have a net energy gain, effectively producing a distortion of the measured spectrum. As the distortion

is more prominent when going through more massive clusters, it can be used as an estimate of the cosmological abundance of DM Kitayama (2014).

- **Baryonic Acoustic Oscillations:** BAOs, and the so-called BAO scale are a direct consequence of the CMB anisotropies so, again, we will defer the detailed discussion to Section 1.2.1. For the time being, the BAO scale is an evidence of DM due to the existence of a privileged scale in the Universe, given by the relation between the baryonic and radiation relative densities in the early Universe, where both of them were coupled in the hot plasma. This scale is the distance at which it is most probable to find two galaxies. By determining the BAO scale we can infer the DM cosmological abundance, which is far from being null according to current measurements.

- **Lyman-$\alpha$ forest:** Another DM evidence can be obtained from the Lyman-$\alpha$ forest, which was discovered in 1970 by Lynds when observing the quasar 4C 05.34 Lynds (1971). It refers to a series of absorption lines in the ultraviolet (UV) produced by the Lyman-$\alpha$ transitions of neutral hydrogen ($n = 2 \rightarrow 1$) in spectra of high-redshift galaxies. The flux power spectrum of this "line forest" can be used to constrain cosmological parameters, such as the DM abundance, which again yields a non-zero contribution. For technical details, see e.g. Hernquist et al. (1996); Croft et al. (2002); Viel et al. (2009); Garzilli et al. (2019) and references therein.

## 1.2 The ΛCDM cosmological model

At this writing, the common understanding of our Universe is within the framework of a cosmological model, ΛCDM (Λ standing for a vacuum negative pressure and CDM for "Cold Dark Matter"). This model is the result of almost a century of scientific breakthroughs. In this Section, we will describe the current theoretical understanding and observational data in support of ΛCDM through a non-exhaustive review of some historical landmarks, and explain the possible DM production mechanisms in the early Universe.

### 1.2.1 Historical notes and mathematical formulation

The birth of modern Cosmology can be marked in 1915, with the final formulation of GR by Einstein, ten years after the publication of Special Relativity. The resulting Einstein equations can be written in modern notation as[3],

$$R_{\mu\nu} - \frac{1}{2} R g_{\mu\nu} = 8\pi G T_{\mu\nu} \tag{1.2}$$

where $R$ is the Ricci scalar, obtained by contraction from the Ricci tensor $R_{\mu\nu}$ with the space-time metric $g_{\mu\nu}$. The Ricci tensor is derived by contracting the Riemann curvature tensor. On the right-hand side of the equation, $G$ is the Newton's gravitational constant and $T_{\mu\nu}$ is the energy-momentum tensor generated by matter. John Wheeler beautifully summarized these equations by reading them left to right or viceversa: "Matter tells space how to curve. Space tells matter how to move" Misner et al. (1973).

An unavoidable consequence of GR when applied to the whole Universe is that this must either expand or contract with time. At the time, it was believed the

[3]Through this Thesis we will assume $h = c = 1$, except where explicitly noted.

Universe was immutable. Einstein manually introduced a "cosmological constant", named $\Lambda$, which would counteract the expansion phenomenon,

$$R_{\mu\nu} - \frac{1}{2}Rg_{\mu\nu} = 8\pi G T_{\mu\nu} + \Lambda g_{\mu\nu} \tag{1.3}$$

$\Lambda$ is usually written on the right-hand side of the Einstein equations, but it is not describing matter. Likewise, it is not a feature of the Universe space-time as the left-hand side of the equation. It can be interpreted as a "vacuum energy" of space-time itself.

By solving the Einstein equations, one can find the dynamics of the Universe as a whole. In general, these equations do not have analytical solution, but they do by assuming two symmetry arguments – that the Universe is i) homogeneous[4] and ii) isotropic[5]. With these assumptions, the line element $ds^2$ can be expressed as the Friedmann–Lemaître–Robertson–Walker (FLRW) metric,

$$ds^2 = g_{\mu\nu}dx^\mu dx^\nu = dt^2 - a(t)^2\left[\frac{dr^2}{1-kr^2} + r^2(d\theta^2 + sin^2\theta\, d\theta\, d\phi)\right] \tag{1.4}$$

where $a(t)$ is a scale factor and $k$ the spatial geometry of the Universe. We can distinguish between open $(k=-1)$, flat $(k=0)$ or closed $(k=1)$ geometries. Some works on this expansion hypothesis were published by de Sitter in 1917 and by Friedmann in 1922 and 1924, but with little repercussion. It was in 1927 when Lemaître published a paper proposing that the Universe was indeed expanding Lemaître (2013). Einstein communicated with Lemaître, and wrote him "Your calculations are correct, but your physics is atrocious" Davis (1985).

Ultimately, Einstein had to admit his error introducing $\Lambda$ in 1929, when Hubble[6] proved with observations the expansion of the Universe by measuring the shift of spectral lines of "nebulæ" (which nowadays we know as galaxies) Hubble (1929). This shift towards lower frequencies (and named accordingly "redshift") was due to the recession velocity, $\mathcal{O}(30)$ times larger than in stars, therefore suggesting there were extragalactic objects.

The Hubble-Lemaître law of the expansion of the Universe can be expressed as,

$$v = H \cdot d \tag{1.5}$$

where $v$ is the recession velocity, $H$ is the Hubble constant and $d$ is the proper distance. This linear relation is valid only for relatively near objects, $d \lesssim 50$ Mpc LIGO Collaboration (2017a). Moreover, the Hubble constant is not constant with time, but only spatially. Therefore, is custom to refer to the Hubble constant as $H_0$, which is its value at present time. By solving the Einstein equations with the FLRW metric, we obtain the Friedmann equations,

$$H^2 \equiv \left(\frac{\dot{a}}{a}\right)^2 + \frac{k}{a^2} = \frac{8\pi G}{3}\rho_{tot} + \frac{\Lambda}{3} \tag{1.6}$$

[4]Supported by galaxy surveys, for distances larger than ∼1 Gpc Mukhanov (2005); SDSS Collaboration (2017).

[5]Supported by CMB observations Planck Collaboration (2020b).

[6]Although Hubble is widely regarded as both the discovered of the expansion of the Universe, the redshift of these galaxies was already measured by Slipher in 1914, and the theory of an expanding Universe was formulated by Lemaître.

where $\rho_{tot}$ is the total average energy density of the Universe and $H$ the Hubble parameter[7]. To make our Universe flat ($k = 0$)[8], the previous equation gives the necessary matter density, the so-called "critical density",

$$\rho_c = \frac{3H^2}{8\pi G} \tag{1.7}$$

This is a very useful unit to express each of the components of the Universe. To do so, we can define $\Omega = \rho_i/\rho_c$ for the $i$ component. We can distinguish four components: matter, radiation, curvature and cosmological constant, which can be expressed as,

$$\begin{aligned} \Omega_m &\equiv \frac{8\pi G\rho_m}{3H_0^2} & \Omega_c &\equiv \frac{-k}{a_0^2 H_0^2} \\ \Omega_r &\equiv \frac{8\pi G\rho_r}{3H_0^2} & \Omega_\Lambda &\equiv \frac{\Lambda}{3H_0^2} \end{aligned} \tag{1.8}$$

$\Omega_\Lambda$ is known as the dark energy, a negative pressure which accelerates the expansion of the Universe. Later on this Section, we will enter into more detail. There is also a "cosmological sum rule", by defining,

$$\Omega \equiv \sum_i \Omega_i = \frac{\rho_{tot}}{\rho_c} \tag{1.9}$$

And therefore, assuming a flat Universe, the Friedmann equations 1.6 can be simply written as,

$$\Omega_m + \Omega_r + \Omega_\Lambda = 1 \tag{1.10}$$

To a very good approximation, we can put $\Omega_r = 0$, as its current value is $\Omega_r \sim 10^{-5}$ Planck Collaboration (2020a). The Friedmann equations describe the expansion of the Universe, implying that the scale factor increases with time. Therefore, light emitted by far objects will suffer a redshift effect on their wavelength. The redshift, expressed as a function of the emitted wavelength $\lambda_{em}$ and the observed wavelength $\lambda_{obs}$ is,

$$1 + z = \frac{\lambda_{obs}}{\lambda_{em}} = \frac{a_0}{a(t_{em})} \tag{1.11}$$

where $a_0$ is the current scale factor, usually set to 1. This equation establishes a one-to-one correspondence between the time at which emission was originated ($t_{em}$) and redshift $z$; therefore, the redshift is a measure of time. The evolution of each Universe component with the redshift is different Dodelson (2003). We can introduce this dependence in the Friedmann equations (Eq. 1.6),

$$H^2(z) = H_0^2 \left[\Omega_m(1+z)^3 + \Omega_r(1+z)^4 + \Omega_k(1+z)^2 + \Omega_\Lambda\right] \tag{1.12}$$

From this equation, we deduce that the relative contribution of each component evolves with time (or redshift). The next milestone in Cosmology may be the discovery in 1965 of the Cosmic Microwave Background (CMB), which was already introduced in Section 1.1.4. As the Universe is expanding, if we reverse the arrow

[7] Although we deemed $\Lambda$ –introduced *ad hoc* to prevent the Universe from expanding– unnecessary, we keep it, as ΛCDM includes a cosmological constant.

[8] Current CMB observations, combined with other probes, yield $\Omega_k = 0.0007 \pm 0.0019$ Planck Collaboration (2020a).

of time, we will necessarily find that the Universe started as an infinitely small, hot and dense material point. This theory is known as the "Big Bang" and it is a widely accepted model for the beginning of the Universe Uzan (2016). The extreme conditions of the early Universe made all different components to be coupled in a hot, ionized plasma. With particles traveling at relativistic speeds, structure formation was impossible. As the Universe expanded, temperature dropped and different species decoupled from the plasma, with their abundances suffering a "freeze-out" process, where it didn't evolve with the rest of the plasma species. This occurs when the interaction rate $\Gamma$ cannot counter the Hubble expansion $H$, i.e, $\Gamma = H$. As DM is non-interacting or very weakly-interacting (as we will see in Section 1.2.2), it decouples in the very early Universe. After all baryonic matter has been formed, the lifetime of neutral atoms was very short, due to the abundance of highly energetic photons which would ionize the atom again. This made the Universe opaque, as no radiation could escape without interacting with matter, given the extreme densities and temperatures. This also sets an absolute limit on the achievable horizon with traditional telescopes[9].

According to Eq. 1.6, we can compute the evolution of each component of the Universe knowing their current values. The matter-radiation equality (when $\Omega_m = \Omega_r$) is produced at $z \sim 3400$. Shortly after, at $z \sim 1100$ (which approximately corresponds to 370.000 years), the temperature of the Universe had lowered to $\sim$3700 K and the recombination phase began, in which electrons and nuclei recombined intro stable, neutral atoms, allowing the radiation to freely travel. Thus, from this moment on, known as the "last scattering surface", the Universe was transparent to radiation Dodelson (2003). This leaves a background radiation in the Universe, which will cool down as its expansion continues. Today, we can still measure it and is known as the CMB.

Although the CMB was theoretically proposed in 1948 Alpher et al. (1948), it was not until 1965 when Penzias and Wilson, technicians working at Bell Laboratories, detected it. As they were installing a new microwave antenna, they found a persistent background noise regardless of the antenna pointing, which didn't seem possible to remove. The measured spectrum was an extraordinarily perfect black body, with temperature $T = 2.726$ K Penzias and Wilson (1965). This itself was a great discovery, as confirmed the Big Bang theory, but physicists expected even more: if the CMB was originated at the last scattering surface, the over- and underdensities of matter should produce tiny anisotropies on the temperature[10]. If, when decoupling, a photon was in a denser patch of space than the average density, some of its energy had to be used to overcome the gravitational pull of the region to escape, thus suffering a redshift (or becoming colder than the average temperature of photons). Likewise, photons located in an underdense patch of the space, lost less energy escaping, appearing blueshifted (i.e., hotter than average).

It was not until 1989 when the *COBE* satellite measured the anisotropies Mather et al. (1990), followed by *WMAP* (launched in 2001) Bennett et al. (2013) and *Planck* (launched in 2009) Lamarre et al. (2003); Planck Collaboration (2020a) satellites. The measured temperature fluctuations are of order $\delta T/T \sim 10^{-5} - 10^{-4}$, and encode information about different cosmological parameters and the properties of the Universe at the recombination epoch. In Figure 1.2 we show the skymap of the anisotropies

[9] Meaning photon telescopes; other probes such as neutrinos and gravitational waves (GWs) allow to access earlier times.

[10] Here we will refer to anisotropies due to the density fluctuations in the early Universe. There is notably a larger dipolar anisotropy, produced by our relative movement with respect to the CMB Kogut et al. (1993).

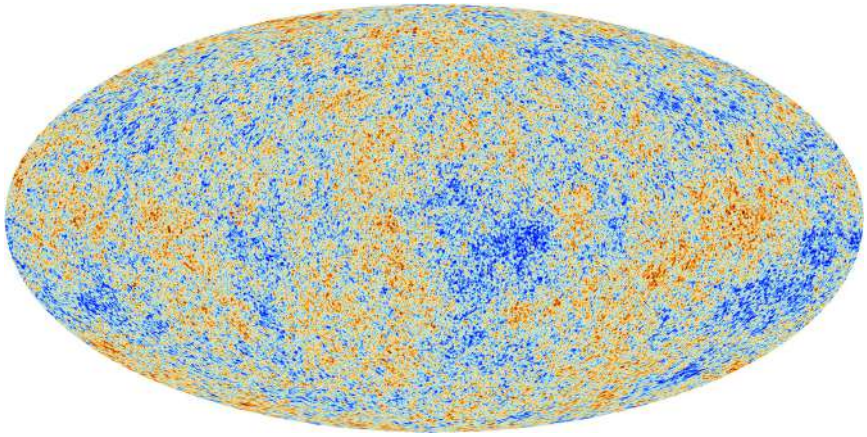

FIGURE 1.2: Skymap of the temperature anisotropies of the CMB as measured by the *Planck* satellite in its third and final data release in 2018. The color scale ranges from $-300\mu$K (blue) to $+300\mu$K (red) temperature variation from the average value. Figure taken from Planck Collaboration (2020b).

as obtained by *Planck*. To extract these properties, the CMB temperature can be decomposed into spherical harmonics $Y_{lm}(\theta, \phi)$ as,

$$\frac{\delta T}{T}(\theta, \phi) = \sum_{l=2}^{\infty} \sum_{m=-1}^{\infty} a_{lm} Y_{lm}(\theta, \phi) \tag{1.13}$$

And the results are usually presented with the power spectrum of the anisotropies (given by $l(l+1)C_l/2\pi$) as a function of the multiple moment $l$,

$$C_l \equiv \langle |a_{lm}|^2 \rangle = \frac{1}{2l+1} \sum_{m=-1}^{l} |a_{lm}|^2 \tag{1.14}$$

According to this formulation and the spherical harmonics, the largest contributions come from fluctuations at scales $\theta \sim 180^\circ/l$. We show this power spectrum as measured by Planck Planck Collaboration (2020a) in Figure 1.3. Indeed, the spectrum presents many features, as multiple peaks with decreasing amplitudes. The position of the first peak, for instance, can be used as proxy of the curvature of the Universe, while the relation between the first and second peak is a measurement of the DM cosmological abundance. Fluctuations at angular scales $\theta \gtrsim 1^\circ$ ($l \lesssim 100$) reflect the inhomogeneous matter distribution on very large scales in the early Universe. At angular scales $\theta \sim 0.1 - 1^\circ$ ($l \sim 100 - 2000$), the power spectrum shows the imprint and oscillation pattern of sound waves present in the fluid of baryonic matter and photons. The interplay between gravity and radiation, i.e., matter attraction and photon pressure, caused a series of compressions and rarefactions in the fluid. Finally, at scales $\theta \lesssim 0.1^\circ$ ($l \gtrsim 2000$), the oscillations are damped due to the photon diffusion, as the decoupling was not an instantaneous process, rather lasting some tens of thousands of years. During this process, collisions between photons and other particles were still happening, yet not as frequently as previously. The effect of these collisions was a photon scattering in different directions, which damped the fluctuations imprint at the smallest scales Dodelson (2003).

As mentioned, DM plays a major role in the CMB anisotropies; indeed, if no DM was present, any fluctuations of the matter density would be strongly suppressed by radiation. In Figure 1.3 we show how ΛCDM provides a remarkable agreement

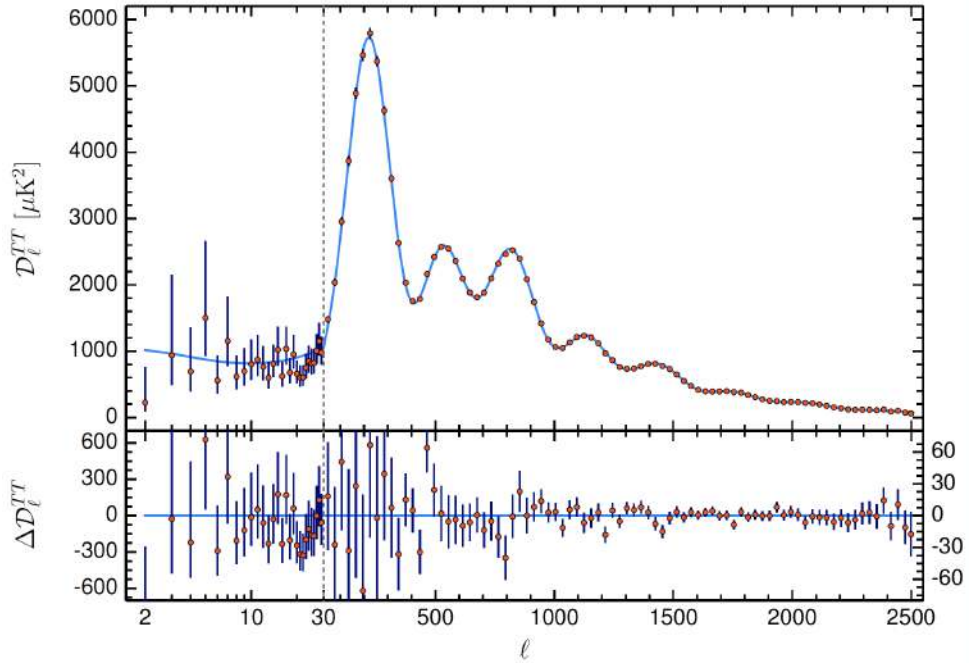


FIGURE 1.3: *Planck* satellite measurements of the CMB temperature power spectrum in its final data release in 2018. The error bars come from cosmic variance (and therefore is larger for low multipoles), approximated as Gaussian. Blue, solid line is the ΛCDM best-fit. Vertical axis is the multipolar moment as defined in Eq. 1.14, and is expressed in units of $\mu K^2$. Figure taken from Planck Collaboration (2020a).

to the data by fitting six parameters: $\Omega_b h^2$ (baryonic matter abundance, where $h$ is the reduced Hubble constant, $h = H_0/100$), $\Omega_c h^2$ (DM abundance), $\tau$ (reonization optical depth), $n_s$ (scalar spectral index), $A_S$ (amplitude parameter), and $\theta_{MC}$ (scale of the sound horizon at decoupling). From them, other parameters such as the Hubble constant $H_0$ or $\Omega_\Lambda$ can be derived. In the final data release, *Planck* reported $\Omega_b h^2 = 0.02233 \pm 0.00015$, $\Omega_c h^2 = 0.1198 \pm 0.0012$, $\Omega_\Lambda = 0.6847 \pm 0.0073$ and $H_0 = 67.37 \pm 0.54$ km $\cdot$ s$^{-1}$ $\cdot$ Mpc$^{-1}$. These values[11], as already pointed out in Section 1.1.4, strongly support DM existence even in the early Universe, accounting up to the $\sim 25\%$ of its total energy content.

The DM overdensities in the matter-radiation decoupling effects do not limit to the temperature power spectrum of the CMB features, but also impacts the baryonic matter distribution in the Universe. As we noted, in radiation-matter coupling in the early Universe, DM overdensities attracted the hot baryon-photon plasma, with an interplay between gravitational pull and photon pressure due to infalling matter. At some point, the pressure drove the baryon-photon plasma away from the initial DM overdensity, producing a spherical acoustic wavefront. This shell then propagated at the speed of sound, $c_s$, of the primordial plasma, given by Eisenstein and Hu (1998); Bassett and Hlozek (2010); Suyu et al. (2018),

$$c_s(z) = \frac{c}{\sqrt{3\left[1 + \frac{3\Omega_b}{4\Omega_r(1+z)}\right]}} \tag{1.15}$$

[11] The reported parameters correspond to those obtained with TT, TE, EE+lowE+lensing modes and a combination of `Plik` and `CAMSpec` likelihoods. See Planck Collaboration (2020a) for technical details.

The propagation of the baryonic wavefront extinguished at the recombination, while radiation kept streaming. This produces both a baryonic overdensity in the center and an underdensity at the sound horizon, i.e., the maximum distance travelled by the sound wave from its creation to the time where radiation pressure stops dragging the baryonic matter. This moment corresponds to a drag redshift $z_{drag} \sim 1060$, briefly after the recombination epoch, equivalent to a comoving radius of the baryonic dragging shell of $r_{drag} \sim 147$ Mpc Planck Collaboration (2020a). At the era where LSS begins to form, an interplay between DM and baryons happen: DM overdensities attract baryonic matter, while DM is attracted by the baryonic shell. As there is not a single, but rather countless of these overdensities through the Universe, there is an overlapping phenomenon between these shells, leading to an interference pattern. This makes galaxies in the center of DM halos prone to have other galaxies at a distance $r_{drag}$. Mathematically, we can express this as the 2-point correlation function of the galaxy field Peebles (1980),

$$\xi_2(|\vec{x_1} - \vec{x_2}|) = \langle \delta(\vec{x_1})\delta(\vec{x_2}) \rangle \tag{1.16}$$

where $\delta(\vec{x}) = (\rho(\vec{x}) - \bar{\rho})/\bar{\rho}$. Given a random galaxy with a certain location, the 2-point correlation function yields the probability that another galaxy will be found within a given distance. This function will therefore peak at $r_{drag}$ Eisenstein et al. (2005). We can also transform this into a galaxy power spectrum $P(k)$ by means of a spherical harmonics (analogous to the CMB temperature power spectrum),

$$\xi(r) = \frac{1}{2\pi^2} \int dk\, k^2 P(k) \frac{sin(kr)}{kr} \tag{1.17}$$

$P(k)$ is a proxy for the matter power spectrum of the Universe. When going to spherical harmonics (which is a Fourier space transformation), the peak of the 2-point correlation function is transformed into a series of acoustic oscillations of the power spectrum, known as *baryonic acoustic oscillations* (BAO). By studying the 2-point correlation function in galaxy surveys, one can search for the position of the BAO peak in the power spectrum Sánchez et al. (2013). This has been found in different galaxy surveys, such as SDSS/BOSS SDSS Collaboration (2019, 2020), 2dFGRS Cole et al. (2005), and, more recently, DES DES Collaboration (2018). In Figure 1.4 we show the distinct peak of the BAO in the case of the WiggleZ DES survey.

As mentioned in Section 1.1.4, BAO is also a strong evidence for DM. Indeed, it proves DM decoupled from the primordial plasma in the very early Universe, seeding the matter density perturbations which create the acoustic waves. As in the case of CMB, if no DM was assumed, the radiation pressure would damp the baryonic overdensities, leving no imprint in the matter power spectrum.

Another breakthrough in ΛCDM came as a a major surprise in 1998, with the discovery of already mentioned dark energy. We recall Einstein introduced Λ *ad hoc* to prevent the Universe from expanding. Riess et al. (1998) computed the distance modulus $\mu$ DES Collaboration (2019a) of Type Ia Supernovæ (SN, occurring as the merging of a binary system in which one star is a white dwarf, as opposed to Type II, core-collapse Supernovæ), which is defined as,

$$\mu = m_B + \alpha x_1 - \beta C + M_0 + \gamma G_{host} + \Delta\mu_{bias} \tag{1.18}$$

where $\alpha x_1$ measures the SNe Ia correlation between the luminosity and width of the light curve, $\beta C$ is the color, $\gamma G_{host}$ is the host-galaxy stellar mass, $M_0$ accounts for both the absolute magnitude of SNe Ia and the Hubble constant, and $\Delta\mu_{bias}$ is a

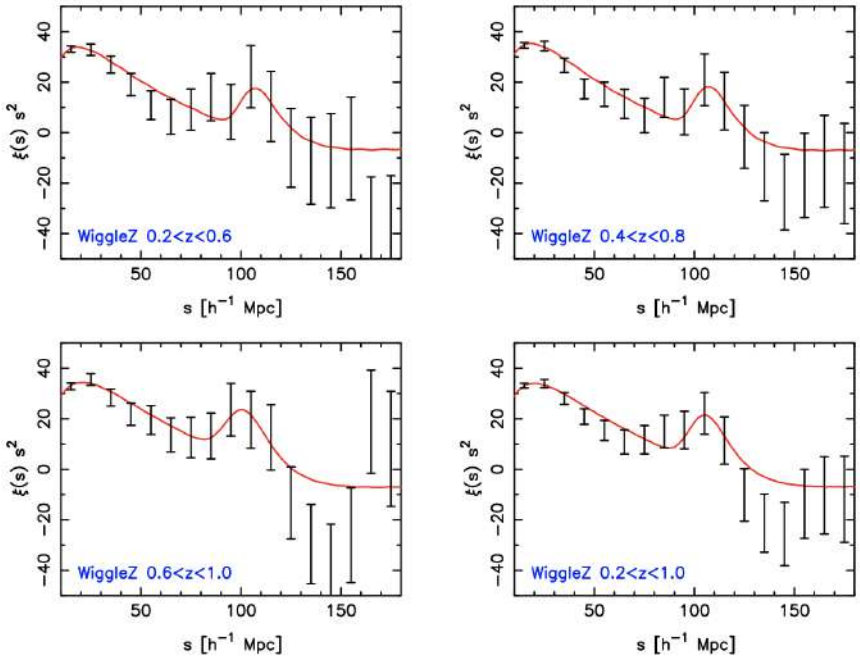


FIGURE 1.4: DES-WiggleZ survey measurements of the 2-point galaxy correlation function $\xi(s)$ times $s^2$, where $s$ is the comoving redshift-space separation. Different panels show different redshift samples. A clear peak is seen at $s \sim 100h^{-1} = 150$ Mpc, assuming *Planck* value $h = 0.67$. Figure taken from Blake et al. (2011).

correction for selection biases, determined by simulations. The luminosity distance to a SN at redshift $z_{SN}$ is given by,

$$d_L(z_{SN}) = c(1+z_{SN}) \int_0^{z_{SN}} \frac{dz}{z \cdot H(z)} \tag{1.19}$$

where $H(z)$ notably depends on $\Omega_m$ and $\Omega_\Lambda$, (which can be derived from Eq. 1.6 introducing the expressions for $\Omega_i$). SNe Ia possess a distinct light curve which allows to use them as "standard candles" for distance determination. When computing this distance modulus as a function of the redshift, a non-zero $\Omega_\Lambda$ had to be introduced to fit the data, roughly doubling the baryonic matter abundance. Moreover, the equation of state of dark energy was $p = \omega\rho$, with $\omega = -1$, indicating that it acted as Einstein's $\Lambda$, but with opposite sign. This is, instead of preventing the Universe from expanding, it drove an accelerated expansion. In Figure 1.5 we plot the recent 3-year data from DES DES Collaboration (2019a), obtaining best-fit parameters $\Omega_m = 0.321, \Omega_\Lambda = 0.679, \omega = -0.978$. These are compatible with the CMB *Planck* results we reviewed.

What came as an additional surprise is the value of $H_0$: as measurements of $H_0$ were more and more precise, CMB and SNe Ia results began to be in tension, with CMB yielding lower values. Indeed, nowadays the tension is statistically significant, around $4-5\sigma$ depending on the combination of probes (see, e.g., Bernal et al. (2016, 2021); Verde et al. (2019) for exhaustive reviews). New measurements, such as gravitational lensing in quasars Wong et al. (2019) are not capable of alleviating this tension. The definitive answer, once again, will probably come from GR's hand as GWs Dirkes (2018).

Predicted by Einstein in 1916 and disregarded as "probably real, yet completely undetectable" Einstein (1918), first indirect evidence of GWs was found in 1975 by

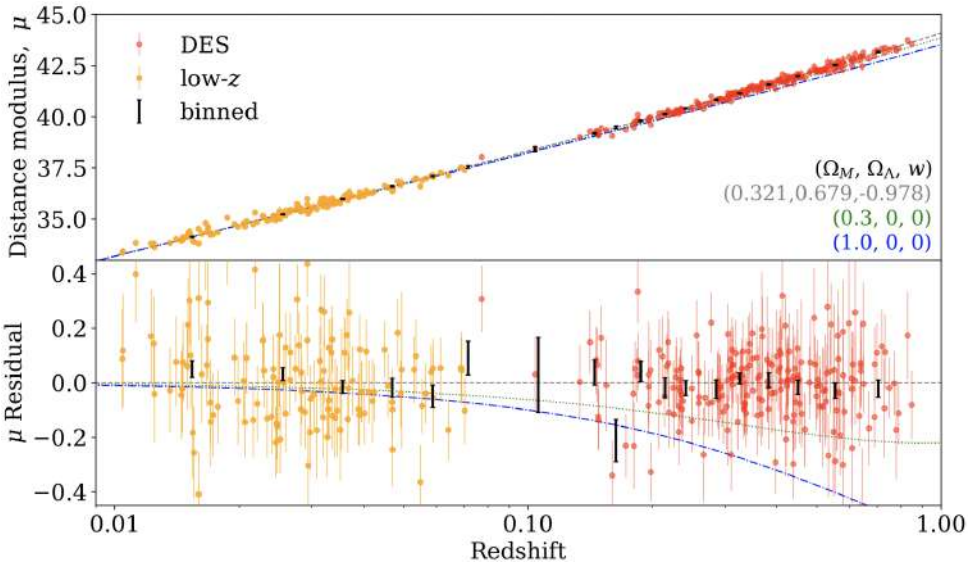


FIGURE 1.5: Hubble diagram for the DES-SN3YR sample. Top panel: distance modulus $\mu$ from Type Ia Supernovæas measured by DES (red, circles) and Harvard-Smithsonian Center for Astrophysics survey Hicken et al. (2012) (orange circles). Dashed, gray line shows the best fit model, while green and blue dotted lines show models assuming no dark energy ($\Omega_\Lambda = 0$) and matter densities $\Omega_m = \{0.3, 1\}$, respectively. Bottom panel: residuals to the best fit model. Figure taken from DES Collaboration (2019a).

Hulse and Taylor with the discovery of the first binary pulsar (PSR) Hulse and Taylor (1975). PSRs are neutron stars (NS), result of late evolution in supergiant stars between $\sim 10 - 25$ M , i.e., not massive enough to collapse into a black hole (BH, see, e.g., Miller and Miller (2015) for a review on the topic). PSRs are characterized for radio emission (synchrotron radiation produced by particle acceleration in strong magnetic fields) with a very precise and short period, due to the high spin[12]. According to GR, this binary system of extremely compact objects should be losing energy in the form of gravitational radiation Dirkes (2018), making the orbital distance to decay with time until merging. By measuring the orbital period change, which perfectly fitted the GR predictions, the existence of GWs was proved, even if not directly detected.

It was not until 2015 when the LIGO[13] instrument, with two interferometers in Handford and Livingstone LIGO Collaboration (2015), directly detected the GWs from the merging of two BHs LIGO Collaboration (2016). Some months later, a conjunction of LIGO, Virgo and different observatories made the first detection of a NS–NS merger with EM counterpart, allowing to precise measurement of the redshift and follow-up multiwavelength campaigns LIGO Collaboration (2017b). Along with a number of Cosmology tests LIGO Collaboration (2019), it permitted an alternative determination of $H_0$ by using GWs as "standard sirens" DES Collaboration (2019b); LIGO Collaboration and Virgo Collaboration (2021). Current data yield a big uncertainty, $H_0 = 67^{+16}_{-8}$ km $\cdot$ s$^{-1}$ $\cdot$ Mpc$^{-1}$, which is fully compatible with both CMB and SNe Ia measurements (which present $\mathcal{O}(1\%)$ uncertainties). Nevertheless,

[12] As the angular moment is conserved, when the star collapses into the $\mathcal{O}(10)$ km NS, it will rapidly rotate, with periods ranging from $\sim 0.001 - 10$s Perrodin and Sesana (2018); Tan et al. (2018).

[13] https://www.ligo.caltech.edu/

as more BH–BH and, especially, NS–NS merging events are detected, the more precise will the $H_0$ value be Chen et al. (2018); Chassande-Mottin et al. (2019). The determination of $H_0$ from standard sirens is, in principle, a model-independent probe which will alleviate the current tension.

### 1.2.2 Production mechanisms of dark matter

In this Section, we briefly review the different DM production mechanisms in the early Universe. There are two main categories, i) thermal relics, where DM is in thermal equilibrium with the primordial plasma, and ii) non-thermal relics, where DM is out of equilibrium due to suppressed coupling to matter and radiation. A detailed review of these mechanisms can be found in, e.g., Bertone et al. (2005); Baer et al. (2015).

#### Thermal production of dark matter

If a DM particle $\chi$ is in the early Universe as a relativistic and stable species in thermal equilibrium with the matter-radiation primordial plasma, we can compute its relic abundance. As long as the temperature of the Universe is larger than the particle mass, i.e., $T > m_\chi$, being in thermal equilibrium makes the rate of annihilation and creation processes identical, this is, the annihilation $\chi\bar{\chi} \longrightarrow p\bar{p}$[14], where $p$ represents different possible particle species, is produced at the same rate as the inverse creation process, $p\bar{p} \longrightarrow \chi\bar{\chi}$. Moreover, scattering processes, $\chi p \longrightarrow \chi p$ have an energy exchange between baryonic matter and radiation such that DM temperature is that of the medium. As commented in Section 1.2.1, $T$ decreases due to the expansion of the Universe until the interaction rate $\Gamma$ is smaller than $H$. At this point, the process which maintained equilibrium stops, and the DM cosmological relic abundance is "frozen out".

To actually compute this relic abundance, we use the Boltzmann equation Dodelson (2003),

$$\hat{L}[f] = \hat{C}[f] \tag{1.20}$$

where $\hat{L}$ is the Liouville operator, $\hat{C}$ is the collision operator, and both act on the particle phase-space distribution $f(x, p)$. This distribution is normally assumed as a Bose-Einstein or Fermi-Dirac distribution for bosons and fermions, respectively. With it, we express the number density of DM particles in equilibrium,

$$n_\chi^{eq} = \frac{g}{(2\pi)^3} \int d^3p \cdot f(x, p) \tag{1.21}$$

This number density will behave as $n_\chi^{eq} \sim T^3$ for $T \gg m_\chi$, i.e., $n_\chi \sim n_\gamma$. On the other hand, when $T \ll m_\chi$, there is a Boltzmann exponential suppression factor, and the number density will be,

$$n_\chi^{eq} \sim g \left(\frac{m_\chi T}{2\pi}\right)^{\frac{3}{2}} e^{-\frac{m_\chi}{T}} \tag{1.22}$$

where $g$ is the number of degrees of freedom of $\chi$. This equation implies that, if the DM particle remained in thermal equilibrium due to a slowly increased expansion rate of the Universe, currently there would be almost no DM due to the exponential

[14] We will assume DM to be a Majorana particle, i.e., $\chi$ is its own antiparticle.

suppression factor. Eq. 1.20 can be expressed as a differential equation on time, which allows to obtain $n_\chi(t)$ Kolb and Turner (1990),

$$\frac{dn_\chi}{dt} + 3Hn_\chi = -\langle\sigma v\rangle \left[n_\chi^2 - (n_\chi^{eq})^2\right] \tag{1.23}$$

where $\langle\sigma v\rangle$ is the velocity-averaged annihilation cross section and $v$ is the relative velocity of DM particles. This equation indicates that, once $T < m_\chi$, $\Gamma = \langle\sigma v\rangle n_\chi < H$, and the annihilation process is not efficient anymore. This will make the annihilation process –as well as the inverse process of creation– to cease, and the number of DM particles will remain constant up to present time. This is known as "chemical freeze-out", followed by the "kinetic freeze-out", when the scattering processes become so inefficient that DM is thermally decoupled from the rest of the Universe Lee and Weinberg (1977). We can rewrite Eq. 1.23 in terms of convenient variables,

$$\begin{aligned} x &\equiv \frac{m_\chi}{T} \\ Y &\equiv \frac{n_\chi}{s} \end{aligned} \tag{1.24}$$

where $s = \frac{2\pi^2 g_* T^3}{45}$ is the entropy density of the Universe depending on $g_*$ relativistic degrees of freedom (which are themselves dependent on $T$). The resulting equation is then,

$$\frac{Y}{x} = -\frac{s\langle\sigma v\rangle}{Hx}\left[Y^2 - (Y^{eq})^2\right] \tag{1.25}$$

No analytical solution exists for this equation; nevertheless, there are some approximations based on reasonable assumptions Lee and Weinberg (1977); Kolb and Turner (1990); Jungman et al. (1996) which can be used to compute the expected relic abundance of DM, yielding,

$$\Omega_\chi h^2 = \frac{m_\chi n_\chi}{\rho_c} \sim \left(\frac{3\cdot 10^{-27}\mathrm{cm}^3\cdot\mathrm{s}^{-1}}{\langle\sigma v\rangle}\right) \tag{1.26}$$

In Figure 1.6, we show $\Omega_\chi h^2$ as a function of $x$ for different values of $\sigma_v$ As seen in Section 1.2.1, *Planck* CMB data yields $\Omega_\chi h^2 = 0.1198$ Planck Collaboration (2020a). This leads to $\langle\sigma v\rangle \sim 2\cdot 10^{-26}\ \mathrm{cm}^3\cdot\mathrm{s}^{-1}$. This value is interesting *per se*, but it is also in the scale of electroweak (EW) interactions[15]. This remarkable coincidence is known as the "WIMP miracle", where WIMP stands for *Weakly Interacting Massive Particle*, one of the most popular DM candidates which will be explained in Section 1.4.1 and throughout this Thesis. This relation can also be inverted to give an upper limit on the mass of the DM particle with unitarity arguments. A value of $m_\chi \lesssim 340$ TeV was derived by Griest and Kamionkowski (1990) assuming $\Omega_\chi h^2 = 1$. More updated calculations lowered the limit to 100 (140) TeV for Dirac (Majorana) DM Smirnov and Beacom (2019), taking into account corrections such as non-perturbative resonances effect such as Sommerfeld enhancement Hisano et al. (2004). Likewise, lower bounds can be obtained by pure particle physics considerations Lee and Weinberg (1977), although they are subject to unknown interactions within the dark sector, which makes their derivation more uncertain Bœhm and Fayet (2004). In any case, stringent bounds can be set by different experiments Boyarsky et al. (2009); Bœ hm et al. (2013); Calibbi et al. (2014); Basu et al. (2020), which yield a lower bound of a few meV at best.

[15] EW interactions present cross sections $\sigma \sim 10^{-36}\mathrm{cm}^2$.

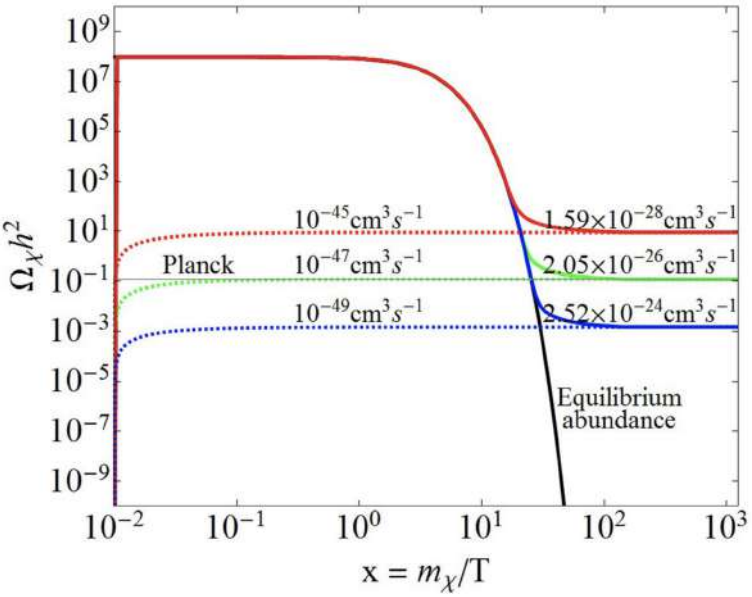


FIGURE 1.6: DM abundance $\Omega_\chi h^2$ as a function of $x = m_\chi/T$. Black, solid line is the abundance if DM remained in equilibrium and therefore was exponentially suppressed (see Eq. 1.22). Different colors show different values of the thermally-averaged annihilation cross section. Black, horizontal line is the inferred abundance from *Planck* CMB data, $\Omega_\chi h^2 = 0.1198$ Planck Collaboration (2020a). Figure taken from Dev et al. (2014).

### Non-thermal production of dark matter

The measured DM cosmological abundance may be produced by non-thermal means, i.e., DM particles not being in thermal equilibrium in the primordial plasma. In this case, the DM coupling to radiation and matter may be too weak to reach an equilibrium state. There are several mechanisms which are able to yield the correct observed relic density. Here we will just cite a few examples, and detail the "freeze-in" mechanism, as opposition to the "freeze-out" thermal relic process.

Some examples of non-thermal production mechanisms (see, e.g., Bertone et al. (2005) for a review) are topological defects of cosmic strings Jeannerot et al. (1999); Cui and Morrissey (2009); Berglund et al. (2021); Packard (2020), mis-alignment mechanisms (which can produce axion-like particles, see Section 1.4.1) Nelson and Scholtz (2011); Marsh (2016); Diez-Tejedor and Marsh (2017); Yang and Di (2017); Luzio et al. (2021), decay of inflaton field Takahashi (2008); Bastero-Gil et al. (2016) and early matter collapse from density fluctuations short after inflation (which can produce DM as PBHs, see Section 1.4.2) Hawking (1971); Ezquiaga and García-Bellido (2018); Allahverdi et al. (2018).

Regarding the "freeze-in" mechanism, it can produce a *Feebly Interacting Massive Particle* (FIMP) Yaguna (2011). Take $X$ as a long-lived particle, feebly coupled to the thermal bath at temperature $T$ (well above the weak scale). Let $m$ to be the mass (in the weak scale) of the heaviest particle sharing an interaction vertex with $X$. Assuming a feeble interaction, the coupling strength is $\lambda \ll 1$[16]. The abundance of $X$ ah high $T$ is negligible; this produces a non-zero abundance of $X$ generated by collisions or decays of particles in the thermal bath. The dominant contribution is

[16]The interaction can either be a Yukawa interaction, which coupling is just $\lambda$, or trilinear interactions with coupling $\lambda m$.

that generated at temperature $T \sim m$, due to the exponential interaction suppression at low temperatures. The yield of particle $X$, defined as $Y_X = n_X/S$ (where $n_X$ is the number density of $X$ and $S$ is the entropy density of the plasma), freezes in at Bernal et al. (2017),

$$Y_X \sim \lambda^2 \frac{M_{pl}}{m} \tag{1.27}$$

where $M_{pl}$ is the Planck mass. Therefore, the abundance of $X$ is proportional to the coupling $\lambda$. This mechanism can yield the correct relic density of FIMPs as DM or as particle which decays into the DM particle. For example, let DM be a FIMP particle $X$ interacting with two particles $\Sigma$ and $\Xi$ according to the operator $\lambda X\Sigma\Xi$ (and imposing $m_\Sigma > m_\Xi + m_X$). In this case, the freeze-in mechanism will make $\Sigma$ decay intro $X$, with a relic abundance given by Hall et al. (2010),

$$\Omega_X h^2 \sim 1.09 \cdot 10^{-27} \Gamma_\Sigma \frac{g_\Sigma}{g_*^{3/2}} \frac{m_X}{m_\Sigma^2} \tag{1.28}$$

where $\Gamma_\Sigma$ is the decay rate of $\Sigma$ into particle $X$, $g_\Sigma$ are the internal degrees of freedom of $\Sigma$, and $g_*$ the degrees of freedom of the thermal bath. Therefore, in this simple case, the correct relic density can be achieved by a non-thermal freeze-in mechanism.

## 1.3 Dark matter distribution in the Universe

In order to search for DM, it is critical to understand not only its cosmological abundance, but its distribution throughout the Universe. Indeed, the latter turns to be a critical ingredient when addressing fundamental questions about the nature of the DM particle, such as if it is relativistic, or the smallest structures formed in $\Lambda$CDM. In this Section, we will review the structure formation mechanisms, how can the DM distribution be studied both from the observational side and N-body simulations, and the current challenges in CDM halos.

### 1.3.1 Structure formation in $\Lambda$CDM

The observed structures in the Universe are a direct consequence of the density fluctuations in the primordial plasma, which imprints are left in the anisotropies of the CMB (Section 1.2.1). These fluctuations turn into matter overdensities, seeding the non-linear structure growth up to the present day Padmanabhan (1993). DM plays a crucial role, attracting the baryonic matter (once it decoupled from radiation) to DM potential wells and enhancing the growth of the initial overdensities. If not thermally-decoupled DM was present, relativistic baryons would escape these overdensities, washing them out and preventing their growth. A decoupled, non-relativistic species is necessary for structure formation according to observations Knobel (2012).

In this model, there is a bottom-up, hierarchical scenario: the smallest structures form first in the Universe as virialized CDM halos; by accretion and merging of these, larger structures arise, and so on. Therefore, $\Lambda$CDM presents DM substructure, with subhalos within halos, sub-subhalos within subhalos, and so on and so forth. This model is able to reproduce the observed LSS, and is one of the main triumphs of $\Lambda$CDM Chamcham et al. (2017). Not only the cosmological abundance of DM is relevant, but also the underlying particle physics governing it. Indeed, if the particle is very light (e.g., neutrinos, as discussed in Section 1.4), the particle will

be relativistic and therefore will free-stream through overdense regions, thus forming only very large structures, erasing small-scale features. This family of models is known as Hot Dark Matter (HDM), which inverts the ΛCDM hierarchy into an up-bottom scenario where, contrary to CDM, very large structures (such as galaxy clusters) form first, and later fragment into smaller structures such as galaxies. Indeed, the free-streaming length of CDM is $\lambda_{CDM} \sim m_\chi^{-1/2}$ Green et al. (2005), while in the case of HDM $\lambda_{HDM} \sim m_\chi^{-1}$ Boyanovsky (2008). Therefore, the colder DM is, the smaller the minimum scale of possible structures.

Currently, HDM is strongly disfavored according to observations, such as the galaxy redshift surveys of 2dF De Propris et al. (2002) or SDSS SDSS Collaboration (2017), which we show in Figure 1.7. Nevertheless, CDM still present some problems, reviewed in Section 1.3.3, which favoured the formulation of a mixed alternative, known as "Warm Dark Matter" (WDM). As shown in Figure 1.8, the amount of substructure significantly changes between HDM and CDM. Therefore, HDM, with DM particle mass below $\sim 0.1$ keV, is discarded as a viable DM model. There is a notable exception to this limit: axion particles (see Section 1.4.1). These are very light particles, $\mathcal{O}(\text{meV})$, which can effectively behave like CDM due to its non-thermal production.

### 1.3.2 N-body cosmological simulations as probes of dark matter substructure

Although the structure formation mechanisms in ΛCDM are well established, our knowledge is still incomplete. The full picture is much more rich and complex, and involves other ingredients such as gas dynamics, radiative transfer and cooling, recombination, baryonic feedback, etc. Due to the highly non-linear growth of structures, the usual approach to address the formation of LSS from the early Universe is by means of N-body cosmological simulations. Since the first attempt to perform a simulation with N bodies to simulate the behaviour of galaxy dynamics by Holmberg (1941), using light bulbs to imitate the $r^{-2}$ radial dependence of gravity, the field has matured into nowadays high-resolution simulations with supercomputers.

In Cosmology, structure evolution can be treated as non-linear gravitational clustering with input initial conditions, and refined by introducing the effects of baryons, chemical processes, radiative transfer and, in general, astrophysical phenomena. N-body simulations are computationally very expensive, as they involve solving 6N differential equations (3N for the position and 3N for the velocity) as a function of time to describe the particle motion in Newtonian gravitation. After surpassing the million- and billion-particle threshold in the first two decades of the XX$^{\text{th}}$ century with simulations such as Via Lactea II ($N = 2 \cdot 10^8$) Diemand et al. (2008), Aquarius ($N = 10^9$) Springel et al. (2009), or Millennium ($N = 10^{10}$) Springel et al. (2005), we are now entering trillion-particle simulations era, e.g., Uchuu ($N = 2.1 \cdot 10^{12}$) Ishiyama et al. (2020). In Figure 1.9 we show some of these simulations.

Since the actual number of interactions to be computed scales as $N^2$, numerically integrating the differential equations is unfeasible, and a number of refinements is necessary. A common practice is to restrict the study to DM-only simulations (recall $\Omega_\chi \sim 5\ \Omega_m$), i.e., ignoring any baryonic effects such as radiative transfer and feedback processes, computing only the gravitational interaction. Nevertheless, there are full hydrodynamic simulations, which devote a signficant fraction of the total computational power to the baryonic effects, such as IllustrisTNG Springel et al. (2017). These are crucial to understand processes with strong baryonic dependence, such as galaxy formation and evolution.

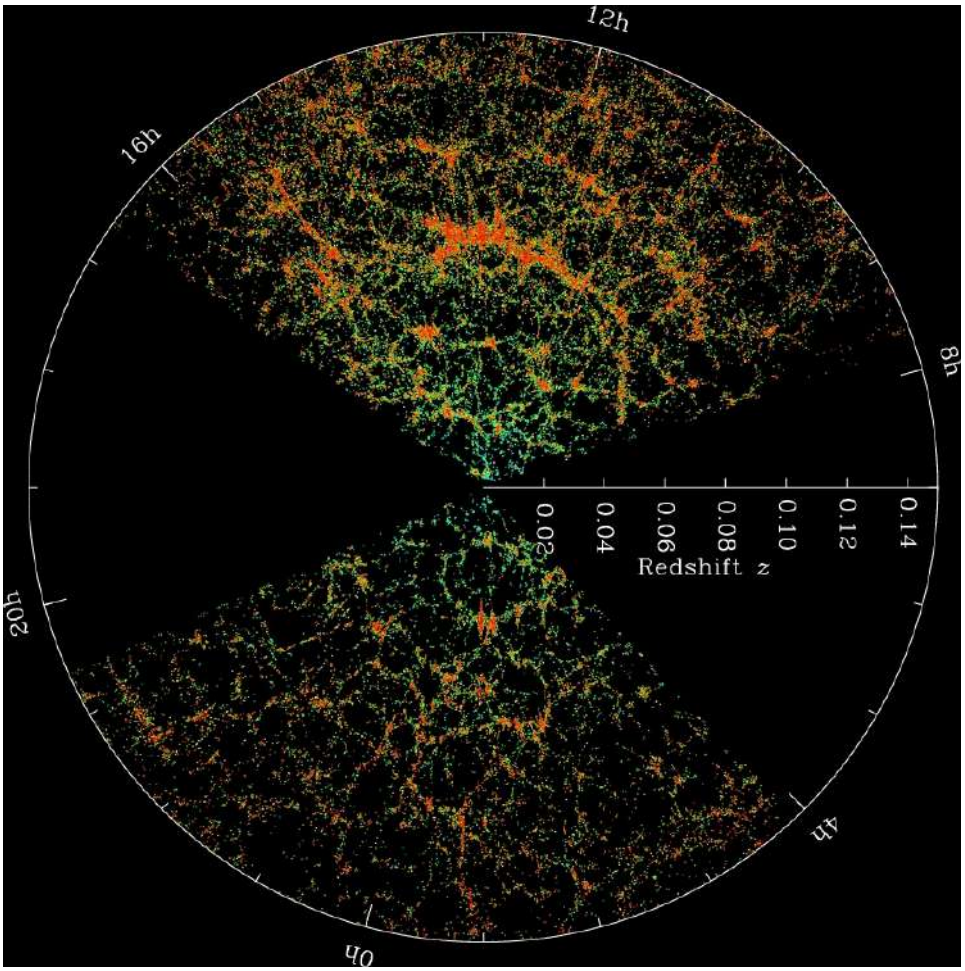


FIGURE 1.7: The Large Scale Structure of the Universe, as observed by the SDSS galaxy redshift survey SDSS Collaboration (2017) up to $z \sim 0.15$ ($d_L \sim 700$ Mpc). It shows the galaxy number distribution as a function of redshift in two observational slices. Each point represents a galaxy, with hotter colors indicating larger number densities. Note the big structure in the top slice, known as the "Great Wall" Leclercq et al. (2017).

The number of particles gives a rough estimate of how powerful is an N-body simulation, but this is ultimately determined by other parameters, such as the mass or length resolution. Structure identification requires a halo or subhalo finder (see e.g. Knebe et al. (2013) for a review), assuming a minimum number of particles (typically $\sim 20$). This makes the mass resolution, i.e., the mass of the smallest resolved structure, to be well above the simulation particle mass, and is therefore limited by numerical power[17]. Likewise, length resolution is limited by the so-called softening scale, which is introduced in order to avoid divergences in the gravitational force computations when particles collide.

Any current simulation is orders of magnitude away from resolving all DM substructure; indeed, the matter power spectrum $P(k)$ is expected to have a mass cutoff, i.e., no further substructure below it, depending on the mass of the DM particle. This can vary from $10^{-12} - 10^{-6}$ M Profumo et al. (2006), being the upper limit roughly

[17] Nevertheless, the simulation is incomplete at mass resolution, and the completion mass is typically a factor $5 - 10$ larger Diemand et al. (2008).

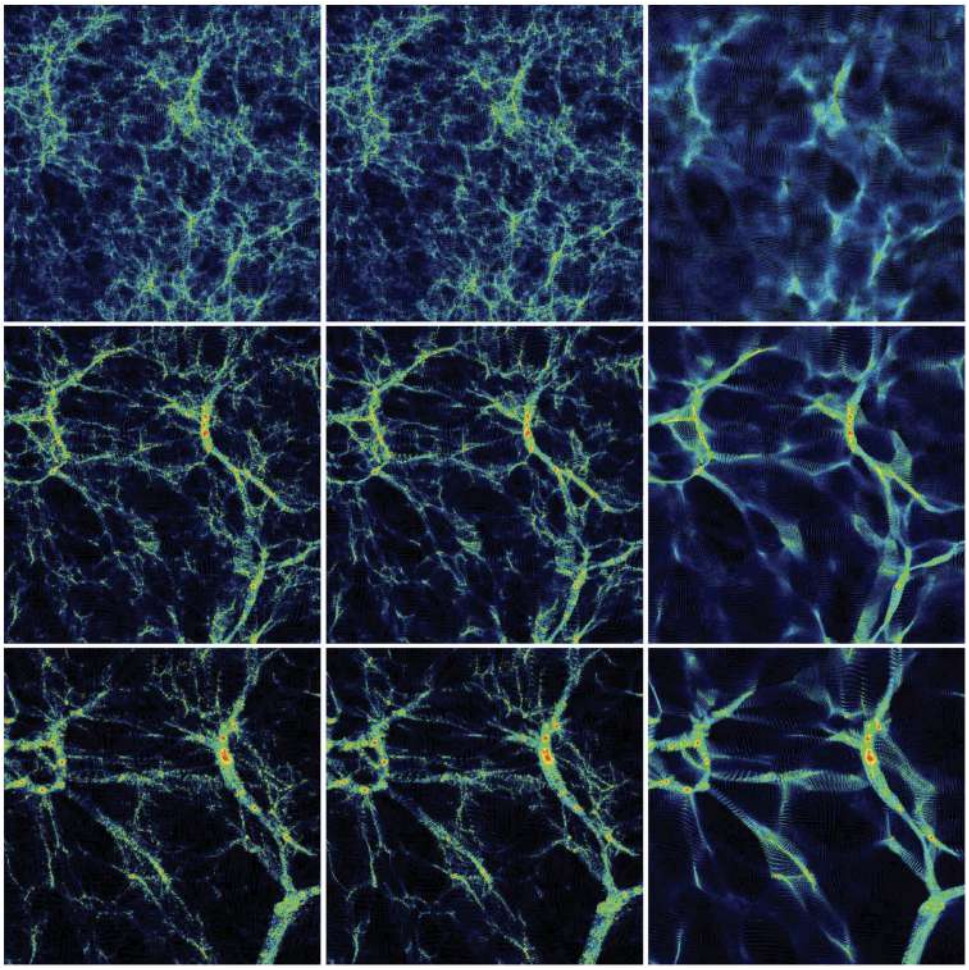

FIGURE 1.8: Large Scale Structure density maps from N-body simulations with a length of $50h^{-1}$ Mpc and a depth of $2.5h^{-1}$ Mpc. From top to bottom, different redshift snapshots are taken at $z = \{4.4, 1.1, 0\}$. From left to right, CDM, WDM ($m_\chi = 1$ keV) and WDM ($m_\chi = 0.25$ keV). WDM effects are barely discernible in the middle panels, while they are prominent in the right panels, where less substructure is present when compared to CDM Schneider et al. (2012).

the mass of the Earth. The subhalo mass function (SHMF) gives the number of subhalos per mass unit, and is of the form $dN/dM \propto M^{-\alpha}$, with $\alpha = 1.9 - 2$ depending on the simulation Springel et al. (2008); Griffen et al. (2016). This means that, as we go to lower masses, the number of subhalos is increased as a power law, with a MW-like galaxy presenting millions of these subhalos below $\sim 10^5$M Diemand et al. (2008). Indeed, subhalos add up to the $10 - 20\%$ of total DM mass in simulations, and, depending on the mass cutoff, can yield up to $\sim 50\%$ in our galaxy Griffen et al. (2016). Typical N-body simulations, on the other hand, present mass resolutions of order $\sim 10^5 - 10^8$ M Springel et al. (2005); Diemand et al. (2008); Springel et al. (2009), with exceptions in the case of microhalo simulations Ishiyama (2014), or halo extrapolations with no subhalos Wang et al. (2020).

A notable feature of the structure of DM halos in simulations is that they seem to be described by an universal radial DM profile, regardless of the mass, epoch and power spectra Navarro et al. (1997). Different profiles have been proposed in the literature, most of which can be agglutinated in a single expression Zhao (1996); Kravtsov et al. (1998),

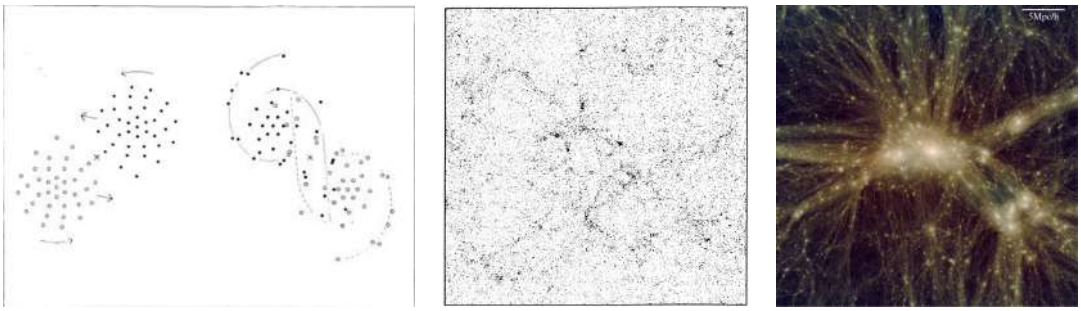

FIGURE 1.9: Eight decades of N-body simulations. **Left panel:** first N-body simulation by Holmberg (1941), using 37x2 light bulbs to model the MW and Andromeda galaxies in collision. **Central panel:** first DM computer-based N-body simulation by Davis et al. (1985), with 32768 particles. **Right panel:** Uchuu N-body simulation of LSS Ishiyama et al. (2020) which comprises $2 \cdot 10^{12}$ particles.

$$\rho_{DM}(r) = \frac{\rho_0}{\left(\frac{r}{r_s}\right)^{\gamma}\left[1+\left(\frac{r}{r_s}\right)^{\alpha}\right]^{\frac{\beta-\gamma}{\alpha}}} \tag{1.29}$$

where $r_s$ is a characteristic scale radius, and $\rho_0$ a density normalization parameter. For $r \ll r_s$, $\rho \sim r^{-\gamma}$, and $\rho \sim r^{-\beta}$ in the inverse case. The $\alpha$ parameter controls the sharpness of change in the logarithmic slope. Depending on the values for $\{\alpha, \beta, \gamma\}$, different DM profiles can be obtained. For instance, the renowned Navarro-Frenk-White profile (NFW) Navarro et al. (1997) presents $\{\alpha, \beta, \gamma\} = \{1, 3, 1\}$, an isothermal profile with core $r_s$ $\{\alpha, \beta, \gamma\} = \{2, 2, 0\}$, the Moore profile Moore et al. (1998) $\{\alpha, \beta, \gamma\} = \{1.5, 3, 1.5\}$ and the Burkert profile Burkert (1995) $\{\alpha, \beta, \gamma\} = \{2, 3, 0.2\}$. Another widely-used profile in the community is the Einasto profile Einasto (1965), parametrized as,

$$\rho_{DM}(r) = \rho_s \exp\left(-\frac{2}{\alpha}\left[\left(\frac{r}{r_s}\right)^{\alpha} - 1\right]\right) \tag{1.30}$$

with $\alpha$ acting as a slope parameter. Einasto profile tends to fit better some N-body simulations such as Aquarius Springel et al. (2008), at the cost of an extra parameter. There are other families of profiles, such as the ones proposed by Kazantzidis et al. (2004), which introduce an exponential cutoff to account for the mass loss beyond the virial radius $R_{vir}$, or the Universal Rotation Curve (URC) Persic et al. (1996).

The distribution of DM subhalos inside the main halos is one of the critical points in this Thesis. Moreover, the information on the profile is normally complemented by the subhalo radial distribution (SRD), which accounts for possible radial dependence on the positions of subhalos in the parent halo. Nevertheless, the structural properties of low-mass subhalos are not well understood, as the mass resolution is well above the whole subhalo population. For example, as many of these subhalos are precisely at the mass resolution limit, they are composed by the threshold number of particles, and its density profile is poorly determined. A way to characterize them is via the concentration parameter. This is traditionally expressed[18] as,

$$c = \frac{R_{vir}}{r_s} \tag{1.31}$$

[18] A similar definition can be done in terms of the velocities of the particles in the simulation, which is a proxy for the mass and, in general, is better defined Moliné et al. (2017).

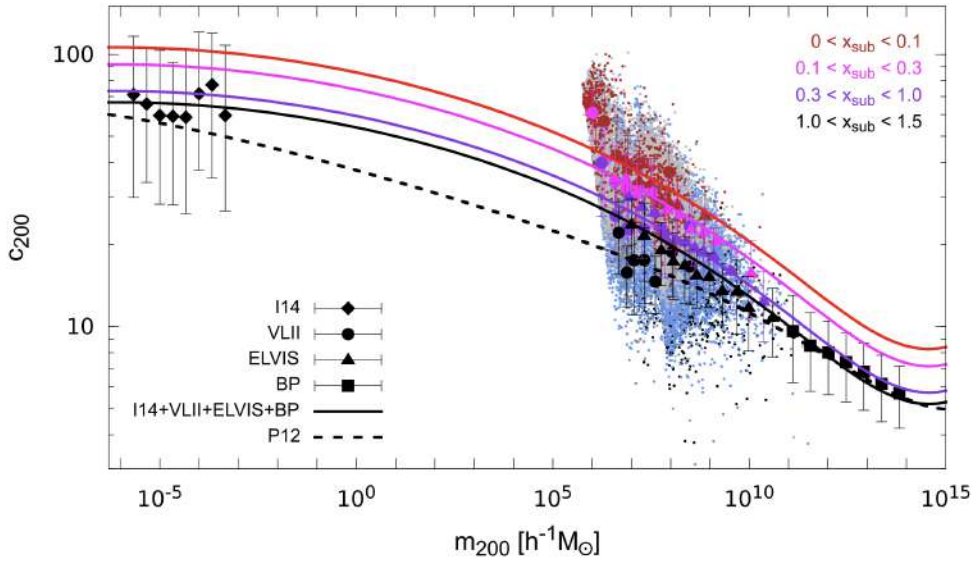


FIGURE 1.10: Median halo (black symbols) and subhalo (colored symbols) concentration parameter $c_{200}$, as a function of $m_{200}$ as found in different N-body simulations. Different colors represent radial bins defined as $x_{sub} = r/R_{vir}$. Background dots are the individual subhalos, and the solid lines are different proposed $c(M)$ models. The $c(M)$ is flattened towards lower masses. See Moliné et al. (2017) for details.

where $R_{vir}$ is the virial radius, defined as the one at which the density is $\rho_{vir} = \Delta\bar{\rho}$. Is usual to assume $\Delta = 200$, i.e., an overdensity of 200 times the mean (or critical, depending on the convention) density in the Universe. The concentration encodes information on the subhalo structure; the larger its value, the more compact the object. This turns out to be critical for the results of this Thesis, as seen in coming Chapters. It is interesting to study the dependence of concentration with mass, $c(M)$. This was though to follow a power-law behaviour, increasing towards lower masses, when using halo masses $10^{10} - 10^{15} h^{-1}$M Prada et al. (2012). Nevertheless, as proved by Sánchez-Conde and Prada (2014), it was flattened at low halo masses. Indeed, this is expected in ΛCDM, as the halo formation time sets its concentration. This will be roughly the same regardless on the mass (but assuming it to be small), due to the matter power spectrum, thus showing a flattening at low masses. Therefore, the initial concentrations of small halos are expected to be very similar, and will remain as so until $z = 0$. Moliné et al. (2017) found a similar trend for subhalos instead of field halos, including a radial dependence on the position of the subhalo within the host halo, with subhalos nearer the host halo center significantly more concentrated than those in the outskirts. This is due to the tidal disruption of material when orbiting close to the central potential, which can remove up to 99.9% of the subhalo mass, yet leaving its core very concentrated van den Bosch and Ogiya (2018).

Nevertheless, this is still a subject of big debate in the community. N-body simulations predict the existence of low-mass subhalos close to the host center, yet not well resolved. Some authors claim these low-$x_{sub}$ subhalos are spurious, and that in reality they will be destroyed by tidal forces. Therefore, these works predict a small surviving probability for low-mass subhalos Berezinsky et al. (2006); Goerdt et al. (2007); Zhao et al. (2007). On the other hand, there are also claims that tidal disruption of subhalos is a numerical artifact of N-body simulations Peñarrubia et al. (2010); van den Bosch and Ogiya (2018); Errani and Peñarrubia (2019); Green and

van den Bosch (2019), and that close-to-center, low-mass subhalos are extremely resilient and concentrated objects which survive up to our days.

Another critical point in subhalo survival probability is the influence of baryons; as we mentioned, simulations are typically DM-only, to dedicate the maximum computational power to push down the resolution limit. Nevertheless, the baryonic counterpart will play a role not only in astrophysical processes such as galaxy formation, but in DM structural properties, as they gravitationally interact. For example, M31 Andromeda galaxy observations favor a baryonic-induced adiabatic contraction in its central region Seigar et al. (2008); Gnedin et al. (2011). Baryons can also be relevant in the cusp/core problem, as we will review in Section 1.3.3. For masses below $\sim 10^8$ M$_\odot$, baryons can significantly affect the subhalo abundance Garrison-Kimmel et al. (2017); Zhu et al. (2016), yet they are not expected to play a significant role in subhalo structural properties as no baryonic content is expected for those.

Indeed, in the ΛCDM picture, galaxies are formed when falling into the gravitational wells generated by DM. As stars are formed by the collapse of molecular clouds, leading to the formation of not a single star but a rich population, the baryonic collapse into DM halos will not form a single galaxy. Any galaxy is within a DM halo which extends much farther than its baryonic content, and, as seen throughout past and current Sections, DM presents a substructure of halos and subhalos going down to very small masses. Therefore, the central galaxy will be surrounded by many other satellite galaxies (see Section 1.1.2). In Figure 1.11 we show this mismatch between the DM subhalo and galaxy populations. According to Sawala et al. (2015); Benitez-Llambay and Frenk (2020), regardless of parameters such as the recombination redshift, the halo occupation fraction (HOF), i.e., the fraction of halos hosting a galaxy, rapidly decays with the halo mass and reaches zero for $M_{halo} \sim 10^8$ M$_\odot$ (assuming $z = 0$). This means no lighter subhalo will be capable of retaining baryonic content and, accordingly, will be a completely DM-dominated object – therefore remaining invisible. Nevertheless, this is one of the central points in this Thesis and, as we will see, they may be visible in gamma rays through DM annihilation or decay (see Sections 1.4.1 and 1.5.3).

### 1.3.3 Challenges in ΛCDM halos

As seen in the previous Sections, ΛCDM predictions provide remarkable agreement with observations of the LSS, where simulations are well characterized. Despite this agreement, there are still some problems at the galactic scales, with some tension between theoretical expectations and observations. In this Section we will briefly explain some of them, but we defer the reader to, e.g., Bullock and Boylan-Kolchin (2017) for an exhaustive review.

- **"Missing satellite" problem:** The low number of discovered satellite galaxies of the MW (see Section 1.1.2) compared to the ΛCDM predictions, where millions of subhalos are expected in the MW, with dozens of them above $10^8$ M$_\odot$ –therefore hosting galaxies Klypin et al. (1999); Read et al. (2005); Strigari et al. (2007)–, triggered the so-called "missing satellite" problem. ΛCDM-predicted number of satellites was in tension with the observed population, leading to a WDM increasing popularity, which erased much of this substructure Bode et al. (2001); Schneider et al. (2012). Nevertheless, as more faint and ultra-faint satellites were discovered in surveys such as SDSS or DES, the tension between observations and predictions disappeared Simon and Geha (2007); Kim et al.

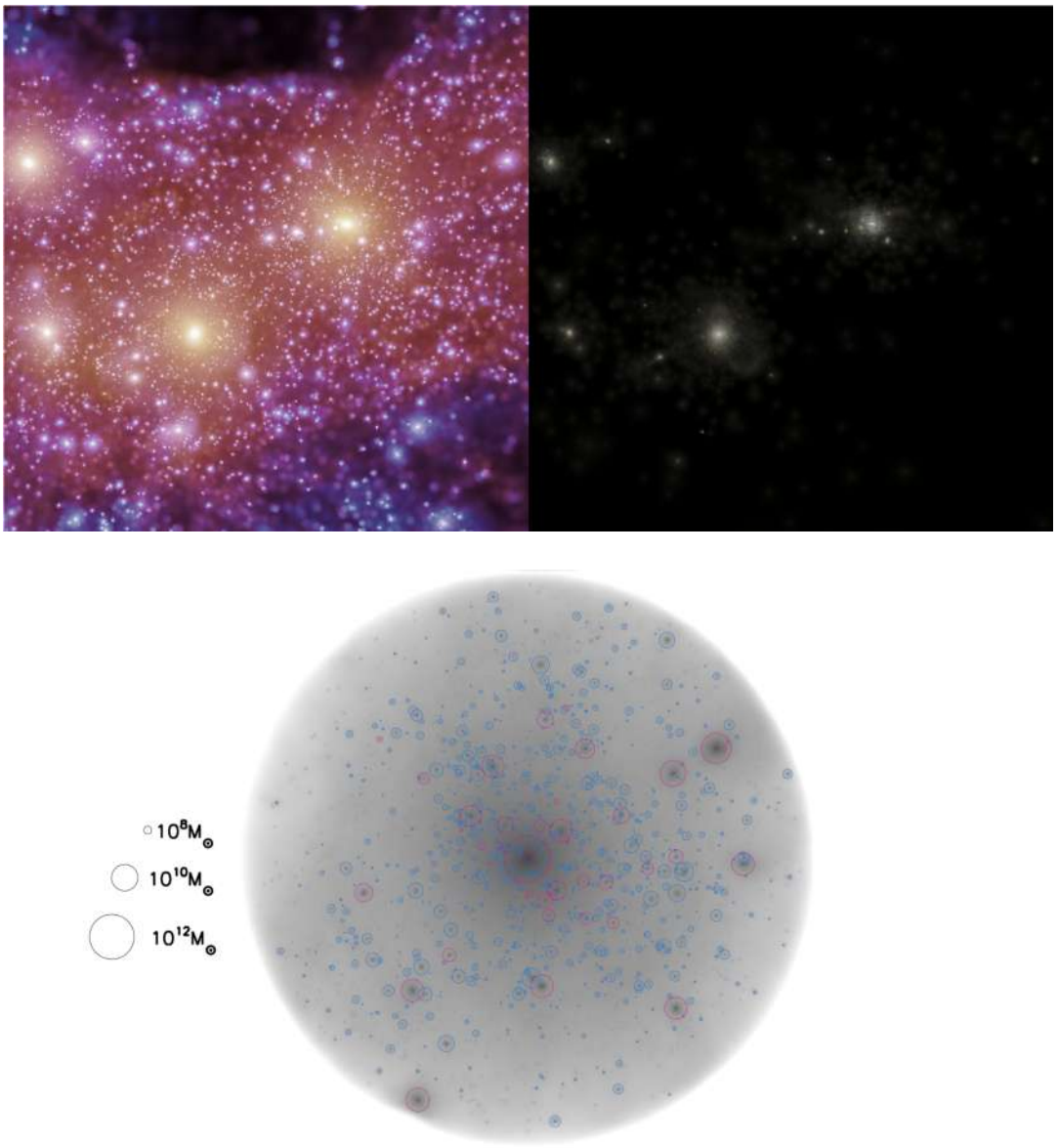


FIGURE 1.11: Not all DM subhalos host a galaxy. **Top row:** 2 Mpc-side cube from the hydrodynamic EAGLE N-body simulation Schaye et al. (2015). Left panel is the DM density map, contrasting with the right panel, where the stellar light distribution is shown. **Bottom panel:** HOF map of one of the two main subhalos of top image, with a 400 kpc radius. Circles show three mass references, while blue (red) colors indicate a dark (luminous) halo, i.e., not hosting (hosting) a galaxy. Figures taken from Sawala et al. (2014, 2015).

(2018). This was never a real problem, but rather a matter of instrumental sensitivity.

- **Cusp/core problem:** as shown in Eq. 1.29, the DM profile close to the center of the halo is expected to behave as $\rho(r) \propto r^{-\gamma}$. While DM-only simulations tend to yield cuspy profiles with $\gamma \sim 0.8 - 1.4$[19] Navarro et al. (2009), observations of DM-dominated objects such as dwarf galaxies prefer more cored profiles where $\gamma \sim 0 - 0.5$ Marchesini et al. (2002); Simon et al. (2005); de Blok et al. (2008). The solution to this problem may come in the form of baryons. Indeed, baryonic physics may effectively lead to the formation of cored DM profiles, as the migration of baryons into the center may boost star formation periods, which create baryonic outflows towards the outer parts Macciò et al. (2011); Oñorbe et al. (2015); Del Popolo and Pace (2016). These outflows affect DM via gravitational pull, which will partly devoid of DM the innermost parts. Successive iterations of this phenomenon will erase the central DM cusp in favour of an almost-constant density core Governato et al. (2010); Di Cintio et al. (2013).

- **"Too-big-to-fail" problem:** The most massive subhalos can have masses up to $\sim$ 10% of the parent halo Moliné et al. (2017). Therefore, one would expect the largest members of the Milky Way[20] to host the most luminous satellites. Nevertheless, measurements of the MW satellite masses yield values systematically lower than those expected in N-body simulations Boylan-Kolchin et al. (2011). This is surprising because massive halos should be more efficient in star formation than lighter ones Boylan-Kolchin et al. (2012). A similar trend has been found in the Andromeda galaxy and its satellites Tollerud et al. (2014). As in the cusp/core problem, the solution may be baryons: interactions between satellite galaxies and the MW, through tidal and ram pressure stripping or disk shocking will suppose additional forms of feedback, which can reduce the central masses of satellites. Indeed, galaxy formation simulations point to the relevance of such interactions Brook and Di Cintio (2015); Dutton et al. (2016), yet no hydrodynamic simulation is yet able to solve the $\sim$ 500 pc scale implementing these processes, critical to understand the real impact of baryons.

- **Planar distribution of satellite galaxies:** Early observations in the 1970s pointed to an unusual distribution of the MW satellites in the halo, which are found along a polar great circle around the MW Lynden-Bell (1976); Kunkel (1979). This has been confirmed with further data, being in tension with the expected isotropic distribution inferred from N-body simulations Samuel et al. (2021). Moreover, the same peculiar bias has been found as a thin disk of satellites in the Andromeda galaxy Metz et al. (2007); Ibata et al. (2013); Conn et al. (2013); Pawlowski et al. (2015). Some works claim this plane to be an observational bias, as the galaxy surveys are incomplete and favour the presence of structures as planes Metz et al. (2009), although other works reject this as the origin of the planar distribution Pawlowski et al. (2015). The combination of the *Hubble* Space Telescope (HST) Holtzman et al. (1995) and future James Webb Space Telescope (JWST) Gardner et al. (2006) will hopefully help to alleviate this tension Bullock and Boylan-Kolchin (2017).

[19] Recall that the NFW profile has $\gamma = 1$.

[20] Recent estimates for the mass of the MW yield values of $M_{200}^{\text{total}} = 1.1 \cdot 10^{12}$ M and $M_{200}^{\text{DM}} = 9.7 \cdot 10^{11}$ M Cautun et al. (2020).

## 1.4 The nature of dark matter: from WIMPs to primordial black holes

In previous Sections we have discussed the observational evidence, theoretical framework and distribution of DM through astrophysical observations and N-body simulations. However, this does not answer the pressing question "what is DM made of?", to which there is still no answer. Indeed, a plethora of candidates have been proposed over the years to explain the ultimate nature of DM, spanning more than 60 orders of magnitude in mass. In this Section, we will do a non-exhaustive review of DM candidates, both particle and macroscopic. For a complete review, we defer the reader to, e.g., Bertone et al. (2005); Steffen (2009); Feng (2010) and references therein.

### 1.4.1 Particle dark matter models

As noted in the literature, according to the observed evidence, a DM particle model should fulfill at least the following requirements, as presented, e.g., in Taoso et al. (2008),

1. DM particles should be "cold", i.e., non-relativistic (see Section 1.3.2).
2. DM particles should be stable or, at least, have a lifetime of the age of the Universe ($\sim$ 13.8 Gyr Planck Collaboration (2020a)).
3. DM particles should account for the observed DM relic density $\Omega_\chi h^2 = 0.1198$ Planck Collaboration (2020a).
4. DM particles should be electrically neutral (no EM interactions), weakly interacting with baryonic matter (no strong interactions), and effectively collisionless, as suggested by, e.g., the Bullet Cluster (see Section 1.1.3).
5. DM particles should be compatible with current observations such as stellar evolution, Big Bang Nucleosynthesis (BBN), LSS, etc., as well as present constraints (see Section 1.5).

As discussed in, e.g., Baltz (2004), the mass range of the current models span more than 60 orders of magnitude, from "fuzzy" CDM to "WIMPzillas". Despite current observations, it is hard to narrow this range, as most probes have no information on the DM particle itself. In the following, we present some of the most popular models in the literature for particle DM.

- **Neutrinos:** Years ago, neutrinos were considered the paramount DM candidate, as they are very weakly interacting particles in the Standard Model (SM), which would not require invoking new physics to account for DM Abazajian (2021). Unfortunately, observational evidence completely ruled out this possibility due to a variety of reasons. Although collisionless, they are relativistic particles at the time of decoupling, acting as HDM and erasing substructure below $\sim 40 \left(\frac{m_\nu}{30\ \mathrm{eV}}\right)$ Mpc Bond et al. (1980); Marulli et al. (2011), which leads to a top-bottom structure formation paradigm, in contradiction with current observations (see Section 1.3.1). Additionally, assuming massive neutrinos[21], the cosmological abundance is given by Dodelson (2003),

[21] We know from flavour oscillations that $m_\nu \neq 0$ Lesgourgues and Pastor (2006).

$$\Omega_\nu h^2 = \frac{\sum_i m_{\nu,i}}{94\text{eV}} \tag{1.32}$$

Current measurements yield $\sum_i m_{\nu,i} < 0.12$ eV at 95% confidence level (c.l.) Planck Collaboration (2020a), which impose $\Omega_\nu h^2 < 0.0012$, therefore allowing them to account for a tiny fraction of DM at most. Nevertheless, a variation of this candidate has been proposed as *sterile neutrinos*, which are neutral leptons with no ordinary weak interactions, except those induced by mixing with active neutrinos Giunti (2016); Naumov (2019), and "sterile" in the sense that they are not charged under any gauge group of the SM, hence non-thermally produced. Furthermore, they are a natural ingredient of the seesaw mechanism Cai et al. (2018), the most popular model to generate neutrino masses[22]. As they lack weak SM interactions other than mixing, they can be much heavier (from a few eV to $\sim 10^{25}$ GeV Drewes (2013)) and therefore become a possible DM candidate. We defer the interested reader to, e.g., Boyarsky et al. (2019) and references therein for a complete review of sterile neutrinos as DM particles.

- **Axions and axion-like particles (ALPs):** Axions were originally proposed as a solution to the strong-CP problem of QCD via the so-called Peccei-Quinn mechanism Peccei and Quinn (1977). This is based on the Nambu-Goldstone theorem and the spontaneous breaking of the global $U(1)_{PQ}$ Peccei-Quinn symmetry, where the axion arises as a pseudo-Goldstone boson. QCD axions are therefore non-thermally produced particles in the early Universe during the Peccei-Quinn phase transition, at temperatures well above the energy scale of QCD, $\Lambda_{QCD} \sim 200$ MeV. When $T < \Lambda_{QCD}$, the axion acquires a non-zero mass due to non-perturbative QCD effects Weinberg (1978). The relic abundance of axions and their mass are closely coupled with non-perturbative QCD effects; if their mass is $\mathcal{O}(\text{meV})$, they will yield the measured DM relic abundance. Therefore, axions are DM particle candidates.

  Once decoupled from its QCD foundation, the concept of axions can be broadly generalised to axion-like particles (ALPs), which arise due to a spontaneously broken $U(1)$ global symmetry. The production of ALPs is similar to axions, yet there are no stringent bounds neither on ALPs masses nor on other parameters such as photon coupling, therefore broadening the possibilities of ALPs as DM candidates Hook (2018). Indeed, the photon coupling is one of the common features between axions and ALPs, via the Lagrangian interaction term,

$$\mathcal{L}^{a\gamma}_{int} = g_{a\gamma\gamma} a F_{\mu\nu} \widetilde{F}^{\mu\nu} \tag{1.33}$$

  where $a$ is the axion/ALP field, $g_{a\gamma\gamma}$ is the photon coupling, which depends on $m_a$, and $F_{\mu\nu}$, $\widetilde{F}^{\mu\nu}$ are the EM field tensor and its dual, respectively. The interaction between ALPs and photons produce radiative ALP-photon conversion through the Primakoff effect Primakoff (1951), making possible their detection with both with direct and indirect detection experiments Marsh (2016), as we will see in Sections 1.5.2 and 1.5.3.

[22] SM neutrinos interact only via weak forces, and they appear in nature as left-handed particles, therefore excluding the Higgs mechanism as the origin of their masses. Neutrinos are in this sense one of the most striking signs for beyond SM (BSM) physics King (2003).

- **Weakly Interacting Massive Particles (WIMPs):** WIMPs are one of the most popular DM particle models. They do not refer to a single particle but rather a family of different BSM, thermally-produced particles, with no general model-building rule or preferred realisation. From a historical point of view, WIMPs were motivated by supersymmetry (SUSY) Martin (1998); Haber and Haskins (2018). SUSY is an extension of SM which aims to solve many of its problems, such as Higgs vacuum stability, via cancellations in the radiative corrections to the Higgs mass Cutright and Ghandour (1975); Machida (2013). SUSY theories provide an enlargement of the Poincaré symmetry group of SM to include transformations between bosons and fermions. This establishes a mapping between SM bosons (fermions) into SUSY fermionic (bosonic) partners, leading to the introduction of a large number of BSM new particles, among which many WIMP DM candidates may arise Ellis et al. (1984); Muñoz (2017).

  SUSY is nevertheless not necessary for WIMPs, and are predicted by other BSM theories such as Grand Unified Theories (GUTs) Arcadi (2016), which attempt to describe the SM symmetry group $SU(3)_c \times SU(2)_L \times U(1)_Y$ as a subgroup of a single, larger group, e.g., $SU(10)$ Arcadi et al. (2017), or Kaluza-Klein models, where the introduction of compactified dimensions, only accessible at very small lengths (or very high energies), give rise to DM particles via the so-called Kaluza-Klein excitations Servant and Tait (2003); Hooper and Profumo (2007). All these candidates present masses between $\sim$ 1 GeV and $\sim$ 500 TeV to stay within current theoretical and experimental allowed range.

  WIMPs popularity arises from the fact that these theories, in particular SUSY, expect the existence of a particle –introducing additional degrees of freedom– with a mass in the GeV–TeV scale. In the "WIMP miracle" (as reviewed in Section 1.2.2), it is a remarkable coincidence that, if DM is composed of WIMPs with a mass of this order, it could naturally yield the required cosmological density through thermal decoupling of the DM component. They are also very popular candidates because their co-annihilation or decay can produce signatures in a variety of experiments, as we will review in Section 1.5. It will be the central candidate throughout this Thesis, although alternative possibilities, such as PBHs (next Section and Chapter 9), will be also explored.

### 1.4.2 Macroscopic dark matter models

Baryonic matter is the first, natural candidate to explain DM. This was rapidly discarded by observations; for example, interstellar dust could account for the DM abundance, yet the extremely large amount necessary to do so would reveal it due to enhanced extinction of light, as well as absorption lines in the spectra of background sources Neininger (2001); Baes et al. (2004). There are also strong arguments from BBN, which disfavour baryonic DM. BBN describes the production of light elements, such as hydrogen, helium or lithium, within the first minutes after the Big Bang, which can be understood with SM physics. The primordial abundances of these elements are in agreement with current observations[23], and constrain the baryonic matter density to a $\sim$ 4% of the critical density, while DM mounts up to $20 - 30\%$ of $\rho_c$. This huge difference indicates that DM should have decoupled from the primordial plasma before BBN, i.e., in the very early Universe (see also Section

[23] While the abundances of hydrogen isotopes $^1$H, $^2$H and helium $^3$He, $^4$He are well understood, there is some tension with the prediction of the primordial $^7$Li abundance when contrasted with astrophysical data. This is known as the "cosmological lithium problem" Fields (2011).

1.2.1). Yet, there are still candidates which require no BSM physics to explain DM, as presented in the following.

- **Massive compact halo objects (MACHOs):** As in the case of neutrinos (Section 1.4.1), a small fraction of DM can be attributed to baryons. Indeed, baryons in the form of Massive Compact Halo Objects (MACHOs) Griest (1993); Freese et al. (1999); Holopainen et al. (2006), are part of the invisible matter content of the Universe. This broad definition includes any compact and massive object which small (below the experimental detection threshold) or null luminosities (black holes, BHs, which we will review in more detail as the next DM candidate). On galactic scales, these would be BHs, remnants of dead stars such as neutron stars and white dwarfs, or objects which are not massive enough to trigger nuclear fusion of hydrogen, such as brown dwarfs and vagabond planets and satellites. At larger scales, the same applies for low-luminosity galaxies. Although invisible, MACHOs can be spotted through gravitational lensing (see Section 1.1.3) Popowski et al. (2003); Calchi Novati (2012). Unfortunately, MACHOs can only account for a small part of the DM content of the Universe; for instance, observations of the LMC and dSphs suggest that, at most, one third of the DM can be in this form Alcock et al. (1996); Brandt (2016). Another MACHO candidate, recently highlighted, are the so-called "Proca stars" Brito et al. (2016), also known as horizonless vector boson stars. Although formally they are not MACHOs, in the sense that they are constituted by a new particle, they would be effectively detected as MACHOs. From LIGO data, it seems that an ultra-light boson with mass $m_\chi \sim 9 \times 10^{-13}$ eV is compatible with most-massive GW events, and can be a candidate for DM Bustillo et al. (2021).

- **Primordial black holes:** BHs from stellar collapse do not emit any radiation (other than theorized Hawking radiation Hawking (1975)), and they are effectively collisionless, given their typical separation and extremely compact size. Despite this, they are not viable DM candidates, as stellar BHs are produced long after BBN. Nevertheless, an alternative production mechanism is possible, which renders *Primordial Black Holes* (PBHs) Hawking (1971); Clesse and García-Bellido (2018). These are currently only theorized, yet are supposed to form in the very early Universe most likely[24] as a consequence of the inflationary phase after the Big Bang Carr et al. (2017), with density fluctuations collapse. Unlike stellar BHs, where their mass is limited by that of the progenitor star, PBHs may be formed in a wide range of masses, from $10^{-5}$ g to thousands of M Masina (2020), spanning more than 40 orders of magnitude. Nevertheless, strong constraints can be placed for them, for example limiting the lower PBH mass, as below $\sim 10^{15}$ g the Hawking radiation would evaporate them in time scales smaller than the age of the Universe, therefore not being viable DM candidates Brevik and Halnes (2003).

  This, together with the different possible mass distributions, from a single mass population to rather complex functions Clesse and García-Bellido (2017); Bellomo et al. (2018), allows to set stringent constraints over the whole range; see Carr et al. (2020) for a comprehensive review. Nevertheless, some mass windows are still open, allowing PBHs to account for 100% of the DM abundance Green and Kavanagh (2020). Interestingly, if accounting up to only a

[24] Although not exclusively, see e.g., Zel'dovich and Novikov (1967).

fraction of DM, they are incompatible with WIMP DM, as they would enhance the WIMP annihilation signal, forming detectable mini-spikes in their surroundings Adamek et al. (2019). The prospects for PBHs observational evidence have been optimistically renewed with GW astronomy, which currently allows for detection of $\sim 10 - 100$ M BHs, one of the open mass windows; the detection of GW190521 LIGO Collaboration and Virgo Collaboration (2020), the first intermediate-mass BH (IMBH) fusion with two BHs of masses 85 and 66 M , in tension with traditional BH production from stellar collapse, may be a hint of a PBH population De Luca et al. (2021); Carr et al. (2021). PBHs as DM candidate will also be explored in Chapter 9.

## 1.5 The quest for dark matter

All of the DM candidates presented in the previous Section are a notable theoretical landmark; nevertheless, as any physical theory, they must be validated with experiments. Thus, the search for DM evidence –which can unveil its ultimate nature– with different approaches has received a great amount of attention in the last two decades. Even if no conclusive DM signal has been found yet, these experiments have ruled out many candidates, as well as constraining the possible parameter space for many others, therefore being interesting *per se*.

Searches for compact objects (e.g., PBHs) have their own, well-established methods such as microlensing, which has already been discussed (see Sections 1.1.3 and 1.4.2)[25]. When assuming particle candidates, as those presented in Section 1.4.1, there is a broad range of detection techniques, based on the small couplings to SM particles that kept the hot primordial plasma and DM in thermal equilibrium in the early Universe. Currently, we distinguish three different experimental approaches in these DM searches. The common picture is to assume a certain interaction between SM and DM particles, with a diagram such as the one in Figure 1.12. Depending on how we read the diagram, we distinguish three possible scenarios,

- **Production**: Referred to $SM + SM \rightarrow \chi + \chi$ processes, i.e., DM particle pair creation from interactions of SM particles. These should happen at high-energy particle colliders and appear as missing momentum/energy in the final states.
- **Direct detection**: Referred to $\chi + SM \rightarrow \chi + SM$ processes, i.e., two-bodies scattering. These are detected in nuclear recoil underground experiments, or annual modulation signal detectors.
- **Indirect detection**: Referred to $\chi + \chi \rightarrow SM + SM$ processes, i.e., DM self-annihilation into SM final states, which may include photons, neutrinos and cosmic rays (CRs). By reconstructing these final states, the original DM particle can be inferred[26].

In this Section, we provide a non-exhaustive review of these three DM search avenues by highlighting state-of-the-art results, detection claims and current constraints on the parameter space of DM particles. We will focus on WIMP-like particles results, yet other candidates such as ALPs will be also reviewed.

[25] Again, we defer the interested reader to Carr et al. (2021) for an exhaustive review on PBH search strategies and constraints.

[26] In some models, DM decay into SM particles can also be an indirect probe.

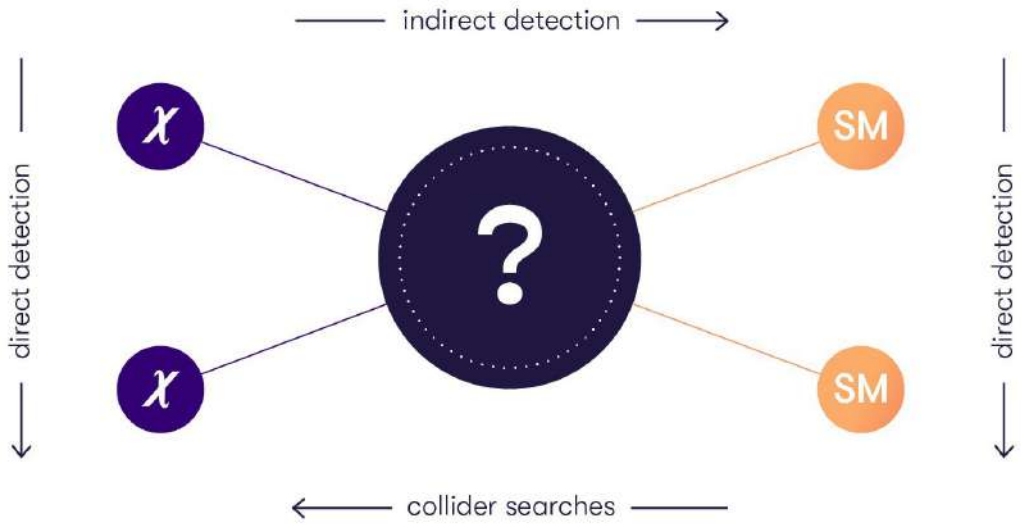


FIGURE 1.12: Schematic view of DM searches based on weak interactions with SM particles. While formally this diagram would only be valid for thermally-produced DM (Section 1.2.2), it may be also applicable to some non-thermally produced particle DM candidates, such as ALPs or sterile neutrinos (Section 1.2.2).

### 1.5.1 Production at colliders

Many of SM particles, such as the gauge bosons Watkins (1986) or the Higgs boson Higgs (1964); Chatrchyan et al. (2012), have been discovered in colliders. The idea of this experimental setup is the collision of SM particles at very high energies/momenta, which produce a cascade of different particles. By reconstructing the energy and momentum of each product in the detectors, new particles may be discovered and characterized. Thus, these are ideal conditions to search for DM if this is weakly interacting with SM.

Nevertheless, there is an experimental limitation in the form of the mass range to probe. Indeed, the most advanced collider at this writing is the *Large Hadron Collider* (LHC)[27] Evans and Bryant (2008), which allows energies as high as 13 TeV (6.5 TeV per beam at the center of mass). Therefore, LHC is capable of probing DM masses up to a few TeV through proton-proton collisions. The current setup in LHC detectors, such as ATLAS ATLAS Collaboration (2008) or CMS CMS Collaboration (2008), roughly consist on calorimeters to reconstruct the energy of each produced particle and chambers to track each trajectory. As DM is electrically neutral and its interaction with SM particles is very weak, the only way to detect them is through missing energy/momentum.

Unfortunately, in the case of LHC it is not possible to check the conservation of energy/momentum on both initial and final particle states, as not the whole proton beams collide, but keep propagating along its original trajectory as particle debris Marsili et al. (2013). Therefore, in this case the useful observables are the missing transverse energy/momentum, which quantify the the fraction of energy/momentum flowing in the perpendicular direction to the beam. The main DM searches at the LHC follow this direction, by searching peculiar morphologies of

[27] https://home.cern/science/accelerators/large-hadron-collider

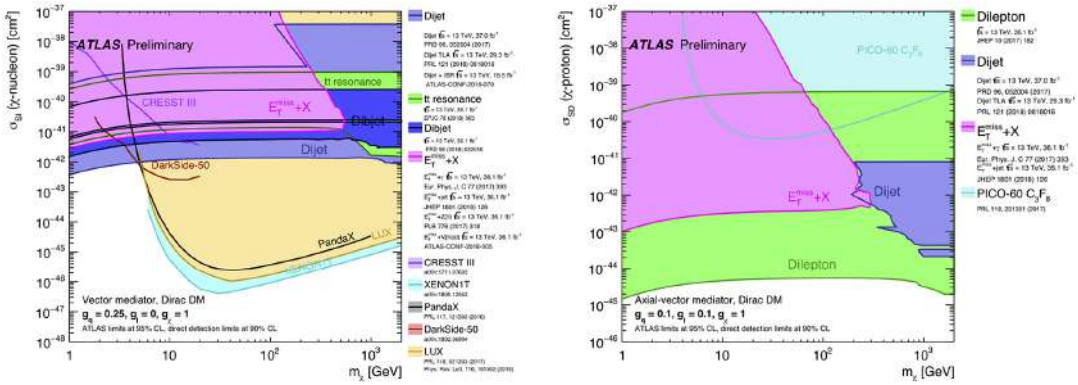


FIGURE 1.13: Comparison of DM constraints from selected direct detection experiments at 90% CL and ATLAS LHC results at 95% CL. **Left panel:** spin-dependent WIMP-proton scattering cross-section in the vector leptophobic model. **Right panel:** spin-independent WIMP-nucleon scattering cross-section constraints in the axial-vector leptophilic model. Figure taken from Giagu (2019).

missing transverse energy in the so-called mono-$X$ final states, where $X$ is a SM particle such as quark/gluon jets, photons or gauge bosons. In these events, the DM particle recoils against the jet, producing particle tracks without an observable particle responsible for it Peskin (2015). The experimental difficulty comes from the fact that not only DM but many other particles can produce these features, such as neutrinos. Therefore, the challenge is to establish criteria which can distinguish between SM background events and DM interactions Abdallah et al. (2015).

Unfortunately, no signal above SM background has been found yet, and only constraints to the DM cross section can be set Giagu (2019). In addition, to connect these constraints to those of direct and indirect probes, a specific DM particle model (for example, a SUSY theory such as $\mu\nu$SSM López-Fogliani and Muñoz (2020)) is necessary. This allows to greatly constrain the parameter space of concrete DM candidates, but usually simplified models and effective field theories are assumed to bracket the possible DM couplings to SM, which are broken down to four-particle operators to describe the interactions Goodman et al. (2010). In Figure 1.13, we plot some of the latest results on LHC DM searches. As mentioned, these are competitive for light DM particles, precisely where the direct search experiments lose sensitivity due to the threshold of recoil energies (see Section 1.5.2). Nevertheless, we must stress that these limits are highly dependent on hidden parameters such as the mediator masses and coupling strengths, and therefore a direct comparison with other search strategies must be done with care Trevisani (2018).

### 1.5.2 Direct detection

As the Earth is orbiting the Sun, which is also orbiting the MW, we are constantly traveling through the MW's DM halo. This effectively translates into a "wind" of billions of DM particles per second penetrating every single object in the Earth, yet completely unaffected given the very weak interaction, if any, with SM particles. Nevertheless, if patient enough, i.e., with sufficient exposure[28], a few DM–SM scattering processes should occur. Direct detection experiments aim to observe

[28] In this Section, exposure is defined as the product of the observation time and the volume (or area) of the detector.

such collisions to extract information on the DM particle nature, as originally proposed in Goodman and Witten (1985). The frequency of these events is enclosed in the so-called differential recoil rate $dR$ per recoil energy $dE_R$ and –assuming elastic scattering– can be computed as Lewin and Smith (1996),

$$\frac{dR}{dE_R} = \frac{M\rho}{m_A m_\chi} \int_{v_{min} \leq v \leq v_{esc}} v f(v) \frac{d\sigma}{dE_r} d^3v \tag{1.34}$$

In this formula there are contributions from particle physics and astrophysics. The first includes $M$ (the total mass of the target), $m_A$ (the mass of the target nuclei), and $d\sigma/dE_r$ (the differential scattering cross section between WIMP and nuclei); the latter includes $\rho$ (the local DM density in the Solar System[29]), $v$ (the velocity of DM particles) and $f(v)$ (their normalized velocity distribution). The integration is done between a minimum velocity $v_{min}$ given by,

$$v_{min} = \left(1 + \frac{m_A}{m_\chi}\right) \sqrt{\frac{E_r}{2m_A}} \tag{1.35}$$

and $v_{esc}$, which is the Galactic escape velocity $v_{esc}$ as determined by $f(v)$, and therefore truncates the velocity integration. This is currently estimated at $v_{esc} \sim 530\,\mathrm{km \cdot s^{-1}}$ Piffl et al. (2014); Deason et al. (2019). $f(v)$, on the other hand, in rather uncertain. The common picture is the so-called Standard Halo Model (SHM) (Green (2012); Cerdeño et al. (2016)), in which the DM halo is spherical and isothermal with a smooth DM density decreasing as $\rho \sim r^{-2}$ from the Galactic Center (GC). This assumption leads to a featureless phase space with a Maxwell-Boltzmann velocity distribution of DM particles in the MW halo, which is supported by hydrodynamic N-Body simulations (see, e.g., Bozorgnia et al. (2016); Kelso et al. (2016); Sloane et al. (2016)). Nevertheless, different simulations also point towards a deviation from a Maxwellian distribution, therefore indicating that the MW's halo morphology is different from the assumed by SHM Petač (2020), including effects such as substructure originating from tidal streams and stellar debris flows Kavanagh and O'Hare (2016).

Regarding the $dR/dE_R$ presented in Eq. 1.34, we can split the total scattering into two terms: a spin-independent (SI) and spin-dependent (SD) contribution. This allows to overcome the actual, unknown scattering process by describing both terms separately, in terms of effective operators. In particular, the Lagrangian for SI processes is based on scalar couplings between DM–SM,

$$\mathcal{L}_{SI} \sim \bar{\chi}\chi\bar{q}q \tag{1.36}$$

While SD processes are based on axial-vector couplings[30], and their Lagrangian is of the form,

$$\mathcal{L}_{SD} \sim \bar{\chi}\gamma^\mu\gamma_5\chi\bar{q}\gamma_\mu\gamma_5 q \tag{1.37}$$

The differential WIMP DM-nucleus scattering cross section can be expressed as a sum of both SI and SD contributions,

$$\frac{d\sigma}{dE_R} = \frac{1}{2m_A v^2}\left(1 + \frac{m_A}{m_\chi}\right)^2 \left[\sigma_{SI}F_{SI}^2(E_R) + \sigma_{SD}F_{SD}^2(E_R)\right] \tag{1.38}$$

[29] Current estimates yield $\rho \sim 0.3 - 0.5\,\mathrm{GeV \cdot cm^{-3}}$ Sivertsson et al. (2018); Guo et al. (2020); de Salas and Widmark (2020).

[30] Vector couplings also lead to SI scattering processes. Such couplings require the DM particle to be a Dirac fermion, while WIMPs are usually assumed to be of Majorana type, i.e., their own antiparticles.

where $F(E_R)$ are the form factors, which account for the shift from coherent to incoherent scattering due to DM and SM particles energies – given the range of probed WIMP masses, $m_\chi \sim 1 - 100$ GeV, the DM particle de Broglie wavelength is larger than the nuclei so scattering is coherent; nevertheless, this may not be true for high kinetic energies or for some nuclei. The form factors will correct for these phenomena and suppress the rate in case of incoherent scattering Barello et al. (2014); Sierra et al. (2019). The cross sections $\sigma_{SI}$ and $\sigma_{SD}$ depend on the target's material, scaling as $A^2$ (where $A$ is the atomic mass number) in the first case, while is determined by the nucleus spin in the latter Lin (2019). Therefore, SI scattering is more frequent in targets composed of heavy nuclei, while SD scattering is not necessarily correlated with increasing atomic mass number, but with the internal spin structure[31].

**Nuclear recoil experiments**

We will first review nuclear recoil experiments, aiming to directly detect the recoil energy of DM-nucleus scattering as described. The most common choices for the target material are Xenon (Xe) and Argon (Ar). Xe-based detectors are the usual setup because is a heavy, stable nucleus, which boosts the SI DM-nucleus scattering events, while being more sensitive to SD DM-neutron scattering. Some of these detectors are LUX LUX Collaboration (2010), PandaX-II Panda Collaboration (2016) and XENON1T Aprile (2013), which is currently the most competitive Xe detector. The hardest challenge in these detectors is to isolate them as much as possible to reduce the SM-interactions background noise. None of these experiments have detected a clear DM signal, therefore setting constraints to the $\sigma - m_\chi$ parameter space. The most stringent limits come from XENON1T, which consists on 3.5 tons of liquid Xe, with accumulated exposure of $10^6$ kg $\times$ d, and excludes at 90% CL SI cross sections $\sigma_{SI} \gtrsim 4.1 \times 10^{-47}\text{cm}^2$ at its peak sensitivity around $m_\chi \sim 30$ GeV Aprile et al. (2019).

Nevertheless, XENON1T has detected a $3.5\sigma$ excess over the expected background at energies between 1–7 keV Aprile et al. (2020). When analyzing the expected events in this energy range, XENON1T observed 285 events, while $232 \pm 15$ were expected. The excess is present at the region where XENON1T is less sensitive, at the peak sensitivity is for $E \gtrsim 20$ keV. Likewise, a local $\sim 4\sigma$ defect is found at 17 keV, which we show in Figure 1.14. At this writing, the most plausible explanations are possible tritium contamination and, regarding new physics, a solar axion signal, a bosonic dark matter signal with $m\chi \sim 2.3$ keV, and a solar neutrino signal with enhanced magnetic moment. The limitation of Xe-based detectors is their sensitivity for DM masses below a few GeV, as they have an energy threshold of $5 - 10$ keV. When dealing with light DM particles, the strongest constraints come from Ar-based detectors such as DarkSide–50 DarkSide Collaboration (2015).

However, future experiments, which are expected to improve the current constraints by 1 or even 2 orders of magnitude, such as PandaX-4T Panda Collaboration (2018), LUX-Zeplin LZ Collaboration (2020) and XENONnT XENON Collaboration (2020), are expected to reach the so-called *neutrino floor* Wyenberg and Shoemaker (2018). This is the level at which SI scattering between SM neutrinos and nuclei happens, therefore not allowing a clear distinction between DM and neutrino events Mayet et al. (2016); Bœhm et al. (2019). Nevertheless, some solutions are possible, such as directional gas time projection chambers, which are able to reconstruct the

[31] "Spin structure" refers to phenomena such as unpaired spins in the nuclei, which may vary between protons and neutrons, enhancing DM-proton or DM-neutron scattering Schumann (2019).

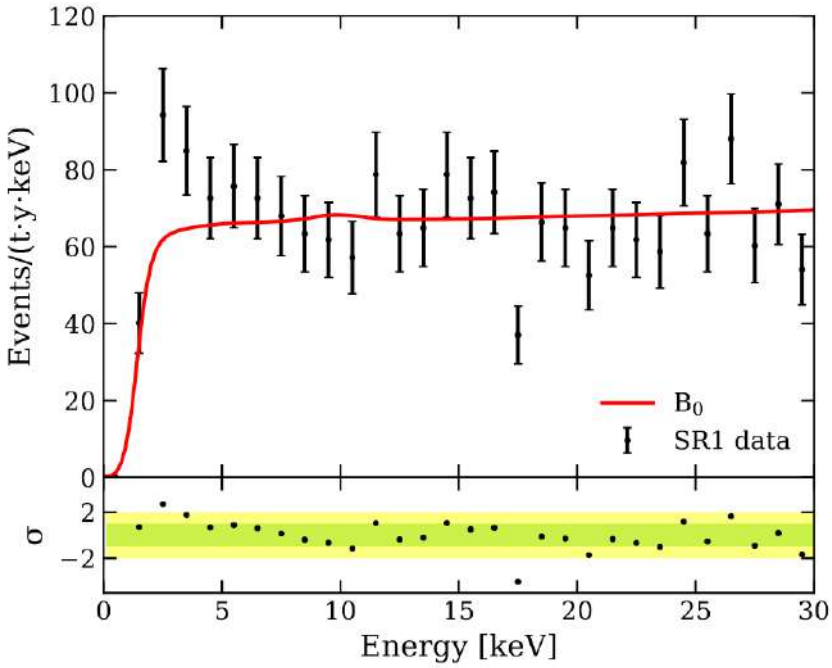


FIGURE 1.14: XENON1T recoil event excess at $1-7$ keV. Black error bars are the binned data, while red line is the background model. An excess is found at the lower bins, while a defect is present at 17 keV. Lower panel shows the difference in standard deviations, with green and yellow bands showing 1 and $2\sigma$ significance, respectively. Figure taken from Aprile et al. (2020).

direction of the incoming particle O'Hare (2020). In Figure 1.15 we show a compilation of different constraints on $\sigma_{SI}$ from direct detection experiments, as well as the theoretical neutrino floor.

There are also results on SD scattering from noble liquid detectors, the most stringent again set by XENON1T, at the level of $\sigma_{SD} \sim 7 \times 10^{-42}\text{cm}^2$ for neutron scattering at the $m_\chi \sim 30$ GeV peak sensitivity. The constraining power for proton scattering is weaker, and can be better probed with fluorine targets, as in the PICO–60 experiment Amole et al. (2019), consisting on a bubble chamber filled with $C_3F_8$. The derived limits for such interaction improved XENON1T results a factor $\sim 10$. Similarly to Figure 1.15, we show a collection of SD constraints in Figure 1.16 for both proton and neutron scattering.

#### Primakoff effect axion searches

Axions and ALPs can also be directly detected, but not with scattering processes as WIMP-like particles. Indeed, the most suitable approach for axions is the Primakoff effect Primakoff (1951). This describes the conversion of axions into photons in the presence of external magnetic fields, a possible interaction thanks to the axion-photon coupling (see Eq. 1.33). Experiments such as ADMX cavity haloscope van Bibber and Carosi (2013) have performed these searches by using strong magnetic fields and a microwave cavity, with a resonance frequency tied to the coupling constant $g_{a\gamma\gamma}$. Therefore, by tuning the cavity resonance frequency, the axion parameter space can be probed. The latest ADMX results rule out QCD axions with masses in the range $m_a = [2.81 - 3.31]\ \mu$eV Braine et al. (2020).

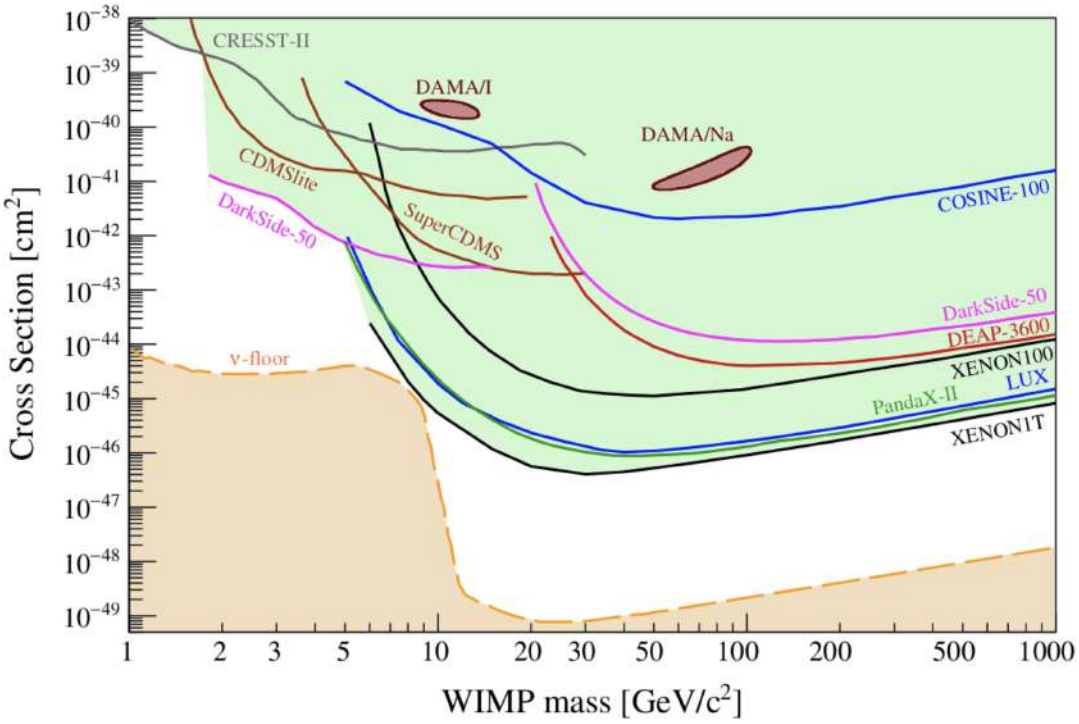


FIGURE 1.15: Compilation of different nuclear recoil experiments 90% CL constraints on $\sigma_{SI}$ for WIMP DM. Orange, dashed line is the so-called neutrino floor, where $\nu-$nuclei interactions are indistinguishable from DM scattering. Figure taken from Lin (2019).

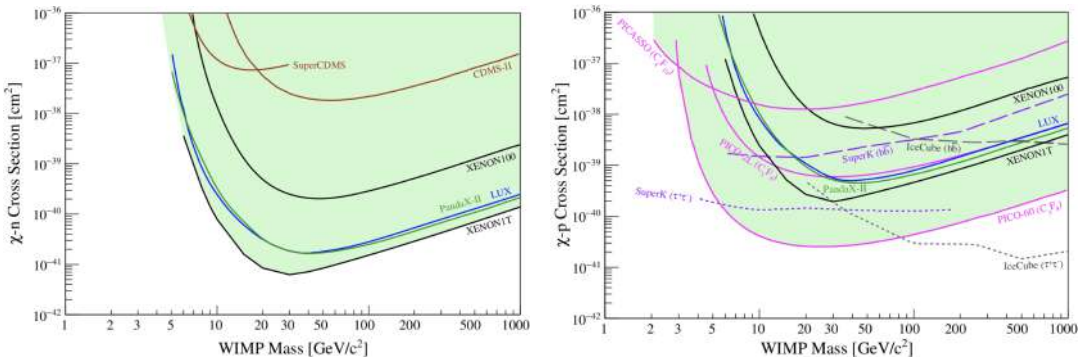


FIGURE 1.16: Same as Figure 1.15, but for SD scattering. **Left panel:** DM-neutron scattering. **Right panel:** DM-proton scattering. Figures taken from Schumann (2019).

### Annual modulation experiments

As we introduced at the beginning of this Section, the expected DM "wind" is produced by the Earth orbiting the Sun at $v_\oplus \sim 30$ km $\cdot$ s$^{-1}$, which orbits the MW at $v \sim 230$ km $\cdot$ s$^{-1}$. Therefore the Earth will be "navigating" in favour of the DM wind half of the year, and viceversa the other half. This will shift the velocity distribution towards larger or smaller values, therefore making the rate of scattering events to suffer a modulation with a yearly period Froborg and Duffy (2020).

The most famous annual modulation experiment is DAMA/LIBRA Bernabei et al. (2008). The experimental setup consists on a 250 kg radio-pure NaI scintillating crystal, which measures the nuclear recoil of DM-nucleus scattering. After 20 years of data taking, DAMA/LIBRA has found an annual modulation signal which

reaches a spectacular $\sim 13\sigma$ significance between 2–6 keV in the latest results, with 1.13 ton $\times$ yr exposure Bernabei et al. (2018). The reported modulation signal, shown in Figure 1.17, is in remarkable agreement with the theoretical prediction.

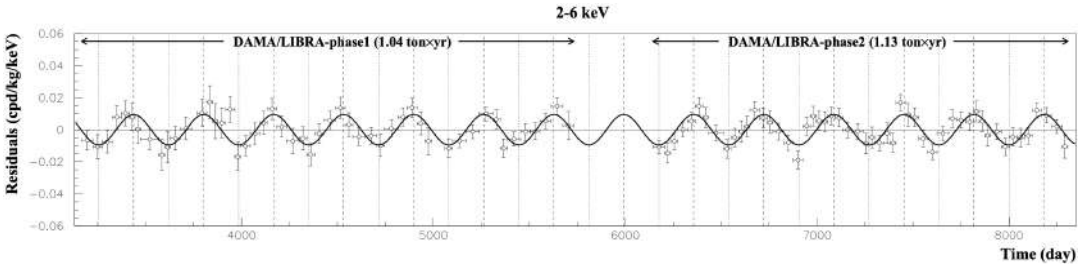


FIGURE 1.17: Experimental residual rate of the scintillation events measured by the DAMA/LIBRA experiment in the 2–6 keV energy range, as function of the time. The overimposed curve is the theoretical prediction for DM modulation in the form of co-sinusoidal function $A \cdot cos[\omega(t - t_0)]$, where the period $T = 2\pi\omega$ is 1 year and the phase is $t_0 = 152.5$ days, corresponding to June 2nd. The modulation amplitude $A$ is obtained with the data best-fit. Figure taken from Bernabei et al. (2018).

Nevertheless, in Figure 1.15 DAMA/LIBRA signal is shown, falling well within the excluded parameter space region by several experiments. This tension has some solutions, such as unknown backgrounds, possible systematic errors in the NaI material, and data analysis issues Blum (2011); Nygren (2011); Klinger and Kudryavtsev (2015); Stiegler et al. (2017); McKinsey (2018). Other detectors, such as currently in operation COSINE–100 COSINE-100 Collaboration (2021), XMASS XMASS Collaboration (2018), and ANAIS–112 Amaré et al. (2019), as well as future SABRE Antonello et al. (2019) have been developed, aiming to enforce or reject the DAMA/LIBRA signal. ANAIS-112, also consisting on NaI scintillators, did not observe annual modulation in the first year and a half of operation Amaré et al. (2019), currently at $\sim 2\sigma$ tension with DAMA/LIBRA results, and expecting to reach a $3\sigma$ significance in the first 4–5 years of data taking.

### 1.5.3 Indirect detection

The last search strategy for DM is based on the detection of by-products of DM annihilation or decay. It is complementary to collider searches (Section 1.5.1) and direct detection (Section 1.5.2), by not observing directly the DM particle in a controlled laboratory, but at a non-controlled environment provided by the Universe itself. Additionally, indirect detection is able to probe properties such as the co-annihilation cross section, responsible for the thermal generation of the relic abundance, therefore linking present-time, local physics with early Universe Cosmology.

Although this co-annihilation is central in WIMP DM models, its ultimate, underlying physics is unknown, yet the outcome of such annihilation must be a pair of SM particles, such as quarks $(t, b, u, d, s, c)$, gauge bosons $(\gamma, W^{\pm}, Z^0)$, leptons $(e^{\pm}, \mu^{\pm})$, or the Higgs boson. These are in general not final, stable states, and will either decay into stable particles or suffer processes such as hadronization. Therefore, the final particles generated by this process will be photons (due to the WIMP typical masses, they will fall within the gamma-ray range), neutrinos, and charged particles, which include $e^{\pm}$, $p/\bar{p}$, and heavier nuclei and antinuclei, i.e., CRs. The major part of the particles in the Earth atmosphere are protons ($\sim$86%), helium nuclei ($\sim$11%),

and electrons (∼2%), being the ∼1% remaining antimatter in different forms Perkins (2003). Therefore, identifying the matter contribution from DM is very challenging due to the high contamination, while it is easier to detect its antimatter products.

Indeed, the possible channels for DM indirect detection are photons, neutrinos and CRs. The two first have the advantage of being neutral particles, therefore not being deflected by the Galactic magnetic fields. This allows, in principle, to track the original source[32]. On the other hand, neutrinos are very difficult to detect due to their very weak interaction rate, which makes photons the "golden channel" for these kind of DM searches. Nevertheless, they are attenuated at cosmological distances due to the *Extragalactic Background Light* (EBL) Primack et al. (2011), as we will further review in Chapter 2, restricting gamma-ray target-based searches to Galactic and galaxy cluster scales.

Another possible search strategy, very recently developed, does not use particle messengers but effects of DM on the dynamics of MW's stellar streams (see Section 1.1.2). Indeed, the gaps in stellar streams can be used to infer not only the population of DM subhalos, but the properties of WDM particles, such as their mass, as proposed in Banik et al. (2018, 2019); Hermans et al. (2020).

In this Section we will summarize the current status of the different venues in indirect DM searches. We will emphasize the gamma-ray channel, as it is the central topic of this Thesis. More detailed reviews are presented in, e.g., Conrad (2014); Cirelli (2015); Gaskins (2016); Slatyer (2017); Leane (2020).

#### Neutrinos

As mentioned, neutrinos are good messengers of DM interactions due to their electrical neutrality. Moreover, their extremely weak interaction with any other SM particle makes them travel in perfect straight lines with almost no flux loss, as their scattering probability is negligible. Thus, they can probe DM at any scales, from MW and its satellites up to cosmological distances. Unfortunately, this advantage is also their biggest drawback, as detecting them is a titanic task. As neutral particles, the only way to detect a neutrino is via the interaction with SM particles. To maximize the probability of observing such event, we must increase as much as possible the exposure as defined in Section 1.5.2, i.e., go to very large volumes and/or times. Indeed, the current generation of neutrino telescopes uses the Cherenkov effect Cherenkov (1960) as signature of these events. This requires a highly pure (transparent), yet dense environment, as shielded as possible from radiation sources. Current observatories use the Antarctica ice, in the case of IceCube IceCube Collaboration (2017), and the Mediterranean Sea water, in the case of ANTARES ANTARES Collaboration (2011).

Given the scarce number of detected neutrinos, and the typical uncertainties associated with their trajectory, it is not possible to study extragalactic objects with neutrinos. In fact, the blazar TXS 0506+056 is the first and only extragalactic known astrophysical source to emit neutrinos, when detected in coincidence with gamma rays during a flaring state IceCube Collaboration (2018). This is just the third source known to emit neutrinos, after the supernova SN 1987a Hirata et al. (1987) (by its nature, a transient source) and the Sun, where the so-called "solar neutrino problem"

[32]Cosmic rays originated in the MW, which can go up to energies ∼PeV, are indeed deviated. Nevertheless, ultra-high energy CRs (UHECRs) with energies even beyond ∼EeV, of extragalactic origin, are barely affected by the Galactic magnetic fields due to their immense energy. This makes UHECRs observatories, such as the Pierre Auger, to have a certain directional sensitivity Farrar and Sutherland (2019).

triggered the discovery of neutrino flavour oscillation Haxton (1995). Therefore, the latter is currently the only viable option among known neutrino-emitter sources to search for DM.

Since its formation, DM is expected to accumulate in the Sun's core, annihilating into SM particles. Photons produced in the core can take a very long time, $\mathcal{O}(10^6)$ years, to reach the surface due to the interaction rate in the extremely dense environment. On the other hand, neutrinos are able to escape due to its low interaction probability. Those neutrinos originated by DM annihilation are much more energetic than standard solar neutrinos, generated by nuclear fusion. Therefore, they just have to be discriminated against the expected neutrino background produced by CRs interactions with the Sun's atmosphere IceCube Collaboration (2021). As already mentioned, the scarce detected neutrino flux makes the accumulated exposure to grow much slower than, e.g., in gamma-ray telescopes, and corresponding constraints will be orders of magnitude weaker than those obtained by other means IceCube Collaboration (2017).

Another possible target is the GC. Although this is not a known neutrino source, the high DM concentration and relatively small distance makes it an excellent target for DM searches (see Section 1.5.3 for a review on the GC gamma-ray searches). Both IceCube and ANTARES have scrutinized the region looking for DM signatures in neutrino events, with null result ANTARES Collaboration and IceCube Collaboration (2020). Nevertheless, the $m_\chi - \langle\sigma v\rangle$ parameter space can be constrained, as we show in Figure 1.18. Again, these are not comparable to the obtained constraints by other means, being $\sim$ 2 orders of magnitude away from the thermal relic cross section value.

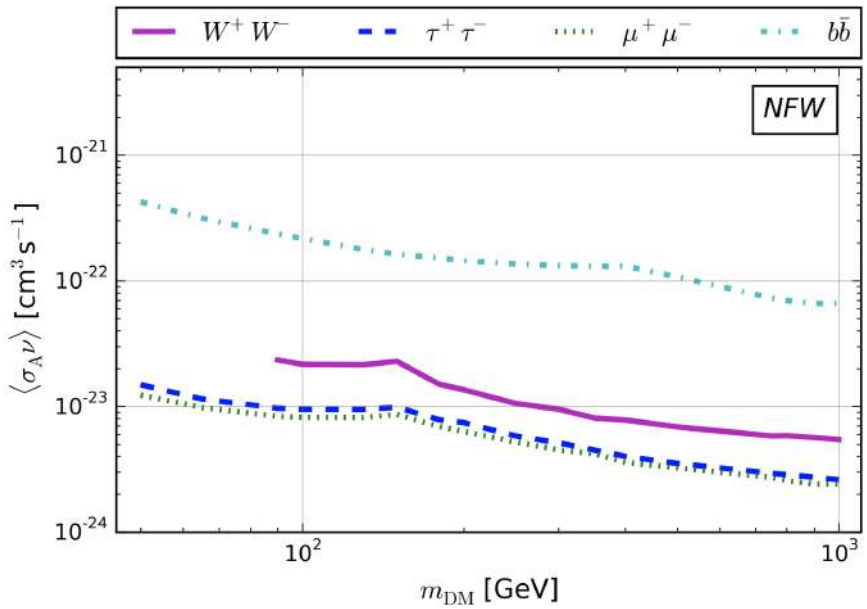


FIGURE 1.18: WIMP DM constraints set by joint observations of the GC by IceCube and ANTARES, for a variety of annihilation channels. An NFW DM density profile is assumed. Figure taken from ANTARES Collaboration and IceCube Collaboration (2020).

Besides these targets, IceCube can study the most energetic neutrinos in a DM context, above $\sim$ 10 PeV Ishihara and IceCube Collaboration (2016). These cannot be due to WIMP DM annihilation, as the corresponding DM particle mass generating them would be beyond the unitarity limit Smirnov and Beacom (2019). Instead, if

originated by DM particles, they have to be due to their decay Esmaili and Serpico (2013); Chianese et al. (2019), where no unitarity bound is violated.

### Cosmic rays

Cosmic rays, in the form of antiparticles, are a standard probe of WIMP DM annihilation. As mentioned, antiparticles are a negligible part of CRs, yet possible products of DM annihilation, therefore being interesting messengers to explore[33]. These are formed by interactions of matter primary CRs with the interstellar medium, from when they are known as secondary CRs. This makes fluxes of both astrophysical- and DM-originated CRs at least of the same order of magnitude.

Current CR-based DM searches are mainly based on positrons, antiprotons and antideuterons. Being charged particles, several effects have to be included, such as EM intra-galactic phenomena. A crucial difference with respect to gamma rays, as we will review in the next Section, is that these searches are restricted to Galactic CRs, because the extragalactic charged antiparticles flux is negligible, as they i) are marginally generated by astrophysical processes, and ii) present a sharp cutoff for energies in the TeV domain AMS Collaboration (2016). The majority of CRs come from the Galactic disk, as they host star-forming regions, which yield a very important fraction of them. The MW disk has a thickness of roughly 25 kpc, which lowers to just $\sim$350 pc in the so-called "thin disk" region. The MW's spiral arms are also embedded in the disk, and can be described as a logarithmic spiral with four arms Shen and Zheng (2020).

Inside the disk we can distinguish several phenomena taking place, such as i) energy losses in inelastic scattering with the interstellar medium, ii) plasma shock-wave induced reacceleration, as well as magnetic anisotropies (so-called *Fermi accelerations* Perkins (2003)), iii) annihilation processes in the interstellar medium, and iv) a stabilising Galactic wind, which will create an outflow of low-energy particles from the disk Maurin et al. (2001). Additionally, CRs will be affected by the Galactic magnetic field, which nowadays can be estimated from observations Ordog et al. (2017); Unger and Farrar (2017). This field is not restricted only to the disk region, but extends up to its outskirts Badhwar and Stephens (1977), thus generating complex CR dynamics.

Indeed, the Galactic magnetic field can be split into two different contributions: a homogeneous part, which is correlated to the spiral arms, and a inhomogeneous and turbulent component Beck and Wielebinski (2013). The latter will affect the propagation of any charged particle, in particlar CRs, through the so-called "Alfvén waves", perturbations due to this irregular magnetic field which will create a Brownian-like, random trajectory for low-energy particles Perkins (2003); Thomas and Pfrommer (2019). The complex propagation of CRs in the MW can be modelled with the transport equation, computing the diffusion and loss of charged particles. This models the spatial and energy distribution of the function $f \equiv dn/dT$, where $n$ is the CR number density and $T$ their kinetic energy. The transport equation is usually written as Boudaud, Cirelli, Giesen and Salati (2015),

$$\frac{\partial f}{\partial t} - \nabla \left[ \mathcal{K}(T) \nabla f - \vec{V}_C(\vec{r}) f \right] - \frac{\partial}{\partial T} \left[ b(T,\vec{r}) f - \mathcal{K}_{EE}(T) \frac{\partial f}{\partial T} \right] = Q(T,\vec{r}) \qquad (1.39)$$

[33] Additionally, the matter-antimatter asymmetry of the Universe makes antiparticles much rarer than "standard" particles.

This complex equation can be broken down into the different terms,

- $\frac{\partial f}{\partial t}$ is the time evolution of $f$; as CRs are usually considered in steady state, this term is generally neglected.
- $\nabla \left[ \mathcal{K}(T) \nabla f - \vec{V}_C(\vec{r}) f \right]$ features the energy-dependent diffusion coefficient $\mathcal{K}(T)$, which describes the overall result of the deflections of the particle in the magnetic field, and is further parametrized as Salati et al. (2010),

$$\mathcal{K}(T) = \mathcal{K}_0 \beta \left( \frac{\mathcal{R}}{GV} \right)^{\delta} \tag{1.40}$$

  where $\mathcal{K}_0$ is a normalization constant, $\beta = v/c$, $\mathcal{R} = pc/Ze$ is the so-called CR rigidity factor, depending on the particle momentum $p$ and proton number $Z$, and $\delta$ is a constant spectral index. This diffusion coefficient is also assumed as constant, therefore lacking a spatial dependence. The second term, $\vec{V}_C(\vec{r}) f$, describes the convective process due to the Galactic wind in the disk, which will create an outflow of particles vertically outwards the disk.
- $\frac{\partial}{\partial T} \left[ b(T, \vec{r}) f - \mathcal{K}_{EE}(T) \frac{\partial f}{\partial T} \right]$ takes into account the energy losses and reacceleration processes suffered by the particles, and also consists of two different terms. $b(T, \vec{r})$ is the energy loss of a CR species, and $\mathcal{K}_{EE}$ parametrizes the drift effect of Alfvén waves on CRs Maurin et al. (2001),

$$\mathcal{K}_{EE}(T) = \frac{2}{9} \frac{E^2 \beta^4}{\mathcal{K}(T)} V_a^2 \tag{1.41}$$

  These drifts are characterized by a velocity $V_a$, which produce diffusive reaccelerations of the particles due to the Fermi accelerations, the diffusion coefficient $\mathcal{K}(T)$, the particle energy $E$ and its velocity $\beta$. Therefore, attending to this expression, the more efficiently CR particles can diffuse, the fewer collisions occur, and the weaker is the energy diffusion Boudaud, Cirelli, Giesen and Salati (2015).
- $Q(T, \vec{r})$ encloses a number of source/sink terms, and codifies both the astrophysical background sources and the possible DM source term.

Therefore, the problem is reduced to solve the transport equation. Semi-analytic solutions are possible with a number of assumptions, such as possible symmetries leading to simplifications and/or cancellations of some of the terms . Nevertheless, to obtain a satisfactory answer which realistically renders the CR transport in the galaxy, the numerical approach is the only solution. This requires a partial differential equation solver code, such as the *Diffusion Reacceleration and Advection of Galactic cosmic rays: an Open New code* DRAGON[34] Evoli et al. (2017) and the *GALactic PROPagation code* GALPROP[35] Vladimirov et al. (2011), two of the most popular, publicly available CR-transport software tools. We will now review the CRs searches with positrons, antiprotons and antinuclei.

[34] https://github.com/cosmicrays
[35] https://galprop.stanford.edu/

1. **Positrons:** These are generated mainly by the spallation of high-energy primary CRs in the interstellar medium. Their main source is the collision between protons and H, producing charged pions, which will eventually decay into muons and these will decay into positrons, i.e., $p + H \rightarrow \pi^+ \rightarrow \mu^+ \rightarrow e^+$. Positron CR flux is measured with the so-called positron fraction (PF) Boudaud et al. (2015),

$$PF = \frac{\Phi(e^+)}{\Phi(L)} = \frac{\Phi(e^+)}{\Phi(e^+) + \Phi(e^-)} \tag{1.42}$$

Where $\Phi(e^\pm)$ is the flux of electrons $(e^-)$ and positrons $(e^+)$ and $\Phi(L)$ is the leptonic flux, sum of positron and electron flux. Working with this fraction instead of just $\Phi(e^+)$ is useful because systematics of both $\Phi(e^\pm)$ will cancel, as they have common sources. From purely astrophysical considerations, $\Phi(e^+)$ is expected to have a drop at GeV energies due to diffuse propagation (Eq. 1.39). Yet, PF is much larger than theoretically expected at those energies, as measured by balloon experiments TS93 and HEAT in the 1990s Golden et al. (1996); HEAT Collaboration (1997). Early DM claims Baltz et al. (2002), based on theoretical proposals such as Turner and Wilczek (1990), were boosted with the measurements of the space-borne *Alpha Magnetic Spectrometer* (AMS-01) AMS-01 Collaboration (2007) and the the *Payload for Antimatter Matter Exploration and Light-nuclei Astrophysics* (PAMELA) PAMELA Collaboration (2009), which confirmed this trend up to 100 GeV. Surprisingly, PAMELA was able to measure the CR antiproton-to-proton ratio, which was in agreement with the theoretical predictions PAMELA Collaboration (2010). A way to reconcile both measurements is "leptophilic" DM Cirelli et al. (2009), which favour the annihilation into leptonic final states, while avoiding quarks. In order to explain the data, the DM particle mass must be in the TeV scale, with large annihilation cross sections, 2–3 orders of magnitude above the thermal relic value Boudaud et al. (2015). This is in tension with measurements from, e.g., CMB Planck Collaboration (2020a), yet it could still be a viable candidate for smaller cross sections, which are reachable provided a sufficient subhalo signal boost or DM decay instead of annihilation processes Ibarra et al. (2013).

More recent measurements of PF by *Fermi*-LAT and the AMS-02 instrument Carquín et al. (2016) confirm this excess. Without invoking a DM origin, a possible explanation may be near PSRs, which produce positrons in their magnetosphere and would act as an additional source term in $Q(T, \vec{r})$ (Eq. 1.39) Di Mauro et al. (2014). This hypothesis, however, seems not enough according to HAWC data from two nearby gamma-ray PSRs HAWC Collaboration (2017). Although PF is convenient, AMS-02 is capable of accurately measuring $\Phi(e^+)$ up to 1 TeV energies AMS Collaboration (2019). This data indicates that the best fit is with the astrophysical positron component from the primary CR spallation on the interstellar medium, and an additional source term which presents an exponential cutoff at 800 GeV. This additional term is preferred at more than $4\sigma$ significance. Additional data is needed to clarify whether this indicates a DM or PSR component.

2. **Antiprotons:** Similarly to positron CRs, antiprotons CRs are produced by spallation of high-energy primary CRs on the H or He present in the interstellar medium. These processes conserve charge and baryonic number, therefore

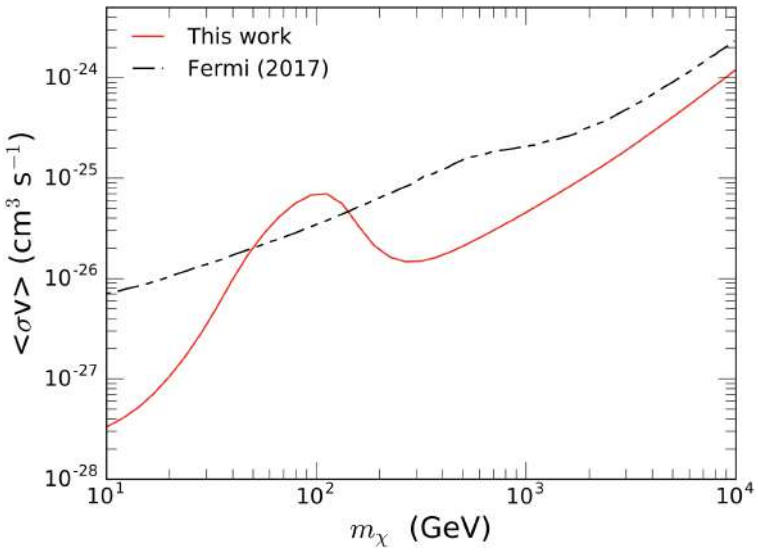


FIGURE 1.19: 95% CL upper limits to the DM annihilation cross section with AMS-02 antiproton data, assuming annihilation into $b\bar{b}$. Dot-dashed line shows the derived limits from the *Fermi*-LAT dSphs (see Section 1.5.3). Figure taken from Cui et al. (2018).

having an energy threshold for the initial primary protons to generate an antiproton Bergstrom et al. (1999). This way, antiproton CRs will be produced at larger kinetic energies. Indeed, the theoretical prediction for the antiproton CR background peaks at a few GeV, while decreasing at lower energies due to the production threshold, and at higher energies for analogous reasons as positrons Bringmann and Salati (2007). Indeed, the analogy with positrons make define the boron-to-carbon ratio (B/C), which is inferred from their respective nuclei fluxes, and can be measured by CRs experiments such as AMS-01 and PAMELA up to ∼180 GeV. Contrary to positrons, the measurements are in agreement with the predictions within uncertainties, coming mainly from the propagation parameters.

This picture has recently changed with the publication of AMS-02 antiproton data, which extends the energy range up to 500 GeV AMS Collaboration (2016). By using these measurements, there is an antiproton excess between 10–20 GeV, although there are claims that it is the result of systematic errors Heisig et al. (2020). The DM interpretation of this excess leads to a $\sim 3\sigma$ preference, pointing to a best-fit mass between 30 and 200 GeV, depending on the assumed annihilation channel, with cross sections around the thermal value Cholis et al. (2019). From a conservative point of view, DM constraints from co-annihilation can be placed, as presented in Figure 1.19.

3. **Antinuclei:** antimatter CRs, heavier than antiprotons, can be produced by the same spallation processes as positrons and antiprotons. However, in this case, the energy threshold is higher than for antiprotons, which will suppress the astrophysical expected background Ibarra and Wild (2013). From a DM point of view, its co-annhihilation or decay may produce low-energy antinuclei, mostly in the form of antideuterium. This is only expected to be produced in these processes, therefore constituting a "smoking gun" for DM detection with CRs Donato et al. (2000). Unfortunately, at this writing no antideuteron has been detected by AMS-02, yet future experiments, such as the *Gaseous Antiparticle*

*Spectometer* (GASP) Aramaki et al. (2016) may further explore this search strategy.

Antihelium, on the other hand, has been detected by AMS-02, which is more surprising than antideuteron, as current models yield as negligible antihelium production due to its much higher threshold Coogan and Profumo (2017). A DM explanation is strongly disfavoured, as no mechanism is able to explain the boosted antihelium production in detriment of antideuterium.

### Gamma rays

As mentioned in the introduction of this Section, gamma rays are a "golden channel" in indirect DM detection. Indeed, being electrically neutral they will not be deviated by magnetic fields, therefore enabling a tracking of the original source, as well as being much easier to detect than neutrinos. Thus, it is possible to study specific targets in the sky, especially those predicted to have high concentrations of DM (see Section 1.3). This is interesting for DM searches because the signal is proportional to the target DM density in case of decay processes, and to the squared DM density for co-annihilation events. These targets will therefore be highly DM-dominated objects, such as dark subhalos, the GC, MW dSphs, field galaxies such as irregular galaxies (dIrrs), and galaxy clusters. Other probes include the extragalactic gamma-ray background (IGRB), which is formally not a specific target but rather a search strategy. Currently, the most stringent constraints on annihilating DM come from dSphs observed with *Fermi*-LAT Fermi-LAT Collaboration and DES Collaboration (2017). In this Section we will review the results of these and other searches, leaving a detailed discussion of gamma-ray observation techniques for Chapter 2.

The DM emission from these targets is characterized by the "DM prompt emission", which refers to gamma rays created by annihilation or decay events, in a quasi-instantaneous regime at the DM particle(s) position. Prompt gamma rays may be the direct product of DM annihilations or decay, e.g., $\chi\chi \rightarrow \gamma\gamma$, or final states from decaying intermediate particles, e.g., $\chi\chi \rightarrow X + Y + ... \rightarrow \gamma + Z + ....$ There may also be secondary gamma rays, mainly produced by the interaction of leptonic primary DM annihilation/decay products with the interstellar medium or the Galactic field. Effects such as Inverse Compton (IC) scattering on low-energy particles, Bremsstrahlung or synchrotron radiation generate gamma rays Cirelli et al. (2011).

DM searches are usually performed looking for the prompt gamma-ray emission. DM co-annihilation can be computed as the differential flux $dN_\gamma$ per energy $E_\gamma$ and solid angle unit $d\Omega$ as Rico (2020),

$$\frac{dN_\gamma}{dE_\gamma d\Omega}(E_\gamma, \psi)_{\text{ann}} = \frac{1}{4\pi}\int_{l.o.s} dl(\psi)\rho_\chi^2(\vec{r})\frac{\langle\sigma v\rangle}{2S_\chi m_\chi^2}\sum_i B_i\left(\frac{dN_\gamma}{dE_\gamma}\right)_i \tag{1.43}$$

where $\psi$ is the direction of the observation, $\rho_\chi$ is the DM density profile (see Section 1.3), and the integration is performed along the line of sight (l.o.s). This encloses the astrophysical information on the source, while the particle physics is codified in the rest of terms, which include the $S_\chi$ factor, which is 1 for Majorana DM and 2 for Dirac particles, the branching ratio $B_i$, which describes the possible distribution of DM annihilation amongst more than one annihilation channels[36], and $\left(\frac{dN_\gamma}{dE_\gamma}\right)_i$ is the number of photons per annihilation into the channel $i$. Assuming the annihilation

[36] Although normally the analysis are performed assuming $B = 1$ for different channels, more complex analysis are possible, assuming up to 3 annihilation channels Di Mauro and Winkler (2021), or even a mass-dependent $B$ in models such as branons Cembranos et al. (2012).

rate and spectrum are independent from the Galactic DM velocities $v(\vec{r})$ (so-called s–wave annihilation, in opposition to p–wave annihilation which depends on it Johnson et al. (2019)), the particle physics part can be pulled out from the integration. In this case, spatial distribution of DM and spectral information are uncorrelated, and the flux from a region $\Delta\Omega$ is proportional to the astrophysical factor, so-called J-factor,

$$J \equiv \int_{\Delta\Omega} d\Omega \int dl\, \rho_\chi^2 \tag{1.44}$$

In a similar fashion, the flux for DM decaying events can be written as,

$$\frac{dN_\gamma}{dE_\gamma d\Omega}(E_\gamma, \psi)_{\text{dec}} = \frac{1}{4\pi} \int_{l.o.s} dl(\psi) \rho_\chi(\vec{r}) \frac{\Gamma}{m_\chi} \sum_i B_i \left(\frac{dN_\gamma}{dE_\gamma}\right)_i \tag{1.45}$$

where $\Gamma$ is the decay width (inverse to its lifetime $\tau$). Note in this case the flux is proportional to $m_\chi$ and not its square, as in the case of annihilation. Similarly to the J-factor, a D-factor can be defined,

$$D \equiv \int_{\Delta\Omega} d\Omega \int dl\, \rho_\chi \tag{1.46}$$

Very little is known about the microphysics taking place in such events, therefore $dN_\gamma/dE_\gamma$ is treated with effective field theories, or simplified models Cirelli et al. (2011). Unfortunately, there is also a big uncertainty in the astrophysical factors determination. To provide a good estimation of the J/D-factor, the DM distribution of the target must be precisely drawn, which is usually not the case due to poor and scarce data. In extragalactic objects measurements with gravitational lensing (Section 1.1.3), gas/stellar kinematics, as well as N-body cosmological simulations (Section 1.3.2), allow an estimation of DM profiles. For nearby targets, such as MW dSphs, DM distribution can be parametrized from stellar velocity dispersion, which heavily depends on the number of stars and quality of the data. In the case of the GC, the uncertainty is very large, as the l.o.s is populated with thousands of astrophysical sources which will avoid a clear view of the region.

In principle, in order to detect a clear DM signal, astrophysical, non DM-related gamma-ray emission from the target should be properly characterized. The exception to this are dark satellites, the central topic of this Thesis, which are not expected to host any baryonic content, therefore allowing a gamma-ray self background-free analysis (see Section 1.3.2). The popularity of dSphs as targets for indirect DM detection mainly comes from the fact that they are generally located at high Galactic latitudes, therefore avoiding intense Galactic diffuse emission in the l.o.s, coming from primary CR spallation in the interstellar medium. Additionally, dSphs are highly DM-dominated systems, with very little gas, therefore being the stars the only luminous baryonic content. dSphs do not have star-forming regions, and generally present old stars, with negligible gamma-ray emission. Thus, the theoretical gamma-ray background in these objects is quite low, and DM analysis are very robust. Nevertheless, the DM density in an individual dSph is very low compared to, e.g., the GC, where is expected to be maximal, and will render much weaker constraints. The way to overcome this is to perform a joint likelihood analysis, known as "stacking", in which several targets are considered in order to globally search for a DM signal, as this is expected to be universal.

In this Section, we will briefly review some of the main results in DM searches with gamma rays, where no clear DM signal has been found, yet some detection

claims have been made over the years. Nevertheless, given the predicted universality of a DM signal, different targets are complementary to each other and make all the constraints more robust, as well as constraining the parameter space. We show a compilation of some of these constraints, as well as probes from direct detection, in Figure 1.20. We defer the interested reader to, e.g., Conrad (2014); Gaskins (2016); Pérez de los Heros (2020) for a complete review on gamma-ray DM searches.

1. **Galactic center:** The GC is the target predicted to have the largest DM density, yet it is also the most complex, with astrophysical sources such as stars, star-forming regions, supernova remnants, PSRs, etc. Many of these will be sources of primary CRs, which will create secondary CRs by spallation with the interstellar medium (see Section 1.5.3) and an intense diffuse gamma-ray emission (see Section 2.3). Regarding the DM modeling, there is a very large uncertainty in the DM distribution of the innermost part of the MW Benito et al. (2019), mainly due to the cusp/core problem, see Section 1.3.3.

   The current approach for gamma-ray DM searches in the GC consists on a detailed astrophysical modeling of all the region components. When doing this, a persistent excess, in the form of gamma-ray residuals, has been found in the region by several authors, extending up to $\sim 10^\circ$ around Goodenough and Hooper (2009); Abazajian and Kaplinghat (2012); Calore et al. (2015); Daylan et al. (2016); Fermi-LAT Collaboration (2016); Di Mauro (2021). This is commonly known as the Galactic Center Excess (GCE). Although varying the assumed background model, e.g., changing the CR propagation parameters in Eq. 1.39 can reduce this excess, it is not possible to completely eliminate it Fermi-LAT Collaboration (2016).

   The spectral shape of the GCE –peaking at $E_\gamma \sim 1-3$ GeV– is fully compatible with a light WIMP DM interpretation with $m_\chi \sim 7-60$ GeV, depending on the annihilation channel(s), and cross sections comparable to the thermal relic value Hooper and Linden (2011); Abazajian et al. (2014); Di Mauro and Winkler (2021). However, astrophysical explanations are also possible, such as an unresolved population of sub-threshold sources, mainly millisecond pulsars (MSPs), which can yield a spectrum very similar to that of DM annihilation Fermi-LAT Collaboration (2012); Mirabal (2013); Mirabal et al. (2016). Indeed, this is the most preferred alternative over hypothesis such as a diffuse emission mismodeling, and a recent analysis based on a wavelet decomposition of the region finds a preference for such explanation Bartels et al. (2016).

   H.E.S.S. has also scrutinized the $1^\circ$ innermost region of the MW between 0.16–70 TeV, not finding any significant excess and deriving the most stringent constraints for heavy WIMP DM H.E.S.S. Collaboration (2016). Future gamma-ray observatories, like the Cherenkov Telescope Array (CTA), will be able to survey the GC with superb sensitivity, and current predictions yield the strongest limits within a number of different assumptions, such as systematics, inner DM profile, or Galactic diffuse emission models CTA Consortium (2021b).

2. **Milky Way halo:** If we mask the GC itself, in order to study the possible DM emission around it, we will have a reduced astrophysical background, at the cost of a somehow smaller DM density. Anyway, a detailed astrophysical modeling is still necessary, by taking into account both prompt DM gamma-ray emission and secondary emission by IC scattering. Such analysis was conducted by *Fermi*-LAT, studying the diffuse emission in two bands in the North

and South of the GC, without any clear DM signal and therefore deriving constraints Fermi-LAT Collaboration (2012).

3. **Gamma-ray line searches:** Processes such as $\chi\chi \rightarrow \gamma\gamma$ will generate two monochromatic photons with energies $E_\gamma = m_\chi$. This is a very singular feature, as gamma-ray spectra are continuous, and therefore the observation of monochromatic lines would constitute a "smoking gun" for DM annihilation. At this writing, no conclusive line has been found in gamma rays. The preferred target for such searches is the GC, as the astrophysical background from spectral lines is very low. Therefore, conservative constraints can be placed with the *Fermi*-LAT Fermi-LAT Collaboration (2015b); Anderson et al. (2016), H.E.S.S. H.E.S.S. Collaboration (2018) and MAGIC MAGIC Collaboration (2014), the latter observing the dSph Segue I instead of the GC. A joint analysis of line searches in dSphs was also performed by VERITAS VERITAS Collaboration (2017).

   Nevertheless, there was a claim of DM line signal from the GC with the *Fermi*-LAT. The authors claimed to have detected a $\sim 3\sigma$ line at $E_\gamma = m_\chi \sim 130$ GeV in 4 years of LAT data Weniger (2012); Su and Finkbeiner (2012). The line was fully compatible with the DM hypothesis; unfortunately, an improved event reconstruction and a larger dataset decreased the significance at the level of statistical fluctuations Fermi-LAT Collaboration (2015b). In fact, it seemed that the line was a instrumental systematic error, and currently is disregarded as DM-related. H.E.S.S. also scrutinized the GC region looking for line features around this energy with 10 years of data, with null result H.E.S.S. Collaboration (2018), therefore definitely disregarding this line candidate.

   Shifting to lower energies –in the X-ray domain– there is a confirmed line feature at 511 keV by INTEGRAL Knödlseder et al. (2005). This is produced by $e^- e^+ \rightarrow \gamma\gamma$ annihilation (recall $m_{e^\pm} = 511$ keV) in the GC. Therefore, a DM explanation is very unlikely, also because of the spatial morphology of the signal, which traces the MW bulge instead of the spherically predicted DM signal Weidenspointner et al. (2008).

4. **Globular clusters:** Globular clusters are star aggregations in the MW, bounded by their gravitational attraction and velocity dispersion. Almost spherical, no DM is in principle necessary to explain their shape. However, a number of these objects may have formed in environments of high DM density, such as DM subhalos, therefore being suitable gamma-ray targets. The interplay between stellar processes, such as SNe, and DM can induce adiabatic contractions on the DM density profile, creating a steeper slope in the innermost parts. This, according to Eq. 1.43, would enhance the DM annihilation signal. Two globular clusters, M15 and NGC 6388, have been observed by H.E.S.S. looking for DM, with null result H.E.S.S. Collaboration (2011).

5. **Dwarf spheroidal galaxies (dSphs):** dSphs are currently the most popular targets for indirect DM detection. Indeed, these are MW satellites (see Section 1.3.2) with low astrophysical background and huge mass-to-light ratio, which favour the expected signal from them. The analysis consists on a template fitting[37] taking into account the nearby sources and components such as the isotropic and Galactic diffuse gamma-ray emission. No significant excess has

[37] This technique, nevertheless, has some drawbacks, and different approaches are possible; see, e.g., Calore et al. (2018); Linden (2020).

been found from any of these objects, neither with *Fermi*-LAT or ground-based observatories such as MAGIC, H.E.S.S. or VERITAS.

No significant signal is found from any dSph. Some of them present local excesses at small significance, without the so-called trials correction for the "look elsewhere" effect, which will greatly decrease the significance value Conrad (2015). These are normally attributed to a mismodel of the region, either from the diffuse emission, nearby sources or the target itself. In the absence of a signal, the flux upper limits can be transformed to a DM likelihood profile, and finally into cross-section limits as a function of the mass. This requires to have a prediction for the J-factor (Eq. 1.44); the uncertainty in such parameter can be introduced in the likelihood computation, which will degrade the obtained constraints Fermi-LAT Collaboration and DES Collaboration (2017); Rico (2020).

As already mentioned, the achievable constraints from individual dSphs are much weaker than other probes, such as the GC. Nevertheless, a joint likelihood analysis is possible, known as "stacking". If a few members of the sample have J-factors much larger than the rest, this stacking will be dominated by them, yet if several targets present similar values, the obtained constraints will be enforced by performing the joint analysis. The derived limits with this technique are the most stringent ones in the WIMP parameter space, ruling out thermal WIMPs up to $\sim 100$ GeV in the case of annihilation into $b\bar{b}$ Fermi-LAT Collaboration and DES Collaboration (2017). Depending on some assumptions, these constraints may be in tension with the GCE DM interpretation.

In addition to different targets, is also possible to combine different instrument observations to compute a global likelihood, such as joint observations of Segue I by *Fermi*-LAT and MAGIC MAGIC Collaboration and Fermi-LAT Collaboration (2016), or the two former plus HAWC, H.E.S.S. and VERITAS Oakes (2019) on a number of dSphs. The main limitation comes from the ground-based telescopes, which are pointing observatories, as opposed to the LAT, which preclude them from observing a large number of targets with large exposure times. Ground-based observatories have also conducted their own DM searches in dSphs H.E.S.S. Collaboration (2014); VERITAS Collaboration (2017); HAWC Collaboration (2018).

6. **Dark subhalos:** Dark subhalos (also known as "dark satellites") are formally the same objects as dSphs, according to ΛCDM. The difference comes form its baryonic content, as below $\sim 10^{7-8}$ M subhalos are not expected to be able to retain baryons, therefore not hosting dSphs (see Section 1.3.2). Contrary to them, dark subhalos' positions in the MW are completely unknown, and can only be studied from a statistical point of view, as inferred from N-body simulations. Nevertheless, within the WIMP model, they could shine in gamma rays from DM annihilation.

   Given their lack of multiwavelength counterparts, they would appear in the sky as unidentified sources (unIDs). The *Fermi*-LAT catalogs, for instance, present $\sim 1/3$ of sources with unknown origin Fermi-LAT Collaboration (2020), therefore being perfect candidates for this kind of search. The major challenge comes from the typically low signal in most unIDs –an observational bias, given that well characterized sources are usually identified–, which precludes the analysis from giving a conclusive answer about the nature of the sources.

Some claims have been done over the years, most notably the source 3FGL J2212.5+0703 Bertoni et al. (2015, 2016), where also spatial extension was found, hailed as a possible "smoking gun" for subhalo searches (see Chapter 5 for extensive details on this statement). Unfortunately, the source was further studied and determined to be two close point sources, and not a single extended object. Being dark subhalos the central subject of this Thesis, we will be constantly discussing about them throughout the next Chapters.

7. **Galaxy clusters:** These are one of the most massive structures in the Universe, and highly DM-dominated objects (see Section 1.1.3). The procedure is similar to that of dSphs, yet they are much farther objects, therefore requiring long exposures. Clusters such as Coma, Fornax and Virgo have been observed with *Fermi*-LAT Fermi-LAT Collaboration (2015b), H.E.S.S. H.E.S.S. Collaboration (2012) and VERITAS VERITAS Collaboration (2012), with no gamma-ray signal detected, and the resulting constraints are weaker than the ones from dSphs. Given the galaxy clusters distance, a proper analysis requires to take into account the EBL absorption in the intergalactic medium, as done in Adam et al. (2021).

8. **Isotropic gamma-ray background (IGRB):** The IGRB is the sum of all unresolved gamma-ray sources of the Universe, which result in a isotropic background, similar to the CMB (see Section 1.2.1). As any DM overdensity would in principle yield gamma rays as product of co-annihilation or decay, the LSS itself can be considered a target for DM detection through the IGRB. The analysis consists on subtracting detected extragalactic sources (mainly Active Galactic Nuclei, AGNs) to study the resulting background searching for DM signatures. Such strategy requires all-sky observations, therefore being *Fermi*-LAT the only current instrument capable to perform it, both for annihilation Fermi-LAT Collaboration (2015a) and decay Blanco and Hooper (2019).

   Additionally, the IGRB can be cross-correlated with the sky mass distribution, as inferred from gravitational lensing or galaxy surveys (see Sections 1.1.3 and 1.3.1). By performing a cross-correlation between the IGRB and the DES lensing map, Ammazzalorso et al. (2020) found two signal features, one at small angular scales, probably due to a blazar population, and a second one at larger scales, which is coincident with the expected emission of DM annihilation at $\sim 3\sigma$ level. More data and improved surveys will be able to further study this novel probe in the future.

Additionally, axion-like particles can be searched with gamma rays via the Primakoff effect (see Section 1.5.2) Primakoff (1951). This can be done by comparing the observed distribution of the highest energy photons from far sources ($z \gtrsim 0.1$) with the theoretical prediction for ALPs, yet no signal has been found and only constraints can be set Sánchez-Conde et al. (2009); Meyer et al. (2017); Buehler et al. (2020); Meyer and Petrushevska (2020). CTA is also expected to further explore this candidate CTA Consortium (2021a).

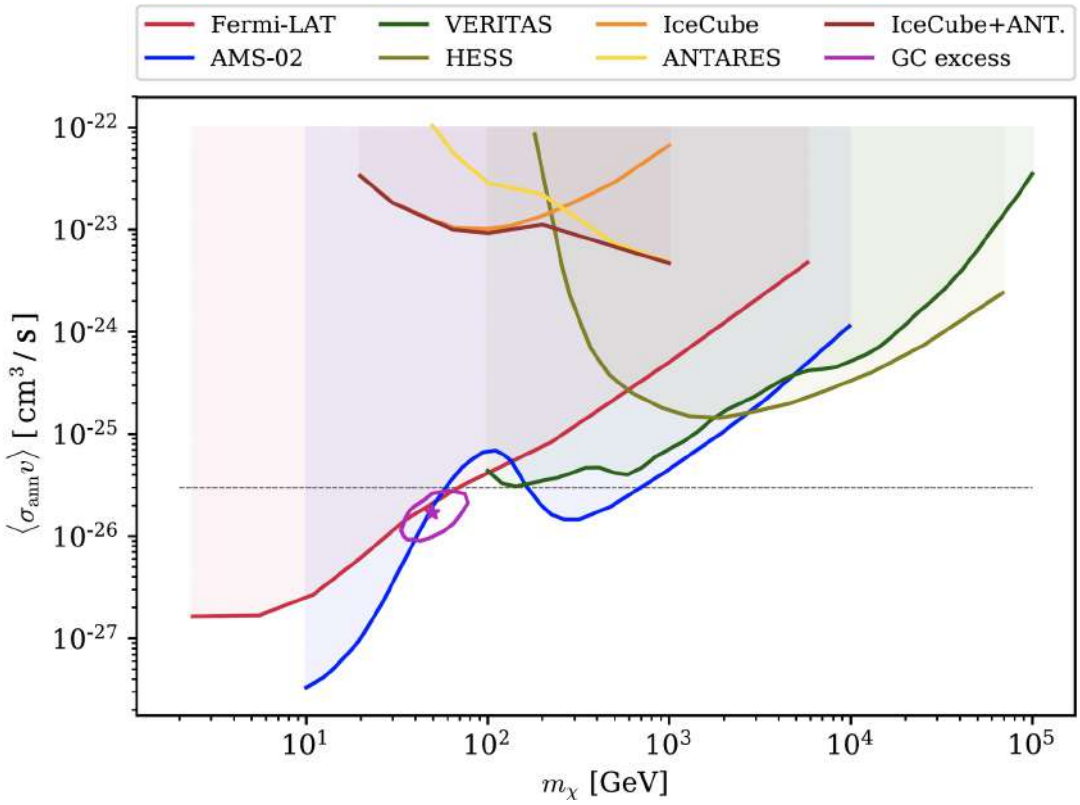


FIGURE 1.20: Compilation of constraints on the annihilation cross section from different DM targets and search strategies, for annihilation into $b\bar{b}$. Dot-dashed gray line is the thermal relic cross section. Red line are *Fermi*-LAT dSphs Fermi-LAT Collaboration and DES Collaboration (2017), blue line antiprotons from AMS-02 Cui et al. (2018), green line dSphs observed by VERITAS VERITAS Collaboration (2017), olive line H.E.S.S. observations of the GC H.E.S.S. Collaboration (2016), orange and yellow lines IceCube and ANTARES neutrino constraints, while brown line is their combined limit ANTARES Collaboration and IceCube Collaboration (2020). The purple star is the DM best fit to the GCE, and the surrounding contour its $1\sigma$ containment region Daylan et al. (2016). Figure adapted from Petač (2019), where a typo in the units was present.

## Bibliography

Abazajian, K. N. (2021). Neutrinos in Astrophysics and Cosmology: Theoretical Advanced Study Institute (TASI) 2020 Lectures.
**URL:** *https://arxiv.org/abs/2102.10183*

Abazajian, K. N., Canac, N., Horiuchi, S. and Kaplinghat, M. (2014). Astrophysical and dark matter interpretations of extended gamma-ray emission from the Galactic Center, *Physical Review D* **90**(2).
**URL:** *http://dx.doi.org/10.1103/PhysRevD.90.023526*

Abazajian, K. N. and Kaplinghat, M. (2012). Detection of a gamma-ray source in the Galactic Center consistent with extended emission from dark matter annihilation and concentrated astrophysical emission, *Physical Review D* **86**(8).
**URL:** *http://dx.doi.org/10.1103/PhysRevD.86.083511*

Abdallah, J., Araujo, H., Arbey, A., Ashkenazi, A., Belyaev, A., Berger, J., Boehm, C., Boveia, A., Brennan, A., Brooke, J. and et al. (2015). Simplified models for dark matter searches at the LHC, *Physics of the Dark Universe* **9-10**: 8–23.
**URL:** *http://dx.doi.org/10.1016/j.dark.2015.08.001*

Adam, R., Goksu, H., Brown, S., Rudnick, L. and Ferrari, C. (2021). $\gamma$-ray detection toward the Coma cluster with Fermi-LAT: Implications for the cosmic ray content in the hadronic scenario, *Astronomy & Astrophysics* **648**: A60.
**URL:** *http://dx.doi.org/10.1051/0004-6361/202039660*

Adamek, J., Byrnes, C. T., Gosenca, M. and Hotchkiss, S. (2019). WIMPs and stellar-mass primordial black holes are incompatible, *Physical Review D* **100**(2).
**URL:** *http://dx.doi.org/10.1103/PhysRevD.100.023506*

Alcock, C., Allsman, R. A., Axelrod, T. S., Bennett, D. P., Cook, K. H., Freeman, K. C., Griest, K., Guern, J. A., Lehner, M. J., Marshall, S. L. and et al. (1996). The MACHO Project First-Year Large Magellanic Cloud Results: The Microlensing Rate and the Nature of the Galactic Dark Halo, *The Astrophysical Journal* **461**: 84.
**URL:** *http://dx.doi.org/10.1086/177039*

Allahverdi, R., Dent, J. and Osinski, J. (2018). Nonthermal production of dark matter from primordial black holes, *Physical Review D* **97**(5).
**URL:** *http://dx.doi.org/10.1103/PhysRevD.97.055013*

Alpher, R. A., Bethe, H. and Gamow, G. (1948). The Origin of Chemical Elements, *Phys. Rev.* **73**: 803–804.
**URL:** *https://link.aps.org/doi/10.1103/PhysRev.73.803*

Amaré, J., Cebrián, S., Coarasa, I., Cuesta, C., García, E., Martínez, M., Oliván, M., Ortigoza, Y., de Solórzano, A. O., Puimedón, J. and et al. (2019). First Results on Dark Matter Annual Modulation from the ANAIS-112 Experiment, *Physical Review Letters* **123**(3).
**URL:** *http://dx.doi.org/10.1103/PhysRevLett.123.031301*

Ammazzalorso, S., Gruen, D., Regis, M., Camera, S., Ando, S., Fornengo, N., Bechtol, K., Bridle, S., Choi, A., Eifler, T. and et al. (2020). Detection of Cross-Correlation between Gravitational Lensing and $\gamma$ Rays, *Physical Review Letters* **124**(10).
**URL:** *http://dx.doi.org/10.1103/PhysRevLett.124.101102*

Amole, C., Ardid, M., Arnquist, I., Asner, D., Baxter, D., Behnke, E., Bressler, M., Broerman, B., Cao, G., Chen, C. and et al. (2019). Dark matter search results from the complete exposure of the PICO-60 $C_3F_8$ bubble chamber, *Physical Review D* **100**(2).
**URL:** http://dx.doi.org/10.1103/PhysRevD.100.022001

AMS-01 Collaboration (2007). Cosmic-ray positron fraction measurement from 1 to 30 GeV with AMS-01, *Physics Letters B* **646**(4): 145–154.
**URL:** http://dx.doi.org/10.1016/j.physletb.2007.01.024

AMS Collaboration (2016). Antiproton Flux, Antiproton-to-Proton Flux Ratio, and Properties of Elementary Particle Fluxes in Primary Cosmic Rays Measured with the Alpha Magnetic Spectrometer on the International Space Station, *Physical Review Letters* **117**(9): 091103.
**URL:** https://ui.adsabs.harvard.edu/abs/2016PhRvL.117i1103A

AMS Collaboration (2019). Towards Understanding the Origin of Cosmic-Ray Positrons, *Physical Review Letters* **122**(4): 041102.
**URL:** https://ui.adsabs.harvard.edu/abs/2019PhRvL.122d1102A

Anderson, B., Zimmer, S., Conrad, J., Gustafsson, M., Sánchez-Conde, M. and Caputo, R. (2016). Search for gamma-ray lines towards galaxy clusters with the Fermi-LAT, *Journal of Cosmology and Astroparticle Physics* **2016**(02): 026–026.
**URL:** http://dx.doi.org/10.1088/1475-7516/2016/02/026

ANTARES Collaboration (2011). ANTARES: The first undersea neutrino telescope, *Nuclear Instruments and Methods in Physics Research Section A: Accelerators, Spectrometers, Detectors and Associated Equipment* **656**(1): 11–38.
**URL:** http://dx.doi.org/10.1016/j.nima.2011.06.103

ANTARES Collaboration and IceCube Collaboration (2020). Combined search for neutrinos from dark matter self-annihilation in the Galactic Center with ANTARES and IceCube, *Physical Review D* **102**(8).
**URL:** http://dx.doi.org/10.1103/PhysRevD.102.082002

Antonello, M., Barberio, E., Baroncelli, T., Benziger, J., Bignell, L. J., Bolognino, I., Calaprice, F., Copello, S., D'Angelo, D., D'Imperio, G. and et al. (2019). The SABRE project and the SABRE Proof-of-Principle, *The European Physical Journal C* **79**(4).
**URL:** http://dx.doi.org/10.1140/epjc/s10052-019-6860-y

Aprile, E. (2013). The Xenon1T Dark Matter Search Experiment, *Springer Proceedings in Physics*, Vol. 148 of *Springer Proceedings in Physics*, p. 93.
**URL:** https://ui.adsabs.harvard.edu/abs/2013SPPhy.148...93A

Aprile, E., Aalbers, J., Agostini, F., Alfonsi, M., Althueser, L., Amaro, F., Antochi, V., Angelino, E., Angevaare, J., Arneodo, F. and et al. (2020). Excess electronic recoil events in xenon1t, *Physical Review D* **102**(7).
**URL:** http://dx.doi.org/10.1103/PhysRevD.102.072004

Aprile, E., Aalbers, J., Agostini, F., Alfonsi, M., Althueser, L., Amaro, F., Antochi, V., Angelino, E., Arneodo, F., Barge, D. and et al. (2019). Light dark matter search with ionization signals in xenon1t, *Physical Review Letters* **123**(25).
**URL:** http://dx.doi.org/10.1103/PhysRevLett.123.251801

Aramaki, T., Hailey, C., Boggs, S., von Doetinchem, P., Fuke, H., Mognet, S., Ong, R., Perez, K. and Zweerink, J. (2016). Antideuteron sensitivity for the GAPS experiment, *Astroparticle Physics* **74**: 6–13.
**URL:** http://dx.doi.org/10.1016/j.astropartphys.2015.09.001

Arca-Sedda, M. and Capuzzo-Dolcetta, R. (2016). Globular clusters as tracers of the host galaxy mass distribution: the Fornax dSph test case, *Monthly Notices of the Royal Astronomical Society* **461**(4): 4335–4342.
**URL:** http://dx.doi.org/10.1093/mnras/stw1647

Arcadi, G. (2016). Dark matter phenomenology of GUT inspired simplified models, *Journal of Physics: Conference Series* **718**: 042003.
**URL:** http://dx.doi.org/10.1088/1742-6596/718/4/042003

Arcadi, G., Lindner, M., Mambrini, Y., Pierre, M. and Queiroz, F. S. (2017). GUT models at current and future hadron colliders and implications to dark matter searches, *Physics Letters B* **771**: 508–514.
**URL:** http://dx.doi.org/10.1016/j.physletb.2017.05.023

ATLAS Collaboration (2008). The ATLAS experiment at the CERN large hadron collider, *Journal of Instrumentation* **3**(08): S08003–S08003.
**URL:** https://doi.org/10.1088/1748-0221/3/08/s08003

Badhwar, G. D. and Stephens, S. A. (1977). Hydrostatic equilibrium of gas, extent of cosmic ray confinement, and radio emission in the Galaxy., *The Astrophysical Journal* **212**: 494–506.
**URL:** https://ui.adsabs.harvard.edu/abs/1977ApJ...212..494B

Baer, H., Choi, K.-Y., Kim, J. E. and Roszkowski, L. (2015). Dark matter production in the early Universe: Beyond the thermal WIMP paradigm, *Physics Reports* **555**: 1–60.
**URL:** http://dx.doi.org/10.1016/j.physrep.2014.10.002

Baes, M., Dejonghe, H. and Davies, J. I. (2004). Dust and the observed dark matter content of galaxies, *in* S. Ryder, D. Pisano, M. Walker and K. Freeman (eds), *Dark Matter in Galaxies*, Vol. 220, p. 343.
**URL:** https://ui.adsabs.harvard.edu/abs/2004IAUS..220..343B

Bahcall, J. N. (1984). Self-consistent determinations of the total amount of matter near the sun., *The Astrophysical Journal* **276**: 169–181.
**URL:** https://ui.adsabs.harvard.edu/abs/1984ApJ...276..169B

Bahcall, N. A. and Fan, X. (1998). The Most Massive Distant Clusters: Determining $\Omega$ and $\sigma_8$, *The Astrophysical Journal* **504**(1): 1–6.
**URL:** https://ui.adsabs.harvard.edu/abs/1998ApJ...504....1B

Baltz, E. A. (2004). Dark Matter Candidates, *arXiv e-prints* pp. astro–ph/0412170.
**URL:** https://ui.adsabs.harvard.edu/abs/2004astro.ph.12170B

Baltz, E. A., Edsjö, J., Freese, K. and Gondolo, P. (2002). Cosmic ray positron excess and neutralino dark matter, *Physical Review D* **65**(6).
**URL:** http://dx.doi.org/10.1103/PhysRevD.65.063511

Banik, N., Bertone, G., Bovy, J. and Bozorgnia, N. (2018). Probing the nature of dark matter particles with stellar streams, *Journal of Cosmology and Astroparticle Physics*

**2018**(07): 061–061.
**URL:** http://dx.doi.org/10.1088/1475-7516/2018/07/061

Banik, N., Bovy, J., Bertone, G., Erkal, D. and de Boer, T. J. L. (2019). Novel constraints on the particle nature of dark matter from stellar streams.

Banik, N., Bovy, J., Bertone, G., Erkal, D. and de Boer, T. J. L. (2021). Evidence of a population of dark subhaloes from Gaia and Pan-STARRS observations of the GD-1 stream, *Monthly Notices of the Royal Astronomical Society* **502**(2): 2364–2380.
**URL:** http://dx.doi.org/10.1093/mnras/stab210

Barello, G., Chang, S. and Newby, C. A. (2014). A model independent approach to inelastic dark matter scattering, *Physical Review D* **90**(9).
**URL:** http://dx.doi.org/10.1103/PhysRevD.90.094027

Barnacka, A. (2018). Gravitational lenses as high-resolution telescopes, *Physics Reports* **778-779**: 1–46.
**URL:** http://dx.doi.org/10.1016/j.physrep.2018.10.001

Bartelmann, M. and Maturi, M. (2016). Weak gravitational lensing.
**URL:** https://arxiv.org/abs/1612.06535

Bartels, R., Krishnamurthy, S. and Weniger, C. (2016). Strong Support for the Millisecond Pulsar Origin of the Galactic Center GeV Excess, *Physical Review Letters* **116**(5).
**URL:** http://dx.doi.org/10.1103/PhysRevLett.116.051102

Bassett, B. and Hlozek, R. (2010). *Baryon acoustic oscillations*, p. 246.
**URL:** https://ui.adsabs.harvard.edu/abs/2010deot.book..246B

Bastero-Gil, M., Cerezo, R. and Rosa, J. G. (2016). Inflaton dark matter from incomplete decay, *Physical Review D* **93**(10).
**URL:** http://dx.doi.org/10.1103/PhysRevD.93.103531

Basu, R., Banerjee, S., Pandey, M. and Majumdar, D. (2020). Lower bounds on dark matter annihilation cross-sections by studying the fluctuations of 21-cm line with dark matter candidate in inert doublet model (IDM) with the combined effects of dark matter scattering and annihilation.
**URL:** https://arxiv.org/abs/2010.11007

Beck, R. and Wielebinski, R. (2013). Magnetic Fields in Galaxies, *Planets, Stars and Stellar Systems* p. 641–723.
**URL:** http://dx.doi.org/10.1007/978-94-007-5612-013

Bellomo, N., Bernal, J. L., Raccanelli, A. and Verde, L. (2018). Primordial black holes as dark matter: converting constraints from monochromatic to extended mass distributions, *Journal of Cosmology and Astroparticle Physics* **2018**(01): 004–004.
**URL:** http://dx.doi.org/10.1088/1475-7516/2018/01/004

Benitez-Llambay, A. and Frenk, C. (2020). The detailed structure and the onset of galaxy formation in low-mass gaseous dark matter haloes, *Monthly Notices of the Royal Astronomical Society* **498**(4): 4887–4900.
**URL:** http://dx.doi.org/10.1093/mnras/staa2698

Benito, M., Cuoco, A. and Iocco, F. (2019). Handling the uncertainties in the Galactic Dark Matter distribution for particle Dark Matter searches, *Journal of Cosmology and Astroparticle Physics* **2019**(03): 033–033.
**URL:** http://dx.doi.org/10.1088/1475-7516/2019/03/033

Bennett, C. L., Larson, D., Weiland, J. L., Jarosik, N., Hinshaw, G., Odegard, N., Smith, K. M., Hill, R. S., Gold, B., Halpern, M. and et al. (2013). Nine-year wilkinson microwave anisotropy probe ( WMAP ) observations: Final maps and results, *The Astrophysical Journal Supplement Series* **208**(2): 20.
**URL:** http://dx.doi.org/10.1088/0067-0049/208/2/20

Berezinsky, V., Dokuchaev, V. and Eroshenko, Y. (2006). Destruction of small-scale dark matter clumps in the hierarchical structures and galaxies, *Physical Review D* **73**(6).
**URL:** http://dx.doi.org/10.1103/PhysRevD.73.063504

Berglund, P., Hübsch, T. and Minic, D. (2021). String Theory, the Dark Sector, and the Hierarchy Problem, *Letters in High Energy Physics* **2021**.
**URL:** http://dx.doi.org/10.31526/lhep.2021.186

Bergstrom, L., Edsjo, J. and Ullio, P. (1999). Cosmic Antiprotons as a Probe for Supersymmetric Dark Matter?, *The Astrophysical Journal* **526**(1): 215–235.
**URL:** http://dx.doi.org/10.1086/307975

Bernabei, R., Belli, P., Bussolotti, A., Cappella, F., Caracciolo, V., Cerulli, R., Dai, C., d' Angelo, A., Di Marco, A. and et al. (2018). First model independent results from DAMA/LIBRA-phase2, *Nuclear Physics and Atomic Energy* **19**(4): 307–325.
**URL:** http://dx.doi.org/10.15407/jnpae2018.04.307

Bernabei, R., Belli, P., Bussolotti, A., Cappella, F., Cerulli, R., Dai, C., d' Angelo, A., He, H., Incicchitti, A., Kuang, H. and et al. (2008). The dama/libra apparatus, *Nuclear Instruments and Methods in Physics Research Section A: Accelerators, Spectrometers, Detectors and Associated Equipment* **592**(3): 297–315.
**URL:** http://dx.doi.org/10.1016/j.nima.2008.04.082

Bernal, J. L., Verde, L., Jimenez, R., Kamionkowski, M., Valcin, D. and Wandelt, B. D. (2021). Trouble beyond $H_0$ and the new cosmic triangles, *Physical Review D* **103**(10).
**URL:** http://dx.doi.org/10.1103/PhysRevD.103.103533

Bernal, J. L., Verde, L. and Riess, A. G. (2016). The trouble with $H_0$, *Journal of Cosmology and Astroparticle Physics* **2016**(10): 019–019.
**URL:** http://dx.doi.org/10.1088/1475-7516/2016/10/019

Bernal, N., Heikinheimo, M., Tenkanen, T., Tuominen, K. and Vaskonen, V. (2017). The dawn of FIMP Dark Matter: A review of models and constraints, *International Journal of Modern Physics A* **32**(27): 1730023.
**URL:** http://dx.doi.org/10.1142/S0217751X1730023X

Bertone, G., Hooper, D. and Silk, J. (2005). Particle dark matter: evidence, candidates and constraints, *Physics Reports* **405**(5-6): 279–390.
**URL:** http://dx.doi.org/10.1016/j.physrep.2004.08.031

Bertoni, B., Hooper, D. and Linden, T. (2015). Examining The Fermi-LAT Third Source Catalog in search of dark matter subhalos, *Journal of Cosmology and Astroparticle Physics* **2015**(12): 035–035.
**URL:** http://dx.doi.org/10.1088/1475-7516/2015/12/035

Bertoni, B., Hooper, D. and Linden, T. (2016). Is the gamma-ray source 3FGL J2212.5+0703 a dark matter subhalo?, *Journal of Cosmology and Astroparticle Physics* **2016**(05): 049–049.
**URL:** http://dx.doi.org/10.1088/1475-7516/2016/05/049

Blake, C., Kazin, E. A., Beutler, F., Davis, T. M., Parkinson, D., Brough, S., Colless, M., Contreras, C., Couch, W., Croom, S. and et al. (2011). The WiggleZ Dark Energy Survey: mapping the distance-redshift relation with baryon acoustic oscillations, *Monthly Notices of the Royal Astronomical Society* **418**(3): 1707–1724.
**URL:** http://dx.doi.org/10.1111/j.1365-2966.2011.19592.x

Blanco, C. and Hooper, D. (2019). Constraints on decaying dark matter from the isotropic gamma-ray background, *Journal of Cosmology and Astroparticle Physics* **2019**(03): 019–019.
**URL:** http://dx.doi.org/10.1088/1475-7516/2019/03/019

Blum, K. (2011). DAMA vs. the annually modulated muon background.

Bode, P., Ostriker, J. P. and Turok, N. (2001). Halo Formation in Warm Dark Matter Models, *The Astrophysical Journal* **556**(1): 93–107.
**URL:** http://dx.doi.org/10.1086/321541

Bœ hm, C., Dolan, M. J. and McCabe, C. (2013). A lower bound on the mass of cold thermal dark matter from Planck, *Journal of Cosmology and Astroparticle Physics* **2013**(08): 041–041.
**URL:** http://dx.doi.org/10.1088/1475-7516/2013/08/041

Bond, J. R., Efstathiou, G. and Silk, J. (1980). Massive Neutrinos and the Large-Scale Structure of the Universe, *Physical Review Letters* **45**(24): 1980–1984.
**URL:** https://ui.adsabs.harvard.edu/abs/1980PhRvL..45.1980B

Boudaud, M., Cirelli, M., Giesen, G. and Salati, P. (2015). A fussy revisitation of antiprotons as a tool for Dark Matter searches, *Journal of Cosmology and Astroparticle Physics* **2015**(05): 013–013.
**URL:** http://dx.doi.org/10.1088/1475-7516/2015/05/013

Boudaud, M. et al. (2015). A new look at the cosmic ray positron fraction, *Astronomy & Astrophysics* **575**: A67.
**URL:** https://doi.org/10.1051/0004-6361/201425197

Boyanovsky, D. (2008). Free streaming in mixed dark matter, *Physical Review D* **77**(2).
**URL:** http://dx.doi.org/10.1103/PhysRevD.77.023528

Boyarsky, A., Drewes, M., Lasserre, T., Mertens, S. and Ruchayskiy, O. (2019). Sterile neutrino dark matter, *Progress in Particle and Nuclear Physics* **104**: 1–45.
**URL:** http://dx.doi.org/10.1016/j.ppnp.2018.07.004

Boyarsky, A., Ruchayskiy, O. and Iakubovskyi, D. (2009). A lower bound on the mass of dark matter particles, *Journal of Cosmology and Astroparticle Physics* **2009**(03): 005–005.
**URL:** http://dx.doi.org/10.1088/1475-7516/2009/03/005

Boylan-Kolchin, M., Bullock, J. S. and Kaplinghat, M. (2011). Too big to fail? The puzzling darkness of massive Milky Way subhaloes, *Monthly Notices of the Royal Astronomical Society: Letters* **415**(1): L40–L44.
**URL:** http://dx.doi.org/10.1111/j.1745-3933.2011.01074.x

Boylan-Kolchin, M., Bullock, J. S. and Kaplinghat, M. (2012). The Milky Way's bright satellites as an apparent failure of ΛCDM, *Monthly Notices of the Royal Astronomical Society* **422**(2): 1203–1218.
**URL:** http://dx.doi.org/10.1111/j.1365-2966.2012.20695.x

Bozorgnia, N., Calore, F., Schaller, M., Lovell, M., Bertone, G., Frenk, C. S., Crain, R. A., Navarro, J. F., Schaye, J. and Theuns, T. (2016). Simulated Milky Way analogues: implications for dark matter direct searches, *Journal of Cosmology and Astroparticle Physics* **2016**(05): 024–024.
**URL:** http://dx.doi.org/10.1088/1475-7516/2016/05/024

Braine, T., Cervantes, R., Crisosto, N., Du, N., Kimes, S., Rosenberg, L., Rybka, G., Yang, J., Bowring, D., Chou, A. and et al. (2020). Extended Search for the Invisible Axion with the Axion Dark Matter Experiment, *Physical Review Letters* **124**(10).
**URL:** http://dx.doi.org/10.1103/PhysRevLett.124.101303

Brandt, T. D. (2016). Constraints on MACHO dark matter from compact stellar systems in ultra-faint dwarf galaxies, *The Astrophysical Journal* **824**(2): L31.
**URL:** http://dx.doi.org/10.3847/2041-8205/824/2/L31

Brevik, I. and Halnes, G. (2003). Cosmic evolution and primordial black hole evaporation, *Physical Review D* **67**(2).
**URL:** http://dx.doi.org/10.1103/PhysRevD.67.023508

Bringmann, T. and Salati, P. (2007). Galactic antiproton spectrum at high energies: Background expectation versus exotic contributions, *Physical Review D* **75**(8).
**URL:** http://dx.doi.org/10.1103/PhysRevD.75.083006

Brito, R., Cardoso, V., Herdeiro, C. A. and Radu, E. (2016). Proca stars: Gravitating Bose–Einstein condensates of massive spin 1 particles, *Physics Letters B* **752**: 291–295.
**URL:** http://dx.doi.org/10.1016/j.physletb.2015.11.051

Brook, C. B. and Di Cintio, A. (2015). Expanded haloes, abundance matching and too-big-to-fail in the Local Group, *Monthly Notices of the Royal Astronomical Society* **450**(4): 3920–3934.
**URL:** http://dx.doi.org/10.1093/mnras/stv864

Brown, A. G. A., Vallenari, A., Prusti, T., de Bruijne, J. H. J., Babusiaux, C., Bailer-Jones, C. A. L., Biermann, M., Evans, D. W., Eyer, L. and et al. (2018). Gaia Data Release 2, *Astronomy & Astrophysics* **616**: A1.
**URL:** http://dx.doi.org/10.1051/0004-6361/201833051

Brownsberger, S. R. and Randall, L. (2020). Stellar profile independent determination of the dark matter distribution of the Fornax Local Group dwarf spheroidal galaxy, *Monthly Notices of the Royal Astronomical Society* **501**(2): 2332–2351.
**URL:** http://dx.doi.org/10.1093/mnras/staa3719

Buehler, R., Gallardo, G., Maier, G., Domínguez, A., López, M. and Meyer, M. (2020). Search for the imprint of axion-like particles in the highest-energy photons of hard $\gamma$-ray blazars, *Journal of Cosmology and Astroparticle Physics* **2020**(9): 027.
**URL:** https://ui.adsabs.harvard.edu/abs/2020JCAP..09..027B

Bullock, J. S. and Boylan-Kolchin, M. (2017). Small-Scale Challenges to the ΛCDM Paradigm, *Annual Review of Astronomy and Astrophysics* **55**(1): 343–387.
**URL:** http://dx.doi.org/10.1146/annurev-astro-091916-055313

Burkert, A. (1995). The Structure of Dark Matter Halos in Dwarf Galaxies, *The Astrophysical Journal Letters* **447**: L25–L28.
**URL:** https://ui.adsabs.harvard.edu/abs/1995ApJ...447L..25B

Burkert, A. (2015). The Structure and Dark Halo Core Properties of Dwarf Spheroidal Galaxies.
**URL:** https://arxiv.org/abs/1501.06604

Bustillo, J. C., Sanchis-Gual, N., Torres-Forné, A., Font, J. A., Vajpeyi, A., Smith, R., Herdeiro, C., Radu, E. and Leong, S. H. (2021). GW190521 as a Merger of Proca Stars: A Potential New Vector Boson of $8.7 \times 10^{-13}$ eV, *Physical Review Letters* **126**(8).
**URL:** http://dx.doi.org/10.1103/PhysRevLett.126.081101

Bœhm, C., Cerdeño, D., Machado, P., Campo, A. O.-D. and Reid, E. (2019). How high is the neutrino floor?, *Journal of Cosmology and Astroparticle Physics* **2019**(01): 043–043.
**URL:** http://dx.doi.org/10.1088/1475-7516/2019/01/043

Bœhm, C. and Fayet, P. (2004). Scalar dark matter candidates, *Nuclear Physics B* **683**(1-2): 219–263.
**URL:** http://dx.doi.org/10.1016/j.nuclphysb.2004.01.015

Cai, Y., Han, T., Li, T. and Ruiz, R. (2018). Lepton Number Violation: Seesaw Models and Their Collider Tests, *Frontiers in Physics* **6**: 40.
**URL:** https://ui.adsabs.harvard.edu/abs/2018FrP.....6..40C

Calchi Novati, S. (2012). Microlensing towards the Magellanic Clouds and M31: is the quest for MACHOs still open?, *Journal of Physics: Conference Series* **354**: 012001.
**URL:** http://dx.doi.org/10.1088/1742-6596/354/1/012001

Calibbi, L., Lindert, J. M., Ota, T. and Takanishi, Y. (2014). A lower bound on light neutralino dark matter from LHC data.
**URL:** https://arxiv.org/abs/1405.3884

Calore, F., Cholis, I., McCabe, C. and Weniger, C. (2015). A tale of tails: Dark matter interpretations of the Fermi GeV excess in light of background model systematics, *Physical Review D* **91**(6).
**URL:** http://dx.doi.org/10.1103/PhysRevD.91.063003

Calore, F., Serpico, P. D. and Zaldivar, B. (2018). Dark matter constraints from dwarf galaxies: a data-driven analysis, *Journal of Cosmology and Astroparticle Physics* **2018**(10): 029–029.
**URL:** http://dx.doi.org/10.1088/1475-7516/2018/10/029

Carlberg, R. G. (2012a). Counting Dark Sub-halos with Star Stream Gaps, *in* W. Aoki, M. Ishigaki, T. Suda, T. Tsujimoto and N. Arimoto (eds), *Galactic Archaeology: Near-Field Cosmology and the Formation of the Milky Way*, Vol. 458 of *Astronomical Society of the Pacific Conference Series*, p. 379.
**URL:** https://ui.adsabs.harvard.edu/abs/2012ASPC..458..379C

Carlberg, R. G. (2012b). Dark Matter Sub-Halo Counts via Star Stream Crossings, *The Astrophysical Journal* **748**(1): 20.
**URL:** http://dx.doi.org/10.1088/0004-637X/748/1/20

Carlberg, R. G., Yee, H. K. C., Morris, S. L., Lin, H., Hall, P. B., Patton, D. R., Sawicki, M. and Shepherd, C. W. (2001). Galaxy groups at intermediate redshift, *The Astrophysical Journal* **552**(2): 427–444.
**URL:** http://dx.doi.org/10.1086/320555

Carquín, E., Díaz, M. A., Gómez-Vargas, G. A., Panes, B. and Viaux, N. (2016). Confronting recent AMS-02 positron fraction and Fermi-LAT extragalactic $\gamma$-ray background measurements with gravitino dark matter, *Physics of the Dark Universe* **11**: 1–10.
**URL:** http://dx.doi.org/10.1016/j.dark.2015.10.002

Carr, B., Clesse, S., García-Bellido, J. and Kühnel, F. (2021). Cosmic conundra explained by thermal history and primordial black holes, *Physics of the Dark Universe* **31**: 100755.
**URL:** http://dx.doi.org/10.1016/j.dark.2020.100755

Carr, B., Kohri, K., Sendouda, Y. and Yokoyama, J. (2020). Constraints on Primordial Black Holes.

Carr, B., Tenkanen, T. and Vaskonen, V. (2017). Primordial black holes from inflaton and spectator field perturbations in a matter-dominated era, *Physical Review D* **96**(6).
**URL:** http://dx.doi.org/10.1103/PhysRevD.96.063507

Cautun, M., Benítez-Llambay, A., Deason, A. J., Frenk, C. S., Fattahi, A., Gómez, F. A., Grand, R. J. J., Oman, K. A., Navarro, J. F. and Simpson, C. M. (2020). The Milky Way total mass profile as inferred from Gaia DR2, *Monthly Notices of the Royal Astronomical Society* **494**(3): 4291–4313.
**URL:** http://dx.doi.org/10.1093/mnras/staa1017

Cembranos, J. A. R., de la Cruz-Dombriz, A., Gammaldi, V. and Maroto, A. L. (2012). Detection of branon dark matter with gamma ray telescopes, *Physical Review D* **85**(4).
**URL:** http://dx.doi.org/10.1103/PhysRevD.85.043505

Cerdeño, D. G., Fornasa, M., Green, A. M. and Peiró, M. (2016). How to calculate dark matter direct detection exclusion limits that are consistent with gamma rays from annihilation in the Milky Way halo, *Physical Review D* **94**(4).
**URL:** http://dx.doi.org/10.1103/PhysRevD.94.043516

Chamcham, K., Silk, J., Barrow, J. D. and Saunders, S. (2017). *The Philosophy of Cosmology*, Cambridge University Press.

Chassande-Mottin, E., Leyde, K., Mastrogiovanni, S. and Steer, D. (2019). Gravitational wave observations, distance measurement uncertainties, and cosmology, *Physical Review D* **100**(8).
**URL:** http://dx.doi.org/10.1103/PhysRevD.100.083514

Chatrchyan, S., Khachatryan, V., Sirunyan, A., Tumasyan, A., Adam, W., Aguilo, E., Bergauer, T., Dragicevic, M., Erö, J., Fabjan, C. and et al. (2012). Observation of a new boson at a mass of 125 GeV with the CMS experiment at the LHC, *Physics Letters B* **716**(1): 30–61.
**URL:** http://dx.doi.org/10.1016/j.physletb.2012.08.021

Chen, H.-Y., Fishbach, M. and Holz, D. E. (2018). A two per cent Hubble constant measurement from standard sirens within five years, *Nature* **562**(7728): 545–547.
**URL:** https://ui.adsabs.harvard.edu/abs/2018Natur.562..545C

Cherenkov, P. A. (1960). Radiation from High-Speed Particles, *Science* **131**(3394): 136–142.
**URL:** https://ui.adsabs.harvard.edu/abs/1960Sci...131..136C

Chianese, M., Fiorillo, D. F., Miele, G., Morisi, S. and Pisanti, O. (2019). Decaying dark matter at IceCube and its signature on High Energy gamma experiments, *Journal of Cosmology and Astroparticle Physics* **2019**(11): 046–046.
**URL:** http://dx.doi.org/10.1088/1475-7516/2019/11/046

Chiappo, A., Cohen-Tanugi, J., Conrad, J., Strigari, L. E., Anderson, B. and Sánchez-Conde, M. A. (2016). Dwarf spheroidal J-factors without priors: A likelihood-based analysis for indirect dark matter searches, *Monthly Notices of the Royal Astronomical Society* **466**(1): 669–676.
**URL:** http://dx.doi.org/10.1093/mnras/stw3079

Cholis, I., Linden, T. and Hooper, D. (2019). A robust excess in the cosmic-ray antiproton spectrum: Implications for annihilating dark matter, *Physical Review D* **99**(10).
**URL:** http://dx.doi.org/10.1103/PhysRevD.99.103026

Cirelli, M. (2015). Status of Indirect (and Direct) Dark Matter searches.
**URL:** https://arxiv.org/abs/1511.02031

Cirelli, M., Corcella, G., Hektor, A., Hütsi, G., Kadastik, M., Panci, P., Raidal, M., Sala, F. and Strumia, A. (2011). PPPC 4 DM ID: a poor particle physicist cookbook for dark matter indirect detection, *Journal of Cosmology and Astroparticle Physics* **2011**(03): 051–051.
**URL:** http://dx.doi.org/10.1088/1475-7516/2011/03/051

Cirelli, M., Kadastik, M., Raidal, M. and Strumia, A. (2009). Model-independent implications of the $e^+$, $e^-$ cosmic ray spectra on properties of Dark Matter, *Nuclear Physics B* **813**(1-2): 1–21.
**URL:** http://dx.doi.org/10.1016/j.nuclphysb.2008.11.031

Clesse, S. and García-Bellido, J. (2018). Seven hints for primordial black hole dark matter, *Physics of the Dark Universe* **22**: 137–146.
**URL:** https://ui.adsabs.harvard.edu/abs/2018PDU...22..137C

Clesse, S. and García-Bellido, J. (2017). The clustering of massive Primordial Black Holes as Dark Matter: Measuring their mass distribution with advanced LIGO, *Physics of the Dark Universe* **15**: 142–147.
**URL:** http://dx.doi.org/10.1016/j.dark.2016.10.002

Clowe, D., Bradač, M., Gonzalez, A. H., Markevitch, M., Randall, S. W., Jones, C. and Zaritsky, D. (2006). A Direct Empirical Proof of the Existence of Dark Matter, *The Astrophysical Journal* **648**(2): L109–L113.
**URL:** http://dx.doi.org/10.1086/508162

CMS Collaboration (2008). The CMS Experiment at the CERN LHC, *Journal of Instrumentation* **3**: S08004.

Cole, S., Percival, W. J., Peacock, J. A., Norberg, P., Baugh, C. M., Frenk, C. S., Baldry, I., Bland-Hawthorn, J., Bridges, T., Cannon, R. and et al. (2005). The 2dF Galaxy Redshift Survey: power-spectrum analysis of the final data set and cosmological implications, *Monthly Notices of the Royal Astronomical Society* **362**(2): 505–534.
**URL:** *http://dx.doi.org/10.1111/j.1365-2966.2005.09318.x*

Conn, A. R., Lewis, G. F., Ibata, R. A., Parker, Q. A., Zucker, D. B., McConnachie, A. W., Martin, N. F., Valls-Gabaud, D., Tanvir, N., Irwin, M. J. and et al. (2013). The three-dimensional structure of the M31 satellite system; strong evidence for an inhomogeneous distribution of satellites, *The Astrophysical Journal* **766**(2): 120.
**URL:** *http://dx.doi.org/10.1088/0004-637X/766/2/120*

Conrad, J. (2014). Indirect Detection of WIMP Dark Matter: a compact review.
**URL:** *https://arxiv.org/abs/1411.1925*

Conrad, J. (2015). Statistical issues in astrophysical searches for particle dark matter, *Astroparticle Physics* **62**: 165–177.
**URL:** *http://dx.doi.org/10.1016/j.astropartphys.2014.09.003*

Coogan, A. and Profumo, S. (2017). Origin of the tentative AMS antihelium events, *Physical Review D* **96**(8).
**URL:** *http://dx.doi.org/10.1103/PhysRevD.96.083020*

COSINE-100 Collaboration (2021). Background modeling for dark matter search with 1.7 years of COSINE-100 data.

Croft, R. A. C., Weinberg, D. H., Bolte, M., Burles, S., Hernquist, L., Katz, N., Kirkman, D. and Tytler, D. (2002). Toward a Precise Measurement of Matter Clustering: Ly$\alpha$ Forest Data at Redshifts 2–4, *The Astrophysical Journal* **581**(1): 20–52.
**URL:** *http://dx.doi.org/10.1086/344099*

CTA Consortium (2021a). Sensitivity of the Cherenkov Telescope Array for probing cosmology and fundamental physics with gamma-ray propagation, *Journal of Cosmology and Astroparticle Physics* **2021**(02): 048–048.
**URL:** *http://dx.doi.org/10.1088/1475-7516/2021/02/048*

CTA Consortium (2021b). Sensitivity of the Cherenkov Telescope Array to a dark matter signal from the Galactic centre, *Journal of Cosmology and Astroparticle Physics* **2021**(01): 057–057.
**URL:** *http://dx.doi.org/10.1088/1475-7516/2021/01/057*

Cui, M.-Y., Pan, X., Yuan, Q., Fan, Y.-Z. and Zong, H.-S. (2018). Revisit of cosmic ray antiprotons from dark matter annihilation with updated constraints on the background model from AMS-02 and collider data, *Journal of Cosmology and Astroparticle Physics* **2018**(06): 024–024.
**URL:** *http://dx.doi.org/10.1088/1475-7516/2018/06/024*

Cui, Y. and Morrissey, D. E. (2009). Nonthermal dark matter from cosmic strings, *Physical Review D* **79**(8).
**URL:** *http://dx.doi.org/10.1103/PhysRevD.79.083532*

Cunha, P. V. P. and Herdeiro, C. A. R. (2018). Shadows and strong gravitational lensing: a brief review, *General Relativity and Gravitation* **50**(4).
**URL:** *http://dx.doi.org/10.1007/s10714-018-2361-9*

Cutright, T. L. and Ghandour, G. I. (1975). Vacuum stability and supersymmetry, *Physics Letters B* **59**(4): 387–390.
**URL:** https://ui.adsabs.harvard.edu/abs/1975PhLB...59..387C

DarkSide Collaboration (2015). First results from the darkside-50 dark matter experiment at laboratori nazionali del gran sasso, *Physics Letters B* **743**: 456–466.
**URL:** http://dx.doi.org/10.1016/j.physletb.2015.03.012

Davis, M. (1985). The Big Bang and Georges Lemaître, *Science* **229**: 644.

Davis, M., Efstathiou, G., Frenk, C. S. and White, S. D. M. (1985). The evolution of large-scale structure in a universe dominated by cold dark matter, *The Astrophysical Journal* **292**: 371–394.
**URL:** https://ui.adsabs.harvard.edu/abs/1985ApJ...292..371D

Daylan, T., Finkbeiner, D. P., Hooper, D., Linden, T., Portillo, S. K., Rodd, N. L. and Slatyer, T. R. (2016). The characterization of the gamma-ray signal from the central Milky Way: A case for annihilating dark matter, *Physics of the Dark Universe* **12**: 1–23.
**URL:** http://dx.doi.org/10.1016/j.dark.2015.12.005

de Blok, W. J. G., Walter, F., Brinks, E., Trachternach, C., Oh, S.-H. and Kennicutt, R. C. (2008). High-resolution rotation curves and galaxy mass models from THINGS, *The Astronomical Journal* **136**(6): 2648–2719.
**URL:** http://dx.doi.org/10.1088/0004-6256/136/6/2648

De Luca, V., Desjacques, V., Franciolini, G., Pani, P. and Riotto, A. (2021). GW190521 Mass Gap Event and the Primordial Black Hole Scenario, *Physical Review Letters* **126**(5).
**URL:** http://dx.doi.org/10.1103/PhysRevLett.126.051101

De Propris, R., Couch, W. J., Colless, M., Dalton, G. B., Collins, C., Baugh, C. M., Bland-Hawthorn, J., Bridges, T., Cannon, R., Cole, S. and et al. (2002). The 2dF Galaxy Redshift Survey: a targeted study of catalogued clusters of galaxies, *Monthly Notices of the Royal Astronomical Society* **329**(1): 87–101.
**URL:** http://dx.doi.org/10.1046/j.1365-8711.2002.04958.x

de Salas, P. F. and Widmark, A. (2020). Dark matter local density determination: recent observations and future prospects.

Deason, A. J., Fattahi, A., Belokurov, V., Evans, N. W., Grand, R. J. J., Marinacci, F. and Pakmor, R. (2019). The local high-velocity tail and the galactic escape speed, *Monthly Notices of the Royal Astronomical Society* **485**(3): 3514–3526.
**URL:** http://dx.doi.org/10.1093/mnras/stz623

Del Popolo, A. and Pace, F. (2016). The Cusp/Core problem: supernovae feedback versus the baryonic clumps and dynamical friction model, *Astrophysics and Space Science* **361**(5).
**URL:** http://dx.doi.org/10.1007/s10509-016-2742-z

DES Collaboration (2015a). Eight new milky way companions discovered in first-year dark energy survey data, *The Astrophysical Journal* **807**(1): 50.
**URL:** http://dx.doi.org/10.1088/0004-637X/807/1/50

DES Collaboration (2015b). Eight ultra-faint galaxy candidates discovered in year two of the dark energy survey, *The Astrophysical Journal* **813**(2): 109.
**URL:** *http://dx.doi.org/10.1088/0004-637X/813/2/109*

DES Collaboration (2018). Dark Energy Survey year 1 results: Cosmological constraints from galaxy clustering and weak lensing, *Physical Review D* **98**(4).
**URL:** *http://dx.doi.org/10.1103/PhysRevD.98.043526*

DES Collaboration (2019a). First Cosmology Results using Type Ia Supernovae from the Dark Energy Survey: Constraints on Cosmological Parameters, *The Astrophysical Journal* **872**(2): L30.
**URL:** *http://dx.doi.org/10.3847/2041-8213/ab04fa*

DES Collaboration, LIGO Collaboration, V. (2019b). First Measurement of the Hubble Constant from a Dark Standard Siren using the Dark Energy Survey Galaxies and the LIGO/Virgo Binary–Black-hole Merger GW170814, *The Astrophysical Journal* **876**(1): L7.
**URL:** *http://dx.doi.org/10.3847/2041-8213/ab14f1*

Desert, F. X. (2000). Sunyaev-Zel'dovich effect review, *35th Rencontres de Moriond: Energy Densities in the Universe*, pp. 107–114.

Dev, P. S. B., Mazumdar, A. and Qutub, S. (2014). Constraining non-thermal and thermal properties of dark matter, *Frontiers in Physics* **2**.
**URL:** *http://dx.doi.org/10.3389/fphy.2014.00026*

Di Cintio, A., Brook, C. B., Macciò, A. V., Stinson, G. S., Knebe, A., Dutton, A. A. and Wadsley, J. (2013). The dependence of dark matter profiles on the stellar-to-halo mass ratio: a prediction for cusps versus cores, *Monthly Notices of the Royal Astronomical Society* **437**(1): 415–423.
**URL:** *http://dx.doi.org/10.1093/mnras/stt1891*

Di Mauro, M. (2021). Characteristics of the Galactic Center excess measured with 11 years of Fermi-LAT data, *Physical Review D* **103**(6).
**URL:** *http://dx.doi.org/10.1103/PhysRevD.103.063029*

Di Mauro, M., Donato, F., Fornengo, N., Lineros, R. and Vittino, A. (2014). Interpretation of AMS-02 electrons and positrons data, *Journal of Cosmology and Astroparticle Physics* **2014**(04): 006–006.
**URL:** *http://dx.doi.org/10.1088/1475-7516/2014/04/006*

Di Mauro, M. and Winkler, M. W. (2021). Multimessenger constraints on the dark matter interpretation of the Fermi-LAT Galactic center excess.
**URL:** *https://ui.adsabs.harvard.edu/abs/2021arXiv210111027D*

Diemand, J., Kuhlen, M., Madau, P., Zemp, M., Moore, B., Potter, D. and Stadel, J. (2008). Clumps and streams in the local dark matter distribution, *Nature* **454**(7205): 735–738.
**URL:** *http://dx.doi.org/10.1038/nature07153*

Diez-Tejedor, A. and Marsh, D. J. E. (2017). Cosmological production of ultralight dark matter axions.

Dirkes, A. (2018). Gravitational waves - a review on the theoretical foundations of gravitational radiation, *International Journal of Modern Physics A*

**33**(14n15): 1830013.
**URL:** http://dx.doi.org/10.1142/S0217751X18300132

Dodelson, S. (2003). *Modern Cosmology*, Academic Press, Amsterdam.

Donato, F., Fornengo, N. and Salati, P. (2000). Antideuterons as a signature of supersymmetric dark matter, *Physical Review D* **62**(4).
**URL:** http://dx.doi.org/10.1103/PhysRevD.62.043003

Drewes, M. (2013). The phenomenology of right handed neutrinos, *International Journal of Modern Physics E* **22**(08): 1330019.
**URL:** http://dx.doi.org/10.1142/S0218301313300191

Dutton, A. A., Macciò, A. V., Frings, J., Wang, L., Stinson, G. S., Penzo, C. and Kang, X. (2016). NIHAO V: too big does not fail – reconciling the conflict between ΛCDM predictions and the circular velocities of nearby field galaxies, *Monthly Notices of the Royal Astronomical Society: Letters* **457**(1): L74–L78.
**URL:** http://dx.doi.org/10.1093/mnrasl/slv193

Einasto, J. (1965). On the Construction of a Composite Model for the Galaxy and on the Determination of the System of Galactic Parameters, *Trudy Astrofizicheskogo Instituta Alma-Ata* **5**: 87–100.
**URL:** https://ui.adsabs.harvard.edu/abs/1965TrAlm...5...87E

Einasto, J. (2010). Dark matter.
**URL:** https://arxiv.org/abs/0901.0632

Einstein, A. (1918). Über Gravitationswellen, *Sitzungsberichte der Königlich Preussischen Akademie der Wissenschaften (Berlin* pp. 154–167.
**URL:** https://ui.adsabs.harvard.edu/abs/1918SPAW.....154E

Eisenstein, D. J. and Hu, W. (1998). Baryonic Features in the Matter Transfer Function, *The Astrophysical Journal* **496**(2): 605–614.
**URL:** http://dx.doi.org/10.1086/305424

Eisenstein, D. J., Zehavi, I., Hogg, D. W., Scoccimarro, R., Blanton, M. R., Nichol, R. C., Scranton, R., Seo, H., Tegmark, M., Zheng, Z. and et al. (2005). Detection of the Baryon Acoustic Peak in the Large-Scale Correlation Function of SDSS Luminous Red Galaxies, *The Astrophysical Journal* **633**(2): 560–574.
**URL:** http://dx.doi.org/10.1086/466512

Ellis, J., Hagelin, J. S., Nanopoulos, D. V., Olive, K. and Srednicki, M. (1984). Supersymmetric relics from the big bang, *Nuclear Physics B* **238**(2): 453–476.
**URL:** https://ui.adsabs.harvard.edu/abs/1984NuPhB.238..453E

Errani, R. and Peñarrubia, J. (2019). Can tides disrupt cold dark matter subhaloes?, *Monthly Notices of the Royal Astronomical Society* **491**(4): 4591–4601.
**URL:** http://dx.doi.org/10.1093/mnras/stz3349

Esmaili, A. and Serpico, P. D. (2013). Are IceCube neutrinos unveiling PeV-scale decaying dark matter?, *Journal of Cosmology and Astroparticle Physics* **2013**(11): 054–054.
**URL:** http://dx.doi.org/10.1088/1475-7516/2013/11/054

European Space Agency (2007). Image credit: X-ray – NASA/CXC/CfA/M.Markevitch, Optical and lensing map – NASA/STScI, Magellan/U.Arizona/D.Clowe, Lensing map – ESO WFI, https://www.esa.int/ESA_Multimedia/Images/2007/07/The_Bullet_Cluster2.

Evans, L. and Bryant, P. (2008). LHC machine, *Journal of Instrumentation* **3**(08): S08001–S08001.
**URL:** *https://doi.org/10.1088/1748-0221/3/08/s08001*

Evoli, C., Gaggero, D., Vittino, A., Bernardo, G. D., Mauro, M. D., Ligorini, A., Ullio, P. and Grasso, D. (2017). Cosmic-ray propagation with DRAGON2: I. numerical solver and astrophysical ingredients, *Journal of Cosmology and Astroparticle Physics* **2017**(02): 015–015.
**URL:** *http://dx.doi.org/10.1088/1475-7516/2017/02/015*

Ezquiaga, J. M. and García-Bellido, J. (2018). Quantum diffusion beyond slow-roll: implications for primordial black-hole production, *Journal of Cosmology and Astroparticle Physics* **2018**(08): 018–018.
**URL:** *http://dx.doi.org/10.1088/1475-7516/2018/08/018*

Faber, S. M. and Gallagher, J. S. (1979). Masses and mass-to-light ratios of galaxies., *Annual Review of Astronomy and Astrophysics* **17**: 135–187.
**URL:** *https://ui.adsabs.harvard.edu/abs/1979ARA&A..17..135F*

Farrar, G. R. and Sutherland, M. S. (2019). Deflections of UHECRs in the Galactic magnetic field, *Journal of Cosmology and Astroparticle Physics* **2019**(05): 004–004.
**URL:** *http://dx.doi.org/10.1088/1475-7516/2019/05/004*

Feng, J. L. (2010). Dark Matter Candidates from Particle Physics and Methods of Detection, *Annual Review of Astronomy and Astrophysics* **48**(1): 495–545.
**URL:** *http://dx.doi.org/10.1146/annurev-astro-082708-101659*

Fermi-LAT Collaboration (2012). Search for Dark Matter Satellites using the Fermi-LAT, *The Astrophysical Journal* **747**(2): 121.
**URL:** *http://dx.doi.org/10.1088/0004-637X/747/2/121*

Fermi-LAT Collaboration (2015a). Limits on dark matter annihilation signals from the Fermi LAT 4-year measurement of the isotropic gamma-ray background, *Journal of Cosmology and Astroparticle Physics* **2015**(09): 008–008.
**URL:** *http://dx.doi.org/10.1088/1475-7516/2015/09/008*

Fermi-LAT Collaboration (2015b). Updated search for spectral lines from Galactic dark matter interactions with pass 8 data from the Fermi Large Area Telescope, *Physical Review D* **91**(12).
**URL:** *http://dx.doi.org/10.1103/PhysRevD.91.122002*

Fermi-LAT Collaboration (2016). Fermi-LAT Observations of High-Energy Gamma-Ray Emission Toward the Galactic Center, *The Astrophysical Journal* **819**(1): 44.
**URL:** *http://dx.doi.org/10.3847/0004-637X/819/1/44*

Fermi-LAT Collaboration (2020). Fermi large area telescope fourth source catalog, *The Astrophysical Journal Supplement Series* **247**(1): 33.
**URL:** *http://dx.doi.org/10.3847/1538-4365/ab6bcb*

Fermi-LAT Collaboration and DES Collaboration (2017). Searching for Dark Matter Annihilation in Recently Discovered Milky Way Satellites with Fermi-LAT, *The Astrophysical Journal* **834**(2): 110.
**URL:** http://dx.doi.org/10.3847/1538-4357/834/2/110

Fields, B. D. (2011). The Primordial Lithium Problem, *Annual Review of Nuclear and Particle Science* **61**(1): 47–68.
**URL:** http://dx.doi.org/10.1146/annurev-nucl-102010-130445

Fleury, P. and García-Bellido, J. (2020). On simple analytic models of microlensing amplification statistics, *Physics of the Dark Universe* **29**: 100567.
**URL:** http://dx.doi.org/10.1016/j.dark.2020.100567

Fong, M., Bowyer, R., Whitehead, A., Lee, B., King, L., Applegate, D. and McCarthy, I. (2018). Prospects for Determining the Mass Distributions of Galaxy Clusters on Large Scales Using Weak Gravitational Lensing, *Monthly Notices of the Royal Astronomical Society* .
**URL:** http://dx.doi.org/10.1093/mnras/sty1339

Foëx, G., Soucail, G., Pointecouteau, E., Arnaud, M., Limousin, M. and Pratt, G. W. (2012). The dark matter distribution in $z \sim 0.5$ clusters of galaxies, *Astronomy & Astrophysics* **546**: A106.
**URL:** http://dx.doi.org/10.1051/0004-6361/201218973

Freeman, K. C. (1970). On the Disks of Spiral and S0 Galaxies, *The Astrophysical Journal* **160**: 811.
**URL:** https://ui.adsabs.harvard.edu/abs/1970ApJ...160..811F

Freese, K., Fields, B. and Graff, D. (1999). What are MACHOs? Limits on stellar objects as the dark matter of our halo, *in* H. V. Klapdor-Kleingrothaus and L. Baudis (eds), *Dark matter in Astrophysics and Particle Physics*, p. 397.
**URL:** https://ui.adsabs.harvard.edu/abs/1999dmap.conf..397F

Froborg, F. and Duffy, A. R. (2020). Annual modulation in direct dark matter searches, *Journal of Physics G: Nuclear and Particle Physics* **47**(9): 094002.
**URL:** http://dx.doi.org/10.1088/1361-6471/ab8e93

Gardner, J. P., Mather, J. C., Clampin, M., Doyon, R., Greenhouse, M. A., Hammel, H. B., Hutchings, J. B., Jakobsen, P., Lilly, S. J., Long, K. S. and et al. (2006). The James Webb Space Telescope, *Space Science Reviews* **123**(4): 485–606.
**URL:** http://dx.doi.org/10.1007/s11214-006-8315-7

Garrison-Kimmel, S., Wetzel, A., Bullock, J. S., Hopkins, P. F., Boylan-Kolchin, M., Faucher-Giguère, C.-A., Kereš, D., Quataert, E., Sanderson, R. E., Graus, A. S. and et al. (2017). Not so lumpy after all: modelling the depletion of dark matter subhaloes by milky way-like galaxies , *Monthly Notices of the Royal Astronomical Society* **471**(2): 1709–1727.
**URL:** http://dx.doi.org/10.1093/mnras/stx1710

Garzilli, A., Magalich, A., Theuns, T., Frenk, C. S., Weniger, C., Ruchayskiy, O. and Boyarsky, A. (2019). The Lyman-$\alpha$ forest as a diagnostic of the nature of the dark matter, *Monthly Notices of the Royal Astronomical Society* **489**(3): 3456–3471.
**URL:** http://dx.doi.org/10.1093/mnras/stz2188

Gaskins, J. M. (2016). A review of indirect searches for particle dark matter, *Contemporary Physics* **57**(4): 496–525.
**URL:** *http://dx.doi.org/10.1080/00107514.2016.1175160*

Gaudi, B. S. (2021). The Demographics of Wide-Separation Planets.

Giagu, S. (2019). WIMP Dark Matter Searches With the ATLAS Detector at the LHC, *Frontiers in Physics* **7**: 75.
**URL:** *https://www.frontiersin.org/article/10.3389/fphy.2019.00075*

Giunti, C. (2016). Light sterile neutrinos: Status and perspectives, *Nuclear Physics B* **908**: 336–353.
**URL:** *http://dx.doi.org/10.1016/j.nuclphysb.2016.01.013*

Gnedin, O. Y., Ceverino, D., Gnedin, N. Y., Klypin, A. A., Kravtsov, A. V., Levine, R., Nagai, D. and Yepes, G. (2011). Halo Contraction Effect in Hydrodynamic Simulations of Galaxy Formation.

Goerdt, T., Gnedin, O. Y., Moore, B., Diemand, J. and Stadel, J. (2007). The survival and disruption of cold dark matter microhaloes: implications for direct and indirect detection experiments, *Monthly Notices of the Royal Astronomical Society* **375**(1): 191–198.
**URL:** *http://dx.doi.org/10.1111/j.1365-2966.2006.11281.x*

Golden, R. L., Stochaj, S. J., Stephens, S. A., Aversa, F., Barbiellini, G., Boezio, M., Bravar, U., Colavita, A., Fratnik, F., Schiavon, P., Vacchi, A., Zampa, N., Mitchell, J. W., Ormes, J. F., Steitmatter, R. E., Bellotti, R., Cafagna, F., Castellano, M., Circella, M., de Cataldo, G., de Marzo, C., Giglietto, N., Marangelli, B., Raino, A., Spinelli, P., Bocciolini, M., Finetti, N., Papini, P., Perego, A., Piccardi, S., Spillantini, P., Basini, G., Massimo Brancaccio, F., Ricci, M., Brunetti, M. T., Codino, A., Grimani, C., Menichelli, M., Bidoli, V., Candusso, M., Casolino, M., de Pascale, M. P., Morselli, A., Picozza, P., Sparvoli, R., Hof, M., Menn, W. and Simon, M. (1996). Measurement of the Positron to Electron Ratio in Cosmic Rays above 5 GeV, *The Astrophysical Journal Letters* **457**: L103.
**URL:** *https://ui.adsabs.harvard.edu/abs/1996ApJ...457L.103G*

Goodenough, L. and Hooper, D. (2009). Possible Evidence For Dark Matter Annihilation In The Inner Milky Way From The Fermi Gamma Ray Space Telescope.
**URL:** *https://arxiv.org/abs/0910.2998*

Goodman, J., Ibe, M., Rajaraman, A., Shepherd, W., Tait, T. M. P. and Yu, H.-B. (2010). Constraints on dark matter from colliders, *Physical Review D* **82**(11).
**URL:** *http://dx.doi.org/10.1103/PhysRevD.82.116010*

Goodman, M. W. and Witten, E. (1985). Detectability of certain dark-matter candidates, *Physical Review D* **31**(12): 3059–3063.
**URL:** *https://ui.adsabs.harvard.edu/abs/1985PhRvD..31.3059G*

Governato, F., Brook, C., Mayer, L., Brooks, A., Rhee, G., Wadsley, J., Jonsson, P., Willman, B., Stinson, G., Quinn, T. and et al. (2010). Bulgeless dwarf galaxies and dark matter cores from supernova-driven outflows, *Nature* **463**(7278): 203–206.
**URL:** *http://dx.doi.org/10.1038/nature08640*

Green, A. M. (2012). Astrophysical uncertainties on direct detection experiments, *Modern Physics Letters A* **27**(03): 1230004.
**URL:** *http://dx.doi.org/10.1142/S0217732312300042*

Green, A. M., Hofmann, S. and Schwarz, D. J. (2005). The first WIMPy halos, *Journal of Cosmology and Astroparticle Physics* **2005**(08): 003–003.
**URL:** http://dx.doi.org/10.1088/1475-7516/2005/08/003

Green, A. M. and Kavanagh, B. J. (2020). Primordial Black Holes as a dark matter candidate, *Journal of Physics G: Nuclear and Particle Physics* **48**(4).

Green, S. B. and van den Bosch, F. C. (2019). The tidal evolution of dark matter substructure – I. subhalo density profiles, *Monthly Notices of the Royal Astronomical Society* **490**(2): 2091–2101.
**URL:** http://dx.doi.org/10.1093/mnras/stz2767

Griest, K. (1993). The Search for the Dark Matter: WIMPs and MACHOs, *Annals of the New York Academy of Sciences* **688**(1): 390–407.
**URL:** http://dx.doi.org/10.1111/j.1749-6632.1993.tb43912.x

Griest, K. and Kamionkowski, M. (1990). Unitarity limits on the mass and radius of dark-matter particles, *Physical Review Letters* **64**(6): 615–618.
**URL:** https://ui.adsabs.harvard.edu/abs/1990PhRvL..64..615G

Griffen, B. F., Ji, A. P., Dooley, G. A., Gómez, F. A., Vogelsberger, M., O'Shea, B. W. and Frebel, A. (2016). The caterpillar project: A large suite of milky way sized halos, *The Astrophysical Journal* **818**(1): 10.
**URL:** http://dx.doi.org/10.3847/0004-637X/818/1/10

Guo, R., Liu, C., Mao, S., Xue, X.-X., Long, R. J. and Zhang, L. (2020). Measuring the local dark matter density with LAMOST DR5 and Gaia DR2, *Monthly Notices of the Royal Astronomical Society* **495**(4): 4828–4844.
**URL:** http://dx.doi.org/10.1093/mnras/staa1483

Haber, H. E. and Haskins, L. S. (2018). Supersymmetric theory and models, *Anticipating the Next Discoveries in Particle Physics* .
**URL:** http://dx.doi.org/10.1142/97898132333480006

Hall, L. J., Jedamzik, K., March-Russell, J. and West, S. M. (2010). Freeze-in production of FIMP dark matter, *Journal of High Energy Physics* **2010**(3).
**URL:** http://dx.doi.org/10.1007/JHEP03(2010)080

HAWC Collaboration (2017). Extended gamma-ray sources around pulsars constrain the origin of the positron flux at Earth, *Science* **358**(6365): 911–914.
**URL:** http://dx.doi.org/10.1126/science.aan4880

HAWC Collaboration (2018). Dark Matter Limits from Dwarf Spheroidal Galaxies with the HAWC Gamma-Ray Observatory, *The Astrophysical Journal* **853**(2): 154.
**URL:** http://dx.doi.org/10.3847/1538-4357/aaa6d8

Hawking, S. (1971). Gravitationally collapsed objects of very low mass, *Monthly Notices of the Royal Astronomical Society* **152**: 75.
**URL:** https://ui.adsabs.harvard.edu/abs/1971MNRAS.152...75H

Hawking, S. W. (1975). Particle creation by black holes, *Communications in Mathematical Physics* **43**(3): 199–220.
**URL:** https://ui.adsabs.harvard.edu/abs/1975CMaPh..43..199H

Haxton, W. C. (1995). The Solar Neutrino Problem, *Annual Review of Astronomy and Astrophysics* **33**(1): 459–503.
**URL:** https://doi.org/10.1146/annurev.aa.33.090195.002331

Hayashi, E. and White, S. D. M. (2006). How rare is the bullet cluster?, *Monthly Notices of the Royal Astronomical Society: Letters* **370**(1): L38–L41.
**URL:** http://dx.doi.org/10.1111/j.1745-3933.2006.00184.x

HEAT Collaboration (1997). Measurements of the Cosmic-Ray Positron Fraction from 1 to 50 GeV, *The Astrophysical Journal* **482**(2): L191–L194.
**URL:** http://dx.doi.org/10.1086/310706

Heisig, J., Korsmeier, M. and Winkler, M. W. (2020). Dark matter or correlated errors: Systematics of the AMS-02 antiproton excess, *Physical Review Research* **2**(4).
**URL:** http://dx.doi.org/10.1103/PhysRevResearch.2.043017

Hermans, J., Banik, N., Weniger, C., Bertone, G. and Louppe, G. (2020). Towards constraining warm dark matter with stellar streams through neural simulation-based inference.

Hernquist, L., Katz, N., Weinberg, D. H. and Miralda-Escudé, J. (1996). The Lyman-Alpha Forest in the Cold Dark Matter Model, *The Astrophysical Journal* **457**(2).
**URL:** http://dx.doi.org/10.1086/309899

H.E.S.S. Collaboration (2011). H.E.S.S. observations of the globular clusters NGC6388 and M15 and search for a Dark Matter signal, *The Astrophysical Journal* **735**(1): 12.
**URL:** http://dx.doi.org/10.1088/0004-637X/735/1/12

H.E.S.S. Collaboration (2012). Search for Dark Matter Annihilation Signals from the Fornax Galaxy Cluster with H.E.S.S, *The Astrophysical Journal* **750**(2): 123.
**URL:** http://dx.doi.org/10.1088/0004-637X/750/2/123

H.E.S.S. Collaboration (2014). Search for dark matter annihilation signatures in H.E.S.S. observations of dwarf spheroidal galaxies, *Physical Review D* **90**(11).
**URL:** http://dx.doi.org/10.1103/PhysRevD.90.112012

H.E.S.S. Collaboration (2016). Search for Dark Matter Annihilations towards the Inner Galactic Halo from 10 Years of Observations with H.E.S.S., *Physical Review Letters* **117**(11).
**URL:** http://dx.doi.org/10.1103/PhysRevLett.117.111301

H.E.S.S. Collaboration (2018). Search for $\gamma$-Ray Line Signals from Dark Matter Annihilations in the Inner Galactic Halo from 10 Years of Observations with H.E.S.S., *Physical Review Letters* **120**(20).
**URL:** http://dx.doi.org/10.1103/PhysRevLett.120.201101

Hicken, M., Challis, P., Kirshner, R. P., Rest, A., Cramer, C. E., Wood-Vasey, W. M., Bakos, G., Berlind, P., Brown, W. R., Caldwell, N. and et al. (2012). Cfa4: Light curves for 94 type Ia supernovae, *The Astrophysical Journal Supplement Series* **200**(2): 12.
**URL:** http://dx.doi.org/10.1088/0067-0049/200/2/12

Higgs, P. W. (1964). Broken Symmetries and the Masses of Gauge Bosons, *Physical Review Letters* **13**(16): 508–509.
**URL:** https://ui.adsabs.harvard.edu/abs/1964PhRvL..13..508H

Hirata, K., Kajita, T., Koshiba, M., Nakahata, M., Oyama, Y., Sato, N., Suzuki, A., Takita, M., Totsuka, Y., Kifune, T., Suda, T., Takahashi, K., Tanimori, T., Miyano, K., Yamada, M., Beier, E. W., Feldscher, L. R., Kim, S. B., Mann, A. K., Newcomer, F. M., van, R., Zhang, W. and Cortez, B. G. (1987). Observation of a neutrino burst from the supernova SN1987A, *Physical Review Letters* **58**(14): 1490–1493.
**URL:** https://ui.adsabs.harvard.edu/abs/1987PhRvL..58.1490H

Hisano, J., Matsumoto, S. and Nojiri, M. M. (2004). Explosive Dark Matter Annihilation, *Physical Review Letters* **92**(3).
**URL:** http://dx.doi.org/10.1103/PhysRevLett.92.031303

Holmberg, E. (1941). On the Clustering Tendencies among the Nebulae. II. a Study of Encounters Between Laboratory Models of Stellar Systems by a New Integration Procedure., *The Astrophysical Journal* **94**: 385.
**URL:** https://ui.adsabs.harvard.edu/abs/1941ApJ...94..385H

Holopainen, J., Flynn, C., Knebe, A., Gill, S. P. and Gibson, B. K. (2006). Microlensing in dark matter haloes, *Monthly Notices of the Royal Astronomical Society* **368**(3): 1209–1222.
**URL:** http://dx.doi.org/10.1111/j.1365-2966.2006.10205.x

Holtzman, J. A., Hester, J. J., Casertano, S., Trauger, J. T., Watson, A. M., Ballester, G. E., Burrows, C. J., Clarke, J. T., Crisp, D., Evans, R. W., Gallagher, John S., I., Griffiths, R. E., Hoessel, J. G., Matthews, L. D., Mould, J. R., Scowen, P. A., Stapelfeldt, K. R. and Westphal, J. A. (1995). The Performance and Calibration of WFPC2 on the Hubble Space Telescope, *Publications of the Astronomical Society of the Pacific* **107**: 156.
**URL:** https://ui.adsabs.harvard.edu/abs/1995PASP..107..156H

Hook, A. (2018). TASI Lectures on the Strong CP Problem and Axions, *TASI 2018 - Theory in an Era of Data*, p. 4.
**URL:** https://ui.adsabs.harvard.edu/abs/2018tasi.confE...4H

Hooper, D. and Linden, T. (2011). Origin of the gamma rays from the Galactic Center, *Physical Review D* **84**(12).
**URL:** http://dx.doi.org/10.1103/PhysRevD.84.123005

Hooper, D. and Profumo, S. (2007). Dark matter and collider phenomenology of universal extra dimensions, *Physics Reports* **453**(2-4): 29–115.
**URL:** http://dx.doi.org/10.1016/j.physrep.2007.09.003

Hubble, E. (1929). A Relation between Distance and Radial Velocity among Extra-Galactic Nebulae, *Proceedings of the National Academy of Science* **15**(3): 168–173.
**URL:** https://ui.adsabs.harvard.edu/abs/1929PNAS...15..168H

Hughes, J. and Wallerstein, G. (2011). Determining Photometric Metallicities of dSph Stellar Populations, *in* A. McWilliam (ed.), *RR Lyrae Stars, Metal-Poor Stars, and the Galaxy*, Vol. 5, p. 249.
**URL:** https://ui.adsabs.harvard.edu/abs/2011rrls.conf..249H

Hulse, R. A. and Taylor, J. H. (1975). Discovery of a pulsar in a binary system., *The Astrophysical Journal Letters* **195**: L51–L53.
**URL:** https://ui.adsabs.harvard.edu/abs/1975ApJ...195L..51H

Ibarra, A., Tran, D. and Weniger, C. (2013). Indirect searches for decaying dark matter, *International Journal of Modern Physics A* **28**(27): 1330040.
**URL:** http://dx.doi.org/10.1142/S0217751X13300408

Ibarra, A. and Wild, S. (2013). Determination of the cosmic antideuteron flux in a Monte Carlo approach, *Physical Review D* **88**(2).
**URL:** http://dx.doi.org/10.1103/PhysRevD.88.023014

Ibata, R. A., Lewis, G. F., Conn, A. R., Irwin, M. J., McConnachie, A. W., Chapman, S. C., Collins, M. L., Fardal, M., Ferguson, A. M. N., Ibata, N. G. and et al. (2013). A vast, thin plane of corotating dwarf galaxies orbiting the Andromeda galaxy, *Nature* **493**(7430): 62–65.
**URL:** http://dx.doi.org/10.1038/nature11717

Ibata, R., Thomas, G., Famaey, B., Malhan, K., Martin, N. and Monari, G. (2020). Detection of Strong Epicyclic Density Spikes in the GD-1 Stellar Stream: An Absence of Evidence for the Influence of Dark Matter Subhalos?, *The Astrophysical Journal* **891**(2): 161.
**URL:** http://dx.doi.org/10.3847/1538-4357/ab7303

IceCube Collaboration (2017). The IceCube Neutrino Observatory: instrumentation and online systems, *Journal of Instrumentation* **12**(03): P03012–P03012.
**URL:** http://dx.doi.org/10.1088/1748-0221/12/03/P03012

IceCube Collaboration (2018). Neutrino emission from the direction of the blazar TXS 0506+056 prior to the IceCube-170922A alert, *Science* **361**(6398): 147–151.
**URL:** http://dx.doi.org/10.1126/science.aat2890

IceCube Collaboration (2021). Search for GeV neutrino emission during intense gamma-ray solar flares with the IceCube Neutrino Observatory, *Physical Review D* **103**(10).
**URL:** http://dx.doi.org/10.1103/PhysRevD.103.102001

Iocco, F., Pato, M. and Bertone, G. (2015). Evidence for dark matter in the inner Milky Way, *Nature Physics* **11**(3): 245–248.
**URL:** http://dx.doi.org/10.1038/nphys3237

Ishihara, A. and IceCube Collaboration (2016). Extremely high energy neutrinos in six years of IceCube data, *Journal of Physics Conference Series*, Vol. 718 of *Journal of Physics Conference Series*, p. 062027.
**URL:** https://ui.adsabs.harvard.edu/abs/2016JPhCS.718f2027I

Ishiyama, T. (2014). Hierarchical formation of dark matter halos and the free streaming scale, *The Astrophysical Journal* **788**(1): 27.
**URL:** http://dx.doi.org/10.1088/0004-637X/788/1/27

Ishiyama, T., Prada, F., Klypin, A. A., Sinha, M., Metcalf, R. B., Jullo, E., Altieri, B., Cora, S. A., Croton, D., de la Torre, S., Millán-Calero, D. E., Oogi, T., Ruedas, J. and Vega-Martínez, C. A. (2020). The Uchuu Simulations: Data Release 1 and Dark Matter Halo Concentrations.

Jeannerot, R., Zhang, X. and Brandenberger, R. (1999). Non-thermal production of neutralino cold dark matter from cosmic string decays, *Journal of High Energy Physics* **1999**(12): 003–003.
**URL:** http://dx.doi.org/10.1088/1126-6708/1999/12/003

Johnson, C., Caputo, R., Karwin, C., Murgia, S., Ritz, S. and Shelton, J. (2019). Search for gamma-ray emission from p-wave dark matter annihilation in the Galactic Center, *Physical Review D* **99**(10).
**URL:** http://dx.doi.org/10.1103/PhysRevD.99.103007

Jungman, G., Kamionkowski, M. and Griest, K. (1996). Supersymmetric dark matter, *Physics Reports* **267**(5-6): 195–373.
**URL:** http://dx.doi.org/10.1016/0370-1573(95)00058-5

Kalirai, J. S., Beaton, R. L., Geha, M. C., Gilbert, K. M., Guhathakurta, P., Kirby, E. N., Majewski, S. R., Ostheimer, J. C., Patterson, R. J. and Wolf, J. (2010). The splash survey: Internal kinematics, chemical abundances, and masses of the andromeda I, II, III, VII, X, and XIV dwarf spheroidal galaxies,, *The Astrophysical Journal* **711**(2): 671–692.
**URL:** http://dx.doi.org/10.1088/0004-637X/711/2/671

Kashlinsky, A. (1998). Determining $\Omega$ from the cluster correlation function, *Physics Reports* **307**(1-4): 67–73.
**URL:** http://dx.doi.org/10.1016/S0370-1573(98)00050-7

Kavanagh, B. J. and O'Hare, C. A. J. (2016). Reconstructing the three-dimensional local dark matter velocity distribution, *Physical Review D* **94**(12).
**URL:** http://dx.doi.org/10.1103/PhysRevD.94.123009

Kazantzidis, S., Mayer, L., Mastropietro, C., Diemand, J., Stadel, J. and Moore, B. (2004). Density Profiles of Cold Dark Matter Substructure: Implications for the Missing-Satellites Problem, *The Astrophysical Journal* **608**(2): 663–679.
**URL:** http://dx.doi.org/10.1086/420840

Kelso, C., Savage, C., Valluri, M., Freese, K., Stinson, G. S. and Bailin, J. (2016). The impact of baryons on the direct detection of dark matter, *Journal of Cosmology and Astroparticle Physics* **2016**(08): 071–071.
**URL:** http://dx.doi.org/10.1088/1475-7516/2016/08/071

Kim, S. Y., Peter, A. H. and Hargis, J. R. (2018). Missing Satellites Problem: Completeness Corrections to the Number of Satellite Galaxies in the Milky Way are Consistent with Cold Dark Matter Predictions, *Physical Review Letters* **121**(21).
**URL:** http://dx.doi.org/10.1103/PhysRevLett.121.211302

King, S. F. (2003). Neutrino mass models, *Reports on Progress in Physics* **67**(2): 107–157.
**URL:** http://dx.doi.org/10.1088/0034-4885/67/2/R01

Kitayama, T. (2014). Cosmological and astrophysical implications of the Sunyaev-Zel'dovich effect, *Progress of Theoretical and Experimental Physics* **2014**(6): 6B111–0.
**URL:** http://dx.doi.org/10.1093/ptep/ptu055

Klinger, J. and Kudryavtsev, V. (2015). Muon-Induced Neutrons Do Not Explain the DAMA Data, *Physical Review Letters* **114**(15).
**URL:** http://dx.doi.org/10.1103/PhysRevLett.114.151301

Klypin, A., Kravtsov, A. V., Valenzuela, O. and Prada, F. (1999). Where Are the Missing Galactic Satellites?, *The Astrophysical Journal* **522**(1): 82–92.
**URL:** http://dx.doi.org/10.1086/307643

Knebe, A., Pearce, F. R., Lux, H., Ascasibar, Y., Behroozi, P., Casado, J., Moran, C. C., Diemand, J., Dolag, K., Dominguez-Tenreiro, R. and et al. (2013). Structure finding in cosmological simulations: the state of affairs, *Monthly Notices of the Royal Astronomical Society* **435**(2): 1618–1658.
**URL:** *http://dx.doi.org/10.1093/mnras/stt1403*

Knobel, C. (2012). An Introduction into the Theory of Cosmological Structure Formation, *arXiv e-prints* p. arXiv:1208.5931.
**URL:** *https://ui.adsabs.harvard.edu/abs/2012arXiv1208.5931K*

Knödlseder, J., Jean, P., Lonjou, V., Weidenspointner, G., Guessoum, N., Gillard, W., Skinner, G., von Ballmoos, P., Vedrenne, G., Roques, J.-P. and et al. (2005). The all-sky distribution of 511 keV electron-positron annihilation emission, *Astronomy & Astrophysics* **441**(2): 513–532.
**URL:** *http://dx.doi.org/10.1051/0004-6361:20042063*

Kogut, A., Lineweaver, C., Smoot, G. F., Bennett, C. L., Banday, A., Boggess, N. W., Cheng, E. S., de Amici, G., Fixsen, D. J., Hinshaw, G. and et al. (1993). Dipole Anisotropy in the COBE Differential Microwave Radiometers First-Year Sky Maps, *The Astrophysical Journal* **419**: 1.
**URL:** *http://dx.doi.org/10.1086/173453*

Kolb, E. W. and Turner, M. S. (1990). *The early universe*, Vol. 69.
**URL:** *https://ui.adsabs.harvard.edu/abs/1990eaun.book.....K*

Kravtsov, A. V., Klypin, A. A., Bullock, J. S. and Primack, J. R. (1998). The Cores of Dark Matter-dominated Galaxies: Theory versus Observations, *The Astrophysical Journal* **502**(1): 48–58.
**URL:** *https://ui.adsabs.harvard.edu/abs/1998ApJ...502...48K*

Kubo, J. M., Stebbins, A., Annis, J., Dell'Antonio, I. P., Lin, H., Khiabanian, H. and Frieman, J. A. (2007). The Mass of the Coma Cluster from Weak Lensing in the Sloan Digital Sky Survey, *The Astrophysical Journal* **671**(2): 1466–1470.
**URL:** *http://dx.doi.org/10.1086/523101*

Kunkel, W. E. (1979). On the origin and dynamics of the Magellanic stream., *The Astrophysical Journal* **228**: 718–733.
**URL:** *https://ui.adsabs.harvard.edu/abs/1979ApJ...228..718K*

Lage, C. and Farrar, G. (2014). Constrained simulation of the bullet cluster, *The Astrophysical Journal* **787**(2): 144.
**URL:** *http://dx.doi.org/10.1088/0004-637X/787/2/144*

Lamarre, J. M., Puget, J. L., Bouchet, F., Ade, P. A. R., Benoit, A., Bernard, J. P., Bock, J., De Bernardis, P., Charra, J., Couchot, F., Delabrouille, J., Efstathiou, G., Giard, M., Guyot, G., Lange, A., Maffei, B., Murphy, A., Pajot, F., Piat, M., Ristorcelli, I., Santos, D., Sudiwala, R., Sygnet, J. F., Torre, J. P., Yurchenko, V. and Yvon, D. (2003). The Planck High Frequency Instrument, a third generation CMB experiment, and a full sky submillimeter survey, *New Astronomy Reviews* **47**(11-12): 1017–1024.
**URL:** *https://ui.adsabs.harvard.edu/abs/2003NewAR..47.1017L*

Leane, R. K. (2020). Indirect Detection of Dark Matter in the Galaxy.
**URL:** *https://arxiv.org/abs/2006.00513*

Leclercq, F., Jasche, J., Lavaux, G., Wandelt, B. and Percival, W. (2017). The phase-space structure of nearby dark matter as constrained by the SDSS, *Journal of Cosmology and Astroparticle Physics* **2017**(06): 049–049.
**URL:** http://dx.doi.org/10.1088/1475-7516/2017/06/049

Lee, B. W. and Weinberg, S. (1977). Cosmological lower bound on heavy-neutrino masses, *Physical Review Letters* **39**(4): 165–168.
**URL:** https://ui.adsabs.harvard.edu/abs/1977PhRvL..39..165L

Lemaître, G. (2013). Republication of: A homogeneous universe of constant mass and increasing radius accounting for the radial velocity of extra-galactic nebulae, *General Relativity and Gravitation* **45**(8): 1635–1646.
**URL:** https://ui.adsabs.harvard.edu/abs/2013GReGr..45.1635L

Lesgourgues, J. and Pastor, S. (2006). Massive neutrinos and cosmology, *Physics Reports* **429**(6): 307–379.
**URL:** http://dx.doi.org/10.1016/j.physrep.2006.04.001

Lewin, J. D. and Smith, P. F. (1996). Review of mathematics, numerical factors, and corrections for dark matter experiments based on elastic nuclear recoil, *Astroparticle Physics* **6**(1): 87–112.
**URL:** https://ui.adsabs.harvard.edu/abs/1996APh.....6..87L

LIGO Collaboration (2015). Advanced LIGO, *Classical and Quantum Gravity* **32**(7): 074001.
**URL:** http://dx.doi.org/10.1088/0264-9381/32/7/074001

LIGO Collaboration (2016). Observation of Gravitational Waves from a Binary Black Hole Merger, *Physical Review Letters* **116**(6).
**URL:** http://dx.doi.org/10.1103/PhysRevLett.116.061102

LIGO Collaboration (2017a). A gravitational-wave standard siren measurement of the Hubble constant, *Nature* **551**(7678): 85–88.
**URL:** http://dx.doi.org/10.1038/nature24471

LIGO Collaboration (2017b). GW170817: Observation of Gravitational Waves from a Binary Neutron Star Inspiral, *Physical Review Letters* **119**(16).
**URL:** http://dx.doi.org/10.1103/PhysRevLett.119.161101

LIGO Collaboration (2019). Tests of General Relativity with GW170817, *Physical Review Letters* **123**(1).
**URL:** http://dx.doi.org/10.1103/PhysRevLett.123.011102

LIGO Collaboration and Virgo Collaboration (2020). GW190521: A Binary Black Hole Merger with a Total Mass of 150 M , *Physical Review Letters* **125**(10): 101102.
**URL:** https://ui.adsabs.harvard.edu/abs/2020PhRvL.125j1102A

LIGO Collaboration and Virgo Collaboration (2021). A Gravitational-wave Measurement of the Hubble Constant Following the Second Observing Run of Advanced LIGO and Virgo, *The Astrophysical Journal* **909**(2): 218.
**URL:** http://dx.doi.org/10.3847/1538-4357/abdcb7

Lin, T. (2019). TASI lectures on dark matter models and direct detection.
**URL:** https://arxiv.org/abs/1904.07915

Linden, T. (2020). Robust method for treating astrophysical mismodeling in dark matter annihilation searches of dwarf spheroidal galaxies, *Physical Review D* **101**(4).
**URL:** http://dx.doi.org/10.1103/PhysRevD.101.043017

LUX Collaboration (2010). Status of the LUX Dark Matter Search, *in* G. Alverson, P. Nath and B. Nelson (eds), *SUSY09: 7th International Conference on Supersymmetry and the Unification of Fundamental Interactions*, Vol. 1200 of *American Institute of Physics Conference Series*, pp. 977–980.
**URL:** https://ui.adsabs.harvard.edu/abs/2010AIPC.1200..977F

Luzio, L. D., Gavela, B., Quilez, P. and Ringwald, A. (2021). Dark matter from an even lighter QCD axion: trapped misalignment.

Lynden-Bell, D. (1976). Dwarf galaxies and globular clusters in high velocity hydrogen streams., *Monthly Notices of the Royal Astronomical Society* **174**: 695–710.
**URL:** https://ui.adsabs.harvard.edu/abs/1976MNRAS.174..695L

Lynds, R. (1971). The Absorption-Line Spectrum of 4c 05.34, *The Astrophysical Journal Letters* **164**: L73.
**URL:** https://ui.adsabs.harvard.edu/abs/1971ApJ...164L..73L

LZ Collaboration (2020). The LUX-ZEPLIN (LZ) experiment, *Nuclear Instruments and Methods in Physics Research Section A: Accelerators, Spectrometers, Detectors and Associated Equipment* **953**: 163047.
**URL:** http://dx.doi.org/10.1016/j.nima.2019.163047

López-Fogliani, D. E. and Muñoz, C. (2020). Searching for supersymmetry: the $\mu\nu$SSM, *The European Physical Journal Special Topics* **229**(21): 3263–3301.
**URL:** http://dx.doi.org/10.1140/epjst/e2020-000114-9

Macciò, A. V., Stinson, G., Brook, C. B., Wadsley, J., Couchman, H. M. P., Shen, S., Gibson, B. K. and Quinn, T. (2011). Halo expansion in cosmological hydro simulations: Toward a baryonic solution of the cusp/core problem in massive spirals, *The Astrophysical Journal* **744**(1): L9.
**URL:** http://dx.doi.org/10.1088/2041-8205/744/1/L9

Machida, N. (2013). Vacuum stability of supersymmetric extended Higgs sectors with a discrete symmetry, *arXiv e-prints* p. arXiv:1305.2374.
**URL:** https://ui.adsabs.harvard.edu/abs/2013arXiv1305.2374M

MAGIC Collaboration (2014). Optimized dark matter searches in deep observations of Segue 1 with MAGIC, *Journal of Cosmology and Astroparticle Physics* **2014**(02): 008–008.
**URL:** http://dx.doi.org/10.1088/1475-7516/2014/02/008

MAGIC Collaboration and Fermi-LAT Collaboration (2016). Limits to dark matter annihilation cross-section from a combined analysis of MAGIC and Fermi-LAT observations of dwarf satellite galaxies, *Journal of Cosmology and Astroparticle Physics* **2016**(02): 039–039.
**URL:** http://dx.doi.org/10.1088/1475-7516/2016/02/039

Malhan, K. and Ibata, R. A. (2018). STREAMFINDER – I. A new algorithm for detecting stellar streams, *Monthly Notices of the Royal Astronomical Society* **477**(3): 4063–4076.
**URL:** http://dx.doi.org/10.1093/mnras/sty912

Malhan, K. and Ibata, R. A. (2019). Constraining the Milky Way halo potential with the GD-1 stellar stream, *Monthly Notices of the Royal Astronomical Society* **486**(3): 2995–3005.
**URL:** http://dx.doi.org/10.1093/mnras/stz1035

Malhan, K., Ibata, R. A., Carlberg, R. G., Bellazzini, M., Famaey, B. and Martin, N. F. (2019). Phase-space Correlation in Stellar Streams of the Milky Way Halo: The Clash of Kshir and GD-1, *The Astrophysical Journal* **886**(1): L7.
**URL:** http://dx.doi.org/10.3847/2041-8213/ab530e

Mandelbaum, R. (2018). Weak Lensing for Precision Cosmology, *Annual Review of Astronomy and Astrophysics* **56**(1): 393–433.
**URL:** http://dx.doi.org/10.1146/annurev-astro-081817-051928

Mantz, A. and Allen, S. W. (2011). Implicit Priors in Galaxy Cluster Mass and Scaling Relation Determinations, *arXiv e-prints* p. arXiv:1106.4052.
**URL:** https://ui.adsabs.harvard.edu/abs/2011arXiv1106.4052M

Marchesini, D., D'Onghia, E., Chincarini, G., Firmani, C., Conconi, P., Molinari, E. and Zacchei, A. (2002). H$\alpha$ Rotation Curves: The Soft Core Question, *The Astrophysical Journal* **575**(2): 801–813.
**URL:** http://dx.doi.org/10.1086/341475

Marsh, D. J. (2016). Axion cosmology, *Physics Reports* **643**: 1–79.
**URL:** http://dx.doi.org/10.1016/j.physrep.2016.06.005

Marsili, A., Bruce, R., Cerutti, F. and Redaelli, S. (2013). Simulations and Measurements of Physics Debris Losses at the 4 TeV LHC, *4th International Particle Accelerator Conference*, p. MOPWO041.

Martin, S. P. (1998). A supersymmetry primer, *Advanced Series on Directions in High Energy Physics* p. 1–98.
**URL:** http://dx.doi.org/10.1142/97898128396570001

Marulli, F., Carbone, C., Viel, M., Moscardini, L. and Cimatti, A. (2011). Effects of massive neutrinos on the large-scale structure of the Universe, *Monthly Notices of the Royal Astronomical Society* **418**(1): 346–356.
**URL:** http://dx.doi.org/10.1111/j.1365-2966.2011.19488.x

Masina, I. (2020). Dark matter and dark radiation from evaporating primordial black holes, *European Physical Journal Plus* **135**(7): 552.
**URL:** https://ui.adsabs.harvard.edu/abs/2020EPJP..135..552M

Mateo, M. (1998). Dwarf galaxies of the local group, *Annual Review of Astronomy and Astrophysics* **36**(1): 435–506.
**URL:** http://dx.doi.org/10.1146/annurev.astro.36.1.435

Mather, J. C., Cheng, E. S., Eplee, R. E., J., Isaacman, R. B., Meyer, S. S., Shafer, R. A., Weiss, R., Wright, E. L., Bennett, C. L., Boggess, N. W., Dwek, E., Gulkis, S., Hauser, M. G., Janssen, M., Kelsall, T., Lubin, P. M., Moseley, S. H., J., Murdock, T. L., Silverberg, R. F., Smoot, G. F. and Wilkinson, D. T. (1990). A Preliminary Measurement of the Cosmic Microwave Background Spectrum by the Cosmic Background Explorer (COBE) Satellite, *The Astrophysical Journal Letters* **354**: L37.
**URL:** https://ui.adsabs.harvard.edu/abs/1990ApJ...354L..37M

Maurin, D., Donato, F., Taillet, R. and Salati, P. (2001). Cosmic Rays below Z=30 in a Diffusion Model: New Constraints on Propagation Parameters, *The Astrophysical Journal* **555**(2): 585–596.
**URL:** http://dx.doi.org/10.1086/321496

Mavromatos, N. E., Sakellariadou, M. and Yusaf, M. F. (2009). Can the relativistic field theory version of modified newtonian dynamics avoid dark matter on galactic scales?, *Physical Review D* **79**(8).
**URL:** http://dx.doi.org/10.1103/PhysRevD.79.081301

Mayet, F., Green, A., Battat, J., Billard, J., Bozorgnia, N., Gelmini, G., Gondolo, P., Kavanagh, B., Lee, S., Loomba, D. and et al. (2016). A review of the discovery reach of directional dark matter detection, *Physics Reports* **627**: 1–49.
**URL:** http://dx.doi.org/10.1016/j.physrep.2016.02.007

McKinsey, D. N. (2018). Is DAMA Bathing in a Sea of Radioactive Argon?

Metz, M., Kroupa, P. and Jerjen, H. (2007). The spatial distribution of the Milky Way and Andromeda satellite galaxies, *Monthly Notices of the Royal Astronomical Society* **374**(3): 1125–1145.
**URL:** http://dx.doi.org/10.1111/j.1365-2966.2006.11228.x

Metz, M., Kroupa, P. and Jerjen, H. (2009). Discs of satellites: the new dwarf spheroidals, *Monthly Notices of the Royal Astronomical Society* **394**(4): 2223–2228.
**URL:** http://dx.doi.org/10.1111/j.1365-2966.2009.14489.x

Meyer, M., Giannotti, M., Mirizzi, A., Conrad, J. and Sánchez-Conde, M. (2017). Fermi Large Area Telescope as a Galactic Supernovae Axionscope, *Physical Review Letters* **118**(1).
**URL:** http://dx.doi.org/10.1103/PhysRevLett.118.011103

Meyer, M. and Petrushevska, T. (2020). Search for Axionlike-Particle-Induced Prompt $\gamma$-Ray Emission from Extragalactic Core-Collapse Supernovae with the Fermi Large Area Telescope, *Physical Review Letters* **124**(23).
**URL:** http://dx.doi.org/10.1103/PhysRevLett.124.231101

Milgrom, M. (2020). MOND vs. dark matter in light of historical parallels, *Studies in History and Philosophy of Science Part B: Studies in History and Philosophy of Modern Physics* **71**: 170–195.
**URL:** http://dx.doi.org/10.1016/j.shpsb.2020.02.004

Milgrom, M. and Sanders, R. H. (2005). MOND predictions of "halo" phenomenology in disc galaxies, *Monthly Notices of the Royal Astronomical Society* **357**(1): 45–48.
**URL:** http://dx.doi.org/10.1111/j.1365-2966.2004.08578.x

Milgrom, M. and Sanders, R. H. (2007). Modified Newtonian Dynamics Rotation Curves of Very Low Mass Spiral Galaxies, *The Astrophysical Journal* **658**(1): L17–L20.
**URL:** http://dx.doi.org/10.1086/513695

Miller, M. C. and Miller, J. M. (2015). The masses and spins of neutron stars and stellar-mass black holes, *Physics Reports* **548**: 1–34.
**URL:** http://dx.doi.org/10.1016/j.physrep.2014.09.003

Mirabal, N. (2013). Dark matter versus pulsars: catching the impostor, *Monthly Notices of the Royal Astronomical Society* **436**(3): 2461–2464.
**URL:** http://dx.doi.org/10.1093/mnras/stt1740

Mirabal, N., Charles, E., Ferrara, E. C., Gonthier, P. L., Harding, A. K., Sánchez-Conde, M. A. and Thompson, D. J. (2016). 3FGL Demographics Outside the Galactic Plane using Supervised Machine Learning: Pulsar and Dark Matter Subhalo Interpretations, *The Astrophysical Journal* **825**(1): 69.
**URL:** http://dx.doi.org/10.3847/0004-637X/825/1/69

Misner, C. W., Thorne, K. S. and Wheeler, J. A. (1973). *Gravitation*, W. H. Freeman, San Francisco.

Moliné, A., Sánchez-Conde, M. A., Palomares-Ruiz, S. and Prada, F. (2017). Characterization of subhalo structural properties and implications for dark matter annihilation signals, *Monthly Notices of the Royal Astronomical Society* p. stx026.
**URL:** http://dx.doi.org/10.1093/mnras/stx026

Moore, B., Governato, F., Quinn, T., Stadel, J. and Lake, G. (1998). Resolving the Structure of Cold Dark Matter Halos, *The Astrophysical Journal* **499**(1): L5–L8.
**URL:** http://dx.doi.org/10.1086/311333

Mukhanov, V. (2005). *Physical Foundations of Cosmology*, Cambridge University Press.

Muñoz, C. (2017). Models of Supersymmetry for Dark Matter, *EPJ Web of Conferences* **136**: 01002.
**URL:** http://dx.doi.org/10.1051/epjconf/201713601002

Nadler, E. O., Birrer, S., Gilman, D., Wechsler, R. H., Du, X., Benson, A., Nierenberg, A. M. and Treu, T. (2021). Dark Matter Constraints from a Unified Analysis of Strong Gravitational Lenses and Milky Way Satellite Galaxies.

Nadler, E. O., Mao, Y.-Y., Green, G. M. and Wechsler, R. H. (2019). Modeling the Connection between Subhalos and Satellites in Milky Way–like Systems, *The Astrophysical Journal* **873**(1): 34.
**URL:** http://dx.doi.org/10.3847/1538-4357/ab040e

Naumov, D. V. (2019). The Sterile Neutrino: A short introduction, *EPJ Web of Conferences* **207**: 04004.
**URL:** http://dx.doi.org/10.1051/epjconf/201920704004

Navarro, J. F., Frenk, C. S. and White, S. D. M. (1997). A Universal Density Profile from Hierarchical Clustering, *The Astrophysical Journal* **490**(2): 493–508.
**URL:** http://dx.doi.org/10.1086/304888

Navarro, J. F., Ludlow, A., Springel, V., Wang, J., Vogelsberger, M., White, S. D. M., Jenkins, A., Frenk, C. S. and Helmi, A. (2009). The diversity and similarity of simulated cold dark matter haloes, *Monthly Notices of the Royal Astronomical Society* **402**(1): 21–34.
**URL:** http://dx.doi.org/10.1111/j.1365-2966.2009.15878.x

Neininger, N. (2001). Contribution to dark matter from extragalactic dust, *in* H. V. Klapdor-Kleingrothaus (ed.), *Dark Matter in Astro- and Particle Physics*, Springer Berlin Heidelberg, Berlin, Heidelberg, pp. 52–59.

Nelson, A. E. and Scholtz, J. (2011). Dark light, dark matter, and the misalignment mechanism, *Physical Review D* **84**(10).
**URL:** *http://dx.doi.org/10.1103/PhysRevD.84.103501*

Nygren, D. (2011). A testable conventional hypothesis for the DAMA-LIBRA annual modulation.

Oakes, L. (2019). Combined Dark Matter Searches Towards Dwarf Spheroidal Galaxies with Fermi-LAT, HAWC, HESS, MAGIC and VERITAS, *36th International Cosmic Ray Conference (ICRC2019)*, Vol. 36 of *International Cosmic Ray Conference*, p. 539.
**URL:** *https://ui.adsabs.harvard.edu/abs/2019ICRC...36.539O*

Ordog, A., Brown, J. C., Kothes, R. and Landecker, T. L. (2017). Three-dimensional structure of the magnetic field in the disk of the Milky Way, *Astronomy & Astrophysics* **603**: A15.
**URL:** *http://dx.doi.org/10.1051/0004-6361/201730740*

Oñorbe, J., Boylan-Kolchin, M., Bullock, J. S., Hopkins, P. F., Kereš, D., Faucher-Giguère, C.-A., Quataert, E. and Murray, N. (2015). Forged in fire: cusps, cores and baryons in low-mass dwarf galaxies, *Monthly Notices of the Royal Astronomical Society* **454**(2): 2092–2106.
**URL:** *http://dx.doi.org/10.1093/mnras/stv2072*

O'Hare, C. A. (2020). Can we overcome the neutrino floor at high masses?, *Physical Review D* **102**(6).
**URL:** *http://dx.doi.org/10.1103/PhysRevD.102.063024*

Packard, R. (2020). Does Dark Matter Consist of Cosmic String Remnants?

Padmanabhan, T. (1993). *Structure Formation in the Universe*.
**URL:** *https://ui.adsabs.harvard.edu/abs/1993sfu..book.....P*

PAMELA Collaboration (2009). An anomalous positron abundance in cosmic rays with energies 1.5–100 GeV, *Nature* **458**(7238): 607–609.
**URL:** *http://dx.doi.org/10.1038/nature07942*

PAMELA Collaboration (2010). PAMELA Results on the Cosmic-Ray Antiproton Flux from 60 MeV to 180 GeV in Kinetic Energy, *Physical Review Letterss* **105**(12): 121101.
**URL:** *https://ui.adsabs.harvard.edu/abs/2010PhRvL.105l1101A*

Panda Collaboration (2016). Dark matter search results from the commissioning run of PandaX-II, *Physical Review D* **93**(12).
**URL:** *http://dx.doi.org/10.1103/PhysRevD.93.122009*

Panda Collaboration (2018). Dark matter direct search sensitivity of the PandaX-4T experiment, *Science China Physics, Mechanics & Astronomy* **62**(3).
**URL:** *http://dx.doi.org/10.1007/s11433-018-9259-0*

Pawlowski, M. S., McGaugh, S. S. and Jerjen, H. (2015). The new Milky Way satellites: alignment with the VPOS and predictions for proper motions and velocity dispersions, *Monthly Notices of the Royal Astronomical Society* **453**(1): 1047–1061.
**URL:** *http://dx.doi.org/10.1093/mnras/stv1588*

Peccei, R. D. and Quinn, H. R. (1977). CP conservation in the presence of pseudoparticles, *Physical Review Letters* **38**(25): 1440–1443.
**URL:** https://ui.adsabs.harvard.edu/abs/1977PhRvL..38.1440P

Peebles, P. J. E. (1980). *The large-scale structure of the universe*.
**URL:** https://ui.adsabs.harvard.edu/abs/1980lssu.book.....P

Penzias, A. A. and Wilson, R. W. (1965). A Measurement of Excess Antenna Temperature at 4080 Mc/s., *The Astrophysical journal* **142**: 419–421.
**URL:** https://ui.adsabs.harvard.edu/abs/1965ApJ...142..419P

Perkins, D. H. (2003). *Particle astrophysics*.
**URL:** https://ui.adsabs.harvard.edu/abs/2003paas.book.....P

Perrodin, D. and Sesana, A. (2018). Radio Pulsars: Testing Gravity and Detecting Gravitational Waves, *Astrophysics and Space Science Library* p. 95–148.
**URL:** http://dx.doi.org/10.1007/978-3-319-97616-73

Persic, M., Salucci, P. and Stel, F. (1996). The universal rotation curve of spiral galaxies — I. The dark matter connection, *Monthly Notices of the Royal Astronomical Society* **281**(1): 27–47.
**URL:** https://ui.adsabs.harvard.edu/abs/1996MNRAS.281...27P

Peskin, M. E. (2015). Supersymmetric dark matter in the harsh light of the Large Hadron Collider, *Proceedings of the National Academy of Sciences* **112**(40): 12256–12263.
**URL:** https://www.pnas.org/content/112/40/12256

Petač, M. (2019). *Galactic Dark Matter distribution and its implications for experimental searches*, PhD thesis, Scuola Internazionale Superiore di Studi Avanzati di Trieste (SISSA).

Petač, M. (2020). Equilibrium axisymmetric halo model for the Milky Way and its implications for direct and indirect dark matter searches, *Physical Review D* **102**(12).
**URL:** http://dx.doi.org/10.1103/PhysRevD.102.123028

Peñarrubia, J., Benson, A. J., Walker, M. G., Gilmore, G., McConnachie, A. W. and Mayer, L. (2010). The impact of dark matter cusps and cores on the satellite galaxy population around spiral galaxies, *Monthly Notices of the Royal Astronomical Society* p. no–no.
**URL:** http://dx.doi.org/10.1111/j.1365-2966.2010.16762.x

Piffl, T., Scannapieco, C., Binney, J., Steinmetz, M., Scholz, R.-D., Williams, M. E. K., de Jong, R. S., Kordopatis, G., Matijevič, G., Bienaymé, O. and et al. (2014). The RAVE survey: the Galactic escape speed and the mass of the Milky Way, *Astronomy & Astrophysics* **562**: A91.
**URL:** http://dx.doi.org/10.1051/0004-6361/201322531

Planck Collaboration (2020a). Planck 2018 results, *Astronomy & Astrophysics* **641**: A6.
**URL:** http://dx.doi.org/10.1051/0004-6361/201833910

Planck Collaboration (2020b). Planck 2018 results. I. Overview and the cosmological legacy of Planck, *Astronomy & Astrophysics* **641**: A1.
**URL:** https://ui.adsabs.harvard.edu/abs/2020A&A...641A...1P

Popowski, P., Nelson, C. A., Bennett, D. P., Drake, A. J., Vandehei, T., Griest, K., Cook, K. H., Alcock, C., Allsman, R. A., Alves, D. R., Axelrod, T. S., Becker, A. C., Freeman, K. C., Geha, M., Lehner, M. J., Marshall, S. L., Minniti, D., Peterson, B. A., Quinn, P. J., Stubbs, C. W., Sutherland, W. and Welch, D. (2003). Recent Microlensing Results from the MACHO Project, *arXiv e-prints* pp. astro–ph/0304464.
**URL:** *https://ui.adsabs.harvard.edu/abs/2003astro.ph..4464P*

Prada, F., Klypin, A. A., Cuesta, A. J., Betancort-Rijo, J. E. and Primack, J. (2012). Halo concentrations in the standard $\Lambda$ cold dark matter cosmology, *Monthly Notices of the Royal Astronomical Society* **423**(4): 3018–3030.
**URL:** *https://ui.adsabs.harvard.edu/abs/2012MNRAS.423.3018P*

Primack, J. R., Domínguez, A., Gilmore, R. C., Somerville, R. S., Aharonian, F. A., Hofmann, W. and Rieger, F. M. (2011). Extragalactic Background Light and Gamma-Ray Attenuation.
**URL:** *http://dx.doi.org/10.1063/1.3635825*

Primakoff, H. (1951). Photo-Production of Neutral Mesons in Nuclear Electric Fields and the Mean Life of the Neutral Meson, *Physical Review* **81**(5): 899–899.
**URL:** *https://ui.adsabs.harvard.edu/abs/1951PhRv..81..899P*

Pritzl, B. J., Venn, K. A. and Irwin, M. (2005). A Comparison of Elemental Abundance Ratios in Globular Clusters, Field Stars, and Dwarf Spheroidal Galaxies, *The Astronomical Journal* **130**(5): 2140–2165.
**URL:** *http://dx.doi.org/10.1086/432911*

Profumo, S., Sigurdson, K. and Kamionkowski, M. (2006). What Mass Are the Smallest Protohalos?, *Physical Review Letters* **97**(3): 031301.
**URL:** *https://ui.adsabs.harvard.edu/abs/2006PhRvL..97c1301P*

Prusti, T., de Bruijne, J. H. J., Brown, A. G. A., Vallenari, A., Babusiaux, C., Bailer-Jones, C. A. L., Bastian, U., Biermann, M., Evans, D. W. and et al. (2016). The Gaia mission, *Astronomy & Astrophysics* **595**: A1.
**URL:** *http://dx.doi.org/10.1051/0004-6361/201629272*

Pérez de los Heros, C. (2020). Status, challenges and directions in indirect dark matter searches, *Symmetry* **12**(10): 1648.
**URL:** *http://dx.doi.org/10.3390/sym12101648*

Read, J. I., Wilkinson, M. I., Evans, N. W., Gilmore, G. and Kleyna, J. T. (2005). The mass of dwarf spheroidal galaxies and the missing satellite problem, *Proceedings of the International Astronomical Union* **1**(C198): 235–239.
**URL:** *http://dx.doi.org/10.1017/S1743921305003807*

Rico, J. (2020). Gamma-Ray Dark Matter Searches in Milky Way Satellites—A Comparative Review of Data Analysis Methods and Current Results, *Galaxies* **8**(1): 25.
**URL:** *http://dx.doi.org/10.3390/galaxies8010025*

Riess, A. G., Filippenko, A. V., Challis, P., Clocchiatti, A., Diercks, A., Garnavich, P. M., Gilliland, R. L., Hogan, C. J., Jha, S., Kirshner, R. P., Leibundgut, B., Phillips, M. M., Reiss, D., Schmidt, B. P., Schommer, R. A., Smith, R. C., Spyromilio, J., Stubbs, C., Suntzeff, N. B. and Tonry, J. (1998). Observational Evidence from Supernovae for an Accelerating Universe and a Cosmological Constant, *The Astronomical Journal* **116**(3): 1009–1038.
**URL:** *https://ui.adsabs.harvard.edu/abs/1998AJ....116.1009R*

Rubin, V. C., Ford, W. K., J. and Thonnard, N. (1980). Rotational properties of 21 SC galaxies with a large range of luminosities and radii, from NGC 4605 (R=4kpc) to UGC 2885 (R=122kpc)., *The Astrophysical Journal* **238**: 471–487.
**URL:** *https://ui.adsabs.harvard.edu/abs/1980ApJ...238..471R*

Rubin, V. C. and Ford, W. Kent, J. (1970). Rotation of the Andromeda Nebula from a Spectroscopic Survey of Emission Regions, *The Astrophysical Journal* **159**: 379.
**URL:** *https://ui.adsabs.harvard.edu/abs/1970ApJ...159..379R*

Salati, P., Donato, F. and Fornengo, N. (2010). Indirect Dark Matter Detection with Cosmic Antimatter.

Samuel, J., Wetzel, A., Chapman, S., Tollerud, E., Hopkins, P. F., Boylan-Kolchin, M., Bailin, J. and Faucher-Giguère, C.-A. (2021). Planes of satellites around Milky Way/M31-mass galaxies in the FIRE simulations and comparisons with the Local Group, *Monthly Notices of the Royal Astronomical Society* **504**(1): 1379–1397.
**URL:** *https://ui.adsabs.harvard.edu/abs/2021MNRAS.504.1379S*

Sanders, R. H. (2003). Clusters of galaxies with modified Newtonian dynamics, *Monthly Notices of the Royal Astronomical Society* **342**(3): 901–908.
**URL:** *http://dx.doi.org/10.1046/j.1365-8711.2003.06596.x*

Sawala, T., Frenk, C. S., Fattahi, A., Navarro, J. F., Bower, R. G., Crain, R. A., Vecchia, C. D., Furlong, M., Helly, J. C., Jenkins, A., Oman, K. A., Schaller, M., Schaye, J., Theuns, T., Trayford, J. and White, S. D. M. (2014). Local Group galaxies emerge from the dark.
**URL:** *https://ui.adsabs.harvard.edu/abs/2014arXiv1412.2748S*

Sawala, T., Frenk, C. S., Fattahi, A., Navarro, J. F., Theuns, T., Bower, R. G., Crain, R. A., Furlong, M., Jenkins, A., Schaller, M. and et al. (2015). The chosen few: the low-mass haloes that host faint galaxies, *Monthly Notices of the Royal Astronomical Society* **456**(1): 85–97.
**URL:** *http://dx.doi.org/10.1093/mnras/stv2597*

Schaye, J., Crain, R. A., Bower, R. G., Furlong, M., Schaller, M., Theuns, T., Dalla Vecchia, C., Frenk, C. S., McCarthy, I. G., Helly, J. C., Jenkins, A., Rosas-Guevara, Y. M., White, S. D. M., Baes, M., Booth, C. M., Camps, P., Navarro, J. F., Qu, Y., Rahmati, A., Sawala, T., Thomas, P. A. and Trayford, J. (2015). The EAGLE project: simulating the evolution and assembly of galaxies and their environments, *Monthly Notices of the Royal Astronomical Society* **446**(1): 521–554.
**URL:** *https://ui.adsabs.harvard.edu/abs/2015MNRAS.446..521S*

Schindler, S. (1996). The accuracy of mass determination in galaxy clusters by X-ray observations., *Astronomy & Astrophysics* **305**: 756.
**URL:** *https://ui.adsabs.harvard.edu/abs/1996A&A...305..756S*

Schneider, A., Smith, R. E., Macciò, A. V. and Moore, B. (2012). Non-linear evolution of cosmological structures in warm dark matter models, *Monthly Notices of the Royal Astronomical Society* **424**(1): 684–698.
**URL:** *http://dx.doi.org/10.1111/j.1365-2966.2012.21252.x*

Schumann, M. (2019). Direct detection of wimp dark matter: concepts and status, *Journal of Physics G: Nuclear and Particle Physics* **46**(10): 103003.
**URL:** *http://dx.doi.org/10.1088/1361-6471/ab2ea5*

SDSS Collaboration (2000). The Sloan Digital Sky Survey: Technical Summary, *The Astronomical Journal* **120**(3): 1579–1587.
**URL:** https://ui.adsabs.harvard.edu/abs/2000AJ....120.1579Y

SDSS Collaboration (2017). Sloan Digital Sky Survey IV: Mapping the Milky Way, Nearby Galaxies, and the Distant Universe, *Astronomy Journal* **154**(1): 28.
**URL:** https://ui.adsabs.harvard.edu/abs/2017AJ....154...28B

SDSS Collaboration (2019). The clustering of the SDSS-IV extended Baryon Oscillation Spectroscopic Survey DR14 LRG sample: structure growth rate measurement from the anisotropic LRG correlation function in the redshift range $0.6 < z < 1.0$, *Monthly Notices of the Royal Astronomical Society* **492**(3): 4189–4215.
**URL:** http://dx.doi.org/10.1093/mnras/stz3602

SDSS Collaboration (2020). The Completed SDSS-IV extended Baryon Oscillation Spectroscopic Survey: measurement of the BAO and growth rate of structure of the luminous red galaxy sample from the anisotropic power spectrum between redshifts 0.6 and 1.0, *Monthly Notices of the Royal Astronomical Society* **498**(2): 2492–2531.
**URL:** http://dx.doi.org/10.1093/mnras/staa2455

Seigar, M. S., Barth, A. J. and Bullock, J. S. (2008). A revised ΛCDM mass model for the Andromeda Galaxy, *Monthly Notices of the Royal Astronomical Society* **389**(4): 1911–1923.
**URL:** http://dx.doi.org/10.1111/j.1365-2966.2008.13732.x

Servant, G. and Tait, T. M. (2003). Is the lightest Kaluza–Klein particle a viable dark matter candidate?, *Nuclear Physics B* **650**(1-2): 391–419.
**URL:** http://dx.doi.org/10.1016/S0550-3213(02)01012-X

Shapley, H. (1938). A Stellar System of a New Type, *Harvard College Observatory Bulletin* **908**: 1–11.
**URL:** https://ui.adsabs.harvard.edu/abs/1938BHarO.908....1S

Shen, J. and Zheng, X.-W. (2020). The bar and spiral arms in the Milky Way: structure and kinematics, *Research in Astronomy and Astrophysics* **20**(10): 159.
**URL:** http://dx.doi.org/10.1088/1674-4527/20/10/159

Sierra, D. A., Liao, J. and Marfatia, D. (2019). Impact of form factor uncertainties on interpretations of coherent elastic neutrino-nucleus scattering data, *Journal of High Energy Physics* **2019**(6).
**URL:** http://dx.doi.org/10.1007/JHEP06(2019)141

Simon, J. D. (2019). The Faintest Dwarf Galaxies, *Annual Review of Astronomy and Astrophysics* **57**(1): 375–415.
**URL:** http://dx.doi.org/10.1146/annurev-astro-091918-104453

Simon, J. D., Bolatto, A. D., Leroy, A., Blitz, L. and Gates, E. L. (2005). High-Resolution Measurements of the Halos of Four Dark Matter–Dominated Galaxies: Deviations from a Universal Density Profile, *The Astrophysical Journal* **621**(2): 757–776.
**URL:** http://dx.doi.org/10.1086/427684

Simon, J. D. and Geha, M. (2007). The Kinematics of the Ultra-faint Milky Way Satellites: Solving the Missing Satellite Problem, *The Astrophysical Journal*

**670**(1): 313–331.
**URL:** http://dx.doi.org/10.1086/521816

Sivertsson, S., Silverwood, H., Read, J. I., Bertone, G. and Steger, P. (2018). The local dark matter density from SDSS-SEGUE G-dwarfs, *Monthly Notices of the Royal Astronomical Society* **478**(2): 1677–1693.
**URL:** http://dx.doi.org/10.1093/mnras/sty977

Slatyer, T. R. (2017). TASI Lectures on Indirect Detection of Dark Matter.
**URL:** https://arxiv.org/abs/1710.05137

Sloane, J. D., Buckley, M. R., Brooks, A. M. and Governato, F. (2016). Assessing astrophysical uncertainties in direct detection with galaxy simulations, *The Astrophysical Journal* **831**(1): 93.
**URL:** http://dx.doi.org/10.3847/0004-637X/831/1/93

Smirnov, J. and Beacom, J. F. (2019). Tev-scale thermal WIMPs: Unitarity and its consequences, *Physical Review D* **100**(4).
**URL:** http://dx.doi.org/10.1103/PhysRevD.100.043029

Springel, V., Pakmor, R., Pillepich, A., Weinberger, R., Nelson, D., Hernquist, L., Vogelsberger, M., Genel, S., Torrey, P., Marinacci, F. and et al. (2017). First results from the IllustrisTNG simulations: matter and galaxy clustering, *Monthly Notices of the Royal Astronomical Society* **475**(1): 676–698.
**URL:** http://dx.doi.org/10.1093/mnras/stx3304

Springel, V., Wang, J., Vogelsberger, M., Ludlow, A., Jenkins, A., Helmi, A., Navarro, J. F., Frenk, C. S. and White, S. D. M. (2008). The Aquarius Project: the subhaloes of galactic haloes, *Monthly Notices of the Royal Astronomical Society* **391**(4): 1685–1711.
**URL:** http://dx.doi.org/10.1111/j.1365-2966.2008.14066.x

Springel, V., White, S. D. M., Jenkins, A., Frenk, C. S., Yoshida, N., Gao, L., Navarro, J., Thacker, R., Croton, D., Helly, J., Peacock, J. A., Cole, S., Thomas, P., Couchman, H., Evrard, A., Colberg, J. and Pearce, F. (2005). Simulations of the formation, evolution and clustering of galaxies and quasars, *Nature* **435**(7042): 629–636.
**URL:** https://ui.adsabs.harvard.edu/abs/2005Natur.435..629S

Springel, V., White, S. D. M., Navarro, J., Jenkins, A., Frenk, C. S., Helmi, A. and Gao, L. (2009). The aquarius project: Cold dark matter under a numerical microscope, *in* S. Wagner, M. Steinmetz, A. Bode and M. Brehm (eds), *High Performance Computing in Science and Engineering, Garching/Munich 2007*, Springer Berlin Heidelberg, Berlin, Heidelberg, pp. 93–108.

Steffen, F. D. (2009). Dark-matter candidates, *The European Physical Journal C* **59**(2): 557–588.
**URL:** http://dx.doi.org/10.1140/epjc/s10052-008-0830-0

Stiegler, T., Sofka, C., Webb, R. C. and White, J. T. (2017). A study of the NaI(Tl) detector response to low energy nuclear recoils and a measurement of the quenching factor in NaI(Tl).

Strigari, L. E., Bullock, J. S., Kaplinghat, M., Diemand, J., Kuhlen, M. and Madau, P. (2007). Redefining the Missing Satellites Problem, *The Astrophysical Journal* **669**(2): 676–683.
**URL:** http://dx.doi.org/10.1086/521914

Su, M. and Finkbeiner, D. P. (2012). Strong evidence for gamma-ray line emission from the inner galaxy.
**URL:** *https://arxiv.org/abs/1206.1616*

Sunyaev, R. A. and Zeldovich, Y. B. (1972). The Observations of Relic Radiation as a Test of the Nature of X-Ray Radiation from the Clusters of Galaxies, *Comments on Astrophysics and Space Physics* **4**: 173.
**URL:** *https://ui.adsabs.harvard.edu/abs/1972CoASP...4..173S*

Suyu, S. H., Chang, T.-C., Courbin, F. and Okumura, T. (2018). Cosmological Distance Indicators, *Space Science Reviews* **214**(5).
**URL:** *http://dx.doi.org/10.1007/s11214-018-0524-3*

Sánchez-Conde, M. A., Paneque, D., Bloom, E., Prada, F. and Domínguez, A. (2009). Hints of the existence of axionlike particles from the gamma-ray spectra of cosmological sources, *Physical Review D* **79**(12).
**URL:** *http://dx.doi.org/10.1103/PhysRevD.79.123511*

Sánchez-Conde, M. A. and Prada, F. (2014). The flattening of the concentration–mass relation towards low halo masses and its implications for the annihilation signal boost, *Monthly Notices of the Royal Astronomical Society* **442**(3): 2271–2277.
**URL:** *http://dx.doi.org/10.1093/mnras/stu1014*

Sánchez, E., Alonso, D., Sánchez, F. J., García-Bellido, J. and Sevilla, I. (2013). Precise measurement of the radial baryon acoustic oscillation scales in galaxy redshift surveys, *Monthly Notices of the Royal Astronomical Society* **434**(3): 2008–2019.
**URL:** *http://dx.doi.org/10.1093/mnras/stt1146*

Takahashi, F. (2008). Gravitino dark matter from inflaton decay, *Physics Letters B* **660**(3): 100–106.
**URL:** *http://dx.doi.org/10.1016/j.physletb.2007.12.048*

Tan, C. M., Bassa, C. G., Cooper, S., Dijkema, T. J., Esposito, P., Hessels, J. W. T., Kondratiev, V. I., Kramer, M., Michilli, D., Sanidas, S. and et al. (2018). LOFAR Discovery of a 23.5 s Radio Pulsar, *The Astrophysical Journal* **866**(1): 54.
**URL:** *http://dx.doi.org/10.3847/1538-4357/aade88*

Taoso, M., Bertone, G. and Masiero, A. (2008). Dark matter candidates: a ten-point test, *Journal of Cosmology and Astroparticle Physics* **2008**(03): 022.
**URL:** *http://dx.doi.org/10.1088/1475-7516/2008/03/022*

Thomas, G. F., Ibata, R., Famaey, B., Martin, N. F. and Lewis, G. F. (2016). Exploring the reality of density substructures in the Palomar 5 stellar stream, *Monthly Notices of the Royal Astronomical Society* **460**(3): 2711–2719.
**URL:** *http://dx.doi.org/10.1093/mnras/stw1189*

Thomas, T. and Pfrommer, C. (2019). Cosmic-ray hydrodynamics: Alfvén-wave regulated transport of cosmic rays, *Monthly Notices of the Royal Astronomical Society* **485**(3): 2977–3008.
**URL:** *http://dx.doi.org/10.1093/mnras/stz263*

Thomson, Baron Kelvin, W. (2010). *Baltimore Lectures on Molecular Dynamics and the Wave Theory of Light*, Cambridge Library Collection - Physical Sciences, Cambridge University Press.

Tollerud, E. J., Boylan-Kolchin, M. and Bullock, J. S. (2014). M31 satellite masses compared to ΛCDM subhaloes, *Monthly Notices of the Royal Astronomical Society* **440**(4): 3511–3519.
**URL:** http://dx.doi.org/10.1093/mnras/stu474

Trevisani, N. (2018). Collider Searches for Dark Matter (ATLAS + CMS), *Universe* **4**(11).
**URL:** https://www.mdpi.com/2218-1997/4/11/131

Tsapras, Y. (2018). Microlensing Searches for Exoplanets, *Geosciences* **8**(10): 365.
**URL:** http://dx.doi.org/10.3390/geosciences8100365

Turner, M. S. and Wilczek, F. (1990). Positron line radiation as a signature of particle dark matter in the halo, *Physical Review D* **42**(4): 1001–1007.
**URL:** https://ui.adsabs.harvard.edu/abs/1990PhRvD..42.1001T

Umetsu, K. (2020). Cluster–galaxy weak lensing, *The Astronomy and Astrophysics Review* **28**(1).
**URL:** http://dx.doi.org/10.1007/s00159-020-00129-w

Unger, M. and Farrar, G. R. (2017). Uncertainties in the Magnetic Field of the Milky Way, *35th International Cosmic Ray Conference (ICRC2017)*, Vol. 301 of *International Cosmic Ray Conference*, p. 558.
**URL:** https://ui.adsabs.harvard.edu/abs/2017ICRC...35..558U

Uzan, J.-P. (2016). The big-bang theory: construction, evolution and status.
**URL:** https://arxiv.org/abs/1606.06112

van Bibber, K. and Carosi, G. (2013). Status of the ADMX and ADMX-HF experiments, *arXiv e-prints* p. arXiv:1304.7803.
**URL:** https://ui.adsabs.harvard.edu/abs/2013arXiv1304.7803V

van den Bosch, F. C. and Ogiya, G. (2018). Dark matter substructure in numerical simulations: a tale of discreteness noise, runaway instabilities, and artificial disruption, *Monthly Notices of the Royal Astronomical Society* **475**(3): 4066–4087.
**URL:** http://dx.doi.org/10.1093/mnras/sty084

Verde, L., Treu, T. and Riess, A. G. (2019). Tensions between the early and late universe, *Nature Astronomy* **3**(10): 891–895.
**URL:** http://dx.doi.org/10.1038/s41550-019-0902-0

VERITAS Collaboration (2012). Constraints on Cosmic Rays, Magnetic Fields, and Dark Matter from Gamma-Ray Observations of the Coma Cluster of Galaxies with VERITAS and Fermi, *The Astrophysical Journal* **757**(2): 123.
**URL:** http://dx.doi.org/10.1088/0004-637X/757/2/123

VERITAS Collaboration (2017). Dark matter constraints from a joint analysis of dwarf Spheroidal galaxy observations with VERITAS, *Physical Review D* **95**(8).
**URL:** http://dx.doi.org/10.1103/PhysRevD.95.082001

Viel, M., Bolton, J. S. and Haehnelt, M. G. (2009). Cosmological and astrophysical constraints from the Lyman-α forest flux probability distribution function, *Monthly Notices of the Royal Astronomical Society: Letters* **399**(1): L39–L43.
**URL:** http://dx.doi.org/10.1111/j.1745-3933.2009.00720.x

Vladimirov, A., Digel, S., Jóhannesson, G., Michelson, P., Moskalenko, I., Nolan, P., Orlando, E., Porter, T. and Strong, A. (2011). GALPROP WebRun: An internet-based service for calculating galactic cosmic ray propagation and associated photon emissions, *Computer Physics Communications* **182**(5): 1156–1161.
**URL:** *http://dx.doi.org/10.1016/j.cpc.2011.01.017*

Walker, M. (2013). Dark Matter in the Galactic Dwarf Spheroidal Satellites, *Planets, Stars and Stellar Systems* p. 1039–1089.
**URL:** *http://dx.doi.org/10.1007/978-94-007-5612-020*

Wang, J., Bose, S., Frenk, C. S., Gao, L., Jenkins, A., Springel, V. and White, S. D. M. (2020). Universal structure of dark matter haloes over a mass range of 20 orders of magnitude, *Nature* **585**(7823): 39–42.
**URL:** *http://dx.doi.org/10.1038/s41586-020-2642-9*

Watkins, P. M. (1986). DISCOVERY OF THE W AND Z BOSONS, *Contemporary Physics* **27**: 291–324.

Weidenspointner, G., Skinner, G., Jean, P., Knödlseder, J., von Ballmoos, P., Bignami, G., Diehl, R., Strong, A. W., Cordier, B., Schanne, S. and Winkler, C. (2008). An asymmetric distribution of positrons in the Galactic disk revealed by $\gamma$-rays, *Nature* **451**(7175): 159–162.
**URL:** *https://ui.adsabs.harvard.edu/abs/2008Natur.451..159W*

Weinberg, S. (1978). A new light boson?, *Physical Review Letters* **40**(4): 223–226.
**URL:** *https://ui.adsabs.harvard.edu/abs/1978PhRvL..40..223W*

Weniger, C. (2012). A tentative gamma-ray line from Dark Matter annihilation at the Fermi Large Area Telescope, *Journal of Cosmology and Astroparticle Physics* **2012**(08): 007–007.
**URL:** *http://dx.doi.org/10.1088/1475-7516/2012/08/007*

Wong, K. C., Suyu, S. H., Chen, G. C.-F., Rusu, C. E., Millon, M., Sluse, D., Bonvin, V., Fassnacht, C. D., Taubenberger, S., Auger, M. W. and et al. (2019). H0LiCOW – XIII. A 2.4 per cent measurement of H0 from lensed quasars: 5.3$\sigma$ tension between early- and late-Universe probes, *Monthly Notices of the Royal Astronomical Society* **498**(1): 1420–1439.
**URL:** *http://dx.doi.org/10.1093/mnras/stz3094*

Wyenberg, J. and Shoemaker, I. M. (2018). Mapping the neutrino floor for direct detection experiments based on dark matter-electron scattering, *Physical Review D* **97**(11).
**URL:** *http://dx.doi.org/10.1103/PhysRevD.97.115026*

XENON Collaboration (2020). Projected WIMP sensitivity of the XENONnT dark matter experiment, *Journal of Cosmology and Astroparticle Physics* **2020**(11): 031–031.
**URL:** *http://dx.doi.org/10.1088/1475-7516/2020/11/031*

XMASS Collaboration (2018). Direct dark matter search by annual modulation with 2.7 years of XMASS-I data, *Physical Review D* **97**(10).
**URL:** *http://dx.doi.org/10.1103/PhysRevD.97.102006*

Yaguna, C. E. (2011). The singlet scalar as FIMP dark matter, *Journal of High Energy Physics* **2011**(8).
**URL:** *http://dx.doi.org/10.1007/JHEP08(2011)060*

Yang, Q. and Di, H. (2017). Sub-MeV bosonic dark matter, misalignment mechanism, and galactic dark matter halo luminosities, *Physical Review D* **95**(7).
**URL:** http://dx.doi.org/10.1103/PhysRevD.95.075032

Zel'dovich, Y. B. and Novikov, I. D. (1967). The Hypothesis of Cores Retarded during Expansion and the Hot Cosmological Model, *Soviet Astronomy* **10**: 602.
**URL:** https://ui.adsabs.harvard.edu/abs/1967SvA...10..602Z

Zhao, H. (1996). Analytical models for galactic nuclei, *Monthly Notices of the Royal Astronomical Society* **278**(2): 488–496.
**URL:** https://ui.adsabs.harvard.edu/abs/1996MNRAS.278..488Z

Zhao, H., Hooper, D., Angus, G. W., Taylor, J. E. and Silk, J. (2007). Tidal Disruption of the First Dark Microhalos, *The Astrophysical Journal* **654**(2): 697–701.
**URL:** http://dx.doi.org/10.1086/509649

Zhu, Q., Marinacci, F., Maji, M., Li, Y., Springel, V. and Hernquist, L. (2016). Baryonic impact on the dark matter distribution in Milky Way-sized galaxies and their satellites, *Monthly Notices of the Royal Astronomical Society* **458**(2): 1559–1580.
**URL:** http://dx.doi.org/10.1093/mnras/stw374

Zwicky, F. (1933). Die Rotverschiebung von extragalaktischen Nebeln, *Helvetica Physica Acta* **6**: 110–127.
**URL:** https://ui.adsabs.harvard.edu/abs/1933AcHPh...6..110Z

# Chapter 2

# Gamma-ray Astronomy: detection techniques and current state

Gamma rays have proven to be a promising window for indirect dark matter searches. Yet, this is the most energetic radiation in the Universe, and the techniques to detect it resemble more the particle physics-based colliders than traditional Astronomy. Indeed, the huge energy carried by gamma-ray photons makes it impossible to focalize them with a lens, as the production of electron-positron pairs is kinematically allowed. Through this Chapter, we will review the gamma-ray astrophysical sources, possible detection methods, and the current and future gamma-ray observatories.

## 2.1 Observation of gamma rays: a historical perspective

After centuries observing the sky in optical wavelengths[1], science was able to open new observational windows in the XX$^{th}$ century. Gamma rays were discovered in 1900 by Paul Villard when studying radium radioactive decay. They are the most energetic form of radiation, with energies above $\sim$MeV, although the border between high-energy X-rays and low-energy gamma rays is diffuse and there is not a formal definition.

The first astrophysical detection of such radiation was by the Vela satellites (1963–1985), a surveillance grid deployed to detect possible nuclear detonations in Earth. In 1967, two of these satellites detected a strong Gamma-Ray Burst (GRB), which was not possible to be originated by a nuclear explosion. The results, published 6 years later given the Vela military nature, opened the window of gamma-ray Astronomy Klebesadel et al. (1973).

The field began to slowly develop with new experiments in the forthcoming decades. Satellites such as the Orbiting Solar Observatory (OSO-3, 1967–1969) or the Small Astronomical Satellite (SAS-2, 1972–1973) detected gamma-ray emission coming from the GC and the Galactic plane, as well as an extragalactic IGRB Kraushaar et al. (1972); Kniffen et al. (1973); Fichtel et al. (1973). A major breakthrough happened in 1975 with the launch of the Celestial Observation Satellite B (COS-B, 1975–1982). This telescope was able to detect gamma radiation from a few keV up to 5 GeV, and was able to compile the first gamma-ray catalog in 1981, consisting on 25

[1] And IR, as infrared radiation was discovered by William Herschel in 1800, initially dubbed as "calorific rays".

objects Swanenburg et al. (1981), yet only 4 of them were identified with known sources[2]. This satellite was also able to observe the Galactic plane between 70 MeV and 5 GeV Mayer-Hasselwander et al. (1982).

The next major leap happened in 1991 with the launch of the Compton Gamma Ray Observatory (CGRO) satellite. One of its instruments was the Energetic Gamma Ray Experiment Telescope (EGRET, 1991–2000), which was able to observe the sky between 20 keV and 30 GeV. This was a pair production instrument, based on the creation of electron-positron pairs through $\gamma \rightarrow e^- e^+$ . Indeed, EGRET had a spark chamber to trigger the detection of such pairs, a calorimeter to measure the energy of the incoming gamma ray, and a plastic scintillator anti-coincidence dome to reject primary CRs in the form of $e^-$ and $e^+$. This setup allowed increased sensitivity and resolution with respect to its predecessors, and its final data release through the 3$^{\text{rd}}$ EGRET Catalog (3EG) EGRET Collaboration (1999) featured 271 gamma-ray sources above 100 MeV. From them, 101 sources were identified, mostly as blazars and other AGNs, as well as some PSRs, the LMC and the Sun.

With the new millennium, Europe launched several space telescopes, such as the INTErnational Gamma-Ray Astrophysics Laboratory (INTEGRAL, 2002–) Winkler (1996), still in operation at this writing. This is a low-energy gamma-ray observatory, sensitive to energies below $\sim$ 10 MeV, therefore being suitable for transient sources such as GRBs. Current space-based telescopes, such as *Fermi*-LAT, are introduced in Section 2.2.

All the reviewed observatories share the space-borne character. Indeed, this is natural from a historical perspective, as the Earth's atmosphere is opaque to gamma rays, due to their small free path in the dense environment. This precludes direct observation of gamma rays from the Earth's surface. Besides such considerations, the main advantage of satellite telescopes is their direct observation of gamma rays, as well as their available observation time. Nevertheless, satellites must be put on orbit, therefore having strict constraints on dimensions and weight. Accordingly, their effective area will be rather small, $\mathcal{O}(1\text{m}^2)$, making impossible to observe gamma rays above $\sim$ 1 TeV.

Therefore, in order to study gamma rays in the TeV domain and above, a different approach is needed. The solution is based on the Cherenkov light emitted by particles traveling in a medium at a speed higher than the speed of light in the medium Cherenkov (1960). In this case, Cherenkov radiation will be emitted by the cascades of relativistic secondary particles, produced by the collision of primary gamma rays with particles in the Earth atmosphere Sciascio (2019). This radiation may be detected by optical telescopes with the Imaging Atmospheric Cherenkov Telescope (IACT) technique if it comes from the high-altitude component of the cascade, i.e., if the Cherenkov medium is air. Additionally, large water tanks with scintillators can be used as detectors if the Cherenkov radiation is produced by secondary particles. In any case, the required areas are huge, in order to be capable of observing gamma rays with energies as high as 1 PeV, as well as an excellent angular resolution. Their main disadvantage from a technical point of view is the day-and-night cycle of the Earth, which will make impossible to take data as efficiently as space-borne instruments.

The pioneering observatory with this technique was the 10-meter IACT Fred Whipple Observatory (1968–), which covered the 0.1–100 TeV range. Despite its poor angular and energy resolution, after years of upgrades it first observed the

[2] Although alleviated, the large fraction of unIDs in gamma-ray Astronomy persists even with modern experiments, as already mentioned in Section 1.5.3, and further detailed in Section 2.3.

Crab nebula at TeV energies Weekes et al. (1989). Its successor was the High Energy Gamma Ray Astronomy array (HEGRA, 1987–2002), sensitive to photons above $\sim 1$ TeV. Consisting on four telescopes, multiple images were available to perform the event reconstruction, leading to improved angular and energy resolution, as well as enhanced CR rejection filters. HEGRA was able to detect flaring activity from the blazar Mrk 501 HEGRA Collaboration (1997) and the first TeV unID in the Cygnus region HEGRA Collaboration (2002). Milagro (2000–2008) improved previous experiments at lower energies, starting at 100 GeV and going up to 100 TeV, by using the water Cherenkov approach. Milagro produced a number of remarkable achievements, such as a full survey of the Northern Hemisphere of the sky Milagro Collaboration (2004), detection of the TeV diffuse emission from the Galactic plane Milagro Collaboration (2008), and the observation of TeV–range unIDs in it (some of them spatially extended) Milagro Collaboration (2007). Additionally, it claimed the unexpected detection of an anisotropic CR flux Milagro Collaboration (2009).

## 2.2 Gamma-ray observatories

In the previous Section, we have briefly reviewed the constant maturing of gamma-ray Astronomy since its birth roughly half a century ago. Indeed, a lot of work has been done in these decades from a experimental point of view, which has permitted to confirm several theories about the high-energy sky, as well as discovering unexpected phenomena. Thus, the current generation of gamma-ray observatories is the evolution of the already introduced precursors. In this Section we will review them, both space-borne, such as AGILE and *Fermi*-LAT, and ground-based, such as MAGIC, VERITAS, H.E.S.S. and HAWC, as well as the future CTA.

### 2.2.1 Space-borne telescopes

The Astrorivelatore Gamma ad Immagini LEggero satellite (AGILE, 2007–) is a small observatory based on the pair-conversion technique (see Section 2.1), sensitive to X-rays between 18–60 keV and gamma rays from 30 MeV to 50 GeV. Its main objective is the characterization of variable sources such as PSRs and AGNs in both bands AGILE Collaboration (2008).

Nevertheless, in the following we will focus on the most renowned space-borne gamma ray observatory, the *Fermi* Large Area Telescope (LAT, 2008–)[3]. The LAT is one of the two instruments onboard the *Fermi* Gamma-ray Space Telescope (FGRST), launched on June 11, 2008, and orbits the Earth at an altitude of 565 km, with 25.6° inclination. At the time of launch, the FGRST was named Gamma-ray Large Space Telescope (GLAST), but the name was changed shortly after to *Fermi* to honor the Italian physicist. The second instrument onboard is the GLAST Burst Monitor (GBM), which operates at low energies (8 keV–40 MeV) looking for GRBs and other transient phenomena.

The LAT is capable of detecting gamma rays with energies as low as 20 MeV up to a few TeV. This upper value is purely statistics-limited, given its reduced dimensions. One of the most powerful assets of the LAT is its huge Field of View (FoV) of 2.4 sr, meaning that roughly sees 1/5 of the celestial sphere, with a full sky survey

[3] https://fermi.gsfc.nasa.gov/

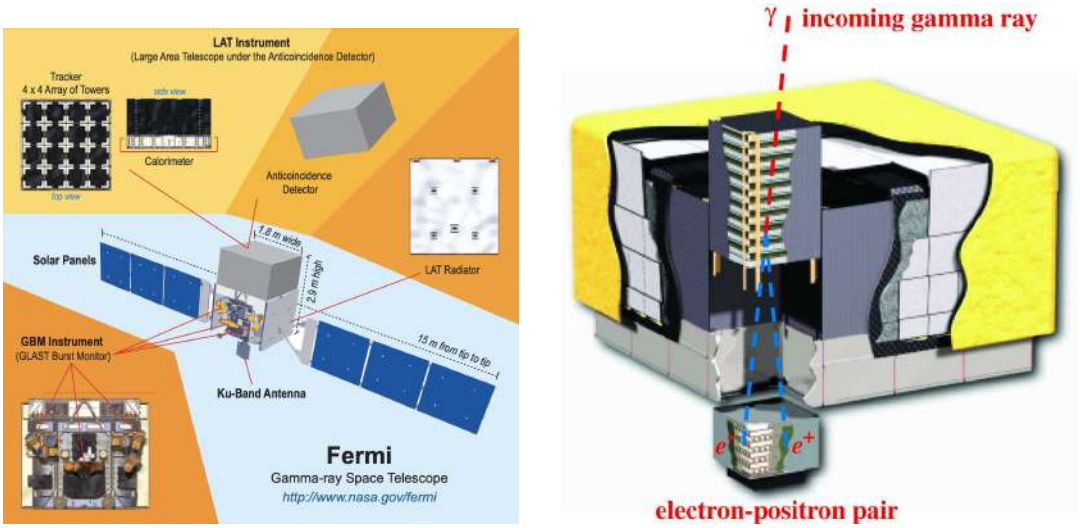


FIGURE 2.1: Schematic view of the Fermi Gamma-ray Space Telescope (left panel), and a more detailed view of the Large Area Telescope instrument, where a pair-conversion event in the tracker is shown (right panel). Taken from Fermi-LAT Collaboration (2009).

every $\sim$ 2.5 hours[4]. It features an energy resolution of $\sim$ 10%, as well as an energy-dependent angular resolution of $\sim 3.5^\circ$ at 100 MeV and $\sim 0.1^\circ$ above 10 GeV[5].

The LAT presents a very similar architecture as EGRET and AGILE, with an anti-coincidente detector wrapping the whole instrument to avoid primary CRs, and a silicon strip tracker to produce the $\gamma \rightarrow e^+e^-$ pair conversion. If a signal is detected by the tracker but not by the anti-coincidence detector, a gamma-ray event is recorded. At one end of the tracker a calorimeter will measure the energy of the pair, therefore reconstructing the original gamma ray energy. We show a schematic view of the instrument in Figure 2.1, yet we defer the interested reader to Fermi-LAT Collaboration (2009) for extensive technical details.

Over more than a decade of operations, *Fermi*-LAT has produced several scientific achievements. Among them, we may count the discovery of the so-called Fermi bubbles, giant hourglass-shaped structures of gamma-ray emission extending above and below the Galactic plane Su et al. (2010). This came as a major surprise, therefore proving that, with sufficient sensitivity, we can unveil the secrets of the high-energy sky. Another scientific breakthrough was the role of the GBM in the discovery of the first NS-NS merger by LIGO and Virgo observatories LIGO Collaboration et al. (2017).

Given the large FoV and constant sky survey of the *Fermi* satellite, it was able to detect the GRB from a NS-NS merger, sending a quick Astronomer Telegram to all the observatories in the world, which could pin down the search for EM counterpart within some square degrees. As LIGO spatial localization is very poor, without *Fermi* a proper search probably could not have been conducted in time and no EM counterpart would have been found. A more recent achievement was the discovery of the first extragalactic neutrino emitter, the blazar TXS 0506+056 (see Section 1.5.3), from which a high-energy neutrino was detected temporally coincident with flaring

[4]Since a solar array failure on March 16 2018, which was the first mechanical failure in almost 10 years of operation, the satellite maintains a fixed angle relative to its orbit in order to maximize solar power. Alternate observation strategies were developed due to power and thermal requirements.

[5]https://www.slac.stanford.edu/exp/glast/groups/canda/lat_Performance.htm

activity reported by the LAT IceCube Collaboration (2018). These two latter highlights represent the dawn of multi-messenger Astronomy, a field which will surely give rise to many discoveries in the coming decades. *Fermi*-LAT has also played a crucial role in indirect DM searches, as reviewed in Section 1.5.3. Given our interest in searches for dark subhalos, where large areas of sky are required, the LAT proves to be the most suitable instrument to perform them, as done in Chapters 3–6.

The future of space-borne gamma-ray observatories is currently uncertain; some proposals to success *Fermi*-LAT have been made in recent years, such as the Russian GAMMA–400 Galper et al. (2018) –designed for an energy range between 0.1–3000 GeV with a factor ∼10 better angular and energy resolution than the LAT–, or the All-sky Medium Energy Gamma-ray Observatory (AMEGO) McEnery (2017), which would be able to detect low-energy gamma rays, from ∼0.2 to 10 GeV.

### 2.2.2 Ground-based observatories

As already pointed out in Section 2.1, direct detection of primary gamma rays is not possible from the surface of the Earth, as the atmosphere is completely opaque to this radiation. To detect them, and particularly those above ∼TeV energies, Cherenkov effect-based telescopes are the optimal solution. Indeed, the interaction of gamma rays with atoms and molecules in the atmosphere produce secondary particle cascades which codify the information of the original photon. Depending on the medium producing Cherenkov radiation, we distinguish between air-based IACTs, and water-based telescopes.

CRs penetrating the atmosphere are mainly hadronic particles, such as protons and heavy nuclei, although positrons, electrons and photons contribute as well. The specific geometry and composition of the secondary particle air showers differ depending on the hadronic or leptonic character of the triggering particles. Therefore, by analysing these properties, gamma-ray observatories are capable of discriminating the hadronic part of the background. Nevertheless, leptonic and gamma-ray showers share a very similar geometry, therefore being almost indistinguishable, and are normally referred together as EM cascades.

In the case of hadronic cascades, hadronic particles (e.g., protons and helium nuclei), will trigger a strongly interacting air shower. Indeed, as hadrons are composite particles, after the initial collision they will disintegrate into new bound quark and leptonic states. Typically, this gives rise mainly to charged and neutral pions $(\pi^{\pm}, \pi^0)$, as well as neutral kaons $K^0$. These are unstable particles, which will rapidly decay, e.g. via $\pi^0 \to \gamma\gamma$, initiating themselves an EM cascade. $\pi^{\pm}$, on the other hand, although unstable, is more stable than $\pi^0$, and will be able to collide with other particles in the atmosphere before disintegrating, inducing secondary hadronic cascades. If they do not collide and disintegrate, they will decay into leptonic states such as $\pi^{\pm} \to \mu^{\pm}\bar{\nu}_{\mu}$. Muons usually are able to survive enough time to reach the surface of the Earth, therefore being one of CRs ground-based observation windows. As hadronic cascade components are massive (in particular, more massive than in EM showers), they will drift apart from the incident CR propagation vector, presenting a wide diameter with non-symmetric substructure. This allows to discriminate between EM and hadronic cascades, permitting an efficient background rejection. Indeed, in the case of IACTs, the false positive ratio in hadronic showers is below 5% Espadanal and Gonçalves (2017). A more efficient filtering can be performed with machine learning (ML), by using deep learning techniques Nieto et al. (2021) to reconstruct the events.

EM cascades, on the other hand, arise from the scattering of an incident high-energy photon with a particle in the atmosphere, inducing a $e^+e^-$ pair creation (assuming $E_\gamma \geq 2m_{e^\pm}$). The resulting pair can produce photons via Bremsstrahlung effect with the surrounding particles. Thus, there is an interaction chain of the form $\gamma \rightarrow e^+e^- \rightarrow e^+e^- + 2\gamma \rightarrow$ ..., which will continue until it is kinematically forbidden, $E_\gamma < 2m_{e^\pm}$. This process is well described by the Heitler model Matthews (2005), which successfully predicts the number and structure of the particles in the EM cascade. Opposite to the hadronic showers, the energy of the initial gamma rays or leptonic CRs is large enough to relativistically boost the secondary shower, therefore presenting a much narrower cascade, which as a first approximation can be taken as rotationally symmetric. Examples of hadronic and EM cascades are shown in Figure 2.2.

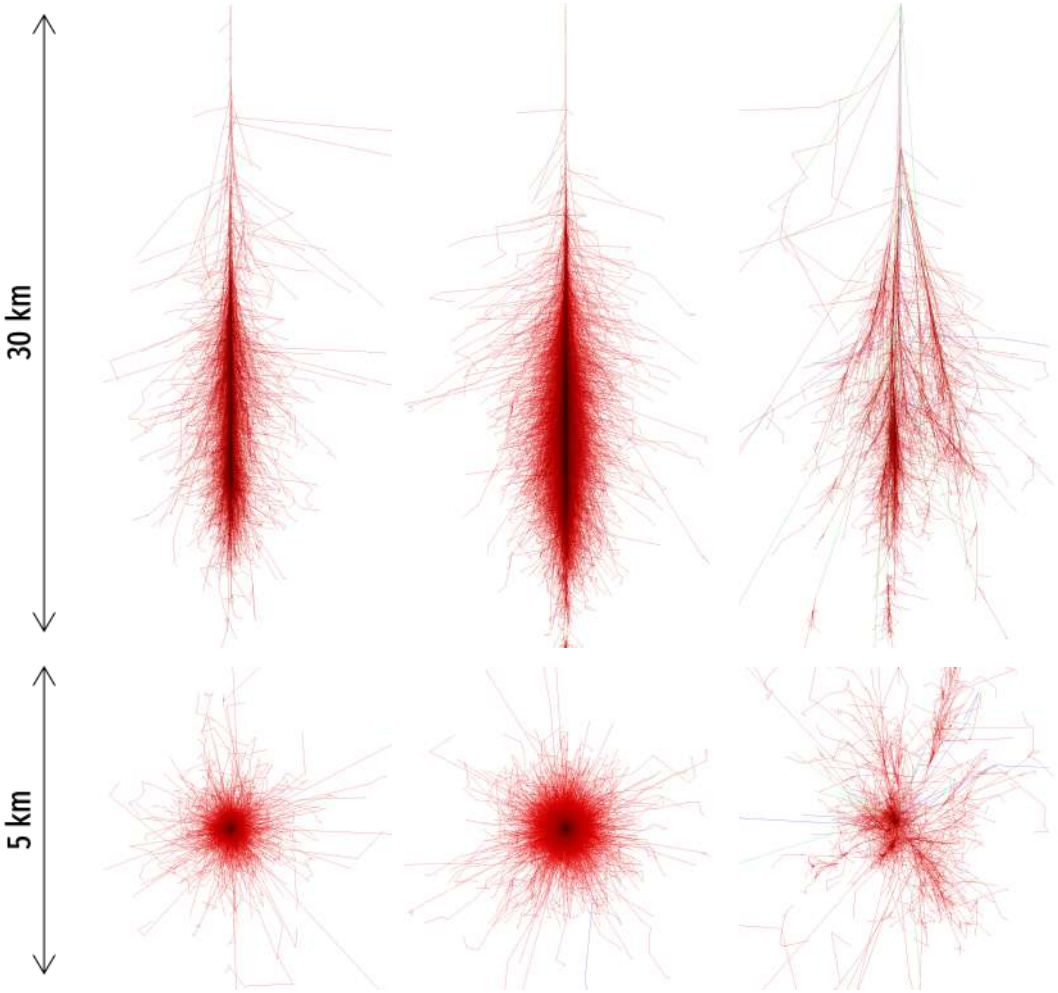


FIGURE 2.2: Examples of particle showers as generated by the CORSIKA software. Upper panels are the XZ plane projection, while lower panels show the XY plane. Colors refer to the particle species, being red for $e^\pm, \gamma$, green for $\mu^\pm$, and blue for hadrons. All cascades are produced at a height of 30 km, and only particles with energies higher than 0.1 MeV (0.1 GeV) are shown in the case of $e^\pm, \gamma$ ($\mu^\pm$, hadrons). **Left panels:** primary gamma ray at 100 GeV. **Central panels:** primary muon at 1 PeV. **Right panels:** primary proton at 100 GeV. Figure adapted from Schmidt and Knapp (2005).

Cherenkov telescopes will be able to detect these showers. The emission of

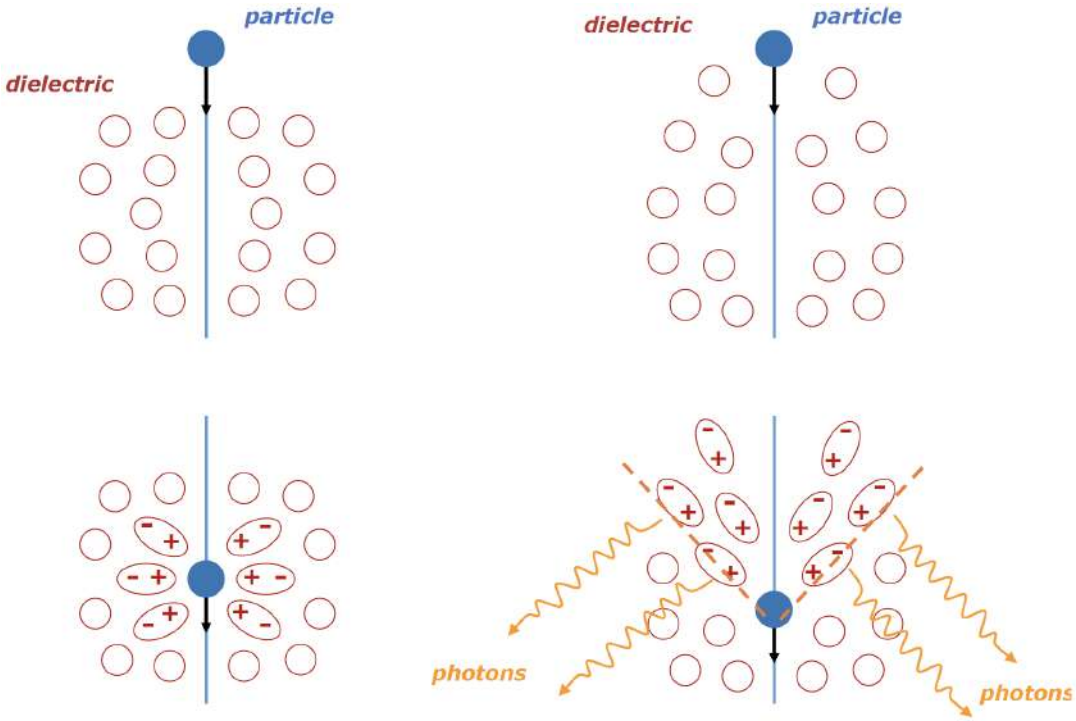


FIGURE 2.3: Cherenkov radiation diagram from a particle (blue) traversing a polarizable medium (red). **Left panel:** the speed of the particle is $v < c/n$, and does not induce a net charge in the medium. **Right panel:** the speed of the particle is $v > c/n$, inducing a dipolar moment which results in a cone-shaped radiation emission (yellow), known as Cherenkov light. Figure taken from Mezek (2019).

Cherenkov radiation is the EM analogue of mechanical shock waves in a supersonic boom. Indeed, as a charged particle is propagating through a polarizable medium (a dielectric) with a velocity $v < c/n$, where $n$ is the refractive index of the medium, it will symmetrically induce a polarization on the surrounding particles. This symmetry will lead to a net-null charge of the particles. Nevertheless, if the particle has a velocity $v > c/n$, the medium will not be able to react instantaneously, therefore presenting a polarization lag behind the traveling particle, which will induce an asymmetrical charge density distribution. This will have a dipole moment, which results in a dipole radiation emission through a characteristic cone-like shape, known as Cherenkov light or radiation. In Figure 2.3 we show a schematic diagram of both cases.

The angular distribution of the Cherenkov radiation is complex, yet is maximum at an angle $\theta = \cos^{-1}(1/n)$ with respect to the propagation direction of the incident particle. In air, where the refractive index is around $n \sim 1.0003$[6], this yields an opening angle of the Cherenkov cone of $2\theta \sim 2.8°$. When this radiation reaches the surface of the Earth, it will create a circular-shaped "light pool" (see Figure 2.2). Typical showers are produced at $h \sim 10 - 30$ km, which will result in a light pool of diameter $d = 2h \cdot \tan\theta \sim 500 - 700$ m. In general, this circle will be an ellipse, with an eccentricity depending on the zenith angle of the incoming particle.

This radiation is nevertheless extremely difficult to detect, as it is a very subdominant energy loss process. Indeed, the number of Cherenkov photons $N$ follows the

[6] https://refractiveindex.info/?shelf=other&book=air

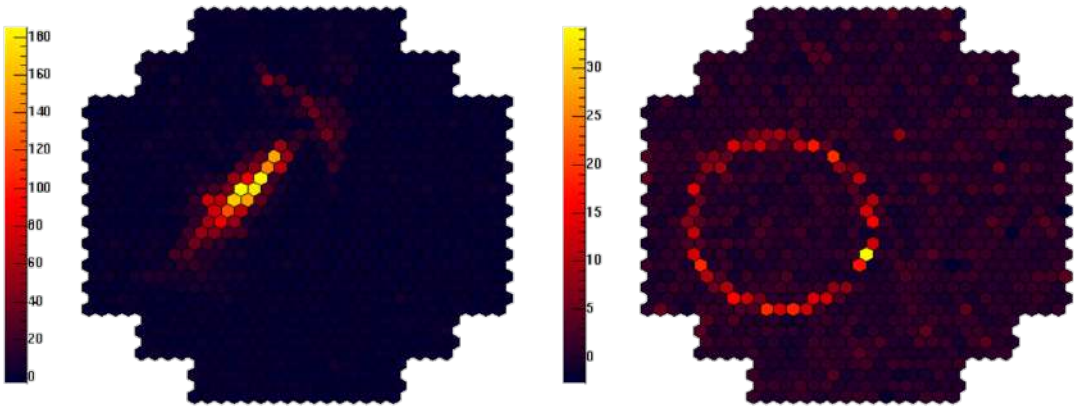


FIGURE 2.4: Examples of photon (left panel) and muon (right panel) events as detected by the first H.E.S.S. telescope camera. While photons tend to leave linear traces, muon cascades show a ring-like feature. Figures taken from H.E.S.S. Collaboration (2002).

Frank-Tamm formula, as the differential number $dN$ per unit length travelled $dx$ and wavelength interval $d\lambda$ Frank and Tamm (1937),

$$\frac{d^2N}{dxd\lambda} = \frac{2\pi\alpha_{em}}{\lambda^2}\left[1 - \frac{1}{(\beta n)^2}\right] \tag{2.1}$$

where $\beta = v/c$, $\alpha_{em} \approx 1/137$ is the fine-structure constant, and $n \equiv n(\lambda)$ is the refraction index of the medium, which depends on the wavelength. By taking finite increments, this formula can be expressed as the number of photons $\Delta N$ traveling a distance $\Delta x$ in a finite energy interval $\Delta E$ (which relates to $\Delta\lambda$ through $\Delta E = hc/\Delta\lambda$),

$$\Delta N \sim 370\left(1 - \frac{1}{(\beta n)^2}\right)\left(\frac{\Delta x}{1\text{ cm}}\right)\left(\frac{\Delta E_\gamma}{1\text{ eV}}\right) \tag{2.2}$$

This increases towards larger energies, and peaks in the UV band, around $\lambda \sim$ 400 nm. Therefore, IACTs must be sensitive to these wavelengths in order to detect the Cherenkov light. Indeed, the usual setup for an IACT consists on a dish with small, adjustable mirrors to reflect the incoming UV Cherenkov radiation and direct it towards a camera. This camera itself is composed by photon detector elements with photomultiplier tubes (PMTs)[7], in order to enhance the signal and produce an image of the shower.

Given the scarce number of Cherenkov photons[8], the dish must be as large as possible. Nowadays, arrays of several telescopes are preferred to a single, large dish. If the individual telescopes are separated, yet close enough, a single air cascade can be detected with multiple detectors, as they will all fall within the Cherenkov light pool. Filtering of background CRs can be done with Monte Carlo simulations, such the as the `CORSIKA` software[9]. In Figure 2.4, we show examples of photon and muon events in the camera plane. The incident gamma ray properties are reconstructed with the spatial distribution and flux of the Cherenkov radiation in the camera (see Eq. 2.1). We defer the reader to, e.g., Aharonian et al. (1997) for a full review on the IACT technique.

[7] Every PMT is effectively a pixel of the reconstructed image.

[8] As an example, the shower produced by a 1 TeV primary gamma ray yields about 100 photons/m$^2$ Hillas (1996).

[9] `https://www.iap.kit.edu/corsika/70.php`

The water-based telescopes work similarly, yet using water tanks with PMTs to detect the Cherenkov radiation of secondary cascades. Their main advantage is the long duty cycle, as, contrary to the sunlight and atmospheric condition-dependent IACTs, water tanks can operate constantly under almost every weather condition, as well as a large FoV. However, as the cascade particles must reach the surface of the Earth, the incident particle must be very energetic, resulting in a higher energy threshold when compared to IACTs. Additionally, discrimination between gamma rays and CRs is harder, as the original particle is more difficult to characterize from the cascade remnants at ground level. Nevertheless, such discrimination is still possible, as gamma-ray showers leave detector hits clustered around the incident direction of the original particle, while hadronic cascades produce a less-structured detector hit pattern.

In the following, we will briefly chronologically review the current-generation of ground-based Cherenkov telescopes, both IACTs and water-based, as well as the future CTA, currently in construction phase. In Table 2.1 we present a summarized version.

- **H.E.S.S.:** The High Energy Spectroscopic System (H.E.S.S., 2002–), named after CRs discoverer Victor Hess, is a 5–telescope IACT array in the Khomas Region, Namibia, 1800 m above sea level. Four of the telescopes are identical, with 12 m diameter dishes, and are situated at the vertices of a square with side length of 120 m. Each one has 382 individual, circular-shaped mirrors, as well as 960 PMTs cameras. The fifth telescope, which saw first light on 2012, is located in the center of the array, with a 28 m diameter dish, 875 hexagonal mirrors and a camera composed of 2048 PMTs. This full configuration is known as the H.E.S.S.–II, as opposed to the original, 4–telescope H.E.S.S.–I Krayzel et al. (2013). Additionally, the cameras of the small telescopes underwent a major upgrade in 2015, which increased their overall performance.

  H.E.S.S. is able to detect photons between $\sim$ 80 GeV and 100 TeV, with a $\sim$ 15% energy resolution and 0.1° angular resolution Holler et al. (2015), with a sensitivity curve shown in Figure 2.6. Its privileged location in the southern hemisphere, unique among the current IACTs, makes it suitable to conduct observations of Galactic targets. Indeed, the GC and most of the Galactic plane lie at high zenith angles, providing the clearest gamma-ray signals. The H.E.S.S. Galactic Plane Survey (HGPS), shown in Figure 2.5, mapped the innermost 4° of the Galactic plane, providing an unprecedented view in very high energies H.E.S.S. Collaboration (2018b). The GC observations have also yielded very interesting results, by discovering emission above 100 GeV from the central 200 pc of the Milky Way, spatially correlated with giant molecular clouds. The hardness of the gamma-ray spectrum indicate that the CRs responsible for this emission are most likely of hadronic origin. Currently, the most plausible explanation is a SN around 10,000 years ago, which injected a huge amount of energy into the region H.E.S.S. Collaboration (2006, 2016). As mentioned in Section 1.5.3, H.E.S.S. observations of the GC currently set the most stringent constraints for heavy, TeV DM H.E.S.S. Collaboration (2018a).

- **MAGIC:** The Major Atmospheric Gamma Imaging Cherenkov array (MAGIC, 2003–) is situated on the Roque de los Muchachos European Northern Observatory, on the Canary Island of La Palma, 2200 m above sea level. It is the direct successor of HEGRA (see Section 2.1), which was built at the same location. Although originally it consisted of a 17 m diameter single dish telescope,

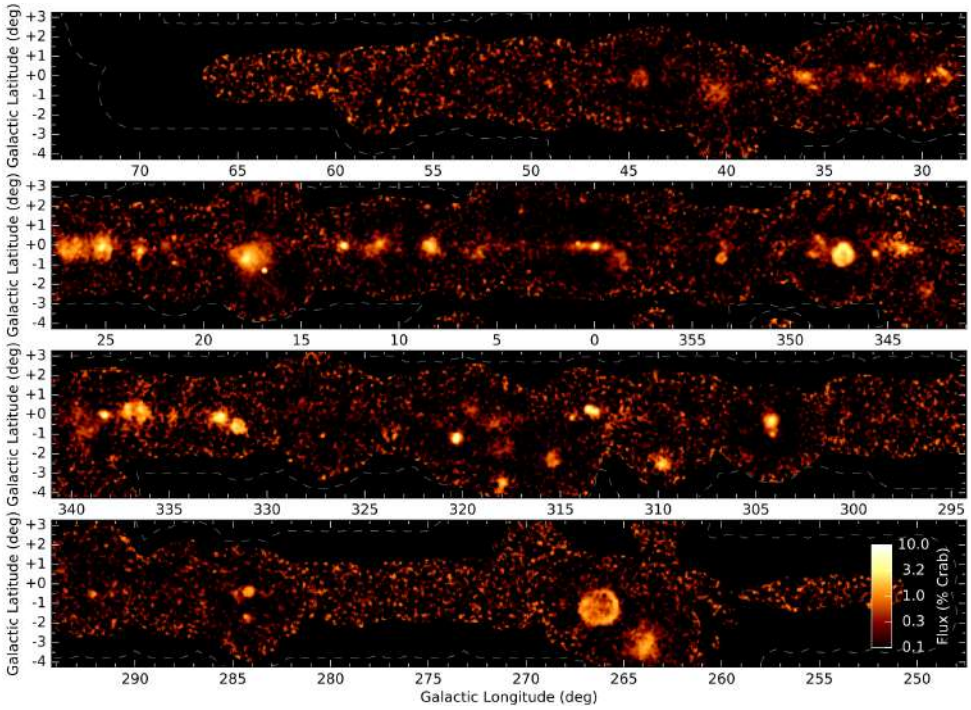


FIGURE 2.5: H.E.S.S. Galactic plane survey. Skymaps show the integral flux above 1 TeV , in units of % of the Crab Nebula flux, a standard candle in gamma-ray Astronomy. The map is only filled where the point-source sensitivity for a $5\sigma$ detection is better than 2.5% of the Crab flux. Note also the intense emission in the GC. Figure taken from H.E.S.S. Collaboration (2018b).

a second, identical telescope was built in 2008, 85 m away from the first, allowing stereoscopic operations. A further improvement was made in 2012, which notably increased its overall performance MAGIC Collaboration (2016b). We show the point-source sensitivity curve in Figure 2.6.

MAGIC is sensitive to photons from 30 GeV up to 100 TeV, with energy resolution about $\sim$ 18% and a superb angular resolution of 0.15° (0.08°) at 0.1 (1) TeV MAGIC Collaboration (2013). MAGIC contribution to indirect DM searches is reviewed in Section 1.5.3; aside from the DM program, it has done remarkable work in other fields. Some highlights are the observation of the most energetic GRB ever, which also lead to constraints on Lorentz invariance violation MAGIC Collaboration (2020), the joint observation of the already mentioned neutrino extragalactic source TXS 0506+056 MAGIC Collaboration (2018b), and the discovery of a very rare binary TeV gamma-ray source MAGIC Collaboration (2018a). A more exhaustive review of MAGIC achievements can be found in Paredes and MAGIC Collaboration (2020).

- **VERITAS:** The Very Energetic Radiation Imaging Telescope Array System (VERITAS, 2007–) is part of the Fred Lawrence Whipple Observatory (and therefore direct successor of the Whipple telescope, see Section 2.1), located in Amado, Arizona, 1268 m above sea level. It consists of four 12 m diameter identical telescopes separated 120 m from each other. Their dishes have 350 faceted mirrors to reflect the Cherenkov photons into a 499 PMTs camera.

VERITAS is sensitive to photons between 50 GeV and 50 TeV, with its sensitivity peak between 0.1–10 TeV, as shown in Figure 2.6, with a 0.08° angular resolution and $\sim$ 17% energy resolution Park and VERITAS Collaboration (2015). Besides the contribution to DM searches (see Section 1.5.3), VERITAS has accomplished a number of scientific achievements; for example, studies to use it as an instrument for intensity interferometry Matthews (2019), and the discovery of the starbust galaxy M82 at very high energies Karlsson (2009).

- **HAWC:** The High-Altitude Water Cherenkov (HAWC, 2015–) instrument is a water-based observatory, locates 4100 m above sea level on the Sierra Negra volcano, near Puebla, Mexico, and is the successor of Milagro (see Section 2.1). Due to the rotation of the Earth and its location, HAWC is able to observe $\sim 2/3$ of the sky every 24 hours, with constant duty cycle, and a FoV of $\sim$ 15% of the sky. HAWC consists of 300 water tanks distributed over an area of 90,000 $m^2$. Each tank is filled with more than 250,000 liters of purified water, as well as four PMTs to detect the Cherenkov light HAWC Collaboration (2017a).

  HAWC is sensitive to energies in the range 0.1–100 TeV, with an angular resolution of 0.1° and energy resolution around $\sim$ 50%. Its 1– and 5–year sensitivity curves are shown in Figure 2.6. HAWC has contributed to DM searches with observations of the MW halo HAWC Collaboration (2018a) and dSphs HAWC Collaboration (2018b). Its large sky coverage makes HAWC an excellent observatory for DM subhalo searches, as detailed in Chapter 7.

- **CTA:** The Cherenkov Telescope Array (CTA), currenty in construction phase, will be the reference instrument for high-energy gamma-ray Astronomy in the coming decades. CTA will consist of two different arrays in both hemispheres –CTA North will be at the MAGIC site, while CTA South will be located in the Atacama desert–, with three different telescope sizes covering different energy ranges. These are known as the Large-, Medium- and Small-Sized Telescopes (LSTs, MSTs and SSTs). The Southern array, which at this writing has not began its construction, will have a symmetric array of 4+25+70 LST–MST-SST telescopes, while the Northern array, due to the geographical conditions, will be a non-symmetric array of 4+15+0. Currently, the first LST of the Northern array –inaugurated in 2018– is on commissioning phase, and is the single largest IACT ever built.

  CTA will be sensitive to energies between $\sim$ 30 GeV and 100 TeV, with a superb angular resolution of 0.05° and energy resolution of $\sim$ 7% above 1 TeV. CTA will provide an unprecedented view of the high-energy sky thanks to its extreme sensitivity, which is roughly a factor $\sim$ 10 better than the current generation of IACTs, as we show in Figure 2.6. There is a number of "Key Science Projects" (KSPs) to be carried out by CTA, as detailed in Cherenkov Telescope Array Consortium (2019). Most notably, a mapping of 1/4 of the extragalactic sky and a Galactic plane survey, similar to the HGPS.

  CTA will also have a heavy DM KSP program, most notably the observation of the GC, dSphs, LMC and SMC and the Perseus galaxy cluster. Indeed, in addition to the allocated time, if a hint of DM signal is detected in any of these targets, more exposure time will be granted. CTA is also a suitable instrument for dark subhalo searches, as we will explore in Chapter 8.

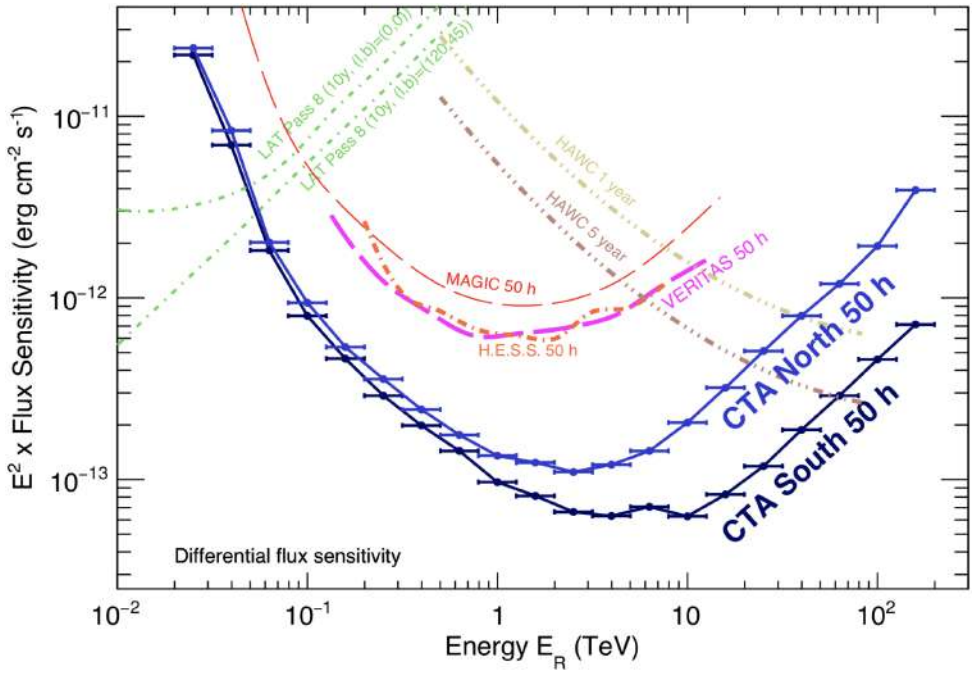


FIGURE 2.6: Comparison of the differential sensitivity (required flux for a $5\sigma$ detection) to a point source in current and future ground-based Cherenkov observatories, assuming diverse exposure times. Figure taken from Cherenkov Telescope Array Consortium (2020).

| | **H.E.S.S.** | **MAGIC** | **VERITAS** | **HAWC** | **CTA** |
|---|---|---|---|---|---|
| Location | Namibia | Spain | Arizona | Mexico | Spain/Chile |
| In operation since | 2002 | 2003 | 2007 | 2015 | – |
| Telescopes/detectors | 5 | 2 | 4 | 300 | 19 + 99 |
| Energy range [TeV] | 0.08–100 | 0.03–100 | 0.05–50 | 0.1–100 | 0.03–100 |
| Energy resolution [%] | 15 | 18 | 17 | 50 | 7 |
| Angular resolution [deg] | 0.1 | 0.1 | 0.08 | 0.1 | 0.05 |

TABLE 2.1: Summary of the current and future generation ground-based gamma-ray observatories.

## 2.3 Composition of the gamma-ray sky

The gamma-ray sky is a complex and rich environment, in which several astrophysical phenomena –which may include DM annihilation or decay– happen. The resulting picture is a combination of many components, persisting over a wide energy range, among which we can distinguish mainly i) localized sources (either point-like or extended), ii) the Galactic diffuse emission, and iii) the isotropic gamma-ray background (already mentioned in Section 1.5.3).

In Figure 2.7, we plot the LAT skymap above 1 GeV, after 10 years of operations (August 4, 2008 – August 4, 2018), containing 6873913 gamma-ray photons Ciprini (2020), which has provided an unprecedented view of the high-energy sky. In order to search for a DM signal, a proper discrimination of different these elements must be performed, especially given our interest on dark subhalos, which are within the sample of unIDs. In the following, we will review the astrophysical origin of each of these constituents.

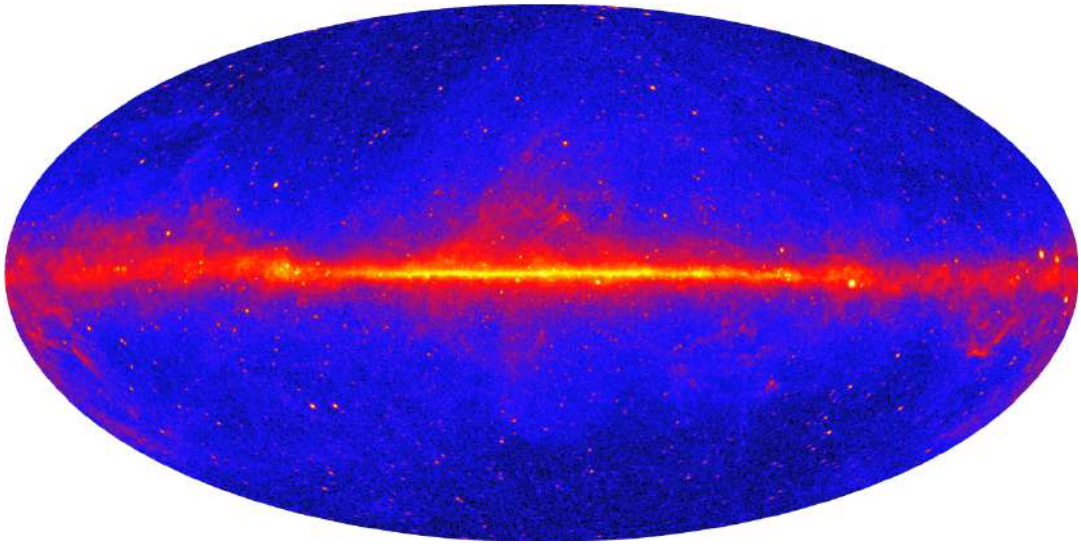

FIGURE 2.7: The gamma-ray sky above 1 GeV, as seen by *Fermi*-LAT in 10 years of operations. The map is shown in Galactic coordinates and a Hammer-Aitoff projection. Hotter colors indicate larger photon fluxes. Figure taken from Ciprini (2020).

### 2.3.1 Galactic diffuse gamma-ray emission

Figure 2.7 presents a prominent horizontal feature, along the equatorial plane of the projected skymap. This is the large-scale gamma-ray emission of the MW, which follows its disk, and together with the localized sources residing in it (see Section 2.3.3) is responsible for $\sim$ 80% of all photons detected by the LAT Fermi-LAT Collaboration (2012a).

Nevertheless, when shifting to higher energies –in the TeV domain– the properties of this diffuse emission are much less defined, and currently only extrapolations from the LAT regime are possible Neronov and Semikoz (2020). Efforts such as the cumulative diffuse emission along the Galactic plane in the HGPS helped to understand it better, although lacked spectral information H.E.S.S. Collaboration (2014). HAWC, being able to observe 2/3 of the sky, has also shed some light on the TeV diffuse emission HAWC Collaboration (2017b).

To understand the interstellar gamma-ray emission, there are a number of processes to take into account. The vicinity of the Galactic plane and, especially, the GC region, are vastly populated with objects such as PSRs, SN remnants (SNRs), pulsar-wind nebulæ (PWNe), and the central supermassive black hole (SMBH), Sgr A$^*$. All these inject accelerated CRs, both leptonic and hadronic, into their surroundings, which may interact with dense gas clouds via spallation processes on the clouds' particles. This will induce a flux of energetic gamma rays due to $\pi^0$ decay and Bremsstrahlung. Additionally, both the stellar population and gas clouds hosting star-formation regions can trigger efficient IC scattering with primary leptonic CRs. Finally, magnetic fields can also produce synchrotron radiation at energies ranging from radio to microwave.

Three processes, $\pi^0$ decay, Bremsstrahlung and IC scattering induce a gamma-ray flux, whose origin cannot be localized, as the primary CR may have travelled long distances before producing the gamma rays. The cumulative emission of these processes is known as the interstellar emission (IE). These components are individually resolved thanks to their morphology, which traces the distribution of gas clouds in the interstellar medium (ISM), and can be produced via leptonic (Bremsstrahlung)

or hadronic ($\pi^0$ decay) processes. The IC scattering, on the other hand, is closely related to the shape of the interstellar radiation field.

A proper modelling of the IE requires a profound understanding of the distribution of gas in the MW, the CR injection spectra and rate of astrophysical objects, the properties of the interstellar radiation field, the diffusion parameter of the CR transport equation (Eq. 1.39) as well as the Galactic magnetic field Fermi-LAT Collaboration (2012a).

The ISM is itself a collection of different elements, in gaseous and plasma states, mainly H, mounting up to $\sim$ 70% of it, which is present in atomic, molecular and ionized form Heiles and Troland (2003). The remaining part is mostly He, whose distribution is expected to follow that of H Cirelli et al. (2013). As mentioned, clouds in the ISM serve as targets for CRs spallation, responsible for the hadronic component of the IE through $\pi^0$ decay and Bremsstrahlung. The distribution of gas within the MW can be inferred from different probes.

The cold HI component is traced with observations of the 21 cm line (see Section 1.1.2). $H_2$ cannot be traced directly, as its emission lines fall into the frequencies blocked by the MW itself. To map its distribution, CO molecules are used as tracers of molecular clouds via its 2.6 mm emission line[10]. This results in the so-called column density measurements, which are a projection of the total density along the l.o.s. The column densities of CO and $H_2$ are usually assumed to be proportional, with a proportionality factor $X_{CO}$. This is the main source of uncertainty when deriving the gas distribution in the MW Cholis et al. (2012); Fermi-LAT Collaboration (2012a). Finally, ionised H –generally extended towards higher Galactic latitudes– only contributes to a small fraction, and usually is mapped with pulsar dispersion measurements Gaensler et al. (2008).

Regarding IC, the gamma-ray flux produced with this process cannot be measured from the Earth, and it must be computed from the transport equation (Eq. 1.39), with input parameters describing the source distribution of CRs (mainly PSRs), interstellar radiation field and propagation parameters Fermi-LAT Collaboration (2012a). The interstellar radiation field itself is produced by emission of stars and scattering–absorption–re-emission chains of this light by the ISM dust. This, together with the CMB photons (see Section 1.2.1), provide targets for IC scatterings Porter et al. (2017).

Another contribution to the Galactic diffuse emission comes from extended structures within the MW. In the GeV domain, two of these structures have been detected by the LAT: the Fermi bubbles (see Section 2.2.1) and the Loop I superbubble. The latter is located in the so-called Scorpius-Centaurus Association region, 100 pc away from the Earth, and contains three independent reservoirs of massive O and B stars Preibisch and Mamajek (2008). Loop I is most likely the result of a series of SNE-induced supersonic shock waves which cleared the inside of the region from the composition of the ISM de Geus (1992). The northern outer rim of Loop I marks a transition towards the denser surrounding environment of the ISM, where diffuse gamma-ray emission has been detected by the LAT after removing the IE components Fermi-LAT Collaboration (2012a).

With respect to the Fermi bubbles, since their discovery in 2010 they have been extensively studied to characterize them both spatially and spectrally Fermi-LAT Collaboration (2014). Its origin is still unknown, yet current theories include nuclear

[10]This is produced by the transition $J = 1 \rightarrow 0$, i.e., de-excitation of excited CO that has been produced by collisions with $H_2$.

starbust activity or remnants of past activity of Sgr A* Yang et al. (2018). The structure of the Fermi bubbles is a two-lobe feature extending up to 55° in latitude, with a maximum width of 40° in longitude. The high-latitude region of the bubbles is best-fit to a exponentially cutoff power law, with a photon spectral index $\Gamma \sim 1.9$ and cutoff energy of $E_{cut} \sim 110$ GeV Su et al. (2010). These parameters are almost constant throughout the high-latitude part of the bubbles, yet the innermost parts are rather unconstrained due to confusion with the GC and Galactic disk.

### 2.3.2 Isotropic gamma-ray background

When all defined components, diffuse emission and localized sources (which we will review next) are substracted, an isotropic, non-zero gamma-ray emission persists over the whole sky, with no clear origin Fermi-LAT Collaboration (2015b); Fornasa and Sánchez-Conde (2015). This is the isotropic gamma-ray background (IGRB), due to the cumulative emission of all far, unresolved extragalactic sources. Indeed, its isotropy is directly related to the LSS. Yet, a fraction of the IGRB can be originated by almost-isotropic Galactic foregrounds which cannot be removed –for instance, high-latitude MSPs Faucher-Giguère and Loeb (2010).

As reviewed in Section 1.5.3, the IGRB may have a component due to DM annihilation in the GC and MW halo, which can also be explored via cross-correlations with galaxy surveys and weak lensing maps Shirasaki et al. (2018). Yet, at the moment, the most accepted explanation is an unresolved population of blazars at high energies ($\gtrsim 100$ GeV) and radio and star-forming galaxies at lower energies Fermi-LAT Collaboration (2015a); Di Mauro (2016) which, together with the Galactic component, are expected to account for $\sim 100\%$ of the IGRB. The IGRB will be further explored in the context of PBH searches in Chapter 9.

### 2.3.3 Point and extended gamma-ray sources

When looking at Figure 2.7, apart from the prominent Galactic diffuse emission and the IGRB, there are several "hotspots" on the map. These, and many more which are not visible at naked eye, are individual gamma-ray sources, appearing as excesses over the expected background. Indeed, the typical analysis is performed with the Test Statistic (TS), defined as Rico (2020),

$$TS = 2 \log \left[ \frac{\mathcal{L}(H_1)}{\mathcal{L}(H_0)} \right] \tag{2.3}$$

where $\mathcal{L}(H_i)$ are the likelihoods under the null ($i = 0$) and source ($i = 1$) hypotheses. The usual convention is to set a detection threshold $TS \geq 25$, which is equivalent to $\sim 5\sigma$ detection over background. Lower values of TS are not conclusive, and usually more data is needed to elucidate whether the excess is a an actual, dim source, or fake, due to e.g., a mere statistical fluctuation or fore/background contamination caused by a mismodeling of the diffuse emission.

As the direction of propagation of gamma rays is (almost) unperturbed, a precise location of the sources can be made. These sources, which are not transient phenomena such as GRBs (although they can undergo flaring periods), are associated with astrophysical objects, which have mechanisms that accelerate particles up to these energies. These objects can be located in the MW or outside it.

In the case of extragalactic sources, these have to be extremely bright to be detected, for two reasons. In the first place, under an isotropic emission assumption, the flux decays as $r^{-2}$, thus having big losses when propagating over large

distances. Additionally, there is an intrinsic attenuation due to the EBL (see Section 1.5.3). This is the cumulative light emitted by stars and accreting compact objects through the whole history of the Universe Dube (1978); Saldana-Lopez et al. (2020). These low-energy photons will interact with the gamma rays via IC scattering $\gamma\gamma \rightarrow e^+e^-$, which results in an effective opacity $\tau$, attenuating the gamma-ray photon flux. The relation between the intrinsic and observed spectrum can be expressed as Domínguez et al. (2010),

$$\left.\frac{dN}{dE}\right|_{obs} = \left.\frac{dN}{dE}\right|_{int} \times e^{-\tau(E,z)} \tag{2.4}$$

The opacity itself is given by,

$$\tau(E,z) = \int_0^z \left(\frac{dl'}{dz}\right) dz' \int_0^2 d\mu \frac{\mu}{2} \int_{\varepsilon_{th}}^{\infty} d\varepsilon' \sigma_{\gamma\gamma}(\beta') n(\varepsilon, z') \tag{2.5}$$

where $dl'/dz' = c|dt'/dz'|$, $\mu = 1 - cos\theta$, $\sigma_{\gamma\gamma}$ is the photon-photon pair production cross section, $\beta = \frac{2m_e^2c^2}{E\varepsilon\mu(1+z)^2}$, and $n$ is the number density per unit energy of EBL photons.

This attenuation is more suppressing for higher energies and farther sources – therefore restricting the distance range of localized sources to the local Universe. Indeed, the most distant source detected at TeV energies is the gravitationally-lensed blazar QSO B0218+357, observed by MAGIC at $z = 0.944$ MAGIC Collaboration (2016a), and most AGNs will present this kind of absorption at very high energies Vassiliev (2000); Fermi-LAT Collaboration (2012c). EBL can also be useful for the determination of other quantities, such as the star formation rate Cooray (2016) or the Hubble constant Domínguez et al. (2019).

There are few extragalactic sources capable of gamma-ray emission luminous enough to reach the Earth. They are AGNs and other individual galaxies, including the cumulative emission of galaxy clusters. The distinction between AGNs and galaxies comes from the fact that AGN is only referred to the central, compact region in the vicinity of the SMBH, while other galaxies may shine in gamma rays due to similar processes that trigger the emission in the MW Galactic plane. Examples of the latter in the Local Group are the LMC, SMC and M31/Andromeda, which have been observed in gamma rays Fermi-LAT Collaboration (2020), and more distant starbust galaxies such as M82, NGC 253, NGC 1068 and NGC 4945 Fermi-LAT Collaboration (2012b).

Associating a gamma-ray source to a known astronomical object is not trivial, and requires a careful, multiwavelength analysis with several instruments. Indeed, in the case of extragalactic sources, AGNs show a high luminosity over a wider range of energies, from radio to gamma rays Beckmann and Shrader (2012). This rich variety is caused by the SMBH, which has an accretion disk, heated up due to the infalling mass and outflowing angular momentum. Additonally, IC scattering is produced in the hot corona above the accretion disk. If only these processes are present, the bulk of the emission is in the X-ray band and towards lower energies. There is, though, additional classes of AGNs, which are caused by the production of very collimated relativistic jets of particles of ionised matter above and below the accretion disk. Details on how does the SMBH produce such jets, especially in the small scales, are not fully understood yet Blandford et al. (2019). Such jets are efficient particle accelerators, powered by the huge magnetic fields in the vicinity of the SMBH. These AGNs will emit radiation over the full EM spectrum, with gamma rays being produced by the IC scattering and hadronic components, such as $\pi^0$ decay.

The current picture of the AGN landscape is a unified scheme, depending on the emission in the radio band and the existence of jets, as well as their orientation towards the Earth. This classification method gives rise to objects such as blazars, quasars, or Seyfert galaxies Urry and Padovani (1995). In particular blazars, which are AGNs with a relativistic jet pointing directly towards the Earth, are the most numerous among all known gamma-ray sources, as we will further detail later in this Section.

Concerning Galactic sources, there is a much richer variety of objects, as their intrinsic low gamma-ray luminosity can be detected from the Earth, given their distances. Among them, we may find PSRs, PWNe, SNRs, star-forming regions, globular clusters, high- and low-mass X-ray binaries, binary star systems, and novæ Fermi-LAT Collaboration (2020). Among these, PSRs, PWNe, SNRs and binaries are the most common Galactic gamma-ray sources, as well as primary sources of accelerated CRs Koyama et al. (1995). This particle acceleration produces a gamma-ray spectrum which is typically best-fit by a power law –reflecting the non-thermal production of such energetic photons. Nevertheless, there are some classes, namely PSRs, SNRs and PWNe, which present a curved spectrum, therefore representing a challenge for DM indirect searches, as both classes share this feature (see Section 1.5.3).

In the case of PSRs, the energy radiated through the synchrotron radiation of accelerated charged particles in their huge magnetic fields are below the gamma-ray domain. Thus, the production of even more energetic photons requires an additional mechanism, which is currently not fully understood. The most accepted picture is that PSRs are slowly spinning down (see Section 1.2.1), with kinetic energy being transferred to $e^{\pm}$ pair creation, which are then accelerated in the PSR magnetosphere. This produces photons via IC scattering and synchrotron radiation, which will then induce a second-generation $e^{\pm}$ pairs, and so forth and so on, resulting in a cascade of emission and pair-creation processes which will render the typical curved gamma-ray spectrum of PSRs, with a sharp cutoff at some GeV Takata et al. (2015).

PSRs also present a very quickly-rotating subclass, with periods around the millisecond, and accordingly known as MilliSecond Pulsars (MSPs). These form when an old PSR is in a binary system, with a much less massive companion star, starts accreting material from it until it reignites with a quicker pulsation period. This leads to luminosities up to 20 times larger than in a young PSR, due to their fast rotation Calore et al. (2014). Due to their age and reignition kick velocity, MSPs tend to appear at higher Galactic latitudes than younger counterparts Cordes and Chernoff (1997).

Regarding extended sources, these are normally characterized with the 68% containment angle of the whole emission. Sources must be larger than the *Point Spread Function* (PSF), which measures the "spill-over" of photons from a source over the ROI due to the instrument angular resolution Fermi-LAT Collaboration (2013). In the case of the LAT, this value is around $\sim 0.1^{\circ}$ for energies above 10 GeV. Therefore, if a source exhibits a 68% containment radius above the PSF value, it will be modeled as extended, and as point-like in the opposite case. Extended gamma-ray sources are very rare, and only a handful of them are known, typically of Galactic origin such as PWNe and SNRs (see Fermi-LAT Collaboration (2017b, 2018) for full details and a complete list). In the case of IACTs, the analysis of extended sources can be more challenging, as their FoV, typically $\sim 0.1^{\circ}$, can be much smaller than the source angular extension, requiring mutiple pointings Mattox et al. (1996); Cardenzana and VERITAS Collaboration (2015). Spatial extension in the context of dark subhalo searches will be further addressed in Chapters 5 and 6.

All this information is ultimately condensed in gamma-ray source catalogs. Depending on the instrument, the nomenclature may vary, but it is typically an alphanumeric chain which marks the instrument and data release, followed by the equatorial coordinates in format J2000, i.e., `JHHMM.m+DDMMa`, although notable sources may be named differently. This allows a quick cross-correlation between multiwavelength catalogs. Additional data such as detection significance, flux, positional error, spectral best-fit model parameters, variability and association(s) is provided.

The latest *Fermi*-LAT catalog, the 4FGL Fermi-LAT Collaboration (2020), is the most complete gamma-ray compendium of sources. In its second data release, which includes 10 years of data, the 4FGL–DR2 comprises 5788 individual sources Ballet et al. (2020), with 75 modeled as extended. More specific catalogs are also released, such as the FHL catalogs of "hard" sources, listing objects well fitted by power law spectral indices higher than -2. Such sources can exhibit significant emission in the TeV range, therefore being interesting targets for IACTs, as well as heavy DM detection. The latest iteration of this catalog is the 3FHL, which lists the 1556 detected sources emitting above 10 GeV with 7 years of LAT data, mostly of extragalactic origin Fermi-LAT Collaboration (2017a)[11].

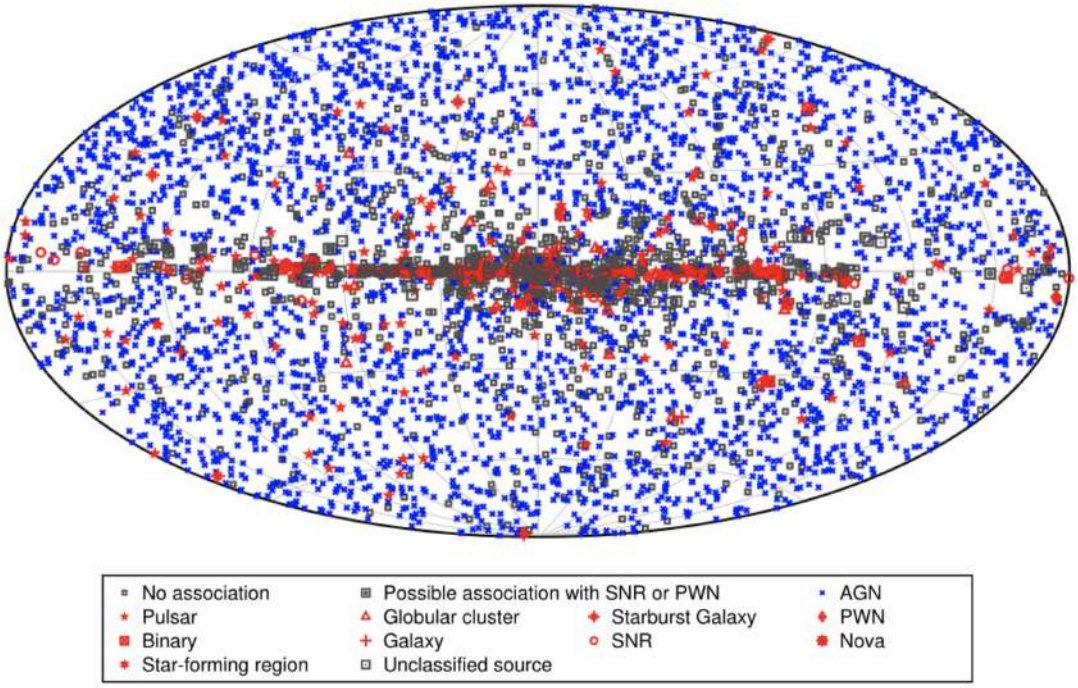


FIGURE 2.8: Map of localized sources in the *Fermi*-LAT 8-year 4FGL catalog, in Hammer-Aitoff projection and Galactic coordinates (see also Figure 2.7). Blue squares are AGNs, the most numerous source type, while grey squares, mounting up to ∼1/3 of the total, are unIDs. Figure taken from Fermi-LAT Collaboration (2020).

Ground-based telescopes, as opposed to the LAT, do not make their data publicly available, being exclusive to each scientific collaboration. Nevertheless, lists of sources, lacking most of the information on the spectral characteristics, have been published. This is the case of the third HAWC data release (3HWC) HAWC Collaboration (2020), with 1523 days of data, which lists 65 TeV sources. VERITAS,

[11] Other catalogs, such as the FGES and FHES, can be found at `https://fermi.gsfc.nasa.gov/ssc/data/access/`

MAGIC and H.E.S.S. do also report their sources, which are collected in the interactive online catalog TeVCAT[12]. At this writing, there are 230 TeV sources reported, with some positional and spectral parameters as referenced in each collaboration's publications. Although this information is limited, it can be used to set constraints to DM annihilation, as we will do in Chapter 7. CTA, on the other hand, is expected to make its data publicly available, therefore being the first TeV open observatory CTA Consortium (2015).

All the gamma-ray source catalogs share a common feature: the large fraction of unIDs. As we show in Figure 2.8, when we decompose the *Fermi*-LAT resolved sky into different classes, we note almost 1/3 of objects are of unknown nature. This is also the typical value in the TeV regime, where 26% of all sources are currently unassociated. Being dark subhalo searches our interest, we therefore have lots of potential DM satellites already detected, just awaiting proper classification. This will be the main research line of this Thesis throughout the next Chapters.

## Bibliography

AGILE Collaboration (2008). The AGILE space mission, *Nuclear Instruments and Methods in Physics Research A* **588**(1-2): 52–62.
**URL:** https://ui.adsabs.harvard.edu/abs/2008NIMPA.588..52T

Aharonian, F. A., Hofmann, W., Konopelko, A. K. and Völk, H. J. (1997). The potential of ground based arrays of imaging atmospheric Cherenkov telescopes. I. Determination of shower parameters, *Astroparticle Physics* **6**(3-4): 343–368.
**URL:** https://ui.adsabs.harvard.edu/abs/1997APh.....6..343A

Ballet, J., Burnett, T. H., Digel, S. W. and Lott, B. (2020). Fermi Large Area Telescope Fourth Source Catalog Data Release 2.

Beckmann, V. and Shrader, C. R. (2012). *Active Galactic Nuclei*.
**URL:** https://ui.adsabs.harvard.edu/abs/2012agn..book.....B

Blandford, R., Meier, D. and Readhead, A. (2019). Relativistic Jets from Active Galactic Nuclei, *Annual Review of Astronomy and Astrophysics* **57**(1): 467–509.
**URL:** http://dx.doi.org/10.1146/annurev-astro-081817-051948

Calore, F., Di Mauro, M. and Donato, F. (2014). Diffuse gamma-ray emission from galactic pulsars, *The Astrophysical Journal* **796**(1): 14.
**URL:** http://dx.doi.org/10.1088/0004-637X/796/1/14

Cardenzana, J. and VERITAS Collaboration (2015). A Novel Method for Detecting Extended Sources with VERITAS, *34th International Cosmic Ray Conference (ICRC2015)*, Vol. 34 of *International Cosmic Ray Conference*, p. 1031.
**URL:** https://ui.adsabs.harvard.edu/abs/2015ICRC...34.1031C

Cherenkov, P. A. (1960). Radiation from High-Speed Particles, *Science* **131**(3394): 136–142.
**URL:** https://ui.adsabs.harvard.edu/abs/1960Sci...131..136C

Cherenkov Telescope Array Consortium (2019). *Science with the Cherenkov Telescope Array*.
**URL:** https://ui.adsabs.harvard.edu/abs/2019scta.book.....C

[12] http://tevcat2.uchicago.edu/

Cherenkov Telescope Array Consortium (2020). CTA Performance.
**URL:** https://www.cta-observatory.org/science/cta-performance/

Cholis, I., Tavakoli, M., Evoli, C., Maccione, L. and Ullio, P. (2012). Diffuse galactic gamma rays at intermediate and high latitudes. I. Constraints on the ISM properties, *Journal of Cosmology and Astroparticle Physics* **2012**(05): 004–004.
**URL:** http://dx.doi.org/10.1088/1475-7516/2012/05/004

Ciprini, S. (2020). Ten years of *Fermi* LAT observations and the new 4FGL and 4LAC catalogs, *PoS* **APCS2018**: 054.

Cirelli, M., Serpico, P. D. and Zaharijas, G. (2013). Bremsstrahlung gamma rays from light dark matter, *Journal of Cosmology and Astroparticle Physics* **2013**(11): 035–035.
**URL:** http://dx.doi.org/10.1088/1475-7516/2013/11/035

Cooray, A. (2016). Extragalactic background light measurements and applications, *Royal Society Open Science* **3**(3): 150555.
**URL:** https://ui.adsabs.harvard.edu/abs/2016RSOS...3.50555C

Cordes, J. M. and Chernoff, D. F. (1997). Neutron star population dynamics. i. millisecond pulsars, *The Astrophysical Journal* **482**(2): 971–992.
**URL:** http://dx.doi.org/10.1086/304179

CTA Consortium (2015). Cherenkov Telescope Array Data Management, *34th International Cosmic Ray Conference (ICRC2015)*, Vol. 34 of *International Cosmic Ray Conference*, p. 947.
**URL:** https://ui.adsabs.harvard.edu/abs/2015ICRC...34..947L

de Geus, E. J. (1992). Interactions of stars and interstellar matter in Scorpio Centaurus., *Astronomy & Astrophysics* **262**: 258–270.
**URL:** https://ui.adsabs.harvard.edu/abs/1992A&A...262..258D

Di Mauro, M. (2016). Isotropic diffuse and extragalactic $\gamma$-ray background: emission from extragalactic sources vs dark matter annihilating particles, *Journal of Physics: Conference Series* **718**: 042019.
**URL:** http://dx.doi.org/10.1088/1742-6596/718/4/042019

Domínguez, A., Primack, J. R., Rosario, D. J., Prada, F., Gilmore, R. C., Faber, S. M., Koo, D. C., Somerville, R. S., Pérez-Torres, M. A., Pérez-González, P. and et al. (2010). Extragalactic background light inferred from AEGIS galaxy-SED-type fractions, *Monthly Notices of the Royal Astronomical Society* **410**(4): 2556–2578.
**URL:** http://dx.doi.org/10.1111/j.1365-2966.2010.17631.x

Domínguez, A., Wojtak, R., Finke, J., Ajello, M., Helgason, K., Prada, F., Desai, A., Paliya, V., Marcotulli, L. and Hartmann, D. H. (2019). A New Measurement of the Hubble Constant and Matter Content of the Universe Using Extragalactic Background Light $\gamma$-Ray Attenuation, *The Astrophysical Journal* **885**(2): 137.
**URL:** http://dx.doi.org/10.3847/1538-4357/ab4a0e

Dube, R. R. (1978). *A measurement of the extragalactic background light*.
**URL:** https://ui.adsabs.harvard.edu/abs/1978mebl.book....D

EGRET Collaboration (1999). The Third EGRET Catalog of High-Energy Gamma-Ray Sources, *The Astrophysical Journal Supplementary Series* **123**(1): 79–202.
**URL:** https://ui.adsabs.harvard.edu/abs/1999ApJS..123...79H

Espadanal, J. and Gonçalves, P. (2017). 3D simulation for Cherenkov emissions in Extensive Air Showers.

Faucher-Giguère, C.-A. and Loeb, A. (2010). The pulsar contribution to the gamma-ray background, *Journal of Cosmology and Astroparticle Physics* **2010**(01): 005–005.
**URL:** http://dx.doi.org/10.1088/1475-7516/2010/01/005

Fermi-LAT Collaboration (2009). The Large Area Telescope on the Fermi Gamma-ray Space Telescope Mission, *The Astrophysical Journal* **697**(2): 1071–1102.
**URL:** http://dx.doi.org/10.1088/0004-637X/697/2/1071

Fermi-LAT Collaboration (2012a). Fermi-LAT Observations of the Diffuse Gamma-Ray Emission: Implications for Cosmic Rays and the Interstellar Medium, *The Astrophysical Journal* **750**(1): 3.
**URL:** http://dx.doi.org/10.1088/0004-637X/750/1/3

Fermi-LAT Collaboration (2012b). GeV Observations of Star-forming Galaxies with *Fermi* LAT, *The Astrophysical Journal* **755**(2): 164.
**URL:** http://dx.doi.org/10.1088/0004-637X/755/2/164

Fermi-LAT Collaboration (2012c). The Imprint of the Extragalactic Background Light in the Gamma-Ray Spectra of Blazars, *Science* **338**(6111): 1190–1192.
**URL:** http://dx.doi.org/10.1126/science.1227160

Fermi-LAT Collaboration (2013). Determination of the Point-Spread Function for the Fermi Large Area Telescope from On-orbit Data and Limits on Pair Halos of Active Galactic Nuclei, *The Astrophysical Journal* **765**(1): 54.
**URL:** http://dx.doi.org/10.1088/0004-637X/765/1/54

Fermi-LAT Collaboration (2014). The Spectrum and Morphology of the Fermi Bubbles, *The Astrophysical Journal* **793**(1): 64.
**URL:** http://dx.doi.org/10.1088/0004-637X/793/1/64

Fermi-LAT Collaboration (2015a). The Origin of the Extragalactic Gamma-Ray Background and Implications for Dark-Matter Annihilation, *The Astrophysical Journal* **800**(2): L27.
**URL:** http://dx.doi.org/10.1088/2041-8205/800/2/L27

Fermi-LAT Collaboration (2015b). The spectrum of isotropic diffuse gamma-ray emission between 100 MeV and 820 GeV, *The Astrophysical Journal* **799**(1): 86.
**URL:** http://dx.doi.org/10.1088/0004-637X/799/1/86

Fermi-LAT Collaboration (2017a). 3FHL: The Third Catalog of Hard Fermi-LAT Sources, *The Astrophysical Journal Supplement Series* **232**(2): 18.
**URL:** http://dx.doi.org/10.3847/1538-4365/aa8221

Fermi-LAT Collaboration (2017b). Search for Extended Sources in the Galactic Plane Using Six Years of Fermi-Large Area Telescope Pass 8 Data above 10 GeV, *The Astrophysical Journal* **843**(2): 139.
**URL:** http://dx.doi.org/10.3847/1538-4357/aa775a

Fermi-LAT Collaboration (2018). The Search for Spatial Extension in High-latitude Sources Detected by the Fermi Large Area Telescope, *The Astrophysical Journal Supplement Series* **237**(2): 32.
**URL:** http://dx.doi.org/10.3847/1538-4365/aacdf7

Fermi-LAT Collaboration (2020). Fermi Large Area Telescope Fourth Source Catalog, *The Astrophysical Journal Supplement Series* **247**(1): 33.
**URL:** http://dx.doi.org/10.3847/1538-4365/ab6bcb

Fichtel, C. E., Kniffen, D. A. and Hartman, R. C. (1973). Celestial Diffuse Gamma Radiation above 30 MeV Observed by SAS-2, *The Astrophysical Journal Letters* **186**: L99.
**URL:** https://ui.adsabs.harvard.edu/abs/1973ApJ...186L..99F

Fornasa, M. and Sánchez-Conde, M. A. (2015). The nature of the Diffuse Gamma-Ray Background, *Physics Reports* **598**: 1–58.
**URL:** http://dx.doi.org/10.1016/j.physrep.2015.09.002

Frank, I. M. and Tamm, I. E. (1937). Coherent visible radiation of fast electrons passing through matter, *Compt. Rend. Acad. Sci. URSS* **14**(3): 109–114.

Gaensler, B. M., Madsen, G. J., Chatterjee, S. and Mao, S. A. (2008). The Vertical Structure of Warm Ionised Gas in the Milky Way, *Publications of the Astronomical Society of Australia* **25**(4): 184–200.
**URL:** http://dx.doi.org/10.1071/AS08004

Galper, A. M., Topchiev, N. P. and Yurkin, Y. T. (2018). GAMMA-400 Project, *Astronomy Reports* **62**(12): 882–889.
**URL:** https://ui.adsabs.harvard.edu/abs/2018ARep...62..882G

HAWC Collaboration (2017a). Observation of the Crab Nebula with the HAWC Gamma-Ray Observatory, *The Astrophysical Journal* **843**(1): 39.
**URL:** http://dx.doi.org/10.3847/1538-4357/aa7555

HAWC Collaboration (2017b). Probing Galactic Diffuse TeV Gamma-Ray Emission with the HAWC Observatory, *35th International Cosmic Ray Conference (ICRC2017)*, Vol. 301 of *International Cosmic Ray Conference*, p. 689.
**URL:** https://ui.adsabs.harvard.edu/abs/2017ICRC...35..689Z

HAWC Collaboration (2018a). A search for dark matter in the Galactic halo with HAWC, *Journal of Cosmology and Astroparticle Physics* **2018**(02): 049–049.
**URL:** http://dx.doi.org/10.1088/1475-7516/2018/02/049

HAWC Collaboration (2018b). Dark Matter Limits from Dwarf Spheroidal Galaxies with the HAWC Gamma-Ray Observatory, *The Astrophysical Journal* **853**(2): 154.
**URL:** https://ui.adsabs.harvard.edu/abs/2018ApJ...853..154A

HAWC Collaboration (2020). 3HWC: The Third HAWC Catalog of Very-high-energy Gamma-Ray Sources, *The Astrophysical Journal* **905**(1): 76.
**URL:** http://dx.doi.org/10.3847/1538-4357/abc2d8

HEGRA Collaboration (1997). Measurement of the flux, spectrum, and variability of TeV $\gamma$-rays from MKN 501 during a state of high activity, *Astronomy & Astrophysics* **327**: L5–L8.
**URL:** https://ui.adsabs.harvard.edu/abs/1997A&A...327L...5A

HEGRA Collaboration (2002). An unidentified TeV source in the vicinity of Cygnus OB2, *Astronomy & Astrophysics* **393**(2): L37–L40.
**URL:** http://dx.doi.org/10.1051/0004-6361:20021171

Heiles, C. and Troland, T. H. (2003). The Millennium Arecibo 21 Centimeter Absorption-Line Survey. II. Properties of the Warm and Cold Neutral Media, *The Astrophysical Journal* **586**(2): 1067–1093.
**URL:** *http://dx.doi.org/10.1086/367828*

H.E.S.S. Collaboration (2002). The H.E.S.S. Telescopes.
**URL:** *https://www.mpi-hd.mpg.de/hfm/HESS/pages/about/telescopes/*

H.E.S.S. Collaboration (2006). Discovery of very-high-energy $\gamma$-rays from the Galactic Centre ridge, *Nature* **439**(7077): 695–698.
**URL:** *http://dx.doi.org/10.1038/nature04467*

H.E.S.S. Collaboration (2014). Diffuse Galactic gamma-ray emission with H.E.S.S., *Physical Review D* **90**(12).
**URL:** *http://dx.doi.org/10.1103/PhysRevD.90.122007*

H.E.S.S. Collaboration (2016). Acceleration of petaelectronvolt protons in the Galactic Centre, *Nature* **531**(7595): 476–479.
**URL:** *http://dx.doi.org/10.1038/nature17147*

H.E.S.S. Collaboration (2018a). Search for $\gamma$-Ray Line Signals from Dark Matter Annihilations in the Inner Galactic Halo from 10 Years of Observations with H.E.S.S., *Physical Review Letters* **120**(20).
**URL:** *http://dx.doi.org/10.1103/PhysRevLett.120.201101*

H.E.S.S. Collaboration (2018b). The H.E.S.S. Galactic plane survey, *Astronomy & Astrophysics* **612**: A1.
**URL:** *http://dx.doi.org/10.1051/0004-6361/201732098*

Hillas, A. M. (1996). Differences between Gamma-Ray and Hadronic Showers, *Space Science Reviews* **75**(1-2): 17–30.
**URL:** *https://ui.adsabs.harvard.edu/abs/1996SSRv...75...17H*

Holler, M., Berge, D., van Eldik, C., Lenain, J. P., Marandon, V., Murach, T., de Naurois, M., Parsons, R. D., Prokoph, H. and Zaborov, D. (2015). Observations of the Crab Nebula with H.E.S.S. Phase II, *arXiv e-prints* p. arXiv:1509.02902.
**URL:** *https://ui.adsabs.harvard.edu/abs/2015arXiv150902902H*

IceCube Collaboration (2018). Neutrino emission from the direction of the blazar TXS 0506+056 prior to the IceCube-170922A alert, *Science* **361**(6398): 147–151.
**URL:** *http://dx.doi.org/10.1126/science.aat2890*

Karlsson, N. (2009). Discovery of VHE Gamma-ray Emission from the Starburst Galaxy M82, *arXiv e-prints* p. arXiv:0912.3807.
**URL:** *https://ui.adsabs.harvard.edu/abs/2009arXiv0912.3807K*

Klebesadel, R. W., Strong, I. B. and Olson, R. A. (1973). Observations of Gamma-Ray Bursts of Cosmic Origin, *The Astrophysical Journal Letters* **182**: L85.
**URL:** *https://ui.adsabs.harvard.edu/abs/1973ApJ...182L..85K*

Kniffen, D. A., Hartman, R. C., Thompson, D. J. and Fichtel, C. E. (1973). SAS-2 Observations of Gamma Rays from the Galactic Plane, *The Astrophysical Journal Letters* **186**: L105.
**URL:** *https://ui.adsabs.harvard.edu/abs/1973ApJ...186L.105K*

Koyama, K., Petre, R., Gotthelf, E. V., Hwang, U., Matsuura, M., Ozaki, M. and Holt, S. S. (1995). Evidence for shock acceleration of high-energy electrons in the supernova remnant SN1006, *Nature* **378**(6554): 255–258.
**URL:** https://ui.adsabs.harvard.edu/abs/1995Natur.378..255K

Kraushaar, W. L., Clark, G. W., Garmire, G. P., Borken, R., Higbie, P., Leong, V. and Thorsos, T. (1972). High-Energy Cosmic Gamma-Ray Observations from the OSO-3 Satellite, *The Astrophysical Journal* **177**: 341.
**URL:** https://ui.adsabs.harvard.edu/abs/1972ApJ...177..341K

Krayzel, F., Maurin, G., Brunetti, L., Dubois, J. M., Fiasson, A., Journet, L., Lamanna, G., Leflour, T., Lieunard, B., Monteiro, I. and Rosier-Lees, S. (2013). Improved Sensitivity of H.E.S.S.-II Through the Fifth Telescope Focus System, *International Cosmic Ray Conference*, Vol. 33 of *International Cosmic Ray Conference*, p. 3084.
**URL:** https://ui.adsabs.harvard.edu/abs/2013ICRC...33.3084K

LIGO Collaboration et al. (2017). Multi-messenger Observations of a Binary Neutron Star Merger, *The Astrophysical Journal Letters* **848**(2): L12.
**URL:** https://ui.adsabs.harvard.edu/abs/2017ApJ...848L..12A

MAGIC Collaboration (2013). Physics Performance of the Upgraded MAGIC Telescopes Obtained with Crab Nebula Data, *International Cosmic Ray Conference*, Vol. 33 of *International Cosmic Ray Conference*, p. 1116.
**URL:** https://ui.adsabs.harvard.edu/abs/2013ICRC...33.1116S

MAGIC Collaboration (2016a). Detection of very high energy gamma-ray emission from the gravitationally lensed blazar QSO B0218+357 with the MAGIC telescopes, *Astronomy & Astrophysics* **595**: A98.
**URL:** http://dx.doi.org/10.1051/0004-6361/201629461

MAGIC Collaboration (2016b). The major upgrade of the MAGIC telescopes, Part II: A performance study using observations of the Crab Nebula, *Astroparticle Physics* **72**: 76–94.
**URL:** http://dx.doi.org/10.1016/j.astropartphys.2015.02.005

MAGIC Collaboration (2018a). Periastron Observations of TeV Gamma-Ray Emission from a Binary System with a 50-year Period, *The Astrophysical Journal* **867**(1): L19.
**URL:** http://dx.doi.org/10.3847/2041-8213/aae70e

MAGIC Collaboration (2018b). The Blazar TXS 0506+056 Associated with a High-energy Neutrino: Insights into Extragalactic Jets and Cosmic-Ray Acceleration, *The Astrophysical Journal Letters* **863**(1): L10.
**URL:** https://ui.adsabs.harvard.edu/abs/2018ApJ...863L..10A

MAGIC Collaboration (2020). Bounds on Lorentz Invariance Violation from MAGIC Observation of GRB 190114C, *Physical Review Letters* **125**(2).
**URL:** http://dx.doi.org/10.1103/PhysRevLett.125.021301

Matthews, J. (2005). A Heitler model of extensive air showers, *Astroparticle Physics* **22**(5-6): 387–397.
**URL:** https://ui.adsabs.harvard.edu/abs/2005APh....22..387M

Matthews, N. (2019). Astrophysical measurements with the VERITAS Stellar Intensity Interferometer, *36th International Cosmic Ray Conference (ICRC2019)*, Vol. 36 of

*International Cosmic Ray Conference*, p. 740.
**URL:** https://ui.adsabs.harvard.edu/abs/2019ICRC...36..740M

Mattox, J. R., Bertsch, D. L., Chiang, J., Dingus, B. L., Digel, S. W., Esposito, J. A., Fierro, J. M., Hartman, R. C., Hunter, S. D., Kanbach, G., Kniffen, D. A., Lin, Y. C., Macomb, D. J., Mayer-Hasselwander, H. A., Michelson, P. F., von Montigny, C., Mukherjee, R., Nolan, P. L., Ramanamurthy, P. V., Schneid, E., Sreekumar, P., Thompson, D. J. and Willis, T. D. (1996). The Likelihood Analysis of EGRET Data, *The Astrophysical Journal* **461**: 396.
**URL:** https://ui.adsabs.harvard.edu/abs/1996ApJ...461..396M

Mayer-Hasselwander, H. A., Bennett, K., Bignami, G. F., Buccheri, R., Caraveo, P. A., Hermsen, W., Kanbach, G., Lebrun, F., Lichti, G. G., Masnou, J. L., Paul, J. A., Pinkau, K., Sacco, B., Scarsi, L., Swanenburg, B. N. and Wills, R. D. (1982). Large-scale distribution of galactic gamma radiation observed by COS-B, *Astronomy & Astrophysics* **105**(1): 164–175.
**URL:** https://ui.adsabs.harvard.edu/abs/1982A&A...105..164M

McEnery, J. E. (2017). All-Sky Medium Energy Gamma-ray Observatory (AMEGO) - A discovery mission for the MeV gamma-ray band, *AAS/High Energy Astrophysics Division #16*, Vol. 16 of *AAS/High Energy Astrophysics Division*, p. 103.13.
**URL:** https://ui.adsabs.harvard.edu/abs/2017HEAD...1610313M

Mezek, G. K. (2019). *Mass composition of ultra-high energy cosmic rays at the Pierre Auger Observatory*, PhD thesis, University of Nova Gorica.

Milagro Collaboration (2004). TeV Gamma-Ray Survey of the Northern Hemisphere Sky Using the Milagro Observatory, *arXiv e-prints* pp. astro–ph/0403097.
**URL:** https://ui.adsabs.harvard.edu/abs/2004astro.ph..3097T

Milagro Collaboration (2007). TeV Gamma-Ray Sources from a Survey of the Galactic Plane with Milagro, *The Astrophysical Journal* **664**(2): L91–L94.
**URL:** http://dx.doi.org/10.1086/520717

Milagro Collaboration (2008). A Measurement of the Spatial Distribution of Diffuse TeV Gamma-Ray Emission from the Galactic Plane with Milagro, *The Astrophysical Journal* **688**(2): 1078–1083.
**URL:** http://dx.doi.org/10.1086/592213

Milagro Collaboration (2009). The large-scale cosmic-ray anisotropy as observed with Milagro, *The Astrophysical Journal* **698**(2): 2121–2130.
**URL:** http://dx.doi.org/10.1088/0004-637X/698/2/2121

Neronov, A. and Semikoz, D. (2020). Galactic diffuse gamma-ray emission at TeV energy, *Astronomy & Astrophysics* **633**: A94.
**URL:** http://dx.doi.org/10.1051/0004-6361/201936368

Nieto, D., Miener, T., Brill, A., Contreras, J. L., Humensky, T. B. and Mukherjee, R. (2021). Reconstruction of IACT events using deep learning techniques with CTLearn.
**URL:** https://arxiv.org/abs/2101.07626

Paredes, J. M. and MAGIC Collaboration (2020). MAGIC Highlights, *Multifrequency Behaviour of High Energy Cosmic Sources - XIII. 3-8 June 2019. Palermo*, p. 43.
**URL:** https://ui.adsabs.harvard.edu/abs/2020mbhe.confE..43P

Park, N. and VERITAS Collaboration (2015). Performance of the VERITAS experiment, *34th International Cosmic Ray Conference (ICRC2015)*, Vol. 34 of *International Cosmic Ray Conference*, p. 771.
**URL:** https://ui.adsabs.harvard.edu/abs/2015ICRC...34..771P

Porter, T. A., Jóhannesson, G. and Moskalenko, I. V. (2017). High-energy Gamma Rays from the Milky Way: Three-dimensional Spatial Models for the Cosmic-Ray and Radiation Field Densities in the Interstellar Medium, *The Astrophysical Journal* **846**(1): 67.
**URL:** http://dx.doi.org/10.3847/1538-4357/aa844d

Preibisch, T. and Mamajek, E. (2008). *The Nearest OB Association: Scorpius-Centaurus (Sco OB2)*, Vol. 5, p. 235.
**URL:** https://ui.adsabs.harvard.edu/abs/2008hsf2.book..235P

Rico, J. (2020). Gamma-Ray Dark Matter Searches in Milky Way Satellites—A Comparative Review of Data Analysis Methods and Current Results, *Galaxies* **8**(1): 25.
**URL:** http://dx.doi.org/10.3390/galaxies8010025

Saldana-Lopez, A., Domínguez, A., Pérez-González, P. G., Finke, J., Ajello, M., Primack, J. R., Paliya, V. S. and Desai, A. (2020). An observational determination of the evolving extragalactic background light from the multiwavelength HST/CANDELS survey in the Fermi and CTA era.

Schmidt, F. and Knapp, J. (2005). CORSIKA Shower Images.
**URL:** https://www-zeuthen.desy.de/~jknapp/fs/showerimages.html

Sciascio, G. D. (2019). Ground-based Gamma-Ray Astronomy: an Introduction, *Journal of Physics: Conference Series* **1263**: 012003.
**URL:** http://dx.doi.org/10.1088/1742-6596/1263/1/012003

Shirasaki, M., Macias, O., Horiuchi, S., Yoshida, N., Lee, C.-H. and Nishizawa, A. J. (2018). Correlation of extragalactic $\gamma$ rays with cosmic matter density distributions from weak gravitational lensing, *Physical Review D* **97**(12).
**URL:** http://dx.doi.org/10.1103/PhysRevD.97.123015

Su, M., Slatyer, T. R. and Finkbeiner, D. P. (2010). Giant Gamma-ray Bubbles from Fermi-LAT: AGN Activity or Bipolar Galactic Wind?, *The Astrophysical Journal* **724**(2): 1044–1082.
**URL:** http://dx.doi.org/10.1088/0004-637X/724/2/1044

Swanenburg, B. N., Bennett, K., Bignami, G. F., Buccheri, R., Caraveo, P., Hermsen, W., Kanbach, G., Lichti, G. G., Masnou, J. L., Mayer-Hasselwander, H. A., Paul, J. A., Sacco, B., Scarsi, L. and Wills, R. D. (1981). Second COS-B catalogue of high-energy gamma-ray sources., *The Astrophysical Journal Letters* **243**: L69–L73.
**URL:** https://ui.adsabs.harvard.edu/abs/1981ApJ...243L..69S

Takata, J., Ng, C. W. and Cheng, K. S. (2015). Probing gamma-ray emissions of Fermi-LAT pulsars with a non-stationary outer gap model, *Monthly Notices of the Royal Astronomical Society* **455**(4): 4249–4266.
**URL:** http://dx.doi.org/10.1093/mnras/stv2612

Urry, C. M. and Padovani, P. (1995). Unified Schemes for Radio-Loud Active Galactic Nuclei, *Publications of the Astronomical Society of the Pacific* **107**: 803.
**URL:** http://dx.doi.org/10.1086/133630

Vassiliev, V. (2000). Extragalactic background light absorption signal in the TeV $\gamma$-ray spectra of blazars, *Astroparticle Physics* **12**(4): 217–238.
**URL:** *http://dx.doi.org/10.1016/S0927-6505(99)00107-3*

Weekes, T. C., Cawley, M. F., Fegan, D. J., Gibbs, K. G., Hillas, A. M., Kowk, P. W., Lamb, R. C., Lewis, D. A., Macomb, D., Porter, N. A., Reynolds, P. T. and Vacanti, G. (1989). Observation of TeV Gamma Rays from the Crab Nebula Using the Atmospheric Cerenkov Imaging Technique, *The Astrophysical Journal* **342**: 379.
**URL:** *https://ui.adsabs.harvard.edu/abs/1989ApJ...342..379W*

Winkler, C. (1996). INTEGRAL. The international gamma-ray astrophysics laboratory., *Astronomy & Astrophysics Supplement* **120**: 637–640.
**URL:** *https://ui.adsabs.harvard.edu/abs/1996A&AS..120C.637W*

Yang, H.-Y., Ruszkowski, M. and Zweibel, E. (2018). Unveiling the Origin of the Fermi Bubbles, *Galaxies* **6**(1): 29.
**URL:** *http://dx.doi.org/10.3390/galaxies6010029*

# Chapter 3

# Unidentified Gamma-ray sources as targets for indirect dark matter detection with the *Fermi* Large Area Telescope

*Based on J. Coronado-Blázquez et al., Journal of Cosmology and Astroparticle Physics* ***1907*** *(2019) 020*

## 3.1 Introduction

Mounting evidence has been found that about 85% of all matter in the Universe is non-baryonic, this is the so-called dark matter (DM) The Planck Collaboration (2016); Garrett and Duda (2011); Bertone et al. (2005); Freese (2009). The composition of this DM remains unknown, and is one of the most important open questions in modern physics.

N-body numerical simulations reveal that DM structures form hierarchically in a bottom-up scenario, with DM particles first collapsing into small gravitationally bound systems known as halos, and then forming more massive halos through a history of mergers. As a consequence, individual DM halos contain a very large number of smaller subhalos Madau et al. (2008).

At large scales, these simulations have been able to test with great success the predictions of the ΛCDM cosmological model. Nevertheless, when dealing with individual DM halos and their corresponding subhalos populations, such as our Galaxy, the situation is more uncertain, as the simulation resolution is limited and does not resolve the full range of possible subhalo masses. The subhalo mass function (SHMF) is found to be of the form $dN/dM \propto M^{-n}$ in the resolved mass range, where $n \in [1.9, 2.0]$, depending on the specific simulation Springel et al. (2008); Diemand et al. (2008). Together with the current resolution limit of MW-size simulations, this implies not only that the number of subhalos increases dramatically at lower masses, but also that the number of subhalos below the current resolution limit of Milky Way (MW) size simulations ($\sim 10^5$ M , while the MW halo is $\sim 10^{12}$ M ) is still very uncertain.

For DM candidates with weak-scale masses and interactions, subhalos with masses from $10^{-11} - 10^{-3}$ M (depending on the model) up to roughly $10^{10}$ M are expected to exist in a galaxy like our own Bertschinger (2006); Profumo et al. (2006); Bringmann (2009). Dwarf spheroidal satellite galaxies (dSphs), such as Draco, are an example of the most massive members of this population Walker (2013). Yet, these dSphs are exceptional objects, in that they are massive enough to retain baryons (i.e.,

gas) and form stars. Conversely, the vast majority of the Galactic DM subhalos are not expected to host baryons and therefore remain completely dark Gao et al. (2004). Given their much larger number density, many of these small subhalos will be much closer to the Earth than the bigger ones, making them potentially interesting for dark matter searches.

Should the *Weakly Interacting Massive Particle* (WIMP) DM model be correct (see, e.g., Roszkowski et al. (2018); Bertone (2010) for a review), these objects may be detectable in the gamma-ray data. WIMPs can achieve the correct relic DM abundance (the so-called "WIMP miracle") through self-annihilation in the early Universe. Self-annihilation of WIMPs gives rise to a Standard Model (SM) particle-antiparticle pair which, among other possible subsequent by-products, typically yields gamma-ray photons. The ongoing self-annihilation of WIMPs in subhalos could be bright enough to be detectable.

Since its launch in 2008, the Large Area Telescope on board the NASA *Fermi Gamma-ray Space Telescope* (*Fermi*-LAT) has been surveying the sky searching for gamma-ray sources Fermi-LAT Collaboration and Atwood (2009). The *Fermi*-LAT is a pair conversion telescope designed to observe the energy band from 20 MeV to greater than 300 GeV. Several point-source *Fermi*-LAT catalogs have been released and contain hundreds to thousands of gamma-ray objects, many of them previously unknown Fermi-LAT Collaboration (2015a, 2016a, 2017a). The various catalogs cover different energy ranges and exposure times, and each was constructed with the best available astrophysical diffuse emission model and instrumental response functions (IRFs).

Many groups have used *Fermi*-LAT data to constrain the WIMP DM parameter space: for example through observations of the diffuse extragalactic emission Ajello et al. (2015), galaxy clusters Fermi-LAT Collaboration (2015b), gamma-ray lines Weniger (2012); Fermi-LAT Collaboration (2013) and the previously mentioned dSphs (Fermi-LAT Collaboration; 2015c), or to claim possible detection of DM in the Galactic Center (GC) Fermi-LAT Collaboration (2016b, 2017b). These gamma-ray DM searches are complemented at larger WIMP masses by ground-based imaging atmospheric Cherenkov telescopes (IACTs) such as MAGIC, VERITAS and H.E.S.S. MAGIC Collaboration (2018); VERITAS Collaboration (2017); H.E.S.S. Collaboration (2016).

An important fraction of objects in the *Fermi*-LAT catalogs are unidentified sources (unIDs), i.e., objects with no clear single association or counterpart, to either a known object identified at other wavelengths, or to a known source type emitting only in gamma rays (such as certain pulsars).[1] There is the exciting possibility that some of these unIDs may actually be DM subhalos. In this work, we will search for DM subhalos in three of the most recent *Fermi*-LAT catalogs: namely the 3FGL Fermi-LAT Collaboration (2015a), 2FHL Fermi-LAT Collaboration (2016a) and 3FHL Fermi-LAT Collaboration (2017a). The number and fraction of the unIDs in each catalog is different; there are 1010 unIDs (33% if the full catalog) in the 3FGL, 48 (13%) in the 2FHL and 177 (11%) in the 3FHL. Both the 3FGL and 2FHL catalogs have been used in previous works Bertoni et al. (2015, 2016); Calore et al. (2017); Schoonenberg et al. (2016); Hooper and Witte (2017); Fermi-LAT Collaboration (2015c), while other works utilized previous catalogs Berlin and Hooper (2014); Zechlin et al. (2012); Zechlin and Horns (2012); Belikov et al. (2012); Buckley and Hooper (2010); Fermi-LAT Collaboration (2012b). Since we do not know the distance to these unIDs, for a signal, the

[1] Is important to note that in many cases there are actually multiple possible associations. In all of these catalogs if a source was not uniquely associated it was categorized as unID.

DM subhalo mass would be degenerate with distance, i.e., the same flux could be produced either by a massive, distant DM subhalo or by a less massive but closer one. This implies that very nearby, low-mass subhalos, may potentially be excellent DM targets.

However, as previously mentioned, there is currently no simulation able to resolve the entire Galactic subhalo population. Thus, when we search for such objects in *Fermi*-LAT data, one of the biggest challenges is to find a good and reliable characterization of the low-mass subhalo population that allows us to make realistic predictions of the expected annihilation fluxes. In our work, we will use a *repopulation* of the Via Lactea II (VL-II) N-body simulation with low-mass subhalos below the resolution limit. We will do so by taking into account what is found above this limit for the abundance and distribution of subhalos, and by adopting state-of-the-art models to describe their structural properties Moliné et al. (2017).

We first perform an exhaustive *filtering* of unID sources from the LAT catalogs, based on the expected DM subhalo properties, in order to find subhalo candidates. With this shortlist of potential DM subhalos, we set constraints on the DM annihilation cross section by comparing the number of observed subhalo candidates with predictions of N-body simulations.

With respect to previous efforts Hooper and Witte (2017); Bertoni et al. (2015, 2016); Schoonenberg et al. (2016); Berlin and Hooper (2014); Buckley and Hooper (2010); Fermi-LAT Collaboration (2012b); Zechlin et al. (2012); Belikov et al. (2012); Zechlin and Horns (2012); Calore et al. (2017), our work includes a new catalog (3FHL), an N-body simulation repopulation, a precise characterization of the instrument sensitivity to DM subhalos, and a more extensive filtering of candidates in the catalogs based on diverse criteria to reject all those unIDs not being compatible with DM.

The structure of this paper is as follows. In Section 3.2, we describe the expected gamma-ray flux from annihilations in DM subhalos, covering the details of the repopulation of the VL-II N-body simulation with the low-mass subhalos, and how the expected J-factor is computed for each subhalo. Section 3.3 describes the *Fermi*-LAT catalogs we considered, and discusses the criteria used to reject unIDs as being potential DM subhalos. The computation of the minimum detectable DM subhalo flux is described in Section 3.4. In Section 9.4, we place constraints on the DM parameter space by comparing the number of unIDs that survive our selection criteria with the number of expected subhalos as obtained from our repopulated N-body simulation. We further discuss the impact of each of the rejection criteria used on the DM limits, and present the sensitivity reach of the method. We conclude in Section 3.6.

## 3.2 Predictions of the gamma-ray annihilation flux from subhalos

Within the WIMP model, the expected gamma-ray flux can be expressed Evans et al. (2004); Bergström et al. (1998) as:

$$F\left(E > E_{th}\right) = J \cdot f_{pp}\left(E > E_{th}\right), \tag{3.1}$$

where $E_{th}$ is the threshold energy (set by the instrument), $J$ is the J-factor, which encloses all the astrophysical considerations, and $f_{pp}$ is the particle physics factor, which contains information on the underlying DM particle theoretical model (i.e., on the specific interaction properties of the DM particle considered).

The full expression for the J-factor is:

$$J = \frac{1}{D^2} \int_{\Delta\Omega} d\Omega \int_{l.o.s} \rho^2_{DM} \left[ r \left( \lambda \right) \right] d\lambda, \tag{3.2}$$

where $D$ is the distance to the target, the first integral is performed over the solid angle of observation ($\Omega$), the second one along the line of sight (l.o.s, $\lambda$), and $\rho_{DM}$ is the dark matter density profile of the object under consideration (in this paper that would be a single subhalo). Interestingly, subhalos are known to be more concentrated than field halos[2] of the same mass, e.g. Moliné et al. (2017). Further discussion on this and other considerations pertaining the DM density profile of subhalos will be given in Section 3.2.2.

The particle physics factor, assuming Majorana DM, is given by:

$$f_{pp} \left( E_{th} \right) = \frac{1}{4\pi} \frac{\langle \sigma v \rangle}{2 m^2_\chi} \sum_f B_f \int_{E_{th}}^{E} \frac{dN_f}{dE} dE, \tag{3.3}$$

where $E_{th}$ is the threshold energy, the upper limit is $E = m_\chi$, the subscript $f$ refers to the annihilation channel, $B_f$ is the branching ratio to that channel (we will take $B_f$ as one for each of the considered channels, so Eq. 3.3 will actually not be a sum), $dN_f/dE$ is the differential spectrum of gamma rays from the annihilation of a pair of DM particles via the channel $f$, $\langle \sigma v \rangle$ is the velocity-averaged annihilation cross section, and $m_\chi$ is the DM particle mass.

### 3.2.1 Annihilation spectra

In our work, we use the PPPC 4 DM ID tables to compute the DM annihilation spectra for different channels and DM masses Cirelli et al. (2011). These tables were constructed using the `PYTHIA 8` Sjöstrand et al. (2015) event generator to model the hadronization processes (including electroweak corrections) and obtain the $dN_f/dE$ spectra. The tables provide the annihilation spectra for DM masses ranging from 5 GeV up to 100 TeV.

We parametrize the DM annihilation spectra with a super-exponential cutoff power law, as done, for instance, by Ref. Calore et al. (2017):

$$\frac{dN_{DM}}{dE} \left( E \right) = K \left( \frac{E}{E_0} \right)^{-\Gamma} e^{-\left( \frac{E}{E_{cut}} \right)^\beta}, \tag{3.4}$$

where $K$ is a prefactor, $E_0 = 10^3$ MeV is the pivot energy, $\Gamma$ is the spectral photon index, $E_{cut}$ is the cutoff energy and $\beta$ is the curvature index. To obtain these parameters for each channel and DM mass, we fit the up to 179 available spectral points from the PPPC 4 DM tables. In each fit we leave the parameters $K, \Gamma, \beta$ and $E_{cut}$ free.

We perform this parametrization for each of the tabulated DM annihilation channels and masses. An example of DM tabulated spectrum and its corresponding parametric fit is shown in the upper panel of Figure 3.1. In Section 3.4 we will use these parametrizations to facilitate computing the sensitivity of the LAT to DM sub-halos. Although the parametrization is not perfect, it is accurate to a few percent.

To compute the annihilation flux as given by Eqs. 3.1 and 3.3, we integrate the DM annihilation spectrum above $E_{th}$:

[2] Those that do not reside inside any other larger halo. Typically an isolation criterion is also applied (i.e. not having a massive neighbor located within a given distance), in which case they are also known as isolated halos.

$$N_\gamma = \int_{E_{th}}^{E} \left( \frac{dN}{dE} \right) dE, \tag{3.5}$$

where $N_\gamma$ is the number of gamma-rays per annihilation produced in the relevant energy range and the upper limit of the integral is $E = m_{DM}$. Scanning over all the tabulated masses from 5 GeV up to 100 TeV, we obtain the value of this integral for each mass. These value can then be interpolated to find $N_\gamma$ for any given mass. An example of this interpolation, which will be useful when computing DM limits in Section 9.4, is plotted in the lower panel of Figure 3.1.

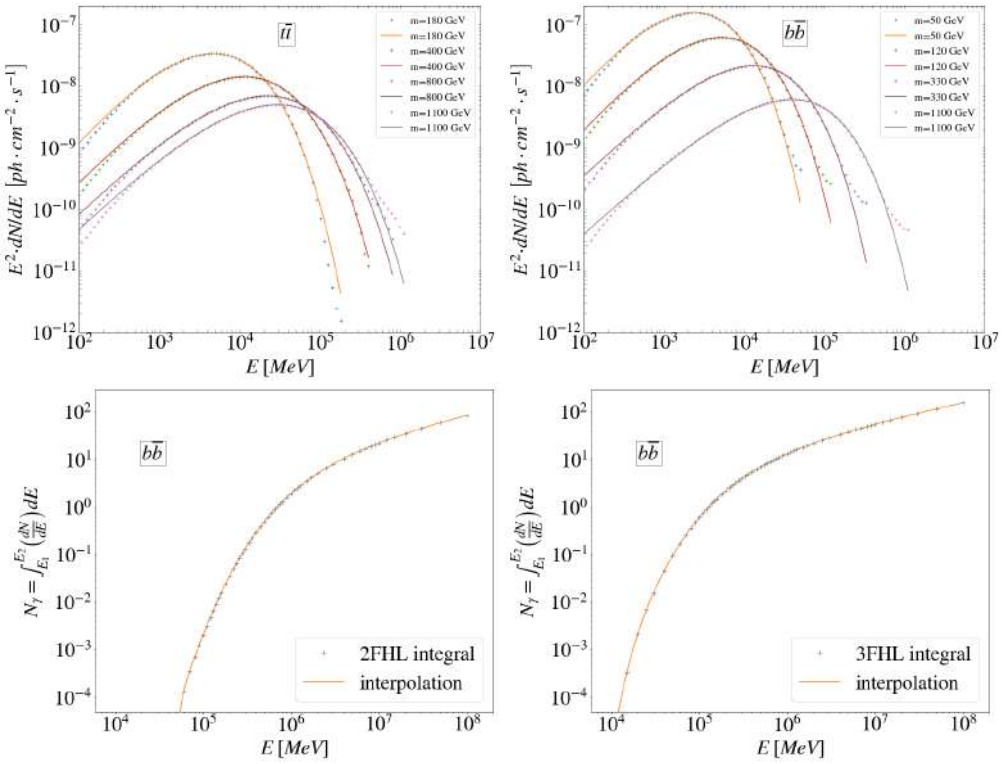


FIGURE 3.1: **Upper panel**: DM annihilation spectra with overlaid Eq. 3.4 parametric fit and interpolation for $t\bar{t}$ (left panel) and $b\bar{b}$ (right panel) for various DM masses. The points from Cirelli et al. (2011) are marked by crosses, while the fit is plotted as solid lines. Note that in the case of $t\bar{t}$ the plotted masses are larger because $m_t = 172$ GeV. **Lower panel**: Integrated DM annihilation spectra ($N_\gamma$) for 2FHL setup (left) and 3FHL (right), for $b\bar{b}$. Both setups differ in the threshold energy. Note that $N_\gamma = 0$ if $E < 50$ GeV ($E < 10$ GeV) in the case of the 2FHL (3FHL) setup, where $E = E_{th}$. Blue crosses are the values of the integral, and orange line is the interpolation between the values of the integral, which is used to compute the DM constraints as described in Section 9.4.

### 3.2.2 Subhalo J-factors

N-body cosmological simulations have become a powerful tool to study the formation and evolution of cold DM halos and their substructure. In particular, state-of-the-art N-body simulations of MW-size halos have provided the most valuable and accurate information on the properties of the present-day subhalo population Springel et al. (2008); Diemand et al. (2008); Stadel et al. (2009); Garrison-Kimmel

et al. (2014). Among these properties, the radial distribution within the MW halo, abundance, and internal subhalo structure are the most relevant ones when computing subhalo J-factors. In our work, we use publicly available results from the VL-II DM-only simulation at redshift zero to perform this task.[3] The VL-II simulation follows the formation and evolution of a MW-like halo in a WMAP3 ΛCDM universe down to present time with a superb particle resolution. Specifically, the VL-II simulation algorithm tracks more than one billion DM particles, each with a mass of $4.1 \times 10^3\ M_\odot$, to resolve the region within the virial radius of the simulated object, i.e., 402 kpc. More than fifty thousand subhalos are identified in the simulated VL-II volume, with masses from 10% of the parent halo mass down to $\sim 10^5\ M_\odot$. This means that VL-II is able to resolve the complex dynamics, merging and accretion histories of structures roughly spanning over 6-7 decades in mass.

Although this is an outstanding result, the masses of the lightest VL-II subhalos are far above the minimum halo mass that is predicted to exist in standard ΛCDM cosmology, e.g. of the order of $10^{-6} M_\odot$ if the DM is made of WIMPs Profumo et al. (2006). These *microhalos* are a natural expectation in the hierarchical structure formation scenario being at work in ΛCDM, and most of them, if not all, should survive to the present time given their early formation times and high DM concentrations, e.g. Diemand et al. (2005); Anderhalden and Diemand (2013); Ishiyama (2014). As previously discussed, in making our predictions of the J-factors of the Galactic subhalo population it is important to include subhalos below the VL-II mass resolution limit, as some of them could yield large annihilation fluxes at Earth if they are nearby. In fact, some of the lightest VL-II subhalos exhibited some of the highest J-factors of the entire subhalo population.

With this in mind, we *repopulate* the original VL-II simulation with subhalos well below its mass resolution limit. To do this we first characterize the SHMF in the mass range well resolved in VL-II data, which we find to be above $M_{cut} = 5 \times 10^6\ M_\odot$. This value corresponds to the mass at which a departure from the power-law behavior of the SHMF is observed, i.e., below $M_{cut}$ the simulation is not complete as it starts to miss subhalos due to lack of resolution. We obtain a power-law index of $n = 1.901 \pm 0.004$ for the SHMF above $M_{cut}$, which is slightly different than the result in Diemand et al. (2007), where a value of $n = 1.97 \pm 0.03$ was reported, but it is still fully with other simulations Springel et al. (2008); Garrison-Kimmel et al. (2017) as well as with theoretical (hardly unavoidable) expectations from the Press–Schechter theory of structure formation in ΛCDM Press and Schechter (1974); Giocoli et al. (2008); Blanchet and Lavalle (2012). As for the subhalo radial distribution, we find that the following parametrization:

$$n_{sub}(r) = \left(\frac{r}{R_0}\right)^a \exp\left(-b\,\frac{r - R_0}{R_0}\right), \tag{3.6}$$

with best-fit parameters $a = 0.94 \pm 0.15$, $b = 10.0 \pm 0.4$, $R_0 = 785 \pm 60$ kpc, provides a reasonably good fit for the number of subhalos as a function of distance to the host halo center, $r$, within its virial radius. We note that we used *all* subhalos in the original simulation in our fit. We also note that Eq. (3.6) does not correspond to any of the parametrizations traditionally used in the literature Pieri et al. (2011), which we found to provide poorer fits to the simulation data. **In particular, we note that the subhalo radial distribution given by Eq. (3.6) does not almost provide subhalos within the inner $\sim 15 - 20$ kpc of the Galaxy, as expected from subhalo disruption due to tidal interactions with the host.**

[3] http://www.ucolick.org/~diemand/vl/

We then include additional subhalos with masses below $M_{cut}$ in the population by assuming that their abundance obeys the power-law found for the SHMF above $M_{cut}$, as expected, and that they distribute following Eq. (3.6). After we draw subhalos from both our derived SHMF and radial distribution, we place the Sun at a different random position along its Galactic orbit (which we assume to be circular and with a radius of 8.5 kpc) and compute the subhalo J-factors. Finally, in order to derive statistically meaningful results, we repeat the whole exercise to produce 1000 realizations of the repopulated VL-II simulation. These realizations perfectly resemble the original VL-II data above $M_{cut}$ but now include subhalos down to $10^3$ $M_\odot$ as well. The latter number is found to be a good compromise between computing effort and relevance of low-mass subhalos for the purposes of this work, as we find that less massive subhalos are already not expected to be among the brightest ones.[4]

The last ingredient needed for the computation of the subhalo J-factors is the description of their structural properties, for which we follow Ref. Moliné et al. (2017). In that work, the inner subhalo structure is conveniently codified in terms of an alternative formulation of the so-called *concentration*[5], which does not depend on the assumed subhalo DM density profile as done previously. Using data from both the VL-II and ELVIS simulations, the authors of Ref. Moliné et al. (2017) find that, when compared to field halos of the same mass, subhalos are typically a factor 2-3 more concentrated. They also find an important dependence of subhalo concentrations on their galactocentric distance: the closer the subhalo to the host halo center the more concentrated it is. These effects are mainly driven by the impact of tidal stripping on the subhalo population. We use the parametrizations in Ref. Moliné et al. (2017) to assign concentration values to each subhalo in the repopulated VL-II 1000 realizations. As we will see later below, the higher concentration values found in Ref. Moliné et al. (2017) will have a critical and direct impact on the J-factor values, as the latter roughly scale as the third power of the concentration.

Our studies of VL-II subhalo abundance, radial distribution and structural properties, as well as our repopulation work with low-mass subhalos down to $10^3 M_\odot$, finally allows us to derive the J-factors associated to the Galactic subhalo population, which, expanding upon Eq. (8.2), we compute using the following expression Moliné et al. (2017):

$$J_T = \frac{1}{D^2} \frac{M_{sub}\, c_{sub}^3(M_{sub})}{[f(c_{sub}(M_{sub}))]^2} \frac{200\,\rho_{crit}}{9} \left(1 - \frac{1}{(1 + r_t(M_{sub}, D)/r_s(M_{sub}))^3}\right), \tag{3.7}$$

where $\rho_{crit}$ is the critical density of the Universe, $M_{sub}$ and $c_{sub}$ are, respectively, the mass and concentration of the subhalo, $r_t$ and $r_s$ refer to its tidal and scale radius, and $f(c) = \log(1+c) - c/(1+c)$. Note that the above equation refers to the integrated J-factor of subhalos within their scale radii.[6] Our J-factor results are summarized in Figure 3.2, which shows the J-factor of all subhalos in a random realization as a function of their distance to the Earth. The subhalo mass is also given by the color

[4] We also apply the Roche criterium Binney and Tremaine (2008) in our repopulated simulations in order to remove any subhalo that might have been included but should not have been. We find that, by doing so, we only remove, on average, an additional 1% of subhalos within 10 kpc, meaning that our proposed fit in Eq. (3.6) is, indeed, a good representation of the actual VL-II subhalo radial distribution.

[5] Formally defined as the ratio between the halo virial radius and its scale radius, i.e. the radius at which the logarithmic slope of the DM density profile is equal to -2.

[6] We note that this is a conservative estimate as it implicitly assumes that all subhalos are truncated at the scale radius due to tidal stripping, while this will only be the case for those in the host's innermost regions.

scale. As can be seen, a number of the lighter subhalos in the repopulation yield some of the largest J-factor values that we inferred for the whole subhalo population.

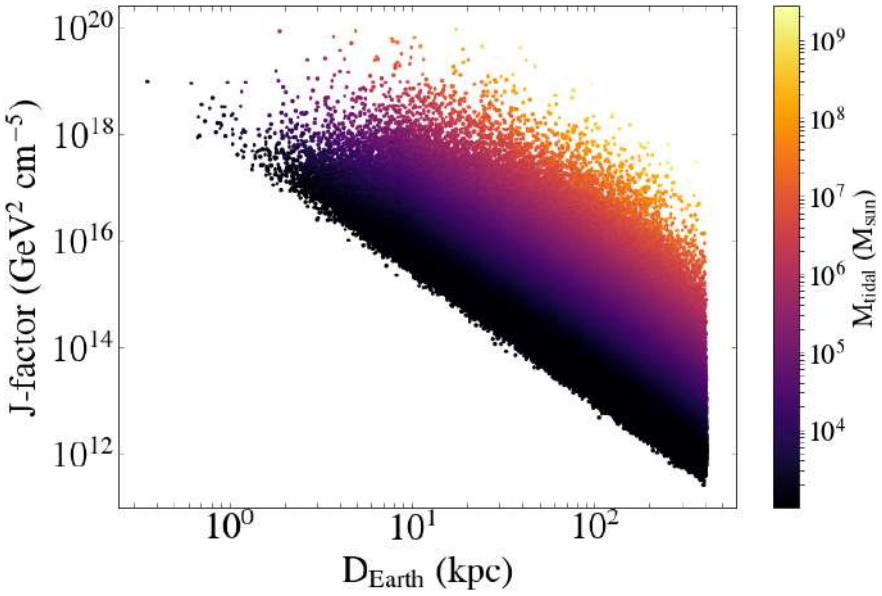


FIGURE 3.2: Subhalo J-factors as a function of distance to the Earth for all subhalos in a random realization of the repopulated VL-II. The repopulation includes low-mass subhalos down to $10^3 M_\odot$; see text for details. The color represents the subhalo mass in $M_\odot$.

With respect to previous work, e.g. Calore et al. (2017), the main difference is the significantly higher J-factors associated to low-mass subhalos in our analysis. We note that this is the first work on subhalo detectability where subhalos are assigned with "proper" subhalo concentrations that take into account both the fact that subhalos are more concentrated than field halos of the same mass, and the dependence of subhalo concentration with distance to host halo center. Also, we note that although Ref. Calore et al. (2017) used both a DM-only and a hydrodynamical simulation, their simulations did not include low-mass subhalos below $\sim 10^7$ M$_\odot$. However, the subhalo J-factor values presented in this section come with some important caveats. It is likely that the main limitation currently affecting every work on this topic is the knowledge of the actual abundance of low-mass subhalos in the innermost region of a galaxy like our own; different works provide very different answers about their survival probability, e.g. van den Bosch et al. (2017); Garrison-Kimmel et al. (2017). Closely related to this issue, the fraction of these small structures surviving from their formation until present time is not well known, due to the violent, non-linear processes that take place during their accretion and merging into larger halos, e.g. Berezinsky et al. (2006); Goerdt et al. (2007); Zhao et al. (2007). The unknown impact of baryons on the subhalo population adds additional uncertainty. In the future, we will repeat our analyses using MW-size hydrodynamical simulations. Baryons are not expected to play a critical effect on the structural properties of subhalos below $\sim 10^8 M_\odot$; yet they could alter the subhalo abundance significantly, e.g. Zhu et al. (2016); Garrison-Kimmel et al. (2017); Calore et al. (2017).

Other second order uncertainties in our study come from the assumed cosmology (VL-II simulation algorithm was run with WMAP3 cosmological parameters instead of Planck), and the non inclusion of subhalos below $10^3 M_\odot$ in the repopulation work (some of them could still yield relevant fluxes; see trend in Figure 3.2).

| Catalog | Year | Energy (GeV) | Observation time (yr) | Sources | UnIDs |
|---|---|---|---|---|---|
| 3FGL | 2015 | 0.1–300 | 4 | 3033 | 1010 |
| 2FHL | 2015 | 50–2000 | 6.7 | 360 | 48 |
| 3FHL | 2017 | 10–2000 | 7 | 1556 | 177 |

TABLE 3.1: Key properties of the *Fermi*-LAT catalogs used in this study.

Although we cannot address these caveats with our current repopulation analysis, our work reflects the best knowledge of the low-mass subhalo population and addresses the uncertainties due to cosmic variance. Numerical work is already ongoing to shed further light on some of the mentioned limitations and open issues pertaining the subhalo population, which will be presented in a future publication.

## 3.3 Search of DM subhalo candidates in *Fermi*-LAT source catalogs

A large number of the gamma-ray sources detected by *Fermi*-LAT lack firm association with known astrophysical objects such as pulsars or blazars Fermi-LAT Collaboration (2016a, 2017a, 2015a). Some of these unIDs can potentially be subhalos of DM whose annihilation produces gamma-rays.

With this in mind, we searched for potential DM subhalo candidates among the unIDs in three LAT catalogs: the 2FHL and 3FHL (second and third catalog of hard *Fermi*-LAT sources), containing sources detected above 10 and 50 GeV and observation time of 6.7 and 7 years, respectively, and the 3FGL (third *Fermi*-LAT source catalog), with a detection threshold of 100 MeV and 4 years of observation time. While the 3FGL is composed mainly of blazars and Galactic pulsars, the high-energy catalogs (2FHL, 3FHL) are composed of an even larger fraction of AGNs Fermi-LAT Collaboration (2016a, 2017a, 2015a). These catalogs contain large numbers of unIDs, 13% of the full catalog in the 2FHL, 11% in the 3FHL, and 33% in the 3FGL. We summarize in 3.1 the most important features of the three catalogs for this particular study.

Our first step will be to build up a list of potential subhalo candidates among the pool of unIDs in these catalogs. Importantly, the smaller the number of potential DM subhalo candidates is, the stronger the DM constraints will be. This will be discussed in further detail in Section 3.5.1. We define several rejection criteria based on the expected properties of DM subhalos versus sources of astrophysical origin, namely:

- Astrophysical association: unIDs already associated to conventional astrophysical sources in follow-up observational campaigns after the catalogs publication will be removed.
- Galactic latitude: a cut around the Galactic plane to decrease contamination due to Galactic sources will be applied.
- Variability: DM subhalos are expected to be steady, so any variable source will be removed.
- Machine learning: we will use information from source classification algorithms to reject unIDs.

- Multiwavelength emission: DM subhalos are expected to emit only in gamma rays; thus unIDs exhibiting emissions at other wavelengths will be removed.
- Complex regions: those unIDs lying on regions of mismodeled diffuse emission, considered as potential artifacts, will be dropped as well.

These criteria and their effect on the number of subhalo candidates are summarized in the flow chart shown in Figure 3.3. Unless specified, the number of rejected unIDs in step $n$ is over the clean list, i.e., taking into account all the cuts in the $n-1$ previous steps. Note also that there is no filter in the list above that explicitly uses either spectral or spatial information of the sources, that is, we did not perform a dedicated *Fermi*-LAT spectral and spatial analysis of the unIDs. That work is ongoing and will be presented in a future publication.

In the following, we describe each rejection criterion in further detail:

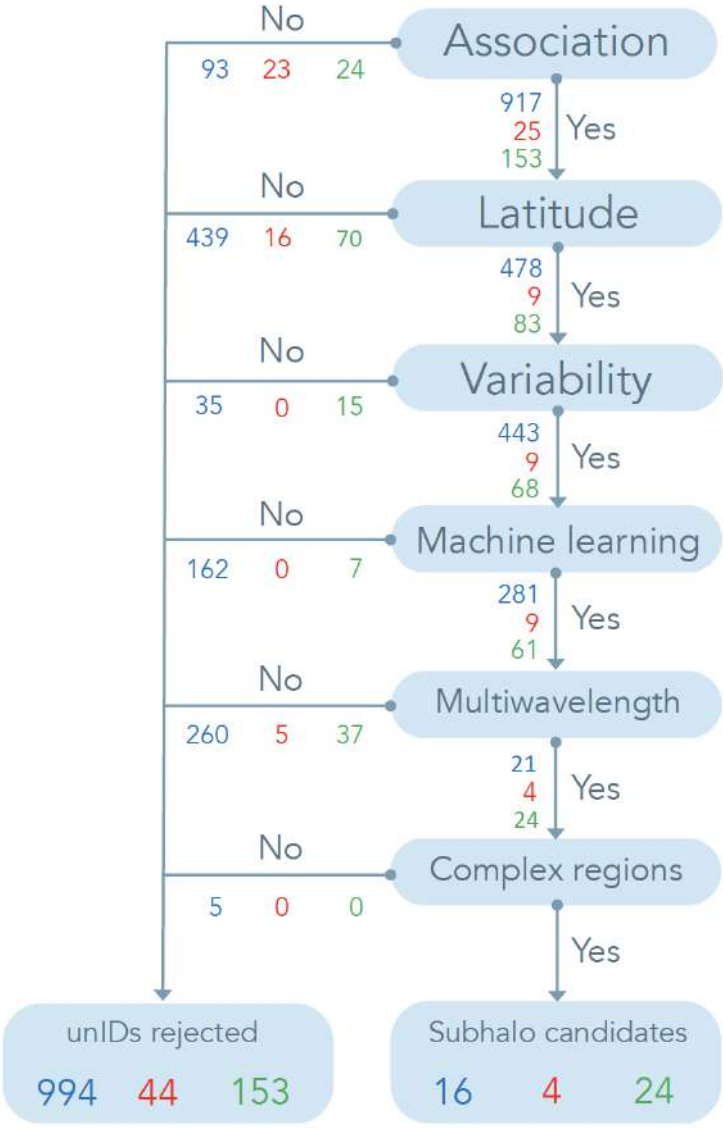


FIGURE 3.3: Flowchart of the rejection criteria. Blue, red and green correspond to numbers in the 3FGL, 2FHL and 3FHL catalogs, respectively. The "yes" flow lists the unIDs that pass a certain filter, while the "no" flow indicates sources that do not, for each criteria. See text for details.

1. **Association**: Many of the unID sources from early catalogs have subsequently received high probability associations, in part because of targeted observation campaigns Saz-Parkinson (2017); Laffon et al. (2015); Smith et al. (2017). This is the case for the 2FHL and 3FHL catalogs, where 22 unIDs of the former appeared later as associated in the latter and therefore are rejected from our sample. One additional source is flagged as unknown rather than as associated; it exhibits emission in X-rays and therefore is discarded as well (see step 4).
   When comparing 3FGL and 3FHL unIDs, although the latter was published almost 2 years later than the former, 7 of the 3FHL unIDs have firm association in the 3FGL and are also removed from our list.
   Seven additional 3FGL sources are associated with blazars in Crespo et al. (2016), although they are all at low latitude (see second criterium below); 31 more in Peña-Herazo et al. (2017), associated with blazars, quasars and galaxies, 10 more blazars in Paiano et al. (2017), and 18 more miscellaneous AGNs collected in Massaro et al. (2016) are rejected. Also, 13 more 3FGL-only sources are removed with a blind search of Einstein@Home Clark et al. (2017) as they are associated to low-latitude pulsars. Within the same project, one more source, a radio-quiet pulsar, is rejected Fermi-LAT Collaboration (2018). Additionally, 5 high latitude sources are removed from the 3FGL candidate sample; one is associated in the 3FHL, and the other four are pulsar associations, and present multiwavelength emission (see criterium number 5): 3FGL J1544.6−1125 Bogdanov and Halpern (2015), 3FGL J2039.6−5618 Salvetti et al. (2015); Romani (2015), 3FGL J1946.4−5403 and 3FGL J1744.1−7619 Camilo et al. (2015).
   We are also able to discard 13 3FGL sources for being recently discovered millisecond pulsars (MSPs) [7]. One of these sources, 3FGL J1016.6−4244, is also present in the 3FHL catalog.
   Recent improvements, including updated positional error ellipses based on 8 years of LAT data and/or a broader energy range compared to the initial catalogs, along with an updated association procedure developed in the context of the future 4FGL catalog, have revealed counterparts to a number of sources initially unidentified in the 3FGL, 2FHL and 3FHL catalogs Fermi-LAT Collaboration (2020). This improvement is especially relevant in the case of the 3FGL catalog, as the new data has almost the double of exposure time and makes use of Pass 8 events. There are two sources which have also been discarded for this reason. Also, there are three 3FGL sources, three 3FHL and four remaining 2FHL sources with no counterpart in the 8-year LAT data, which are likely to be flaring objects or artifacts. Yet, they are conservatively not discarded from our list. Further observations will be needed in order to determine their true nature.

   As a final remark, we note that there exists the possibility of a misassociation. This rate of false positives is expected to be under 5% according to the Bayesian analysis in the considered catalogs, although this number can be significantly smaller, e.g. a 1% in the 3FHL Fermi-LAT Collaboration (2017a).

2. **Latitude**: Galactic astrophysical sources present in *Fermi*-LAT catalogs, such as pulsars, pulsar wind nebulae or supernova remnants, are observed to be strongly concentrated along the Galactic plane. Since many objects of this class

[7] http://astro.phys.wvu.edu/GalacticMSPs/

are expected to also be hidden among the pool of unIDs awaiting higher confidence classification, we expect the distribution of unIDs to peak around zero Galactic latitudes as well. Indeed, this can clearly seen in Figure 3.4, where the latitude histograms for the all the unIDs in the catalogs are shown.

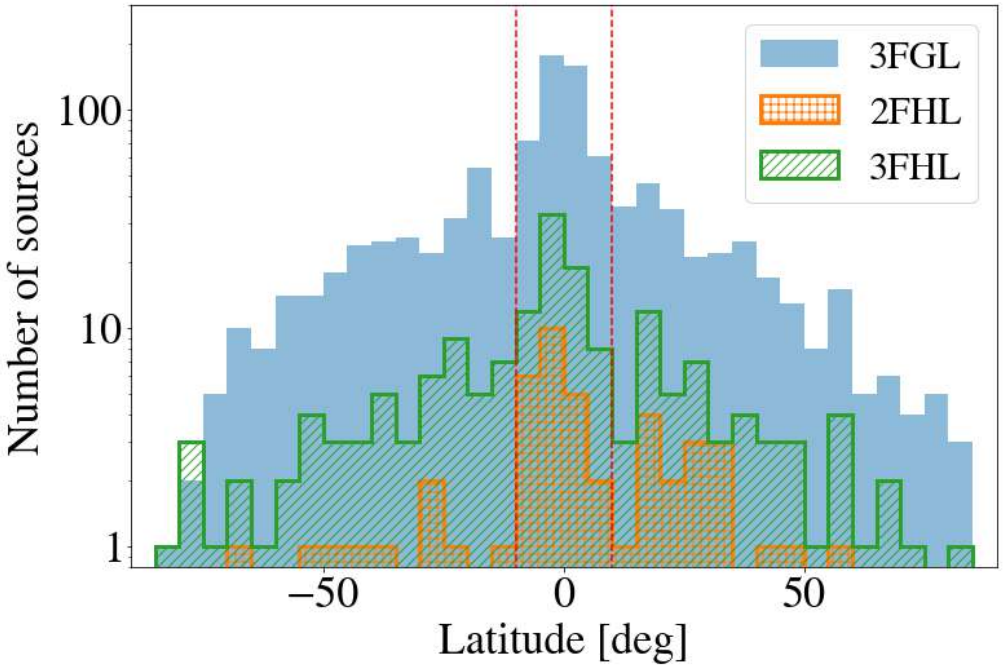


FIGURE 3.4: Galactic latitude distribution of unIDs in the 2FHL, 3FHL, and 3FGL catalogs. Those sources between the red dashed lines are excluded from our analysis ($|b| \leq 10^{\circ}$).

For our purposes, these low-latitude sources (especially pulsars, which can fake DM annihilation spectra at low energies Fermi-LAT Collaboration (2012b)) are not interesting and only add contamination to our sample of potential DM subhalo candidates. Furthermore, from N-body simulations we expect the subhalos to be isotropically distributed over the sky; thus we apply a cut at Galactic latitudes $|b| \leq 10^{\circ}$. [8]
After having applied this latitude cut to the catalogs, 16 2FHL, 70 3FHL and 439 3FGL sources are removed from our list. More of the 3FGL sources are rejected by the Galactic latitude cut because that catalog has a lower energy threshold and thus contains a large fraction of Galactic (though unidentified) sources. Conversely, the harder sources found in both the 2FHL and 3FHL catalogs, are mostly AGNs.

3. **Variability**: DM annihilation in subhalos is expected to be steady, i.e., to not display flux variability over time. We will use two different methodologies to identify and eliminate variable sources: the variability reported in the catalogs and our own studies performed with the the Fermi All-sky Variability Analysis (FAVA) Fermi-LAT Collaboration (2017c) tool. Regarding the first one, in order to be conservative, we only remove sources marked as variable at 99% C.L. in the catalogs. Specifically, the variability statistics in the catalogs are $\chi^2$-distributed reported, with different degrees of freedom depending on the

[8] The same cut is also be applied on the N-body simulation data. Assuming an isotropic distribution of subhalos, the cut removes, on average, 11% of the simulated subhalos.

catalog. For each catalog we cut on the variability statistics at a value corresponding to 99% C.L. This removes 2 unIDs from the 3FHL sample (note that one of these is marked as not variable in the 3FHL but as variable in the 3FGL), 16 in the 3FGL (note that there are 9 more variable sources, but already rejected by latitude) and none in the 2FHL.
These flux variations are computed taking into account the Galactic diffuse emission model Fermi-LAT Collaboration (2012a). Yet, ideally, we would be interested in systematic deviations around the mean flux of the source, without relying on any background model to model the region around the sources.
As previously mentioned, our second methodology is based upon FAVA. By default, FAVA scans the sky in a weekly time lapse searching for deviations from the median detected flux in each direction, presenting lightcurves refered to the collection of pixels within the corresponding PSF centered on the source position. It performs this analysis in a low-energy band (100-800 MeV) and a high-energy band (800 MeV-10 GeV), where there is still enough photon statistics to perform a proper variability analysis.
In order for us to reject an unID due to variability, and with the intention to be conservative, we require the presence of a flare at $5\sigma$ significance in the data, searching for flares at the reported unIDs sky positions.

Note that in some cases the mean of the difference between the flux and average flux may be null, yet an hypothetical flare lasting a tiny fraction of the whole dataset would reject automatically a DM subhalo origin. When performing variability studies with FAVA a flaring source can induce fake variability in its surrounding sources/regions. This is so because of the spill-over of photons coming from the point spread function (PSF) of the LAT (highly energy-dependent and of the order of $2^\circ$ at few hundred MeV)[9]. Therefore, should we find a variable unID with FAVA, an inspection of the significance map of the region around the unID is necessary in order to conclude that the variability is real and not induced by spill-over from a nearby, flaring source. An example of this effect can be seen in figures 3.5 and 3.6. Having checked that the variability is not induced and, thus, that the source presents a flare over $5\sigma$ significance (see Figure 3.7), the source is rejected.
The weekly time binning used by FAVA, in comparison to the catalog monthly binning, proves to be very useful when dealing with short flaring episodes, and allow us to search in narrower time bins than those in the catalogs, and to detect very short flares which would get diluted on longer time scales. Our study can also find additional variable sources with respect to the catalogs as we extend beyond the observation times of the catalogs, using all available data up to March 1st, 2018 (MET 541555205).
In summary, the FAVA analysis allows us to discard 13 3FHL sources and 11 3FGL sources, with no source overlap between catalogs.
Interestingly, we also found two source coincidences or *duplicities*, i.e., sources very near to each other and present in different catalogs which, apparently, are not related but nevertheless possess highly correlated lightcurves and similar spectra, and therefore seem to be actually the same source. These are the pairs (2FHL J0738.6+1741, 3FGL J0738.1+1741) and (2FHL J1630.0+7644, 3FGL J1628.2+7703).

[9] http://www.slac.stanford.edu/exp/glast/groups/canda/lat_Performance.htm

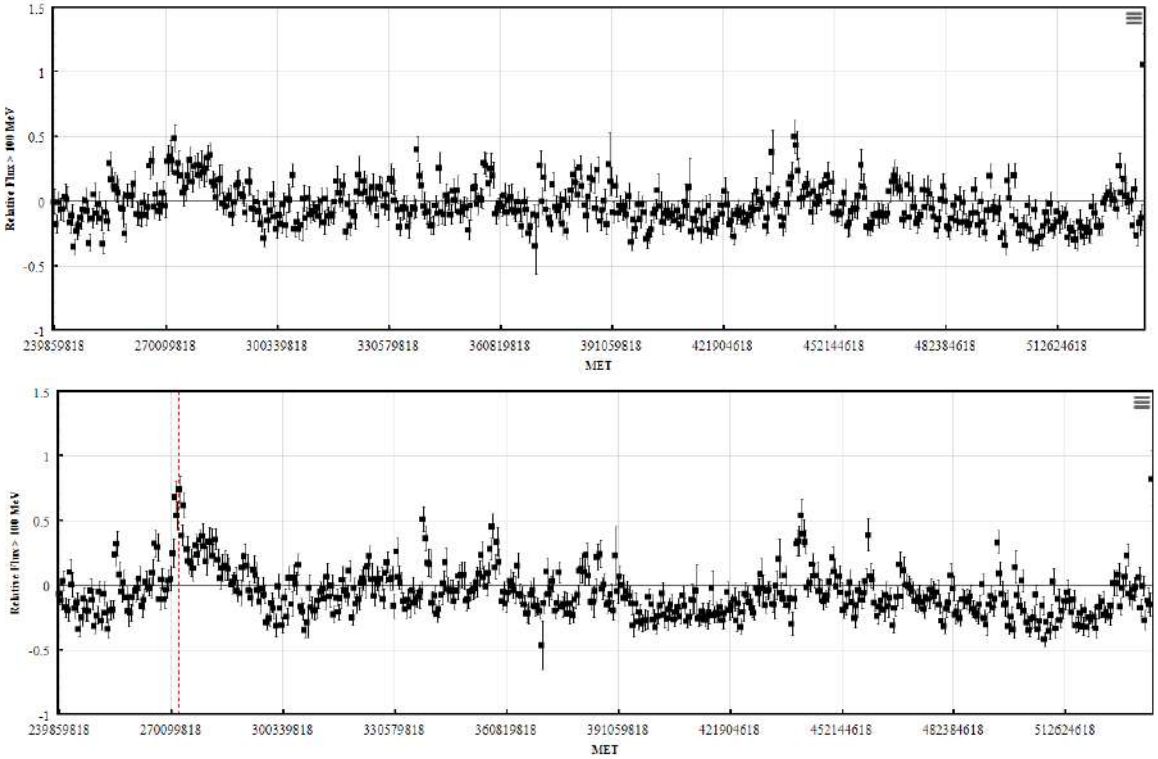


FIGURE 3.5: Example of "fake" variability induced by the spill over of photons due to the PSF. **Top panel**: FAVA lightcurve of 3FGL J2043.8-4801. **Low panel**: FAVA lightcurve of 3FGL J2056.2-4714 (associated with a flat-spectrum radio quasar) flare in week 55 (mission elapsed time (MET) 272519018), indicated by the dashed red line. Note the tight correlation between the variations in both curves. These two sources are 2.3° from each other in the sky.

4. **Machine-learning algorithms**: these have been used to classify unIDs into different types of sources. Typically, the machine learning algorithm is trained with the associated sources and then is run over the unidentified sample, assigning each of the unIDs a probability to be a particular type of source. We use the results from Salvetti et al. (2017); Lefaucheur and Pita (2017), both of them trained and run over the 3FGL. Since this is the catalog with the largest number of sources we expect the most accurate results, because the training sample is the largest. In both works, the algorithms use time-series and spectral information to search for AGN candidates, so the classification is made and optimized for this type of sources. Many of the sources classified as AGNs are common to both of the mentioned works. Note a source being in just one of them is discarded, i.e., we do not require an "and" criterium, but an "or". We reject a total of 162 3FGL sources with this method, which are not discarded by previous filters (the total number is 559 for Salvetti et al. (2017) and 595 for Lefaucheur and Pita (2017)). Also, by cross-checking the results of these works for the 3FGL with the 2FHL and 3FHL catalogs, 7 3FHL sources are discarded. The expected false positive ratio is estimated to be of order 4% in both works. As we use 162 sources for the 3FGL catalog, a 4% are approximately 6 false positives. We will be taking into account this uncertainty when setting the DM constraints in Section 9.4. Further information about the propagation of this uncertainty can be found in 3.7.1.

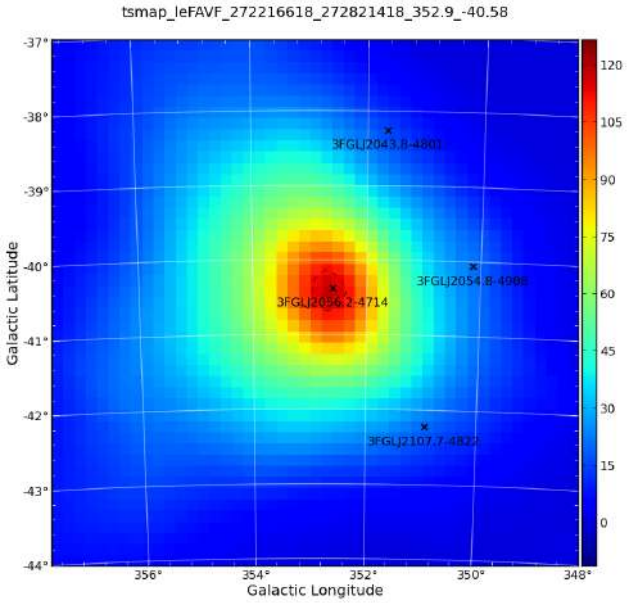


FIGURE 3.6: TS map of 3FGL J2056.2−4714. This object shows a flare in week 55 (MET 272519018). There is still a relatively high significance ($TS = 17$) at the position of 3FGL 2043.8−4801, which lies only 2.3° away from the flaring source. Thus, we can conclude that the flare of 3FGL J2056.2−4714 is causing the variability observed for 3FGL 2043.8−4801 (the timing coincides as well, see Figure 3.5)

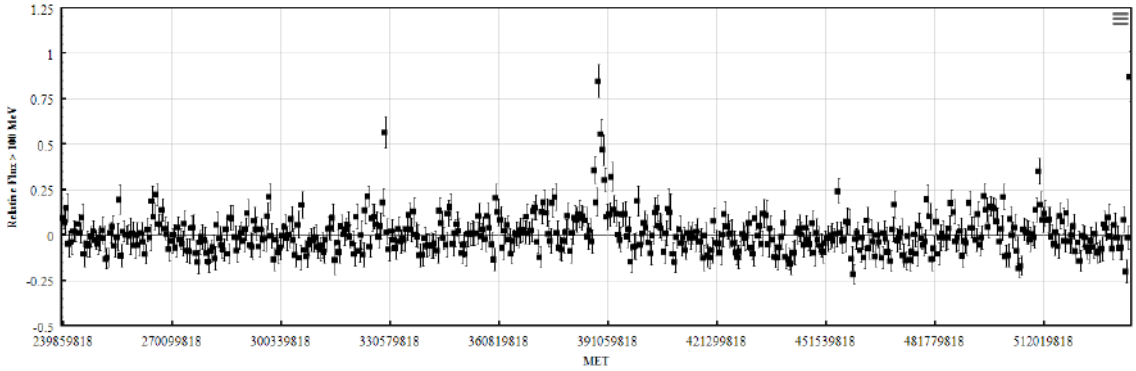


FIGURE 3.7: FAVA lightcurve of 3FHL J0500.6+1903. No other source flare is temporally and spatially coincident with the flare centered on week 247 (MET 388640618), and therefore this object is rejected as DM subhalo due to its intrinsic variability.

Another machine learning work Mirabal et al. (2016) used a similar algorithm but for pulsars instead of AGNs. In this case, it is not possible to discard the obtained pulsar candidates, as they have a spectrum compatible with DM annihilation. Yet, for this same reason, they actually are interesting sources for our purposes. From their 34 reported pulsar candidates, we are left with only 3 sources in the 3FGL which have not been rejected by any other of our selection criteria (3FGL J0336.1+7500, 3FGL J0953.7−1510 and 3FGL J1225.9+2953). These sources may be especially interesting for future observational follow-up campaigns.

5. **Multi-wavelength emission**: If the gamma-ray emission of the unIDs is indeed produced by DM annihilation, we do not expect to see these objects emitting in other wavelengths. Therefore, the observation of any of these sources in IR, Optical, UV or X-ray would represent another reason for rejection. Note that subhalos with masses larger than $\gtrsim 10^7$ M$_\odot$ are expected to have baryonic content and consequently they could emit and be observed at other wavelengths (see Section 3.2.2 and Section 3.5.1). As said, in this work we will focus on the search for less massive DM subhalos with no visible astrophysical counterparts.
   We follow three different approaches when looking for multiwavelength (MWL) emission. First of all, we manually search for additional emission in the ASDC repository[10]. To reject a source, we require i) that any additional emission to be within a 5 arcmin radius of the catalog source position for the 2FHL and 3FHL sources[11] and ii) no other known source is present in this region. In the case of 3FGL sources, we search within their corresponding 95% confidence level positional error ellipses. We are able to discard 4 2FHL, 12 3FHL and 7 3FGL sources. For these, there are observations in the search area by WISE Wright et al. (2010), 2MASS Skrutskie et al. (2006), USNO Monet et al. (2003), SDSS SDSS Collaboration (2018) and NVSS Condon et al. (1998).
   When considering the 3FGL sources, we also made use of the observational campaign performed by authors in Ref. Stroh and Falcone (2013) using the *Swift* X-ray telescope[12]. In this case, we reject 3FGL sources that have been detected at least once by *Swift*. This removes 16 additional sources, 2 of which are also in the 3FHL catalog.
   We also search for associated *Fermi*-LAT sources in the *Swift* Master Catalog on HEASARC[13]. The search is extended to other X-ray telescopes as well, such as Chandra, Hitomi, NICER, NuSTAR, ROSAT, RXTE, Suzaku and XMM-Newton. By using this tool, we remove 207 3FGL, 1 2FHL and 30 3FHL sources. 25 out of these 30 are common to the 3FGL.

6. **Complex regions**: As reported in the 3FGL and previous low-energy threshold catalogs (such as 2FGL), sources with moderate Test Statistics (TS) are labeled with a "c" in case they lie in complex regions with a poor modeling of the diffuse emission, thus having significantly higher probability of being artifacts (see § 3.8 in Fermi-LAT Collaboration (2015a)). These sources are mostly concentrated along the Galactic plane, and very close to the Galactic center, although some of them are also at higher latitude. We remove them from our list of potential subhalo candidates as they are probably star-forming regions or just mere artifacts, as described by Fermi-LAT Collaboration (2015a). From our remaining candidate list, this filter removes 5 additional sources in the 3FGL catalog, none of which are present in the other catalogs. The fraction of the sky affected is by this cut is negligible, so we do not attempt to mask these regions when analyzing the N-body simulation data, or to correct the subhalo sensitivity predictions for this cut.

After the above filtering procedure, we are left with 4 2FHL (8% of the original unIDs sample), 24 3FHL (14%) and 16 3FGL (2%) candidates. We note that

[10] https://tools.asdc.asi.it/

[11] The typical LAT PSF at these high energies is below 0.1°, i.e., 6 arcmin. Therefore, we can conservatively exclude a source showing any kind of emission within this area.

[12] The results of this survey can be retrieved at www.swift.psu.edu/unassociated/

[13] https://heasarc.gsfc.nasa.gov

| Filter | Efficiency | Treatment |
|---|---|---|
| Association | >95% | Neglected |
| Latitude | ∼89% | Applied to N-body simulations |
| Variability | 99.9999% | Neglected |
| Machine learning | >96% | Used to correct number of observed candidates |
| Complex regions | >99% | Neglected |

TABLE 3.2: Estimated efficiency for each of the applied filters in Section 3.3. The third column refers to the treatment adopted in each case for the remaining unIDs "beyond" the efficiency of our cuts. Note that we omit the multi-wavelength emission filter in this table given the difficulty to provide a realistic estimate as of today: among other ingredients, one would need to compute the expected source number density of each of the considered catalogs at other wavelengths, which is beyond the scope of this work.

no source flagged as extended in the catalogs survived our cuts. In particular, the source 3FGL J2212.5+0703, which is marked as possible DM subhalo by Bertoni et al. (2016), is rejected by its multiwavelength emission, and 3FGL J1924.8-1034, which is also marked as a possible extended DM subhalo by Xia et al. (2017), is classified as an AGN by the machine-learning algorithms.

Table 3.2 summarizes the expected efficiency, defined as the fraction of each filtering effect which is univocally applied (i.e., with no possibility of a false positive), and how we dealt in each case with the fact of not having 100% efficiency.

## 3.4 *Fermi*-LAT sensitivity to DM subhalos

Most of previous works Bertoni et al. (2015, 2016); Schoonenberg et al. (2016); Berlin and Hooper (2014); Buckley and Hooper (2010); Zechlin et al. (2012) assumed that the sensitivity of the LAT to DM subhalos is the same across the sky and equal to the detection threshold of the catalog under consideration. Yet, the reality is that the minimum flux required to have a $\sim 5\sigma$ (where $\sigma$ is the significance expressed in standard deviations) detection with the LAT, $F_{min}$, depends on the source spectrum and position in the sky. In fact, the threshold for detection is strictly performed in terms of another parameter, i.e., the Test Statistic:

$$TS = -2 \cdot \log \left[ \frac{\mathcal{L}(H_1)}{\mathcal{L}(H_0)} \right], \tag{3.8}$$

where $\mathcal{L}(H_0)$ and $\mathcal{L}(H_1)$ are the likelihood under the null (no source) and alternative (existing source) hypotheses, respectively. We note that $TS \sim \sigma^2$, and each of the catalogs we used applied a TS $\geq 25$ threshold. Thus, when it comes to DM subhalo detection, $F_{min}$ will depend on the adopted annihilation channel and WIMP mass, as well as on the position of the object in the sky. Indeed, this $F_{min}$ could significantly differ from the characteristic detection threshold of the catalog, which is typically computed assuming a power-law spectrum of spectral index $\Gamma = 2$ ($dN/dE \propto E^{-\Gamma}$), a fairly typical spectrum for conventional astrophysical emitters. This is not the case for DM annihilation spectra, as seen in Section 3.2.1, where curvature and a cut-off are present.

Also, there is a strong dependence on the latitude of the considered source due to the variations of the diffuse emission: at high Galactic latitudes, the Galactic diffuse

emission is much lower when compared to regions along the Galactic plane. Thus, a low-latitude source needs a comparatively larger flux in order to reach the TS $\geq$ 25 detection threshold.

To compute the dependence of the minimum detection flux, we use *Fermipy*[14] v0.17.0 Wood et al. (2017), a `PYTHON`-based code to analyze *Fermi*-LAT data. We begin by generating all-sky sensitivity maps for each annihilation channel and DM mass. This must be done for each catalog, as they cover different energy ranges. The sensitivity at each (l,b) Galactic coordinate is obtained by placing a putative (point-like) DM subhalo there and computing the integrated flux needed to reach TS = 25.

The input to the sensitivity maps generation procedure consists of the spectral parameters of the DM subhalo annihilation emission (implicitly set by annihilation channel and particle mass, which are obtained with the parametrization of Section 3.2.1), a threshold for the test statistics (set to 25), a minimum number of photon counts (set to 3), diffuse and isotropic templates (catalog dependent), energy range (depending on the catalog), spatial extension (set to point-like) and type of Healpix Górski et al. (2005) pixelisation (NESTED ordering, NSIDE=64). The Galactic diffuse emission templates are `gll_iem_v06.fits` (2FHL, 3FHL) and `gll_iem_v05_rev1.fit` (3FGL), while the isotropic templates are `iso_P8R2_SOURCE_V6_v06.txt` (2FHL, 3FHL) and `iso_source_v05.txt` (3FGL). The output is an all-sky map for each annihilation channel, particle mass and source catalog. As an example, the minimum detection flux ($F_{min}$) for the $\tau^+\tau^-$ channel and two different DM masses is plotted in Figure 3.8 for the 3FGL catalog.

At this point we remove the 10° above and below the Galactic plane, following our latitude cut described in Section 3.3, and take the mean and standard deviation of the $F_{min}$ values over the remaining sky.

We note that the differences in $F_{min}$ between the North and South hemispheres is found to be always under 1%. This whole procedure allows us to characterize in detail the $F_{min}$ function for each catalog, channel and mass, which will be later used to place the constraints in Section 9.4.

Some examples of the mean and standard deviation of $F_{min}$ and its dependencies are plotted in Figure 3.9. As it can be seen, for the $\tau^+\tau^-$ channel, the behavior of $F_{min}$ is significantly different depending on the adopted catalog. For example, for 3FGL and at a fixed latitude, $F_{min}$ decreases rapidly as the mass increases, reaching a minimum and then remaining almost constant at the largest DM masses. For 3FHL, $F_{min}$ slightly worsen (i.e. larger flux values) as the mass increases to slowly decrease at larger masses. The maximum variation in this case is approximately a factor 2, while in the case of the 3FGL setup it is roughly an order of magnitude. In all cases, the associated uncertainties become smaller at higher latitudes. This is expected because of the morphology of the Galactic diffuse emission (see also Figure 3.8).

A comparison between the size of the uncertainties associated to both the J-factor and $F_{min}$ is described in 3.7.1.

## 3.5 DM Constraints

After the unIDs filtering performed in Section 3.3, we are left with a certain number of DM subhalo candidates in each *Fermi*-LAT point-source catalog. In the absence of a conclusive answer about the nature of these remaining unIDs,[15] we will place

[14] `http://fermipy.readthedocs.io/en/latest/`

[15] A careful spectral and spatial scrutiny is ongoing for these sources, which will be presented in further work.

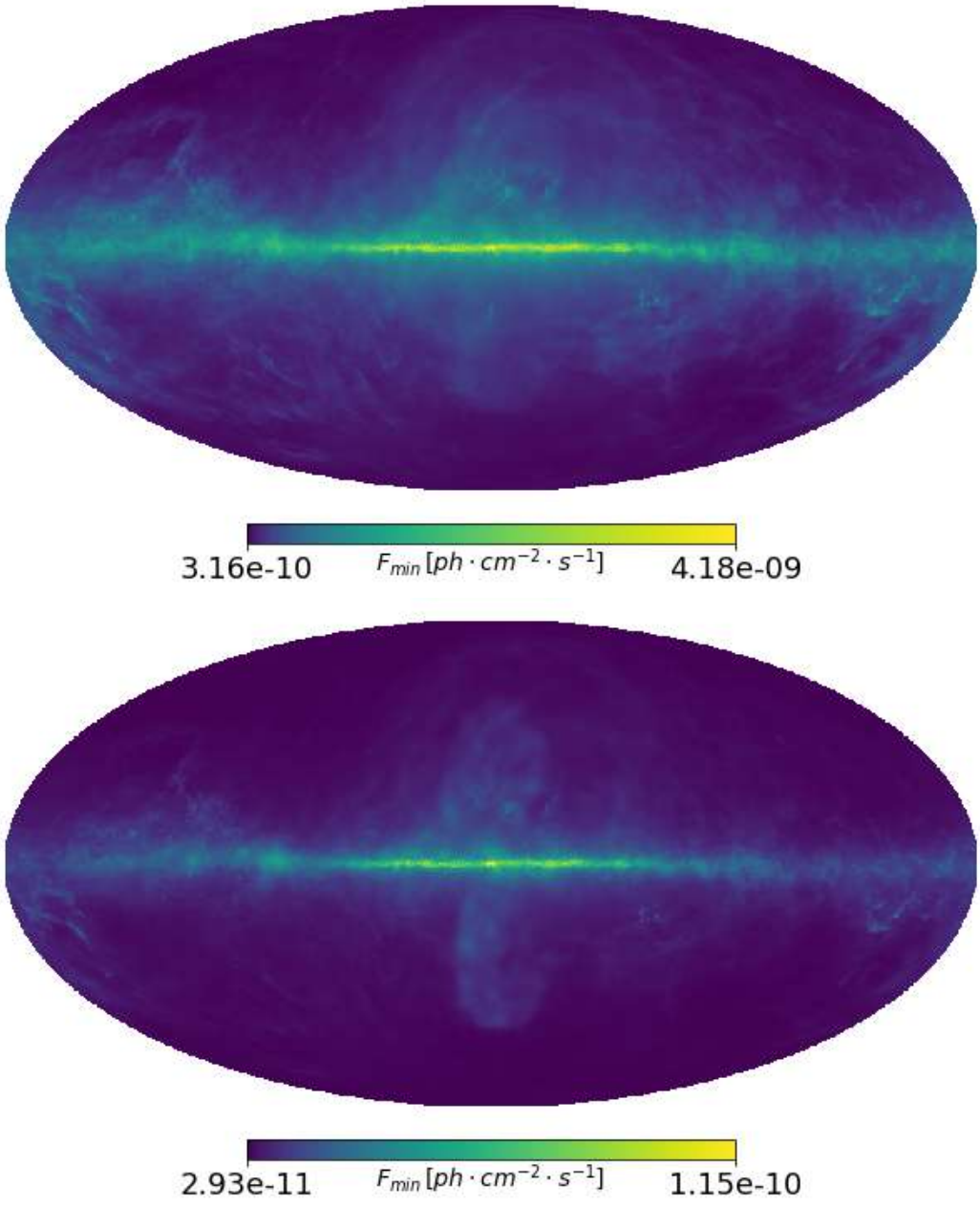


FIGURE 3.8: LAT sensitivity to DM subhalos for $\tau^+\tau^-$ annihilation and the 3FGL setup, for $m_\chi = 10$ GeV (top) and $m_\chi = 1$ TeV (bottom).

constraints on the WIMP annihilation cross section. To do so, we make use of Eqs. 3.1–3.3, to set a relation between $\langle\sigma v\rangle$ and $m_\chi$,

$$\langle\sigma v\rangle = \frac{8\pi \cdot m_\chi^2 \cdot F_{min}}{J \cdot N_\gamma}, \tag{3.9}$$

where $F_{min}$ is the minimum detection flux (see Section 3.4), $J$ the J-factor (see Section 3.2.2) and $N_\gamma$ the integrated DM spectra (see Eq. 3.5). Note that $\langle\sigma v\rangle$ is proportional to the DM particle mass squared, thus the constraints will be weaker for larger masses if $F_{min}$ was constant, yet $F_{min}$ exhibits a dependence on the energy, so at the end the exact shape of the constraints will depend on a combination of these parameters.

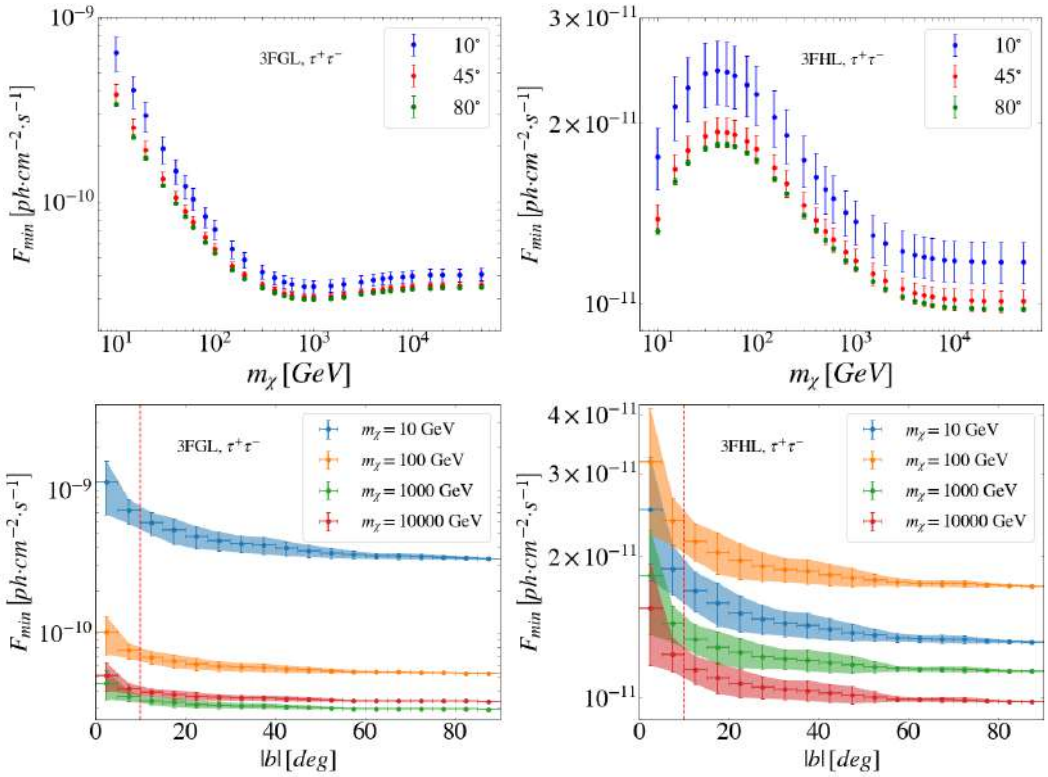


FIGURE 3.9: LAT sensitivity to DM subhalos annihilating to $\tau^+\tau^-$ as a function of DM mass for various absolute Galactic latitudes (top panels) and as a function of absolute Galactic latitude for various DM masses (bottom panels). Left and right panels refer, respectively, to the 3FGL and 3FHL setups. A vertical red dashed line is plotted in the bottom panels to mark our latitude cut, $|b| < 10°$.

### 3.5.1 Procedure to set DM limits

Our procedure to set limits is based on a comparison of the number of surviving candidates with the predictions from our N-body simulation work (see Section 3.2.2). More precisely, we allow for the possibility that the DM subhalo candidates we identified in *Fermi*-LAT catalogs are actually subhalos, and that they correspond to our brightest subhalos in the simulations.[16] To do this, we sort the simulated subhalos by J-factor, and confront this list with the remaining unIDs number. For example, in the case of 3FGL, where we are left with 16 subhalo candidates, we take the 16th largest J-factor subhalo in each realization of the simulation as the subhalo J-factor to be used in Eq. 8.3.

More precisely, as we are interested in obtaining the limits at 95% confidence level (C.L.), what we actually do for the generic case of having $n$ remaining candidates, is to draw the distribution of J-factors corresponding to the $n^{th}$ brightest subhalo across all the N-body realizations, and pick the J-factor value above which 95% of this distribution is contained. To be consistent with our filtering procedure of Section 3.3, this J-factor distribution is obtained with a cut at $|b| \leq 10°$ (to match the latitude filter) and $M \geq 10^7 M_\odot$ (to ensure that we only consider dark subhalos).

[16] We only refer here to subhalos with no baryonic components and thus completely "dark". In our work, we will adopt an upper mass limit of $M < 10^7 M_\odot$ for these objects. Above this limit, we assume that subhalos host visible dwarf satellites and thus are observed. Indeed, some dwarfs are known with inferred masses as light as few times $10^7 M_\odot$, e.g., Ref. Simon et al. (2011). Also, we note that our mass cut is conservative, since the adoption of a larger value would translate into even stronger DM limits.

As an example, we show in Figure 3.10 the J-factor distribution for the 3FGL setup, i.e. 16 remaining unIDs, with and without the mentioned cuts.

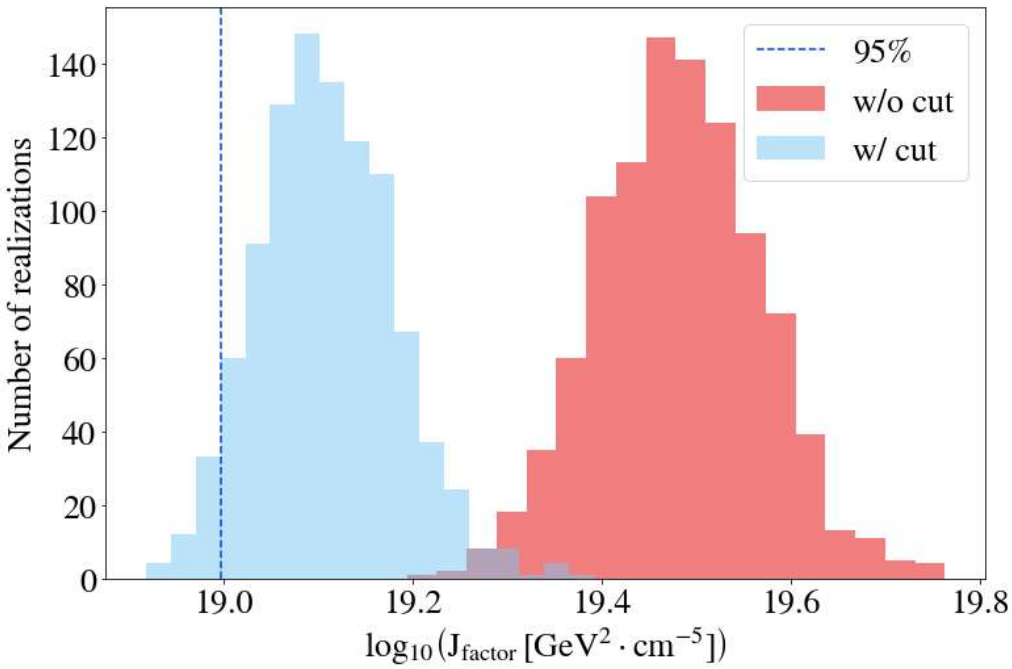


FIGURE 3.10: Distribution of the 16th (i.e. the number of remaining DM candidates in the 3FGL catalog) brightest subhalo J-factor in each of the 1000 VL-II repopulation realizations. The red (blue) distribution refers to the case without (with) a cut in both subhalo mass ($M \geq 10^7 M_\odot$) and latitude ($|b| \leq 10°$); see text for details. The dark blue vertical dashed line marks the J-factor above which 95% of the blue J-factor distribution is contained. This is the J-factor we would adopt for the computation of the 95% C.L. limits in this particular case.

Clearly, the number of surviving DM subhalo candidates has a direct impact on the constraints: the fewer the candidates, the larger the adopted J-factor in Eq. 8.3 will be, as the value to be used will correspond to a brighter simulated subhalo. As $\langle\sigma v\rangle \propto J^{-1}$, by lowering the number of surviving subhalo candidates we will be improving the derived limits on $\langle\sigma v\rangle$. This can be seen in Figure 3.11, which shows the ratio between the J-factor that corresponds to having a certain number of remaining unIDs as subhalo candidates, and the J-factor to be used when the full list of unIDs is used instead. Both of them refer to the values above which 95% of the corresponding J-factors distributions are contained, for each number of candidates. This ratio of J-factors is shown versus the normalized number of unIDs we are left with, for the three considered catalogs.

The figure summarizes the need for decreasing the number of unIDs as potential subhalo candidates, for which the careful filtering of sources performed in Section 3.3 becomes critical. Indeed, from Figure 3.11 it can be seen that by rejecting up to ∼80% of unIDs in a given catalog the improvement with respect to the full catalog (i.e., no filtering) is not relevant (around a factor 3-4 in the constraints), yet for bigger rejection rates the gain becomes exponential: every additional source we are able to remove will have a significant impact on the limits.

The maximum improvement that is possible to achieve depends on the catalog:

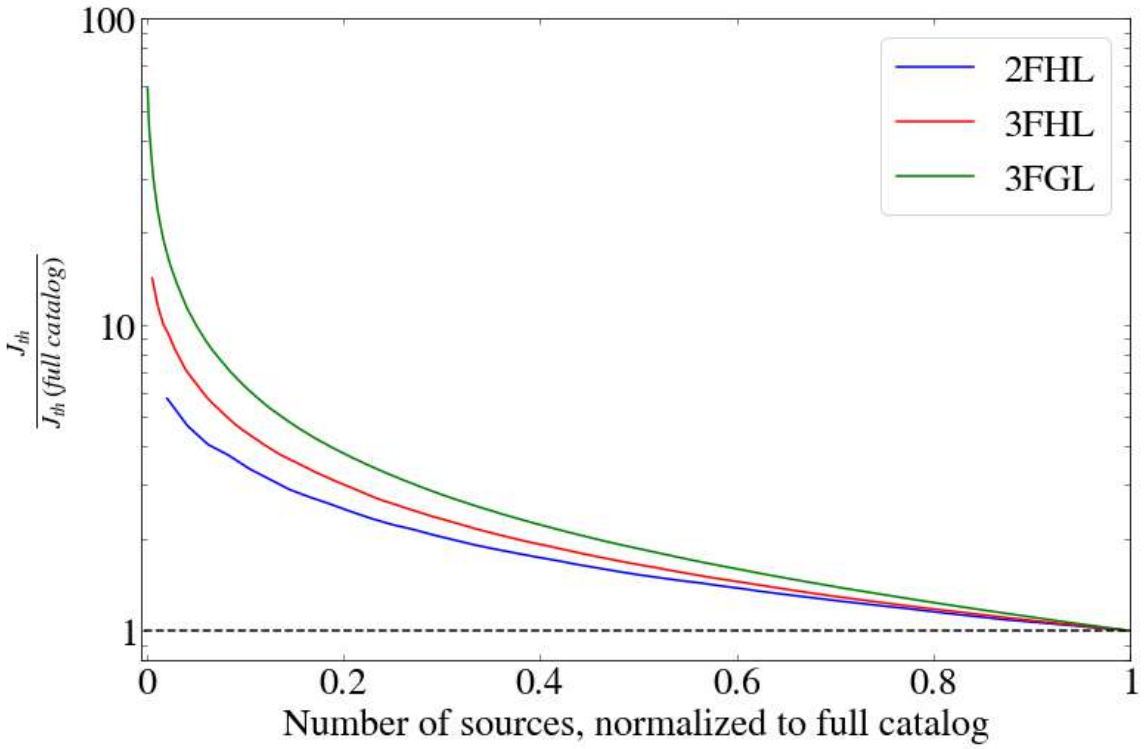


FIGURE 3.11: Improvement in the DM constraints as a function of number of remaining unIDs in the catalogs. The improvement is codified in terms of a ratio of J-factors: the one to be used for the number of remaining sources after filtering, and the one corresponding to the full unID catalog (i.e. no unID rejection). Both J-factors refer to the values above which 95% of the corresponding J-factor distributions, for each number of candidates, are contained; see text and Figure 3.10 for details. The horizontal dashed line shows no improvement at all due to (lack of) unIDs filtering, and it is computed with respect to the case of having a single remaining unID (sensitivity reach of the method; see Figure 3.13). Note the exponential rise of constraining power once less than ∼20% of sources are left.

for small catalogs, such as the 2FHL (48 unIDs), discarding 30 to 40 sources is almost equal to discarding the full catalog, while for the 3FGL (1010 unIDs) this same number represents just a tiny fraction. In other words, removing 80% of unIDs in a catalog (to lie on the 20% turnover of Figure 3.11) is more difficult the more sources we have on the catalog. This explains e.g. that for the case of considering the minimum number of sources (1) in Figure 3.11 we obtain a different percentage for each catalog ($1/48 = 0.02$ for 2FHL; $1/177 = 0.006$ for 3FHL; $1/1010 = 0.001$ for 3FGL). And this is why the maximum improvement (i.e., removing all sources but one) is different between catalogs and equal to a factor 16 for 2FHL, 38 for 3FHL and 140 for 3FGL unIDs, with respect to having the full catalog of unIDs.

We note that, after the filtering performed in Section 3.3 we are left with 8%, 12% and 2% of the full list of unIDs in the 2FHL, 3FHL and 3FGL catalogs, respectively. These numbers already lie in the exponential-growing part of the curve shown in Figure 3.11, showing the power of the unID filtering we performed. Since the 3FHL is the most recent catalog, a smaller fraction of its unIDs have been associated yet. Thus the corresponding DM constraints are not so competitive with respect to the other catalogs.

In short, we must reduce the number of potential subhalos to improve the DM constraints. The maximum potential of this method corresponds to the scenario in which we derive constraints for zero DM subhalo candidates, i.e., no unIDs compatible with DM subhalos. In the following, we will derive DM constraints to the annihilation cross section by i) adopting the number of potential DM subhalos in each catalog after our filtering work, and ii) by assuming that only 1 unID survives our cuts and is therefore compatible with being a subhalo. The latter case will be close to the sensitivity reach of the method as mentioned above.

### 3.5.2 Current DM limits

We first derive the constraints for the most realistic scenario, i.e., the one in which we consider all the unIDs that survive our proposed cuts in Section 3.3 as potential DM subhalos. This means that we are left with 16 candidates in the 3FGL, 4 in the 2FHL and 24 in the 3FHL. The results are shown in Figure 3.12 for both the $b\bar{b}$ and $\tau^+\tau^-$ annihilation channels and for the three catalogs.

We show in Figure 3.12 the 95% C.L limits computed as explained in Section 3.5.1. We also show the 1-$\sigma$ uncertainty band coming from the $F_{min}$ uncertainties, due to the average over the whole considered sky. Additionally, we conservatively include the 4% false-rate positive as the error associated to the machine learning classification algorithms. We discuss in further detail on the computations of these errors in Appendix 3.7.1. In Appendix 3.7.2 the limits are compared with those obtained with no repopulation.

As expected, the 3FGL catalog provides the best constraints in the low-mass range, while the 2FHL setup dominates the high-mass end covered by the LAT. More precisely, for $b\bar{b}$ ($\tau^+\tau^-$) the 2FHL provides the best constraints above $\sim$1 TeV (200 GeV). On the other hand, the 3FHL does not improve significantly the constraints for medium masses with respect to the other two due to the more inefficient filtering. Note also that the 2FHL and 3FHL constraints go to infinity at their respective energy thresholds, 50 and 10 GeV. This is an expected result according to Eq. 8.3, because $N_\gamma = 0$ below the catalog thresholds.

### 3.5.3 Sensitivity reach of the method

The maximum potential of the method is reached for the case in which no unID is compatible with the DM subhalo scenario. However, even in this case we must adopt a J-factor in order to set constraints. We do this by using the J-factor of the brightest object in the simulation. This may look similar to the case in which still one unID is compatible with DM. However, it is conceptually different: in the latter case the resulting sensitivity curve refers to the cross section needed to have one subhalo detected, while in the zero unID case this same sensitivity curve will indeed represent an upper limit to the allowed values. Note, also, that for this reason the sensitivity reach obtained this way will be conservative.

Although it may seem overly optimistic and unlikely that we are able to eliminate all the unIDs in a given catalog as potential DM subhalos, in fact many efforts are currently ongoing to associate the largest possible number of unIDs with known objects. Thus, it may be possible to actually reach this goal in the future.

Figure 3.13 shows the sensitivity reach for the three catalogs under consideration. In the figure, we also include the projected limits for *Fermi*-LAT 60 dwarf galaxies in 15 years of operation Charles et al. (2016), and the latest CTA prospects for the

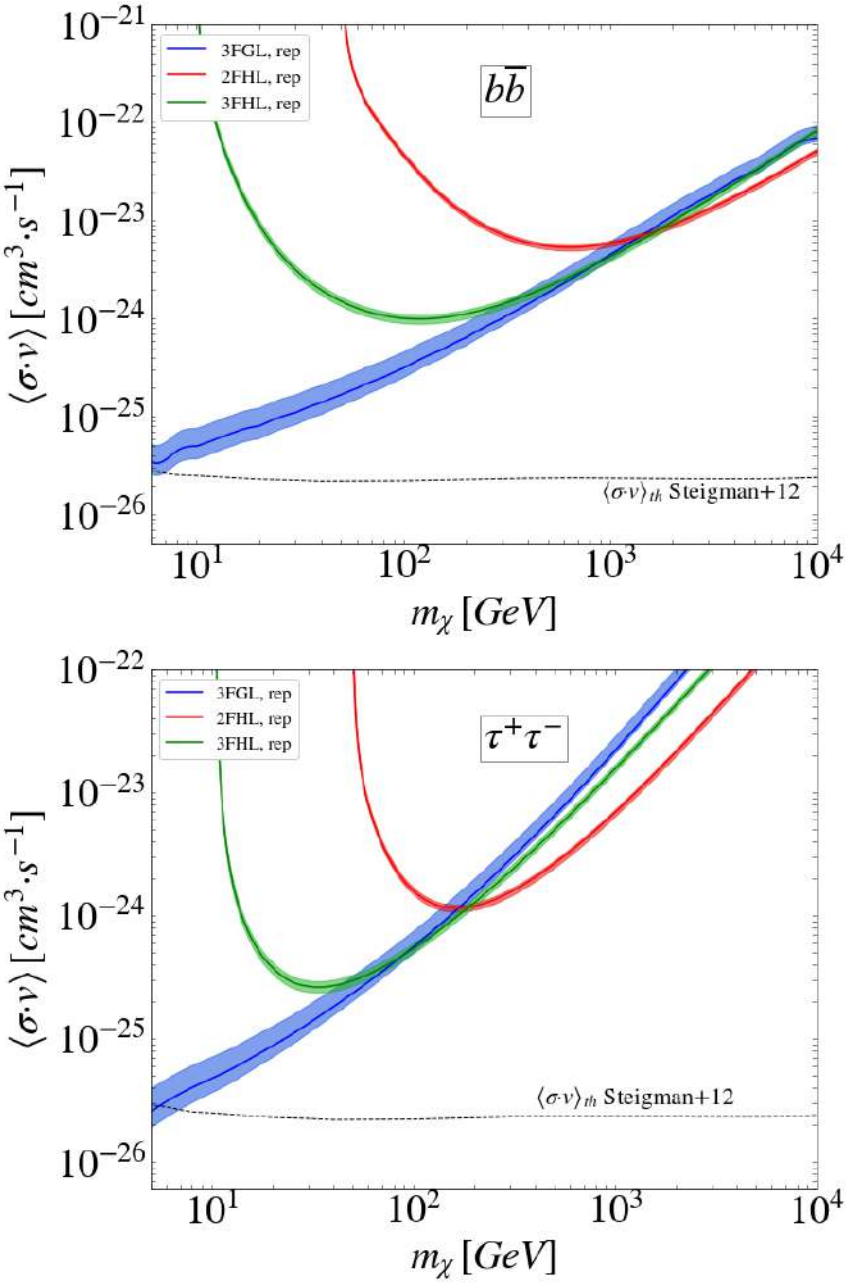


FIGURE 3.12: Limits on the DM annihilation cross section for $b\bar{b}$ (top) and $\tau^+\tau^-$ (bottom) for the three LAT catalogs used in this work, and once the unID filtering detailed in Section 3.3 has been applied to each of them. More precisely, 16, 4 and 24 unIDs remain in the 3FGL, 2FHL and 3FHL catalogs, respectively. The shaded bands refer to the 1-$\sigma$ uncertainty band coming from $F_{min}$; see text for details. The dashed line represents the thermal value of the annihilation cross section Steigman et al. (2012). The "rep" label stands for repopulated.

Milky Way halo The Cherenkov Telescope Array Consortium (2017) (note that these assume no uncertainties).

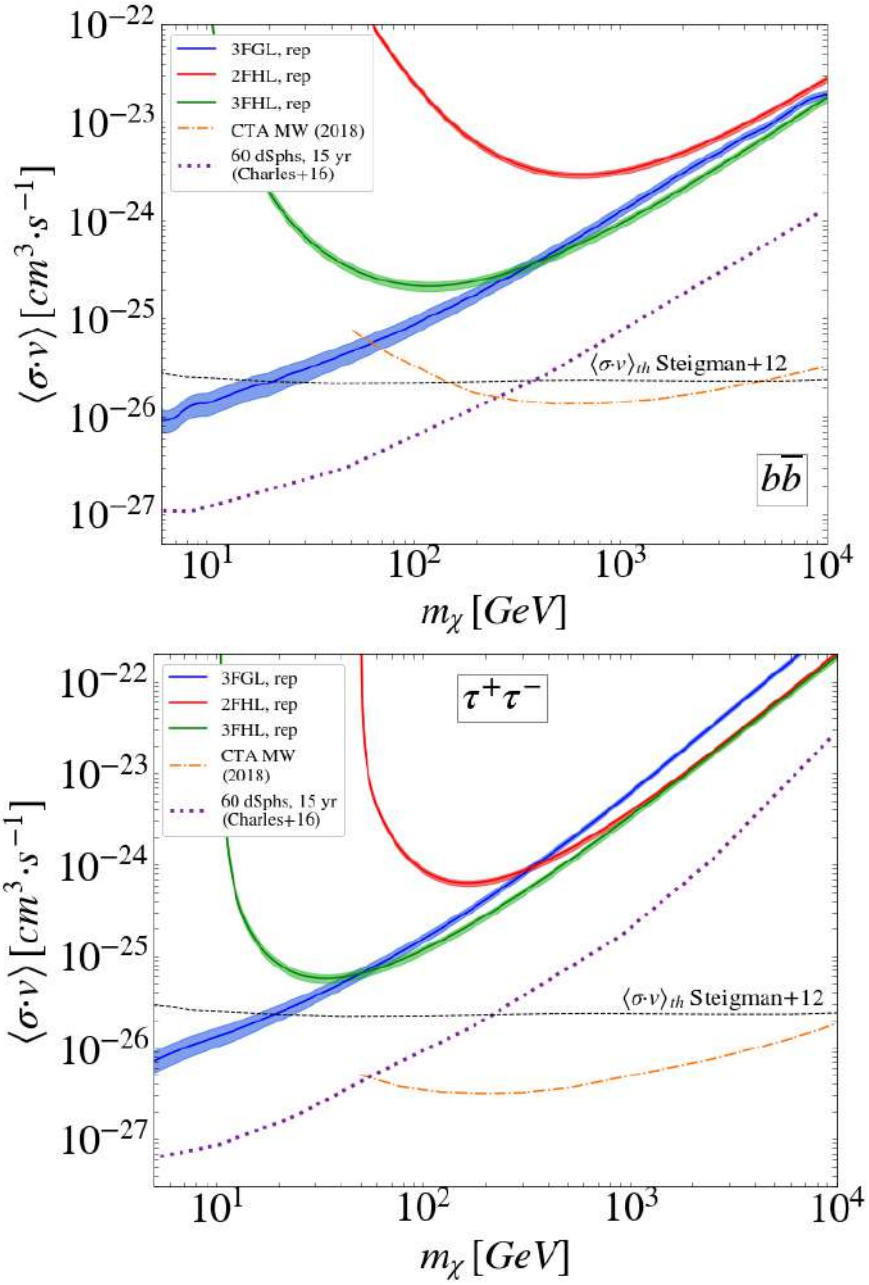


FIGURE 3.13: Same as Figure 3.12, but for the sensitivity reach scenario presented in Section 3.5.3, where only 1 unID is left in each corresponding catalog. We also compare our projections with the predictions for dwarfs with the Fermi LAT Charles et al. (2016) and from the Milky Way halo with CTA Lefranc and Moulin (2016).

## 3.6 Discussion and conclusions

We have presented a competitive method to constrain the nature of DM, assuming the WIMP model. Our method is based on the search for DM subhalo candidates among the sample of unID sources in *Fermi*-LAT point-source catalogs. We performed an exhaustive unID filtering in Section 3.3 with the intention to remove all those unIDs with features not compatible with being a DM subhalo. Our selection cuts included: (1) astrophysical associations; (2) a Galactic latitude cut to avoid issues with the bulk of the Galactic astrophysical sources and diffuse contamination;

(3) variability studies in the official catalogs and with the FAVA tool; (4) machine learning classification algorithms; (5) unambiguous multiwavelength emission of the unID; (6) previously identified complex regions. These selection criteria did not include a dedicated LAT spectral and spatial analysis. This work is ongoing and will be presented elsewhere.

Lacking knowledge on the actual nature of the remaining unIDs after our filtering process (16, 4 and 24 in the 3FGL, 2FHL and 3FHL catalogs, respectively), and in the absence of a clear hint of DM annihilation, we set 95% upper limits on the $\langle\sigma v\rangle - m_\chi$ parameter space. Three basic ingredients were needed to do so. First, we computed the DM annihilation spectra for different annihilation channels and WIMP masses by making use of the PPPC4ID tables of Ref. Cirelli et al. (2011). Second, we characterized the LAT sensitivity to DM with unprecedented accuracy by simulating a population of (point-like) DM subhalos at each sky position, annihilation channel and DM mass, and by computing the minimum integrated flux needed to to have a $TS = 25$ signal in the LAT, i.e., a source detection. This was done for each considered catalog by mimicking its exact configuration, like exposure time, and diffuse and isotropic templates. Third, we relied on results from the VL-II N-body cosmological simulation to compute subhalo J-factors. Since our work focused on low-mass, completely "dark" subhalos, we performed an additional simulation work to *repopulate* the original VL-II with low-mass subhalos well below its formal resolution limit so as not to miss any potential bright dark subhalo. This was done by assuming the same radial distribution and mass function for subhalos as observed in the mass range well resolved in the parent simulation. Subhalo structural properties were modeled using the state-of-the-art subhalo mass-concentration relation by Ref. Moliné et al. (2017). This repopulation exercise was repeated 1000 times to derive statistically meaningful results. The final outcome was a prediction of the distribution of expected subhalo J-factors in ΛCDM.

With a precise characterization of these three basic ingredients at hand, we were able to set conservative yet competitive constraints in Figure 3.12. We also put our results in context by comparing them with other state-of-the-art constraints coming from H.E.S.S., Planck and LAT in Figure 3.14. The obtained DM limits reach the level of the thermal relic cross section for both $b\bar{b}$ and $\tau^+\tau^-$ at the smallest WIMP masses considered, indeed ruling out thermal WIMPs up to 6 GeV in the case of $\tau^+\tau^-$. Our constraints are complementary and independent to the ones obtained by means of other targets such as dSphs Fermi-LAT Collaboration (2015c).

The results of this paper can be compared with those found in Ref. Calore et al. (2017), where a study of LAT sensitivity to DM subhalos was also performed. The $F_{min}$ results for $b\bar{b}$ and $\tau^+\tau^-$ are fully compatible. We here extend the calculation to many other channels and use a much finer grid. In our work, we performed a filtering of unIDs that allowed us to derive a conservative number of catalog sources that cannot be discarded as DM subhalos at present time, and set *realistic* DM limits according to this number. In contrast, Ref. Calore et al. (2017) did not perform an unID filtering and simply fixed the number of remaining candidates (namely 20, 5, 0) when presenting their limits[17]. For the same number of considered sources, we improve their results roughly one order of magnitude once our low-mass subhalo repopulation work and the latest subhalo mass-concentration relation are implemented. Yet, we must bear in mind that the repopulation and characterization of the subhalo population was done with VL-II, a DM-only, WMAP-cosmology N-body

[17] Indeed, they implicitly adopted one remaining source instead of zero for their sensitivity reach; V. de Romeri, private communication.

cosmological simulation. In the next years, new Milky-Way-size simulations should be available that will adopt the Planck cosmology and will include baryonic physics as well. All together, this may significantly alter the current subhalo predictions. Work is already ongoing to help clarify the properties of the subhalo population that are expected to be more relevant for DM annihilation searches (abundance, radial distribution, inner structure).

We also made an effort to quantify the involved uncertainties in our limits, which we summarized in 3.7.1. In short, for a small number of sources we are dominated by the uncertainty in the J-factor, which is implicitly taken into account in the computation of the 95% limits, while for large unID samples the uncertainty in $F_{min}$ is the largest.

In order to put the DM limits derived in this work into a more general context, we compare them in Figure 3.14 to those obtained by the *Fermi*-LAT from dSphs Fermi-LAT Collaboration (2015c), by the H.E.S.S. Collaboration from the Milky Way halo H.E.S.S. Collaboration (2016) and by the Planck Collaboration using the Cosmic Microwave Background (CMB) DR3 recent results The Planck Collaboration (2020). For this figure, we only show the envelope of the (mean) limits presented in Figure 3.12 for the three catalogs. This allows a single, best-curve representation of the three sets of limits. Figure 3.14 shows, once again, that DM subhalos can yield very competitive limits compared to other targets and probes.

We also studied the maximum potential or sensitivity reach of our method to set limits. More precisely, we obtained that by having one single DM subhalo candidate left in each of the catalogs, the method would potentially yield the best limits to the annihilation cross section so far, discarding the thermal relic cross section value up to $\sim$20 GeV in the case of annihilation into $b\bar{b}$ and $\tau^+\tau^-$. This sensitivity reach scenario is indeed a plausible one, as the increasing quantity and quality of available data, as well as several ongoing observational campaigns at other wavelengths could definitely unveil the true nature of the remaining unID sources. Also, as already mentioned, a dedicated spectral and spatial analysis is currently ongoing, which will hopefully be able to either reject additional sources as DM subhalos (thus improving the current constraints significantly, as illustrated in Figure 3.11), or point out very interesting sources from the DM perspective. At larger WIMP masses, the Cherenkov Telescope Array (CTA) in the near future The Cherenkov Telescope Array Consortium (2017) will provide results at higher energies than *Fermi*-LAT. A combination of both instruments may be able for the first time to test the WIMP paradigm over more than 4 decades in energy.

The most relevant results from this work are being made public for community's use. In particular, the tabulated DM constraints for both the conservative and sensitivity reach scenarios; tables of $F_{min}$ for the whole considered WIMP masses and channels; and the full list of rejected unID sources containing the rejection criteria applied in each case.

## 3.7 Appendix

### 3.7.1 Impact of uncertainties

In this paper we have considered those uncertainties associated to $F_{min}$, J-factor, and machine learning techniques. We assumed the DM annihilation spectra (see Section 3.2.1) to have negligible errors.

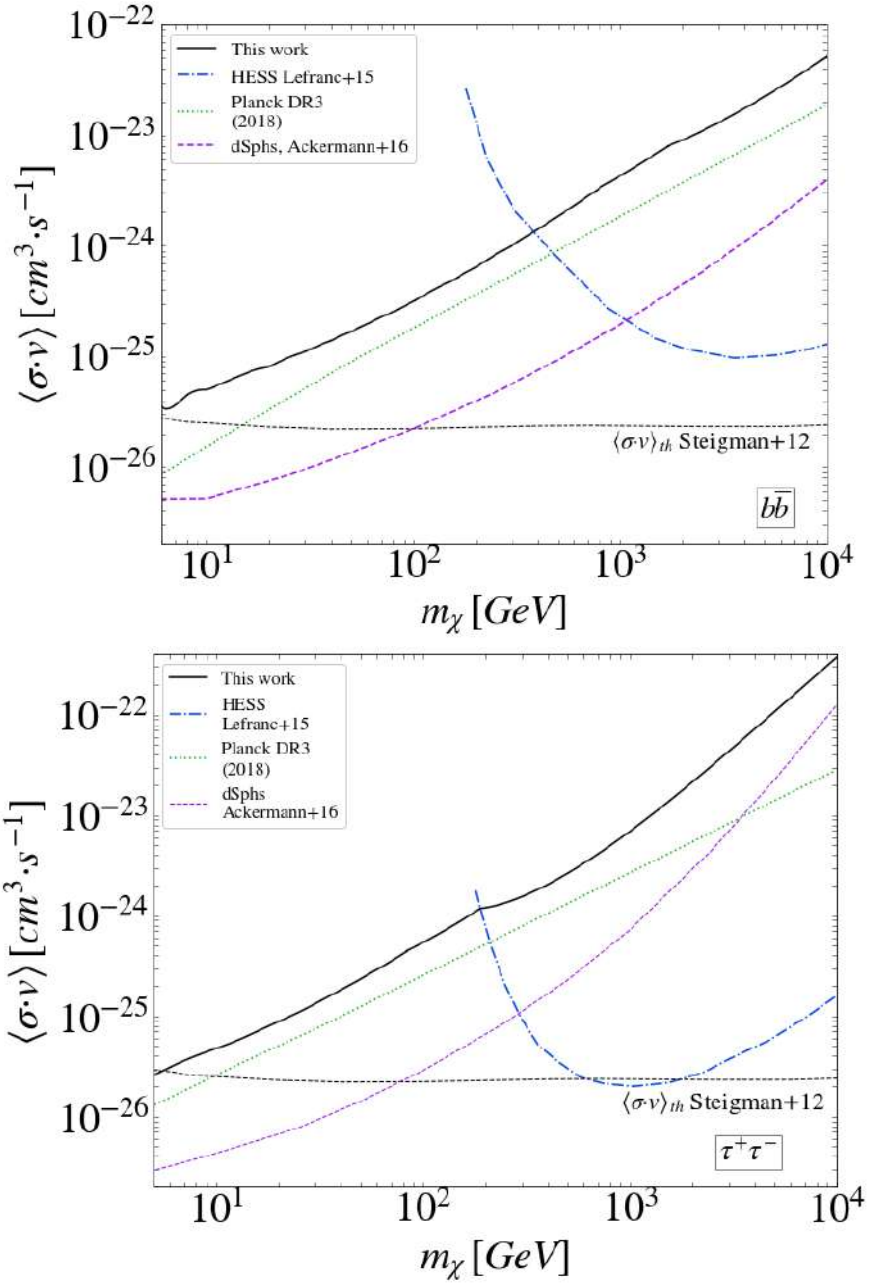


FIGURE 3.14: Comparison of DM limits for different targets and probes. Solid line corresponds to the envelope of the three sets of limits shown in Figures 3.12 and 3.13 for the realistic scenario (Section 9.4). dot-dashed, dashed and dotted lines are, respectively, the DM constraints derived by H.E.S.S. for the Milky Way halo Lefranc et al. (2015), by the *Fermi*-LAT for dSphs Fermi-LAT Collaboration (2015c), and by Planck using the CMB DR3 latest release The Planck Collaboration (2020). Top panel is for $b\bar{b}$ and bottom panel for $\tau^+\tau^-$ annihilation channel.

Here, we perform a study to understand how these uncertainties behave with the considered catalog, DM mass and annihilation channel. Note that the J-factor uncertainty does not depend on the DM mass, as it only depends on the number of unID sources left (see Section 3.5.1).

The $F_{min}$ relative error can be computed as:

$$\varepsilon_F = 100 \cdot \frac{\sigma_F}{F_{min}^{avg}}, \tag{3.10}$$

where $F_{min}^{avg}$ is the average minimum flux and $\sigma_F$ is the standard deviation of the corresponding log-normal distribution, both computed over the whole sky but the $|b| \leq 10^\circ$ band. We note that in some cases this log-normal distribution may significantly differ from being Gaussian. Also, we note that there may be other second-order effects in the characterization of this quantity, such as inhomogeneities or slight deviations with respect to the mean values across the sky, yet they are expected to be subdominant.

The J-factor uncertainty comes from the cosmic variance across 1000 realizations from the N-body simulations, and may be computed as:

$$\varepsilon_J = 100 \cdot \frac{\sigma_J}{J^{avg}} \tag{3.11}$$

where $J^{avg}$ is the average of the J-factors over the different realizations of the repopulated simulation, and $\sigma_J$ is their standard deviation, using the $n^{th}$ J-factor for the considered $n$ subhalos. This implicitly assumes that the J-factor distribution is well represented by a Gaussian; however we warn that for a very low number of sources ($n < 3$) this distribution may exhibit significant departures from it.

We show a comparison between both $\varepsilon_F$ and $\varepsilon_J$ as given by the above expressions in Figure 3.15. We stress that $\sigma_J$ refers to the mean J-factor ($J^{avg}$) and not to the one we used to set the 95% C.L. upper limits (see Section 9.4). As it can be seen, $\varepsilon_J$ is sub-dominant with respect to $\varepsilon_F$ when the number of unIDs is large. Then, below $\sim$15 unIDs, $\varepsilon_J$ comes comparable or even larger than $\varepsilon_F$.

As for the dependency of these uncertainties with annihilation channel: the general trend is a decrease of $\varepsilon_F$ as the DM mass increases. There are some exceptions: $Z^0Z^0$, $\mu^+\mu^-$ and $e^+e^-$. For these, $\varepsilon_F$ increases mildly for the heaviest DM masses. It is worth noting that the $Z^0Z^0$ channel behaves slightly different under the 2FHL setup, while the other channels behave always very similarly independently of the catalog.

Concerning the different catalog setups, $\varepsilon_F$ is typically larger for the 3FGL setup because of the larger variations of $F_{min}$ in this case compared to the other catalogs (the diffuse emission is more intense at lower energies, and the 3FGL energy threshold is 100 MeV so it is the most affected one).

Finally, the 4% false association rate from the use of the machine learning criterium in our work has also been implemented in the DM constraints by adopting all of this 4% rate as an uncertainty. The net effect is a broadening of the J-factor (upper) uncertainty band, since a slightly larger number of unIDs cannot be discarded. This effect is only non-negligible in the case of the 3FGL catalog, where we applied the machine learning to 162 sources and therefore this 4% false rate uncertainty translates into 6 potentially wrongly rejected sources. Namely, the number of unIDs left after our filtering procedure increases from 16 to a maximum of 22.

### 3.7.2 Impact of the low-mass subhalo repopulation on DM limits

Here we compare the DM constraints presented on Section 9.4 to those without repopulating VL-II with low-mass subhalos below the resolution limit of the simulation. Figure 3.16 shows such a comparison for both the case that adopts the current remaining number of DM subhalo candidates in the catalogs (Section 3.3), and the

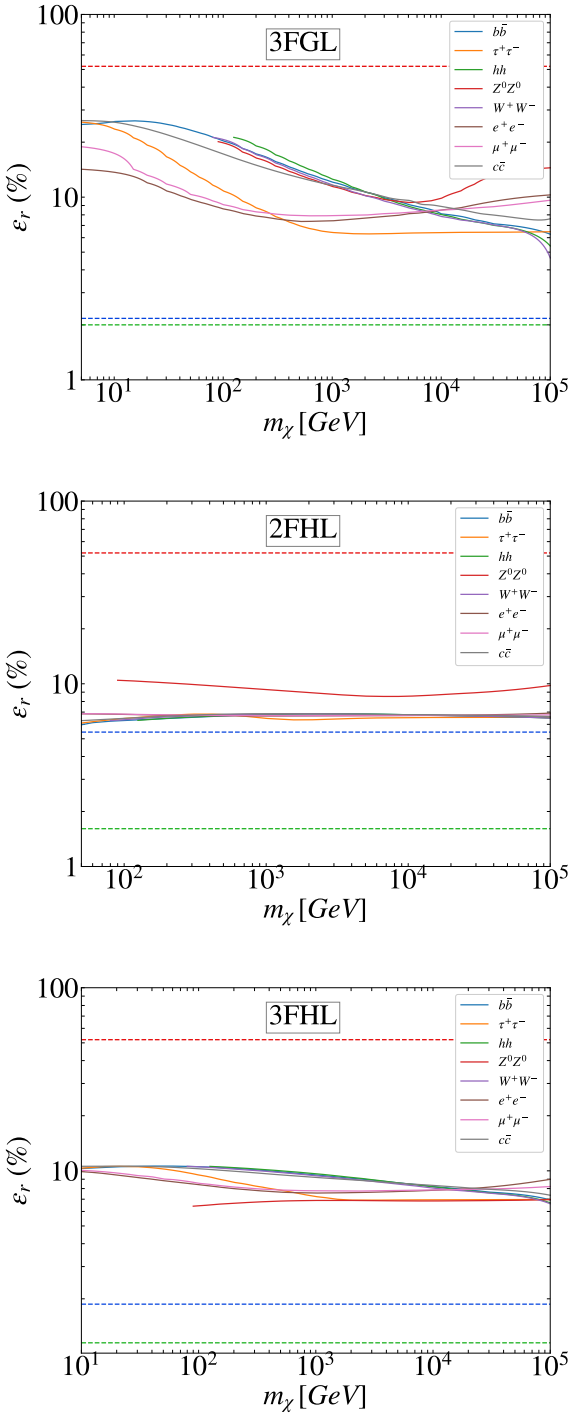


FIGURE 3.15: Comparison of $\varepsilon_F$ versus $\varepsilon_J$, i.e. the relative errors associated to the $F_{min}$ (solid lines) and J-factor (dashed lines), respectively, as a function of the DM particle mass and different annihilation channels. From bottom to top, for the 3FGL, 2FHL and 3FHL catalogs. The dashed lines are, from bottom to top, the $\varepsilon_J$ of the full number of unIDs in the corresponding catalog (green), the number of unIDs in the realistic scenario detailed in Section 9.4 (blue) and the 1-source sensitivity reach of Section 3.5.3 (red).

sensitivity reach case (Section 3.5.3) as well as the constraints both with and without the repopulation.

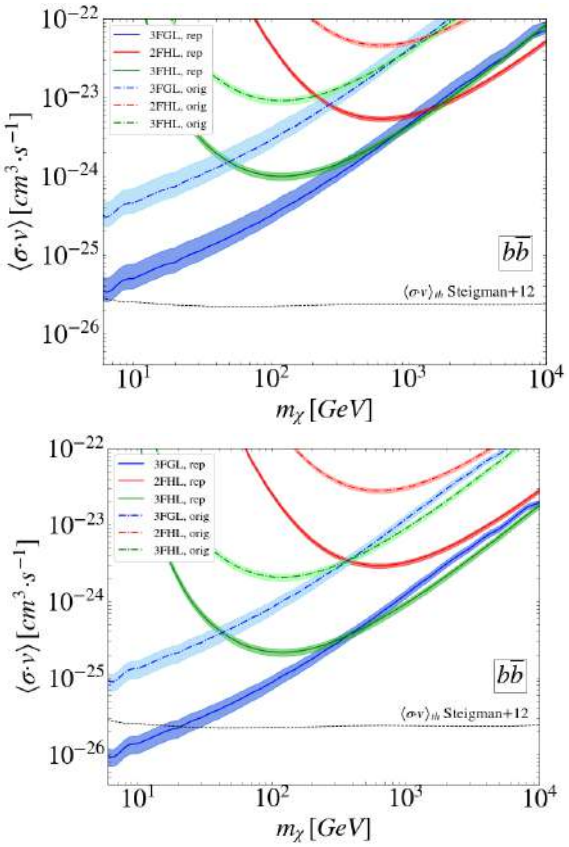


FIGURE 3.16: Comparison of DM 95% C.L. upper limits found with and without low-mass subhalo repopulation below the resolution limit of the original VL-II simulation. Both panels are for $b\bar{b}$, in the three catalog setups. Dot-dashed lines are the constraints from the original VL-II simulation ("orig"), while the solid lines use the repopulated simulation ("rep"). Left: current number of DM subhalo candidates in the catalogs (see Figure 3.12); right: sensitivity reach of the method (see Figure 3.13).

The differences in the J-factor distribution between the original and repopulated VL-II simulation are large enough to improve the limits by a factor $\sim$ 10. At high masses, limits worsen due to the loss of sensitivity of the *Fermi*-LAT, and all three catalog setups converge to approximately the same value. Similar improvements are found when considering either the realistic scenario or the sensitivity reach.

From these results, we find low-mass subhalos to be especially relevant for this work, as a significant number of them are expected to exhibit similar annihilation fluxes than resolved, more massive objects in the original simulation. We note that there may be still room for some further improvement by extending our repopulation work to include even smaller subhalos masses (i.e., below $\gtrsim 10^3$ M ). This additional numerical work will be done elsewhere.

### 3.7.3 Full set of DM constraints

In this Appendix, we provide the DM constraints for various channels, namely $c\bar{c}$ (Figure 3.17), $t\bar{t}$ (Figure 3.18), $W^+W^-$ (Figure 3.19), $Z^0Z^0$ (Figure 3.20), $hh$ (Figure

3.21), $e^+e^-$ (Figure 3.22), $\mu^+\mu^-$ (Figure 3.23), in addition to the $b\bar{b}$ and $\tau^+\tau^-$ channels, which were shown in Figure 3.12. We note that all the plots have the VL-II low-mass subhalo repopulation implemented.

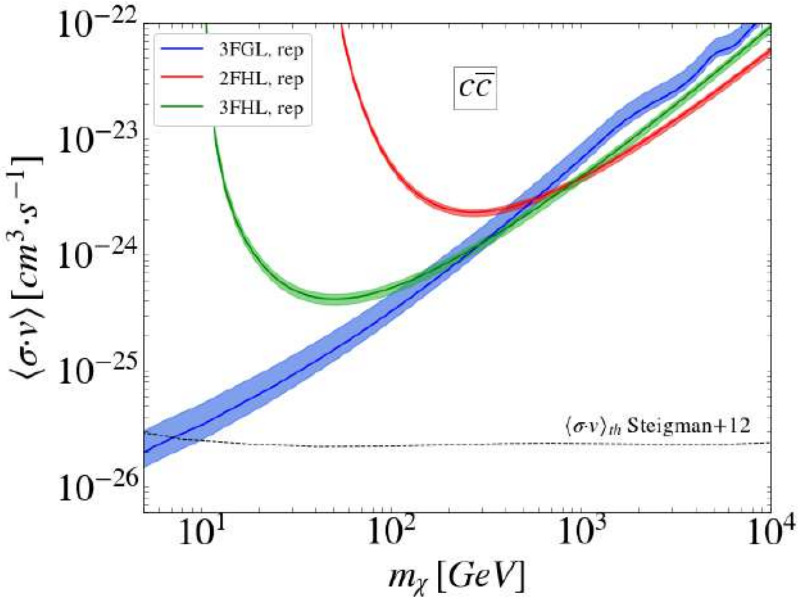


FIGURE 3.17: Same as Figure 3.12 but for $c\bar{c}$ annihilation channel.

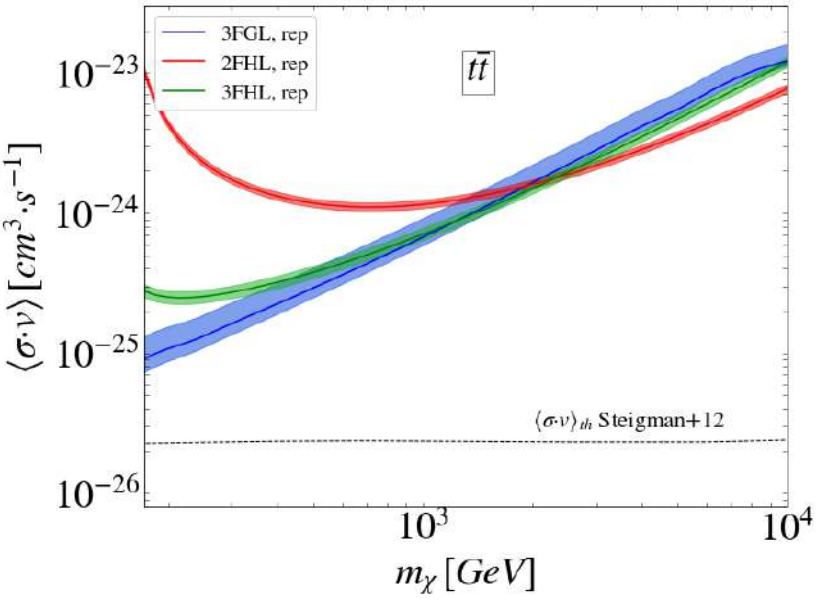


FIGURE 3.18: Same as Figure 3.12 but for $t\bar{t}$ annihilation channel.

## Bibliography

Ajello, M., Gasparrini, D., Sanchez-Conde, M., Zaharijas, G., Gustafsson, M., Cohen-Tanugi, J., Dermer, C. D., Inoue, Y., Hartmann, D., Ackermann, M., Bechtol, K., Franckowiak, A., Reimer, A., Romani, R. W. and Strong, A. W. (2015). The Origin of the Extragalactic Gamma-Ray Background and Implications for Dark-Matter

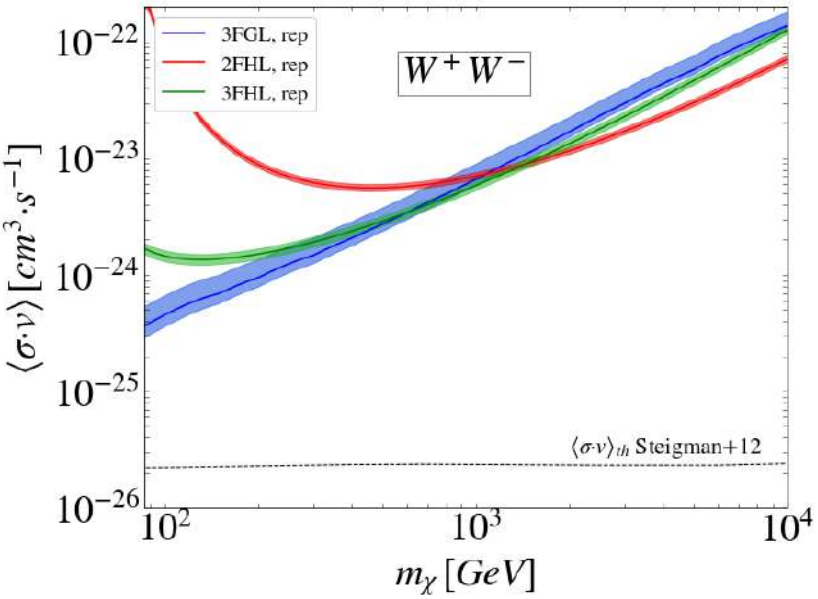


FIGURE 3.19: Same as Figure 3.12 but for $W^+W^-$ annihilation channel.

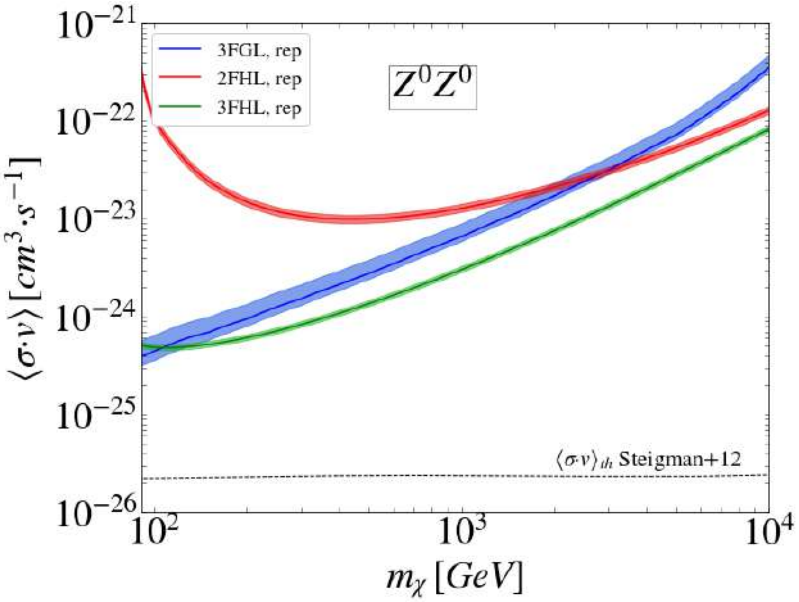


FIGURE 3.20: Same as Figure 3.12 but for $Z^0Z^0$ annihilation channel.

Annihilation, *The Astrophysical Journal Letter* **800**: L27.
**URL:** *http://adsabs.harvard.edu/abs/2015ApJ...800L..27A*

Anderhalden, D. and Diemand, J. (2013). Density profiles of CDM microhalos and their implications for annihilation boost factors, *Journal of Cosmology and Astroparticle Physics* **2013**(04): 009–009.

Belikov, A. V., Buckley, M. R. and Hooper, D. (2012). Searching for dark matter subhalos in the Fermi-LAT second source catalog, *Physical Review D* **86**(4).

Berezinsky, V., Dokuchaev, V. and Eroshenko, Y. (2006). Destruction of small-scale dark matter clumps in the hierarchical structures and galaxies, *Physical Review D*

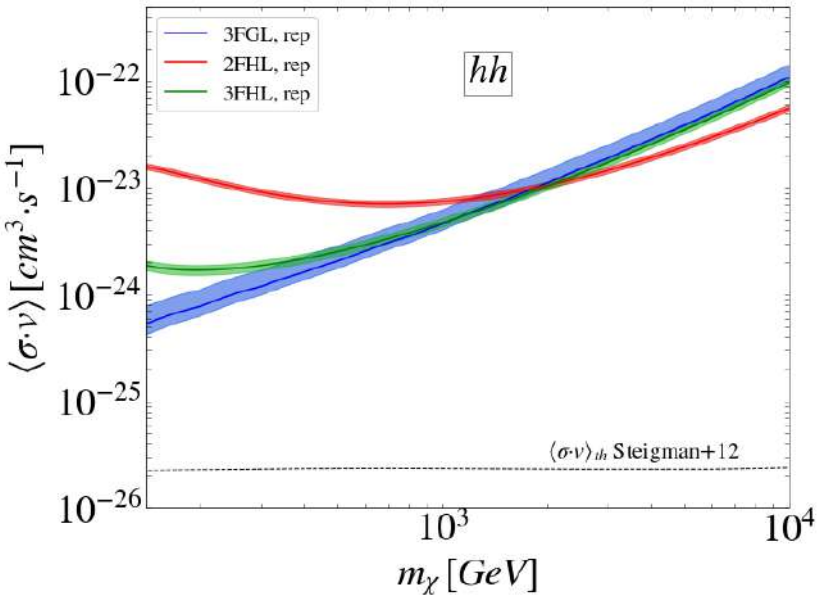


FIGURE 3.21: Same as Figure 3.12 but for *hh* annihilation channel.

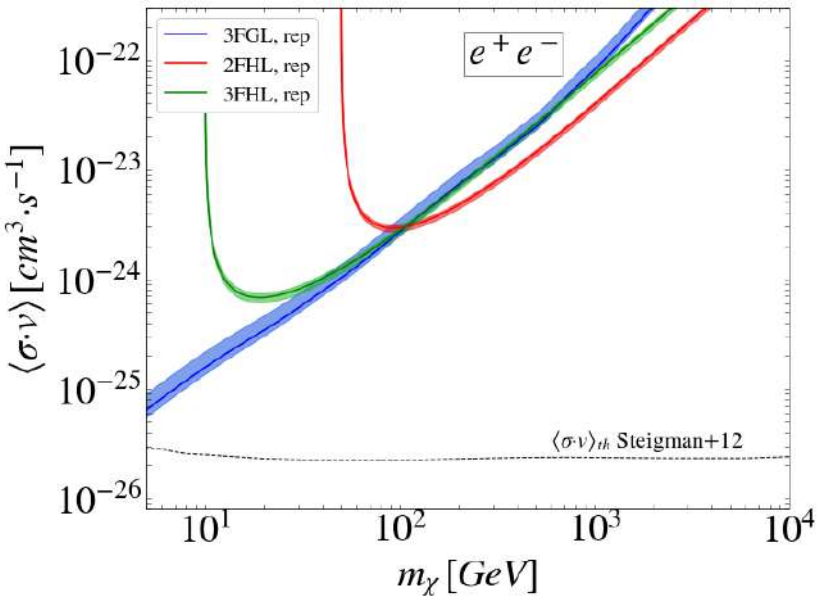


FIGURE 3.22: Same as Figure 3.12 but for $e^+e^-$ annihilation channel.

**73**(6).

Bergström, L., Ullio, P. and Buckley, J. H. (1998). Observability of gamma rays from dark matter neutralino annihilations in the Milky Way halo, *Astroparticle Physics* **9**(2): 137–162.

Berlin, A. and Hooper, D. (2014). Stringent Constraints On The Dark Matter Annihilation Cross Section From Subhalo Searches With The Fermi Gamma-Ray Space Telescope, *Physical Review D* **89**(1).
**URL:** http://dx.doi.org/10.1103/PhysRevD.89.016014

Bertone, G. (2010). The moment of truth for WIMP Dark Matter, *Nature* **468**(7322): 389–393.

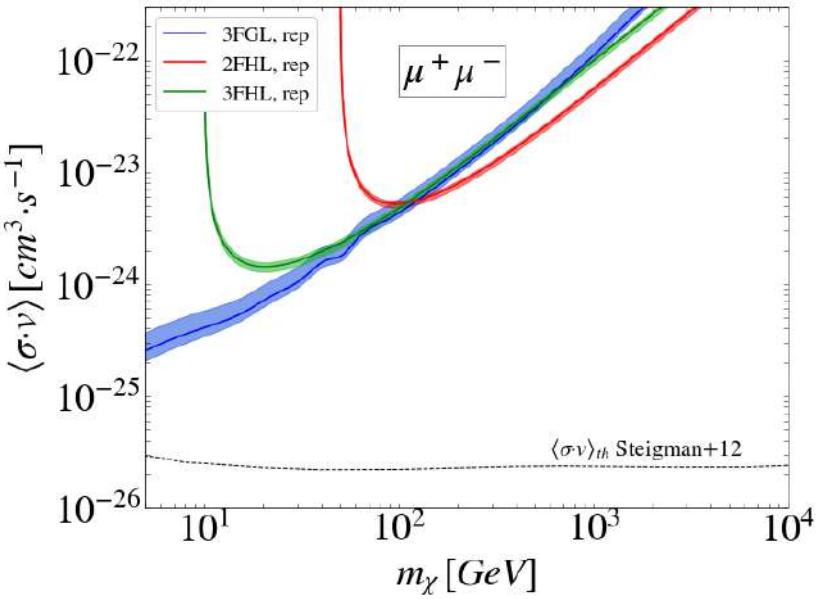


FIGURE 3.23: Same as Figure 3.12 but for $\mu^+\mu^-$ annihilation channel.

**URL:** http://dx.doi.org/10.1038/nature09509

Bertone, G., Hooper, D. and Silk, J. (2005). Particle dark matter: evidence, candidates and constraints, *Physics Reports* **405**(5-6): 279–390.

Bertoni, B., Hooper, D. and Linden, T. (2015). Examining The Fermi-LAT Third Source Catalog In Search Of Dark Matter Subhalos, *Journal of Cosmology and Astroparticle Physics* **12**: 035.
**URL:** http://dx.doi.org/10.1088/1475-7516/2015/12/035

Bertoni, B., Hooper, D. and Linden, T. (2016). Is The Gamma-Ray Source 3FGL J2212.5+0703 A Dark Matter Subhalo?, *Journal of Cosmology and Astroparticle Physics* **5**: 049.
**URL:** http://dx.doi.org/10.1088/1475-7516/2016/05/049

Bertschinger, E. (2006). Effects of cold dark matter decoupling and pair annihilation on cosmological perturbations, *Physical Review D* **74**(6).

Binney, J. and Tremaine, S. (2008). *Galactic Dynamics: Second Edition (Princeton Series in Astrophysics)*, Princeton University Press.

Blanchet, S. and Lavalle, J. (2012). Diffuse gamma-ray constraints on dark matter revisited I: the impact of subhalos, *Journal of Cosmology and Astroparticle Physics* **2012**(11): 021–021.

Bogdanov, S. and Halpern, J. P. (2015). Identification of the High-Energy Gamma-Ray Source 3FGL J1544.6-1125 as a Transitional Millisecond Pulsar Binary in an Accreting State, *The Astrophysical Journal Letter* **803**: L27.
**URL:** http://adsabs.harvard.edu/abs/2015ApJ...803L..27B

Bringmann, T. (2009). Particle Models and the Small-Scale Structure of Dark Matter, *New Journal of Physics* **11**(10): 105027.
**URL:** http://dx.doi.org/10.1088/1367-2630/11/10/105027

Buckley, M. R. and Hooper, D. (2010). Dark Matter Subhalos In the Fermi First Source Catalog, *Physical Review D* **82**(6).
**URL:** http://dx.doi.org/10.1103/PhysRevD.82.063501

Calore, F., Romeri, V. D., Mauro, M. D., Donato, F. and Marinacci, F. (2017). Realistic estimation for the detectability of dark matter sub-halos with Fermi-LAT, *Physical Review D* **96**(6).
**URL:** http://dx.doi.org/10.1103/PhysRevD.96.063009

Camilo, F., Kerr, M., Ray, P. S., Ransom, S. M., Sarkissian, J., Cromartie, H. T., Johnston, S., Reynolds, J. E., Wolff, M. T., Freire, P. C. C., Bhattacharyya, B., Ferrara, E. C., Keith, M., Michelson, P. F., Parkinson, P. M. S. and Wood, K. S. (2015). Parkes radio searches of Fermi gamma-ray sources and millisecond pulsar discoveries, *The Astrophysical Journal* **810**: 85.
**URL:** http://adsabs.harvard.edu/abs/2015ApJ...810...85C

Charles, E., Sánchez-Conde, M., Anderson, B., Caputo, R., Cuoco, A., Mauro, M. D., Drlica-Wagner, A., Gomez-Vargas, G., Meyer, M., Tibaldo, L., Wood, M., Zaharijas, G., Zimmer, S., Ajello, M., Albert, A., Baldini, L., Bechtol, K., Bloom, E., Ceraudo, F., Cohen-Tanugi, J., Digel, S., Gaskins, J., Gustafsson, M., Mirabal, N. and Razzano, M. (2016). Sensitivity projections for dark matter searches with the Fermi large area telescope, *Physics Reports* **636**: 1–46.

Cirelli, M., Corcella, G., Hektor, A., Hütsi, G., Kadastik, M., Panci, P., Raidal, M., Sala, F. and Strumia, A. (2011). PPPC 4 DM ID: A Poor Particle Physicist Cookbook for Dark Matter Indirect Detection, *Journal of Cosmology and Astroparticle Physics* **2011**(03): 051–051.
**URL:** http://dx.doi.org/10.1088/1475-7516/2011/03/051

Clark, C. J., Wu, J., Pletsch, H. J., Guillemot, L., Allen, B., Aulbert, C., Beer, C., Bock, O., Cuéllar, A., Eggenstein, H. B., Fehrmann, H., Kramer, M., Machenschalk, B. and Nieder, L. (2017). The Einstein@Home Gamma-Ray Pulsar Survey. I. Search Methods, Sensitivity and Discovery of New Young Gamma-Ray Pulsars, *The Astrophysical Journal* **834**(2): 106.

Condon, J. J., Cotton, W. D., Greisen, E. W., Yin, Q. F., Perley, R. A., Taylor, G. B. and Broderick, J. J. (1998). The NRAO VLA Sky Survey, *The Astronomical Journal* **115**(5): 1693–1716.

Crespo, N. Á., Massaro, F., Milisavljevic, D., Landoni, M., Chavushyan, V., Patiño-Álvarez, V., Masetti, N., Jiménez-Bailón, E., Strader, J., Chomiuk, L., Katagiri, H., Kagaya, M., Cheung, C. C., Paggi, A., D'Abrusco, R., Ricci, F., Franca, F. L., Smith, H. A. and Tosti, G. (2016). Optical Spectroscopic Observations of Gamma-Ray Blazar Candidates. VI. Further Observations from TNG, WHT, OAN, SOAR and MAGELLAN Telescopes, *The Astronomical Journal* **151**(4): 95.

Diemand, J., Kuhlen, M. and Madau, P. (2007). Formation and Evolution of Galaxy Dark Matter Halos and Their Substructure, *The Astrophysical Journal* **667**(2): 859–877.

Diemand, J., Kuhlen, M., Madau, P., Zemp, M., Moore, B., Potter, D. and Stadel, J. (2008). Clumps and streams in the local dark matter distribution, *Nature* **454**(7205): 735–738.
**URL:** http://dx.doi.org/10.1038/nature07153

Diemand, J., Moore, B. and Stadel, J. (2005). Earth-mass dark-matter haloes as the first structures in the early Universe, *Nature* **433**(7024): 389–391.

Evans, N., Ferrer, F. and Sarkar, S. (2004). A travel guide to the dark matter annihilation signal, *Physical Review D* **69**(12).

Fermi-LAT Collaboration (2012a). Fermi-LAT Observations of the Diffuse Gamma-Ray Emission: Implications for Cosmic Rays and the Interstellar Medium, *The Astrophysical Journal* **750**(1): 3.
**URL:** *http://dx.doi.org/10.1088/0004-637X/750/1/3*

Fermi-LAT Collaboration (2012b). Search for Dark Matter Satellites using the FERMI-LAT, *The Astrophysical Journal* **747**(2): 121.
**URL:** *http://dx.doi.org/10.1088/0004-637X/747/2/121*

Fermi-LAT Collaboration (2013). Search for Gamma-ray Spectral Lines with the Fermi Large Area Telescope and Dark Matter Implications, *Physical Review D* **88**(8).
**URL:** *http://dx.doi.org/10.1103/PhysRevD.88.082002*

Fermi-LAT Collaboration (2015a). Fermi Large Area Telescope Third Source Catalog, *The Astrophysical Journal Supplementary Series* **218**(2): 23.
**URL:** *https://ui.adsabs.harvard.edu/abs/2015ApJS..218..23A*

Fermi-LAT Collaboration (2015b). Search for extended gamma-ray emission from the Virgo galaxy cluster with Fermi-LAT, *The Astrophysical Journal* **812**(2): 159.
**URL:** *http://dx.doi.org/10.1088/0004-637X/812/2/159*

Fermi-LAT Collaboration (2015c). Searching for Dark Matter Annihilation from Milky Way Dwarf Spheroidal Galaxies with Six Years of Fermi-LAT Data, *Physical Review Letters* **115**(23).
**URL:** *http://dx.doi.org/10.1103/PhysRevLett.115.231301*

Fermi-LAT Collaboration (2016a). 2FHL: The Second Catalog of Hard Fermi-LAT Sources, *The Astrophysical Journal Supplement Series* **222**: 5.
**URL:** *http://adsabs.harvard.edu/abs/2016ApJS..222...5A*

Fermi-LAT Collaboration (2016b). Fermi-LAT Observations of High-Energy Gamma-Ray Emission Toward the Galactic Center, *The Astrophysical Journal* **819**: 44.
**URL:** *http://adsabs.harvard.edu/abs/2016ApJ...819...44A*

Fermi-LAT Collaboration (2017a). 3FHL: The Third Catalog of Hard Fermi-LAT Sources, *The Astrophysical JournalS* **232**: 18.
**URL:** *http://adsabs.harvard.edu/abs/2017ApJS..232...18A*

Fermi-LAT Collaboration (2017b). The Fermi Galactic Center GeV Excess and Implications for Dark Matter, *The Astrophysical Journal* **840**: 43.
**URL:** *http://adsabs.harvard.edu/abs/2017ApJ...840...43A*

Fermi-LAT Collaboration (2017c). The second catalog of flaring gamma-ray sources from the Fermi All-sky Variability Analysis, *The Astrophysical Journal* **846**(1): 34.
**URL:** *http://dx.doi.org/10.3847/1538-4357/aa8092*

Fermi-LAT Collaboration (2018). Einstein@Home discovers a radio-quiet gamma-ray millisecond pulsar, *Science Advances* **4**(2): eaao7228.

Fermi-LAT Collaboration (2020). Fermi Large Area Telescope Fourth Source Catalog, *The Astrophysical Journal Supplement Series* **247**(1): 33.
**URL:** http://dx.doi.org/10.3847/1538-4365/ab6bcb

Fermi-LAT Collaboration and Atwood, W. B. (2009). The Large Area Telescope on the Fermi Gamma-ray Space Telescope Mission, *The Astrophysical Journal* **697**(2): 1071–1102.
**URL:** http://dx.doi.org/10.1088/0004-637X/697/2/1071

Freese, K. (2009). *Review of Observational Evidence for Dark Matter in the Universe and in upcoming searches for Dark Stars*, Vol. 36 of *EAS Publications Series*.
**URL:** http://adsabs.harvard.edu/abs/2009EAS...36..113F

Gao, L., White, S. D. M., Jenkins, A., Stoehr, F. and Springel, V. (2004). The subhalo populations of ΛCDM dark haloes, *Monthly Notices of the Royal Astronomical Society* **355**: 819–834.
**URL:** http://dx.doi.org/10.1111/j.1365-2966.2004.08360.x

Garrett, K. and Duda, G. (2011). Dark Matter: A Primer, *Advances in Astronomy* **2011**: 1–22.
**URL:** http://dx.doi.org/10.1155/2011/968283

Garrison-Kimmel, S., Boylan-Kolchin, M., Bullock, J. S. and Lee, K. (2014). ELVIS: Exploring the Local Volume in Simulations, *Monthly Notices of the Royal Astronomical Society* **438**(3): 2578–2596.

Garrison-Kimmel, S., Wetzel, A., Bullock, J. S., Hopkins, P. F., Boylan-Kolchin, M., Faucher-Giguère, C.-A., Kereš, D., Quataert, E., Sanderson, R. E., Graus, A. S. and Kelley, T. (2017). Not so lumpy after all: modelling the depletion of dark matter subhaloes by Milky Way-like galaxies , *Monthly Notices of the Royal Astronomical Society* **471**(2): 1709–1727.

Giocoli, C., Pieri, L. and Tormen, G. (2008). Analytical approach to subhalo population in dark matter haloes, *Monthly Notices of the Royal Astronomical Society* **387**(2): 689–697.

Goerdt, T., Gnedin, O. Y., Moore, B., Diemand, J. and Stadel, J. (2007). The survival and disruption of cold dark matter microhaloes: implications for direct and indirect detection experiments, *Monthly Notices of the Royal Astronomical Society* **375**(1): 191–198.

Górski, K. M., Hivon, E., Banday, A. J., Wandelt, B. D., Hansen, F. K., Reinecke, M. and Bartelmann, M. (2005). HEALPix: A Framework for High-Resolution Discretization and Fast Analysis of Data Distributed on the Sphere, *The Astrophysical Journal* **622**.

H.E.S.S. Collaboration (2016). Search for Dark Matter Annihilations towards the Inner Galactic Halo from 10 Years of Observations with H.E.S.S., *Physical Review Letters* **117**(11).

Hooper, D. and Witte, S. J. (2017). Gamma Rays From Dark Matter Subhalos Revisited: Refining the Predictions and Constraints, *Journal of Cosmology and Astroparticle Physics* **4**: 018.
**URL:** http://dx.doi.org/10.1088/1475-7516/2017/04/018

Ishiyama, T. (2014). Hierarchical Formation of Dark Matter Halos and the Free Streaming Scale, *The Astrophysical Journal* **788**(1): 27.

Laffon, H., Smith, D. A., Guillemot, L. and for the Fermi-LAT Collaboration (2015). New pulsars detected in gamma-rays with the Fermi-LAT.
**URL:** *https://arxiv.org/abs/1502.03251*

Lefaucheur, J. and Pita, S. (2017). Research and characterisation of blazar candidates among the Fermi-LAT 3FGL catalogue using multivariate classifications, *Astronomy & Astrophysics* **602**: A86.
**URL:** *http://dx.doi.org/10.1051/0004-6361/201629552*

Lefranc, V. and Moulin, E. (2016). Dark matter search in the inner Galactic halo with H.E.S.S. II, *Proceedings of The 34th International Cosmic Ray Conference — PoS(ICRC2015)*, Sissa Medialab.

Lefranc, V., Moulin, E. and for the H. E. S. S. collaboration (2015). Dark matter search in the inner Galactic halo with H.E.S.S. I and H.E.S.S. II.
**URL:** *https://arxiv.org/abs/1509.04123*

Madau, P., Diemand, J. and Kuhlen, M. (2008). Dark Matter Subhalos and the Dwarf Satellites of the Milky Way, *The Astrophysical Journal* **679**(2): 1260–1271.

MAGIC Collaboration (2018). Indirect dark matter searches in the dwarf satellite galaxy Ursa Major II with the MAGIC telescopes, *Journal of Cosmology and Astroparticle Physics* **2018**(03): 009–009.

Massaro, F., Crespo, N. Á., D'Abrusco, R., Landoni, M., Masetti, N., Ricci, F., Milisavljevic, D., Paggi, A., Chavushyan, V., Jiménez-Bailón, E., Patiño-Álvarez, V., Strader, J., Chomiuk, L., Franca, F. L., Smith, H. A. and Tosti, G. (2016). The gamma-ray blazar quest: new optical spectra, state of art and future perspectives, *Astrophysics and Space Science* **361**(10).

Mirabal, N., Charles, E., Ferrara, E. C., Gonthier, P. L., Harding, A. K., Sánchez-Conde, M. A. and Thompson, D. J. (2016). 3FGL Demographics Outside the Galactic Plane using Supervised Machine Learning: Pulsar and Dark Matter Subhalo Interpretations, *The Astrophysical Journal* **825**: 69.
**URL:** *http://adsabs.harvard.edu/abs/2016ApJ...825...69M*

Moliné, A., Sánchez-Conde, M. A., Palomares-Ruiz, S. and Prada, F. (2017). Characterization of subhalo structural properties and implications for dark matter annihilation signals, *Monthly Notices of the Royal Astronomical Society* **466**: 4974–4990.
**URL:** *http://dx.doi.org/10.1093/mnras/stx026*

Monet, D. G., Levine, S. E., Canzian, B., Ables, H. D., Bird, A. R., Dahn, C. C., Guetter, H. H., Harris, H. C., Henden, A. A., Leggett, S. K., Levison, H. F., Luginbuhl, C. B., Martini, J., Monet, A. K. B., Munn, J. A., Pier, J. R., Rhodes, A. R., Riepe, B., Sell, S., Stone, R. C., Vrba, F. J., Walker, R. L., Westerhout, G., Brucato, R. J., Reid, I. N., Schoening, W., Hartley, M., Read, M. A. and Tritton, S. B. (2003). The USNO-B Catalog, *The Astronomical Journal* **125**(2): 984–993.

Paiano, S., Falomo, R., Franceschini, A., Treves, A. and Scarpa, R. (2017). Optical Spectroscopic Survey of a Sample of Unidentified Fermi Objects, *The Astrophysical Journal* **851**(2): 135.

Peña-Herazo, H. A., Marchesini, E. J., Crespo, N. Á., Ricci, F., Massaro, F., Chavushyan, V., Landoni, M., Strader, J., Chomiuk, L., Cheung, C. C., Masetti, N., Jiménez-Bailón, E., D'Abrusco, R., Paggi, A., Milisavljevic, D., Franca, F. L., Smith, H. A. and Tosti, G. (2017). Optical spectroscopic observations of gamma-ray blazar candidates. VII. Follow-up campaign in the southern hemisphere, *Astrophysics and Space Science* **362**(12).

Pieri, L., Lavalle, J., Bertone, G. and Branchini, E. (2011). Implications of high-resolution simulations on indirect dark matter searches, *Physical Review D* **83**(2).

Press, W. H. and Schechter, P. (1974). Formation of Galaxies and Clusters of Galaxies by Self-Similar Gravitational Condensation, *The Astrophysical Journal* **187**: 425.

Profumo, S., Sigurdson, K. and Kamionkowski, M. (2006). What Mass Are the Smallest Protohalos?, *Physical Review Letters* **97**(3).

Romani, R. W. (2015). A binary counterpart for 2FGL J2039.6-5620, *The Astrophysical Journal Letter* **812**: L24.
**URL:** http://adsabs.harvard.edu/abs/2015ApJ...812L..24R

Roszkowski, L., Sessolo, E. M. and Trojanowski, S. (2018). Wimp dark matter candidates and searches—current status and future prospects, *Reports on Progress in Physics* **81**(6): 066201.
**URL:** http://dx.doi.org/10.1088/1361-6633/aab913

Salvetti, D., Chiaro, G., La Mura, G. and Thompson, D. J. (2017). 3FGLzoo: classifying 3FGL unassociated Fermi-LAT $\gamma$-ray sources by artificial neural networks, *Monthly Notices of the Royal Astronomical Society* **470**(2): 1291–1297.
**URL:** http://dx.doi.org/10.1093/mnras/stx1328

Salvetti, D., Mignani, R. P., Luca, A. D., Delvaux, C., Pallanca, C., Belfiore, A., Marelli, M., Breeveld, A. A., Greiner, J., Becker, W. and Pizzoccaro, D. (2015). Multi-wavelength observations of 3FGL J2039.6-5618: a candidate redback millisecond pulsar, *The Astrophysical Journal* **814**: 88.
**URL:** http://adsabs.harvard.edu/abs/2015ApJ...814...88S

Saz-Parkinson, P. (2017). Latest results on gamma-ray pulsars with Fermi, *Il Nuovo Cimento C* **40**(3): 1–5.

Schoonenberg, D., Gaskins, J., Bertone, G. and Diemand, J. (2016). Dark matter subhalos and unidentified sources in the Fermi 3FGL source catalog, *Journal of Cosmology and Astroparticle Physics* **5**: 028.
**URL:** http://dx.doi.org/10.1088/1475-7516/2016/05/028

SDSS Collaboration (2018). The Fourteenth Data Release of the Sloan Digital Sky Survey: First Spectroscopic Data from the extended Baryon Oscillation Spectroscopic Survey and from the second phase of the Apache Point Observatory Galactic Evolution Experiment, *The Astrophysical Journal Supplementary Series* **235**(2): 42.
**URL:** https://ui.adsabs.harvard.edu/abs/2018ApJS..235...42A

Simon, J. D., Geha, M., Minor, Q. E., Martinez, G. D., Kirby, E. N., Bullock, J. S., Kaplinghat, M., Strigari, L. E., Willman, B., Choi, P. I., Tollerud, E. J. and Wolf, J. (2011). A Complete Spectroscopic Survey of the Milky Way Satellite Segue 1: The Darkest Galaxy, *The Astrophysical Journal* **733**(1): 46.

Sjöstrand, T., Ask, S., Christiansen, J. R., Corke, R., Desai, N., Ilten, P., Mrenna, S., Prestel, S., Rasmussen, C. O. and Skands, P. Z. (2015). An Introduction to PYTHIA 8.2, *Computer Physics Communications* **191**: 159–177.
**URL:** http://adsabs.harvard.edu/abs/2015CoPhC.191..159S

Skrutskie, M. F., Cutri, R. M., Stiening, R., Weinberg, M. D., Schneider, S., Carpenter, J. M., Beichman, C., Capps, R., Chester, T., Elias, J., Huchra, J., Liebert, J., Lonsdale, C., Monet, D. G., Price, S., Seitzer, P., Jarrett, T., Kirkpatrick, J. D., Gizis, J. E., Howard, E., Evans, T., Fowler, J., Fullmer, L., Hurt, R., Light, R., Kopan, E. L., Marsh, K. A., McCallon, H. L., Tam, R., Dyk, S. V. and Wheelock, S. (2006). The Two Micron All Sky Survey (2MASS), *The Astronomical Journal* **131**(2): 1163–1183.

Smith, D. A., Guillemot, L., Kerr, M., Ng, C. and Barr, E. (2017). Gamma-ray pulsars with Fermi, *Proceeding of the 11th INTEGRAL Conference* .
**URL:** https://arxiv.org/abs/1706.03592

Springel, V., Wang, J., Vogelsberger, M., Ludlow, A., Jenkins, A., Helmi, A., Navarro, J. F., Frenk, C. S. and White, S. D. M. (2008). The Aquarius Project: the subhalos of galactic halos, *Monthly Notices of the Royal Astronomical Society* **391**(4): 1685–1711.
**URL:** http://dx.doi.org/10.1111/j.1365-2966.2008.14066.x

Stadel, J., Potter, D., Moore, B., Diemand, J., Madau, P., Zemp, M., Kuhlen, M. and Quilis, V. (2009). Quantifying the heart of darkness with GHALO - a multibillion particle simulation of a galactic halo, *Monthly Notices of the Royal Astronomical Society* **398**(1): L21–L25.

Steigman, G., Dasgupta, B. and Beacom, J. F. (2012). Precise Relic WIMP Abundance and its Impact on Searches for Dark Matter Annihilation, *Physical Review D* **86**(2).
**URL:** http://dx.doi.org/10.1103/PhysRevD.86.023506

Stroh, M. C. and Falcone, A. D. (2013). Swift X-ray Telescope Monitoring of Fermi-LAT Gamma Ray Sources of Interest, *The Astrophysical JournalS* **207**: 28.
**URL:** http://adsabs.harvard.edu/abs/2013ApJS..207...28S

The Cherenkov Telescope Array Consortium (2017). Science with the Cherenkov Telescope Array, *ArXiv e-prints* .
**URL:** http://adsabs.harvard.edu/abs/2017arXiv170907997C

The Planck Collaboration (2016). Planck 2015 results. XIII. Cosmological parameters, *Astronomy & Astrophysics* **594**: A13.
**URL:** http://dx.doi.org/10.1051/0004-6361/201525830

The Planck Collaboration (2020). Planck 2018 results. VI. Cosmological parameters, *Astronomy & Astrophysics* **641**: A6.
**URL:** http://dx.doi.org/10.1051/0004-6361/201833910

van den Bosch, F. C., Ogiya, G., Hahn, O. and Burkert, A. (2017). Disruption of dark matter substructure: fact or fiction?, *Monthly Notices of the Royal Astronomical Society* **474**(3): 3043–3066.

VERITAS Collaboration (2017). Dark matter constraints from a joint analysis of dwarf Spheroidal galaxy observations with VERITAS, *Physical Review D* **95**: 082001.
**URL:** https://link.aps.org/doi/10.1103/PhysRevD.95.082001

Walker, M. G. (2013). *Dark Matter in the Milky Way's Dwarf Spheroidal Satellites*.
**URL:** http://adsabs.harvard.edu/abs/2013pss5.book.1039W

Weniger, C. (2012). A Tentative Gamma-Ray Line from Dark Matter Annihilation at the Fermi Large Area Telescope, *Journal of Cosmology and Astroparticle Physics* **2012**(08): 007–007.
**URL:** http://dx.doi.org/10.1088/1475-7516/2012/08/007

Wood, M., Caputo, R., Charles, E., Mauro, M. D., Magill, J. and for the Fermi-LAT Collaboration, J. P. (2017). Fermipy: An open-source Python package for analysis of Fermi-LAT Data.
**URL:** https://arxiv.org/abs/1707.09551

Wright, E. L., Eisenhardt, P. R. M., Mainzer, A., Ressler, M. E., Cutri, R. M., Jarrett, T., Kirkpatrick, J. D., Padgett, D., McMillan, R. S., Skrutskie, M., Stanford, S. A., Cohen, M., Walker, R. G., Mather, J. C., Leisawitz, D., III, T. N. G., McLean, I., Benford, D., Lonsdale, C. J., Blain, A., Mendez, B., Irace, W. R., Duval, V., Liu, F., Royer, D., Heinrichsen, I., Howard, J., Shannon, M., Kendall, M., Walsh, A. L., Larsen, M., Cardon, J. G., Schick, S., Schwalm, M., Abid, M., Fabinsky, B., Naes, L. and Tsai, C.-W. (2010). The Wide-field Infrared Survey Explorer (WISE): Mission Description and Initial On-orbit Performance, *The Astronomical Journal* **140**(6): 1868–1881.
**URL:** http://dx.doi.org/10.1088/0004-6256/140/6/1868

Xia, Z.-Q., Duan, K.-K., Li, S., Liang, Y.-F., Shen, Z.-Q., Yue, C., Wang, Y.-P., Yuan, Q., Fan, Y.-Z., Wu, J. and Chang, J. (2017). 3FGL J1924.8-1034: A spatially extended stable unidentified GeV source?, *Physical Review D* **95**(10).

Zechlin, H.-S., Fernandes, M. V., Elsässer, D. and Horns, D. (2012). Dark matter subhaloes as gamma-ray sources and candidates in the first Fermi-LAT catalogue, *Astronomy & Astrophysics* **538**: A93.
**URL:** http://dx.doi.org/10.1051/0004-6361/201117655

Zechlin, H.-S. and Horns, D. (2012). Unidentified sources in the fermi-lat second source catalog: the case for dm subhalos, *Journal of Cosmology and Astroparticle Physics* **2012**(11): 050–050.
**URL:** http://dx.doi.org/10.1088/1475-7516/2012/11/050

Zhao, H., Hooper, D., Angus, G. W., Taylor, J. E. and Silk, J. (2007). Tidal Disruption of the First Dark Microhalos, *The Astrophysical Journal* **654**(2): 697–701.

Zhu, Q., Marinacci, F., Maji, M., Li, Y., Springel, V. and Hernquist, L. (2016). Baryonic impact on the dark matter distribution in Milky Way-sized galaxies and their satellites, *Monthly Notices of the Royal Astronomical Society* **458**(2): 1559–1580.

# Chapter 4

# Spectral and spatial analysis of the dark matter subhalo candidates among *Fermi* Large Area Telescope unidentified sources

*Based on J. Coronado-Blázquez et al., Journal of Cosmology and Astroparticle Physics* ***1911*** *(2019) 045*

## 4.1 Introduction

During the last years, different search strategies have been employed in the quest for dark matter (DM) detection Garrett and Duda (2011); Roszkowski et al. (2018). Among these, we find direct detection experiments, designed to observe the elastic scattering of DM-nuclei interactions, DM production in accelerators such as the LHC, and indirect searches that look for the annihilation or decay products of DM. These approaches are in many cases complementary, allowing us to probe different classes of DM candidates, subject to different uncertainties.

Gamma rays have been hailed as the "golden channel" for indirect DM detection, as they are not deflected by magnetic fields as opposed to antimatter produced in DM annihilation or decays, and are easier to detect than neutrinos. With gamma-ray telescopes, many different observational targets have been pursued. Among the most promising sources are the Galactic center (GC) Fermi-LAT Collaboration (2016b, 2017c); H.E.S.S. Collaboration (2016); Pierre et al. (2014), dwarf spheroidal galaxies (dSphs) Fermi-LAT Collaboration (2015c); Oakes et al. (2019); Ahnen, M. L. et al. (2016) and galaxy clusters Fermi-LAT Collaboration (2015b). Although the GC is expected to be the brightest source of gamma rays produced by DM annihilation, the astrophysical gamma-ray background, in the form of unresolved diffuse Galactic emission, is significant and poorly understood Fermi-LAT Collaboration (2017b); Bartels et al. (2017). In contrast, while the astrophysical background for dSphs is expected to be quite low, its DM annihilation signal is predicted to be comparatively fainter, and subject to large uncertainties due to the imprecise DM content modelling.

Another interesting and complementary target in gamma-ray searches are the dark satellites. Within the standard ΛCDM paradigm, the DM halos that host galaxies are expected to contain a large amount of substructure (subhalos) as a consequence of the bottom-up hierarchical formation history Madau et al. (2008). The largest members of this subhalo population (above $\sim 10^7$ M ) will host dSphs, yet most of them are not massive enough to retain baryonic (i.e. gas) content and form

stars, and therefore should remain completely dark Walker (2013). These objects are predicted to be compact and concentrated, and therefore, if near enough and composed of *Weakly Interacting Massive Particles* (WIMPs), they would yield a significant flux of gamma rays that could be detectable by gamma-ray observatories such as *Fermi*-LAT Fermi-LAT Collaboration and Atwood (2009). The main advantage of these sub-halos are that they are not expected to host any non-DM astrophysical gamma-ray emitters, their large number density in the Galaxy and their high concentrations of DM. The main disadvantages come from uncertainties in their structural properties, their exact number and their distribution in the Galaxy. These also translate into a total lack of knowledge on their sky position. Although subhalos are expected to be almost isotropically distributed from the Earth point of view Springel, White, Frenk, Navarro, Jenkins, Vogelsberger, Wang, Ludlow and Helmi (2008), in general terms, only those located close to us may yield annihilation fluxes large enough to be detected.

A large number of *Fermi*-LAT detected sources lack proper astrophysical association and remain as unidentified sources (unIDs), therefore being perfect candidates to perform this search of Galactic DM subhalos or dark satellites. Many works have already used these targets for indirect DM detection Bertoni et al. (2015, 2016); Calore et al. (2017); Schoonenberg et al. (2016); Hooper and Witte (2017); Berlin and Hooper (2014); Zechlin et al. (2012); Zechlin and Horns (2012); Belikov et al. (2012); Buckley and Hooper (2010); Fermi-LAT Collaboration (2012b). In a previous work Coronado-Blázquez et al. (2019) we performed a filtering of those unIDs present in the latest point-source catalogs (namely 3FGL Fermi-LAT Collaboration (2015a), 2FHL Fermi-LAT Collaboration (2016a), and 3FHL Fermi-LAT Collaboration (2017a)) according to the expected emission from DM subhalo annihilation. Then, we combined these catalog filtering results with a state-of-the-art N-body simulation, conveniently repopulated with low-mass subhalos below the original mass resolution limit, to set constraints on the DM annihilation cross section. To do so, it was necessary to perform a full characterization of the *Fermi*-LAT sensitivity to DM annihilation for different annihilation channels and sky positions. The obtained constraints were competitive, ruling out canonical thermal WIMPs up to $\sim$6 GeV in the case of $\tau^+\tau^-$ annihilation.

In Coronado-Blázquez et al. (2019), from a total of 1235 (1010 3FGL + 48 2FHL + 177 3FHL) unIDs, we were able to discard all but 44 unIDs (16 3FGL + 1 2FHL + 24 3FHL) as DM subhalos outside the Galactic plane ($|b| \geq 10^\circ$). Although no spectral information was explicitly used, the filter based on machine learning results Lefaucheur and Pita (2017); Salvetti et al. (2017) to reject unIDs as DM subhalo candidates implicitly did. However, we note that such filter referred to just a general and coarse analysis which searched for active galactic nuclei (AGN) features, such as the spectral index of the source, and only relying on the official, 4-year LAT data Fermi-LAT Collaboration (2015a). In this work, we perform a full, dedicated spectral analysis of these 44 remaining candidates using all 10-year *Fermi*-LAT available data, in order to confirm or discard their DM origin. With all this new spectral information at hand, we can reduce the number of potential subhalos among unIDs even further, to point out the best DM candidates, and to update our previous DM constraints, following the procedure described in Coronado-Blázquez et al. (2019) (see also Calore et al. (2017)). As it was shown in that analysis, the fewer the sources compatible with DM, the stronger the DM constraints.

In the process, it will be also necessary to address the long-standing problem of confusion between gamma-ray emission from pulsars and DM Mirabal (2013); Mirabal et al. (2016). This confusion is due to annihilating WIMP DM having similar

spectra to most pulsars Fermi-LAT Collaboration (2012b) for low, $\mathcal{O}(10)$ GeV WIMP masses, especially for annihilation into $b\bar{b}$ quarks. As we will show in this work, a more clear separation between both classes of sources may be possible should the work be done in an optimal parameter space entirely built upon the available spectral information.

Additionally, spatial source extension has been pointed out to be a "smoking gun" for this kind of indirect DM searches Bertoni et al. (2016). Therefore, we also perform a spatial analysis for the candidates surviving the DM spectral analysis. Should any of the considered sources exhibit significant extension, a DM origin would become a plausible option.

The structure of this paper is as follows: in Section 4.2, we perform the spectral analysis and apply the relevant statistical tests needed to confidently evaluate the DM origin hypothesis. In Section 9.4, we set DM constraints taking into account what is learnt from our spectral analysis. Section 4.4 presents a promising new tool to discriminate between DM annihilation and pulsars. Our search for spatial extension on the most interesting candidates that we found after our spectral analysis is presented in Section 4.5. A search for potential stellar streams in *Gaia* DR2 within our best candidates is done in Section 4.6. We conclude our report in Section 4.7.

## 4.2 Spectral analysis of DM candidates

### 4.2.1 Technical setup and analysis pipeline

The spectral analysis is performed with *Fermipy* Wood et al. (2017). We use almost 10 years of data (MET[1] 239557417 to 541779795). The energy range is chosen to avoid photons under 300 MeV due to the intense diffuse emission, which would make the analysis very time-consuming. We use Pass 8 events Atwood et al. (2013), with the `P8R3_SOURCE_V2` instrumental response functions (IRFs, Bruel et al. (2018)), and utilize all available photons (FRONT+BACK), excluding those arriving with zenith angles greater than 100° below 1 GeV and 105° above.

To compute the detection significance of the source, we adopt the Test Statistic,

$$\mathrm{TS} = -2 \cdot \log \left[ \frac{\mathcal{L}(H_1)}{\mathcal{L}(H_0)} \right] \tag{4.1}$$

where $\mathcal{L}(H_0)$ and $\mathcal{L}(H_1)$ are respectively the likelihoods under the null (no source) and alternative (existing source) hypotheses.

A region of interest (ROI) of $18° \times 18°$ around the reported position is chosen for each source, with an angular bin size of 0.06° and 8 (4) evenly spaced logarithmic energy bins for sources with TS>100 (TS<100). To model point sources lying within the ROI, we use the preliminary 8-year point source catalog, the so-called FL8Y[2]. In this analysis, the `gll_iem_v06.fits` diffuse and `iso_P8R3_SOURCE_V2.txt` isotropic templates are used[3]. A summary of the analysis setup can be found in Table 4.1.

First of all, we run `GTAnalysis`[4] and define the full analysis setup. Then, we perform the initial fit running the `GTAnalysis.free_sources`, `GTAnalysis.fit` and `GTAnalysis.optimize` modules. We remove sources under the $TS = 25$ ($\sim 5\sigma$) detection threshold and find new sources over it with `GTAnalysis.find_sources`. If

[1] MET: *Mission Ellapsed Time*

[2] https://fermi.gsfc.nasa.gov/ssc/data/access/lat/fl8y/

[3] https://fermi.gsfc.nasa.gov/ssc/data/access/lat/BackgroundModels.html

[4] https://fermipy.readthedocs.io/en/latest/

| | |
|---|---|
| Time domain (ISO 8601) | 2008-08-04 to 2018-03-03 |
| Time domain (MET) | 239557417 to 541779795 |
| Energy range | 300 MeV - 800 GeV |
| IRF | `P8R3_SOURCE_V2` |
| Event type | FRONT+BACK |
| Point-source catalog | FL8Y |
| ROI size | $18^\circ \times 18^\circ$ |
| Angular bin size | $0.06^\circ$ |
| Bins per energy decade | 4 (TS<100) or 8 (TS>100) |
| Galactic diffuse model | `gll_iem_v06.fits` |
| Isotropic diffuse model | `iso_P8R3_SOURCE_V2.txt` |

TABLE 4.1: Summary of the spectral analysis technical setup. See Section 4.2 for details.

the unID source is found to have $TS \geq 25$, we recalculate its sky position with the `GTAnalysis.localize` module. We also obtain a TS detection map of the whole ROI, removing the candidate source to verify that the residuals look good in the rest of the region and the found excess is indeed due to the unID. Also, the gamma-ray spectral energy distribution (SED) of the source is generated with the `GTAnalysis.sed` module.

Now we perform the spectral fit using the three different parametric functions given below,

- Power law (PL):

$$\frac{dN}{dE} = K \left( \frac{E}{E_0} \right)^{-\Gamma} \tag{4.2}$$

  where $K$ is the normalization, $\Gamma$ is the photon spectral index and $E_0$ sets the energy scale. This form is widely used to fit gamma-ray AGNs and other sources.

- Log-parabola (LP):

$$\frac{dN}{dE} = K \left( \frac{E}{E_0} \right)^{-\Gamma - \beta \cdot \log(E/E_0)} \tag{4.3}$$

  where, in addition to those parameters in Eq. 4.2, the parameter $\beta$ or spectral curvature index is included. This parametric form is used to fit both blazars and pulsars, although it can also provide a good spectral description for DM in certain cases. Further details on $\beta$ in the context of DM searches will be discussed in Section 4.4.

- Power law with super-exponential cutoff (PLE):

$$\frac{dN}{dE} = K \left( \frac{E}{E_0} \right)^{-\Gamma} e^{-\left(\frac{E}{E_{cut}}\right)^{\beta}} \tag{4.4}$$

  that includes $E_{cut}$ as the cutoff energy and $\beta$ as the super-exponential index. This spectral shape is normally used to fit pulsars, although it also fits well some possible DM annihilation spectra Coronado-Blázquez et al. (2019) Calore

et al. (2017). This fact reflects the above-mentioned spectral confusion between pulsars and DM Fermi-LAT Collaboration (2012b); Mirabal (2013); Mirabal et al. (2016).

The fit is performed with `GTAnalysis.optimize` and `GTAnalysis.fit` for these three parametric forms, leaving free the normalization of the sources within a radius of 2° from the center of the ROI. We obtain the log-likelihood and the spectral parameters with their $1\sigma$ uncertainties. By comparing the log-likelihoods obtained for each of the three parametric forms, we are able to determine the best-fit model. In many cases, though, we anticipated that two or even the three of these models will yield similar likelihoods due to typically poor photon statistics.

Figure 4.1 shows the results of some of the steps in our analysis, for two different types of sources in our unIDs list, i.e., with SEDs well described by PL and PLE in each corresponding case.

From the DM perspective, this procedure assumes that the SED is entirely produced by DM annihilations. The fit is performed with `DMFitFunction` Jeltema and Profumo (2008)[5]. The differential spectrum for a pure annihilation channel[6] is given by

$$\frac{dN}{dE} = K \cdot F_{m_\chi, C}, \tag{4.5}$$

where $K = \langle \sigma v \rangle \cdot J$ is the normalization, product of velocity-averaged annihilation cross section times the so-called J-factor, $F_{m_\chi, C}$ is the photon flux for channel $C$ and DM particle mass $m_\chi$ at the energy under consideration. We fit the spectra to eight different annihilation channels, namely $b\bar{b}$, $\tau^+\tau^-$, $t\bar{t}$, $c\bar{c}$, $Z^0Z^0$, $W^+W^-$, $e^+e^-$ and $\mu^+\mu^-$. For each channel then, this DM fit will return the log-likelihood, the DM mass and $K$ with their $1\sigma$ uncertainties.

Once both the best-fit astrophysical and DM models have been obtained, our goal is to evaluate the statistical preference of DM against an astrophysical origin of the emission for each source in our DM subhalo candidates' list.

### 4.2.2 Analysis results and DM hypothesis test

We perform the analysis of the 44 (4 2FHL, 24 3FHL and 16 3FGL) unID candidates that were found to be compatible with DM in Coronado-Blázquez et al. (2019). The full list with all unIDs can be found in the supplementary material of Coronado-Blázquez et al. (2019). Two out of these 44 unIDs, 3FHL J0350.4−5153 and 3FHL J1650.9+0430, are rejected as DM subhalos, as an X-ray counterpart was found in a multiwavelength search with *Swift*-XRT Kaur et al. (2019). An additional source, 3FHL J0233.0+3742, is also removed as it is associated as an active galaxy of uncertain type (BCU) in the 4FGL catalog Fermi-LAT Collaboration (2020).

We note that the detection significance of a true source is expected to increase as the square root of time. Yet, a total of nine sources (2FHL J1630.0+7644, 3FGL J0244.4+4745, 3FGL J0538.8−0341, 3FGL J1958.2−1413, 3FHL J0055.8+4507, 3FHL J0121.8+3808, 3FHL J0550.9+5657, 3FHL J1403.4+4319 and 3FHL J1726.2−1710) lie now below the detection threshold ($TS = 25$) and therefore are removed from our

[5] We will later use the DM spectra as computed by Cirelli et al. (2011), which only differs from this one for very heavy WIMPs, beyond the WIMP masses that this study probes.

[6] We focus on pure annihilation channels in order to stay agnostic to the underlying particle physics model.

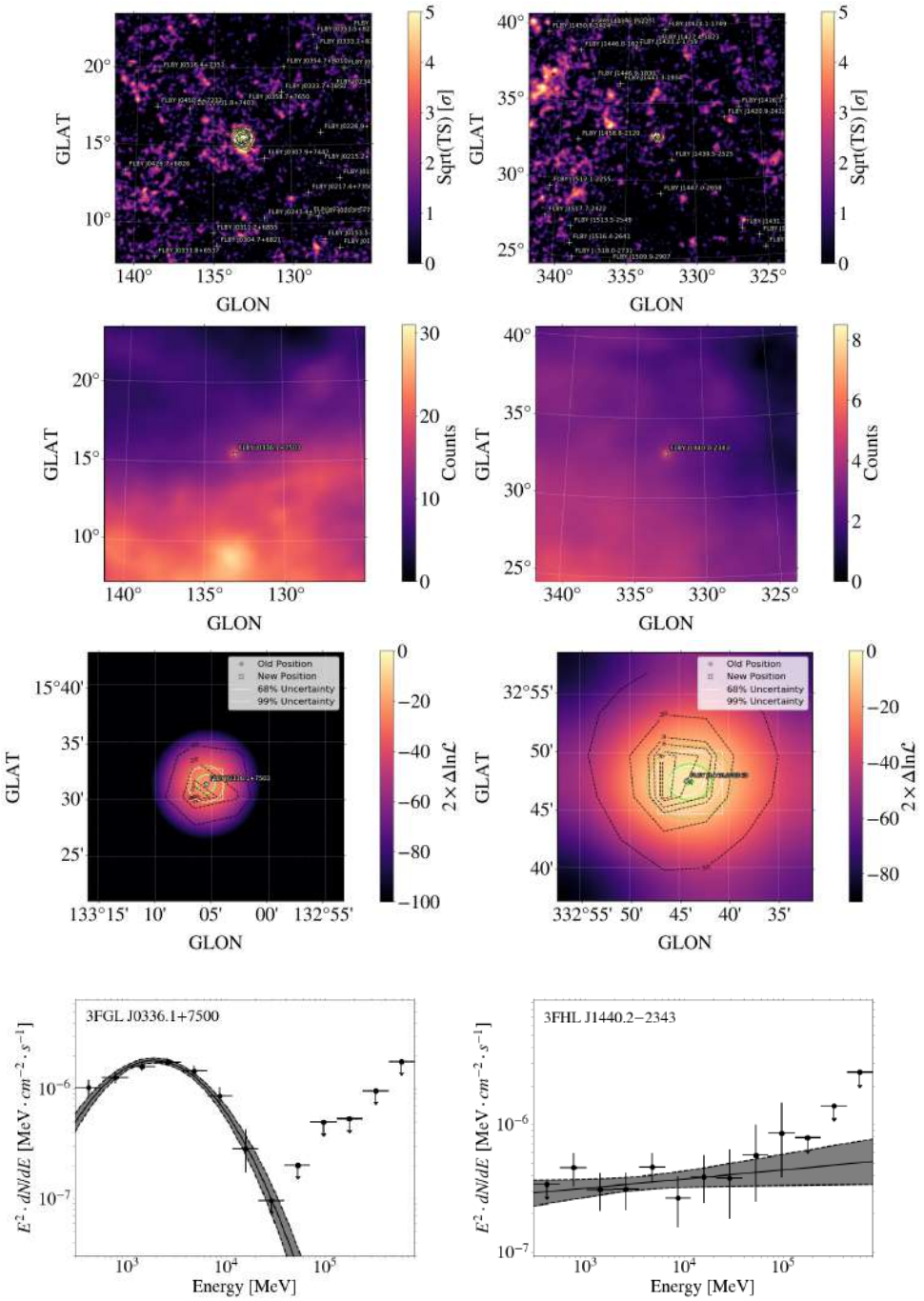


FIGURE 4.1: Results examples of our spectral analysis, for two different types of sources in our unIDs' list: 3FGL J0336.1+7500 (left panels) and 3FHL J1440.2−2343 (right panels). The first is a bright source (detected at TS=1095) whose SED is best described by a PLE (see Eq. 4.4); while the second is a faint (TS=135) object for which a PL (Eq. 4.2) is preferred. First row is the ROI residual map leaving the unID unmodelled, so that the TS peak is clearly visible. Second row shows the model of expected counts in the ROI. The location of the source, compared with the FL8Y reported position (green circle), is shown in the third row. The fourth row features the gamma-ray SED with the best-fit spectral model and $1\sigma$ uncertainties overimposed (solid line with gray shaded regions).

sample[7]. We also found some sources for which the corresponding detection TS ($TS_d$) did not change as expected when considering a larger integration time, indeed still remaining near the detection threshold. This may be a hint of statistical artifacts due to mis-modeling of the diffuse emission. 3FHL J0041.7−1608 ($TS_d = 29.48$), 3FHL J0115.4−2916 ($TS_d = 30.77$) and 3FHL J0838.5+4006 ($TS_d = 26.66$) show this behavior[8]. Nevertheless, in the conservative spirit of this work, we do not discard these sources as potential DM subhalos, as doing it would improve the constraints.

For the remaining 32 unIDs, we test the DM hypothesis against the astrophysical origin of the emission. In order to compare the log-likelihoods of the best astrophysical model vs. DM, we must take into account the degrees of freedom (d.o.f.), $k$, of each model Wang et al. (2016). Indeed, from Eqs. 4.2 to 4.5, it can be seen that PL has the same number of d.o.f. as `DMFit`, $k = 3$, while LP has $k = 4$ and PLE $k = 5$. Therefore, those models with more d.o.f. might provide better fits in some cases just because they have more parameters.

To penalize those models with higher d.o.f, we use the Akaike Information Criterion (AIC) Akaike (1974),

$$\Delta TS = 2 \cdot \left[ (k_0 - k_\chi) + \log\left(\frac{\mathcal{L}_\chi}{\mathcal{L}_0}\right) \right] \tag{4.6}$$

where $k_0$ and $k_\chi$ are the d.o.f. of the astrophysical and DM best-fit models, respectively, and $\mathcal{L}_\chi$ ($\mathcal{L}_0$) is the likelihood of the DM (astrophysical) best-fit model.

Figure 4.2 shows the ΔTS distribution for all fitted sources and channels. The most successful annihilation channel is $b\bar{b}$, followed by $c\bar{c}$ and $\tau^+\tau^-$. Other leptonic channels such as $e^+e^-$ and $\mu^+\mu^-$ are able to fit only five and two sources, respectively. The less successful channels are $W^+W^-$, that can only fit two sources, and $t\bar{t}$, with no sources.

From our analysis, no unID in our initial list is found to prefer a DM origin significantly. Indeed, only seven sources have (at least) one annihilation channel marginally preferred over an astrophysical model (ΔTS>0). However, all of them are far from being significant. Indeed, the maximum ΔTS reached is 10.3, well below the $5\sigma$ significance threshold (ΔTS∼25) Fermi-LAT Collaboration (2015c). Only in a couple of cases there is a $\sim 3\sigma$ preference for DM. For a given channel, we will reject as DM subhalos those sources with ΔTS>-9, i.e., the astrophysical model preferred at most at $\sim 3\sigma$. This ensures the false-negative ratio to be negligible. In any case, we note that the obtained ΔTS are pre-trials. Any potential factor that should be applied to correct for trials would go in the direction of decreasing the DM significance values. We do not perform such correction here, as the largest DM significances we found are already very low and thus the derivation of post-trials significances is not necessary.

In Table 4.2, we summarize the best fit DM models for those cases in which ΔTS>0. The table provides the annihilation channel, the ΔTS and the DM mass of the best fit. The SEDs of these seven objects, with the best-fit DM annihilation channel overimposed, are shown in Figure 4.3. Note that the choice of number of bins is found to only marginally affect the ΔTS. A full table with the selection criteria for all unIDs can be found in Appendix 4.8.

[7] The reason why they do not reach the threshold may be different in each case. For the 3FGL sources we use different diffuse and isotropic models, as well as Pass 8 events instead of Pass 7. For 2FHL and 3FHL a possible cause may be that these sources were previously detected in a flaring state, which is now over (though given their low detection significances, just above the threshold, a statistical fluctuation is actually more plausible than a past flaring state.

[8] In fact, the TS is found to hardly increase with respect to the TS in the published catalogs.

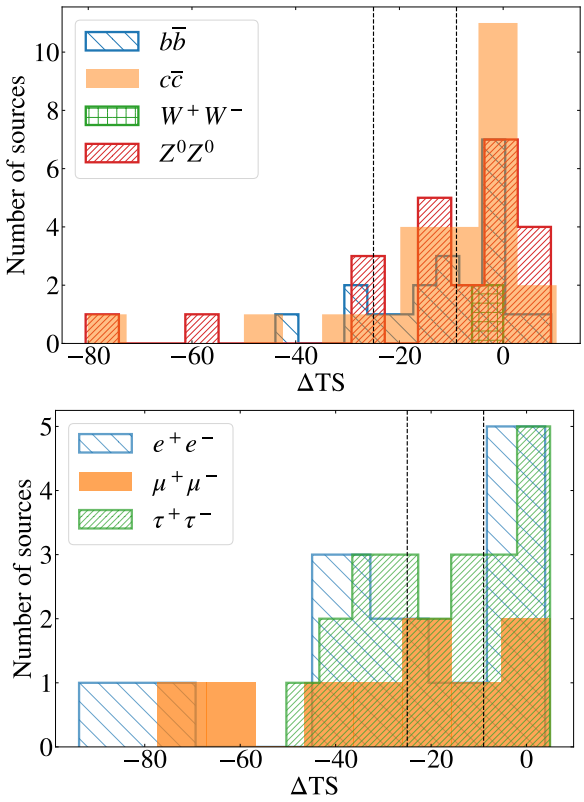


FIGURE 4.2: Distribution of ΔTS values as defined in Eq. 4.6 for the comparison between astrophysical models and DM fits. The left (right) panel is for hadronic (leptonic) annihilation channels. The two vertical dashed lines mark $\Delta TS = -25$ and $\Delta TS = -9$, i.e., the best-fit astrophysical model is preferred against DM at $\sim 5$ and $\sim 3\sigma$, respectively. Note that the $t\bar{t}$ channel does not appear in these plots, as no source is found to be well fitted by it.

## 4.3 Limits on the DM annihilation cross section

Our analysis of unID spectral properties in Section 4.2 has been useful to safely decrease the original number of DM subhalo candidates. In the absence of outstanding DM candidates in the remaining list (see, e.g., the ΔTS values in Table 4.2), we now proceed to set constraints on the DM annihilation cross section.

The procedure is the same as in Coronado-Blázquez et al. (2019), and, thus, we refer the reader to the mentioned work for further details. The methodology consists on a comparison between the predicted number of subhalos in the simulations that should outshine in gamma rays for the LAT, and the actual number of remaining unIDs in LAT catalogs that may still be potential DM subhalos according to our studies. The smaller the number of remaining unIDs the stronger the DM constraints. In this sense, the constraints in this section represent an updated version of the constraints presented in Coronado-Blázquez et al. (2019). Following our previous work, the velocity-averaged annihilation cross section can be expressed as:

$$\langle \sigma v \rangle = \frac{8 \cdot \pi \cdot m_\chi^2 \cdot F_{min}}{J \cdot N_\gamma} \tag{4.7}$$

where $F_{min}$ is the instrumental sensitivity to DM, $J$ the nominal value of the subhalos' J-factor, and $N_\gamma$ the DM spectrum for a particular annihilation channel integrated

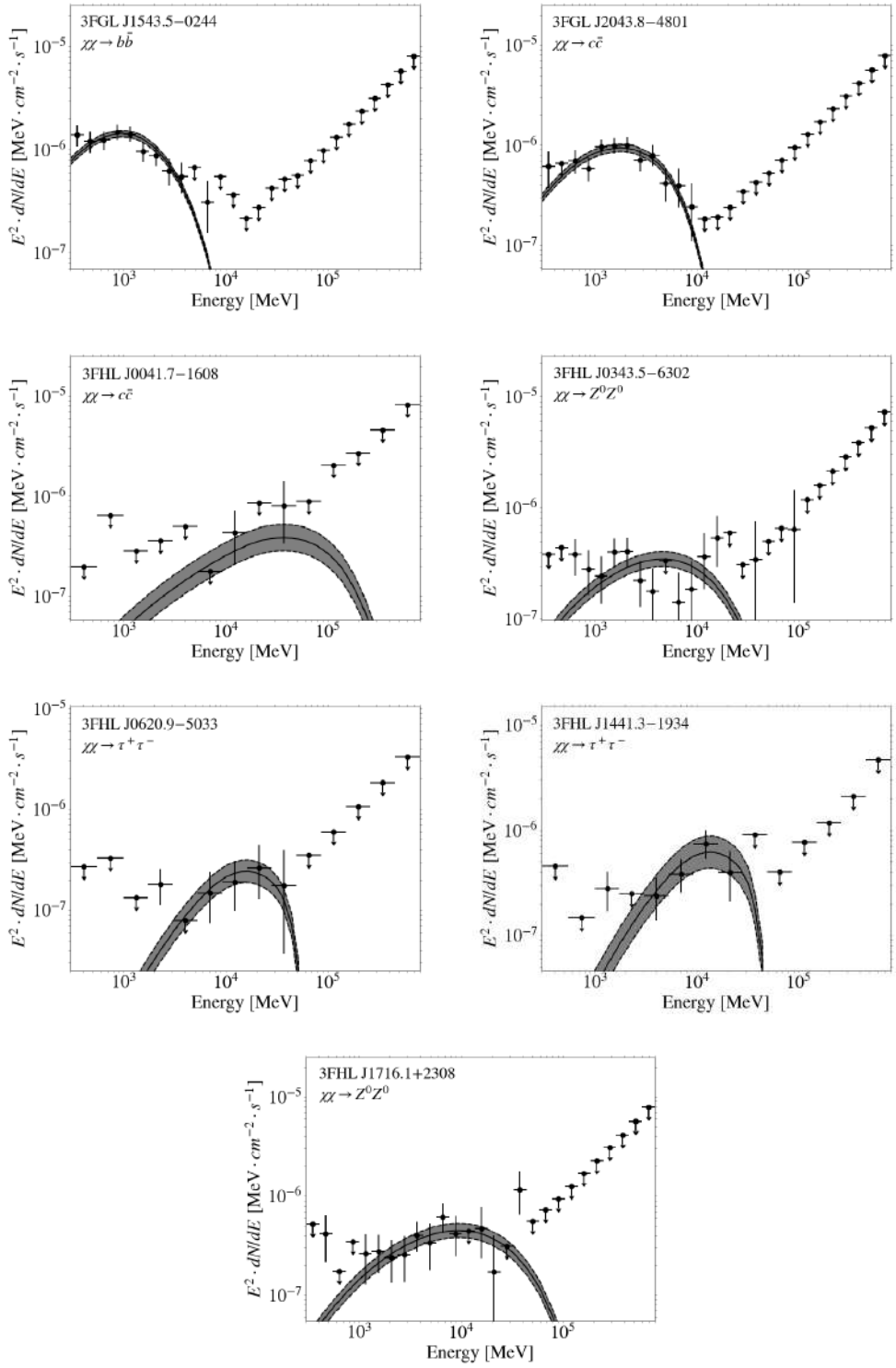


FIGURE 4.3: SED of the seven candidates with ΔTS>0 listed in Table 4.2. Overimposed is the best-fit DM annihilation channel in each case. Note the significantly smaller model uncertainties in the case of the 3FGL sources (top panels).

within the energy range under consideration. In the current work, the constraining power depends on the number of sources that can be fitted by each annihilation channel, e.g., while for $b\bar{b}$ we have five 3FGL and six 3FHL sources that cannot be

| Source name | DM channel(s) | ΔTS | $m_\chi$ (GeV) | Astro. models |
|---|---|---|---|---|
| 3FGL J1543.5−0244 | $b\bar{b}$ | 9.26 | $15.2 \pm 1.3$ | LP, PLE |
| | $Z^0Z^0$ | 8.29 | $11.1 \pm 0.9$ | |
| | $c\bar{c}$ | 6.27 | $11.8 \pm 0.7$ | |
| 3FGL J2043.8−4801 | $c\bar{c}$ | 10.31 | $22.4 \pm 1.7$ | PLE, LP |
| | $Z^0Z^0$ | 9.21 | $23.3 \pm 5.7$ | |
| | $\tau^+\tau^-$ | 3.21 | $8.5 \pm 0.4$ | |
| 3FHL J0041.7−1608 | $c\bar{c}$ | 1.87 | $666 \pm 99$ | PL |
| 3FHL J0343.5−6302 | $Z^0Z^0$ | 3.89 | $112 \pm 14$ | PL, LP |
| | $c\bar{c}$ | 0.59 | $67.1 \pm 6.7$ | |
| 3FHL J0620.9−5033 | $\tau^+\tau^-$ | 0.63 | $56.7 \pm 9.2$ | PL, PLE |
| 3FHL J1441.3−1934 | $\tau^+\tau^-$ | 4.92 | $48.1 \pm 13.3$ | PLE, PL |
| | $\mu^+\mu^-$ | 4.91 | $29.6 \pm 2.9$ | |
| | $e^+e^-$ | 3.89 | $29.6 \pm 3.0$ | |
| | $b\bar{b}$ | 2.79 | $328 \pm 45$ | |
| | $c\bar{c}$ | 2.68 | $197 \pm 22$ | |
| | $Z^0Z^0$ | 2.12 | $299 \pm 32$ | |
| 3FHL J1716.1+2308 | $Z^0Z^0$ | 3.19 | $207 \pm 25$ | PLE, PL |
| | $c\bar{c}$ | 2.59 | $162 \pm 47$ | |

TABLE 4.2: Sources exhibiting positive ΔTS values, sorted by catalog and right ascension (RA), following its definition in Eq. 4.6, i.e., in these cases DM is preferred against astrophysical models. The second column shows the DM channel(s) for which we have positive ΔTS. For almost all these sources, there are different channels providing ΔTS>0. The third column gives their corresponding ΔTS. These values are far from being significant; see also discussion in the text. The fourth column shows best-fit DM mass with $1\sigma$ uncertainty. The last column reports the best-fit astrophysical models.

ruled out as DM subhalos, for $\tau^+\tau^-$ we have just one 3FGL and four 3FHL unIDs. There are not 2FHL sources in any channel.

We conservatively consider as potential DM subhalos those unIDs for which the ΔTS as defined in Eq. 4.6, and obtained from spectral fits to DM and astrophysical models, is $\Delta TS \geq -9$, i.e., the spectral astrophysical models are preferred against DM at less than $3\sigma$. The weakest limits are for $\tau^+\tau^-$, with one 3FGL and four 3FHL sources and $c\bar{c}$, with seven sources both in 3FGL and 3FHL (see Table 4.3 for all channels and catalogs). The strongest limits are for the $t\bar{t}$ channel, as it does not provide good fits to any source[9]. No DM subhalo annihilating into pure channels is present in the 2FHL catalog according to our spectral analysis, and therefore the corresponding DM constraints for this catalog are already at the level of sensitivity reach (i.e., the maximum potential of the method) for all considered channels.

As in Coronado-Blázquez et al. (2019), and in order to obtain 95% C.L. upper limits for a given number $n$ of remaining unIDs, we integrate the distribution of J-factor values corresponding to the $n^{th}$ brightest subhalo as obtained from our 1000 VL-II realizations, and take the J-factor above which 95% of the whole distribution is contained as the value of $J$ to be used in Eq. 8.3.

In Figure 8.5 we present the constraints for $b\bar{b}$ and $\tau^+\tau^-$ annihilation channels. They are able to rule out canonical thermal WIMPs with masses up to ∼10 GeV for

[9] As stated in Coronado-Blázquez et al. (2019), we are in the sensitivity reach scenario.

| | $b\bar{b}$ | $c\bar{c}$ | $t\bar{t}$ | $\tau^+\tau^-$ | $e^+e^-$ | $\mu^+\mu^-$ | $W^+W^-$ | $Z^0Z^0$ |
|---|---|---|---|---|---|---|---|---|
| 2FHL | 0 | 0 | 0 | 0 | 0 | 0 | 0 | 0 |
| 3FHL | 6 | 8 | 0 | 4 | 4 | 2 | 1 | 6 |
| 3FGL | 5 | 7 | 0 | 1 | 1 | 0 | 1 | 6 |

TABLE 4.3: Summary of the number of sources from the three different catalogs which are fitted to DM annihilation channels with $\Delta TS \geq -9$. There is no overlap between catalogs, i.e., no source from a particular catalog is present in one of the other two. There is no 2FHL source or $t\bar{t}$ channel fit present in the final result.

$b\bar{b}$ and $\sim$20 GeV for $\tau^+\tau^-$. With respect to our previous work, these constraints improve between a factor 2-5 depending on the annihilation channel. The uncertainty bands correspond to the $1\sigma$ uncertainty obtained after averaging $F_{min}$ over the whole sky. Also, in the case of the 3FGL constraint, we note that the upper half of the uncertainty band is larger than the lower half due to the way the machine learning conservative false positive rate is implemented in the unID filtering of Coronado-Blázquez et al. (2019)[10]. As done in our previous work, in those cases where no unID is compatible with DM, we prefer to stay conservative and still adopt the J-factor of the brightest subhalo in the simulation. For the limits in Figure 8.5, this is the case of the ones derived from the 2FHL catalog for $b\bar{b}$, and $\tau^+\tau^-$.

Figure 4.5 shows the envelope of the limits presented in Figure 8.5, together with other independent limits from targets such as the MW halo with H.E.S.S. Lefranc et al. (2015), the cosmic microwave background with *Planck* DR3 The Planck Collaboration (2020) and the dSphs with *Fermi*-LAT Fermi-LAT Collaboration (2015c). Our limits are a factor 2-4 weaker than the dSphs constraints, while they are more competitive than H.E.S.S. below $\sim 200 - 400$ GeV (depending on the channel). Also, in the case of $\tau^+\tau^-$, they improve *Planck* DR3 constraints by a factor $\sim$ 2 up to 300 GeV.

## 4.4 The $\beta$ plot: a technique to address DM/pulsar confusion

Spectral confusion between pulsars and DM annihilation signals has been a long issue in the quest for DM in gamma rays (see for example Mirabal (2013); Mirabal et al. (2016); Fermi-LAT Collaboration (2012b)), especially for low, $\mathcal{O}(10)$ GeV DM masses, and when considering hadronic channels such as $b\bar{b}$. In this section we propose a test that could help distinguish them, at least in some particular cases.

The test starts from the preliminary 4FGL *Fermi*-LAT source catalog Fermi-LAT Collaboration (2020). More precisely, we focus on those sources in the catalog that are well fitted by a LP (see Eq. 4.3). We take the curvature spectral index, $\beta$, of the sources in the catalog and the peak energy, $E_{peak}$, i.e., the energy at which the energy flux reaches its maximum, computed from 4FGL parameters as,

$$E_{peak} = E_0 \cdot e^{\frac{2-\alpha}{2\beta}} \tag{4.8}$$

[10] In short, the expected false positive ratio ($\leq$ 4%) is taken into account defining as the upper band the limit obtained considering a J-factor corresponding to six more sources (4% of the used sample) remaining.

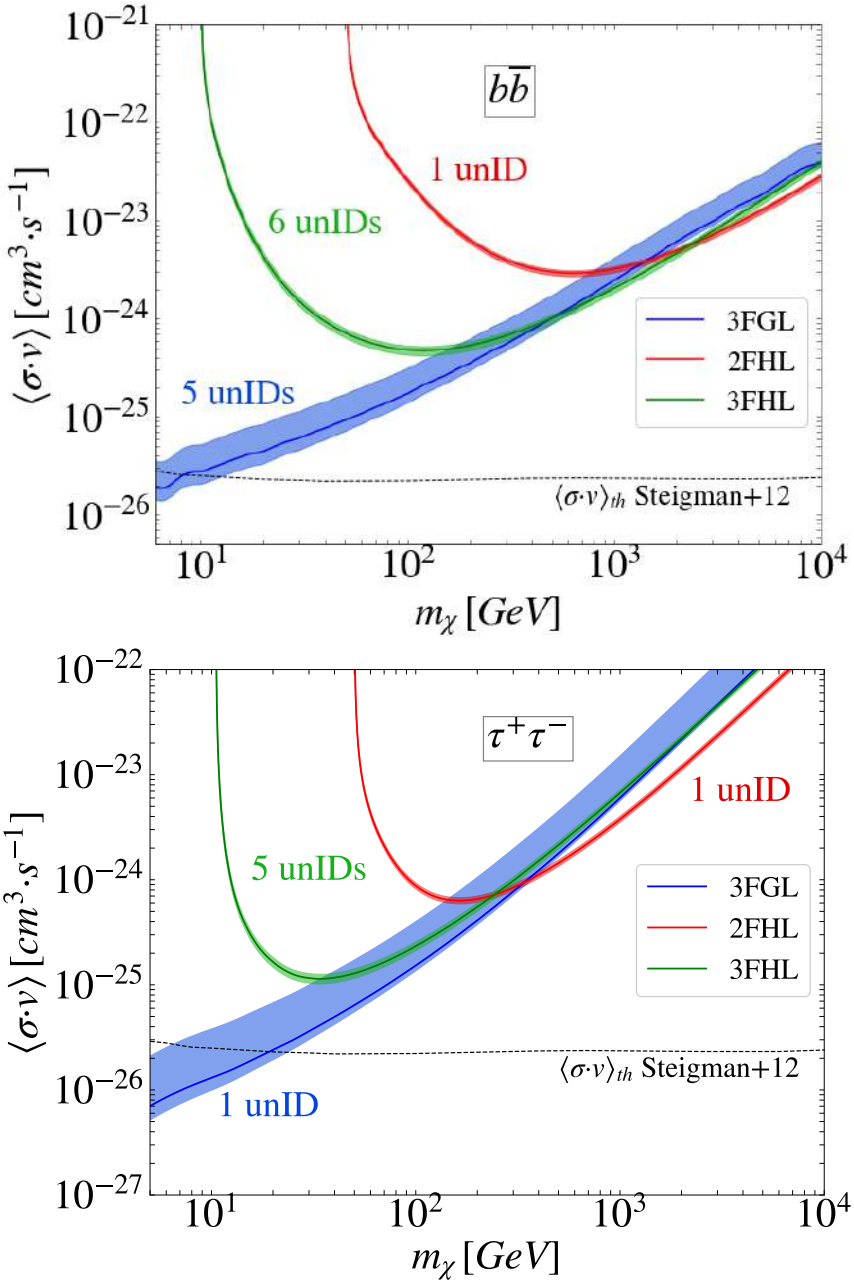


FIGURE 4.4: Limits on the DM annihilation cross section for $b\bar{b}$ (top) and $\tau^+\tau^-$ (bottom) for the 3FGL, 2FHL and 3FHL LAT catalogs and the number of unIDs that are still compatible with a DM annihilation origin after our spectral analyses of Section 4.2 and Section 4.4. The wide uncertainty band in the case of the 3FGL constraint is due to false positive rates in the machine learning classification algorithms used in the unID filtering work of Ref. Coronado-Blázquez et al. (2019). The dashed line represents the thermal value of the annihilation cross section Steigman et al. (2012).

where $E_0$ is the pivot energy and $\alpha$ the photon spectral index. In this peculiar parameter space, for the brightest sources ($TS_d > 1000$[11]), there is a clear separation between pulsars, BL Lacs (BLLs), and flat-spectrum radio quasars (FSRQs), as shown

[11] We will assume $TS_d \sim \sigma^2$, where $\sigma$ is the significance of detection.

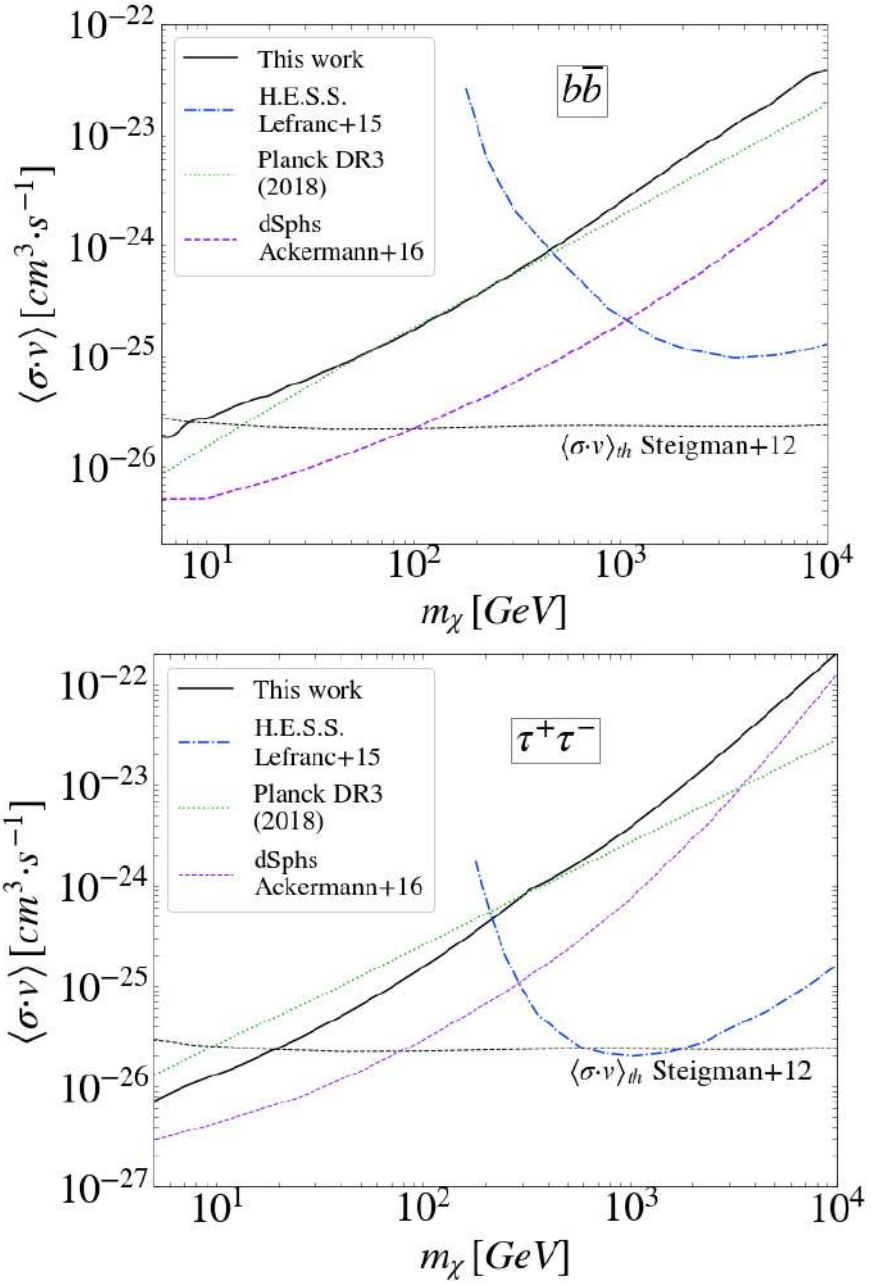


FIGURE 4.5: Comparison of DM limits from different targets and probes. Solid line corresponds to the envelope of the three sets of limits shown in Figure 8.5. Dot-dashed, dashed and dotted lines are, respectively, the DM constraints derived by H.E.S.S. for the Milky Way halo Lefranc et al. (2015), by the *Fermi*-LAT for dSphs Fermi-LAT Collaboration (2015c), and by Planck using the CMB DR3 latest release The Planck Collaboration (2020). Top panel is for $b\bar{b}$ and bottom panel for $\tau^+\tau^-$ annihilation channel.

in Figure 4.6. In particular, bright blazars present $\beta < 0.2$ (i.e., less curved spectrum), while pulsars typically exhibit $0.1 < \beta < 1$ (higher curvature). Also, BLLs peak at higher energies than FSRQs.

The separation of classes with parameters such as the spectral curvature or the photon index has been addressed by different authors in the past Lefaucheur and Pita (2017); Fermi-LAT Collaboration (2012a), but none of them included DM as

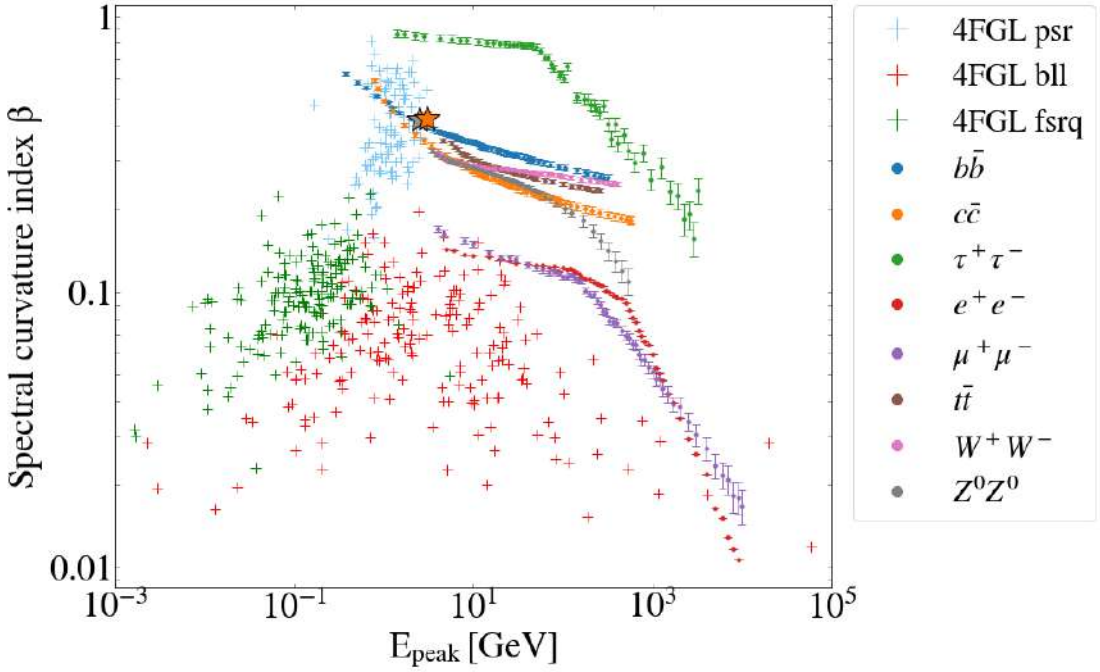


FIGURE 4.6: Spectral curvature index ($\beta$) vs. the peak energy ($E_{peak}$) for 4FGL pulsars (psr, blue crosses), BL Lacs (bll, red crosses) and flat spectrum radio quasars (fsrq, green crosses) with TS of detection ($TS_d$) greater than 1000. Colored data symbols with error bars correspond to the ($E_{peak}$, $\beta$) with $1\sigma$ uncertainty, for different DM annihilation channels (see legend). Large gray and orange stars correspond to the best-fit annihilation channels for the two unID sources with $TS_d > 1000$ that are well fitted by a LP model out of the 44 unIDs in our list.

a possible class in their analyses. Previous work Calore et al. (2017); Coronado-Blázquez et al. (2019) showed that the PLE represents a fair approximation to the DM annihilation spectrum. Following the same arguments, and since LP exhibits a spectral curvature as well, we now perform a fit to LP for every annihilation channel. We do so, first, by producing spectral DM data points as given by PPPC4IDDM Cirelli et al. (2011), which are then fitted with LP. The fit behaves better for hadronic channels compared to leptonic ones, as expected. We do not perform fits for $m_\chi > 10$ TeV, as higher-order electroweak corrections, not included in PPPC4IDDM, may be relevant approximately above this energy. As can be seen in Figure 4.6, for each considered channel, $E_{peak}$ can look quite different depending on the considered channel and mass. For example, for $b\bar{b}$, $E_{peak} \sim m/20$ $(m/50)$ for low (high) DM masses, while $\tau^+\tau^-$ roughly peaks at $m/3$ independently of the mass. We now populate the $E_{peak} - \beta$ parameter space with the $E_{peak}, \beta$ values derived from these DM fits to LP performed for different masses and channels. Interestingly, a good portion of the region of the parameter space where the DM resides is radically different from the one where astrophysical sources lie; again, see Figure 4.6. We note that a similar exercise and argument was already proposed and explored by Geringer-Sameth et al. (2018), in that case to specifically address a potential annihilation signal from the Reticulum-II dwarf satellite galaxy.

DM and pulsars only share a region in the parameter space for DM masses ranging approximately from 5 to 70 GeV, and for the $b\bar{b}$ and $c\bar{c}$ annihilation channels. This is the region where the mentioned pulsar/DM confusion is present. We also

show in Figure 4.6 the result of using LP for two sources with $TS_d$>1000 and ΔTS>-25 (see Eq. 4.6), namely 3FGL J0336.1+7500 ($Z^0Z^0$, $TS_d$=1095, ΔTS=-6.60) and 3FGL J1225.9+2953 ($c\bar{c}$, $TS_d$=1149, ΔTS=-0.02). They both lie precisely in the parameter space typical of pulsars (yet not far from the DM area).

The test described above is particularly powerful for bright sources. In Figure 4.7, we repeat the same test for all sources instead, i.e., without a cut in $TS_d$. As can be seen, the same parameter space gets very crowded when including weak sources. For instance, now the blazars' and quasars' curvature spectral indices range up to 1, though in all these cases $E_{peak}$ still remains below 100 GeV with a few exceptions (and, interestingly, all of them with $\beta < 0.1$). Also, the pulsars keep confined to $\beta > 0.1$, with the exception of only two sources which lie very close to this value. All in all, for weak sources the $E_{peak} - \beta$ parameter space can still be useful to shed light on the type of objects, e.g. by rejecting the pulsar interpretation for objects exhibiting $\beta < 0.1$ or, alternatively, $E_{peak} > 10$ GeV.

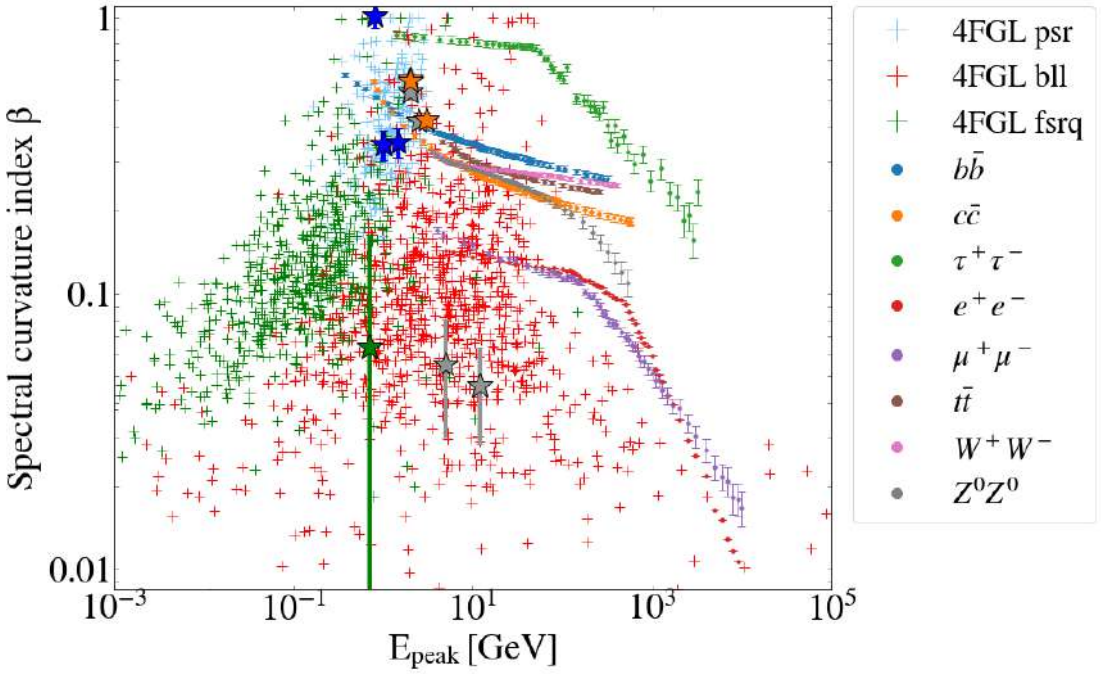


FIGURE 4.7: Same as Figure 4.6 but without cut in detection TS. Also shown as stars are those unIDs that are well fitted by LP (i.e., ΔTS ≥ −25). The color of each star refers to the best-fit DM channel in each case; see legend.

From a DM perspective, the proposed test will be particularly valid for energies higher than 100 GeV, i.e., where no astrophysical source peaks but DM can. This roughly corresponds to DM masses larger than ∼1 TeV (depending on the specific annihilation channel). Figure 4.7 also plots the 11 sources with a fit to DM (ΔTS ≥ −25) which are also well fitted with LP. None of these sources lie in the region of the parameter space exclusive to DM. Yet, it is possible to draw some useful conclusions from the DM perspective from this exercise. Three unID sources (3FGL J0539.2−0536, 3FHL J0343.5−6302 and 3FHL J1440.2−2343) exhibit values of $\beta$ much lower than the ones expected for DM annihilation, i.e., ∼0.05 versus values around $0.3 - 0.9$, respectively. Also, the 1-$\sigma$ error bars, with $\Delta\beta$ ranging from ∼0.025 to 0.1, are not large enough to reach the DM parameter space. These sources may be discarded as DM subhalos, although as the statistical significance of these uncertainties

is unclear, we conservatively do not discard any of them for this reason. Although two of them are already discarded for not fitting any DM channel with ΔTS>-9, it is worth remembering that 3FHL J0343.5−6302 is one of the sources with ΔTS(DM)>0 (see Table 4.2). Although the uncertainty in $\beta$ is high, all these unIDs are well below the expected DM $E_{peak} - \beta$ values. Also, we predict these sources to be most likely blazars.

With respect to the remaining seven unID sources, well fitted by $b\bar{b}$, $c\bar{c}$ and $Z^0Z^0$, they all lie close to the DM region, thus conservatively we cannot discard a DM hypothesis or classify them either as pulsars or blazars due to the high confusion in this part of the parameter space for the case of weak sources.

As a summary, this discriminating tool based on the $E_{peak} - \beta$ parameter space can potentially discard unIDs as DM subhalos, when these exhibit low ($E_{peak}$, $\beta$) values of order $(0.01 - 0.3, 0.01 - 1)$, or to point out particularly interesting DM candidates. Indeed, there is a specific region of the parameter space that is only reachable by DM annihilation with high ($E_{peak}$, $\beta$), roughly larger than $(0.1 - 1, 1 - 10)$. No unIDs among our list of best candidates are found there though. A more quantitative assessment of the boundaries of each source class in this parameter space is under study using machine learning techniques and will be published elsewhere.

## 4.5 Spatial analysis of remaining DM candidates

### 4.5.1 Technical setup and data analysis results

Spatial extension has been studied by many authors as a possible "smoking gun" for DM annihilation (see e.g. Bertoni et al. (2015, 2016); Zechlin and Horns (2012); Hütten and Maier (2018); Chou et al. (2018); Fermi-LAT Collaboration and Biteau (2018)). In this section we search for spatial extension, in the 7 best DM candidates ($\Delta TS > 0$ in Eq. 4.6) that are left after the spectral analysis in Section 4.2. The spatial extension is defined as the 68% containment width of the signal. We choose two different templates, a 2D uniform disk and a Gaussian profile. The `GTAnalysis.extension` *fermipy* module fits the source with the mentioned spatial profiles in concentric circles of increasing radii, centered at the position of the source, and computes the likelihood values for each of them. The fit is computed in 40 linear radial bins between 0.01 and 0.5°.

We perform a TS analysis to study the preference of the extended model over a point-like source, similarly to what done via Eq. 4.1 to estimate detection significances, but where now $H_1$ represents the extended source model (alternative hypothesis) and $H_0$ the point-like source (null hypothesis). The latter is defined as the one with an extension smaller than the point spread function (PSF) at the energy under consideration. On the other extreme, should significant extension be found, larger than the maximum allowed angular size of 0.5° (i.e. the log-likelihood is monotonically increasing in that range), the latter upper limit is increased.

None of the candidates is found to have significant spatial extension. Figure 4.8 shows the log-likelihood profiles and corresponding TS values of the extension evaluated with the Gaussian profile. Changing the spatial template to the 2D disk provides similar results.

### 4.5.2 ΛCDM predictions of subhalo angular sizes

State-of-the-art N-body simulations of Milky Way (MW) size halos have become a powerful tool to study halo substructure and have provided the most valuable

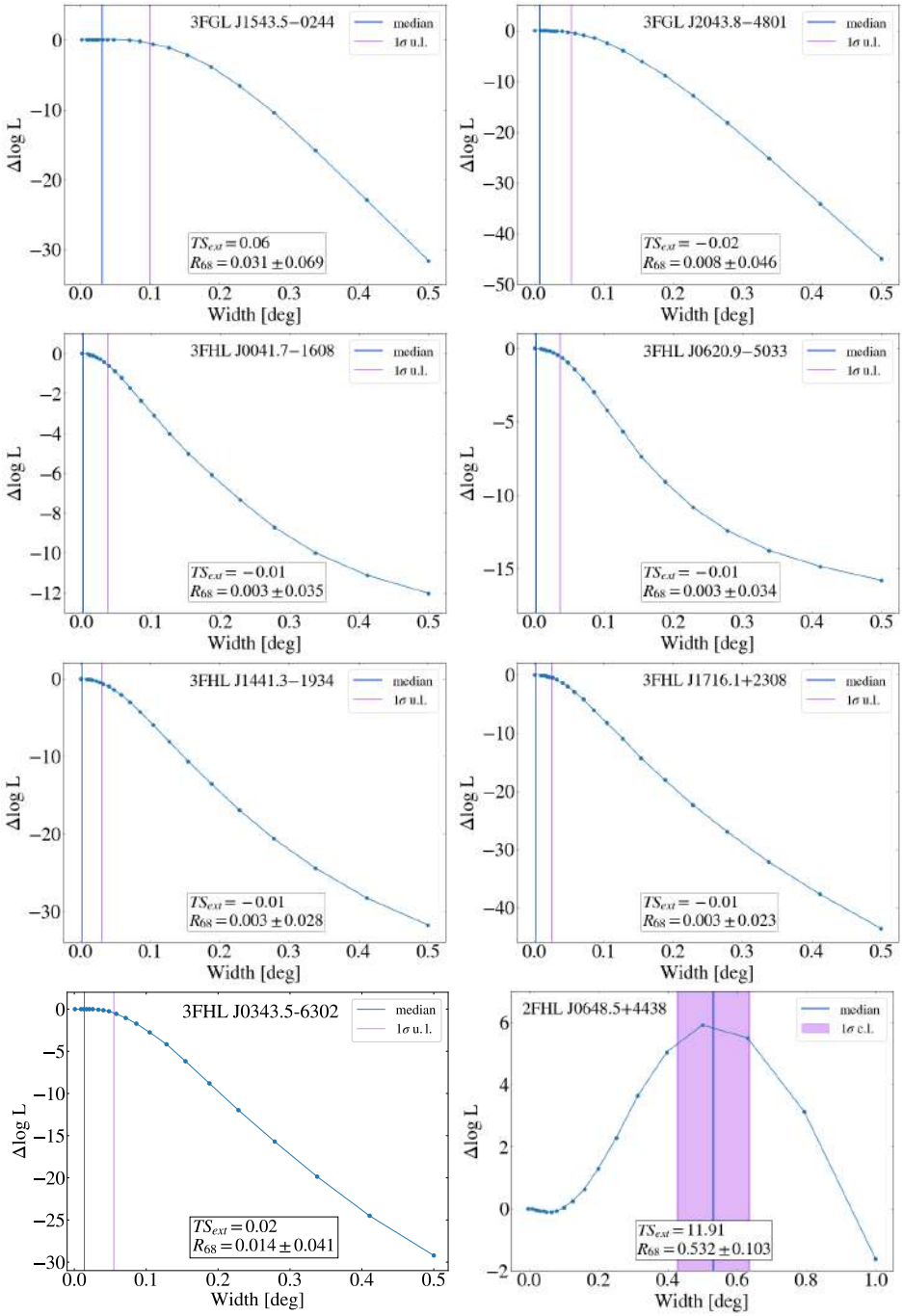


FIGURE 4.8: Spatial extension log-likelihood profiles of the seven DM candidates from Table 4.2 and one known extended source, for the case of adopting a Gaussian spatial template. The blue, vertical line is the median best-fit value, while the violet line refers to the $+1\sigma$ uncertainty of the mean (in the last source, where there is a preference for extension, this is an uncertainty band). All DM candidates appear as point-like. The use of a 2D disk spatial template instead of a Gaussian one leads to similar results. Only for illustrative purposes, we also show in the bottom right panel the source 2FHL J0648.5+4438, which is not well fitted to any DM channel but is found to have a 68% containment width of $0.5 \pm 0.1^\circ$ at $\sim 3\sigma$ significance.

and accurate information on the properties of the present-day subhalo population Springel, Wang, Vogelsberger, Ludlow, Jenkins, Helmi, Navarro, Frenk and White (2008); Diemand et al. (2008); Stadel et al. (2009); Garrison-Kimmel et al. (2014). In Coronado-Blázquez et al. (2019), we used publicly available results from the Via Lactea II (VL-II) DM-only simulation at redshift zero[12] to perform this task. More specifically, we obtained ΛCDM predicted annihilation fluxes of the Galactic subhalos to, ultimately, set DM constraints by comparing predictions with data. To do so, we first replicated the original VL-II and repopulated it with millions of low-mass subhalos below the resolution of the parent simulation. We then placed the observer at arbitrary positions at 8.5 kpc from the Galactic center in order to obtain multiple realizations.

Yet, in Coronado-Blázquez et al. (2019) we did not study the *typical* angular extent of subhalos in the sky. This feature may turn out to be relevant for the current work, for which the spatial extension of the best DM subhalo candidates among our list of remaining unIDs was analyzed. Thus, we now compute the angular size of subhalos in our realizations of the repopulated VL-II as well. We do so by defining it in the following way:

$$\theta_{sub}[\mathrm{deg}] = \frac{180}{\pi}\mathrm{atan}\left(\frac{r_s(m_{sub})}{D_{Earth}}\right) \tag{4.9}$$

where $r_s$ is the scale radius of the subhalo, with mass $m_{sub}$, when a Navarro-Frenk-White (NFW) DM density profile is assumed Navarro et al. (1997), and $D_{Earth}$ is the distance to the Earth. We recall that for an NFW profile 90% of the total annihilation flux originates within $r_s$. As subhalos exhibit a truncated NFW (see, e.g., Ref. Kazantzidis et al. (2004); Moliné et al. (2017)), the use of $r_s$ in Eq. 4.9 represents a very good approximation for the size of the region where most of the DM flux was originated. The angular extension for the 100 brightest subhalos below $10^7\ M_\odot$ in 1000 repopulated VL-II realizations is shown in Figure 4.9. The typical *Fermi*-LAT PSF at $E > 10$ GeV, $\sim 0.2$, is also shown in the same figure[13]. According to this figure, every subhalo should appear as extended for the LAT. However, no unID was found to be extended in our spatial analysis of Section 4.5.1. In principle, this means that none of the seven best candidates are DM subhalos. Yet, as these unIDs correspond to faint sources, it is not totally clear that they would appear as extended in our analyses even if being actual DM subhalos. We conclude that more work is needed before being able to use ΛCDM predictions of subhalo angular sizes to rule out unIDs as potential DM subhalos. This work will be done elsewhere. For the time being, in the spirit of the conservative approach of this work, we do not reject any source as DM subhalo for this reason.

The brightest subhalos in Figure 4.9 are all expected to be significantly extended, with typical sizes of the order of 10°. Also, some of them are expected to be light, with masses as low as $10^5 M_\odot$ or even less. Thus, these small subhalos should be close to Earth ($\sim$ 2 kpc) in order to be among the brightest ones. These subhalos, with the largest predicted angular sizes of $\mathcal{O}(10^\circ)$, are the ones used to set the DM constraints in Section 9.4.

[12] http://www.ucolick.org/~diemand/vl/

[13] http://www.slac.stanford.edu/exp/glast/groups/canda/lat_Performance.htm

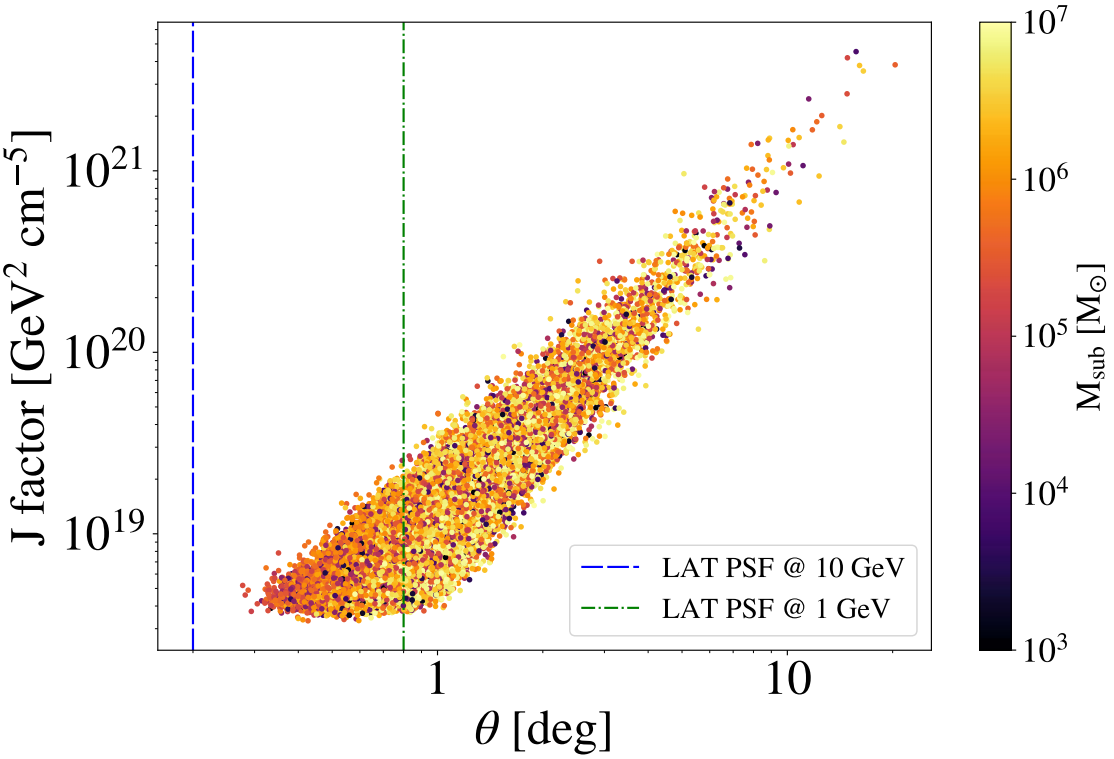


FIGURE 4.9: Angular extension of subhalos following our definition in Eq. 4.9 as predicted by the N-body simulation work of Coronado-Blázquez et al. (2019). The figure shows the 100 brightest subhalos in each of the 1000 realizations of the repopulated VL-II simulation, which include subhalos with masses down to $10^3 M_\odot$, i.e. well below the resolution of the original VL-II. The typical *Fermi*-LAT PSF at $E > 1$ GeV and $E > 10$ GeV are also shown as vertical dashed lines. Most subhalos are expected to be extended for *Fermi*-LAT, especially the brightest ones.

## 4.6 Search for Stellar Counterparts with *Gaia* DR2

Our DM candidate sources in Table 4.2 have no obvious associated stellar counterparts such as dwarf galaxies. If a dwarf galaxy is observed in the same region as a gamma-ray source which has a similar spectrum to what is expected from the DM annihilation, it would provide stronger support for the gamma-ray source to be a "smoking gun" for DM annihilation (e.g. Bertoni et al.; 2015, 2016; Calore et al.; 2017). The European Space Agency's *Gaia* mission (Gaia Collaboration; 2016) has made the second data release of their unprecedented parallax and proper motion measurements for more than one billion stars brighter than $G < 20$ mag (*Gaia* DR2; Gaia Collaboration; 2018a,b). This provides us with a new window to find an overdensity of stars, which could be dwarf galaxies, using proper motions in the inner Galactic halo, where the stellar density is too high to detect them from the photometric data alone Antoja et al. (2015). In Ciucă et al. (2018) the authors used both parallax and proper motion data from *Gaia* DR2, and searched for a dwarf galaxy in the fields of the eight *Fermi*-LAT extended sources suggested by Bertoni et al. (2015, 2016); Xia et al. (2017); Fermi-LAT Collaboration and Biteau (2018). Unfortunately, they did not find any stellar counterpart in the *Gaia* data. Still, using mock data, Ciucă et al. (2018)

obtained a conservative limit on the stellar mass of $M_* < 10^4$ M for $d < 20$ kpc, which provided a constraint on the potential stellar counterpart. However, their targeted sources are either not found in the follow-up studies Fermi-LAT Collaboration and Biteau (2018) or are located at lower Galactic latitudes. Hence, it is interesting to apply this new window of searching dwarf galaxies to our DM candidate sources that are carefully selected from the improved spectral analysis.

Following the approach of Ciucă et al. (2018), we selected a region of the sky within 2° of each of the best seven dark matter candidates shown in Table 4.2, namely 3FGL J1543.5−0244 ($l = 4.07°$, $b = 38.90°$), 3FGL J2043.8−4801 ($l = 351.75°$, $b = -38.47°$), 3FHL J0041.7−1608 ($l = 110.90°$, $b = -78.79°$), 3FHL J0343.5−6302 ($l = 277.20°$, $b = -44.54°$), 3FHL J0620.9−5033 ($l = 258.80°$, $b = -25.29°$), 3FHL J1441.3−1934 ($l = 335.55°$, $b = 36.24°$) and 3FHL J1716.6+2308 ($l = 45.04°$, $b = 30.64°$), from the data in *Gaia* DR2. We then used both spatial and proper motion information from *Gaia* DR2 to find the stellar signature of a co-moving stellar component at the position of each field of our DM candidate sources. Depending on the distance at which we are searching for a stellar counterpart, i.e. either closer or farther than $d = 10$ kpc, we apply a parallax filter to minimize the background contamination. In the case of search distances greater than 10 kpc, we apply the same parallax filter used in Antoja et al. (2015), where we discard stars for which $\varpi - \sigma_\varpi > 0.1$ mas, where $\varpi$ represents the parallax and $\sigma_\varpi$ is the parallax uncertainty. This filtering is equivalent to removing stars closer than 10 kpc within parallax uncertainties and aims to minimize contamination from foreground stars. If the dSph is assumed to be closer than $d < 10$ kpc, we employ a distance-dependent parallax cut, namely $1/(2d_{\rm in}) < \varpi < 1.0/d_{\rm in}$, which changes as we are probing a distance range between 1.0 and 10 kpc in increments of $d_{\rm in}$ of 1 kpc up to 5 kpc, and then 2 kpc up to 9 kpc.

Following Ciucă et al. (2018), we used an Extreme-Deconvolution (XD, Bovy et al.; 2011) Gaussian Mixture Model (XDGMM, Holoien et al.; 2017), to detect a stellar overdensity associated with a stellar counterpart as a density enhancement in the four-dimensional data vector comprised of the stellar position in Galactic longitude and latitude, and the RA and DEC proper motion measurements as we are looking to find a concentration of stars both in proper motion space and in the sky. Ciucă et al. (2018) demonstrated that this method allows us to take into account the correlation between the measurement of RA and DEC proper motions. As done in Ciucă et al. (2018), for practical purposes, we applied a small constant uncertainty of 0.01° in the stellar positions, whose effect on our results is thought to be insignificant, and we do not take into account the correlations between proper motion and position as they are very small.

We used an XDGMM with 25 four-dimensional Gaussian components, to retrieve the structure present in the data, to the samples of stars with d < 10 kpc and d > 10 kpc, filtered as mentioned above, in the seven fields of our DM candidate sources. 25 Gaussian components are found to be a large enough number of components to detect a co-moving stellar structure in the relatively high Galactic latitude regions like our target regions Ciucă et al. (2018). In that same work, the detectability of a dwarf galaxy depending on the number of Gaussian components by placing a synthetic mock dwarf galaxy data in the background data created using the Gaia data with the same size as that of the field of view used for our search is tested, and demonstrated that the detected mock dwarf galaxy showed up as a narrow Gaussian component in the RA and DEC proper motions. In fact, an excessive number of components in the XDGMM does not penalize the detection of the dwarf galaxy (see also Ciucă et al. (2018); Anderson et al. (2018)). Therefore it is not necessary to search for the optimum number of the components, rather using a large enough

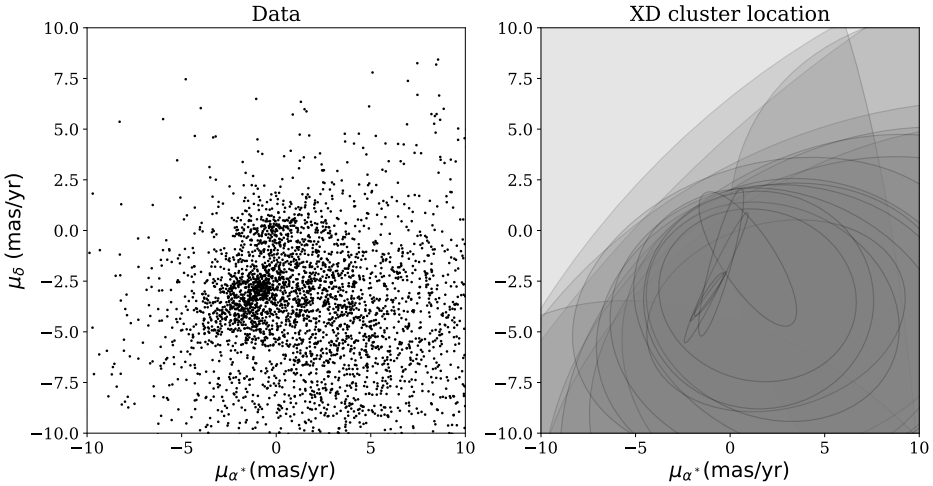


FIGURE 4.10: A detection of a kinematical structure in the field of 3FHL J0041.7−1608. The left panel shows the data after filtering with $d > 10$ kpc. The right panel shows the results from the Gaussian Mixture Model (Holoien et al.; 2017) used to perform density estimation using the XD method (Bovy et al.; 2011) with 25 components. Ellipses represent detected Gaussian components to describe the data and the darker gray color indicates more components overlapping. The small ellipse around $(\mu_{\alpha^*}, \mu_\delta) = (-1.12, -3.15)$ mas yr$^{-1}$ is believed to be part of the Sagittarius stream in the right panel.

number of the Gaussian components is sufficient.

We found no evidence for any co-moving stellar group in the fields, except in the field of 3FHL J0041.7−1608. A clear overdensity of stars highlighted by a small narrow ellipse is detected in the proper motion space as shown in Figure 4.10. However, we believe that this is not evidence of a dwarf galaxy associated with 3FHL J0041.7−1608. It is worth noticing that this is a part of the known Sagittarius stream. Our detected proper motion is $(\mu_{\alpha^*}, \mu_\delta) = (-1.12, -3.15)$ mas yr$^{-1}$, which is consistent with the expected proper motion from the Sagittarius stream (e.g. see Hayes et al. (2018)). We also explored the proper motion distribution in a much larger region of the sky around this source (as far as 90° away), and found the excess of the proper motion to be extended in the large region of the sky where the Sagittarius stream is expected in the Southern Galactic region (e.g. see (Mateu and Vivas; 2018) for a compilation of the known stellar streams). It is interesting to find that one of our DM candidate sources coincides with the Sagittarius stream. However, considering the fraction of the sky covered by the Sagittarius stream, this coincidence is not surprising. Still, this remains a compelling fact, although it is difficult to confirm or reject that this is an annihilation emission signal from a DM subhalo in the Sagittarius stream.

## 4.7 Conclusions and prospects

In this work, we have presented a dedicated LAT analysis of those unIDs that were identified as the best DM subhalo candidates within the latest *Fermi*-LAT catalogs by Coronado-Blázquez et al. (2019). Now, we are able to discard most of these candidates, mainly based upon their spectral information.

First, we performed a full spectral analysis with *Fermipy*, using all 10-year available gamma-ray data. With the new data set, not all our previous candidates reach the standard detection threshold of $TS_d = 25$. In fact, by just improving the LAT statistics from 48 to 116 months, and by using the new multi-wavelength information available, we are able to reduce the number of candidates in 9 and 3 sources, respectively. More precisely, we are left with 32 unIDs out of an initial poll of 44. For these remaining 32 unIDs, we performed a spectral analysis in the 300 MeV-800 GeV range. Three different parametric models were used to perform the SED fitting: a power law, log-parabola and a power law with super-exponential cutoff. Also, we used `DMFit` to fit the SED to different DM annihilation channels. The goal of the fitting procedure was to find the spectral model that best fits the data and, thus, to understand if a DM origin was statistically preferred over typical astrophysical gamma-ray emitters for any of the studied unIDs.

We found a significant number of sources that preferred a non-exotic, astrophysical origin at high ($> 3\sigma$) significance. These sources were rejected from our list of potential DM subhalos. On the other hand, only seven unIDs (two 3FGL, five 3FHL and zero 2FHL sources) were found to marginally prefer a DM origin for at least one annihilation channel. Yet, in all cases the slight preference for DM was found to not be statistically significant.

After our spectral analysis, that allows us to disregard some of the unIDs as due to DM annihilation, and in the absence of outstanding DM subhalo candidates in the list of remaining sources, we set stringent constraints on the $m_\chi$-$\langle\sigma v\rangle$ parameter space. We do so by adopting the same methodology that was presented in Coronado-Blázquez et al. (2019), which is based on a comparison between number of predicted observable subhalos from simulations, and actual number of remaining unIDs in our catalogs. By adopting a conservative view, we keep in our list of potential DM subhalo candidates all those unIDs that do *not* exhibit a preference for an astrophysical spectral model at more than $3\sigma$. Our derived DM constraints rule out canonical thermal WIMPs up to $\sim$10 GeV for $b\bar{b}$ and $\sim$20 GeV for $\tau^+\tau^-$ annihilation channels.

In Section 4.4, we described a test that can be potentially used for discriminating astrophysical sources from DM. This can be particularly interesting in the case of disentangling low-mass WIMPs from pulsars. The method is based on the parameter that controls the spectral curvature in the log-parabola SED model, $\beta$, and on the peak energy of the source, $E_{peak}$. Sources of a particular type tend to cluster in this particular ($E_{peak}$, $\beta$) parameter space, indeed astrophysical sources and DM populating different regions of it. Although the discrimination power of this "$\beta$ plot" behaves differently depending on the TS of detection (the larger its value the better for discrimination), we are able to mark one of our best candidates as very unlikely due to DM annihilation, although we conservatively do not reject it due to the uncertain statistical significance. In the rest of cases the test is not conclusive. Work is already ongoing to further scrutinize the nature of unIDs using this promising tool for source type discrimination.

In Section 4.5 we searched for spatial extension of our seven best candidates, using two different spatial templates (an uniform 2D disk and a Gaussian profile). All of the candidates are found as point-like sources. Interestingly, our N-body simulation work predicts that the brightest members of the subhalo population should exhibit a large extension, of the order of several degrees. It is unclear though that we can safely use these results to reject unIDs as potential subhalos so we decide not to do so and stay conservative: weak unIDs may appear as point sources even if they

were intrinsically extended. Further work will be presented to properly address this issue as well.

Finally, using *Gaia* DR2 and an advanced density estimation technique, we search for kinematical signature of a stellar counterpart in the fields of our seven best DM candidates listed in Table 4.2. We find that one of the fields, the one surrounding 3FHL J0041.7−1608, coincides with the Sagittarius stream. This may point to a potential association of the DM annihilation signal with a hidden DM subhalo within the tidal stream of the Sagittarius dwarf galaxy. However, considering the large sky coverage of the Sagittarius stream, this is likely to be just a coincidence.

Looking into the imminent future, the release of new *Fermi*-LAT catalogs (e.g. 4FGL Fermi-LAT Collaboration (2020)) will provide new targets to work with and better photon statistics. The 4FGL will allow for a better discrimination power in the $\beta$-plot that could be further used to remove additional sources. Current *Imaging Atmospheric Cherenkov Telescopes* (IACTs) and, very especially, the future Cherenkov Telescope Array (CTA) The Cherenkov Telescope Array Consortium (2017) could also be used to perform dedicated analyses of the best DM subhalo candidates at higher energies. In this sense, also ongoing or future observational campaigns at other wavelengths, such as X-ray or radio, may shine a light on the origin of some of the candidates presented in this work. Moreover, instruments with an improved angular resolution, such as AMEGO Caputo et al. (2017), or even CTA itself, may further explore the potential spatial extension of the unIDs.

## 4.8 Rejection criteria for the unIDs

In Table 4.8 we detail the rejection criteria for the 44 unIDs considered in this work.

| Source Name | Rejection | Source Name | Rejection |
|---|---|---|---|
| 3FGL J0003.4+3100 | F | 3FHL J0301.4−5618 | - |
| 3FGL J0244.4+4745 | TS | 3FHL J0302.6+3354 | F |
| 3FGL J0336.1+7500 | - | 3FHL J0343.5−6302 | - |
| 3FGL J0538.8−0341 | TS | 3FHL J0350.4−5153 | X |
| 3FGL J0539.2−0536 | F | 3FHL J0359.4−0235 | F |
| 3FGL J0600.4−1934 | F | 3FHL J0550.9+5657 | TS |
| 3FGL J0905.8−2127 | F | 3FHL J0620.9−5033 | - |
| 3FGL J0953.7−1510 | F | 3FHL J0838.5+4006 | F |
| 3FGL J1106.6−1744 | - | 3FHL J0954.2−2520 | - |
| 3FGL J1225.9+2953 | - | 3FHL J1403.4+4319 | TS |
| 3FGL J1543.5−0244 | - | 3FHL J1421.5−1654 | - |
| 3FGL J1936.6−4215 | F | 3FHL J1440.2−2343 | F |
| 3FGL J1947.4−1121 | F | 3FHL J1441.3−1934 | - |
| 3FGL J1958.2−1413 | TS | 3FHL J1503.3+1651 | - |
| 3FGL J2029.5−4232 | - | 3FHL J1650.9+0430 | X |
| 3FGL J2043.8−4801 | - | 3FHL J1705.3+5434 | F |
| 3FHL J0041.7−1608 | - | 3FHL J1716.1+2308 | - |
| 3FHL J0055.8+4507 | TS | 3FHL J1726.2−1710 | TS |
| 3FHL J0110.9+4346 | F | 2FHL J0648.5+4438 | F |
| 3FHL J0115.4−2916 | - | 2FHL J0906.8+3530 | F |
| 3FHL J0121.8+3808 | TS | 2FHL J1516.1+3702 | F |
| 3FHL J0233.0+3742 | A | 2FHL J1630.0+7644 | TS |

**Table A** Selection criteria for the 44 unIDs considered in this work. Last column indicates the rejection criteria, if any: TS - the source did not reach the TS=25 detection threshold; F - no annihilation channel was found to fit the SED with $\Delta TS \geq -9$; A - associated in 4FGL Fermi-LAT Collaboration (2020); X - X-ray counterpart with *Swift*-XRT Kaur et al. (2019).

## Bibliography

Ahnen, M. L. et al. (2016). Limits to dark matter annihilation cross-section from a combined analysis of MAGIC and Fermi-LAT observations of dwarf satellite galaxies, *Journal of Cosmology and Astroparticle Physics* **2016**(02): 039–039.

Akaike, H. (1974). A new look at the statistical model identification, *IEEE Transactions on Automatic Control* **19**(6): 716–723.

Anderson, L., Hogg, D. W., Leistedt, B., Price-Whelan, A. M. and Bovy, J. (2018). Improving Gaia Parallax Precision with a Data-driven Model of Stars, *The Astronomical Journal* **156**(4): 145.
**URL:** *https://ui.adsabs.harvard.edu/abs/2018AJ....156..145A*

Antoja, T., Mateu, C., Aguilar, L., Figueras, F., Antiche, E., Hernández-Pérez, F., Brown, A. G. A., Valenzuela, O., Aparicio, A., Hidalgo, S. and Velázquez, H. (2015). Detection of satellite remnants in the Galactic halo with Gaia- III. Detection limits for ultrafaint dwarf galaxies, *Monthly Notices of the Royal Astronomical Society* **453**: 541–560.
**URL:** *http://dx.doi.org/10.1093/mnras/stv1622*

Atwood, W., Albert, A., Baldini, L., Tinivella, M., Bregeon, J., Pesce-Rollins, M., Sgrò, C., Bruel, P., Charles, E., Drlica-Wagner, A., Franckowiak, A., Jogler, T., Rochester, L., Usher, T., Wood, M., Cohen-Tanugi, J. and for the Fermi-LAT Collaboration, S. Z. (2013). Pass 8: Toward the Full Realization of the Fermi-LAT Scientific Potential.
**URL:** *https://arxiv.org/abs/1303.3514*

Bartels, R., Hooper, D., Linden, T., Mishra-Sharma, S., Rodd, N. L., Safdi, B. R. and Slatyer, T. R. (2017). Comment on "Characterizing the population of pulsars in the Galactic bulge with the Fermi Large Area Telescope" [arXiv:1705.00009v1].
**URL:** *https://arxiv.org/abs/1710.10266*

Belikov, A. V., Buckley, M. R. and Hooper, D. (2012). Searching for dark matter subhalos in the Fermi-LAT second source catalog, *Physical Review D* **86**(4).

Berlin, A. and Hooper, D. (2014). Stringent Constraints On The Dark Matter Annihilation Cross Section From Subhalo Searches With The Fermi Gamma-Ray Space Telescope, *Physical Review D* **89**(1).
**URL:** *http://dx.doi.org/10.1103/PhysRevD.89.016014*

Bertoni, B., Hooper, D. and Linden, T. (2015). Examining The Fermi-LAT Third Source Catalog In Search Of Dark Matter Subhalos, *Journal of Cosmology and Astroparticle Physics* **12**: 035.
**URL:** *http://dx.doi.org/10.1088/1475-7516/2015/12/035*

Bertoni, B., Hooper, D. and Linden, T. (2016). Is The Gamma-Ray Source 3FGL J2212.5+0703 A Dark Matter Subhalo?, *Journal of Cosmology and Astroparticle Physics* **5**: 049.
**URL:** *http://dx.doi.org/10.1088/1475-7516/2016/05/049*

Bovy, J., Hogg, D. W. and Roweis, S. T. (2011). Extreme deconvolution: Inferring complete distribution functions from noisy, heterogeneous and incomplete observations, *Annals of Applied Statistics* **5**.
**URL:** *http://adsabs.harvard.edu/abs/2011AnApS...5.1657B*

Bruel, P., Burnett, T. H., Digel, S. W., Johannesson, G., Omodei, N. and on behalf of the Fermi-LAT Collaboration, M. W. (2018). Fermi-LAT improved Pass 8 event selection.
**URL:** *https://arxiv.org/abs/1810.11394*

Buckley, M. R. and Hooper, D. (2010). Dark Matter Subhalos In the Fermi First Source Catalog, *Physical Review D* **82**(6).
**URL:** *http://dx.doi.org/10.1103/PhysRevD.82.063501*

Calore, F., Romeri, V. D., Mauro, M. D., Donato, F. and Marinacci, F. (2017). Realistic estimation for the detectability of dark matter sub-halos with Fermi-LAT, *Physical Review D* **96**(6).
**URL:** *http://dx.doi.org/10.1103/PhysRevD.96.063009*

Caputo, R., Meyer, M. and Sanchez-Conde, M. (2017). AMEGO: Dark Matter Prospects, *Proceedings of 35th International Cosmic Ray Conference — PoS(ICRC2017)*, Sissa Medialab.

Chou, T.-L., Tanoglidis, D. and Hooper, D. (2018). Resolving Dark Matter Subhalos With Future Sub-GeV Gamma-Ray Telescopes, *Physics of the Dark Universe* **21**: 1.
**URL:** *https://ui.adsabs.harvard.edu/abs/2018PDU...21...1C*

Cirelli, M., Corcella, G., Hektor, A., Hütsi, G., Kadastik, M., Panci, P., Raidal, M., Sala, F. and Strumia, A. (2011). PPPC 4 DM ID: A Poor Particle Physicist Cookbook for Dark Matter Indirect Detection, *Journal of Cosmology and Astroparticle Physics* **2011**(03): 051–051.
**URL:** *http://dx.doi.org/10.1088/1475-7516/2011/03/051*

Ciucă, I., Kawata, D., Ando, S., Calore, F., Read, J. I. and Mateu, C. (2018). A Gaia DR2 search for dwarf galaxies towards Fermi-LAT sources: implications for annihilating dark matter, *Monthly Notices of the Royal Astronomical Society* **480**: 2284–2291.

Coronado-Blázquez, J., Sánchez-Conde, M. A., Domínguez, A., Aguirre-Santaella, A., Mauro, M. D., Mirabal, N., Nieto, D. and Charles, E. (2019). Unidentified gamma-ray sources as targets for indirect dark matter detection with the fermi-large area telescope, *Journal of Cosmology and Astroparticle Physics* **2019**(07): 020–020.

Diemand, J., Kuhlen, M., Madau, P., Zemp, M., Moore, B., Potter, D. and Stadel, J. (2008). Clumps and streams in the local dark matter distribution, *Nature* **454**(7205): 735–738.
**URL:** *http://dx.doi.org/10.1038/nature07153*

Fermi-LAT Collaboration (2012a). A Statistical Approach to Recognizing Source Classes for Unassociated Sources in the First Fermi-LAT Catalog, *The Astrophysical Journal* **753**(1): 83.

Fermi-LAT Collaboration (2012b). Search for Dark Matter Satellites using the FERMI-LAT, *The Astrophysical Journal* **747**(2): 121.
**URL:** http://dx.doi.org/10.1088/0004-637X/747/2/121

Fermi-LAT Collaboration (2015a). Fermi Large Area Telescope Third Source Catalog, *The Astrophysical Journal Supplementary Series* **218**(2): 23.
**URL:** https://ui.adsabs.harvard.edu/abs/2015ApJS..218...23A

Fermi-LAT Collaboration (2015b). Search for extended gamma-ray emission from the Virgo galaxy cluster with Fermi-LAT, *The Astrophysical Journal* **812**(2): 159.
**URL:** http://dx.doi.org/10.1088/0004-637X/812/2/159

Fermi-LAT Collaboration (2015c). Searching for Dark Matter Annihilation from Milky Way Dwarf Spheroidal Galaxies with Six Years of Fermi-LAT Data, *Physical Review Letters* **115**(23).
**URL:** http://dx.doi.org/10.1103/PhysRevLett.115.231301

Fermi-LAT Collaboration (2016a). 2FHL: The Second Catalog of Hard Fermi-LAT Sources, *The Astrophysical Journal Supplement Series* **222**: 5.
**URL:** http://adsabs.harvard.edu/abs/2016ApJS..222....5A

Fermi-LAT Collaboration (2016b). Fermi-LAT Observations of High-Energy Gamma-Ray Emission Toward the Galactic Center, *The Astrophysical Journal* **819**: 44.
**URL:** http://adsabs.harvard.edu/abs/2016ApJ...819...44A

Fermi-LAT Collaboration (2017a). 3FHL: The Third Catalog of Hard Fermi-LAT Sources, *The Astrophysical JournalS* **232**: 18.
**URL:** http://adsabs.harvard.edu/abs/2017ApJS..232...18A

Fermi-LAT Collaboration (2017b). Characterizing the population of pulsars in the Galactic bulge with the Fermi Large Area Telescope.
**URL:** https://arxiv.org/abs/1705.00009

Fermi-LAT Collaboration (2017c). The Fermi Galactic Center GeV Excess and Implications for Dark Matter, *The Astrophysical Journal* **840**: 43.
**URL:** http://adsabs.harvard.edu/abs/2017ApJ...840...43A

Fermi-LAT Collaboration (2020). Fermi Large Area Telescope Fourth Source Catalog, *The Astrophysical Journal Supplement Series* **247**(1): 33.
**URL:** http://dx.doi.org/10.3847/1538-4365/ab6bcb

Fermi-LAT Collaboration and Atwood, W. B. (2009). The Large Area Telescope on the Fermi Gamma-ray Space Telescope Mission, *The Astrophysical Journal* **697**(2): 1071–1102.
**URL:** http://dx.doi.org/10.1088/0004-637X/697/2/1071

Fermi-LAT Collaboration and Biteau, J. (2018). The Search for Spatial Extension in High-latitude Sources Detected by the Fermi Large Area Telescope, *The Astrophysical JournalS* **237**(2): 32.

Gaia Collaboration (2016). The Gaia mission, *Astronomy & Astrophysics* **595**: A1.
**URL:** *http://adsabs.harvard.edu/abs/2016A%26A...595A...1G*

Gaia Collaboration (2018a). Gaia Data Release 2. Summary of the contents and survey properties, *Astronomy & Astrophysics* **616**: A1.
**URL:** *http://dx.doi.org/10.1051/0004-6361/201833051*

Gaia Collaboration (2018b). Gaia Data Release 2: The astrometric solution, *Astronomy & Astrophysics* **616**: A2.
**URL:** *http://dx.doi.org/10.1051/0004-6361/201832727*

Garrett, K. and Duda, G. (2011). Dark Matter: A Primer, *Advances in Astronomy* **2011**: 1–22.
**URL:** *http://dx.doi.org/10.1155/2011/968283*

Garrison-Kimmel, S., Boylan-Kolchin, M., Bullock, J. S. and Lee, K. (2014). ELVIS: Exploring the Local Volume in Simulations, *Monthly Notices of the Royal Astronomical Society* **438**(3): 2578–2596.

Geringer-Sameth, A., Koushiappas, S. M., Walker, M. G., Bonnivard, V., Combet, C. and Maurin, D. (2018). Astrophysical explanations of suspected dark matter signals in dwarf galaxies.
**URL:** *https://arxiv.org/abs/1807.08740*

Hayes, C. R., Law, D. R. and Majewski, S. R. (2018). Constraining the Solar Galactic Reflex Velocity using Gaia Observations of the Sagittarius Stream, *The Astrophysical Journal* **867**(2): L20.

H.E.S.S. Collaboration (2016). Search for Dark Matter Annihilations towards the Inner Galactic Halo from 10 Years of Observations with H.E.S.S., *Physical Review Letters* **117**(11).

Holoien, T. W.-S., Marshall, P. J. and Wechsler, R. H. (2017). EmpiriciSN: Re-sampling Observed Supernova/Host Galaxy Populations Using an XD Gaussian Mixture Model, *Astronomical Journal* **153**: 249.
**URL:** *http://adsabs.harvard.edu/abs/2017AJ....153..249H*

Hooper, D. and Witte, S. J. (2017). Gamma Rays From Dark Matter Subhalos Revisited: Refining the Predictions and Constraints, *Journal of Cosmology and Astroparticle Physics* **4**: 018.
**URL:** *http://dx.doi.org/10.1088/1475-7516/2017/04/018*

Hütten, M. and Maier, G. (2018). Observing small-scale gamma anisotropies with the Cherenkov Telescope Array, *Journal of Cosmology and Astroparticle Physics* **2018**(08): 032–032.

Jeltema, T. E. and Profumo, S. (2008). Fitting the gamma-ray spectrum from dark matter with DMFIT: GLAST and the galactic center region, *Journal of Cosmology and Astroparticle Physics* **2008**(11): 003.

Kaur, A., Ajello, M., Marchesi, S. and Omodei, N. (2019). Identifying the 3FHL catalog: I. Archival Swift Observations and Source Classification, *The Astrophysical Journal* **871**(1): 94.
**URL:** *http://dx.doi.org/10.3847/1538-4357/aaf649*

Kazantzidis, S., Mayer, L., Mastropietro, C., Diemand, J., Stadel, J. and Moore, B. (2004). Density Profiles of Cold Dark Matter Substructure: Implications for the Missing-Satellites Problem, *The Astrophysical Journal* **608**(2): 663–679.

Lefaucheur, J. and Pita, S. (2017). Research and characterisation of blazar candidates among the fermi/LAT 3fgl catalogue using multivariate classifications, *A&A* **602**: A86.

Lefranc, V., Moulin, E. and for the H. E. S. S. collaboration (2015). Dark matter search in the inner Galactic halo with H.E.S.S. I and H.E.S.S. II.
**URL:** *https://arxiv.org/abs/1509.04123*

Madau, P., Diemand, J. and Kuhlen, M. (2008). Dark Matter Subhalos and the Dwarf Satellites of the Milky Way, *The Astrophysical Journal* **679**(2): 1260–1271.

Mateu, C. and Vivas, A. K. (2018). The Galactic thick disc density profile traced with RR Lyrae stars, *Monthly Notices of the Royal Astronomical Society* **479**(1): 211–227.
**URL:** *http://dx.doi.org/10.1093/mnras/sty1373*

Mirabal, N. (2013). Dark matter versus pulsars: catching the impostor, *Monthly Notices of the Royal Astronomical Society* **436**(3): 2461–2464.

Mirabal, N., Charles, E., Ferrara, E. C., Gonthier, P. L., Harding, A. K., Sánchez-Conde, M. A. and Thompson, D. J. (2016). 3FGL demographics outside the Galactic plane using supervised machine learning: pulsar and dark matter subhalo interpretations, **825**(1): 69.

Moliné, A., Sánchez-Conde, M. A., Palomares-Ruiz, S. and Prada, F. (2017). Characterization of subhalo structural properties and implications for dark matter annihilation signals, *Monthly Notices of the Royal Astronomical Society* **466**: 4974–4990.
**URL:** *http://dx.doi.org/10.1093/mnras/stx026*

Navarro, J. F., Frenk, C. S. and White, S. D. M. (1997). A Universal Density Profile from Hierarchical Clustering, *The Astrophysical Journal* **490**: 493–508.
**URL:** *http://adsabs.harvard.edu/abs/1997ApJ...490..493N*

Oakes, L., Armand, C., Charles, E., di Mauro, M., Giuri, C., Harding, J. P., Kerszberg, D., Miener, T., Moulin, E., Poireau, V., Pueschel, E., Rico, J., Rinchiuso, L., Salazar-Gallegos, D., Tollefson, K. and Zitzer, B. (2019). Combined Dark Matter searches towards dwarf spheroidal galaxies with Fermi-LAT, HAWC, HESS, MAGIC and VERITAS, *Proc. of ICRC 2019* .
**URL:** *https://arxiv.org/abs/1909.06310*

Pierre, M., Siegal-Gaskins, J. M. and Scott, P. (2014). Sensitivity of CTA to dark matter signals from the Galactic Center, *Journal of Cosmology and Astroparticle Physics* **2014**(06): 024–024.

Roszkowski, L., Sessolo, E. M. and Trojanowski, S. (2018). Wimp dark matter candidates and searches—current status and future prospects, *Reports on Progress in Physics* **81**(6): 066201.
**URL:** *http://dx.doi.org/10.1088/1361-6633/aab913*

Salvetti, D., Chiaro, G., La Mura, G. and Thompson, D. J. (2017). 3FGLzoo: classifying 3FGL unassociated Fermi-LAT $\gamma$-ray sources by artificial neural networks, *Monthly Notices of the Royal Astronomical Society* **470**: 1291–1297.

**URL:** http://adsabs.harvard.edu/abs/2017MonthlyNoticesoftheRoyalAstronomicalSociety.470.1291S

Schoonenberg, D., Gaskins, J., Bertone, G. and Diemand, J. (2016). Dark matter subhalos and unidentified sources in the Fermi 3FGL source catalog, *Journal of Cosmology and Astroparticle Physics* **5**: 028.
**URL:** http://dx.doi.org/10.1088/1475-7516/2016/05/028

Springel, V., Wang, J., Vogelsberger, M., Ludlow, A., Jenkins, A., Helmi, A., Navarro, J. F., Frenk, C. S. and White, S. D. M. (2008). The Aquarius Project: the subhalos of galactic halos, *Monthly Notices of the Royal Astronomical Society* **391**(4): 1685–1711.
**URL:** http://dx.doi.org/10.1111/j.1365-2966.2008.14066.x

Springel, V., White, S. D. M., Frenk, C. S., Navarro, J. F., Jenkins, A., Vogelsberger, M., Wang, J., Ludlow, A. and Helmi, A. (2008). Prospects for detecting supersymmetric dark matter in the Galactic halo, *Nature* **456**(7218): 73–76.

Stadel, J., Potter, D., Moore, B., Diemand, J., Madau, P., Zemp, M., Kuhlen, M. and Quilis, V. (2009). Quantifying the heart of darkness with GHALO - a multibillion particle simulation of a galactic halo, *Monthly Notices of the Royal Astronomical Society* **398**(1): L21–L25.

Steigman, G., Dasgupta, B. and Beacom, J. F. (2012). Precise Relic WIMP Abundance and its Impact on Searches for Dark Matter Annihilation, *Physical Review D* **86**(2).
**URL:** http://dx.doi.org/10.1103/PhysRevD.86.023506

The Cherenkov Telescope Array Consortium (2017). Science with the Cherenkov Telescope Array, *ArXiv e-prints* .
**URL:** http://adsabs.harvard.edu/abs/2017arXiv170907997C

The Planck Collaboration (2020). Planck 2018 results. VI. Cosmological parameters, *Astronomy & Astrophysics* **641**: A6.
**URL:** http://dx.doi.org/10.1051/0004-6361/201833910

Walker, M. G. (2013). *Dark Matter in the Milky Way's Dwarf Spheroidal Satellites*.
**URL:** http://adsabs.harvard.edu/abs/2013pss5.book.1039W

Wang, Y.-P., Duan, K.-K., Ma, P.-X., Liang, Y.-F., Shen, Z.-Q., Li, S., Yue, C., Yuan, Q., Zang, J.-J., Fan, Y.-Z. and Chang, J. (2016). Testing the dark matter subhalo hypothesis of the gamma-ray source 3FGL J2212.5+0703, *Physical Review D* **94**(12).

Wood, M., Caputo, R., Charles, E., Mauro, M. D., Magill, J. and for the Fermi-LAT Collaboration, J. P. (2017). Fermipy: An open-source Python package for analysis of Fermi-LAT Data.
**URL:** https://arxiv.org/abs/1707.09551

Xia, Z.-Q., Duan, K.-K., Li, S., Liang, Y.-F., Shen, Z.-Q., Yue, C., Wang, Y.-P., Yuan, Q., Fan, Y.-Z., Wu, J. and Chang, J. (2017). 3FGL J1924.8-1034: A spatially extended stable unidentified GeV source?, *Physical Review D* **95**(10): 102001.
**URL:** http://adsabs.harvard.edu/abs/2017PhRvD..95j2001X

Zechlin, H.-S., Fernandes, M. V., Elsässer, D. and Horns, D. (2012). Dark matter subhaloes as gamma-ray sources and candidates in the first Fermi-LAT catalogue, *Astronomy & Astrophysics* **538**: A93.
**URL:** http://dx.doi.org/10.1051/0004-6361/201117655

Zechlin, H.-S. and Horns, D. (2012). Unidentified sources in the fermi-lat second source catalog: the case for dm subhalos, *Journal of Cosmology and Astroparticle Physics* **2012**(11): 050–050.
**URL:** http://dx.doi.org/10.1088/1475-7516/2012/11/050

# Chapter 5

# Spatial extension as a "smoking gun" for dark subhalo detection with *Fermi*-LAT and implications for WIMP constraints

*Based on J. Coronado-Blázquez et al., Submitted to Journal of Cosmology and Astroparticle Physics (2021)*

## 5.1 Introduction

The nature of dark matter (DM), a non-baryonic component of the Universe accounting for ∼25% of its matter-energy density Planck Collaboration (2020), is one of the most pressing questions in modern physics. Many candidates have been proposed to explain its ultimate nature, such as the *Weakly Interacting Massive Particles* (WIMPs) Bertone (2010). These are well-motivated particles that decouple from the thermal plasma through a freeze-out mechanism, and are able to reproduce the measured cosmological abundance with an interaction cross section coincident with the electroweak scale, known as the "WIMP miracle" Bertone et al. (2005). In the last few years, different strategies have been employed in the quest for WIMP DM detection Garrett and Duda (2011). From direct detection experiments, aiming to observe the scattering of DM-nuclei interactions; and DM production in particle accelerators such as the *Large Hadron Collider* (LHC), to indirect searches, looking for the annihilation (or decay) products of DM. These approaches are in many cases complementary, which allow different models of DM to be probed, subject to different uncertainties Schumann (2019); Kahlhoefer (2017); Gaskins (2016).

In the case of indirect detection, gamma rays have been considered a "golden channel", as they are not deflected by magnetic fields (as opposed to antimatter produced in DM annihilation or decays), and are easier to detect than neutrinos Conrad and Reimer (2017). With gamma-ray telescopes, many different targets have been observed. Among the most promising sources are the Galactic center (GC), e.g., Fermi-LAT Collaboration (2016b, 2017c); H.E.S.S. Collaboration (2016); CTA Consortium (2021), dwarf spheroidal galaxies (dSphs) Fermi-LAT Collaboration (2015c); Oakes et al. (2019); MAGIC Collaboration and Fermi-LAT Collaboration (2016) and galaxy clusters Fermi-LAT Collaboration (2015b, 2010); MAGIC Collaboration (2018), as well as the M31 galaxy, where a gamma-ray signal has been detected both from the inside and towards the outer halo Karwin et al. (2019, 2021). The GC is expected to be the brightest source of gamma rays produced by DM annihilation, yet the astrophysical gamma-ray background in the area, in the form of unresolved point

sources (PS) or diffuse Galactic emission, is dominant and still poorly understood Fermi-LAT Collaboration (2017b); Bartels et al. (2017). On the other hand, while the astrophysical background in dSphs is expected to be negligible Winter et al. (2016), their predicted DM annihilation signal is comparatively fainter.

An interesting and complementary target for gamma-ray searches are the so-called dark subhalos (also known as dark satellites). Within the standard Λ–Cold Dark Matter (ΛCDM) cosmological paradigm, the DM halos that host galaxies should contain a large amount of substructure (subhalos, i.e., halos within halos) as a consequence of the bottom-up hierarchical structure formation scenario Madau et al. (2008). The largest members of this subhalo population (above $\sim 10^7$ M ) will host dSphs, yet most of them are not massive enough to retain baryonic content, i.e., gas, and form stars, and therefore should remain completely dark Walker (2013); Sawala et al. (2015). These objects are predicted to be compact and very concentrated and so, if near enough and composed of WIMPs, they would yield a significant flux of gamma rays that could be detected by gamma-ray telescopes such as the *Fermi*-Large Area Telescope (LAT) on board the NASA Fermi satellite Fermi-LAT Collaboration and Atwood (2009).

The main advantages of these subhalos compared to other competitive DM targets are i) they are not expected to host any non-DM astrophysical gamma-ray emitters, as they do not retain baryonic content and, thus, no astrophysical background is expected; ii) their large number density in the Galaxy; and iii) their high concentrations of DM, as inferred from DM-only N-body sims within ΛCDM Diemand et al. (2008); Springel, White, Frenk, Navarro, Jenkins, Vogelsberger, Wang, Ludlow and Helmi (2008); Moliné et al. (2017). The main disadvantages come from uncertainties related to the lack of observations/identification of these objects in the sky, such as their precise structural properties, abundance (particularly at the smallest predicted scales) and radial distribution within the Galaxy. Indeed, there is an absolute lack of knowledge on their exact position in the sky. Dark subhalos are expected to be almost isotropically distributed from the Earth's point of view; yet, in general terms, only those located very close to us may yield annihilation fluxes large enough to be detected.

A large number of *Fermi*-LAT sources lack clear astrophysical association and have no multi-wavelength counterparts, remaining as unidentified sources (unIDs) at present. These are perfect candidates to perform a search for Galactic dark subhalos, as WIMPs may be annihilating within them, appearing as unIDs in the LAT sky. Many works have already used these targets for indirect DM detection Bertoni et al. (2015, 2016); Calore et al. (2016); Schoonenberg et al. (2016); Hooper and Witte (2017); Berlin and Hooper (2013); Zechlin et al. (2011); Zechlin and Horns (2012); Belikov et al. (2012); Buckley and Hooper (2010); Fermi-LAT Collaboration (2012); Coronado-Blázquez and Sánchez-Conde (2020); Coronado-Blázquez et al. (2021). In previous works, which we will refer to as Paper I and Paper II respectively, starting from a total of 1235 unIDs in the latest LAT point-source catalogs, we applied a series of filters according to the expected emission from dark subhalo annihilation. Once the number was greatly reduced to a pool of just 44 unIDs compatible with DM annihilation in Paper I, a careful, dedicated spectral analysis was performed in Paper II, to enforce or reject the DM hypothesis. Only a handful of them, with marginal statistical significance, were more compatible with a DM origin over a traditional astrophysical explanation. Therefore, we proceeded to set upper limits on the $\langle\sigma v\rangle - m_\chi$ parameter space. As it was shown in Paper I, the fewer the sources compatible with DM among the poll of unIDs, the stronger the DM constraints. To set constraints, the catalog filtering results were combined with expectations from

state-of-the-art N-body simulations, that were conveniently repopulated with low-mass subhalos below the original mass resolution limit using well-motivated ΛCDM recipes. In parallel to this N-body simulation work, it was also necessary to perform a full characterization of the *Fermi*-LAT point-source sensitivity to DM annihilation for different annihilation channels and sky positions. The obtained constraints were competitive, ruling out canonical thermal WIMPs up to ∼20 GeV in the case of $\tau^+\tau^-$ annihilation, this way also being complementary to constraints obtained by other methods and targets.

In Paper II, source spatial extension was pointed out to be a "smoking gun" for this kind of indirect DM search, as already noted by many authors Bertoni et al. (2015, 2016); Hooper and Witte (2017); Xia et al. (2017); Facchinetti et al. (2020); Di Mauro et al. (2020). Indeed, in Paper II we quantified for the first time the expected extension of the brightest (and therefore, easiest to detect) subhalos, as obtained from our repopulated N-body simulations. Very large angular sizes, $\mathcal{O}(5^\circ)$ were found when integrating the annihilation signal up to the scale radius.

Aside from known extended sources (e.g., Fermi-LAT Collaboration (2018)), all sources in official LAT catalogs Fermi-LAT Collaboration (2015a, 2016a, 2017a, 2020) are modeled as point sources, and no additional spatial analysis is performed. Therefore, this allows for a dedicated spatial analysis on the candidates surviving the DM spectral analysis. Yet, none of them shown any preference for a spatially extended signal over a point-like model in Paper II. This would in principle rule out all remaining candidates, or at least put some tension between simulations and data. Nevertheless, it is important to note that a cuspy DM annihilation profile can appear point-like if the extended emission is below the detection threshold, as is likely the case for faint unIDs. For this reason, we could not discard our candidates straight away in Paper II. In Di Mauro et al. (2020) this issue was assessed for the first time with simulated data. In this work, we will address it quantitatively using a realistic sky model based on LAT data for the first time.

We will first characterize the properties of Milky Way (MW) subhalos as well as their expected annihilation fluxes in 5.2. More precisely, in 5.2.1 we will select representative cases of the subhalo population in the Galaxy. These will be studied in detail in 5.2.2, where also their expected annihilation fluxes will be computed. Indeed, we will build DM profiles for these objects and will compute the expected DM annihilation signal as two-dimensional templates accounting for the spatial morphology. Then, we will compute the LAT sensitivity (i.e., the threshold flux) to extended dark subhalos in 5.3, and will study how this sensitivity is degraded with respect to the point-like case computed in Paper I.

We will consider a grid of possible scenarios, varying different analysis parameters such as the annihilation channel or the WIMP mass. For these scenarios, we will look for any hint of angular extension and will characterize it in case of detection. After performing this exercise, we will be able to determine if spatial extension is, indeed, a "smoking gun" for dark subhalo detection and, if so, in which cases and under which configurations. In 5.4 we will discuss and quantify the impact of this subhalo extension study on the DM constraints, namely those presented in Paper I and Paper II, where point-like subhalos were assumed. Finally, we will conclude in 8.6.

## 5.2 Gamma-ray signal from Milky Way subhalos

### 5.2.1 Building of the subhalo DM density profile

As said before, we can distinguish between dSphs, which have a baryonic counterpart, and dark satellites, which do not have it. Most Galactic DM subhalos are expected to be dark satellites, lacking the baryonic content of dSphs. We apply the same conservative[1] upper mass limit of of $M_{sub} < 10^7$M for these objects, as in Paper I and Paper II, thus we will stick to this bound here as well.

Formerly, in Paper I, we analyzed how useful state-of-the-art N-body cosmological simulations of MW-like halos are to learn about the properties of the subhalo population existing at the present time. In both Paper I and Paper II, we made use of the outcome of one of them, namely the Via Lactea II DM-only simulation (VL-II, Diemand et al. (2008)), which resolves subhalo masses as light as $10^4$M and is complete in terms of subhalo abundance down to $\sim 10^6$M . In particular, in our previous work we repopulated the original VL-II to also include subhalos less massive than those in the parent simulation, as some of these small subhalos could still be relevant for DM searches. We did so using theoretically-motivated recipes arising within the ΛCDM structure formation scenario. Once this was done, we also obtained subhalo annihilation fluxes. Furthermore, in Paper II we computed the angular extension of the brightest subhalos in our repopulated simulation, using their scale radii (defined as the radius at which the slope of the density profile is $-2$) as a proxy for subhalo extension. From this study, we found large angular extensions of $\sim 1 - 10^\circ$, and concluded that the majority of them should be actually seen as extended by *Fermi*-LAT, given the instrument's point-spread function (PSF), i.e., its angular resolution (see Figure 9 from Paper II).

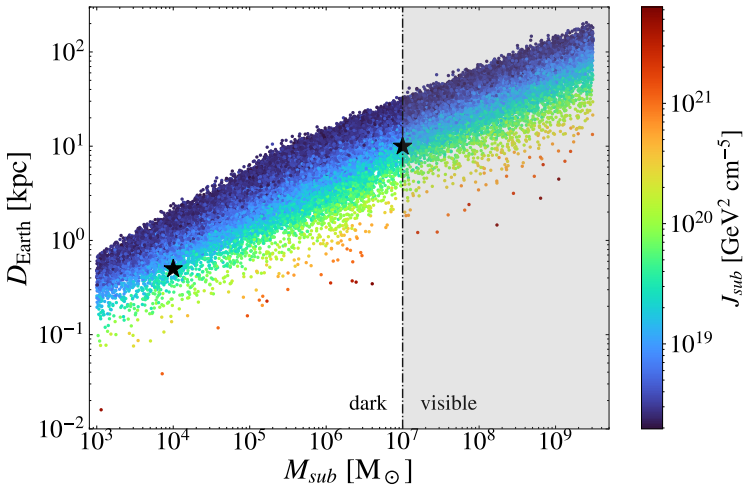


FIGURE 5.1: Distance to the Earth versus the subhalo mass for the 100 brightest subhalos in 1000 repopulations of the VL-II N-body cosmological simulation. The colored z-axis represents the J-factor. The vertical, dark dash-dotted line separates between dSphs and dark subhalos, and the black stars show the mass and distance of the two subhalos that were chosen as representative to perform the *Fermi*-LAT analysis in the next sections.

[1] Conservative in the sense that this will reject some subhalos with large J-factors in the simulation. Objects above $10^7$M may not host baryonic content and be dark subhalos, yet only below this value it is completely safe to rule out dSphs formation Sawala et al. (2015).

We use this study as the starting point to perform the analysis of detecting a possible extension of these objects with *Fermi*-LAT. To quantitatively measure the expected annihilation flux, we define the so-called J-factor for a subhalo as:

$$J_{sub}(\Delta\Omega, l.o.s) = \int_0^{\Delta\Omega} d\Omega \int_{l.o.s} \rho^2(r) dl, \tag{5.1}$$

where $\Delta\Omega = 2\pi(1 - \cos\alpha_{int})$, with $\alpha_{int}$ the integration angle, the integration is calculated along the line of sight ($l.o.s.$) and $\rho(r)$ is the DM density profile. We show in Figure 5.1 the J-factor as a function of mass and distance to the Earth for the brightest subhalos in the repopulated VL-II. We note that subhalos with the highest expected annihilation fluxes, i.e., at least $J_{sub} \gtrsim 10^{19}$ GeV$^2$ cm$^{-5}$, are the most interesting for our purposes. Given the large number of subhalos above this value, as well as the large spread in their masses and distances, it becomes unfeasible to perform a *Fermi*-LAT analysis simulation for each of them. In view of this, we decided to select two representative scenarios. As already stated before, we want to restrict ourselves to dark subhalos. This implies that the highest mass we can reach would be $10^7$ M$_\odot$, following our previous work and results found, e.g., in Sawala et al. (2015). With this in mind, and taken into account what is shown in the top panel of Figure 5.1:

- the first chosen scenario is a subhalo with a small mass of $M_{sub} = 10^4$ M$_\odot$ located near Earth ($D_{\rm Earth} = 0.5$ kpc);
- the second scenario is a subhalo with a mass in the limit of $M_{sub} = 10^7$ M$_\odot$ and situated far from Earth ($D_{\rm Earth} = 10$ kpc).

With this selection of representative cases, we aim at covering the range in masses, distances and expected angular extensions of the fraction of the subhalo population expected to be relevant for our purposes. In Section 5.2.2, we will study in further detail the expected DM-induced emission from these two scenarios as well as their similarities and differences.

For each of these two representative subhalos, we construct a consistent DM density profile following the results found in N-body, DM-only cosmological simulations in a ΛCDM universe Diemand et al. (2008); Springel, Wang, Vogelsberger, Ludlow, Jenkins, Helmi, Navarro, Frenk and White (2008); Hellwing et al. (2016); Ishiyama et al. (2020), which points to a universal DM density profile. More precisely, we adopt the Navarro-Frenk-White (NFW) profile Navarro et al. (1997). We note though that deviations from this universal profile are particularly expected for subhalos, which are subject to multiple and complex processes within their hosts (e.g. tidal stripping, dynamical friction, interaction with baryonic material, etc.). The magnitude and impact of these effects on the subhalo population is still a matter of debate, e.g. van den Bosch et al. (2018); van den Bosch and Ogiya (2018); Ogiya et al. (2019). These deviations are expected to be particularly relevant in the outer regions of the subhalos, where the mass loss is more significant.

Yet, in such regions the annihilation flux has already decreased very significantly compared to the one originated in the inner regions. For this reason, for the sake of our work we will proceed with an NFW profile to model the inner structure of

subhalos[2]. The NFW profile can be written as

$$\rho_{\rm NFW}(r) = \frac{\rho_0}{\left(\frac{r}{r_s}\right)\left(1+\frac{r}{r_s}\right)^2}, \tag{5.2}$$

where $r_s$ and $\rho_0$ are the scale radius and the normalization density, respectively.

One key ingredient to build this NFW profile is to define a mass for an enclosed overdensity of $\Delta_{200} = 200$ within the virial radius of the object, with respect to the critical density $\rho_{crit} = 135.99$ M kpc$^{-3}$ , $M_{200}$. However, for subhalos we recall that the meaning of this quantity becomes unclear. After repeatedly suffering tidal stripping, which removes part of the mass, the profile gets modified, especially in the outermost regions. This causes the standard definition of virialized objects to lack a physical meaning in the subhalo case, motivating new definitions Moliné et al. (2017). Thus, in order to construct an NFW profile from the value of $M_{200}$, a specific concentration-mass relation for the subhalos must be adopted. In Moliné et al. (2017), the authors propose a parametrization of this relation specifically for subhalos, that involves the dependence of the concentration not only with mass but also with subhalo position within the host halo. With this new parametrization, the problem of the definition of $M_{200}$ in subhalos is accounted for by properly correcting their concentrations. This makes this parametrization ideal for our purposes. This relation is expressed as:

$$c_{200}(M_{sub}, x_{sub}) = c_0 \left[1 + \sum_{i=0}^{3}\left[a_i \ln\left(\frac{M_{sub}}{10^8 h^{-1}\mathrm{M}}\right)\right]^i\right] \times [1 + b\ln(x_{sub})], \tag{5.3}$$

where $h = 0.7$ is the reduced Hubble constant and $c_0$, $a_i$ and $b$ are obtained from fits to N-body cosmological simulations at different subhalo mass scales. The concentration is written as a function of the masses of the subhalos $M_{sub}$ and as a function of their positions within the host halo ($D_{sub}$) through $x_{sub} \equiv D_{sub}/R_{host}$. In order to compute $x_{sub}$ for subhalos, we assume $R_{host} = 402$ kpc, i.e. the virial radius of the Milky Way in the VL-II simulation. For our two representative subhalos, $D_{sub}$ is estimated to simply be $D_{sub} = D_{\rm Earth} + d$ , with $d$ = 8.5 kpc the galactocentric distance from the Sun. This is indeed the maximum distance at which both subhalos could lie, which in turn provides a conservative estimate of the annihilation flux (as the concentration decreases with increasing distance to the host halo center). Having computed the subhalo concentration via the Eq. 5.3, we can then obtain $r_s$:

$$r_s = R_{sub}/c_{200}, \tag{5.4}$$

for which we previously computed $R_{sub}$ via the definition of the overdensity $\Delta_{200}$:

$$R_{sub} = \left(\frac{3M_{sub}}{4\pi\Delta_{200}\rho_{crit}}\right)^{1/3}. \tag{5.5}$$

We stress that the purpose of obtaining $R_{sub}$ is only to build a coherent NFW profile for subhalos, since by adopting the $c_{200}(M_{sub})$ relation in Moliné et al. (2017)

[2]We note that, since we are interested in the innermost region of the subhalo, i.e. the one within its scale radius where most of the annihilation is produced, any other realistic DM density profile such as Einasto Einasto (1965) or a truncated NFW Kazantzidis et al. (2004) is expected to render similar results. Only core profiles would potentially yield significantly different results, however these profiles are not expected for these small objects, as they are already devoid of baryons, which are the ones that drive the formation of cores Pontzen and Governato (2012); Cintio et al. (2014).

we mostly overcome the problem to describe subhalos with standard, non-truncated and less concentrated NFW profiles. Indeed, the variable that we will use to estimate the actual spatial extension of the subhalos is the tidal radius $R_{tidal}$, obtained by applying the Roche criterium King (1962):

$$R_{tidal} = D_{GC} \left( \frac{M_{sub}}{M(< D_{GC})} \right)^{1/3}, \tag{5.6}$$

where $D_{GC}$ is the distance to the GC. The last parameter that is needed to build the subhalos DM density profiles is the normalization density, $\rho_0$. We impose the normalization condition $M_{sub} = \int_0^{R_{sub}} \rho_{NFW}(r) r^2 dr d\Omega$, and rewriting this in terms of the concentration parameters, we can finally compute $\rho_0$ as

$$\rho_0 = \frac{2\,\Delta_{200}\,\rho_{crit}\,c_{200}}{3\,F(c_{200})}, \tag{5.7}$$

where $F(c_{200}) = \frac{2}{c_{200}^2} \left( \ln(1 + c_{200}) - \frac{c_{200}}{1+c_{200}} \right)$. The obtained profile parameters for each of the two representative subhalo scenarios are given in Table 5.1.

| Name | $D_{\rm Earth}$ [kpc] | $M_{sub}$ [M$_\odot$] | $c_{200}$ | $r_s$ [kpc] | $R_{tidal}$ [kpc] | $\log_{10}\rho_0$ [M$_\odot$/kpc$^3$] |
|---|---|---|---|---|---|---|
| Subhalo 1 | 0.5 | $10^4$ | 71.36 | 0.006 | 0.036 | 9.00 |
| Subhalo 2 | 10 | $10^7$ | 42.31 | 0.107 | 0.516 | 2.95 |

TABLE 5.1: Parameters needed to build the NFW DM profiles of our two subhalo scenarios, each of them representatives of the fraction of the Galactic dark subhalo population that is relevant in terms of expected annihilation flux. See Section 5.2.1 for details on the derivation of these parameters.

### 5.2.2 Gamma-ray flux from subhalos

The DM modeling performed in the previous section is the starting point for obtaining the expected DM-induced gamma-ray flux for the two representative subhalo cases. Assuming that the DM is made of Majorana WIMPs, the annihilation flux can be computed as:

$$\frac{d\phi_\gamma}{dE}(E, \Delta\Omega, l.o.s.) = \frac{1}{8\pi} \frac{\langle \sigma v \rangle}{m_{DM}^2} \frac{dN_\gamma}{dE}(E) \times J(\Delta\Omega, l.o.s.), \tag{5.8}$$

where $\frac{d\phi_\gamma}{dE}$ is the differential gamma-ray flux, $\langle \sigma v \rangle$ is the velocity-averaged annihilation cross-section, $m_{DM}$ is the DM mass, $\frac{dN_\gamma}{dE}$ is the photon spectrum and $J$ is the astrophysical factor or J-factor defined as in Eq. 5.1. We notice that two main dependencies can be identified in the flux. First, an energy dependence that appears only in the particle physics term, carrying all the information of the mass of the DM candidate and the annihilation channels. Secondly, the spatial dependence appearing as the J-factor. This allows us to factorize these terms independently, and to model the spatial distribution of the DM independently of energy. The photon spectrum from DM annihilation strongly depends on the mass of the dark matter particle and on the annihilation channel, which indeed leads to very different spectra depending on which combinations are selected. We will explore the impact on the gamma-ray flux of these dependencies in Section 5.3.2.

The computation of the J-factors is performed using the CLUMPY code Charbonnier et al. (2012); Bonnivard et al. (2016); Hütten et al. (2019). CLUMPY is a very flexible code written in C++, which allows us to model the DM profiles of the subhalos as described above and to compute J-factors, annihilation fluxes, etc. The obtained values of the integrated J-factors for each considered subhalo model are shown in Table 5.2 and also highlighted in Figure 5.1. We note that, since we do not expect subhalos to host a significant population of sub-subhalos, we do not add further levels of subhalo substructure to the computation of the J-factors, as this effect has been shown to be very subdominant Moliné et al. (2017).

| Name | $\log_{10} J_{sub}$ [GeV$^2$cm$^{-5}$] | $\log_{10} J_s$ [GeV$^2$cm$^{-5}$] |
|---|---|---|
| Subhalo 1 | 19.20 | 19.17 |
| Subhalo 2 | 19.14 | 19.10 |

TABLE 5.2: Total, integrated J-factors for the two representative subhalo scenarios, in the first column integrated up to the whole object ($R_{sub}$), and up to $r_s$ in the second.

The results shown in Table 5.2 show an emerging degeneracy between the two considered physical scenarios chosen as representative of the population of subhalos in the MW relevant in terms of annihilation flux. Indeed, both scenarios will be nearly indistinguishable in terms of the expected annihilation flux, despite the fact that both physical scenarios were defined independently in Section 5.2.1. In order to take a closer look at this degeneracy, we can also use CLUMPY to create two-dimensional templates, reproducing the spatial morphology of the expected DM annihilation signal. These maps are shown in Figure 5.2 for the two representative subhalos, and represent, indeed, the main CLUMPY result that will be later used for the LAT analysis. The figure also exhibits the same degeneracy between the two scenarios that appeared before in Table 5.2 for the integrated J-factors. To better characterize both the spatial morphology and this apparent degeneracy, we define two angular quantities. The first one is the angular extension in the sky associated to the scale radius:

$$\theta_s = \arctan\left(\frac{r_s}{D_{\rm Earth}}\right). \tag{5.9}$$

Also, it is convenient to define the angular extension associated to the angle that contains 68% of the DM annihilation flux, $\theta_{68}$, i.e.:

$$J(\theta_{68}) = 68\% \times J_{sub}. \tag{5.10}$$

These two quantities as well as the annihilation flux profile within the two representative subhalos are illustrated in Figure 5.3. From this Figure, we can observe that the two scenarios exhibit very similar flux profiles, with only small differences arising in the outermost regions, for angles above 1°. As it will be shown later on, the fact that the selected scenarios are mostly indistinguishable from the spatial point of view will impact the *Fermi*-LAT analysis of these objects, where we expect this degeneracy to persist.

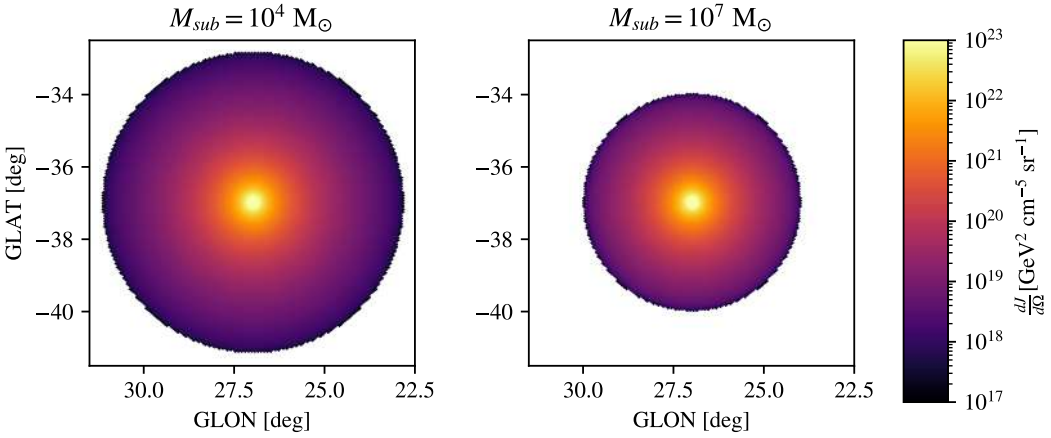


FIGURE 5.2: Two-dimensional templates of the DM-induced gamma-ray spatial morphology for the two representative subhalo scenarios defined in Section 5.2.1. The z axis represents the differential J-factor $\left(\frac{dJ}{d\Omega}\right)$ computed according to the DM modeling of Section 5.2.1.

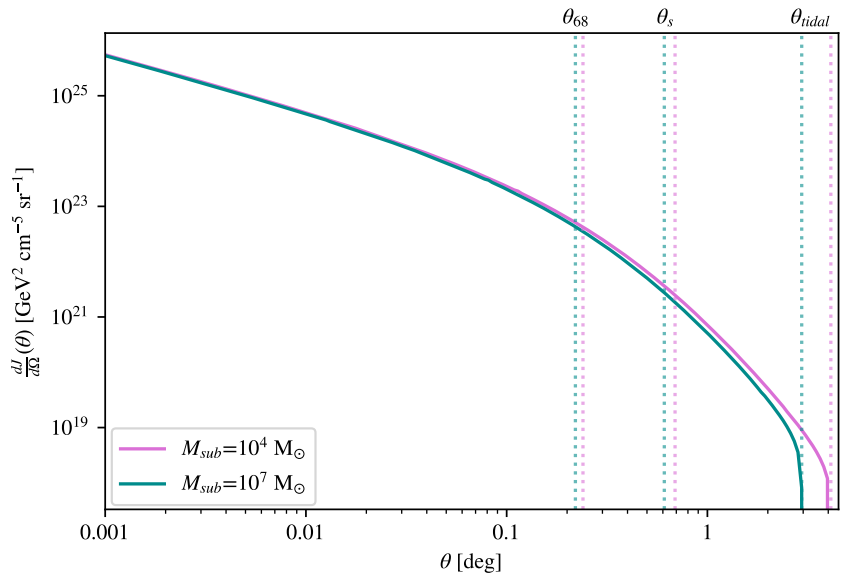


FIGURE 5.3: Differential J-factor versus the radial angle for the two representative subhalo scenarios defined in Section 5.2.1. Here, we also show $\theta_{tidal}$, which represents the angle subtended by $R_{tidal}$, $\theta_s$ as defined in Eq. 5.9 and $\theta_{68}$ as defined in Eq. 5.10, all depicted with a different color in each subhalo case. The spatial distributions of the J-factor are almost identical until about 1°, emphasizing the degeneracy discussed in the main text.

## 5.3 LAT sensitivity to extended dark matter subhalos

In this section, we will compute the actual sensitivity of the LAT to an extended DM subhalo in the two subhalo mass modeling scenarios described in Section 5.2. For each subhalo model, we will consider two benchmark annihilation channels: $b\bar{b}$, representative of hadronic final states, and $\tau^+\tau^-$, representative of leptonic ones. We first compute the minimum flux required to detect an extended subhalo in Section 7.3.1, and compare it with the case of point-like sources. Then, in Section 5.3.2 we

extend the computation to a grid of different setups to study the LAT response to an extended signal.

### 5.3.1 Threshold flux for extended subhalo detection

First, we compute the minimum flux that is needed in order to detect an extended subhalo with the *Fermi*-LAT. To do so, we simulate the LAT sensitivity by placing a putative, extended DM subhalo in the sky. Then, we vary the normalization of the source until it reaches detection – at that very moment the integrated flux will be the minimum detection flux.

To perform such computation, we rely on *fermipy* Wood et al. (2017). We use 11 years of LAT data, with an energy range between 500 MeV and 2 TeV, Pass 8 events Atwood et al. (2013), with the `P8R3_SOURCE_V2` instrumental response functions (IRFs, Bruel et al. (2018)), and utilize all available photons (FRONT+BACK), excluding those arriving with zenith angles greater than 105°.

As we are interested in high-latitude sources, like in Paper I and Paper II, we first performed some tests placing the subhalo at different, high Galactic latitudes; yet we found the corresponding variations in our results to be negligible when compared to other uncertainties that will be presented in this work. Nevertheless, we assume the subhalo to lie in a relatively clean patch of the sky, with no sources nearby ($\leq 1°$).[3] Because of that, the results in this section refer only to a specific region of interest (ROI) of $15° \times 15°$ centered at $(l, b) = (27°, -37°)$. To model point sources lying within the ROI, we use the second release of the latest LAT point-source catalog, 4FGL–DR2 Fermi-LAT Collaboration (2020); Ballet et al. (2020), version `gll_psc_v27.fit`. In the analysis, the `gll_iem_v07.fits` and `iso_P8R3_SOURCE_V2.txt` templates[4] are used to model the Galactic and isotropic diffuse emission, respectively. Table 6.1 summarizes the analysis setup, with an spatial extension given by the templates shown in Figure 5.2.

| | |
|---|---|
| Coordinates $(l, b)$ | $(27°, -37°)$ |
| Time domain (ISO 8601) | 2008-08-04 to 2019-08-03 |
| Time domain (MET) | 239557417 to 586490000 |
| Energy range | 500 MeV – 2 TeV |
| IRFs | `P8R3_SOURCE_V2` |
| Event type | FRONT+BACK |
| Point-source catalog | 4FGL–DR2 |
| ROI size | $15° \times 15°$ |
| Max zenith angle | 105° |
| Galactic diffuse model | `gll_iem_v07.fits` |
| Isotropic diffuse model | `iso_P8R3_SOURCE_V2.txt` |

TABLE 5.3: Summary of the *fermipy* analysis setup.

The subhalo is injected with `gta.add_source()` and, adopting a specific input WIMP spectrum (defined by its mass and annihilation channel) as obtained by means of DMFit Jeltema and Profumo (2008), we run `gta.simulate_roi()` to simulate the

[3] We note that, in case that the subhalo is close enough to another gamma-ray emitter due to projection effects, it is likely that Fermi will identify it as an extended source when in reality there are two distinct objects, e.g., Chou et al. (2018). This could also alter the spectral properties due to the spillover of photons in the ROI. Further tests were performed with no near sources closer than 2° with no difference in the results.

[4] `https://fermi.gsfc.nasa.gov/ssc/data/access/lat/BackgroundModels.html`

full ROI with the photon events[5]. Then, we free the subhalo flux normalization, defined as,

$$\mathcal{N} = J \times \langle \sigma v \rangle \quad \left[ \mathrm{GeV}^2 \cdot \mathrm{cm}^{-2} \cdot \mathrm{s}^{-1} \right], \tag{5.11}$$

where $J$ is the J-factor and $\langle \sigma v \rangle$ is the velocity-averaged annihilation cross section as both introduced in Eq. 5.1. Indeed, the spectrum normalization is completely degenerate between these two quantities, and therefore we will discuss the results based on this overall normalization from now on. In practice, given a certain value of J-factor or $\langle \sigma v \rangle$, it will be trivial to obtain the complementary quantity as a function of $\mathcal{N}$. To compute the detection significance of the source, we adopt the Test Statistic Rico (2020),

$$\mathrm{TS}_{\mathrm{det}} = 2 \cdot \log \left[ \frac{\mathcal{L}(H_1)}{\mathcal{L}(H_0)} \right], \tag{5.12}$$

where $\mathcal{L}(H_0)$ and $\mathcal{L}(H_1)$ are, respectively, the likelihoods under the null (no source) and alternative (existing DM source) hypotheses. In a similar fashion, one can define the extension significance of a source,

$$\mathrm{TS}_{\mathrm{ext}} = 2 \cdot \log \left[ \frac{\mathcal{L}(EXT)}{\mathcal{L}(PS)} \right] \tag{5.13}$$

where $\mathcal{L}(EXT)$ is the likelihood of the extended hypothesis and $\mathcal{L}(PS)$ is the one of the point source. To ensure either a robust source detection or an unequivocal extended source, we will search for the minimum flux value ($F_{min}$) that would yield at least $\mathrm{TS}_{\mathrm{det}} = 25$ or $\mathrm{TS}_{\mathrm{ext}} = 25$, respectively.[6] Note that, as it will be shown later in this same section, it is not possible to simultaneously have $\mathrm{TS}_{\mathrm{det}} = \mathrm{TS}_{\mathrm{ext}} = 25$, as for a source to appear unequivocally as extended in the analysis, ($\mathrm{TS}_{\mathrm{ext}} = 25$), the required signal must be properly characterized, thus exhibiting $\mathrm{TS}_{\mathrm{det}} \gg 25$.

We use the `gta.optimize` and `gta.fit` *fermipy* subroutines to simultaneously fit all the sources in the ROI and to compute the spectral properties of the subhalo, including its $\mathrm{TS}_{\mathrm{det}}$. We then run the code iteratively, increasing or decreasing the normalization, until the source exhibits just $\mathrm{TS}_{\mathrm{det}} = 25$.[7] At this point, the obtained integrated flux is $F_{min}^{det}$.

In order to compute $F_{min}^{ext}$, i.e., the minimum flux required to have $\mathrm{TS}_{\mathrm{ext}} = 25$, we will follow a similar procedure: once the source is detected, a fit to the spatial extension is performed via `gta.extension()`. There are two available 2D fitting templates in *fermipy*, a 2D uniform disk and a 2D Gaussian profile. We adopt the latter from now on, as no differences were found when using the 2D disk. Although neither the Gaussian nor the disk profile are a perfect model of the expected DM source spatial profile, an important advantage of using these generic spatial templates is that they are agnostic to the real, underlying annihilation profile. Indeed, should a DM subhalo be detected with the LAT, the specific spatial template would be unknown and, therefore, the computations reported in this work would be actually closer to reality. This time, as we are only interested in the preference for extension with respect to the PS hypothesis, $\mathrm{TS}_{\mathrm{ext}}$ (Eq. 6.2), we vary iteratively the normalization until

[5] This procedure assumes a perfect description of the background components. Yet, being our interest subhalos well outside the Galactic plane with no nearby sources, large deviations from this assumptions are not expected.

[6] This threshold is approximately a 5-$\sigma$ significance in the case of detection, as $TS_{det} \sim \sigma^2$.

[7] Throughout this section, we will assume a $\pm 3$ numerical tolerance in all TS computations in order to ensure convergence.

we reach the required $TS_{ext} = 25$. At that point, we save the integrated flux of the source, $F_{min}^{ext}$.[8]

Finally, in order to have proper statistics, we repeat each configuration of subhalo modeling, WIMP mass, and annihilation channel 10 times for both our evaluation of subhalo detection and detection of extension. The results of both $F_{min}^{det}$ and $F_{min}^{ext}$ for every channel and subhalo model are shown in Figure 5.4, where the threshold flux is lowered for larger masses in every case. As can be seen, the two considered subhalo models are completely degenerate from the point of view of detection and extension analysis. As a result, in the remaining of this section we will focus on only one of them, being the conclusions identical for the other.

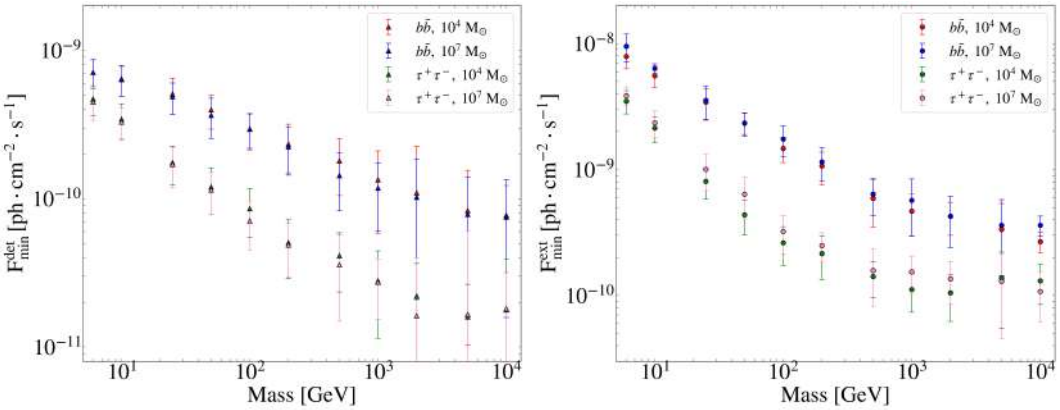


FIGURE 5.4: Comparison between minimum fluxes for extended subhalos. **Left panel:** Minimum flux for detection ($TS_{det} = 25$), for the two considered annihilation channels and subhalo models. **Right panel:** The same for the case of minimum flux for extension ($TS_{ext} = 25$). The uncertainty bars come from averaging across ten realizations. Note the different flux scale in each panel.

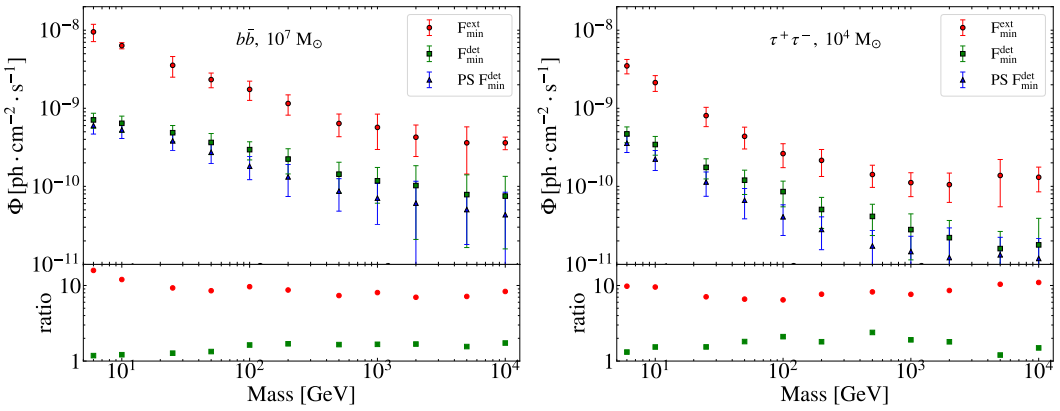


FIGURE 5.5: Minimum fluxes for point-source $TS_{det} = 25$ detection (PS), extended subhalo $TS_{det} = 25$ detection ($F_{min}^{det}$), and extension with $TS_{ext} = 25$ ($F_{min}^{ext}$), for $b\bar{b}$ (left panel) and $\tau^+\tau^-$ (right panel) annihilation channels. Lower panels show the ratio between $F_{min}^{det}$ (green squares) and $F_{min}^{ext}$ (red circles) when compared to the PS threshold.

[8] We note that the convergence of the code in this case is slower, as the analysis of extension does not behave as smoothly as the detection, due to the photon spill over, which makes the relation between $TS_{ext}$ and normalization more unstable (see Figure 5.15 in Appendix 5.6.2).

We can also compare the detection and extension fluxes with respect to the PS case, i.e., with no spatial template. This is shown in Figure 5.5. In both Figure 5.4 and 5.5 we note that annihilation into $\tau^+\tau^-$, yielding a harder spectrum than the $b\bar{b}$ annihilation channel, is easier to detect (i.e., requires a lower flux). There is a consistent trend of obtaining lower fluxes for larger WIMP masses in every case. Moreover, it is interesting to compare the ratios between the three of them; when analyzing detection ($TS_{det} = 25$), we can distinguish between the PS and extended cases. The latter turns out to be a factor $1.5 - 2$ larger (meaning more difficult to detect), as the photons are spatially spread, and therefore the sensitivity is slightly decreased. Nevertheless, being that the DM annihilation profile is very cuspy (see Section 5.2), most of the signal comes from the innermost part of the profile, and there is little difference with respect to the PS case. This is no longer true for the case of detection of extension ($TS_{ext} = 25$), where the required fluxes are a factor $8 - 10$ larger than in the PS case (and therefore a factor $4 - 6$ larger than the $F^{det}_{min}$ for the extended template). This trend is observed in every channel and subhalo model.

Overall, the different behaviors found for both annihilation channels can be explained due to the convolution of the LAT sensitivity and the peak energy of the DM spectrum: the LAT is more sensitive to energies $\sim 1 - 10$ GeV, while the DM spectrum peaks at energies $\sim m_\chi/30$ in the case of $b\bar{b}$ and $\sim m_\chi/3$ in the case of $\tau^+\tau^-$. Therefore, depending on the annihilation channel, increasing the WIMP mass will either improve the instrument's performance or reach a sensitivity plateau. In the case of $b\bar{b}$, the spectrum peaks at the LAT maximum sensitivity for WIMP masses $m_\chi \sim 50 - 500$ GeV, while in the case of $\tau^+\tau^-$, this maximum sensitivity is reached for masses $m_\chi \sim 5 - 50$ GeV. Thus, for masses larger than these values, the corresponding $TS_{det}$ required to have $TS_{ext} = 25 \pm 3$ is approximately constant. These trends are observed in Figure 5.6.

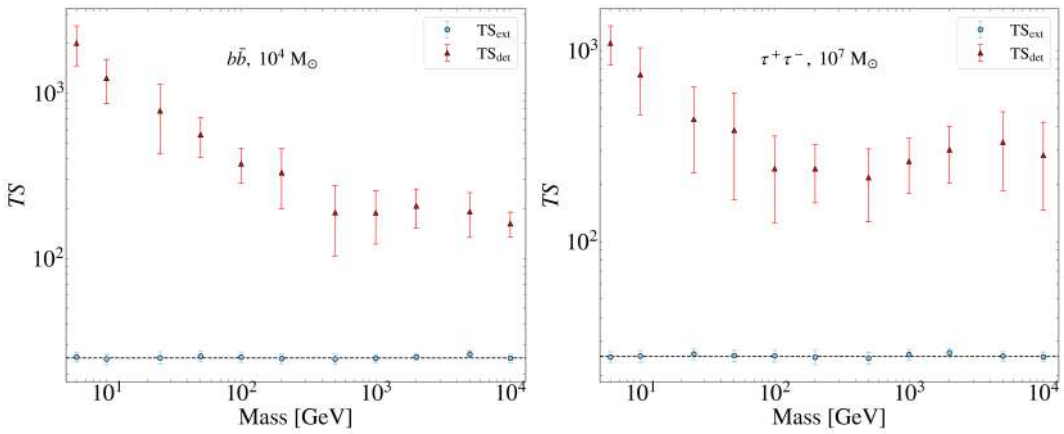


FIGURE 5.6: Comparison between the TS of detection ($TS_{det}$) and TS of extension ($TS_{ext}$) for the case of achieving $F^{ext}_{min}$, i.e., $TS_{ext} = 25$ (we use a tolerance of $\pm 3$). Left panel shows the results for $b\bar{b}$ and right panel for $\tau^+\tau^-$ annihilation channel.

As a general conclusion of this section, our results allow for a quick evaluation of a potential DM subhalo candidate found among the LAT unIDs – depending on the value of $(TS_{det}, TS_{ext})$, one can evaluate how likely it is that the emission is coming from a DM subhalo, according to the previous figures. This is especially interesting when considering the currently best LAT DM constraints Fermi-LAT Collaboration and The DES Collaboration (2017), which do not constrain canonical thermal WIMPs for masses larger than $\sim$ 50 GeV and $\sim$ 100 GeV in the case of $b\bar{b}$ and $\tau^+\tau^-$ final

states, respectively. A putative candidate, not discarded by these constraints, should be evaluated according to the results in this section, taking the information on expected spatial extension as an additional DM "filter" to spot potential dark subhalos.

### 5.3.2 Recovery of spatial information from dark subhalos

Once the LAT threshold sensitivity to extended dark subhalos has been properly characterized, we can study a more general performance of the instrument in a wider range of subhalo configurations, varying the same parameters as in Section 7.3.1 (different subhalo models, WIMP masses, annihilation channels) and including new normalization values – not searching for a specific value of detection/extension significance but rather blindly studying the output with different normalizations.

To do so, we will first define the grid of models to be studied. As in Section 7.3.1, we consider two subhalo models, ($10^4$ M$_\odot$, 0.5 kpc) and ($10^7$ M$_\odot$, 10 kpc), that were fully described in Section 5.2. We will consider 11 WIMP masses that span over the WIMP range, $m_\chi = [6, 10, 25, 50, 100, 200, 500, 1000, 2000, 5000, 10000]$ GeV, and the same two annihilation channels as before are selected as benchmark models, $b\bar{b}$ and $\tau^+\tau^-$. Finally, we choose an $\mathcal{N}$ grid which will be representative of viable DM models (even if extreme in some cases), with 15 values logarithmically spaced between $\mathcal{N} = 10^{-6} - 10^{-3}$ (i.e., 5 values per order of magnitude). The lower limit would be representative of, e.g., a $\langle\sigma v\rangle = 10^{-26}$ cm$^3 \cdot$ s$^{-1}$ and $J = 10^{20}$ GeV$^2 \cdot$ cm$^{-5}$, this is, a (quasi)canonical thermal WIMP with a J-factor similar to that of the best dSphs. The upper limit would correspond to, e.g., a $\langle\sigma v\rangle = 10^{-24}$ cm$^3 \cdot$ s$^{-1}$ and $J = 10^{21}$ GeV$^2 \cdot$ cm$^{-5}$ model, i.e., an annihilation cross section roughly 2 orders of magnitude above the thermal value, and an extreme J-factor value according to our results from N-body simulations (see Figure 5.1), therefore an extreme yet possible DM scenario.

With this grid definition and set of models, we proceed similarly to Section 7.3.1, this time directly saving the output of each setup rather than forcing the analysis to converge to some predefined TS values. This is, for each 10 repetitions of the ($m_\chi$, $\mathcal{N}$, channel, subhalo model) combination, we perform the analysis of the ROI and, provided the source is detected ($\mathrm{TS_{det}} \geq 25$), we search for spatial extension and perform a spectral fit to DM. A discussion on the precision of *fermipy* to recover the spectral information is deferred to Appendix 5.6.1. This way we obtain a full characterization of the source, including its detection significance, integral flux, extension significance, angular extension and best-fit DM parameters.

Figure 5.7 shows the photon flux versus both the detection and extension significances. The relations are remarkably linear (in log-space), meaning that the more flux emitted by the subhalo, the easier will be to have a signal detection and the more preference for extension will be found, both as expected. Additionally, the uncertainty in the flux among the 10 realizations gets smaller for larger $\mathcal{N}$, as the source can be better characterized for higher fluxes.

Interestingly, low WIMP masses are easier to detect and to characterize. Indeed, as the input $\mathcal{N}$ values are all the same for every WIMP mass in Figure 5.7, we can conclude that the lowest WIMP masses considered in our analysis are always detected and spatially resolved, while this is not true for heavier WIMPs. The reason is mainly twofold: i) for a fixed $\mathcal{N}$, the DM spectrum per annihilation is dimmer as we go towards higher energies, and ii) the sensitivity of the LAT peaks at roughly 1–5 GeV, while the energy peak of a DM spectrum is $E^{b\bar{b}}_{peak} \sim m_\chi/30$ for $b\bar{b}$ and $E^{\tau^+\tau^-}_{peak} \sim m_\chi/3$ for $\tau^+\tau^-$. Therefore, masses larger than $m_\chi \sim 150$ (50) GeV for

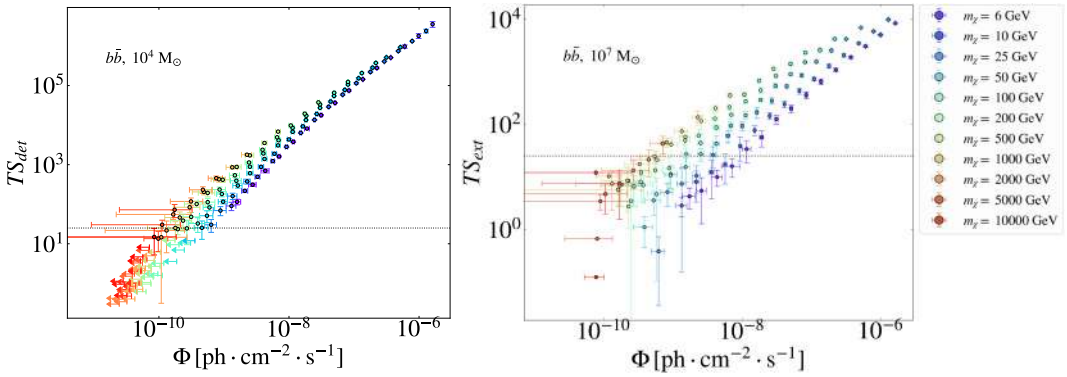


FIGURE 5.7: Comparison of the integrated source flux with the corresponding detection ($TS_{det}$; left panel) and extension significances ($TS_{ext}$; right panel), for the two subhalo models and $b\bar{b}$ annihilation channel. Each point is averaged across the 10 different realizations of the same setup. As in Section 7.3.1, the two subhalo models that we consider turn out to be completely indistinguishable within errors, and therefore we show only one of them in each case.

$b\bar{b}$ ($\tau^+\tau^-$) will be increasingly difficult to detect, and therefore progressively more difficult to be spatially resolved as well.

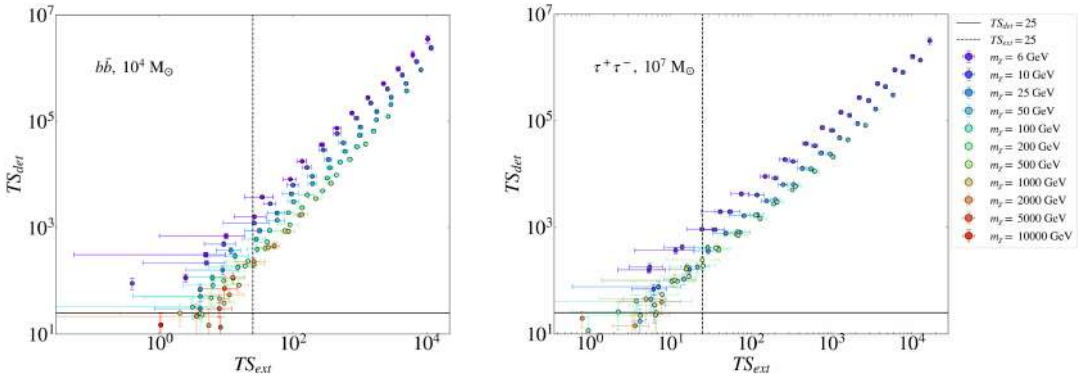


FIGURE 5.8: Detection $TS_{det}$ and extension $TS_{ext}$ significances for the ($b\bar{b}$, $10^4$ M$_\odot$) and the ($\tau^+\tau^-$, $10^7$ M$_\odot$) models (left and right panels, respectively). Vertical and horizontal lines mark, respectively, $TS_{ext} = 25$ and $TS_{det} = 25$. Each point is averaged across the 10 different realizations of the same setup.

In Figure 5.8, we show the relation, again linear, between detection and extension significances for both $b\bar{b}$ and $\tau^+\tau^-$, a complementary version of the previous figure. The data points, averaged over the 10 different realizations for each analysis setup, also exhibit a trend of decreasing uncertainty[9] with increasing $\mathcal{N}$ values, as expected. Note that the uncertainties associated to $TS_{ext}$ are consistently larger than the ones for $TS_{det}$ (see Appendix 5.6.2). This can also be seen in Figure 5.9, where $\mathcal{N}$ is shown against $TS_{det}$ and $TS_{ext}$, in this case for every single realization of the analysis. For small normalization values, only low masses yield a detection, while for the largest values heavy WIMPs also show up.

Figures 5.7 to 5.9 were mainly focused on the detection/extension significances, yet it is worth also asking what is the actual spatial extension we can recover in

[9]We define our uncertainty as quadratic combination of individual error plus standard deviation among realizations.

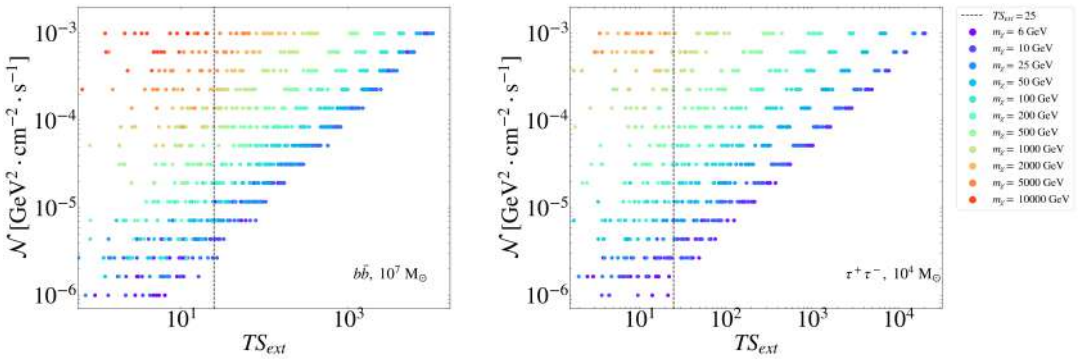


FIGURE 5.9: Normalization of the source (J-factor $\times$ $\langle\sigma v\rangle$) versus the extension significance $TS_{ext}$, for the ($b\bar{b}$, $10^7$ M$_\odot$) and the ($\tau^+\tau^-$, $10^4$ M$_\odot$) models, in all individual realizations. Vertical, black line marks $TS_{ext} = 25$.

case of having an extended signal. This is shown in Figure 5.10, where the best-fit angular extension $R_{68}$ (containing 68% of the DM-induced emission) is given versus both $TS_{det}$ and $TS_{ext}$. We recall here that the predicted $\theta_{68}$ value for the considered subhalo models is 0.22°.

As found in previous figures, one can see that the lowest WIMP masses are the ones better resolved for every $\mathcal{N}$ value, while larger masses have associated larger error bars, and these increase for lower $\mathcal{N}$ values as naturally expected. Additionally, we note that, for a fixed WIMP mass, the central value of $R_{68}$ is stable, regardless of $\mathcal{N}$, while $R_{68}$ will shift to lower values as we increase the WIMP mass. Focusing e.g., on the $b\bar{b}$ case, the lowest WIMP mass predicts $R_{68} \sim 0.28°$, larger than the theoretical value. For $m_\chi \sim 25$ GeV they coincide, while it shifts down to $R_{68} \sim 0.18°$ for $m_\chi \sim 1$ TeV. This is possibly due to i) the fact that we are modeling the spatial extension with a Gaussian profile, which represents only a fair approximation of the input spatial DM profile, as previously discussed; ii) the DM spectrum peaking at higher energies for heavier WIMPs, which, convoluted with the IRFs and PSF, may also partially produce this shift; or iii) most likely, a combination of both effects.

The angular sizes and their associated uncertainties as a function of $TS_{det}$ and $TS_{ext}$ may allow us to define an additional "filter" that unIDs should pass should they be viable DM subhalo candidates (see Paper I). Indeed, our results in this Section allow to predict the expected angular extension and significance of the subhalo candidate provided that the unID is bright enough and is well fitted to a DM spectrum. In the most optimistic case, a bright unID source with a spectrum compatible with DM but appearing as strictly point-like could in principle be ruled out as a viable DM candidate. However, in practice most point-like sources cannot be safely ruled out as DM, except for sufficiently large detection significances that would unequivocally predict angular extension. This is so given the typical uncertainties present in the case of low $\mathcal{N}$ values (i.e., faint sources, which is the case for most unIDs). Likewise, if an unID turns out to be a potential subhalo candidate, i.e., it exhibits both a significant spatial extension and prefers a spectral fit to DM, one could start from its $TS_{det}$, $TS_{ext}$, $R_{68}$ and $m_\chi$ and see where it falls in Figure 5.10. This exercise will be performed elsewhere on particular dark subhalo candidates among the LAT unIDs.

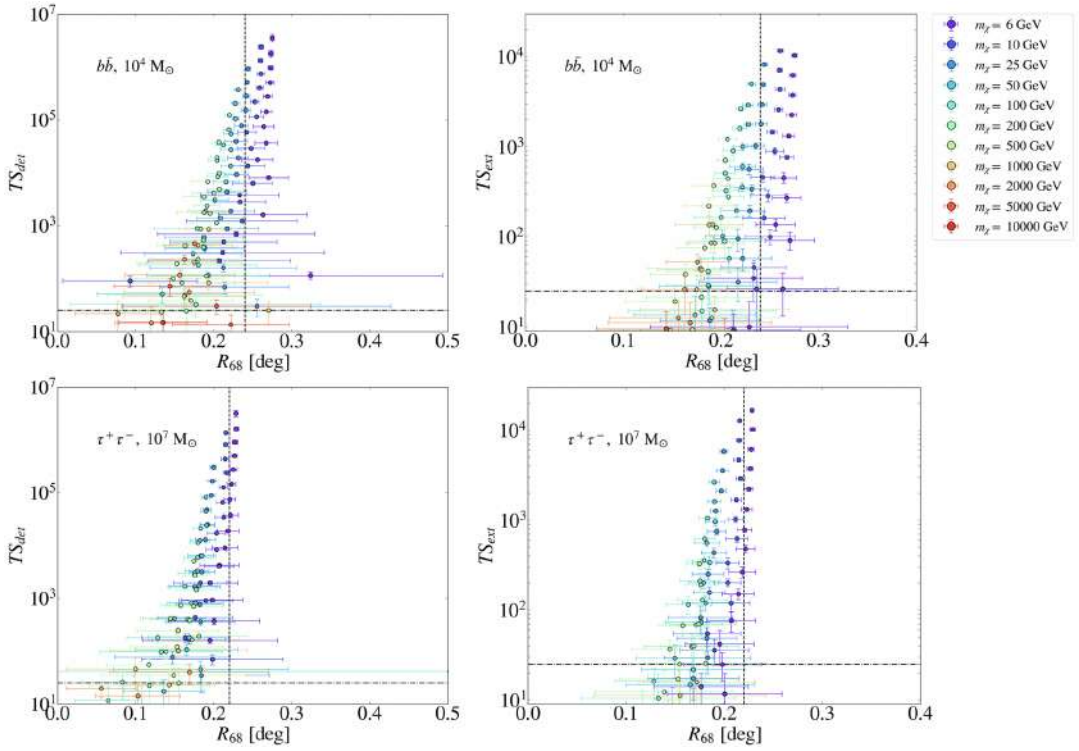


FIGURE 5.10: Best-fit extension $R_{68}$ versus the extension ($TS_{ext}$) and detection ($TS_{det}$) significance, for the ($b\bar{b}$, $10^4$ M$_\odot$) and the ($\tau^+\tau^-$, $10^7$ M$_\odot$) models. Each $R_{68}$ is the average value of the 10 realizations, while their uncertainties are computed via a quadratic sum of the individual realization uncertainties and the $1\sigma$ spread across realizations.

## 5.4 Implications for WIMP dark matter constraints

Our study on the characterization of the spatial extension of a potential dark subhalo signal in LAT data could have relevant implications for the case of setting DM constraints with unIDs. Following the methodology in Paper I, the constraints on the WIMP mass vs. annihilation cross section parameter space we can set are given by,

$$\langle \sigma v \rangle_{UL} = \frac{8\pi \cdot F_{min}^{det}}{J \cdot N_\gamma} \, m_\chi^2, \tag{5.14}$$

where $F_{min}^{det}$ is the minimum detection flux (see Section 7.3.1), $J$ the J-factor (see Section 5.2) and $N_\gamma$ the integrated DM spectrum per annihilation, also known as the "particle physics factor", which is obtained from Cirelli et al. (2011) (see Section 5.2 and Eq. 5.8). The DM spectrum is integrated from 500 MeV, to match the $F_{min}$ computations through this paper. As in our previous papers, the J-factor is defined as the one above which 95% of the J-factor distribution across different realizations of the Galactic subhalo population is contained, thus allowing us to derive 95% C.L. upper limits (see Paper I for more details). Throughout this Section, we will assume this same definition when discussing specific J-factor values.

There are two main differences with respect to our previous constraints in Paper I and Paper II, namely:

- Point sources: The constraints were set assuming point-like sources, i.e., using

a detection threshold flux $F^{PS}_{min}$, while in Section 7.3.1 we computed how the actual flux for extended source detection is degraded by a factor $\sim$ 1.5 (see Figure 5.6).

- J-factor: The J-factor was computed by integrating the signal up to the scale radius ($J_s$), as we expected this to be representative of the emission that may be observed by the LAT. However, as seen in Figure 5.3, $\theta_s$, i.e., the radius subtended by the scale radius, is a factor $\sim$ 3 larger than the one given by $\theta_{68}$, containing 68% of the emission – the theoretical equivalent of the *fermipy* $R_{68}$.

Our work in the previous sections allows us to finally quantify the expected spatial signal of dark subhalos, whose angular size is far from being $\theta_s$. In Figure 5.10 it can be seen that the *recovered* angular extension is centered around 0.3°, and can take larger or lower values depending on the WIMP mass (this is also true for the considered subhalo models). Therefore, we now study the impact in the DM constraints of integrating the J-factor just up to the innermost 0.3° of subhalos (we refer to it as $J_{03}$ instead of up to $\theta_s$ as before in Paper I and Paper II).

We can also estimate how the resulting J-factor will degrade compared to the one used in Paper I and Paper II. In Figure 5.11, we show how the distribution of the 95% C.L. J-factor changes when integrating the signal either up to the scale radius or to the innermost 0.3°, for the brightest subhalo[10]. As in the previous papers, we draw the distribution filtered by mass (M $\leq 10^7$ M$_\odot$) and Galactic latitude ($|b| > 10°$). The J-factor shifts towards lower values, up to a factor $\sim$ 4, which will directly impact the achievable constraints.

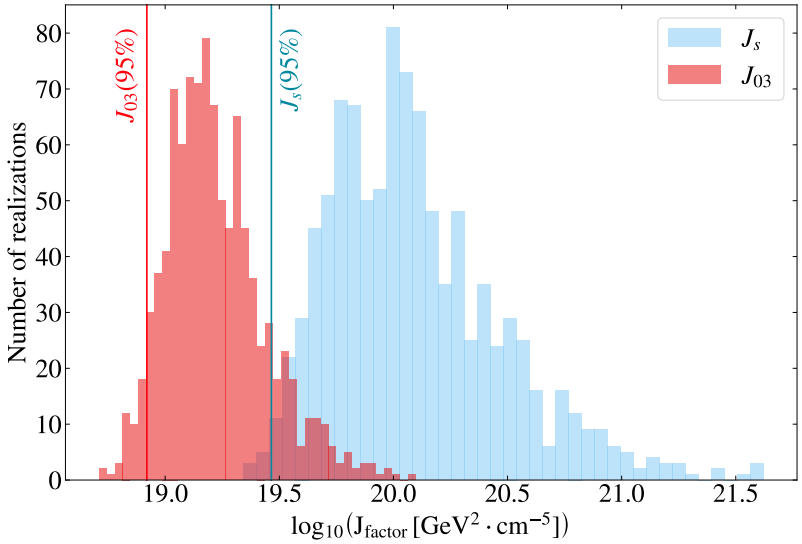


FIGURE 5.11: Distribution of the brightest subhalo J-factor, across 1000 realizations of the N-body simulation (see Paper I for more details), integrating the signal either up to the scale radius (blue) or the innermost 0.3° (red). Vertical lines mark the value at which 95% of the distribution is contained, i.e., the J-factor used to set the DM constraints.

In Figure 5.12, we show the constraints for both the $\tau^+\tau^-$ and $b\bar{b}$ annihilation channels as a function of the number of sources (in log-scale) compatible with DM.

[10] Indeed, this would coincide with our result in Paper II for the $\tau^+\tau^-$ annihilation channel, where only one source was found to be compatible with a DM hypothesis.

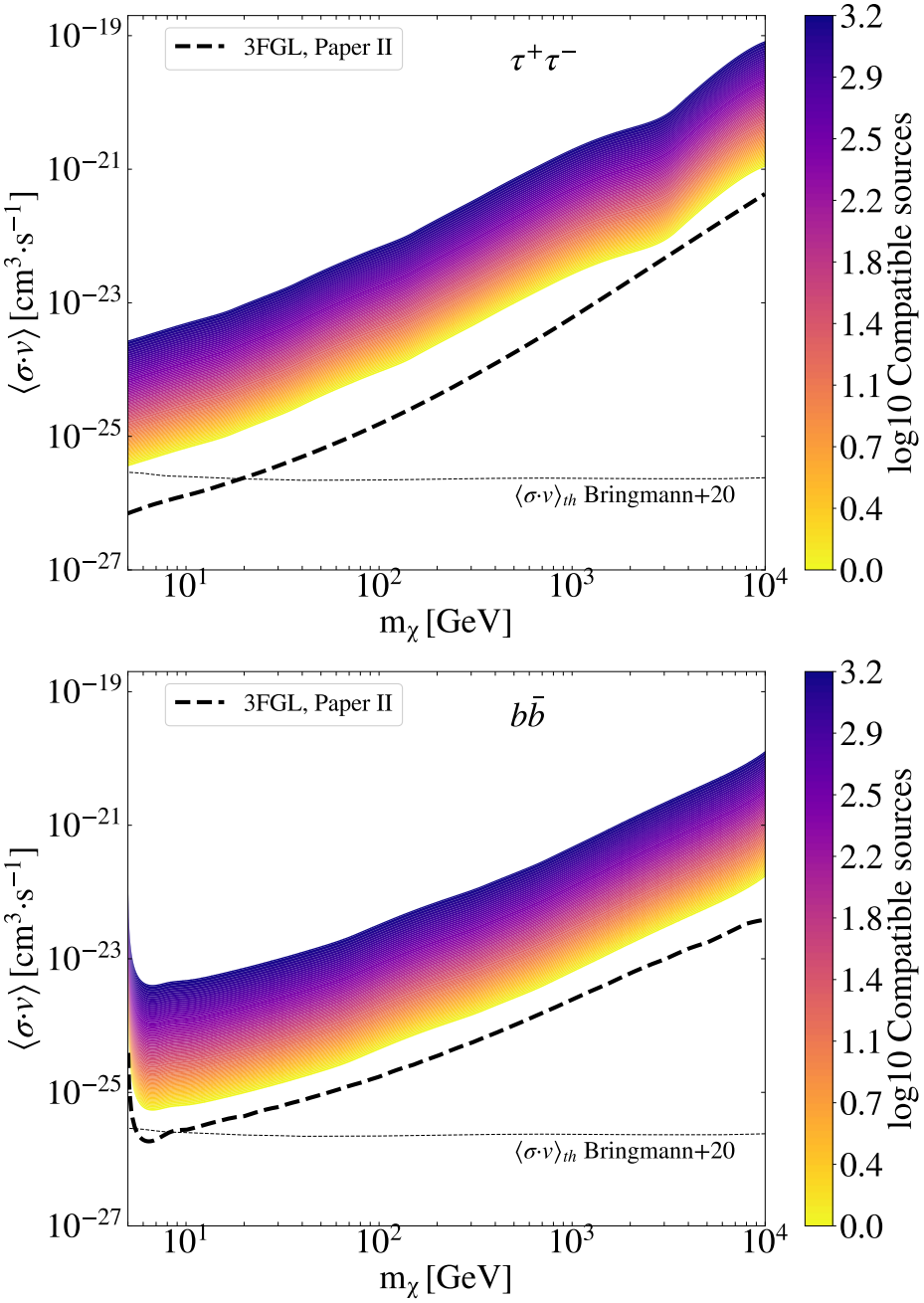


FIGURE 5.12: 95% C.L. limits for DM annihilating to $\tau^+\tau^-$ (top panel) and $b\bar{b}$ (bottom panel), as a function of the number of 4FGL–DR2 unIDs compatible with DM. Black, dashed line is the constraint obtained in Paper II using the previous 3FGL catalog Fermi-LAT Collaboration (2015a) with 1 (5) compatible sources in the case of $\tau^+\tau^-$ ($b\bar{b}$) channel, starting the analysis at 100 MeV, assuming point-like sources and integrating the J-factor up to the scale radius. The horizontal dashed line is the thermal relic cross section Bringmann et al. (2021).

Even in the sensitivity reach case (one source), we do not achieve the constraints we set in Paper II by means of the 3FGL catalog Fermi-LAT Collaboration (2015a). We recall that in the case of Paper II, the constraints for the $\tau^+\tau^-$ channel were already at the sensitivity reach level, which are now a factor ∼8 away for low WIMP masses

and a factor ∼5 away for the heaviest WIMPs. The difference in this factor at small and large masses is probably due to the fact of having started this data analysis at 500 MeV instead of 100 MeV as in Paper II. Indeed, this is expected to particularly impact the constraints at low WIMP masses, as observed. Overall, in the sensitivity reach case, our new constraints are right at the thermal relic cross section value for the lowest considered WIMP masses and a factor $\sim$ 10 away at 100 GeV in the case of $\tau^+\tau^-$ annihilation channel, while similar conclusions can be drawn for $b\bar{b}$, yet a factor $\sim$ 4 far from the thermal value at best.

As already pointed out in Paper I, Figure 5.12 shows that the constraints would only marginally improve if we filtered less than $\sim$ 80% of the unID sources in the catalog, while the improvement will be more than two orders of magnitude from this number of sources down to zero.

Finally, we also note that in this work we assumed two different subhalo models, representative of the subhalo population that would be most relevant from the point of view of annihilation flux (see top panel in Figure 5.1). Yet, when setting constraints we adopt the J-factor above which 95% of the realizations are contained. This is conservative, as using e.g. the median value of the subhalo J-factor instead would improve our limits by a factor $\sim$ 2.

## 5.5 Discussion and conclusions

In this work, we have presented a quantitative assessment of the role of spatial extension in DM subhalo detection with the *Fermi*-LAT using actual data. In the first place, we have chosen two representative physical scenarios for the subhalos, a massive and far subhalo, and a lighter and closer one, covering all interesting ranges. Relevant properties of such representative subhalos, namely angular extension and annihilation flux, were chosen following our previous results from the VL-II N-body cosmological simulation of a MW size halo Paper I. In Section 5.2 we built coherent DM density profiles taking into account the N-body simulation work and taking into account processes like tidal disruption (Moliné et al.; 2017). Both the computed J-factors and the spatial distribution of the corresponding putative DM signals revealed a degeneracy between our selected representative subhalos, as noted in Figure 5.1. This effect can be understood by analysing the dependencies of the J-factor computation for NFW DM density profiles, which can be described as:

$$J_{sub} \propto \frac{M_{sub} c_{200}^3}{D_{\rm Earth}^2} \rho_{crit}. \tag{5.15}$$

Indeed, the combination of the involved masses, distances and obtained concentrations for the selected subhalos resulted in similar values of their J-factors, as shown in Table 5.2.

Using `CLUMPY`, we built spatial templates for the annihilation signal (see Figure 5.2), that were later used as inputs for the LAT data analysis. We performed two types of analysis. First, we computed the threshold flux to detect an unequivocal extension, $F_{min}^{ext}$, i.e., the minimum flux to have an extension TS of 25, equivalent to $\sim 5\sigma$. We also computed the detection minimum flux, $F_{min}^{det}$, and compared it to the point-source case. We found that, in order to detect an extended subhalo, the LAT requires a factor $\sim$ 2 more flux than the one needed to detect a point-like source, and a factor $\sim$ 10 more flux to properly characterize the spatial extension of the subhalo, as reported in Figure 5.5. The two subhalo models, as guessed from the `CLUMPY` templates, are indistinguishable also from the point of view of the data analysis.

In a second stage of the analysis, we performed "blind" computations to characterize the LAT sensitivity to extended subhalos, by analysing a larger grid of different parameters such as the WIMP mass, annihilation channel, subhalo model and the normalization of the DM spectrum. We defined the latter as the product of the cross section and the J-factor, $\langle\sigma v\rangle \times J$. This provides a unified framework in which, given one of the two magnitudes, the other can be easily estimated. The explored normalizations were chosen to lie within a range of extreme, yet possible DM scenarios, such as cross sections two orders of magnitude larger than the thermal relic value or "outlier" J-factors according to the N-body simulation results. From our full grid analysis computations, we found that the LAT should be capable of resolving the angular extension for most WIMP masses (Figures 5.8–5.10). Indeed, for low WIMP masses, whose spectra peak around the maximum sensitivity of the LAT, even low normalization values provide a good signal characterization, both spectrally and spatially. Nevertheless, as we shift towards large WIMP masses, the annihilation spectrum yields less photons; this, together with the decreased sensitivity at high energies, provides no detection for most considered normalization values, as well as a poor (if any) spatial characterization.

With respect to the previous work of Di Mauro et al. (2020) on extended subhalo detection with the LAT, we note a number of differences: Di Mauro et al. (2020) finds a factor $\sim$ 2 variation on the recovered $R_{68}$ when varying the cross section, with a constant uncertainty, while we find a variation of a factor $\sim$ 1.5, with uncertainties consistently much larger for small normalizations (see Figure 5.10 and Appendix 5.6.2). Moreover, Di Mauro et al. (2020) does not report any variation of the recovered $R_{68}$ with the WIMP mass, while we note a factor $\sim$ 2 variation from light ($\sim$ 5 GeV) to heavy ($\sim$ 500 GeV) WIMPs. We must stress that the results in Di Mauro et al. (2020) are based on simulated data, while this work injects the subhalo model into actual LAT data[11].

Finally, we explored the impact of this subhalo spatial extension study on the DM constraints. In our previous works Paper I; Paper II and Coronado-Blázquez and Sánchez-Conde (2020), DM constraints were always derived assuming point-source subhalos, namely adopting a J-factor equal to the integration of the annihilation signal up to the subhalo scale radius. In our work, we found that a better estimate of the subhalo J-factor, as it could be actually observed by the LAT, would be the one integrated up to the innermost 0.3° instead (see Figure 5.11). Thus, we now updated the DM constraints with this new information at hand, shown in Figure 5.12 as a function of the number of sources compatible with a DM origin.

Our analysis allows us to define, in a similar fashion to the work done in Paper I, an additional "filter" to identify DM subhalo candidates among the pool of unidentified LAT sources. Indeed, we conclude that, in most cases – especially for low WIMP masses – the LAT should be able to detect at least a hint of spatial extension if the source (subhalo) is bright enough[12]. An analysis of spatial extension in the latest gamma-ray catalogs is already ongoing and will be presented elsewhere. This additional DM filter, now robustly defined, together with new generation instruments such as the Cherenkov Telescope Array Coronado-Blázquez et al. (2021) or AMEGO The AMEGO Collaboration (2019), will be able to explore the whole WIMP range. CTA will be specially sensitive to large, TeV WIMP masses and will also possess a superb angular resolution of about 0.03° in the TeV energy range, while AMEGO will

[11] Recall our procedure assumes a perfect knowledge of the background (see footnote 5).

[12] Yet, as mentioned in Section 5.3, the LAT may detect as extended source two nearby, individual point-like objects Chou et al. (2018).

be sensitive to lower energies than the LAT with 5 times better angular resolution, therefore ideal for this extension search as well.

## 5.6 Precision of recovered signal

In this Section, we discuss how well *fermipy* can reconstruct an injected DM signal. This reconstruction check will be divided in two parts: first, we will study how precise are the recovered mass and normalization values, i.e., the spectral parameters. In the second part, we will focus on the evolution of the signal as we increase the normalization, both spectral ans spatially.

### 5.6.1 DM spectrum

As discussed, we study how well *fermipy* can reconstruct the DM spectral parameters, this is, how precise the WIMP mass and normalization (J-factor $\times$ $\langle\sigma v\rangle$) fitted values are with respect to the injected values. We show the results in Figure 5.13 and Figure 5.14. For the sake of clarity, we only show results for the $b\bar{b}$ annihilation channel, although the same is found for the $\tau^+\tau^-$ channel. To ensure proper statistics, as in the rest of the paper, 10 realizations of the same WIMP mass/normalization setup are run, thus we report average values and $1-\sigma$ error bars corresponding to the standard deviation of these realizations.

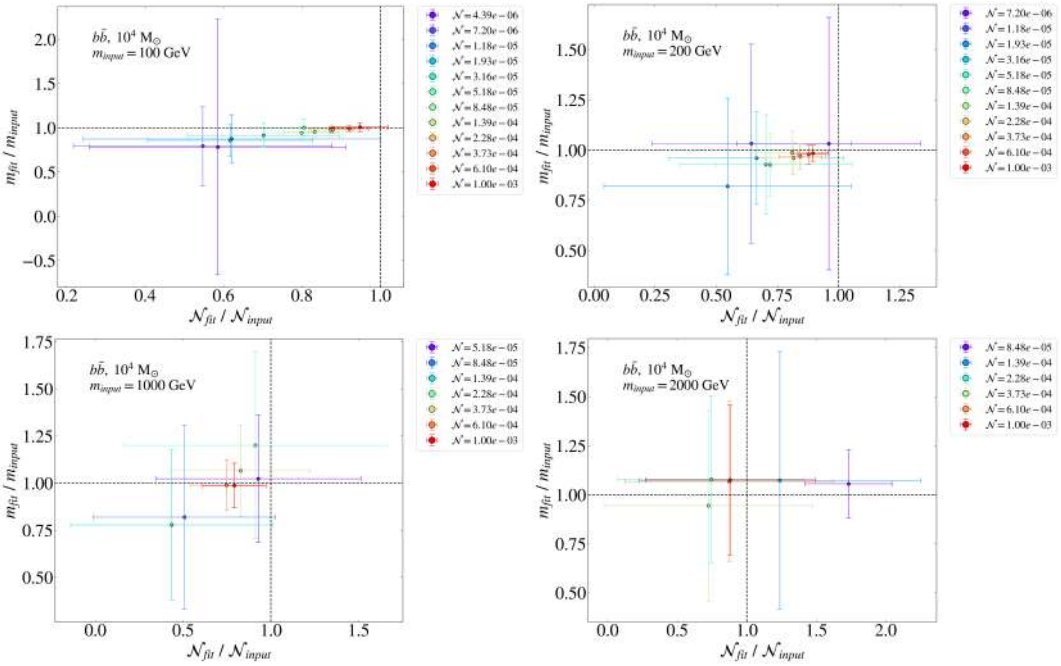


FIGURE 5.13: Comparison between the injected DM signal and the recovered one, in terms of recovered WIMP mass and normalization (J-factor $\times$ $\langle\sigma v\rangle$, with units GeV$^2 \cdot$ cm$^{-2} \cdot$ s$^{-1}$), for the $b\bar{b}$ annihilation channel and the $10^4$ M subhalo model. Note that, as the input mass is increased, less points are present, as the lowest normalization values do not provide detection, indeed only the largest normalizations allowing for a proper characterization of the DM spectrum. Values and error bars refer to average and standard deviation as obtained from 10 realizations. Black, dashed line marks the true values of WIMP mass and normalization (unity ratios).

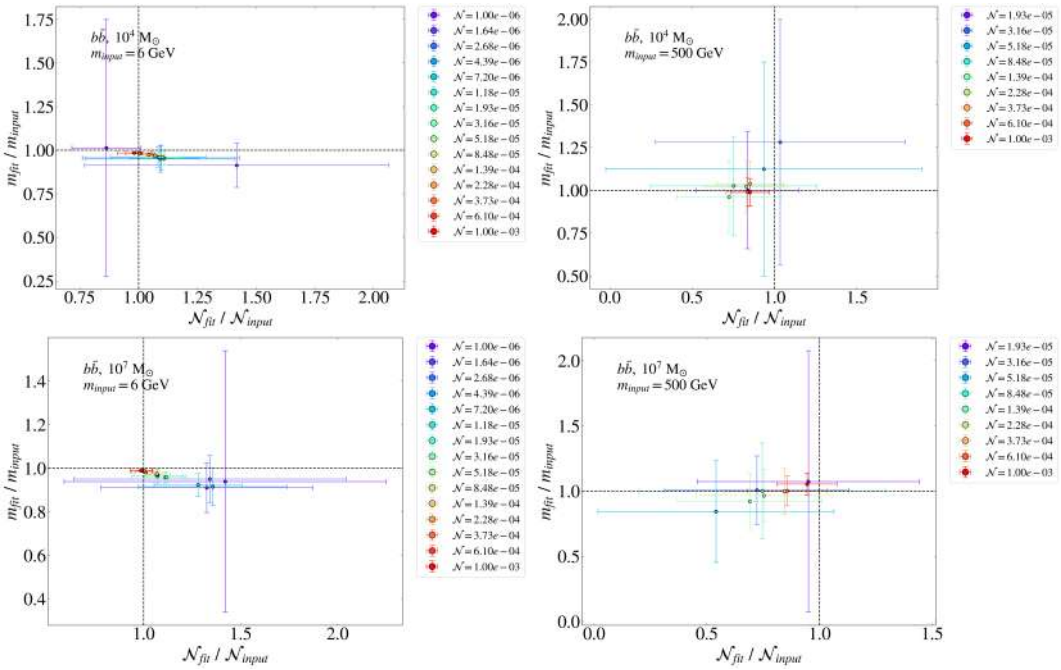


FIGURE 5.14: Same as Figure 5.13, but comparing the two subhalo models considered in our work. **Upper panels:** $10^4$ M$_\odot$ subhalo. **Bottom panels:** $10^7$ M$_\odot$ subhalo.

From Figure 5.13 we find that, the lighter the WIMP, the better the accuracy of the recovered WIMP mass/normalization values. In addition, according to Figure 5.14, the two subhalo models provide similar results.

Therefore, as general conclusions, we find that:

- *fermipy* is generally able to recover the DM spectra with a few percent uncertainty in WIMP mass and normalization values, finding figures compatibles with the injected ones within 1-$\sigma$ uncertainties.
- The code is more precise when injecting signals with large normalizations, i.e., for large normalizations there are smaller uncertainties both in normalization and WIMP mass. In fact, since the overall normalization of the DM spectrum decreases when considering large DM masses, and our normalization grid is the same for all of them, the number of normalizations for which *fermipy* detects the source is decreasing, not being able to detect a 10 TeV WIMP in any case.
- Both the WIMP mass and the normalization tend to be slightly underestimated – a $\sim$ 25% for the mass and a $\sim$ 50% for the normalization at most, for the dimmest setups.
- There are no significant differences when considering different subhalo modelings and/or annihilation channels.

### 5.6.2 Evolution of the signal with the normalization

In this subsection, we study how the signal spatial morphology, DM spectral energy distribution (SED), and the likelihood curves of the extended analysis behave as a

function of the input normalization. To do so, we consider a 100 GeV WIMP, annihilating into $b\bar{b}$, for the ($10^4$ M , 0.5 kpc) subhalo model, although similar conclusions are found for the remaining configurations. In the next figures, these quantities are displayed for normalization values $\mathcal{N} = \{5 \cdot 10^{-6}, 10^{-5}, 10^{-4}, 10^{-3}\}$ GeV$^2$ cm$^{-2}$ s$^{-1}$. We start at $\mathcal{N} = 5 \cdot 10^{-6}$ instead of $10^{-6}$ because there is no signal in the latter case. In Figure 5.15 we show the evolution of the spatial morphology; in Figure 5.17 the DM SED; and, in Figure 5.16, the likelihood curves of the spatial extension analysis.

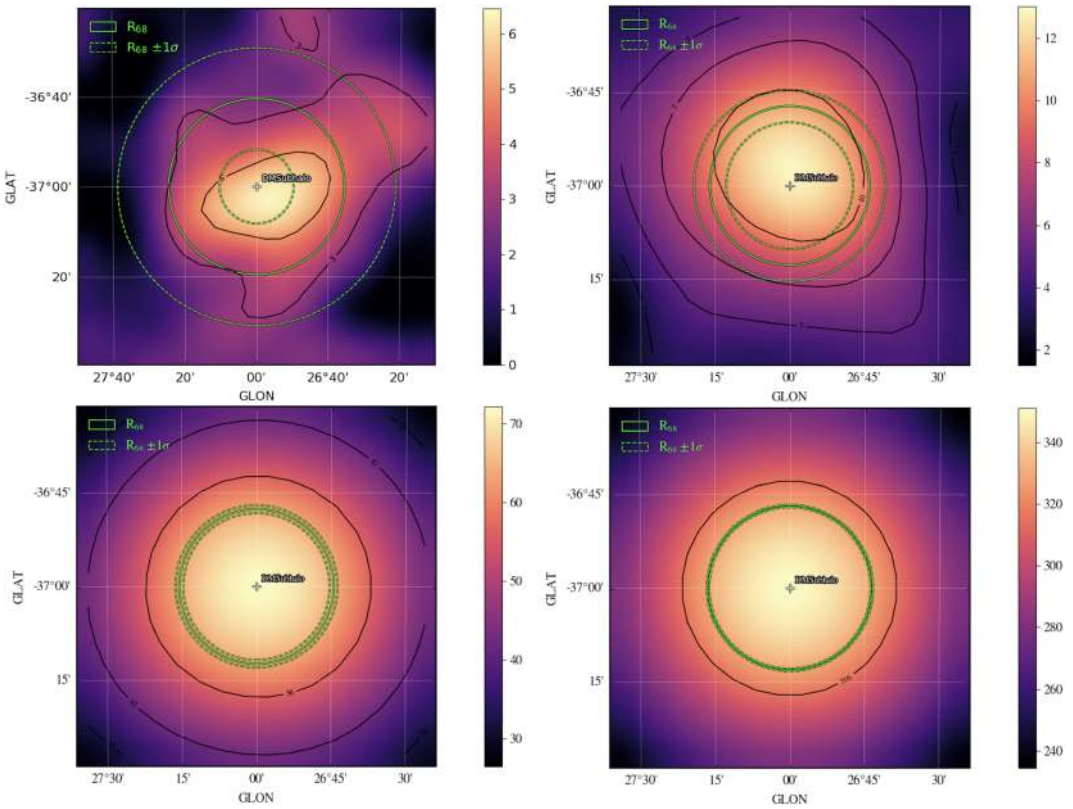


FIGURE 5.15: Spatial morphology of the simulated DM subhalo for $\mathcal{N} = 5 \cdot 10^{-6}$ (top left), $10^{-5}$ (top right), $10^{-4}$ (bottom left), and $10^{-3}$ (bottom right). Green, continuous circle is the best-fit extension, while dashed green circles are the $\pm 1\sigma$ uncertainty. The color scale provides the delta log-likelihood values, being the black curves iso-contours for some particular values (note the different z-axis scale in each plot). See text for details of the analysis parameters.

There is a similar general trend in the three figures: as the normalization is increased, the recovery is more precise, i.e., the corresponding uncertainties are reduced. Indeed, Figures 5.15 and 5.16 show that, although the best-fit $R_{68}$ is always stable, its uncertainty is reduced from almost 50% to less than 2%. Also, the preference for an extended source over the point-source model ($TS_{ext}$, see Eq. 6.2) increases accordingly. This is prominent in Figure 5.15, where the morphology of the signal evolves from an irregular "blob" to a perfect reconstruction of the input spatial template (see Figure 5.2).

The same conclusions apply to the DM SEDs in Figure 5.17: the SED starts as a poorly resolved spectrum, well fitted by either DM or a power law, and evolves to a refined, very well characterized spectrum with a much smaller uncertainty in most bins (indeed allowing for a finer analysis, with 8 bins per energy decade).

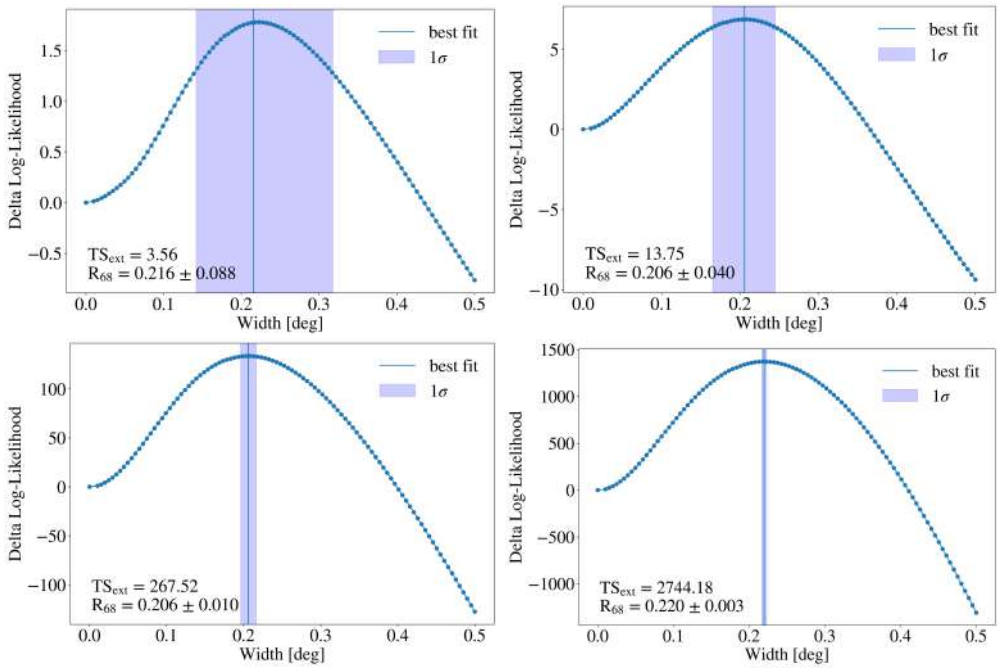


FIGURE 5.16: Extension likelihood curves for $\mathcal{N} = 5 \cdot 10^{-6}$ (top left), $10^{-5}$ (top right), $10^{-4}$ (bottom left), and $10^{-3}$ (bottom right). Blue, vertical line is the extension best-fit, while the violet band is the $1\sigma$ uncertainty. See text for details of the analysis parameters.

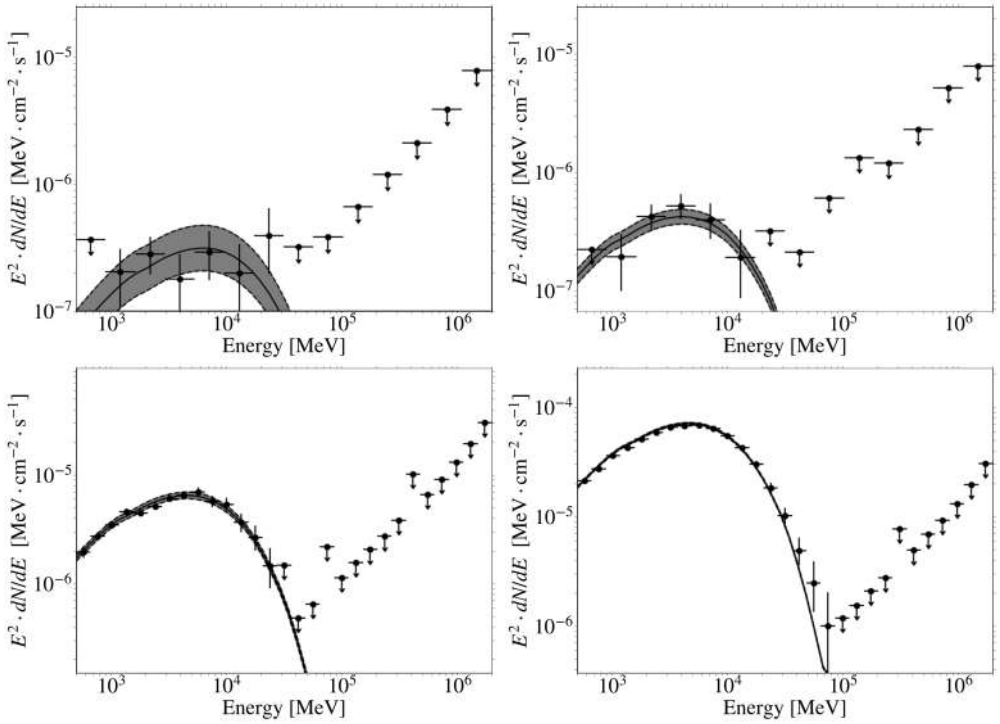


FIGURE 5.17: Spectral energy distribution (SED) of a 100 GeV WIMP annihilating to $b\bar{b}$, for normalization values $\mathcal{N} = 5 \cdot 10^{-6}$ (top left), $10^{-5}$ (top right), $10^{-4}$ (bottom left), and $10^{-3}$ (bottom right). The black band is the best-fit DM spectrum with $1\sigma$ uncertainty. The analyses in the two first cases are performed with 4 bins per energy decade, while the two latter 8, as the signal is bright enough to allow a finer binning. See text for details of the analysis parameters.

## Bibliography

Atwood, W., Albert, A., Baldini, L., Tinivella, M., Bregeon, J., Pesce-Rollins, M., Sgrò, C., Bruel, P., Charles, E., Drlica-Wagner, A., Franckowiak, A., Jogler, T., Rochester, L., Usher, T., Wood, M., Cohen-Tanugi, J. and Zimmer, S. (2013). Pass 8: Toward the Full Realization of the Fermi-LAT Scientific Potential.

Ballet, J., Burnett, T. H., Digel, S. W. and Lott, B. (2020). Fermi Large Area Telescope Fourth Source Catalog Data Release 2.

Bartels, R., Hooper, D., Linden, T., Mishra-Sharma, S., Rodd, N. L., Safdi, B. R. and Slatyer, T. R. (2017). Comment on "Characterizing the population of pulsars in the Galactic bulge with the *Fermi* Large Area Telescope" [arXiv:1705.00009v1].

Belikov, A. V., Buckley, M. R. and Hooper, D. (2012). Searching for dark matter subhalos in the Fermi-LAT second source catalog, *Physical Review D* **86**(4).

Berlin, A. and Hooper, D. (2013). Stringent Constraints On The Dark Matter Annihilation Cross Section From Subhalo Searches With The Fermi Gamma-Ray Space Telescope, *Phys. Rev D89* .

Bertone, G. (2010). The moment of truth for WIMP dark matter, *Nature* **468**(7322): 389–393.

Bertone, G., Hooper, D. and Silk, J. (2005). Particle dark matter: evidence, candidates and constraints, *Physics Reports* **405**(5-6): 279–390.

Bertoni, B., Hooper, D. and Linden, T. (2015). Examining The Fermi-LAT Third Source Catalog In Search Of Dark Matter Subhalos, *Journal of Cosmology and Astroparticle Physics* **12**: 035.
**URL:** http://dx.doi.org/10.1088/1475-7516/2015/12/035

Bertoni, B., Hooper, D. and Linden, T. (2016). Is The Gamma-Ray Source 3FGL J2212.5+0703 A Dark Matter Subhalo?, *Journal of Cosmology and Astroparticle Physics* **5**: 049.
**URL:** http://dx.doi.org/10.1088/1475-7516/2016/05/049

Bonnivard, V., Hütten, M., Nezri, E., Charbonnier, A., Combet, C. and Maurin, D. (2016). CLUMPY : Jeans analysis, $\gamma$-ray and $\nu$ fluxes from dark matter (sub-)structures, *Computer Physics Communications* **200**: 336–349.

Bringmann, T., Depta, P. F., Hufnagel, M. and Schmidt-Hoberg, K. (2021). Precise dark matter relic abundance in decoupled sectors, *Physics Letters B* **817**: 136341.
**URL:** http://dx.doi.org/10.1016/j.physletb.2021.136341

Bruel, P., Burnett, T. H., Digel, S. W., Johannesson, G., Omodei, N. and Wood, M. (2018). Fermi-LAT improved Pass 8 event selection.

Buckley, M. R. and Hooper, D. (2010). Dark Matter Subhalos In the Fermi First Source Catalog, *Phys. Rev. D82* .

Calore, F., Romeri, V. D., Mauro, M. D., Donato, F. and Marinacci, F. (2016). Realistic estimation for the detectability of dark matter sub-halos with Fermi-LAT, *Phys. Rev. D96* .

Charbonnier, A., Combet, C. and Maurin, D. (2012). CLUMPY: A code for $\gamma$-ray signals from dark matter structures, *Computer Physics Communications* **183**(3): 656–668.

Chou, T.-L., Tanoglidis, D. and Hooper, D. (2018). Resolving dark matter subhalos with future sub-GeV gamma-ray telescopes, *Physics of the Dark Universe* **21**: 1.

Cintio, A. D., Brook, C. B., Dutton, A. A., Macciò, A. V., Stinson, G. S. and Knebe, A. (2014). A mass-dependent density profile for dark matter haloes including the influence of galaxy formation, *Monthly Notices of the Royal Astronomical Society* **441**(4): 2986–2995.
**URL:** *http://dx.doi.org/10.1093/mnras/stu729*

Cirelli, M., Corcella, G., Hektor, A., Hütsi, G., Kadastik, M., Panci, P., Raidal, M., Sala, F. and Strumia, A. (2011). PPPC 4 DM ID: a poor particle physicist cookbook for dark matter indirect detection, *Journal of Cosmology and Astroparticle Physics* **2011**(03): 051–051.

Conrad, J. and Reimer, O. (2017). Indirect dark matter searches in gamma and cosmic rays, *Nature Physics* **13**(3): 224–231.

Coronado-Blázquez, J. and Sánchez-Conde, M. A. (2020). Constraints to dark matter annihilation from high-latitude HAWC unidentified sources, *Galaxies* **8**(1): 5.

Coronado-Blázquez, J., Sánchez-Conde, M. A., Domínguez, A., Aguirre-Santaella, A., Mauro, M. D., Mirabal, N., Nieto, D. and Charles, E. (2019). Unidentified gamma-ray sources as targets for indirect dark matter detection with the Fermi-Large Area Telescope, *Journal of Cosmology and Astroparticle Physics* **2019**(07): 020–020.

Coronado-Blázquez, J., Sánchez-Conde, M. A., Mauro, M. D., Aguirre-Santaella, A., Ciucă, I., Domínguez, A., Kawata, D. and Mirabal, N. (2019). Spectral and spatial analysis of the dark matter subhalo candidates among Fermi Large Area Telescope unidentified sources, *Journal of Cosmology and Astroparticle Physics* **2019**(11): 045–045.

Coronado-Blázquez, J., Doro, M., Sánchez-Conde, M. A. and Aguirre-Santaella, A. (2021). Sensitivity of the Cherenkov Telescope Array to dark subhalos.
**URL:** *http://dx.doi.org/10.1016/j.dark.2021.100845*

CTA Consortium (2021). Sensitivity of the Cherenkov Telescope Array to a dark matter signal from the Galactic centre, *Journal of Cosmology and Astroparticle Physics* **2021**(01): 057–057.
**URL:** *http://dx.doi.org/10.1088/1475-7516/2021/01/057*

Di Mauro, M., Stref, M. and Calore, F. (2020). Investigating the detection of dark matter subhalos as extended sources with Fermi-LAT, *Physical Review D* **102**(10).

Diemand, J., Kuhlen, M., Madau, P., Zemp, M., Moore, B., Potter, D. and Stadel, J. (2008). Clumps and streams in the local dark matter distribution, *Nature* **454**(7205): 735–738.

Einasto, J. (1965). On the Construction of a Composite Model for the Galaxy and on the Determination of the System of Galactic Parameters, *Trudy Astrofizicheskogo Instituta Alma-Ata* **5**: 87–100.
**URL:** *https://ui.adsabs.harvard.edu/abs/1965TrAlm...5...87E*

Facchinetti, G., Lavalle, J. and Stref, M. (2020). Statistics for dark matter subhalo searches in gamma rays from a kinematically constrained population model. I: Fermi-LAT-like telescopes.

Fermi-LAT Collaboration (2010). Constraints on dark matter annihilation in clusters of galaxies with the Fermi Large Area Telescope, *Journal of Cosmology and Astroparticle Physics* **2010**(05): 025–025.
**URL:** http://dx.doi.org/10.1088/1475-7516/2010/05/025

Fermi-LAT Collaboration (2012). Search for Dark Matter Satellites using the Fermi-LAT, *The Astrophysical Journal* (2).
**URL:** http://dx.doi.org/10.1088/0004-637X/747/2/121

Fermi-LAT Collaboration (2015a). Fermi Large Area Telescope Third Source Catalog, *The Astrophysical Journal Supplement Series* **218**(2): 23.

Fermi-LAT Collaboration (2015b). Search for extended gamma-ray emission from the Virgo galaxy cluster with Fermi-LAT, *The Astrophysical Journal* .

Fermi-LAT Collaboration (2015c). Searching for Dark Matter Annihilation from Milky Way Dwarf Spheroidal Galaxies with Six Years of Fermi Large Area Telescope Data, *Physical Review Letters* **115**(23).

Fermi-LAT Collaboration (2016a). 2FHL: The Second Catalog of Hard Fermi-LAT Sources, *The Astrophysical Journal Supplement Series* **222**(1): 5.

Fermi-LAT Collaboration (2016b). Fermi-LAT Observations of High-Energy Gamma-Ray Emission Toward the Galactic Center, *The Astrophysical Journal* **819**: 44.
**URL:** http://adsabs.harvard.edu/abs/2016ApJ...819..44A

Fermi-LAT Collaboration (2017a). 3FHL: The Third Catalog of Hard Fermi-LAT Sources, *The Astrophysical Journal Supplement Series* **232**(2): 18.

Fermi-LAT Collaboration (2017b). Characterizing the population of pulsars in the Galactic bulge with the *Fermi* Large Area Telescope.

Fermi-LAT Collaboration (2017c). The Fermi Galactic Center GeV Excess and Implications for Dark Matter, *The Astrophysical Journal* **840**: 43.
**URL:** http://adsabs.harvard.edu/abs/2017ApJ...840...43A

Fermi-LAT Collaboration (2018). The Search for Spatial Extension in High-latitude Sources Detected by the Fermi Large Area Telescope, *The Astrophysical Journal Supplement Series* **237**(2): 32.
**URL:** http://dx.doi.org/10.3847/1538-4365/aacdf7

Fermi-LAT Collaboration (2020). Fermi Large Area Telescope Fourth Source Catalog, *The Astrophysical Journal Supplement Series* **247**(1): 33.

Fermi-LAT Collaboration and Atwood, W. B. (2009). The Large Area Telescope on the Fermi Gamma-ray Space Telescope Mission, *The Astrophysical Journal* .

Fermi-LAT Collaboration and The DES Collaboration (2017). Searching for Dark Matter Annihilation in Recently Discovered Milky Way Satellites with Fermi-Lat, *The Astrophysical Journal* **834**(2): 110.
**URL:** https://ui.adsabs.harvard.edu/abs/2017ApJ...834..110A

Garrett, K. and Duda, G. (2011). Dark Matter: A Primer, *Advances in Astronomy* **2011**: 1–22.
**URL:** http://dx.doi.org/10.1155/2011/968283

Gaskins, J. M. (2016). A review of indirect searches for particle dark matter, *Contemporary Physics* **57**(4): 496–525.

Hellwing, W. A., Frenk, C. S., Cautun, M., Bose, S., Helly, J., Jenkins, A., Sawala, T. and Cytowski, M. (2016). The Copernicus Complexio: a high-resolution view of the small-scale Universe, *Monthly Notices of the Royal Astronomical Society* **457**(4): 3492–3509.
**URL:** https://ui.adsabs.harvard.edu/abs/2016MNRAS.457.3492H

H.E.S.S. Collaboration (2016). Search for Dark Matter Annihilations towards the Inner Galactic Halo from 10 Years of Observations with H.E.S.S., *Physical Review Letters* **117**(11).
**URL:** http://dx.doi.org/10.1103/PhysRevLett.117.111301

Hooper, D. and Witte, S. J. (2017). Gamma rays from dark matter subhalos revisited: refining the predictions and constraints, *Journal of Cosmology and Astroparticle Physics* **2017**(04): 018–018.

Hütten, M., Combet, C. and Maurin, D. (2019). CLUMPY v3: $\gamma$-ray and $\nu$ signals from dark matter at all scales, *Computer Physics Communications* **235**: 336–345.

Ishiyama, T., Prada, F., Klypin, A. A., Sinha, M., Metcalf, R. B., Jullo, E., Altieri, B., Cora, S. A., Croton, D., de la Torre, S., Millán-Calero, D. E., Oogi, T., Ruedas, J. and Vega-Martínez, C. A. (2020). The Uchuu Simulations: Data Release 1 and Dark Matter Halo Concentrations, *arXiv e-prints* p. arXiv:2007.14720.
**URL:** https://ui.adsabs.harvard.edu/abs/2020arXiv200714720I

Jeltema, T. E. and Profumo, S. (2008). Fitting the gamma-ray spectrum from dark matter with DMFIT: GLAST and the galactic center region, *Journal of Cosmology and Astroparticle Physics* **2008**(11): 003.

Kahlhoefer, F. (2017). Review of LHC dark matter searches, *International Journal of Modern Physics A* **32**(13): 1730006.

Karwin, C. M., Murgia, S., Campbell, S. and Moskalenko, I. V. (2019). Fermi-LAT Observations of $\gamma$-Ray Emission toward the Outer Halo of M31, *The Astrophysical Journal* **880**(2): 95.
**URL:** https://doi.org/10.3847/1538-4357/ab2880

Karwin, C. M., Murgia, S., Moskalenko, I. V., Fillingham, S. P., Burns, A.-K. and Fieg, M. (2021). Dark matter interpretation of the Fermi-LAT observations toward the outer halo of M31, *Physical Review D* **103**(2).
**URL:** http://dx.doi.org/10.1103/PhysRevD.103.023027

Kazantzidis, S., Kravtsov, A. V., Zentner, A. R., Allgood, B., Nagai, D. and Moore, B. (2004). The Effect of Gas Cooling on the Shapes of Dark Matter Halos, *The Astrophysical Journal* **611**(2): L73–L76.
**URL:** http://dx.doi.org/10.1086/423992

King, I. (1962). The structure of star clusters. I. an empirical density law, *The Astrophysical Journal* **67**: 471.
**URL:** http://adsabs.harvard.edu/abs/1962AJ.....67..471K

Madau, P., Diemand, J. and Kuhlen, M. (2008). Dark Matter Subhalos and the Dwarf Satellites of the Milky Way, *The Astrophysical Journal* **679**(2): 1260–1271.

MAGIC Collaboration (2018). Constraining dark matter lifetime with a deep gamma-ray survey of the Perseus galaxy cluster with MAGIC, *Physics of the Dark Universe* **22**: 38–47.
**URL:** http://dx.doi.org/10.1016/j.dark.2018.08.002

MAGIC Collaboration and Fermi-LAT Collaboration (2016). Limits to dark matter annihilation cross-section from a combined analysis of MAGIC and fermi-LAT observations of dwarf satellite galaxies, *Journal of Cosmology and Astroparticle Physics* **2016**(02): 039–039.

Moliné, A., Sánchez-Conde, M. A., Palomares-Ruiz, S. and Prada, F. (2017). Characterization of subhalo structural properties and implications for dark matter annihilation signals, *Monthly Notices of the Royal Astronomical Society* **466**: 4974–4990.
**URL:** http://adsabs.harvard.edu/abs/2017MNRAS.466.4974M

Navarro, J. F., Frenk, C. S. and White, S. D. M. (1997). A universal density profile from hierarchical clustering, *The Astrophysical Journal* **490**(2): 493–508.

Oakes, L., Armand, C., Charles, E., Mauro, M. D., Giuri, C., Harding, J. P., Kerszberg, D., Miener, T., Moulin, E., Poireau, V., Pueschel, E., Rico, J., Rinchiuso, L., Salazar-Gallegos, D., Tollefson, K. and Zitzer, B. (2019). Combined Dark Matter searches towards dwarf spheroidal galaxies with Fermi-LAT, HAWC, HESS, MAGIC and VERITAS, *Proc. of ICRC 2019* .

Ogiya, G., van den Bosch, F. C., Hahn, O., Green, S. B., Miller, T. B. and Burkert, A. (2019). DASH: a library of dynamical subhalo evolution, *Monthly Notices of the Royal Astronomical Society* **485**(1): 189–202.
**URL:** https://ui.adsabs.harvard.edu/abs/2019MNRAS.485..1890

Planck Collaboration (2020). Planck 2018 results, *Astronomy & Astrophysics* **641**: A6.

Pontzen, A. and Governato, F. (2012). How supernova feedback turns dark matter cusps into cores, *Monthly Notices of the Royal Astronomical Society* **421**(4): 3464–3471.
**URL:** http://dx.doi.org/10.1111/j.1365-2966.2012.20571.x

Rico, J. (2020). Gamma-Ray Dark Matter Searches in Milky Way Satellites—A Comparative Review of Data Analysis Methods and Current Results, *Galaxies* **8**(1): 25.
**URL:** http://dx.doi.org/10.3390/galaxies8010025

Sawala, T., Frenk, C. S., Fattahi, A., Navarro, J. F., Theuns, T., Bower, R. G., Crain, R. A., Furlong, M., Jenkins, A., Schaller, M. and et al. (2015). The chosen few: the low-mass haloes that host faint galaxies, *Monthly Notices of the Royal Astronomical Society* **456**(1): 85–97.
**URL:** http://dx.doi.org/10.1093/mnras/stv2597

Schoonenberg, D., Gaskins, J., Bertone, G. and Diemand, J. (2016). Dark matter subhalos and unidentified sources in the Fermi 3FGL source catalog, *Journal of Cosmology and Astroparticle Physics* **5**: 028.
**URL:** http://dx.doi.org/10.1088/1475-7516/2016/05/028

Schumann, M. (2019). Direct detection of WIMP dark matter: concepts and status, *Journal of Physics G: Nuclear and Particle Physics* **46**(10): 103003.

Springel, V., Wang, J., Vogelsberger, M., Ludlow, A., Jenkins, A., Helmi, A., Navarro, J. F., Frenk, C. S. and White, S. D. M. (2008). The Aquarius Project: the subhaloes of galactic haloes, *Monthly Notices of the Royal Astronomical Society* **391**(4): 1685–1711.
**URL:** https://ui.adsabs.harvard.edu/abs/2008MNRAS.391.1685S

Springel, V., White, S. D. M., Frenk, C. S., Navarro, J. F., Jenkins, A., Vogelsberger, M., Wang, J., Ludlow, A. and Helmi, A. (2008). Prospects for detecting supersymmetric dark matter in the Galactic halo, *Nature* **456**(7218): 73–76.

The AMEGO Collaboration (2019). All-sky Medium Energy Gamma-ray Observatory: Exploring the Extreme Multimessenger Universe.

van den Bosch, F. C. and Ogiya, G. (2018). Dark matter substructure in numerical simulations: a tale of discreteness noise, runaway instabilities, and artificial disruption, *Monthly Notices of the Royal Astronomical Society* **475**(3): 4066–4087.
**URL:** https://ui.adsabs.harvard.edu/abs/2018MNRAS.475.4066V

van den Bosch, F. C., Ogiya, G., Hahn, O. and Burkert, A. (2018). Disruption of dark matter substructure: fact or fiction?, *Monthly Notices of the Royal Astronomical Society* **474**(3): 3043–3066.
**URL:** https://ui.adsabs.harvard.edu/abs/2018MNRAS.474.3043V

Walker, M. G. (2013). *Dark Matter in the Milky Way's Dwarf Spheroidal Satellites*.
**URL:** http://adsabs.harvard.edu/abs/2013pss5.book.1039W

Winter, M., Zaharijas, G., Bechtol, K. and Vandenbroucke, J. (2016). Estimating the GeV Emission of Millisecond Pulsars in Dwarf Spheroidal Galaxies, *The Astrophysical Journal Letters* **832**(1): L6.

Wood, M., Caputo, R., Charles, E., Mauro, M. D., Magill, J. and Perkins, J. (2017). Fermipy: An open-source Python package for analysis of Fermi-LAT Data.

Xia, Z.-Q., Duan, K.-K., Li, S., Liang, Y.-F., Shen, Z.-Q., Yue, C., Wang, Y.-P., Yuan, Q., Fan, Y.-Z., Wu, J. and Chang, J. (2017). 3FGL J1924.8-1034: A spatially extended stable unidentified GeV source?, *Physical Review D* **95**(10).

Zechlin, H. S., Fernandes, M. V., Elsaesser, D. and Horns, D. (2011). Dark matter subhaloes as gamma-ray sources and candidates in the first Fermi-LAT catalogue, *A&A* .

Zechlin, H.-S. and Horns, D. (2012). Unidentified sources in the Fermi-LAT second source catalog: the case for DM subhalos, *Journal of Cosmology and Astroparticle Physics* .

# Chapter 6

# Hints of dark subhalo detection with the *Fermi*-LAT

*Based on J. Coronado-Blázquez and M. A. Sánchez-Conde, 2021, to be submitted*

## 6.1 Introduction

Roughly 26% of the matter-energy density of the Universe is made of non-baryonic, cold dark matter (DM) Planck Collaboration (2020). One of the most popular DM models are weakly interacting massive particles (WIMPs) Bertone (2010). These can account for the whole DM density via a freeze-out process when thermally decoupling from the primordial plasma in the early Universe. The WIMP relic abundance is determined by their annihilation cross section – if this is in the weak interactions scale, WIMPs can yield the measured DM abundance Bertone et al. (2005).

These annihilation processes may produce Standard Model (SM) particles which final states renders sub-products such as gamma rays, cosmic rays and neutrinos. In particular, gamma rays are a privileged probe, easier to detect than neutrinos yet with neutral electrical charge, as opposed to cosmic rays, and can be detected by observatories such as the Fermi Large Area Telescope (LAT), sensitive to energies from $\sim$ 20 MeV to $\sim$ 2 TeV Fermi-LAT Collaboration and Atwood (2009).

Several targets have been explored in DM searches with gamma rays, among which we may highlight the Galactic center (GC) Goodenough and Hooper (2009); Fermi-LAT Collaboration (2016, 2017), dwarf spheroidal galaxies (dSphs) Fermi-LAT Collaboration (2015b); Oakes et al. (2019); MAGIC Collaboration and Fermi-LAT Collaboration (2016) and galaxy clusters Fermi-LAT Collaboration (2015a, 2010); MAGIC Collaboration (2018). A complementary target are DM subhalos, $\Lambda$CDM-predicted objects due to the bottom-up hierarchical structure formation model, which merge and accrete into larger halos Madau et al. (2008). If not massive enough –below $\sim 10^7$ M$_\odot$ – to retain baryons, they will remain invisible at any wavelength Sawala et al. (2015). Thus, if DM annihilation takes place in these subhalos, only a gamma-ray signal is expected, therefore appearing in the sky as unidentified gamma-ray sources (unIDs).

The main advantages of these targets are that they are not expected to have any astrophysical background, their large number density in the Galaxy, and their high concentrations of DM Diemand et al. (2008); Springel et al. (2008); Moliné et al. (2017). The main disadvantage of such searches is the lack of knowledge of the actual subhalos' positions, as opposed to the aforementioned targets. In principle, only the closest subhalos to the Earth may yield annihilation fluxes large enough to be detected Coronado-Blázquez et al. (2019b).

Statistical studies can be performed, confronting the actual data to the expected population from N-body cosmological simulations. Nevertheless, one can also study individual unIDs from a DM perspective, by a spectral and spatial dedicated analysis. In previous works Coronado-Blázquez et al. (2019a,b), both approaches are followed, and the latter rendered a handful of promising candidates, which showed mild preference for a DM origin over an astrophysical explanation.

From the perspective of their spatial extension, all candidates were point-like. This was in tension with the predicted angular sizes from N-body simulations for the brightest subhalos. Yet, when carefully studying the expected angular extension convoluted with real LAT data, and by analysing a fine grid of models, not all subhalo configurations should present spatial extension (see Chapter 5). Indeed, depending on the annihilation channel, subhalo modeling, overall normalization and WIMP mass, the signal may be detected as point-like or extended, with extensions $\mathcal{O}(0.1 - 0.3^\circ)$.

In this work, we update the previous analysis of Coronado-Blázquez et al. (2019a) searching for new candidates. From the spectral point of view, we now have more years of data and a new source catalog with more potential candidates. From the spatial extension perspective, we now know in which cases we should expect a hint of spatial extension and, more importantly, in which ones it would act as a "smoking gun", i.e., supposes an unequivocal sign of a dark matter subhalo.

## 6.2 Sample selection

The latest release of *Fermi*-LAT data, the 4FGL–DR2 catalog Ballet et al. (2020), presents 1667 unIDs. The vast majority of the unIDs are expected to be astrophysical gamma-ray emitters, such as AGNs, pulsars or supernova remnants. Although there is a great confusion between pulsars and DM Mirabal (2013); Mirabal et al. (2016), we can apply a selection of "filters" Coronado-Blázquez et al. (2019b) to reduce the pool of candidates compatible with a DM origin, namely:

- **Low latitude sources** – by applying a $|b| > 10^\circ$ selection, we eliminate the Galactic plane region, thus avoiding dealing with the intense diffuse emission and possible source confusion Eckner et al. (2018).
- **Variability** – DM annihilation is not expected to present any time variability, and therefore any variable source (at 99% C.L.[1]) can be rejected.
- **Curved spectrum** – The astrophysical emitters are typically fitted to three spectral models: a power law (PL), a log-parabolic model (LP, which is a curved power law), and a power law with super exponential cutoff (PLE, similar to DM in many cases)[2]. While the latter may be similar to DM annihilation, the first cannot (at least for the channels we will consider throughout this paper, $b\bar{b}$ and $\tau^+\tau^-$). Therefore, we will eliminate any source which is best fit by a power law.
- **No flags** – Flags are warnings issued in the LAT catalogs, which are typically due to mismodels either in the diffuse emission or the source. These tend to be spurious sources and thus we will reject any flagged unID.

[1] The variability statistics in the catalog are $\chi^2$-distributed, which allows to use this confidence level.
[2] https://fermi.gsfc.nasa.gov/ssc/data/analysis/scitools/source_models.html

After we perform this "filtering", our pool of subhalo candidates is reduced from 1667 to 127, which allows an individual, detailed spectral and spatial analysis. It is worth noting that the official LAT catalogs do not search for spatial extension Fermi-LAT Collaboration (2020), modeling the whole population as point-like except for well-known sources, and therefore one may expect some of the unIDs to be spatially extended.

## 6.3 Dark subhalo candidates analysis

To analyze the 127 unIDs, we rely on `fermipy` Wood et al. (2017). The analysis parameters match the ones of Chapter 5, and are summarized in Table 6.1.

| | |
|---|---|
| Time domain (ISO 8601) | 2008-08-04 to 2020-08-03 |
| Energy range | 500 MeV – 2 TeV |
| IRFs | `P8R3_SOURCE_V2` |
| Event type | FRONT+BACK |
| Point-source catalog | 4FGL–DR2 |
| ROI size | $15^\circ \times 15^\circ$ |
| Max zenith angle | $105^\circ$ |
| Galactic diffuse model | `gll_iem_v07.fits` |
| Isotropic diffuse model | `iso_P8R3_SOURCE_V2.txt` |

TABLE 6.1: Summary of the *fermipy* analysis setup.

For each source, we perform the fitting of the ROI and, if the source is detected, we search for spatial extension and fit to DM. To evaluate the source detection, we adopt the Test Statistic Rico (2020),

$$\mathrm{TS}_{\mathrm{det}} = 2 \cdot \log\left[\frac{\mathcal{L}(H_1)}{\mathcal{L}(H_0)}\right] \tag{6.1}$$

where $\mathcal{L}(H_0)$ and $\mathcal{L}(H_1)$ are, respectively, the likelihoods under the null (no source) and alternative (existing source) hypotheses. The detection threshold is set to $\mathrm{TS}_{\mathrm{det}} = 25$ [3]. Similarly, the extension significance of a source, i.e., how likely is that it exhibits angular extension, can be computed as,

$$\mathrm{TS}_{\mathrm{ext}} = 2 \cdot \log\left[\frac{\mathcal{L}(\mathrm{EXT})}{\mathcal{L}(\mathrm{PS})}\right] \tag{6.2}$$

where $\mathcal{L}(\mathrm{EXT})$ is the likelihood of the extended hypothesis and $\mathcal{L}(\mathrm{PS})$ is the one of the point source.

Furthermore, as in Chapter 4, we compute the preference for a DM model over an astrophysical emission origin via a generalized likelihood ratio test built upon the spectral information,

$$\mathrm{TS}_{\mathcal{X}} = 2\left[(\mathrm{k}_{\mathcal{X}} - \mathrm{k}_0) + \log\left(\frac{\mathcal{L}_{\mathcal{X}}}{\mathcal{L}_0}\right)\right] \tag{6.3}$$

where $\chi$ is the DM model (we will consider $b\bar{b}$ and $\tau^+\tau^-$) and 0 refers to the astrophysical one, $k$ is the degrees of freedom of each model, and $\mathcal{L}$ is the likelihood under each hypothesis. The difference in the degrees of freedom will be taken into account

[3] This threshold is approximately a $5\sigma$ preference, as $TS \sim \sigma^2$, and is the usual value in gamma-ray astronomy.

here in the computation of the TS, via the Akaike Information Criterion (AIC, Akaike (1998)).

We find a handful of sources, $\mathcal{O}(10)$, with large values of $\mathrm{TS}_{\mathcal{X}}$, $\mathcal{O}(10-70)$. Yet, to properly quantify the statistical preference for DM, we first need to compute the associated local p-values ($p_{loc}$), for which the actual TS distribution must be used. Using the ideal TS, $\chi^2/2$-distributed with one degree of freedom (Chernoff's theorem Chernoff (1952, 1956)) would overestimate the actual significance of the signal Atwood et al. (2013). Therefore, we use the results from Fermi-LAT Collaboration and DES Collaboration (2017), where blank sky regions are simulated to assess the actual TS distribution for DM annihilation[4]. The difference between this TS distribution and the theoretical $\chi^2/2$ distribution is notable at large TS values, and using the latter would lead to $p_{loc} \sim 10^{-18} - 10^{-9}$ for the best sources.

The summary of this analysis is in Table 6.2. The obtained local significances ($\sigma_{loc}$), computed from $p_{loc}$ with the actual TS distribution, are around $2-2.5\sigma$ at best. Yet, we should consider a trials factor to account for the "look-elsewhere" effect, i.e., penalizing the fact that the analysis is trying different models with very diverse underlying particle physics scenarios. This correction may be applied on the p-value in the following way Conrad (2015); Algeri et al. (2016); Fermi-LAT Collaboration and DES Collaboration (2017),

$$p_{glob} = 1 - (1 - p_{loc})^{N_{trials}} \tag{6.4}$$

where $p_{loc}$ is the local p-value, $N_{trials}$ the number of different models considered, and $p_{glob}$ is the trials-corrected p-value. Here $N_{trials} = 48$, due to 2 annihilation channels and 24 different masses. Even when penalizing by trials some sources exhibit large p-values. Indeed, four of them present a $p_{glob} < 0.05$ (approximately $2\sigma$). This may challenge an astrophysical explanation, and could be considered a hint of dark subhalo discovery, as these four sources are located at high latitudes, possess no counterparts, are non variable, and exhibit a curved spectrum well fitted by DM. It is also interesting to note that the best-fit WIMP masses are very similar (within $2\sigma$) in all four cases, $\mathcal{O}(10)$ GeV, as expected from an universal DM signal.

In Figure 6.1, we show the Spectral Energy Distribution (SED) of the two best $b\bar{b}$ and $\tau^+\tau^-$ sources (4FGL J1641.3−2908 and 4FGL 1717.5−5804), which have a preference for DM with post-trials p-values of 0.047 and 0.012, respectively. We show the spectral points obtained with the LAT as well as the best-fit DM annihilation spectrum overimposed.

From the four sources with $p_{glob} < 0.05$, three result as point-like in the spatial analysis, but one (4FGL J1641.3−2908) is extended with a $3\sigma$ preference. In Figure 6.2 we focus on the latter, showing its extension likelihood curve and its position in the expected $\mathrm{TS}_{\mathrm{det}} - \mathrm{TS}_{\mathrm{ext}}$ DM subhalo parameter space, as obtained in Chapter 5. Interestingly, the source falls where we should expect a DM subhalo to, this way reinforcing even further the DM hypothesis, and becoming more challenging to be explained by an alternative astrophysical class.

[4]We use their averaged results for all WIMP masses and $|b| > 30°$. Their reported results are valid for the $b\bar{b}$ annihilation channel, yet using them for both $b\bar{b}$ and $\tau^+\tau^-$ channels is conservative, as the latter, being a harder channel, would render a distribution closer to the theoretical one.

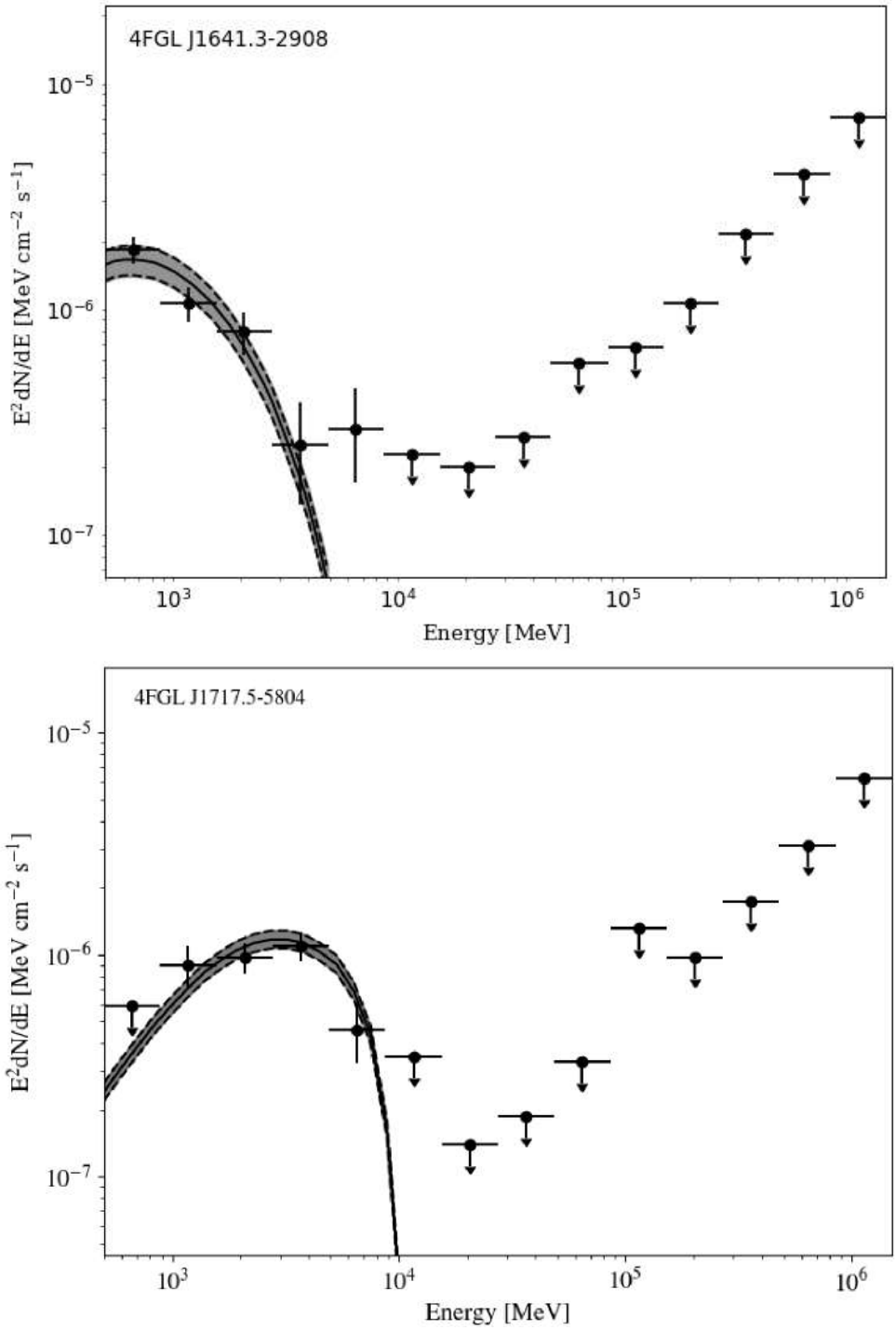


FIGURE 6.1: SED of the two best DM subhalo candidates in Table 6.2, overimposed with the best-fit DM annihilation spectrum. **Top panel:** 4FGL J1641.3−2908, annihilating to $b\bar{b}$ with $m_\chi = 10.3 \pm 0.6$ GeV. **Bottom panel:** 4FGL 1717.5−5804, annihilating to $\tau^+\tau^-$with $m_\chi = 10.6 \pm 0.7$ GeV.

## 6.4 Discussion and conclusions

Based on the results of our previous work in Chapters 3, 4 and 5, we analyzed 12 years of Fermi-LAT gamma-ray data, searching for WIMP annihilation in dark subhalos. To do so, we examined the sample of unIDs from the latest LAT catalog,

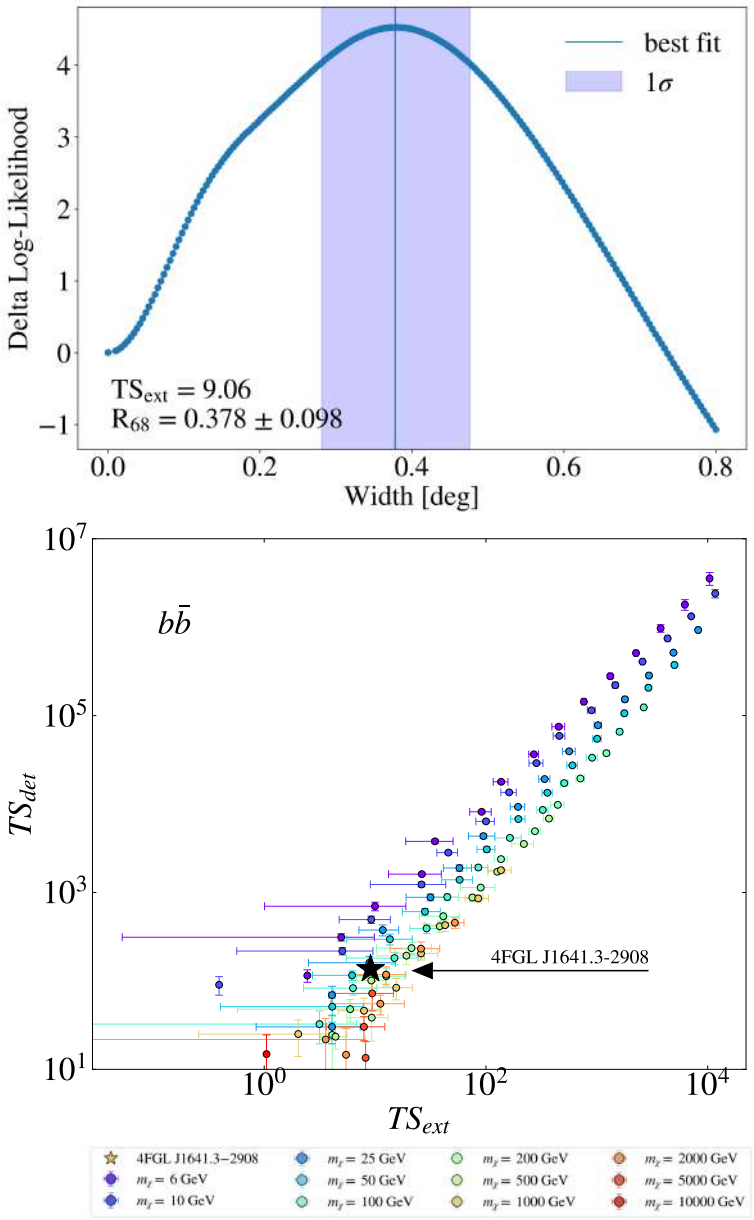


FIGURE 6.2: **Top panel:** Spatial extension likelihood profile of 4FGL J1641.3−2908, exhibiting an extension of $0.38 \pm 0.10$ degrees at $3\sigma$ level (see Table 6.2). **Bottom panel:** Based on previous work in Chapter 5, we show the position of this same source (golden star) in the expected $TS_{det}$ vs. $TS_{ext}$ parameter space for DM subhalos and the LAT.

| 4FGL-DR2 127 unIDs sample analysis | | | | | | | | | |
|---|---|---|---|---|---|---|---|---|---|
| $b\bar{b}$ annihilation channel | | | | | | | | | |
| Source name | $TS_{det}$ | $TS_{ext}$ | $R_{68}$ [deg] | $TS_{b\bar{b}}$ | $p_{loc}$ | $\sigma_{loc}$ | $p_{glob}$ | $\sigma_{glob}$ | $m_\chi^{b\bar{b}}$ [GeV] |
| 4FGL J1225.9+2951 | 1167 | - | - | 14.2 | $7.53 \cdot 10^{-3}$ | 1.83 | 0.304 | 0.51 | $49.4 \pm 1.1$ |
| 4FGL J1641.3−2908 | 136 | 9.1 | $0.38 \pm 0.10$ | 36.9 | $1.01 \cdot 10^{-3}$ | 2.22 | 0.047 | 1.35 | $10.3 \pm 0.6$ |
| 4FGL J1204.5−5032 | 198 | 1.1 | $0.08 \pm 0.05$ | 19.2 | $4.04 \cdot 10^{-3}$ | 1.97 | 0.176 | 0.83 | $21.5 \pm 1.5$ |
| $\tau^+\tau^-$ annihilation channel | | | | | | | | | |
| Source name | $TS_{det}$ | $TS_{ext}$ | $R_{68}$ [deg] | $TS_{\tau^+\tau^-}$ | $p_{loc}$ | $\sigma_{loc}$ | $p_{glob}$ | $\sigma_{glob}$ | $m_\chi^{\tau^+\tau^-}$ [GeV] |
| 4FGL J1711.9−1922 | 131 | - | - | 42.5 | $7.63 \cdot 10^{-4}$ | 2.28 | 0.036 | 1.44 | $13.6 \pm 0.9$ |
| 4FGL J1717.5−5804 | 257 | - | - | 75.4 | $2.50 \cdot 10^{-4}$ | 2.47 | 0.012 | 1.74 | $10.6 \pm 0.7$ |
| 4FGL J1924.8−1035 | 253 | - | - | 42.3 | $7.70 \cdot 10^{-4}$ | 2.27 | 0.036 | 1.43 | $12.6 \pm 0.6$ |
| 4FGL J1204.5−5032 | 198 | 1.1 | $0.08 \pm 0.05$ | 15.6 | $6.31 \cdot 10^{-3}$ | 1.87 | 0.262 | 0.61 | $7.0 \pm 0.5$ |
| 4FGL J2318.6−3827 | 64 | - | - | 11.5 | $1.34 \cdot 10^{-2}$ | 1.71 | 0.476 | 0.24 | $10.0 \pm 1.3$ |

TABLE 6.2: Summary of the analysis of the 127 4FGL-DR2 unIDs sample, selected with the cuts detailed in Section 6.2. We only report the results for the best subhalo candidates, i.e., with the largest preferences for DM ($TS_\mathcal{X} > 10$). First (second) sub-table shows the candidates fitted to $b\bar{b}$ ($\tau^+\tau^-$). The $TS_\mathcal{X}$ values refer to the difference w.r.t the best-fit astrophysical model, corrected by the difference in d.o.f. with the Akaike criterium. The local p-value ($p_{loc}$) and corresponding local significance ($\sigma_{loc}$) are computed with the realistic TS distribution for DM annihilation from Fermi-LAT Collaboration and DES Collaboration (2017), while the global p-value ($p_{glob}$) accounts for the number of trials and is computed with Eq. 6.4. The global significance $\sigma_{glob}$ is obtained from $p_{glob}$. Note that one source, 4FGL J1204.5−5032, is well fitted to both annihilation channels and therefore is present in both sub-tables.

4FGL–DR2, containing 1667 candidates. We reduced the pool of unIDs to 127 by applying well-motivated cuts attending to the expected gamma-ray properties of DM annihilation.

For the analysis, we relied on `fermipy`. We re-evaluated the significance of detection and searched for spatial extension as well. We then fitted the spectrum to $b\bar{b}$ and $\tau^+\tau^-$ annihilation channels. Then, the preference for DM over standard astrophysical spectra was explored, taking into account the degrees of freedom of each model (Akaike criterion) and the "look elsewhere effect" (trials factor). For the latter, we used a realistic TS distribution derived from blank-sky regions when fit to DM annihilation spectra.

We found four unIDs with post-trials p-values $< 0.05$ when analysing the preference for a WIMP DM origin, one of them being also extended with a $3\sigma$ significance and falling in the expected $TS_{det}$ vs. $TS_{ext}$ parameter space for a DM subhalo, as derived in previous work. These results challenge alternative astrophysical explanations, as the sources successfully passed a number of different, demanding tests for DM annihilation. We conclude that some of the unIDs highlighted in Table 6.2 constitute promising DM subhalo candidates, and encourage further studies to shed definitive light on their nature. This additional work should necessarily include multi-wavelength campaigns as well.

## Bibliography

Akaike, H. (1998). Information theory and an extension of the maximum likelihood principle, *Springer Series in Statistics*, Springer New York, pp. 199–213.

Algeri, S., van Dyk, D., Conrad, J. and Anderson, B. (2016). On methods for correcting for the look-elsewhere effect in searches for new physics, *Journal of Instrumentation* **11**(12): P12010–P12010.

Atwood, W., Albert, A., Baldini, L., Tinivella, M., Bregeon, J., Pesce-Rollins, M., Sgrò, C., Bruel, P., Charles, E., Drlica-Wagner, A., Franckowiak, A., Jogler, T., Rochester, L., Usher, T., Wood, M., Cohen-Tanugi, J. and for the Fermi-LAT Collaboration, S. Z. (2013). Pass 8: Toward the Full Realization of the Fermi-LAT Scientific Potential.
**URL:** *https://arxiv.org/abs/1303.3514*

Ballet, J., Burnett, T. H., Digel, S. W. and Lott, B. (2020). Fermi Large Area Telescope Fourth Source Catalog Data Release 2.

Bertone, G. (2010). The moment of truth for WIMP dark matter, *Nature* **468**(7322): 389–393.

Bertone, G., Hooper, D. and Silk, J. (2005). Particle dark matter: evidence, candidates and constraints, *Physics Reports* **405**(5-6): 279–390.

Chernoff, H. (1952). A measure of asymptotic efficiency for tests of a hypothesis based on the sum of observations, *The Annals of Mathematical Statistics* **23**(4): 493–507.

Chernoff, H. (1956). Large-sample theory: Parametric case, *The Annals of Mathematical Statistics* **27**(1): 1–22.

Conrad, J. (2015). Statistical issues in astrophysical searches for particle dark matter, *Astroparticle Physics* **62**: 165–177.

Coronado-Blázquez, J. et al. (2019a). Spectral and spatial analysis of the dark matter subhalo candidates among Fermi Large Area Telescope unidentified sources, *Journal of Cosmology and Astroparticle Physics* **2019**(11): 045–045.

Coronado-Blázquez, J. et al. (2019b). Unidentified gamma-ray sources as targets for indirect dark matter detection with the Fermi-Large Area Telescope, *Journal of Cosmology and Astroparticle Physics* **2019**(07): 020–020.

Diemand, J., Kuhlen, M., Madau, P., Zemp, M., Moore, B., Potter, D. and Stadel, J. (2008). Clumps and streams in the local dark matter distribution, *Nature* **454**(7205): 735–738.

Eckner, C., Hou, X., Serpico, P. D., Winter, M., Zaharijas, G., Martin, P., Mauro, M. d., Mirabal, N., Petrovic, J., Prodanovic, T. and et al. (2018). Millisecond pulsar origin of the galactic center excess and extended gamma-ray emission from andromeda: A closer look, *The Astrophysical Journal* **862**(1): 79.
**URL:** *http://dx.doi.org/10.3847/1538-4357/aac029*

Fermi-LAT Collaboration (2010). Constraints on dark matter annihilation in clusters of galaxies with the Fermi Large Area Telescope, *Journal of Cosmology and Astroparticle Physics* **2010**(05): 025–025.
**URL:** *http://dx.doi.org/10.1088/1475-7516/2010/05/025*

Fermi-LAT Collaboration (2015a). Search for extended gamma-ray emission from the Virgo galaxy cluster with Fermi-LAT, *The Astrophysical Journal* .

Fermi-LAT Collaboration (2015b). Searching for Dark Matter Annihilation from Milky Way Dwarf Spheroidal Galaxies with Six Years of Fermi Large Area Telescope Data, *Physical Review Letters* **115**(23).

Fermi-LAT Collaboration (2016). Fermi-LAT Observations of High-Energy Gamma-Ray Emission Toward the Galactic Center, *The Astrophysical Journal* **819**: 44.
**URL:** *http://adsabs.harvard.edu/abs/2016ApJ...819...44A*

Fermi-LAT Collaboration (2017). The Fermi Galactic Center GeV Excess and Implications for Dark Matter, *The Astrophysical Journal* **840**: 43.
**URL:** *http://adsabs.harvard.edu/abs/2017ApJ...840...43A*

Fermi-LAT Collaboration (2020). Fermi Large Area Telescope Fourth Source Catalog, *The Astrophysical Journal Supplement Series* **247**(1): 33.

Fermi-LAT Collaboration and DES Collaboration (2017). Searching for Dark Matter Annihilation in Recently Discovered Milky Way Satellites with Fermi-LAT, *The Astrophysical Journal* **834**(2): 110.
**URL:** *http://dx.doi.org/10.3847/1538-4357/834/2/110*

Fermi-LAT Collaboration and Atwood, W. B. (2009). The Large Area Telescope on the Fermi Gamma-ray Space Telescope Mission, *The Astrophysical Journal* .

Goodenough, L. and Hooper, D. (2009). Possible Evidence For Dark Matter Annihilation In The Inner Milky Way From The Fermi Gamma Ray Space Telescope.
**URL:** *https://arxiv.org/abs/0910.2998*

Madau, P., Diemand, J. and Kuhlen, M. (2008). Dark matter subhalos and the dwarf satellites of the milky way, *The Astrophysical Journal* **679**(2): 1260–1271.

MAGIC Collaboration (2018). Constraining dark matter lifetime with a deep gamma-ray survey of the Perseus galaxy cluster with MAGIC, *Physics of the Dark Universe* **22**: 38–47.
**URL:** http://dx.doi.org/10.1016/j.dark.2018.08.002

MAGIC Collaboration and Fermi-LAT Collaboration (2016). Limits to dark matter annihilation cross-section from a combined analysis of MAGIC and Fermi-LAT observations of dwarf satellite galaxies, *Journal of Cosmology and Astroparticle Physics* **2016**(02): 039–039.

Mirabal, N. (2013). Dark matter versus pulsars: catching the impostor, *Monthly Notices of the Royal Astronomical Society* **436**(3): 2461–2464.
**URL:** http://dx.doi.org/10.1093/mnras/stt1740

Mirabal, N., Charles, E., Ferrara, E. C., Gonthier, P. L., Harding, A. K., Sánchez-Conde, M. A. and Thompson, D. J. (2016). 3FGL Demographics Outside the Galactic Plane using Supervised Machine Learning: Pulsar and Dark Matter Subhalo Interpretations, *The Astrophysical Journal* **825**(1): 69.
**URL:** http://dx.doi.org/10.3847/0004-637X/825/1/69

Moliné, A., Sánchez-Conde, M. A., Palomares-Ruiz, S. and Prada, F. (2017). Characterization of subhalo structural properties and implications for dark matter annihilation signals, *Monthly Notices of the Royal Astronomical Society* **466**: 4974–4990.
**URL:** http://adsabs.harvard.edu/abs/2017MNRAS.466.4974M

Oakes, L., Armand, C., Charles, E., di Mauro, M., Giuri, C., Harding, J. P., Kerszberg, D., Miener, T., Moulin, E., Poireau, V., Pueschel, E., Rico, J., Rinchiuso, L., Salazar-Gallegos, D., Tollefson, K. and Zitzer, B. (2019). Combined Dark Matter searches towards dwarf spheroidal galaxies with Fermi-LAT, HAWC, HESS, MAGIC and VERITAS, *Proc. of ICRC 2019* .

Planck Collaboration (2020). Planck 2018 results, *Astronomy & Astrophysics* **641**: A6.

Rico, J. (2020). Gamma-Ray Dark Matter Searches in Milky Way Satellites—A Comparative Review of Data Analysis Methods and Current Results, *Galaxies* **8**(1): 25.
**URL:** http://dx.doi.org/10.3390/galaxies8010025

Sawala, T., Frenk, C. S., Fattahi, A., Navarro, J. F., Theuns, T., Bower, R. G., Crain, R. A., Furlong, M., Jenkins, A., Schaller, M. and et al. (2015). The chosen few: the low-mass haloes that host faint galaxies, *Monthly Notices of the Royal Astronomical Society* **456**(1): 85–97.
**URL:** http://dx.doi.org/10.1093/mnras/stv2597

Springel, V., White, S. D. M., Frenk, C. S., Navarro, J. F., Jenkins, A., Vogelsberger, M., Wang, J., Ludlow, A. and Helmi, A. (2008). Prospects for detecting supersymmetric dark matter in the Galactic halo, *Nature* **456**(7218): 73–76.

Wood, M., Caputo, R., Charles, E., Mauro, M. D., Magill, J. and Perkins, J. (2017). Fermipy: An open-source Python package for analysis of Fermi-LAT Data.

# Chapter 7

# Constraints to dark matter annihilation from high-latitude HAWC unidentified sources

*Based on J. Coronado-Blázquez and M. A. Sánchez-Conde, Galaxies 2020, 8(1), 5*

## 7.1 Introduction

As of today, we believe that about 85% of all the matter in the Universe is of non-baryonic nature The Planck Collaboration (2016); Garrett and Duda (2011); Freese (2009). Despite its large abundance, the ultimate nature of this so-called dark matter (DM) remains unknown, being at present one of the most puzzling questions in modern physics.

N-body cosmological simulations reveal that DM structures form hierarchically in a bottom-up scenario: the DM particles first collapse into small gravitationally bound systems (known as halos), and then form more massive structures through a complex history of merging and accretion. As a result, DM halos contain a very large number of smaller *subhalos* Madau et al. (2008); Zavala and Frenk (2019).

For DM candidates with weak-scale masses and interactions, as those preferred by supersymmetric particle physics theories Jungman et al. (1996), subhalos with masses between approximately $10^{-11} - 10^{-3}$ M Bertschinger (2006); Profumo et al. (2006); Bringmann (2009) (depending on the specific DM particle model) up to roughly $10^{10}$ M are expected to exist in a Milky Way-like galaxy. The vast majority of the Galactic DM subhalos are not expected to be massive enough to host baryons and therefore remain completely dark, with no visible counterparts Gao et al. (2004); Ocvirk et al. (2016); Sawala, Frenk, Fattahi, Navarro, Theuns, Bower, Crain, Furlong, Jenkins, Schaller and Schaye (2015); Sawala, Frenk, Fattahi, Navarro, Bower, Crain, Vecchia, Furlong, Jenkins, McCarthy, Qu, Schaller, Schaye and Theuns (2015); Fitts et al. (2018). Yet, many of these light subhalos or *dark satellites* will lie much closer to the Earth compared to the most massive ones, given both their much larger number density and higher survival probability at small Galactocentric radii against tidal disruption Diemand et al. (2008); Springel et al. (2008).

If the DM is made of the so-called *Weakly Interacting Massive Particles* (WIMPs) DM Roszkowski et al. (2018); Bertone (2010), these small subhalos may outshine in gamma rays. WIMPs can achieve the correct relic DM abundance (the so-called "WIMP miracle"), through self-annihilation in the early Universe. This process gives rise to a Standard Model (SM) particle-antiparticle pair which, among other possible subsequent by-products, may yield gamma-ray photons Bertone et al. (2005); Bertone (2009). Small subhalos may be potentially interesting for this kind of *indirect*

dark matter search since, as mentioned, many of them may be located close enough to Earth to yield high enough gamma-ray fluxes Anderson et al. (2010); Calore et al. (2017); Coronado-Blázquez, Sánchez-Conde, Domínguez, Aguirre-Santaella, Mauro, Mirabal, Nieto and Charles (2019). Interestingly, an important fraction of objects (typically between $30-40\%$, depending on the catalog) in the very high energy (VHE, $E > 100$ GeV) sky are unidentified sources (unIDs), i.e., objects with no clear single association or counterpart. Some of these unIDs may actually be DM subhalos Bertoni et al. (2015, 2016); Buckley and Hooper (2010); Calore et al. (2017); Fermi-LAT Collaboration (2012b); Hooper and Witte (2017); Egorov et al. (2018); A. De Angelis et al. (2018); Zechlin et al. (2012); Zechlin and Horns (2012); Coronado-Blázquez, Sánchez-Conde, Domínguez, Aguirre-Santaella, Mauro, Mirabal, Nieto and Charles (2019). In our work, we will explore this possibility focusing on the unIDs recently detected in the VHE regime by the High Altitude Water Cherenkov Observatory (HAWC) The HAWC Collaboration (2013a, 2019).

One of the greatest challenges when using dark satellites to search for DM is to come up with a reliable characterization of the low-mass subhalo population that would allow for robust predictions of their DM annihilation fluxes. Indeed, there is no N-body cosmological simulation at present able to resolve the entire Galactic subhalo population all the way down to the expected minimum subhalo mass. In this paper, we will adopt the results in Coronado-Blázquez, Sánchez-Conde, Domínguez, Aguirre-Santaella, Mauro, Mirabal, Nieto and Charles (2019), where the authors devised an algorithm to repopulate the original Via Lactea II (VL-II) Diemand et al. (2008) N-body cosmological simulation with low-mass subhalos below its resolution limit, of about $\sim 10^5$M . To do so, they first studied what found for the abundance and distribution of resolved subhalos in the simulation, and extrapolated the relevant quantities to smaller subhalo masses. In addition, they adopted state-of-the-art models to describe the subhalo structural properties Moliné et al. (2017). With the predictions of Coronado-Blázquez, Sánchez-Conde, Domínguez, Aguirre-Santaella, Mauro, Mirabal, Nieto and Charles (2019) at hand, and in the absence of an obvious DM subhalo candidate among the pool of HAWC unIDs, which is actually reduced to just one source in the end, 2HWC J1040+308, we will show in this work that it is possible to place competitive constraints on the WIMP DM parameter space following the procedure described in Calore et al. (2017); Coronado-Blázquez, Sánchez-Conde, Domínguez, Aguirre-Santaella, Mauro, Mirabal, Nieto and Charles (2019).

The structure of this paper is as follows. In Section 7.2 we briefly describe the observational status of the VHE sky, paying special attention to the HAWC observatory. We also address our specific target selection in this section. Section 9.4 is devoted to the computation of the DM constraints taking into account the different instrumental parameters and the theoretical predictions from N-body simulations. We conclude in Section 7.4, where we also make explicit the caveats in our analysis, compare our results to previous work and make qualitative assessments for future unID-based DM search strategies and experiments.

## 7.2 HAWC unidentified sources

In this section, we briefly review the HAWC observatory and discuss the target selection we made for this work.

### 7.2.1 HAWC and the TeV sky

The High Altitude Water Cherenkov Observatory (HAWC) is a VHE gamma-ray detector with a one-year sensitivity of $5 - 10\%$ of the flux of the Crab Nebula. Unlike imaging atmospheric Cherenkov telescopes (IACTs), such as H.E.S.S. The H.E.S.S. Collaboration (2004), MAGIC The MAGIC Collaboration (2016) or VERITAS The VERITAS Collaboration (2006), which detect the Cherenkov light emitted by the extensive air showers produced by the gamma rays in the atmosphere, HAWC detects particles of these air showers that reach ground level with water-based Cherenkov detectors. Therefore, HAWC is able to operate continuously and to achieve a field of view (FoV) larger than 1.5 sr Andrew J. Smith for the HAWC Collaboration (2007). HAWC is located on the flanks of the Sierra Negra volcano near Puebla, Mexico, and consists on a large pond of water tanks, each of 7.3m of diameter, located at 4100 m elevation. The pond contains 900 photomultiplier tubes (PMTs), while each tank contains 200,000 liters of purified water Andrew J. Smith for the HAWC Collaboration (2015). Starting operations in 2012 with 30 tanks, they were progressively increased to 300 in 2015, detecting TeV gamma and cosmic rays with a high duty cycle (>95%) Dingus (2007); The HAWC Collaboration (2013b).

Currently, there are about 200 known VHE gamma-ray sources detected by a handful of observatories, compiled within the TeVCat[1] catalog Wakely and Horan (2008). A Galactic map in Hammer-Aitoff projection with all TeVCat sources and their class is plotted in Figure 7.1. From these, roughly 60 sources remain with no clear association. Most of them are probably astrophysical sources of Galactic origin, since many were discovered after the Galactic plane survey by H.E.S.S The H.E.S.S. Collaboration (2018). Yet, there are several unIDs located at high Galactic latitudes, in particular three of them reported in the 2HWC catalog – the second HAWC catalog The HAWC Collaboration (2017b) comprising 507 days of instrument operation. In this work, we will focus on these sources.

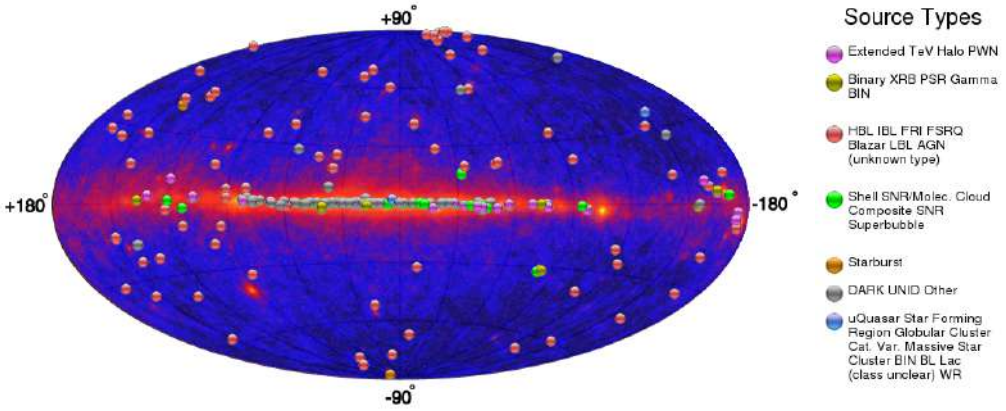


FIGURE 7.1: VHE sources listed in the TeVCat online catalog as of November 2019, here shown in Hammer-Aitoff projection and Galactic coordinates. Background is the gamma-ray sky as seen by Fermi-LAT in 4 years of operation. Note the higher density of sources, in particular of unIDs, along the Galactic plane. The figure was generated with the TeVCat online tool Wakely and Horan (2008).

[1] tevcat2.uchicago.edu

### 7.2.2 Target selection

We chose to work only with the high-latitude unIDs listed in the 2HWC catalog mainly for two reasons:

- **Why HAWC?** - HAWC is currently the only VHE observatory able to survey a significant fraction of the whole sky. Indeed, the combination of its 1.5 sr FoV, Earth rotation and location in Mexican soil, 19° above the Equator, makes it possible to observe 2/3 of the sky every day.[2] In contrast, IACTs are pointing telescopes, i.e., they need to know the location of the sources in advance and, thus, just point towards specific targets. For the purposes of this work, it becomes critical to have observations of a large fraction of the sky. This is so because we adopt the methodology introduced in Coronado-Blázquez, Sánchez-Conde, Domínguez, Aguirre-Santaella, Mauro, Mirabal, Nieto and Charles (2019) to set constraints on the DM annihilation parameter space using unIDs. The method is based on a comparison between the number of catalogued unID sources and subhalo predictions derived from N-body cosmological simulations. Large fractions of the sky, observed with a nearly uniform exposure, will allow for a more accurate comparison to N-body simulations, as we can derive a more robust statistical determination of the subhalo annihilation fluxes for significantly large sky areas. We remind that these fluxes are proportional to the so-called J-factor:

$$J = \int_{\Delta\Omega} d\Omega \int_{l.o.s} \rho^2_{DM} \left[ r\left(\lambda\right) \right] d\lambda, \tag{7.1}$$

  where the first integral is performed over the solid angle of observation ($\Delta\Omega$), the second one along the line of sight (l.o.s, $\lambda$), and $\rho_{DM}$ is the dark matter density profile of a given subhalo.

- **Why high latitude?** $\Lambda$CDM predicts the existence of DM subhalos at all Galactic latitudes distributed nearly isotropically from the Sun's position in the Galaxy. On the other hand, the majority of Galactic VHE astrophysical sources, such as pulsars, binaries, supernova remnants and pulsar wind nebulae, are expected to cluster heavily along the Galactic plane, where most of the stars and gas reside. Since many of these objects are expected to also be hidden among the pool of unIDs awaiting for a proper classification, we expect the distribution of unIDs to peak around zero Galactic latitude as well (as already discussed in Figure 7.1). For our purposes, these low-latitude sources only add contamination to our sample of potential DM subhalo candidates. Therefore, we apply a cut in our analysis at Galactic latitudes $|b| \leq 10°$. For consistency, this cut will also need to be done on our predicted subhalo distribution. On average, our Galactic cut removes only ∼11% of the simulated subhalos, while 87% of 2HWC unIDs are left out. Actually, in practice we cut a larger region $|b| \leq 30°$ in the N-body simulation in order to match the 2/3 sky coverage of HAWC, this way having a totally fair one-to-one comparison among observed and simulated sky.

After this selection, we are left with only three candidates in the 2HWC catalog, namely 2HWC J1309−054, 2HWC J1040+308 and 2HWC J0819+157. All three

[2] In fact, HAWC applies a zenith cut of 45°, which for a daily exposure translates in 8.4sr, corresponding exactly to 66.85% of the sky.

candidates are reported as very faint, i.e. near the source detection threshold of the catalog. In fact, The HAWC Collaboration (2019) recently analyzed 760 days of HAWC data, i.e., approximately 50% more integration time than the original 2HWC catalog, and found both 2HWC J0819+157 and 2HWC J1309−054 to be under the detection threshold. This behaviour of source flux versus integration time is not expected for actual sources but from spurious ones instead. Thus, in the following we only consider the remaining candidate for our analysis, 2HWC J1040+308. We note that a spectral analysis was already performed for this source in The HAWC Collaboration (2019), no preference for DM being found. Yet, more data are probably needed before being able to definitely reject this unID as a DM subhalo. Thus, we conservatively keep this source as the only surviving target in our list of potential subhalo candidates and set DM limits by assuming the existence of one single DM subhalo candidate in HAWC data.

### 7.2.3 2HWC J1040+308 as a DM subhalo candidate

Before proceeding to set DM limits in the next section, we would like to highlight here some properties of 2HWC J1040+308 that make this unID particularly appealing in a DM context, as such properties may be compatible with a DM origin for the observed emission:

- **Spatial extension** – Spatial extension has been hailed as a "smoking gun" for DM annihilation Bertoni et al. (2015, 2016); Coronado-Blázquez, Sánchez-Conde, Mauro, Aguirre-Santaella, Ciucă, Domínguez, Kawata and Mirabal (2019). Indeed, low-mass yet sufficiently close DM subhalos may be expected to appear as extended unID sources. 2HWC J1040+308 is found to be spatially extended in HAWC data with a radius of 0.5° The HAWC Collaboration (2017b). This fact is even more notable for the case of very high latitude sources like this one ($b = 61°$), as sources at high latitudes are typically extragalactic and thus the majority of them are expected to be point-like. Indeed,it would be hard to explain all these features with a single astrophysical source – AGNs would appear as point-like sources, while Galactic sources could appear as extended, yet this source's high latitude would imply a small distance and thus it would be surprising not to have a detection in any other wavelengths. On the other hand, as these unIDs correspond to very faint sources near the detection threshold, it is currently unclear whether they would appear as extended, even if being actual DM subhalos, as the DM annihilation flux profile decreases very rapidly with distance to the subhalo center.

- **Multi-wavelength search** – As already mentioned, dark satellites are not massive enough to retain baryons and, as a result, they are not expected to shine at any wavelengths due to astrophysical processes. However, gamma-ray emission is expected to happen should these objects be composed of WIMP DM.[3] A dedicated search at different wavelengths was performed for 2HWC J1040+308, with null results. In particular, a combined search in less energetic gamma rays with *Fermi*-LAT and VERITAS was performed in The Fermi-LAT, HAWC and VERITAS Collaborations (2018), with no detection. An additional search can

[3] DM-induced emission may also be expected in radio due to synchrotron radiation from secondary particles Colafrancesco et al. (2006, 2007); Marchegiani et al. (2018); Cembranos et al. (2020); yet the high density of radio sources would make any potential association probably very challenging.

be performed with the SSDC online tool,[4] where no significant emission at lower energies is found.

- **Heavy WIMP mass** – It is interesting to note that a joint analysis of Fermi LAT Fermi-LAT Collaboration and Atwood (2009), VERITAS Nahee Park for the VERITAS Collaboration (2015) and HAWC data was recently done in The Fermi-LAT, HAWC and VERITAS Collaborations (2018) and no gamma-ray emission was reported for 2HWC J1040+308 in the comparatively lower energy range covered by the LAT and VERITAS. This is so despite the fact that 2HWC J1040+308 exhibits a *hard* spectrum with a photon spectral index of $\Gamma = 2.08 \pm 0.25$ in the HAWC energy range The HAWC Collaboration (2017b), which would in principle make a detection at low energies easier to realize. If interpreted in a DM scenario, these results suggest heavy, TeV WIMP masses as we would not expect a detection by Fermi LAT or VERITAS only in case of significantly high values of the WIMP mass, for which a DM spectrum beyond the range of sensitivity of these two instruments would be generated. Also, interestingly, this unID slightly prefers a fit to a "Cutoff Power Law" instead of a "Simple Power Law" The HAWC Collaboration (2019), which is a parametric form that better reproduces a typical DM annihilation spectrum Calore et al. (2017); Coronado-Blázquez, Sánchez-Conde, Domínguez, Aguirre-Santaella, Mauro, Mirabal, Nieto and Charles (2019). Heavy WIMPs are well motivated Gammaldi (2019); Cembranos et al. (2003); Cembranos et al. (2012) and, probably, favoured in the light of current DM constraints in the usual $\langle \sigma v \rangle$ (velocity-averaged annihilation cross section) vs. $m_\chi$ (WIMP mass) parameter space: IACTs are still far from being able to probe the *thermal relic* cross section values Steigman et al. (2012) for large, TeV WIMP masses, while for much lighter, $\mathcal{O}$(GeV) masses there are already robust and strong constraints, e.g., Fermi-LAT Collaboration (2015); Coronado-Blázquez, Sánchez-Conde, Domínguez, Aguirre-Santaella, Mauro, Mirabal, Nieto and Charles (2019).

All the above considerations make 2HWC J1040+308 an excellent candidate for being a DM subhalo. Yet, lacking a definitive answer for the moment we will proceed and will set constraints to DM annihilation using HAWC unIDs, just assuming that we cannot discard 2HWC J1040+308 as a DM subhalo.

## 7.3 DM constraints

The methodology we follow to set our DM constraints is explained in full detail in Coronado-Blázquez, Sánchez-Conde, Domínguez, Aguirre-Santaella, Mauro, Mirabal, Nieto and Charles (2019). In short, these are computed according to i) the number of remaining HAWC unIDs as potential DM subhalo candidates, i.e. just one source (2HWC J1040+308), as discussed in Section 7.2; ii) the flux sensitivity of the instrument to DM annihilation; and iii) the J-factor predictions for the Galactic DM subhalo population as derived from N-body cosmological simulations. The annihilation cross section and WIMP mass $\langle \sigma v \rangle$ and $m_\chi$ are related by Coronado-Blázquez, Sánchez-Conde, Domínguez, Aguirre-Santaella, Mauro, Mirabal, Nieto and Charles (2019):

[4] https://tools.ssdc.asi.it/

$$\langle \sigma v \rangle = \frac{8\pi \cdot m_\chi^2 \cdot F_{min}}{J \cdot \int_{E_{th}}^{\infty} \left(\frac{dN}{dE}\right) dE} \tag{7.2}$$

where $F_{min}$ is the minimum flux needed for a point-source detection, $J$ is the astrophysical J-factor (see Eq. 8.2), and $\int_{E_{th}}^{\infty} \left(\frac{dN}{dE}\right) dE = N_\gamma$ is the integrated DM spectrum. This DM spectrum is obtained from the PPPC4 DM ID tables Cirelli et al. (2011), including electroweak corrections, and integrated from $E_{th} = 300$ GeV for a variety of annihilation channels. Hereafter, though, and for the sake of clarity, we will focus on $b\bar{b}$ and $\tau^+\tau^-$ channels, considering only pure annihilations (unity branching ratio).

### 7.3.1 Minimum detection flux

As mentioned previously, the minimum detection flux ($F_{min}$) is defined as the one required by the instrument to have a detection. More specifically, it is the source flux that is needed to reach $TS = 25$ over the background, where TS is the Test Statistic, defined as,

$$TS = -2 \log \left[\frac{\mathcal{L}(H_1)}{\mathcal{L}(H_0)}\right] \tag{7.3}$$

$\mathcal{L}(H_1)$ and $\mathcal{L}(H_0)$ are, respectively, the likelihoods under the source and no source (null hypothesis) assumptions. Ideally, as done in Coronado-Blázquez, Sánchez-Conde, Domínguez, Aguirre-Santaella, Mauro, Mirabal, Nieto and Charles (2019), one would need to account for the variations of this quantity across different instrumental setups (integration time, energy threshold, instrument response functions, etc.) and adopting different DM spectra.[5] Finally, the source latitude should also be taken into account, however this is a second-order effect once the Galactic plane is removed from the analysis, as it is the case.

Unfortunately, the VHE sky still lacks a proper model for the all-sky Galactic diffuse gamma-ray emission, which exists at lower energies Fermi-LAT Collaboration (2012a). This, and the fact that we do not possess the HAWC instrumental response functions (IRFs), private for this Collaboration's internal use at the moment, precludes a precise characterization of the HAWC $F_{min}$. Instead, we will have to rely only on the differential sensitivity from Figure 16 of The HAWC Collaboration (2017a).[6] At each energy, the $F_{min}$ can be obtained by dividing the differential sensitivity (in TeV $\cdot$ cm$^{-2}$ $\cdot$ s$^{-1}$) value by the log-central energy value in each considered bin (to obtain ph $\cdot$ cm$^{-2}$ $\cdot$ s$^{-1}$). In our case, we need the $F_{min}$ corresponding to a declination of 30.87°, which turns out to be very near the absolute minimum of the curve shown in Figure 16 of The HAWC Collaboration (2017a).[7] Note, however, that the reported flux in The HAWC Collaboration (2017a) assumes a power law spectrum with a photon spectral index $\Gamma = 2.63$ (Crab-like), while our DM subhalo candidate

[5] This is so because, by default, this quantity is computed for a source spectrum with a power law index $\Gamma \sim 2$, while the DM is better parametrized by a "Power Law with SuperExponential Cutoff" Coronado-Blázquez, Sánchez-Conde, Domínguez, Aguirre-Santaella, Mauro, Mirabal, Nieto and Charles (2019), where the index and cutoff energy vary over the annihilation channel and WIMP mass.

[6] This sensitivity is computed for the Crab, which is located at DEC$\sim$ 22°, while our source is at $\sim$ 30° instead. Fortunately, the HAWC sensitivity for both locations is expected to be very similar The HAWC Collaboration (2013a).

[7] We note that, should we have had more than one unID, we would have computed a mean value after averaging the corresponding differential sensitivities for each source's declination.

exhibits a considerably harder spectrum, $\Gamma = 2.08$, and therefore it should be comparatively easier to detect. Also, the sensitivity is expected to scale as $\sim \sqrt{t}$ (assuming Poisson photon statistics), where $t$ is the exposure time. Thus, as the reported flux in The HAWC Collaboration (2017b) was computed for 507 days of operation, the performance of HAWC would be underestimated for the 760 days of the current analysis.

With these limitations in mind, it is actually possible to compute a better estimate for $F_{min}$ than the one described above. We will define the improvement factor as the ratio between our estimation of $F_{min}$ and the official one. First, we take into account the improvement due to the photon spectral index – a source with smaller index (harder spectrum), will be easier to detect than a source with larger index (softer spectrum). We can use the scaling relation reported in The HAWC Collaboration (2017b), i.e., the variation of $F_{min}$ with the source spectral index, for an energy value of 7 TeV, used as the pivot energy. By calibrating the improvement at this energy, we can extend it to all the considered energy range (300 GeV – 100 TeV), taking into account the spectral shapes of both power laws. Then, we rescale the obtained $F_{min}$ by differences in exposure times, i.e., a factor $\sqrt{507/760} = 0.82$.

Also, as our unID is an extended source, with a reported extension of 0.5°, the HAWC sensitivity is expected to worsen with respect to that for a point-like source. Indeed, according to The HAWC Collaboration (2013a), a 0.5° source would require a flux 1.93 times larger to be detected at the same significance, independently of the assumed spectral index. As we are tailoring the sensitivity to our candidate, we will take this correction factor into account. As a result, the disagreement between our results and those in The HAWC Collaboration (2019) is reduced to a factor $\sim 25$.

A comparison between both the originally reported $F_{min}$ in The HAWC Collaboration (2017a) ($\Gamma = 2.63$, $t = 507$ days, point-like) and the "improved" $F_{min}$ here described for our candidate ($\Gamma = 2.08$, $t = 760$ days, 0.5°) is shown in Figure 8.3 as the blue and red curves, respectively. The latter is the one that will be used to set our DM constraints in Section 7.3.3.[8]

### 7.3.2 J-factor

The last ingredient needed to set the DM constraints is the J-factor. In the case of unID-based DM searches, we conservatively assume that all $N$ DM subhalo candidates in our unID list ($N = 1$ in this work) are in fact DM subhalos Calore et al. (2017); Coronado-Blázquez, Sánchez-Conde, Domínguez, Aguirre-Santaella, Mauro, Mirabal, Nieto and Charles (2019). Then, we require consistency of this supposedly observed number of DM subhalos with that obtained from N-body simulations, by assuming that the J-factor of the $N^{th}$ ($1^{st}$, in this work) most brilliant DM subhalo in our simulation sets the border between the population of detected and non-detectable subhalos.

As input, we use the N-body simulation work by Coronado-Blázquez, Sánchez-Conde, Domínguez, Aguirre-Santaella, Mauro, Mirabal, Nieto and Charles (2019), specifically designed to assess the relevance of low-mass subhalos for this kind of studies. The authors of Coronado-Blázquez, Sánchez-Conde, Domínguez, Aguirre-Santaella, Mauro, Mirabal, Nieto and Charles (2019) *repopulate* the original Via Lactea II DM-only N-body cosmological simulation of a Milky-Way-size halo Diemand et al. (2008) with subhalos well below its resolution limit by applying bootstrapping

[8] The spectral index is reported to have an uncertainty $\Gamma = 2.08 \pm 0.25$. We checked that this uncertainty translates into a factor $\sim$4 uncertainty in $F_{min}$ at most (factor 2 when compared to the benchmark $\Gamma = 2.08$).

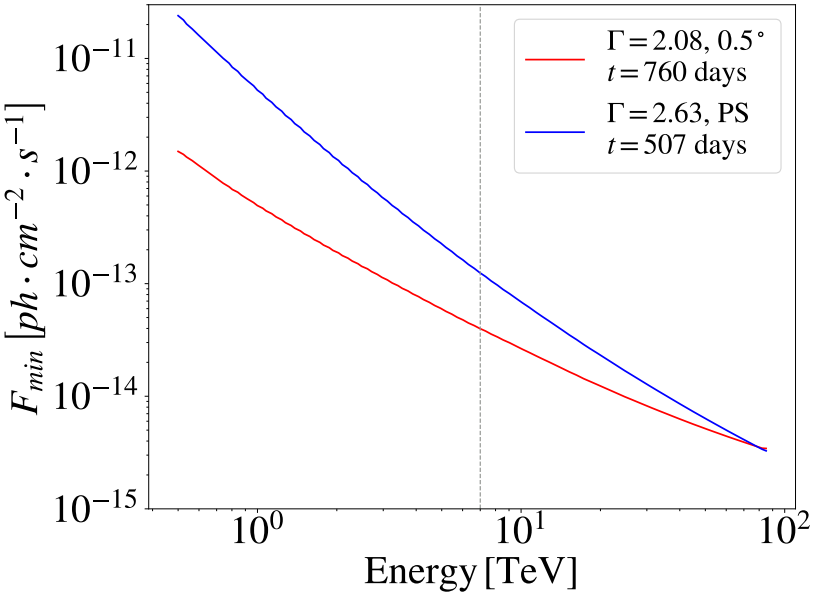


FIGURE 7.2: HAWC minimum flux, $F_{min}$, needed to reach source detection ($TS = 25$) at a sky declination equal to 30.87°. In blue, the $F_{min}$ as originally reported in The HAWC Collaboration (2017a) for the case of a point source described by a power law spectrum with index $\Gamma = 2.63$ and 507 days of exposure. The red curve shows the $F_{min}$ for our DM subhalo candidate instead (with a spatial extension of 0.5°, $\Gamma = 2.08$ and 760 days of exposure). This one is computed taking into account i) the improvement factor of $\sim 5$ derived for this unID at a pivot energy of 7 TeV The HAWC Collaboration (2017b), marked in the figure as a dashed grey vertical line; ii) the difference in exposure times, which makes the $F_{min}$ improve by a factor $\sqrt{507/760} = 0.82$; and iii) a factor $\sim$2 worsening due to the extension of the source, according to The HAWC Collaboration (2013a). See text for further details on these computations. The overall $F_{min}$ improvement is roughly an order of magnitude at low energies, while at the highest energies there is no improvement at all.

techniques and semi-analytical extrapolations of the relevant quantities. In particular, the subhalo mass function is extended down to $10^3$M , the subhalo distribution within the host halo is assumed to be similar to that of the resolved subhalos in the parent simulation, and a state-of-the-art concentration model Moliné et al. (2017) is used to model the subhalo structural properties and, ultimately, to compute the J-factors. Actually, hundreds of realizations of the parent simulation are performed that allow to derive statistical meaningful J-factor results. More precisely, as done in Coronado-Blázquez, Sánchez-Conde, Domínguez, Aguirre-Santaella, Mauro, Mirabal, Nieto and Charles (2019), in order to derive 95% C.L. upper limits on the DM annihilation cross section, we obtain the distribution of J-factor values for the $N^{th}$ subhalo under consideration and then as reference J-factor the one above which 95% of the J-factor distribution is contained; see Figure 7.3.

In this particular case, we cut out from the simulation results the Galactic region $|b| \leq 10°$ in order to match the cut that we applied on the data to avoid the Galactic plane contamination (see Section 7.2.2). We also take into account that HAWC, unlike Fermi-LAT, does not achieve a uniform exposure for the whole sky but only for $\sim 2/3$ of it. Specifically, to mimic this effect in the simulation side, we cut out the $|b| \leq 30°$ region (i.e., we only keep 2/3 of the whole sky) in every realization.

Finally, as we are interested in dark satellites alone, only M$\leq 10^7$M$_\odot$ subhalos (i.e., not massive enough to retain baryons) are considered. We checked that the resulting distribution looks isotropic as seen from the Earth. The result of applying and of not applying cuts on the J-factor distributions for the most brilliant subhalo in the simulations is shown in Figure 7.3. The value used to set the constraints, above which 95% of the distribution is contained, is $\log_{10}(J) = 19.47$, a factor 4.26 smaller than the value before cuts.[9]

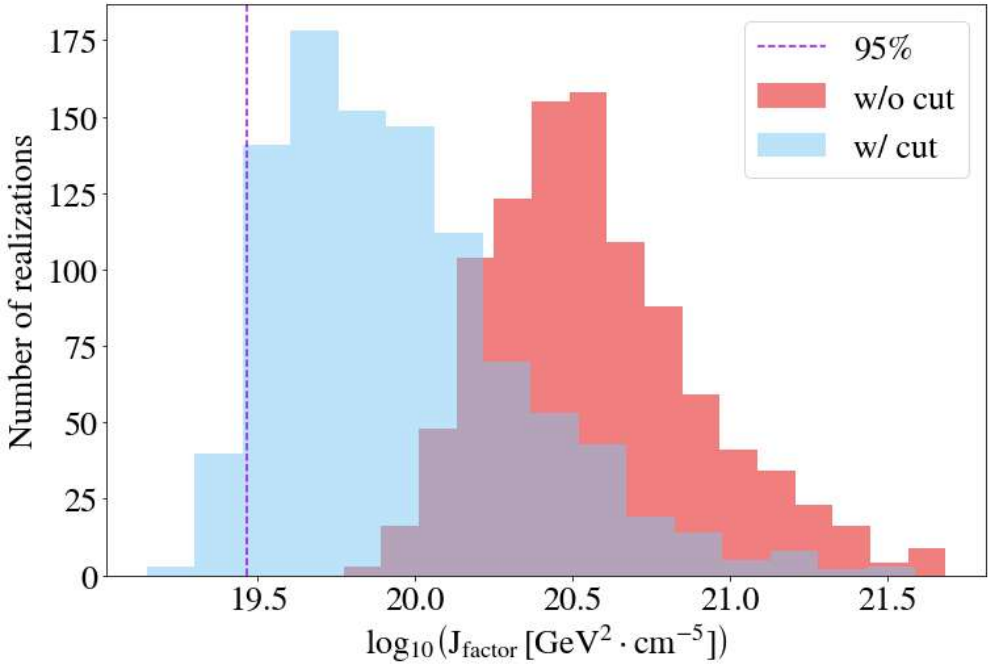


FIGURE 7.3: J-factor distributions for the brightest subhalo across 1000 realizations of the DM subhalo population as derived in Coronado-Blázquez, Sánchez-Conde, Domínguez, Aguirre-Santaella, Mauro, Mirabal, Nieto and Charles (2019) from the Via Lactea II N-body simulation. Red and blue histograms show, respectively, the values before and after applying our selection cuts on the simulated DM subhalos, namely a mass cut ($M \leq 10^7$M$_\odot$) and a coordinate cut ($|b| > 30°$). The dashed, purple vertical line marks the value of the J-factor that will be used to set the 95% C.L. DM limits in Section 9.4, and it is defined as the one above which 95% of the J-factor distribution is contained.

### 7.3.3 Results

Once all involved quantities in Equation 8.3 have been properly characterized, we can set constraints on the DM parameter space at 95% confidence level. These are

[9] The J-factor of our brightest subhalo is comparable to the one typically quoted for dwarf spheroidal satellite galaxies (see e.g. The Fermi-LAT Collaboration (2017)), which are expected to be well above the extragalactic isotropic DM-induced gamma ray background. On the other hand, the value of the DM-induced Galactic diffuse emission is comparable to the isotropic contribution at high latitudes The Fermi-LAT Collaboration (2015), and therefore also negligible compared to the brightest subhalo J-factor. Finally, the boost due to Galactic unresolved substructure contributing to the diffuse emission in the line of sight of this unID is expected to be at the level of few percent and, thus, not relevant here. The boost due to substructures is only particularly important when integrating the subhalo signal for the whole host halo; see e.g. the discussions and results in Moliné et al. (2017).

plotted in Figure 7.4 for the $b\bar{b}$ and $\tau^+\tau^-$ annihilation channels. We remind, once again, that these limits adopt a single HAWC unID as being a potential DM subhalo (2HWC J1040+308).

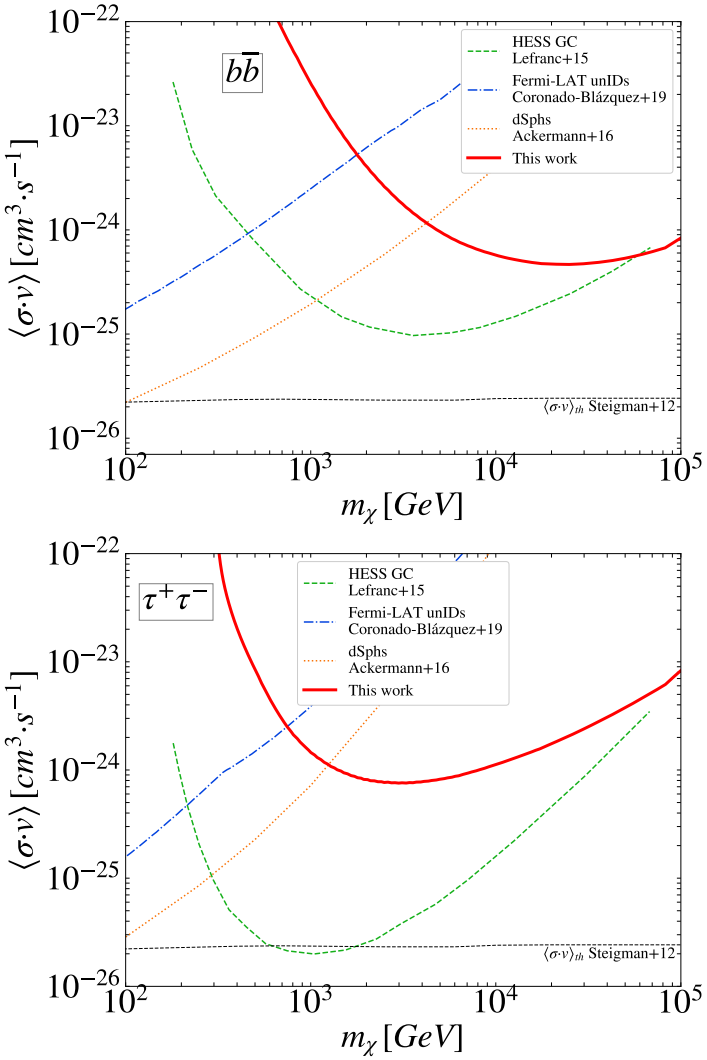


FIGURE 7.4: 95% upper limits on the DM annihilation cross section as derived from HAWC unIDs and predictions from N-body cosmological simulations. Indeed, these constraints use 2HWC J1040+308 alone, i.e., the only HAWC unID located at $|b| \geq 10^\circ$ and surviving our selection criteria in Section 7.2.2. Left (right) panel shows the 95% C.L. upper limits for the $b\bar{b}$ ($\tau^+\tau^-$) annihilation channel. For comparison, we also show as a blue, dot-dashed line the DM constraints obtained from Fermi-LAT unIDs using the same methodology Coronado-Blázquez, Sánchez-Conde, Mauro, Aguirre-Santaella, Ciucă, Domínguez, Kawata and Mirabal (2019). Limits from the observation of the Galactic center region by H.E.S.S., i.e., the best DM constraints achieved from IACT observations at present, are included in both panels as well as a green, dashed line Lefranc et al. (2015). Finally, a dotted, orange line shows the constraints from *Fermi*-LAT observations of dSphs Fermi-LAT Collaboration (2015). We did not include in this Figure the results in The HAWC Collaboration (2019), as a one-to-one comparison would be misleading given the fact that the methodology and underlying assumptions in both works are significantly different; see discussion in Section 9.4 for details.

The obtained 95% upper limits to the DM annihilation cross section are most stringent for masses of ∼20 (2) TeV for the $b\bar{b}$ ($\tau^+\tau^-$) annihilation channel, reaching cross section values around $5 \cdot 10^{-25}$ ($8 \cdot 10^{-25}$) $cm^3 s^{-1}$. This is roughly one order of magnitude far from the thermal relic cross section value, yet they are competitive with today's IACTs best constraints (derived from H.E.S.S. observations of the Galactic center Lefranc et al. (2015)) for very heavy WIMPs annihilating to $b\bar{b}$ above ∼50 TeV. It is worth emphasizing that our DM constraints are independent and complementary to the ones obtained for other astrophysical targets and by means of different analysis techniques.

We must note here that we observe a mismatch between the DM constraints obtained in this work and the ones shown in The HAWC Collaboration (2019). This disagreement, that reaches a factor ∼ 25 for $\tau^+\tau^-$, is hard to understand in detail but it is probably due to several factors. In particular, our $F_{min}$ is expected to be a fair approximation while The HAWC Collaboration (2019) adopts the actual sensitivity of HAWC to a DM spectrum (only computable with the IRFs). In that work, the structural properties of subhalos were described according to Sánchez-Conde and Prada (2014), which is well-suited for field halos, not subhalos. Indeed, we use Moliné et al. (2017), where subhalos exhibit concentration values a factor 2-3 larger than field halos of the same mass. As the J-factor is roughly proportional to the third power of the concentration, this correction would thus yield J-factors about a factor 8-9 times larger, leading to better constraints. Other possible systematics, such as those coming from the Galactic diffuse emission model and the observation strategy adopted in The HAWC Collaboration (2019), may turn out to be particularly relevant. Also, we note that they show cross-section values needed for detection, while we here show 95% upper limits. All in all, a precise one-to-one comparison with the results in The HAWC Collaboration (2019) is not possible, as the methodology and underlying assumptions are different.

For the sake of comparison, we also show in Figure 7.4 the constraints found by Coronado-Blázquez, Sánchez-Conde, Domínguez, Aguirre-Santaella, Mauro, Mirabal, Nieto and Charles (2019) following a similar methodology, but using unIDs in *Fermi*-LAT catalogs instead. Both these low and high energy unID-based DM limits meet at roughly 2 (0.7) TeV for $b\bar{b}$ ($\tau^+\tau^-$) annihilation channel.

Finally, it is important to note that our DM limits are subject to potentially large uncertainties. In addition to the already mentioned caveats in the computation of the minimum detection flux (see Section 7.3.1),[10] there exist important theoretical uncertainties in the N-body simulation predictions, such as the survival probability of the lightest subhalos near the Galactic center van den Bosch et al. (2017); Garrison-Kimmel et al. (2017); Errani and Peñarrubia (2019),[11] the precise subhalo structural properties, the impact of baryons on the subhalo population Kelley et al. (2019); Calore et al. (2017) or the value of the minimum subhalo mass that is adopted to separate between visible and dark satellites Sawala et al. (2017). These and other issues that affect the Galactic subhalo population will be addressed elsewhere. Also, for WIMP masses above ∼ 10 TeV, the theoretical spectra of Cirelli et al. (2011) should

[10] Namely, the lack of both the HAWC IRFs and a Galactic diffuse TeV emission model.

[11] We note that tidal stripping is implicitly included in our simulations. Yet, we note that the mentioned works claim that the disruption of a large fraction of low-mass subhalos in simulations may be artificial and numerical in origin – if this was indeed the case, the distribution of J-factors of the entire subhalo population would surely reach larger values, as we would expect more and closer-to-Earth subhalos. Therefore, our results are conservative, as the DM limits would become even more stringent for resilient subhalos.

include higher-order EW corrections, although these are expected to be potentially relevant only for leptonic channels such as $e^+e^-$ and $\mu^+\mu^-$.

## 7.4 Summary and conclusions

In this work, we have studied the HAWC unIDs reported in the 2HWC catalog to search for potential DM subhalos. HAWC proves to be the best VHE gamma-ray observatory to perform this kind of search at present, as it is the only one that surveys a significant portion of the sky in this energy window.

Starting from a total of 23 unIDs in the 2HWC, we apply several selection criteria in Section 7.2.2 based on expected DM signal and subhalo properties. More precisely, at first we only select those HAWC unIDs located at Galactic latitudes $|b| \geq 10^\circ$ to avoid contamination from astrophysical sources along the Galactic plane. 87% of the 2HWC unIDs do not pass this cut, i.e. we are left with only three unIDs. We then consider these three unIDs as DM subhalo candidates, yet two of them do not even reach the flux detection threshold when adding ∼250 more days of data The HAWC Collaboration (2019). Therefore, only one unID, labeled as 2HWC J1040+308, remains as a potential DM subhalo after our filtering procedure. Indeed, the measured flux of this unID grows as expected when considering more integration time, which reinforces its actual existence.

When scrutinized in further detail, 2HWC J1040+308 turns out to be specially interesting in a DM context, as it is reported in the 2HWC catalog as spatially extended, it exhibits a hard spectrum and does not possess visible counterparts neither at other wavelengths nor for other gamma-ray observatories operating at lower energies such as *Fermi*-LAT and VERITAS. The combination of the latter with the hard source spectrum might point towards particularly heavy WIMP masses, if the gamma-ray emission was actually produced by DM annihilation.

While waiting for more data that can help to shed further light on the true nature of 2HWC J1040+308, we proceed in Section 9.4 and set limits on the DM annihilation cross section by conservatively assuming that this source is actually a subhalo. To do so, we follow the methodology in Coronado-Blázquez, Sánchez-Conde, Domínguez, Aguirre-Santaella, Mauro, Mirabal, Nieto and Charles (2019) and compare the HAWC unID observations with predictions for the Galactic subhalo population as derived from N-body cosmological simulations of a galaxy like our own. In particular, we follow the simulation work in Coronado-Blázquez, Sánchez-Conde, Domínguez, Aguirre-Santaella, Mauro, Mirabal, Nieto and Charles (2019), where the VL-II DM-only simulation was repopulated to include subhalos with masses down to $10^3$M . This work provides the expected subhalo J-factors, which we combine with our own estimate of the HAWC instrumental sensitivity to DM subhalos in order to set 95% C.L. upper limits in the $\langle\sigma v\rangle$-$m_\chi$ parameter space.

Our DM limits are most stringent for masses of ∼20 (2) TeV for the $b\bar{b}$ ($\tau^+\tau^-$) annihilation channel, reaching cross section values around $5 \cdot 10^{-25}$ ($8 \cdot 10^{-25}$) $cm^3s^{-1}$. Although roughly one order of magnitude far from the thermal relic cross section value, our limits are competitive with today's IACTs best constraints Lefranc et al. (2015)) above ∼ 50 TeV for $b\bar{b}$ annihilation channel. Also, these constraints are independent and complementary, yet competitive, to those obtained for other astrophysical targets adopting diverse analysis techniques.

The analysis presented in this work is subject to some potentially important uncertainties. In particular, a proper determination of the minimum HAWC detection flux taking into account the specific instrumental setup used in the observations, as

well as the DM spectrum, annihilation channel and WIMP mass, would be required. The HAWC IRFs are nevertheless not public, thus this study is beyond the scope of the current paper. Instead, we used public information in The HAWC Collaboration (2017b,a) to come up with a fair estimate of the HAWC sensitivity to DM subhalos (Section 7.3.1). Another source of uncertainty is the lack of a proper Galactic diffuse gamma-ray background model, which prevents us from including it in our estimate of the HAWC sensitivity to DM. Yet, as in the end only one unID survives our cuts, this single unID is located at high Galactic latitudes (where the diffuse emission is expected to be subdominant) and exhibits a hard spectrum well fitted by a power law, we expect this uncertainty from the Galactic diffuse model to be a second order effect. Finally, there are also theoretical uncertainties hidden behind the adopted N-body simulation work. In particular, the survival probability of the smallest subhalos near the Galactic center – thus subject to strong tidal forces – is a matter of fierce debate in the community at present, with different works van den Bosch et al. (2017); Garrison-Kimmel et al. (2017); Errani and Peñarrubia (2019) providing diverse answers. In addition, the impact of baryons on the subhalo population was not considered here. Baryons may induce a reduction of the number of subhalos near the Sun's position, which would worsen our DM constraints probably by a factor of a few Calore et al. (2017); Kelley et al. (2019).

Looking into the future, more data, preferably not only in the VHE regime, are needed in order to elucidate the true nature of 2HWC J1040+308, i.e., the only HAWC unID that survives our selection cuts and, indeed, a promising DM subhalo candidate. Related to this, we note that the simplest and most robust way to improve our DM constraints is to also associate 2HWC J1040+308 to a known astrophysical source. In fact, a simple detection of variability or multi-wavelength emission would be enough to discard it as a DM subhalo (see several examples of unID rejections in Coronado-Blázquez, Sánchez-Conde, Domínguez, Aguirre-Santaella, Mauro, Mirabal, Nieto and Charles (2019)). As HAWC accumulates exposure time, also its minimum detectable flux will be lowered, thus allowing for better DM limits for a fixed number of unIDs. New HAWC observations and additional exposure time will surely bring up new unIDs though, thus in the end the resulting DM limits may improve or worsen depending on the number of unIDs that will be potential DM subhalos Calore et al. (2017); Coronado-Blázquez, Sánchez-Conde, Domínguez, Aguirre-Santaella, Mauro, Mirabal, Nieto and Charles (2019).

Finally, the upcoming Cherenkov Telescope Array (CTA) The Cherenkov Telescope Array Consortium (2017), with its superb instrumental capabilities, enhanced sensitivity to DM, improved angular resolution to pinpoint source extension, and already planned surveys of large portions of the VHE sky with unprecedented sensitivity, should be able to set the most competitive DM limits in the TeV energy range by means of the unID-based method used in this work. Alternatively, it is also possible that CTA may bring the first robust DM subhalo discovery.

## Bibliography

A. De Angelis et al. (2018). Science with e-ASTROGAM, *Journal of High Energy Astrophysics* **19**: 1–106.

Anderson, B., Kuhlen, M., Diemand, J., Johnson, R. P. and Madau, P. (2010). Fermi-LAT Sensitivity to Dark Matter Annihilation in Via Lactea II Substructure, *The Astrophysical Journal* **718**(2): 899–904.

Andrew J. Smith for the HAWC Collaboration (2007). HAWC: A next generation all-sky gamma-ray telescope, *Journal of Physics: Conference Series* **60**: 131–134.

Andrew J. Smith for the HAWC Collaboration (2015). HAWC: Design, Operation, Reconstruction and Analysis, *PoS* .
**URL:** *https://arxiv.org/abs/1508.05826*

Bertone, G. (2010). The moment of truth for WIMP Dark Matter, *Nature* **468**(7322): 389–393.
**URL:** *http://dx.doi.org/10.1038/nature09509*

Bertone, G. (ed.) (2009). *Particle Dark Matter*, Cambridge University Press.

Bertone, G., Hooper, D. and Silk, J. (2005). Particle dark matter: evidence, candidates and constraints, *Physics Reports* **405**(5-6): 279–390.

Bertoni, B., Hooper, D. and Linden, T. (2015). Examining The Fermi-LAT Third Source Catalog In Search Of Dark Matter Subhalos, *Journal of Cosmology and Astroparticle Physics* **12**: 035.
**URL:** *http://dx.doi.org/10.1088/1475-7516/2015/12/035*

Bertoni, B., Hooper, D. and Linden, T. (2016). Is The Gamma-Ray Source 3FGL J2212.5+0703 A Dark Matter Subhalo?, *Journal of Cosmology and Astroparticle Physics* **5**: 049.
**URL:** *http://dx.doi.org/10.1088/1475-7516/2016/05/049*

Bertschinger, E. (2006). Effects of cold dark matter decoupling and pair annihilation on cosmological perturbations, *Physical Review D* **74**(6).

Bringmann, T. (2009). Particle Models and the Small-Scale Structure of Dark Matter, *New Journal of Physics* **11**(10): 105027.
**URL:** *http://dx.doi.org/10.1088/1367-2630/11/10/105027*

Buckley, M. R. and Hooper, D. (2010). Dark Matter Subhalos In the Fermi First Source Catalog, *Physical Review D* **82**(6).
**URL:** *http://dx.doi.org/10.1103/PhysRevD.82.063501*

Calore, F., Romeri, V. D., Mauro, M. D., Donato, F. and Marinacci, F. (2017). Realistic estimation for the detectability of dark matter sub-halos with Fermi-LAT, *Physical Review D* **96**(6).
**URL:** *http://dx.doi.org/10.1103/PhysRevD.96.063009*

Cembranos, J. A. R., de La Cruz-Dombriz, A., Gammaldi, V. and Maroto, A. L. (2012). Detection of branon dark matter with gamma ray telescopes, *Physical Review D* **85**(4).

Cembranos, J. A. R., de la Cruz-Dombriz, Á., Gammaldi, V. and Méndez-Isla, M. (2020). SKA-Phase 1 sensitivity to synchrotron radio emission from multi-TeV Dark Matter candidates, *Physics of the Dark Universe* **27**: 100448.
**URL:** *http://dx.doi.org/10.1016/j.dark.2019.100448*

Cembranos, J. A. R., Dobado, A. and Maroto, A. L. (2003). Brane-World Dark Matter, *Physical Review Letters* **90**(24).

Cirelli, M., Corcella, G., Hektor, A., Hütsi, G., Kadastik, M., Panci, P., Raidal, M., Sala, F. and Strumia, A. (2011). PPPC 4 DM ID: A Poor Particle Physicist Cookbook for Dark Matter Indirect Detection, *Journal of Cosmology and Astroparticle Physics* **2011**(03): 051–051.
**URL:** http://dx.doi.org/10.1088/1475-7516/2011/03/051

Colafrancesco, S., Profumo, S. and Ullio, P. (2006). Multi-frequency analysis of neutralino dark matter annihilations in the Coma cluster, *Astronomy & Astrophysics* **455**(1): 21–43.

Colafrancesco, S., Profumo, S. and Ullio, P. (2007). Detecting dark matter WIMPs in the Draco dwarf: A multiwavelength perspective, *Physical Review D* **75**(2).

Coronado-Blázquez, J., Sánchez-Conde, M. A., Domínguez, A., Aguirre-Santaella, A., Mauro, M. D., Mirabal, N., Nieto, D. and Charles, E. (2019). Unidentified gamma-ray sources as targets for indirect dark matter detection with the Fermi-Large Area Telescope, *Journal of Cosmology and Astroparticle Physics* **2019**(07): 020–020.

Coronado-Blázquez, J., Sánchez-Conde, M. A., Mauro, M. D., Aguirre-Santaella, A., Ciucă, I., Domínguez, A., Kawata, D. and Mirabal, N. (2019). Spectral and spatial analysis of the dark matter subhalo candidates among Fermi Large Area Telescope unidentified sources, *Journal of Cosmology and Astroparticle Physics* **2019**(11): 045–045.

Diemand, J., Kuhlen, M., Madau, P., Zemp, M., Moore, B., Potter, D. and Stadel, J. (2008). Clumps and streams in the local dark matter distribution, *Nature* **454**(7205): 735–738.
**URL:** http://dx.doi.org/10.1038/nature07153

Dingus, B. L. (2007). HAWC (High Altitude Water Cherenkov) Observatory for Surveying the TeV Sky, *AIP Conference Proceedings*, AIP.

Egorov, A. E., Galper, A. M., Topchiev, N. P., Leonov, A. A., Suchkov, S. I., Kheymits, M. D. and Yurkin, Y. T. (2018). Detactability of Dark Matter Subhalos by Means of the GAMMA-400 Telescope, *Physics of Atomic Nuclei* **81**(3): 373–378.

Errani, R. and Peñarrubia, J. (2019). Can tides disrupt cold dark matter subhaloes?, *Monthly Notices of the Royal Astronomical Society* **491**(4): 4591–4601.
**URL:** http://dx.doi.org/10.1093/mnras/stz3349

Fermi-LAT Collaboration (2012a). Fermi-LAT Observations of the Diffuse Gamma-Ray Emission: Implications for Cosmic Rays and the Interstellar Medium, *The Astrophysical Journal* **750**(1): 3.
**URL:** http://dx.doi.org/10.1088/0004-637X/750/1/3

Fermi-LAT Collaboration (2012b). Search for Dark Matter Satellites using the FERMI-LAT, *The Astrophysical Journal* **747**(2): 121.
**URL:** http://dx.doi.org/10.1088/0004-637X/747/2/121

Fermi-LAT Collaboration (2015). Searching for Dark Matter Annihilation from Milky Way Dwarf Spheroidal Galaxies with Six Years of Fermi-LAT Data, *Physical Review Letters* **115**(23).
**URL:** http://dx.doi.org/10.1103/PhysRevLett.115.231301

Fermi-LAT Collaboration and Atwood, W. B. (2009). The Large Area Telescope on the Fermi Gamma-ray Space Telescope Mission, *The Astrophysical Journal* **697**(2): 1071–1102.
**URL:** *http://dx.doi.org/10.1088/0004-637X/697/2/1071*

Fitts, A., Boylan-Kolchin, M., Bullock, J. S., Weisz, D. R., El-Badry, K., Wheeler, C., Faucher-Giguère, C.-A., Quataert, E., Hopkins, P. F., Kereš, D., Wetzel, A. and Hayward, C. C. (2018). No assembly required: mergers are mostly irrelevant for the growth of low-mass dwarf galaxies, *Monthly Notices of the Royal Astronomical Society* **479**(1): 319–331.

Freese, K. (2009). *Review of Observational Evidence for Dark Matter in the Universe and in upcoming searches for Dark Stars*, Vol. 36 of *EAS Publications Series*.
**URL:** *http://adsabs.harvard.edu/abs/2009EAS....36..113F*

Gammaldi, V. (2019). Multimessenger Multi-TeV Dark Matter, *Frontiers in Astronomy and Space Sciences* **6**.

Gao, L., White, S. D. M., Jenkins, A., Stoehr, F. and Springel, V. (2004). The subhalo populations of ΛCDM dark haloes, *Monthly Notices of the Royal Astronomical Society* **355**: 819–834.
**URL:** *http://dx.doi.org/10.1111/j.1365-2966.2004.08360.x*

Garrett, K. and Duda, G. (2011). Dark Matter: A Primer, *Advances in Astronomy* **2011**: 1–22.
**URL:** *http://dx.doi.org/10.1155/2011/968283*

Garrison-Kimmel, S., Wetzel, A., Bullock, J. S., Hopkins, P. F., Boylan-Kolchin, M., Faucher-Giguère, C.-A., Kereš, D., Quataert, E., Sanderson, R. E., Graus, A. S. and Kelley, T. (2017). Not so lumpy after all: modelling the depletion of dark matter subhaloes by Milky Way-like galaxies , *Monthly Notices of the Royal Astronomical Society* **471**(2): 1709–1727.

Hooper, D. and Witte, S. J. (2017). Gamma Rays From Dark Matter Subhalos Revisited: Refining the Predictions and Constraints, *Journal of Cosmology and Astroparticle Physics* **4**: 018.
**URL:** *http://dx.doi.org/10.1088/1475-7516/2017/04/018*

Jungman, G., Kamionkowski, M. and Griest, K. (1996). Supersymmetric dark matter, *Physics Reports* **267**(5-6): 195–373.

Kelley, T., Bullock, J. S., Garrison-Kimmel, S., Boylan-Kolchin, M., Pawlowski, M. S. and Graus, A. S. (2019). Phat ELVIS: The inevitable effect of the Milky Way's disc on its dark matter subhaloes, *Monthly Notices of the Royal Astronomical Society* **487**(3): 4409–4423.

Lefranc, V., Moulin, E. and for the H. E. S. S. collaboration (2015). Dark matter search in the inner Galactic halo with H.E.S.S. I and H.E.S.S. II.
**URL:** *https://arxiv.org/abs/1509.04123*

Madau, P., Diemand, J. and Kuhlen, M. (2008). Dark Matter Subhalos and the Dwarf Satellites of the Milky Way, *The Astrophysical Journal* **679**(2): 1260–1271.

Marchegiani, P., Colafrancesco, S. and Khanye, N. F. (2018). The role of dark matter annihilation in the radio emission of the galaxy cluster A520, *Monthly Notices of the Royal Astronomical Society* **483**(2): 2795–2800.

Moliné, A., Sánchez-Conde, M. A., Palomares-Ruiz, S. and Prada, F. (2017). Characterization of subhalo structural properties and implications for dark matter annihilation signals, *Monthly Notices of the Royal Astronomical Society* **466**: 4974–4990.
**URL:** http://dx.doi.org/10.1093/mnras/stx026

Nahee Park for the VERITAS Collaboration (2015). Performance of the VERITAS experiment, *Proceedings of the 34th ICRC* .
**URL:** https://arxiv.org/abs/1508.07070

Ocvirk, P., Gillet, N., Shapiro, P. R., Aubert, D., Iliev, I. T., Teyssier, R., Yepes, G., Choi, J.-H., Sullivan, D., Knebe, A., Gottlöber, S., D'Aloisio, A., Park, H., Hoffman, Y. and Stranex, T. (2016). Cosmic Dawn (CoDa): the first radiation-hydrodynamics simulation of reionization and galaxy formation in the Local Universe, *Monthly Notices of the Royal Astronomical Society* **463**(2): 1462–1485.

Profumo, S., Sigurdson, K. and Kamionkowski, M. (2006). What Mass Are the Smallest Protohalos?, *Physical Review Letters* **97**(3).

Roszkowski, L., Sessolo, E. M. and Trojanowski, S. (2018). Wimp dark matter candidates and searches—current status and future prospects, *Reports on Progress in Physics* **81**(6): 066201.
**URL:** http://dx.doi.org/10.1088/1361-6633/aab913

Sánchez-Conde, M. A. and Prada, F. (2014). The flattening of the concentration-mass relation towards low halo masses and its implications for the annihilation signal boost, *Monthly Notices of the Royal Astronomical Society* **442**(3): 2271–2277.

Sawala, T., Frenk, C. S., Fattahi, A., Navarro, J. F., Bower, R. G., Crain, R. A., Vecchia, C. D., Furlong, M., Jenkins, A., McCarthy, I. G., Qu, Y., Schaller, M., Schaye, J. and Theuns, T. (2015). Bent by baryons: the low-mass galaxy-halo relation, *Monthly Notices of the Royal Astronomical Society* **448**(3): 2941–2947.

Sawala, T., Frenk, C. S., Fattahi, A., Navarro, J. F., Theuns, T., Bower, R. G., Crain, R. A., Furlong, M., Jenkins, A., Schaller, M. and Schaye, J. (2015). The chosen few: the low-mass haloes that host faint galaxies, *Monthly Notices of the Royal Astronomical Society* **456**(1): 85–97.

Sawala, T., Pihajoki, P., Johansson, P. H., Frenk, C. S., Navarro, J. F., Oman, K. A. and White, S. D. M. (2017). Shaken and stirred: the Milky Way's dark substructures, *Monthly Notices of the Royal Astronomical Society* **467**(4): 4383–4400.

Springel, V., Wang, J., Vogelsberger, M., Ludlow, A., Jenkins, A., Helmi, A., Navarro, J. F., Frenk, C. S. and White, S. D. M. (2008). The Aquarius Project: the subhaloes of galactic haloes, *Monthly Notices of the Royal Astronomical Society* **391**(4): 1685–1711.

Steigman, G., Dasgupta, B. and Beacom, J. F. (2012). Precise Relic WIMP Abundance and its Impact on Searches for Dark Matter Annihilation, *Physical Review D* **86**(2).
**URL:** http://dx.doi.org/10.1103/PhysRevD.86.023506

The Cherenkov Telescope Array Consortium (2017). Science with the Cherenkov Telescope Array, *ArXiv e-prints* .
**URL:** http://adsabs.harvard.edu/abs/2017arXiv170907997C

The Fermi-LAT Collaboration (2015). Limits on dark matter annihilation signals from the Fermi LAT 4-year measurement of the isotropic gamma-ray background, *Journal of Cosmology and Astroparticle Physics* **2015**(09): 008–008.

The Fermi-LAT Collaboration (2017). Searching for Dark Matter Annihilation in Recently Discovered Milky Way Satellites with Fermi-LAT, *The Astrophysical Journal* **834**(2): 110.

The Fermi-LAT, HAWC and VERITAS Collaborations (2018). VERITAS and Fermi-LAT Observations of TeV Gamma-Ray Sources Discovered by HAWC in the 2HWC Catalog, *The Astrophysical Journal* **866**(1): 24.

The HAWC Collaboration (2013a). Sensitivity of the high altitude water Cherenkov detector to sources of multi-TeV gamma rays, *Astroparticle Physics* **50-52**: 26–32.

The HAWC Collaboration (2013b). The HAWC Gamma-Ray Observatory: Design, Calibration, and Operation, *PoS ICRC 2013* .
**URL:** *https://arxiv.org/abs/1310.0074*

The HAWC Collaboration (2017a). Observation of the Crab Nebula with the HAWC Gamma-Ray Observatory, *The Astrophysical Journal* **843**(1): 39.

The HAWC Collaboration (2017b). The 2HWC HAWC Observatory Gamma-Ray Catalog, *The Astrophysical Journal* **843**(1): 40.

The HAWC Collaboration (2019). Searching for dark matter sub-structure with HAWC, *Journal of Cosmology and Astroparticle Physics* **2019**(07): 022–022.

The H.E.S.S. Collaboration (2004). Calibration of cameras of the H.E.S.S. detector, *Astroparticle Physics* **22**(2): 109–125.

The H.E.S.S. Collaboration (2018). The H.E.S.S. Galactic plane survey, *Astronomy & Astrophysics* **612**: A1.

The MAGIC Collaboration (2016). The major upgrade of the MAGIC telescopes, Part II: A performance study using observations of the Crab Nebula, *Astroparticle Physics* **72**: 76–94.

The Planck Collaboration (2016). Planck 2015 results. XIII. Cosmological parameters, *Astronomy & Astrophysics* **594**: A13.
**URL:** *http://dx.doi.org/10.1051/0004-6361/201525830*

The VERITAS Collaboration (2006). The first VERITAS telescope, *Astroparticle Physics* **25**(6): 391–401.

van den Bosch, F. C., Ogiya, G., Hahn, O. and Burkert, A. (2017). Disruption of dark matter substructure: fact or fiction?, *Monthly Notices of the Royal Astronomical Society* **474**(3): 3043–3066.

Wakely, S. P. and Horan, D. (2008). TeVCat: An online catalog for Very High Energy Gamma-Ray Astronomy, *Proc. of ICRC 2008* **3**: 1341–1344.
**URL:** *http://adsabs.harvard.edu/abs/2008ICRC....3.1341W*

Zavala, J. and Frenk, C. S. (2019). Dark matter haloes and subhaloes, *Galaxies* **7**(4): 81.

Zechlin, H.-S., Fernandes, M. V., Elsässer, D. and Horns, D. (2012). Dark matter subhaloes as gamma-ray sources and candidates in the first Fermi-LAT catalogue, *Astronomy & Astrophysics* **538**: A93.
**URL:** *http://dx.doi.org/10.1051/0004-6361/201117655*

Zechlin, H.-S. and Horns, D. (2012). Unidentified sources in the fermi-lat second source catalog: the case for dm subhalos, *Journal of Cosmology and Astroparticle Physics* **2012**(11): 050–050.
**URL:** http://dx.doi.org/10.1088/1475-7516/2012/11/050

# Chapter 8

# Sensitivity of the Cherenkov Telescope Array to dark subhalos

*Based on J. Coronado-Blázquez et al., Physics of the Dark Universe* ***32*** *(2021), 100845*

## 8.1 Introduction

Ground-based very-high-energy (VHE) gamma-ray astronomy, using the so-called imaging air Cherenkov technique, has been profusely developed in the last decades. There are several Imaging Atmospheric Cherenkov Telescopes (IACTs) currently in operation, namely H.E.S.S. (since 2003; one 28 m and four 12 m telescopes in Namibia) (Hinton; 2004), MAGIC (since 2004, two 17 m telescopes in La Palma) (Lorenz; 2004) and VERITAS (since 2007, four 12 m telescopes in Arizona) (VERITAS Collaboration; 2002).

When compared to space-based gamma-ray observatories, such as the Large Area Telescope (LAT) on board the Fermi satellite Fermi-LAT Collaboration (2009), IACTs feature better energy and angular resolution, at the cost of a reduced field of view (FoV): while IACTs present a FoV of $\mathcal{O}(5^\circ)$, *Fermi*-LAT observes roughly a fifth of the whole sky in a single exposure. The range of energies of both type of observatories is complementary, as satellites have significantly smaller effective areas, which degrade the sensitivity at high energies, precisely where ground-based observatories start to be competitive.

IACTs have been able to discover a significant number of VHE sources in the gamma-ray sky, producing catalogs with more than two hundred TeV sources as of today. The most populated classes are those of active galactic nuclei (AGNs), supernova remnants (SNRs) and pulsar wind nebulae (PWNe). When it comes to dark matter (DM) searches, IACT observations have been used to place competitive limits on TeV-scale DM candidates, although unable to probe the theoretically motivated annihilation thermal relic cross section value (Doro; 2014a; Gammaldi; 2019; Fermi-LAT Collaboration and MAGIC Collaboration; 2016; VERITAS Collaboration; 2017; H.E.S.S. Collaboration; 2020).

The Cherenkov Telescope Array (CTA) The Cherenkov Telescope Array Consortium (2017) is the next-generation ground-based gamma-ray observatory. Currently under construction phase, it will consist of two arrays, a Southern one located at the ESO site in the Atacama desert, Chile (24º 41′ 0.34" S, 70º 18′ 58.84" W), and a Northern one located at the Roque de los Muchachos in La Palma, Canary Islands, Spain (17º 53′ 31.22" W, 28º 45′ 43.79" N). These two arrays, in both hemispheres, will make CTA the first ground-based gamma-ray telescope able to observe almost the whole sky. CTA will feature three types of telescopes, each with different sizes and therefore sensitive to different energy ranges: i) Large–Size Telescopes (LSTs),

with 23 m diameter, sensitive to the scarce Cherenkov photons coming from gamma rays in the 20 – 150 GeV range, ii) Medium–Size Telescopes (MSTs), 11.5 m diameter, which will observe energies between 150 GeV and 5 TeV, and iii) a large number of Small–Size Telescopes (SSTs, foreseen only in the Southern Hemisphere array) with 4 m diameter to detect the less frequent, most energetic gamma rays above 5 TeV. While the North array will be distributed within ca. 1 square kilometer in an array of 19 telescopes, CTA-South will occupy several square kilometers in an array of 99 telescopes.

As a result of this ambitious setup, all together CTA will cover energies ranging from a few GeV up to about hundreds of TeV. The large number of telescopes will also enable CTA to perform, for the first time, large surveys of extended sky regions at the highest energies[1]. Indeed, performing an extragalactic survey with CTA is one of the so-called *key science projects* (KSPs). These represent the core topics within the CTA Consortium science program to be addressed over the first years of operations. In addition to VHE astrophysics and cosmology, these KSPs include a total of nearly 1,500 hours devoted to the search of DM (The Cherenkov Telescope Array Consortium; 2017).[2] Especially relevant in this context will be the dedicated search for annihilating DM with CTA at the Galactic Center, amply discussed in the recent Ref. (The Cherenkov Telescope Array Consortium; 2021). It is important to stress out that the detailed specifics of CTA KSPs are still a matter of debate, and can be refined before CTA actually starts observations.

In addition to the already "traditional" astrophysical targets to search for DM annihilation (e.g., Galactic center, dwarf galaxies), there is the possibility to use CTA for less explored DM scenarios such as the one offered by the so-called Galactic *dark subhalos*. These represent the less massive components of DM halo substructures in our galaxy, not massive enough to retain a baryonic, visible counterpart, as opposed to the case of the larger subhalos that host dwarf galaxy satellites. Being invisible in most of the electromagnetic spectrum, dark subhalos are hard to locate. Evidence of their passage may be obtained from their gravitational interaction on e.g., the surrounding stellar fields or by the imprint on the stellar velocity distribution (Banik et al.; 2018; Erkal et al.; 2016; Carlberg; 2009, 2012; Ibata et al.; 2002). Yet, despite their unknown location, they can be excellent candidates for gamma-ray DM searches given their typical number densities, masses and distances (Diemand et al.; 2008; Springel et al.; 2008; Brun et al.; 2011; Doro et al.; 2013; Calore et al.; 2017; Hooper and Witte; 2017) and, indeed, several groups already searched for dark subhalos in gamma-ray data and catalogs, and were able to set competitive constraints in the absence of them (Buckley and Hooper; 2010; Belikov et al.; 2012; Mirabal et al.; 2012; Zechlin et al.; 2012; Fermi-LAT Collaboration; 2012; Zechlin and Horns; 2012; Berlin and Hooper; 2014; Bertoni et al.; 2015; Schoonenberg et al.; 2016; Mirabal et al.; 2016; HAWC Collaboration; 2019; Coronado-Blázquez, Sánchez-Conde, Domínguez, Aguirre-Santaella, Mauro, Mirabal, Nieto and Charles; 2019; Coronado-Blázquez, Sánchez-Conde, Mauro, Aguirre-Santaella, Ciucă, Domínguez, Kawata and Mirabal; 2019; Coronado-Blázquez and Sánchez-Conde; 2020). In principle, CTA is less suitable than e.g. *Fermi*-LAT to perform blind dark subhalo searches, due to its smaller FoV and more limited exposure times (orders of magnitude below that of *Fermi*-LAT,

[1] Although H.E.S.S. performed a Galactic plane survey, CTA will be able to do these kind of surveys through all the sky with extended sensitivity.

[2] We note that this observation time is not motivated by fundamental physics alone and will be used for other purposes and science cases as well; e.g., observations of the Galactic center, the Large Magellanic Cloud or the Perseus galaxy cluster.

which has been operating for 12 years and performs an all-sky survey every only 3 hours). A more careful discussion is deferred to Section 8.2. Yet, for this work we identify at least three different scenarios in which a subhalo may appear in the CTA FoV:

**EGAL scenario: the CTA planned Extragalactic Survey.** CTA plans to perform the largest sky survey ever performed by IACTs, covering a fraction of 25% of the extragalactic ($b > 5°$) sky with an uniform exposure of 3 h per pointing and a total of 1000 h (The Cherenkov Telescope Array Consortium; 2017). This scenario was the one also scrutinized for CTA and dark subhalos by Hütten et al. (2016), although several differences are noted with that work, most notably our conservative use of the Northern array, updated instrumental response functions and different N-body simulation suites.

**DEEP Scenario: a deep exposure over a specific sky area.** CTA will be operated as an open observatory with a consistent guest observation program. Possible requests could be aimed at deep wide-field sky observation, in which a specific sky region is observed for prolonged time (say $100 - 150$ hours, or more). Thanks to the possibility of divergent pointing mode (Lucie Gérard for the CTA Consortium; 2015), CTA can scan a region of sky as narrow as about $8 \times 8$ deg$^2$ or as large as $20 \times 20$ deg$^2$ without need of repointing.

**EXPO scenario: overall CTA 10 years exposure.** After 10 years of continous operations, CTA is expected to have covered a considerable fraction of the sky as overall sum of its individual pointings. One could therefore use the envelope of all individual exposures and argue that potential dark subhalos could appear as serendipitous sources within the FoV of such pointings and exposures.

The goal of this paper is to evaluate the sensitivity of the CTA to dark subhalos for each of these different observational strategies. We will also provide constraints on the annihilating dark matter $\langle \sigma v \rangle - m_\chi$ parameter space in case none of these observing scenarios would provide a detection. As shown e.g. in Coronado-Blázquez, Sánchez-Conde, Domínguez, Aguirre-Santaella, Mauro, Mirabal, Nieto and Charles (2019), this can be done with the help of predictions from N-body cosmological simulations for a Milky-Way-size galaxy in a ΛCDM universe.

This paper is structured as follows. In Sec. 8.2, we discuss the different observational search strategies. Sec. 8.3 presents the sensitivity of CTA to dark subhalos. The expected dark subhalo population and limits to the annihilation cross section are computed in Sec. 9.4 and discussed in Sec. 8.5, while we conclude in Sec. 8.6.

## 8.2 Dark subhalo search scenarios

Unless directly spotted by gravitational probes or detected in gamma-rays by wide FoV instruments such as those hosted in satellites (e.g. *Fermi*-LAT, AGILE, HERD, DAMPE or the planned e-Astrogam or Amigo) or atmospheric shower ground-based particle detectors (e.g. HAWC, LHAASO or the planned SWGO), dark subhalos can be found only serendipitously in the CTA FoV. This can be attained in scenarios that provide either a large sky area or a large exposure: an extragalactic sky scan, a deep wide-field over a certain sky region or as unanticipated excess signals within the FoV of regular operation observations. Note that other potentially interesting CTA programs, such as a Galactic plane survey, would be sub-optimal for subhalo

searches, if one considers both the intense diffuse emission and the high density of astrophysical sources present in that region of the Galaxy.[3]

In the following, we discuss in more details the putative detection scenarios identified above.

### 8.2.1 EGAL

The EGAL survey has been flagged as a CTA KSP by the CTA Consortium, as it will offer an unprecedented, unbiased view of the TeV extragalactic sky (The Cherenkov Telescope Array Consortium; 2017). Never before a wide sky region was observed by IACTs with constant exposure, as IACTs mostly work on target of opportunity and specific target programs. The current plan is to scan 25% of the sky with an uniform exposure of 3 h per pointing, for a total of 1000 h over 3 years (see the survey footprint in Figure 8.1).

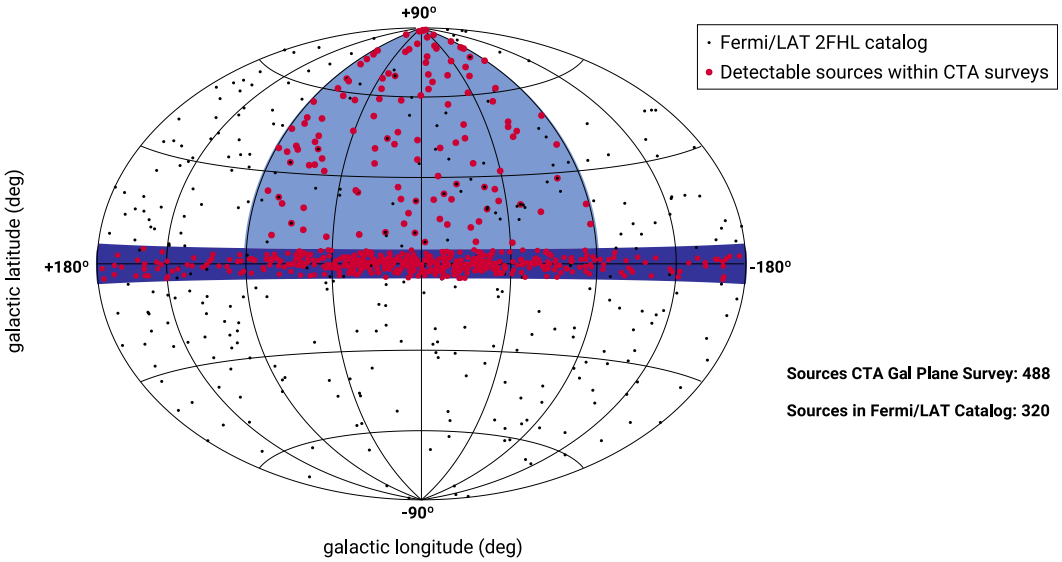


FIGURE 8.1: Skymap of the EGAL Survey, including also simulated sources potentially detectable by CTA. Figure adapted from Ref. (The Cherenkov Telescope Array Consortium; 2017).

The main advantage of this search strategy is having access to a wide area of the sky surveyed with homogeneous acceptance, thus allowing for unbiased results. Furthermore, being a CTA KSP, its execution is guaranteed, although the exact sky region is not fixed yet. It is then possible that within this wide area a few optimal DM targets of interest will be present – subhalos in the form of either visible known (or yet to be discovered) dwarf satellite galaxies (dSphs) or dark subhalos.

A drawback of this observing strategy is the relatively short exposure per pointing, with a reported average sensitivity of the full survey of around 6 mCrab ($\sim 3.04 \times 10^{-13}$ ph cm$^{-2}$ s$^{-1}$) for an energy threshold of 125 GeV.

[3] Yet, nothing impedes that subhalo resides in the Galactic plane. In theory, by using the different spectral features of DM spectra to astrophysical ones, one could be able to disentangle them in case of detection. The prospects for such search are left for future works.

### 8.2.2 DEEP

A dedicated, long exposure of $100 - 200$ h on a specific sky region of extended FoV between $8 \times 8$ deg$^2$ and $20 \times 20$ deg$^2$ appears as a possible observation mode in CTA and consequently a viable scenario for dark subhalo searches with CTA as well. Currently, a specific observation program of such kind is foreseen within the CTA core program, focused on the observation of the LMC (The Cherenkov Telescope Array Consortium; 2017). However, further deep-field observations can be proposed in the future to CTA either by Consortium members or via the CTA guest observational program,which will constantly increase the fraction of CTA observation time granted to external proposals, becoming the major observational mode in few years from the CTA start of observation. For example, a deep wide-field survey of the Virgo cluster was proposed by Doro et al. (2013). Such regions could be observed by CTA in two modes: with either focused, patched observation, in which a large sky region is observed in "tiles", or divergent pointing mode, in which the FoV is enlarged by slightly misaligning the telescopes within the array, as discussed in 8.7.1.

Dark subhalos could serendipitously fall within the FoV, whereas the probability of detection depends on the chosen sky region and its area. As a benchmark model, we will adopt a deep wide-field of $10 \times 10$ deg$^2$ with 100 h of exposure. Note though that different sky regions, different extensions, and different exposures could be required for specific science cases.

The main drawback of this mode is that the surveyed area is relatively small, and therefore the probability to spot a dark subhalo by chance is low. Furthermore, deep, long-duration observations may be subject to higher systematics related, e.g., to the background fluctuations, inevitable over large period of times, considering the background rate depends both on the position in the sky and the atmospheric conditions during a specific data-taking (see The Cherenkov Telescope Array Consortium (2021) for a detailed discussion). Such systematics effects are not taken into account in our estimates below.

### 8.2.3 EXPO

Regardless the specific observational proposal, during its lifetime CTA will be accumulating exposures on several directions of the sky, observation by observation. It is thus certainly possible that a dark subhalo may serendipitously appear within one of these sky regions.

While it is not possible to predict exactly the overall CTA exposure and its sky footprint, one can make educated guesses based on available data from currently operating IACTs. In this scenario, a good modeling of the astrophysical target for which the observation was motivated is particularly critical. Only in this way it would be possible to look for any other sources hidden under potential residuals in the FoV. Another probable issue of using this third scenario for dark subhalo searches is the potentially significant loss of sensitivity a few degrees off the center of the FoV (off-axis sensitivity). For this reason, in the following we will assume the region of the FoV in which the sensitivity is expected to be almost constant.

We have based our calculation of the total, integrated CTA observation area/time as obtained after its first years of data forecasting it from the actual operations of MAGIC, an IACT currently in operation (MAGIC Collaboration; 2016a,b). MAGIC is located at the Roque de los Muchachos Observatory (ORM) in the island La Palma (Spain), the same place of the northern CTA array. The MAGIC overall exposure

map allows us to predict a *plausible* exposure map for CTA. We defer the details of the MAGIC-to-CTA extrapolation method in 8.7.2.

We extrapolated MAGIC observations in stereo configuration from November 2012 to June 2019, i.e., 6.5 years of data into a projected exposure map for CTA for 10 years of operation. Our results are shown in Figure 8.2. The total CTA predicted observed area is roughly 45% of the sky. This is almost twice that of the previously-discussed EGAL survey footprint, yet in this case unevenly sampled in terms of exposure time.

The bottom panel of Figure 8.2 shows the distribution of exposure times for all the simulated CTA pointings in a random realization. One can see that ∼33% of the total exposure time is devoted to short ($< 5$) h observations, ∼47% of $(5 - 50)$ h duration dominate the observational program, and ∼20% observation time is spent for very deep $(> 50)$ h observations. For a fixed survey area, chances of serendipitous detection of dark subhalos are maximized during long or very long observations, as they will allow detection of DM candidates with small annihilation cross sections. Note that, in case of no-detection, DM limits can still be computed by using the full exposure map available at the time. We will do so later on in Section 9.4.

## 8.3 Dark subhalo detectability

### 8.3.1 CTA sensitivity to DM spectra

In this section, we evaluate the different performance of CTA to specific DM annihilation spectra. Indeed, the CTA sensitivity to DM-induced signals is expected to be different that the one for more common astrophysical "featureless" power-law spectra. Thus, the computation of this CTA DM sensitivity is critical should we wanted to properly address the actual chances of dark subhalo discovery.

For instance, for the EGAL survey, an integral sensitivity of ∼6 mCrab is quoted[4]. Yet, this sensitivity was computed for a Crab Nebula-like spectrum, that can be well approximated by a single power-law with a spectral index $-2.62$. Instead, DM annihilations show more complex, highly-curved spectra, strongly dependent on the mass of the WIMP and specifics of the considered annihilation channel, and with a more or less sharp cutoff at the DM mass. To correctly compute the CTA sensitivity to DM spectra, we use the public `ctools`[5] software (Knödlseder et al.; 2016), v1.7.

We compute the sensitivity of CTA to dark subhalos in the EGAL survey following these steps:

1. We place a simulated point-like subhalo –made of WIMPs of a given mass and annihilating via a particular channel– in a position of the Northern Galactic hemisphere covered by the EGAL scan and close to the zenith angle of the instrumental response function (IRF)[6] we use (i.e., 40°). Note that the specific coordinates of the subhalo will not change the results, as no underlying diffuse

[4]The flux of VHE gamma rays from the Crab nebula is set to that measured by HEGRA Collaboration (2004), given by $dN/dE = 2.83 \times 10^{-11}(E/1\ \text{TeV})^{-2.62}\ \text{cm}^{-2}\text{s}^{-1}\text{TeV}^{-1}$, while the integral flux is computed with an energy threshold of 125 GeV

[5]`http://cta.irap.omp.eu/ctools/`

[6]IRFs are files containing the full characterization of a specific CTA observation mode in terms of energy resolution and bias, energy threshold, angular resolution, photon arrival direction, and effective area throughout the FoV, based on tailored optimized event cuts. More specifically, the IRFs provide the relations between the event properties as measured in the detector and the actual physical properties of the incident photon, i.e., they enclose the response of the instrument to gamma rays depending on their properties.

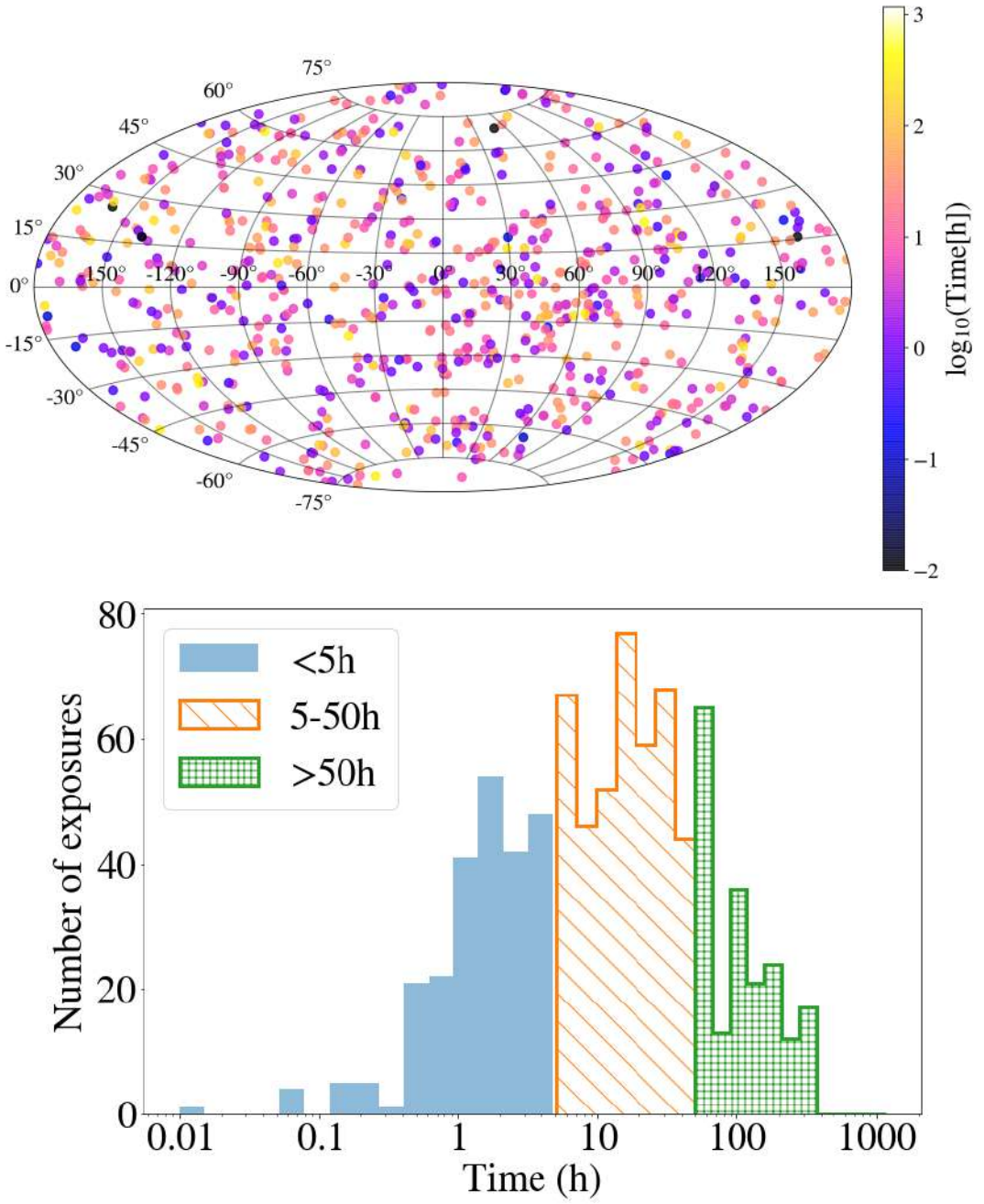


FIGURE 8.2: **Upper panel**: overall 10-year exposure map for CTA in Galactic coordinates, extrapolated from 6.5 years of MAGIC stereo observations. The shown map corresponds to a random realization of our extrapolation algorithm. Color code traces the observation time per pointing. **Lower panel**: distribution of the observation time of the EXPO strategy for three bins: 0-5h, 5-50h and >50h, for the same random realization.

emission model is considered[7]. We adopt 3 hours per pointing so as to match the EGAL survey setup reported in Ref. (The Cherenkov Telescope Array Consortium; 2017).

[7] This contribution is rather unknown in the TeV energy domain. As we are interested in extragalactic ($|b| > 5°$) sources, a cosmic-ray induced gamma-ray diffuse emission would be negligible (Gaggero et al.; 2015, 2017; Cataldo et al.; 2019)

2. Individual events with energies between 30 GeV up to 100 TeV are generated for a particular DM annihilation channel and WIMP mass by means of the `ctobssim` Monte Carlo generator. The input is a spectral file function obtained from PPPC4DMID (Cirelli et al.; 2010), generated with `PYTHIA 8` and including electroweak corrections. Only $b\bar{b}$ and $\tau^+\tau^-$ annihilation channels are considered in this work as representative of "soft" and "hard" DM spectra, respectively, i.e., spectra exhibiting shallower and steeper cutoffs at the DM mass. For the sake of computational time, we use 29 of the 62 available masses in the PPPC4DMID tables for each channel.[8] The events are generated using the latest IRFs, `prod3b-v2`, with the `North_z40_5h`[9] (i.e., CTA Northern array, for a source located at a zenith angle of 40°, azimuth-averaged for 5 h observation time).

3. Once the events are simulated, we use `ctlike` to compute the detection significance via the likelihood-ratio test statistic (TS), defined as:

$$\mathrm{TS} = -2\log\left[\frac{\mathcal{L}(H_1)}{\mathcal{L}(H_0)}\right] \tag{8.1}$$

where $\mathcal{L}(H_0)$ and $\mathcal{L}(H_1)$ are, respectively, the likelihood functions under the null (no source) and alternative (existing source) hypotheses. The detection threshold is set to $\mathrm{TS} = 25$, corresponding to about 5 standard deviations (Cowan et al.; 2011; Conrad; 2015). Additionally, as the reconstructed event energy may differ from the true photon energy, particularly at low energies, we take into account the energy dispersion in the computation of the likelihood.[10]

4. For each mass and annihilation channel, the normalization of the source flux is varied by running `ctlike` iteratively until the detection threshold is reached. We adopt a tolerance of $TS = 25 \pm 1$ to ensure numerical convergence. The flux obtained this way is the minimum detection flux, $F_{min}$.

5. Finally, the random seed initially used by `ctobssim` to generate the events is changed in order to randomize the distribution and create another simulated observation. We notice a smooth convergence after 10-20 realizations; nevertheless we perform 100 simulations so that we can obtain reliable uncertainty bands at 68% and 95% confidence levels.

The results of our DM sensitivity computation are shown in Figure 8.3 for the $b\bar{b}$ and $\tau^+\tau^-$ annihilation channels. Both channels present similar behaviours. Standard Crab-based integral sensitivity overestimates the actual DM performance by a

[8] For masses larger than $\sim$ 10 TeV, especially for the case of $\tau^+\tau^-$, the effect of electroweak corrections are unclear and therefore the results above this mass must be taken with caution. Concretely, these "model-independent" corrections assume that any effect of weakly interacting bosons radiated from the initial DM states (or from virtual internal propagators) are negligible (Ciafaloni et al.; 2011). Moreover, all these radiative corrections only take into account leading order effects, while higher-order effects can potentially be included by consistently treating leading logarithms (Beneke et al.; 2018; Baumgart et al.; 2019). Finally, it is worth noting that an additional photon in the final state can both significantly enhance the annihilation rate (Bergström; 1989) and lead to very characteristic spectral features (Flores et al.; 1989; Bringmann et al.; 2008), while final state gluons would only mildly modify the photon spectrum from quark final states, such as $b\bar{b}$ (Bringmann et al.; 2016).

[9] Publicly available at `https://www.cta-observatory.org/science/cta-performance/`

[10] In any case, we checked that enabling and disabling this energy dispersion affects only marginally our results.

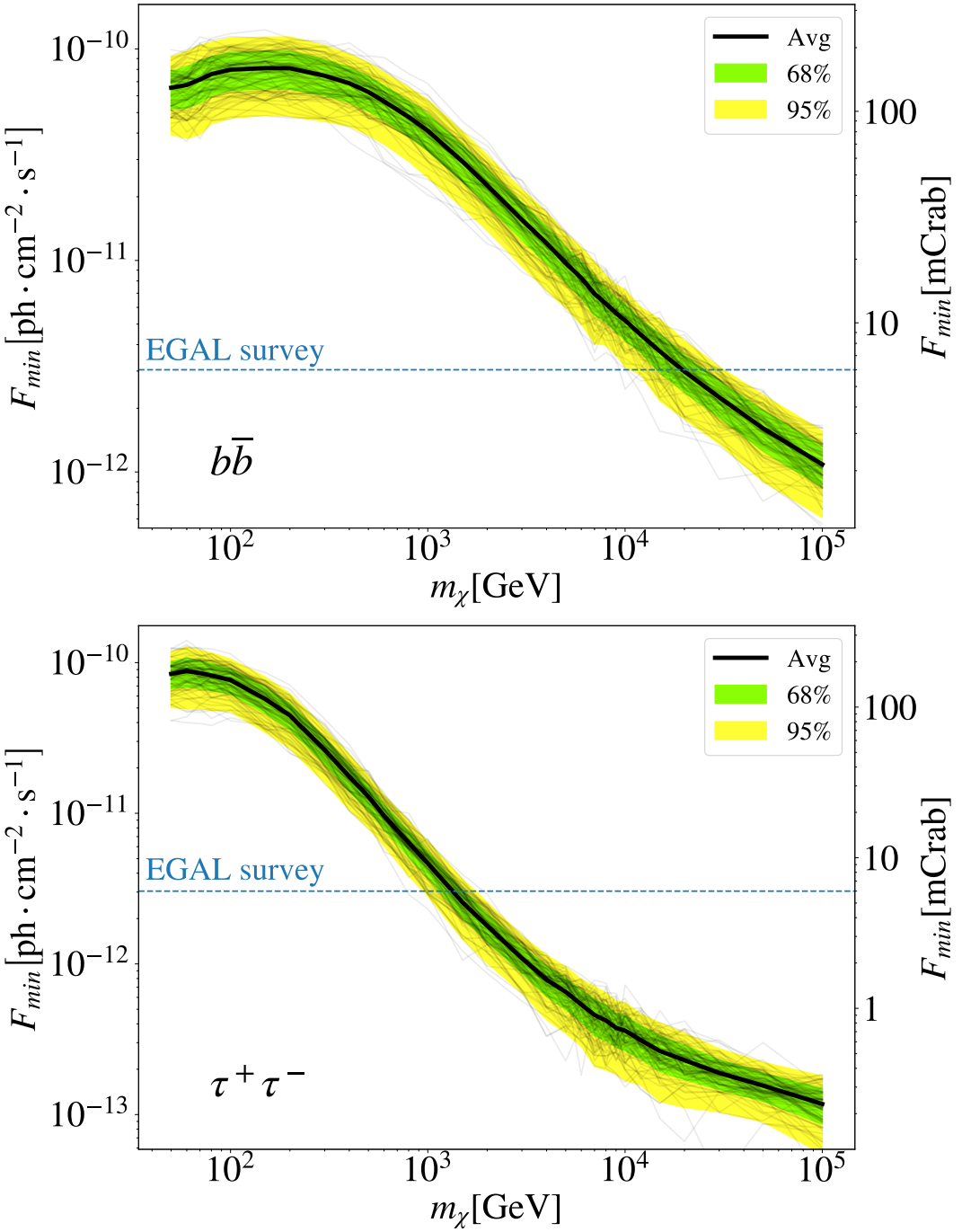


FIGURE 8.3: Minimum flux ($F_{min}$) to detect a dark subhalo annihilating to $b\bar{b}$ (top panel) and $\tau^+\tau^-$ (bottom panel) in the EGAL survey, assuming the Northern array and 3h of normal pointing observation with an energy threshold of 30 GeV. Gray lines are the individual 100 realizations, black solid line is the average value, and green and yellow bands are, respectively, the 68% and 95% confidence level. Right $y$ axis is expressed in units of mCrab flux. Blue dashed, horizontal line is the nominal 6 mCrab flux sensitivity of the EGAL scan.

factor of $10 - 100$ for low DM mass (depending on the specific channel), while the sensitivity to DM spectra reaches the standard one toward larger masses, to become even better (by a factor of up to 10 at the heaviest considered WIMP) in the case of

the $\tau^+\tau^-$ channel. This is expected, as $\tau^+\tau^-$ is a harder channel compared to $b\bar{b}$. Indeed, the former peaks at $E^{\tau^+\tau^-}_{peak} \sim m_\chi/3$, while the latter peaks at $E^{b\bar{b}}_{peak} \sim m_\chi/30$. As the best sensitivity of CTA is reached at $\sim 3-5$ TeV, this means that the peak of the DM annihilation spectrum coincides with CTA's best sensitivity for $m_\chi \sim 90-150$ TeV for $b\bar{b}$, and $m_\chi \sim 9-15$ TeV for $\tau^+\tau^-$. This roughly coincides with our results, as the $b\bar{b}$ sensitivity curve shown in the right panel of Figure 8.3 reaches its best sensitivity at 100 TeV (the largest considered mass), and $\tau^+\tau^-$'s best sensitivity is reached and starts to flatten at masses $m_\chi \gtrsim 10$ TeV in the bottom panel of the same figure.

Note that, as pointed out above, Figure 8.3 refers to the CTA sensitivity to dark subhalos under the EGAL survey setup. To compute the $F_{min}$ in either the DEEP or the EXPO scenarios, we will assume that the sensitivity scales as the square root of the observation time (using the same 40° zenith IRFs). This saves a significant amount of computation time, as its direct calculation is computationally too expensive due to the large involved exposure times (∼40 and 100 h, instead of 3h in the EGAL survey). We checked that this is a good approximation, by running some full simulations for both the 42h and 100 h setups. In these checks, we adopted 50h-IRFs (the available IRFs are for 0.5, 5 and 50 h) and three different DM masses (0.1, 1 and 10 TeV). The square-root-of-time scaling turns out to be, indeed, an excellent representation of the actual scaling, within errors, for the three considered masses. In an actual observation, we note that we expect this square-root scaling to be accurate as long as there is not significant diffuse emission, a condition that is fulfilled at latitudes far from the Galactic plane.

Table 8.1 displays the results for the minimum flux ($F_{\rm min}$) to detect a dark subhalo computed for the three different observational strategies under scrutiny, and for three benchmark WIMP masses (0.1, 1 and 10 TeV) and for both $b\bar{b}$ and $\tau^+\tau^-$ annihilation channels.

| **Minimum flux for detection $F_{\rm min}$ [ph cm$^{-2}$ s$^{-1}$]** | | | |
|---|---|---|---|
| DM mass | 0.1 TeV | 1 TeV | 10 TeV |
| Scenario 1: EGAL (T=3h) | | | |
| $b\bar{b}$ | $7.98 \times 10^{-11}$ | $4.10 \times 10^{-11}$ | $5.21 \times 10^{-12}$ |
| $\tau^+\tau^-$ | $7.65 \times 10^{-11}$ | $4.66 \times 10^{-12}$ | $3.61 \times 10^{-13}$ |
| Scenario 2: DEEP (T=100h) | | | |
| $b\bar{b}$ | $1.39 \times 10^{-11}$ | $7.14 \times 10^{-12}$ | $9.03 \times 10^{-13}$ |
| $\tau^+\tau^-$ | $1.31 \times 10^{-11}$ | $8.02 \times 10^{-13}$ | $6.21 \times 10^{-14}$ |
| Scenario 3: EXPO (T=42h) | | | |
| $b\bar{b}$ | $2.14 \times 10^{-11}$ | $1.07 \times 10^{-11}$ | $1.32 \times 10^{-12}$ |
| $\tau^+\tau^-$ | $2.05 \times 10^{-11}$ | $1.22 \times 10^{-12}$ | $9.11 \times 10^{-14}$ |

TABLE 8.1: Average $F_{min}$ values with an energy threshold of 30 GeV, in ph $\cdot$ cm$^{-2} \cdot$ s$^{-1}$, for the three observational strategies under discussion, and for three benchmark WIMP masses annihilating via either $b\bar{b}$ or $\tau^+\tau^-$ annihilation channels.

There are some caveats to these computations. First, we assume the DM subhalos to be point-like sources, while N-body cosmological simulations (Coronado-Blázquez, Sánchez-Conde, Mauro, Aguirre-Santaella, Ciucă, Domínguez, Kawata and Mirabal; 2019) found possible large angular sizes, up to $\mathcal{O}(5°)$ for some dark

subhalos according to their distance, when adopting the scale radius as the extension of the subhalo.[11] In principle, a dedicated *target-by-target* discussion would be needed, in which the specific extension is treated individually. However, applying such an approach in this study would have introduced an additional level of degeneracy with target distance, target intensity and telescope acceptance, which we prefer to avoid. In fact, understanding that the expected signal from a dark subhalo is always peaked toward its center, it is plausible to assume that a point-like search in the FoV of the three scenarios above will not provide significantly different outcomes than a specific search for moderately extended sources. This is especially true for CTA, in which the acceptance is flat throughout the inner degrees of the camera.[12]

Additionally, the $F_{min}$ computation did not take into account any underlying Galactic diffuse emission. This contribution is unknown in the TeV energy domain. Yet, as we are restricting our search to extragalactic ($|b| > 5^{\circ}$) sources, a cosmic-ray induced gamma-ray diffuse emission would be negligible (Gaggero et al.; 2015, 2017; Cataldo et al.; 2019), and, as a consequence, it would only slightly worsen the obtained $F_{min}$. A related issue can be the diffuse emission that may be generated by DM annihilation itself in the halo of the Galaxy, which may indeed outshine some of these subhalos (Facchinetti et al.; 2020).

Finally, we assumed that the EGAL survey will be performed by CTA-North. However, the actual coordinates and area are still under discussion. Should the EGAL survey be performed, at least partially, with CTA-South in the end, the reached $F_{min}$ could be better than the one in our study above.[13]

### 8.3.2 Subhalo annihilation flux

We now continue in elucidating the number and the flux of expected dark subhalos for each specific sky region of the three scenarios described in Section 8.2.

To perform this task, we choose the procedure to populate N-body simulations with low-mass dark clumps as described by Coronado-Blázquez, Sánchez-Conde, Domínguez, Aguirre-Santaella, Mauro, Mirabal, Nieto and Charles (2019); Coronado-Blázquez, Sánchez-Conde, Mauro, Aguirre-Santaella, Ciucă, Domínguez, Kawata and Mirabal (2019), which are based on the Via Lactea II (VL-II) N-body cosmological simulation of a Milky Way-sized halo (Diemand et al.; 2008). In the mentioned works, the original VL-II simulation was "repopulated" below its mass limit, due to numerical resolution, to include subhalos as light as $10^3$ M$_\odot$ (well below the original minimum subhalo mass with completeness in the simulation, of about $10^6$ M$_\odot$).[14] The repopulated VL-II provides very light yet very near subhalos, indeed some of them exhibiting annihilation fluxes comparable to those of more massive yet farther ones. With the repopulation algorithm of Coronado-Blázquez, Sánchez-Conde, Domínguez, Aguirre-Santaella, Mauro, Mirabal, Nieto and Charles (2019);

[11] The choice for the scale radius is motivated because, for a Navarro-Frenk-White (NFW) (Navarro et al.; 1997) DM density profile, ∼90% of the total annihilation flux comes from the region subtended by it.

[12] https://www.cta-observatory.org/science/cta-performance/#1472563544190-020879e1-468f

[13] For energies higher than ∼1 TeV, CTA-South is roughly a factor 2 more sensitive than CTA-North, while the improvement below this energy is minimal. Therefore, one can put an upper bound of this factor 2 in the $F_{min}$ improvement, which, if relevant, will be for very heavy WIMPs, which peak at energies higher than this ∼1 TeV.

[14] Since the subhalo mass function is not fully reproduced below one million solar masses in VL-II, and we expect those subhalos to exist in ΛCDM, we generate more of them adopting the subhalo radial distribution and an extrapolation of the subhalo mass function as found above the mass resolution of the original simulation.

Coronado-Blázquez, Sánchez-Conde, Mauro, Aguirre-Santaella, Ciucă, Domínguez, Kawata and Mirabal (2019), we generate 1000 realizations of VL-II so that the distribution of subhalo fluxes can be properly drawn. From the astrophysical point of view, the DM-induced "brightness" is codified into the so-called J-factor, which accounts for all the astrophysical considerations:

$$J = \int_{\Delta\Omega} d\psi \int_{l.o.s} \rho^2_{DM}(r(l))\, dl, \tag{8.2}$$

where the first integral is performed along the sky line $\psi$ over the solid angle defined from the signal region ($\Delta\Omega$), the second one along the line of sight (l.o.s, $l$), and $\rho_{DM}$ is the DM density profile of the object under consideration.

In the following, we adopt for the J-factor the so-called $J_{max}$ value. This is the J-factor of the brightest subhalo, but averaged across our 1000 realizations of VL-II, and in such a way that we take the value above which 95% of the brightest subhalo J-factor distribution is contained (i.e., out of 1000 realizations, 95% of the time their maximum J-factors will be larger than the value we adopt). $J_{max}$ will also depend on the sky area considered, as explained below. The J-factor distribution of all realizations is drawn imposing $M \leq 10^8 M$ as to ensure we deal with dark subhalos (more massive subhalos will surely host a visible dSph and therefore become visible at other wavelengths (Okamoto et al.; 2010; Sawala et al.; 2015, 2017; Kelley et al.; 2019)). In order to evaluate the detectability of dark subhalos, we follow the method by Coronado-Blázquez, Sánchez-Conde, Domínguez, Aguirre-Santaella, Mauro, Mirabal, Nieto and Charles (2019).

As we increase the observation area, the chance of having subhalos of larger $J_{max}$ also increases, as shown in Figure 8.4. For the case of observing 100 square degrees, $J_{max} \sim 10^{17.5}$ GeV$^2$ cm$^{-5}$. When adopting e.g. 400 square degrees, subhalos with $\sim 10^{18}$ GeV$^2$ cm$^{-5}$ can be expected to be observed. In the EGAL survey, with about 25% of the sky, we can expect to have dark subhalos as bright as $J_{max} \sim 10^{19}$ GeV$^2$ cm$^{-5}$. Note that, up to very large portions of the sky ($\gtrsim$80%), the dependence of $\log_{10}(J_{max})$ with the area is a power law: doubling the observation area increases the logarithm of $J_{max}$ by a factor 1.6 according to the slope of the curve in Figure 8.4. These results are in agreement with those of Dubus et al. (2013); Hütten et al. (2016).

It is evident that, for a given total observation time, increasing the area will result in less time per pointing and a poorer sensitivity. Thus, the optimal strategy must rely on a a compromise between area and time. If we assume a square-root scaling of the sensitivity with exposure time (see Section 8.3.1), then doubling the latter will improve the sensitivity by a factor $\sqrt{2} = 1.4$. This is to be compared to the factor 1.6 mentioned before for the relation between area and $J_{max}$. Therefore, in principle it is better to increase the area at the expense of less exposure time. This will make the EXPO scenario the optimal one, as it is the one in which the observed area is the largest.

## 8.4 Results

### 8.4.1 Expected number of dark subhalos

For each of the three different observation strategies discussed in Section 8.2, and making use of the subhalo annihilation flux computed in Section 8.3.2, it is now possible to estimate the number of expected subhalos in the CTA FoV above a certain

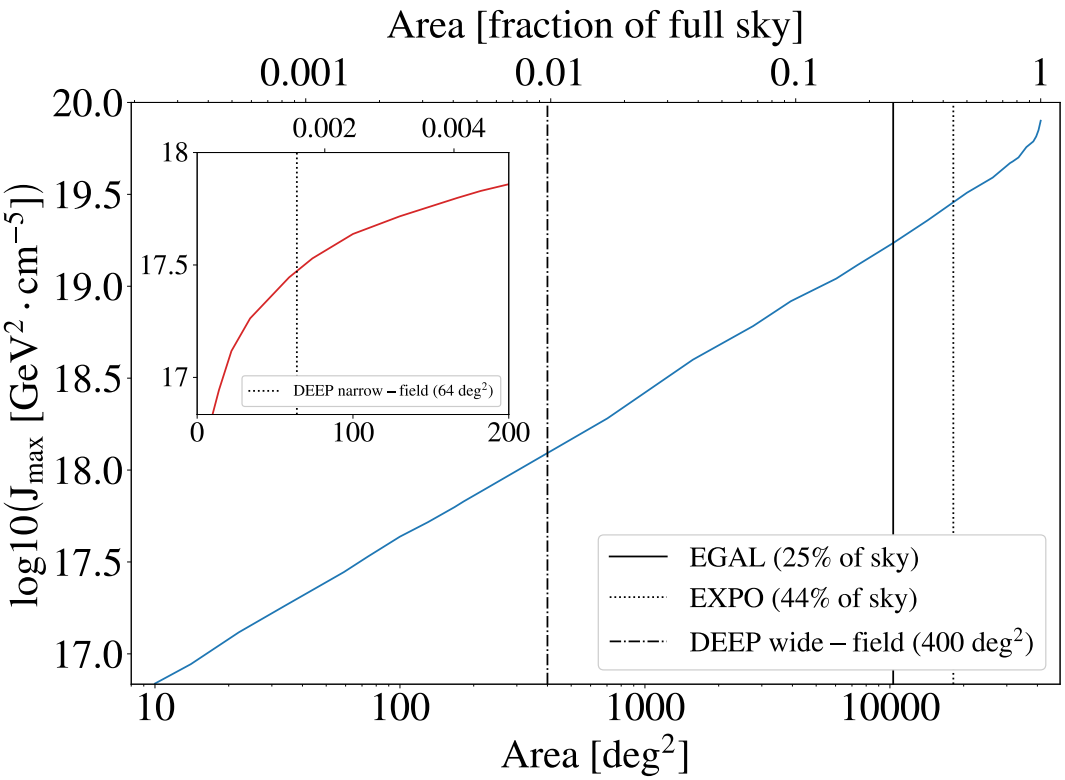


FIGURE 8.4: Scaling of $J_{max}$ with the total observation area; see text for details. Only subhalos with M $\leq 10^8$M are considered, as more massive subhalos are expected to host dSphs and thus be visible. The horizontal axes are expressed in square degrees (bottom axis) and as fraction of the full sky (top axis). We show four vertical lines, respectively, at 64 square degrees ($8 \times 8$ deg$^2$ DEEP scenario with narrow-field), 400 square degrees ($20 \times 20$ deg$^2$ DEEP with wide-field), 25% of the sky (EGAL) and 44% of the sky (EXPO). The zoom panel shows the scaling for the smallest areas, in linear scale.

J-factor, $J_{min}$. The results are summarized in Table 8.2, where the reported uncertainties are due to the variance averaging across realizations of the VL-II simulation and across different sky positions of the observed patch.[15]

| | $N\,(\geq J_{min})$ | | |
|---|---|---|---|
| $\log_{10}(J_{min})$ | EGAL | DEEP | EXPO |
| 17 | $392 \pm 18$ | $26 \pm 8$ | $728 \pm 23$ |
| 18 | $115 \pm 11$ | $5.1 \pm 2.5$ | $206 \pm 14$ |
| 19 | $6.5 \pm 2.6$ | $0.3 \pm 0.5$ | $13 \pm 4$ |
| 20 | $0.3 \pm 0.5$ | 0 | $0.5 \pm 0.7$ |

TABLE 8.2: Average number of subhalos above a given $J_{min}$ in the CTA FoV for the three observation strategies of Section 8.2, across 1000 realizations of the repopulated VL-II N-body simulation as described in Section 8.3.2.

[15]The latter is only relevant in the case of the DEEP exposure, where the variance across sky positions is of the order of the variance across realizations. In the EGAL and EXPO strategies this uncertainty is negligible.

Table 8.2 shows that there are two scenarios: EXPO and possibly EGAL, in which it will be statistically plausible to have a dark subhalo with $J = 10^{20}$ GeV$^2$cm$^{-5}$ in the data. Such high value, predicted by our simulations, would compete with or even surpass the $J-$factors of the most DM dominated ultra-faint dSphs, such as Ret II with an estimated $J-$factor of $J \sim 7 \times 10^{19}$ GeV$^2$cm$^{-5}$ (Bonnivard et al.; 2015), or that of the Large Magellanic Cloud ($\geq 10^{20}$ GeV$^2$cm$^{-5}$) (Buckley et al.; 2015). This result is in agreement with Hütten et al. (2016) for their most optimistic scenario.[16]

Assuming as working hypothesis a DM mass of 1 TeV, a cross-section as the thermal one $\langle\sigma v\rangle \sim 10^{-26}$ cm$^3$s$^{-1}$, the annihilation into purely $b\bar{b}$ and a target located in Northern hemisphere, a $J = 10^{20}$ GeV$^2$cm$^{-5}$ subhalo would give a flux at the CTA telescopes of the order of $\Phi \sim 5 \times 10^{-13}$ ph cm$^2$ s$^{-1}$. This can be compared with the corresponding value computed in Table 8.1 that is $F_{min} = 4.1 \times 10^{-11}$ ph cm$^2$ s$^{-1}$, roughly two orders of magnitude larger. In order to obtain a detection, this putative subhalo should require thousands of hours of exposure, far more than what achievable in the EGAL and EXPO scenarios. Similar exposures are found for all the masses and annihilation channels of Figure 8.3.

### 8.4.2 Exclusion curve for the no-detection case

However, even if no dark subhalo is detected by CTA, it will be still possible to set constraints to the $\langle\sigma v\rangle - m_\chi$ DM parameter space. The methodology is the same as in Refs. (Coronado-Blázquez, Sánchez-Conde, Domínguez, Aguirre-Santaella, Mauro, Mirabal, Nieto and Charles; 2019; Coronado-Blázquez, Sánchez-Conde, Mauro, Aguirre-Santaella, Ciucă, Domínguez, Kawata and Mirabal; 2019), and is based on a comparison between the N-body simulation prediction $J_{max}$ and the gamma-ray data $F_{min}$ via:

$$\langle\sigma v\rangle = \frac{8\pi \cdot m_\chi^2 \cdot F_{min}}{J_{max} \cdot N_\gamma} \tag{8.3}$$

where $m_\chi$ is the DM particle mass, $F_{min}$ the instrumental sensitivity to DM as defined in Section 8.3.1, $J_{max}$ the 95% c.l. nominal value of the brightest subhalo J-factor among the different VL-II realizations, as described in Section 8.3.2, and $N_\gamma$ is the DM spectrum for a particular annihilation channel integrated within the energy range under consideration.

Figure 8.5 shows the 95% c.l. upper limits to the DM annihlation cross section for the $b\bar{b}$ (top panel) and $\tau^+\tau^-$ (bottom panel) annihilation channels for the three observational strategies under consideration in this work. The most stringent limits are obtained for the EXPO method, while the weakest ones are those for which the DEEP scenario is adopted.

These constraints reach their best sensitivity for masses of $\sim 1$ TeV (500 GeV) for the $b\bar{b}$ ($\tau^+\tau^-$) annihilation channel, of the order of $3 \times 10^{-24}$ ($7 \times 10^{-25}$) cm$^3 \cdot$ s$^{-1}$. Interestingly, the behavior around the maximum sensitivity is fairly flat over more than an order of magnitude in DM mass, especially in the case of $b\bar{b}$. We recall that values roughly two orders of magnitude above the thermal relic cross section are ruled out for canonical WIMPs.

We also include in Figure 8.5 the 68% containment uncertainty bands on $F_{min}$ for the three observational strategies. In the case of the EXPO method we also include, via quadrature, the uncertainty in both our estimate of the total observed sky area and the average exposure time. Nevertheless, the latter uncertainties turn out to

[16] Indeed, in Ref. (Hütten et al.; 2016) this would be the EGAL survey and their aggressive, so-called "HIGH", configuration.

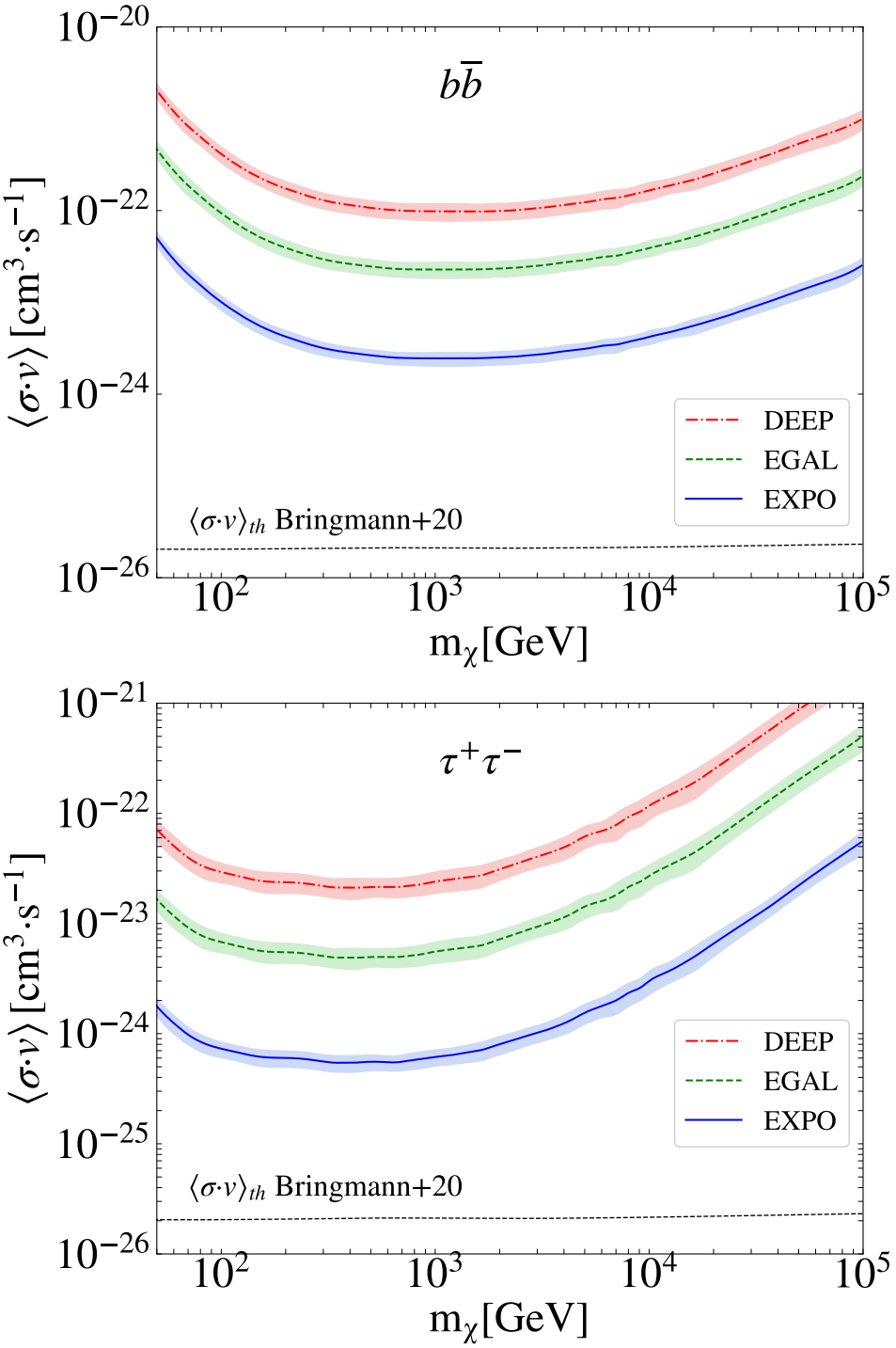


FIGURE 8.5: 95% C.L. upper limits to the DM annihilation cross section for $b\bar{b}$ (top) and $\tau^+\tau^-$ (bottom) assuming no unIDs are detected by CTA under any of the three observational strategies proposed in Sec. 8.2: a dedicated $10 \times 10$ deg$^2$, 100h deep-field, the EGAL survey, and the EXPO scenario. The dashed line represents the thermal value of the annihilation cross section (Bringmann et al.; 2020). See main text for details on the uncertainty bands, which, in short, come from the uncertainty in $F_{min}$ and, in the EXPO case, the uncertainty in the total sky area extrapolation.

be completely negligible when compared to the $F_{min}$ uncertainty (see 8.7.2). This reinforces the accuracy of our results: should the actual EXPO time significantly differ from the one we anticipated here, the impact of these variations would still be subdominant in the computation of DM limits when compared to uncertainties in $F_{min}$.

Finally, we remind the reader that, for the computation of these DM limits, we assumed Galactic subhalos to be indeed dark for masses $M_{sub} < 10^8 M_\odot$. Note that the precise value of this mass cut will directly impact the value of $J_{max}$ and, thus, ultimately, the DM constraints. This particular ansatz is discussed and relaxed in 8.7.3.

## 8.5 Discussion

In Figure 8.6, we put our results into context by showing a selection of exclusion limits obtained by other instruments that can be compared to ours, as they aim for setting constraints with unidentified sources (unIDs), namely the *Fermi*-LAT (Coronado-Blázquez, Sánchez-Conde, Mauro, Aguirre-Santaella, Ciucă, Domínguez, Kawata and Mirabal; 2019), HAWC (Coronado-Blázquez and Sánchez-Conde; 2020), and the previous work on unIDs detection with CTA (Hütten et al.; 2016). For the sake of clarity, only the best limits, i.e., the ones obtained with the EXPO strategy, are plotted.

The EXPO limits are most competitive for masses above $\sim$ 1 TeV (500 GeV) for the $b\bar{b}$ ($\tau^+\tau^-$) annihilation channel, of the order of $3 \times 10^{-24}$ ($7 \times 10^{-25}$) cm$^3 \cdot$ s$^{-1}$. Our work also improves by a factor $\sim$2 the CTA limits derived in a previous work in this subject by Hütten et al. (2016) – where authors adopted a different methodology and observation strategy, as well as different CTA IRFs – being therefore compatible. Note that the behavior around the peak sensitivity is remarkably flat over more than an order of magnitude in the WIMP mass, especially for $b\bar{b}$. We recall that values roughly two orders of magnitude above the thermal relic cross section are ruled out for canonical WIMPs.

In terms of limits, this work also complements previous works on dark subhalo detection for other gamma-ray telescopes, namely the *Fermi*-LAT (Coronado-Blázquez, Sánchez-Conde, Mauro, Aguirre-Santaella, Ciucă, Domínguez, Kawata and Mirabal; 2019) and the HAWC (Coronado-Blázquez and Sánchez-Conde; 2020) observatory. Indeed, the synergy between the three mentioned instruments, LAT, HAWC and CTA, is evident: LAT dominates the sensitivity for energies below few hundred of GeV and HAWC above few tens of TeV, with CTA bridging the gap in the region in between. Should a dark subhalo candidate appear in one of the telescopes, this complementarity among instruments would allow for, e.g., follow-up observations with the others.

The LAT–HAWC–CTA constraints from Coronado-Blázquez, Sánchez-Conde, Mauro, Aguirre-Santaella, Ciucă, Domínguez, Kawata and Mirabal (2019); Coronado-Blázquez and Sánchez-Conde (2020) and this work, as shown in Figure 8.6, have the advantage that they were obtained with the exact same methodology and adopting the same N-body simulation results. This means that these limits are fully consistent one another. Yet, there are important caveats to note: our CTA limits are a projection over a large amount of time. We recall that, in order for the EXPO program to be accomplished, 10 years of CTA operation shall pass. Therefore, the respective weight of the limits at present may change with time: LAT results will probably slowly improve, dominating for long time the constraints below the TeV. In the meantime,

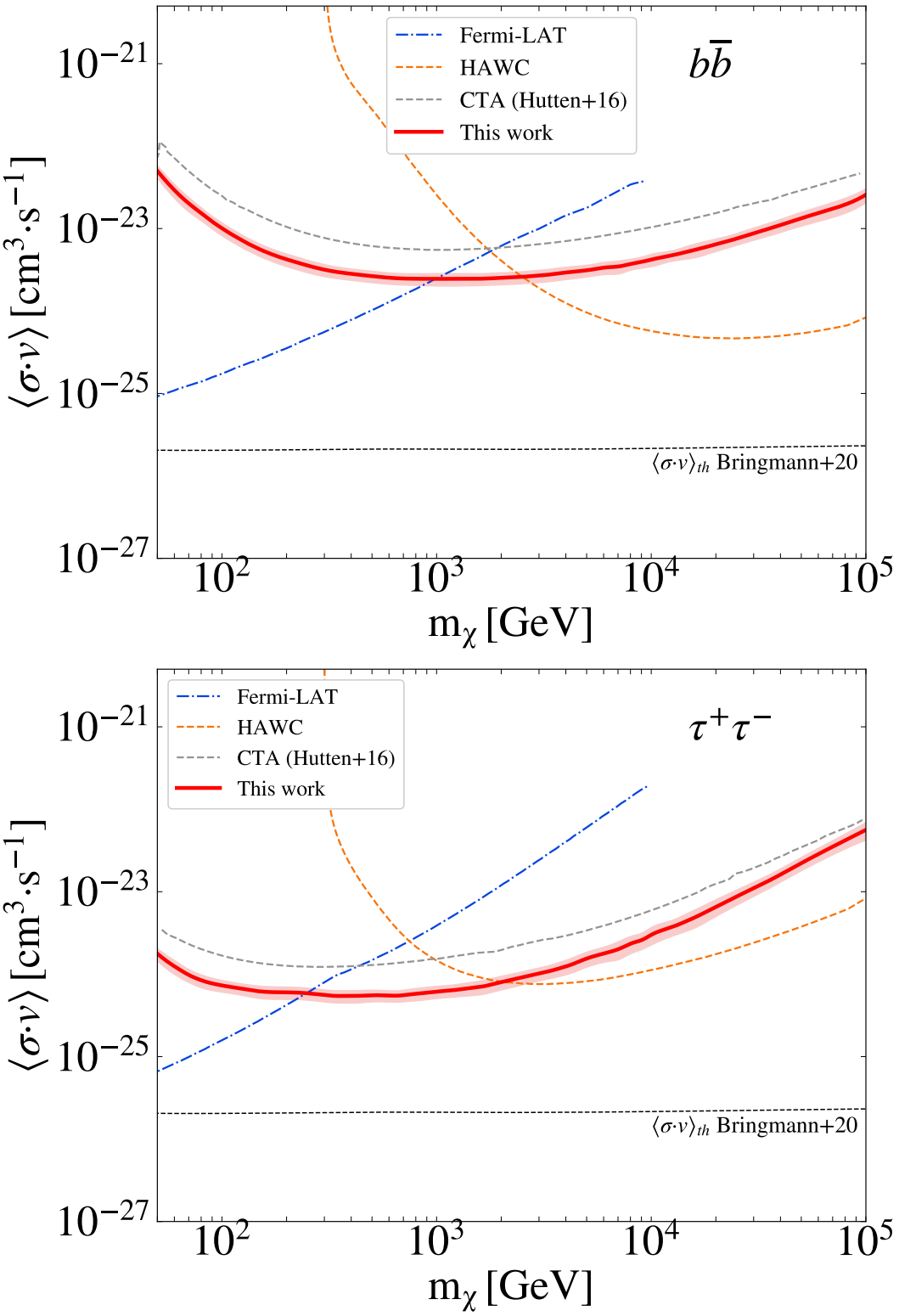


FIGURE 8.6: Same as Figure 8.5, but showing only the EXPO constraints and the comparison with previous works, namely the *Fermi*-LAT unIDs (Coronado-Blázquez, Sánchez-Conde, Mauro, Aguirre-Santaella, Ciucă, Domínguez, Kawata and Mirabal; 2019), HAWC unIDs (Coronado-Blázquez and Sánchez-Conde; 2020), and the previous work on unIDs detection with CTA (Hütten et al.; 2016).

HAWC will have several years of data to close the gap from higher energies. CTA will come later and will probably update results over intermediate times (say after ca. 5 years of operation) and possibly extending over 10 years of operation.[17]

For the moment, we did not include in these discussions at least two players that will enter the scene in the near future: the LHAASO Sciascio (2016) instrument in Tibet and the planned SWGO SWGO Collaboration (2019) observatory in South America, which might provide stronger constraints than HAWC in the TeV range due to their greater dimensions and thus improved sensitivity.

We do not include in Figure 8.6 other limits obtained for other DM targets such as the dwarf satellite galaxies of the Milky Way or the Galactic center. There is an ample literature on those results (see, e.g., Doro; 2014b, for a collection of them). Both classes of results yield more competitive results than those presented here. Yet, we note that those results are built upon the exact knowledge of the astrophysical factor of the individual target in consideration, and may be therefore subject to larger uncertainties than the results obtained here. For example, the assumption of a cored DM profile in the Galactic center may deteriorate the results by two orders of magnitude, as shown in The Cherenkov Telescope Array Consortium (2021). In this regard, our results have the advantage of being based on conservative assumptions on the statistical properties of the subhalo population as obtained from N-body cosmological simulations, this way being less sensitive to individual target uncertainties.

## 8.6 Summary and conclusions

In this paper, we assessed the detectability of dark subhalos with the Cherenkov Telescope Array (CTA). We proposed three different observational strategies based on the current Key Science Programs (KSPs) and the predictions for the sky pointings: i) EGAL scenario, based on a planned extragalactic survey that will scan 25% of the sky (Figure 8.1); ii) DEEP scenario, consisting of a deep-field exposure of 100 h over a region of $10 \times 10$ deg$^2$; and iii) EXPO scenario, based on the total exposure gathered over 10 years of CTA operation (Figure 8.2).

A careful characterization of the sensitivity of CTA to dark subhalos in these observation scenarios was then performed by means of 100 simulations of a putative subhalo made of WIMPs annihilating via two different annihilation channels ($b\bar{b}$ and $\tau^+\tau^-$). We considered 29 WIMP masses ranging from 50 GeV up to 10 TeV (Figure 8.3 and Table 8.1) and the latest instrument response functions for CTA. Based on hundreds of realizations of the Via Lactea II N-body cosmological simulation, "repopulated" with subhalos well below the resolution limit of the original simulation, we generated a scaling relation between sky area and maximum (statistically expected) subhalo J-factor achievable in such area (Figure 8.4), and computed the expected number of dark subhalos above a certain J-factor in the three different scenarios (Table 8.2). In the most optimistic scenario, corresponding to EXPO, we found that on average one dark subhalo ($0.5 \pm 0.7$) with $J_{min} > 10^{20}$ GeV$^2 \cdot$ cm$^{-5}$ can be expected. Such a value is similar to that of the most competitive dSphs.

However we note that this result is based on a simplified model that does not take into account neither a possible signal spatial extension nor any baryonic-induced effects within the subhalos. The former will probably have negligible effects on our results, while the precise relevance of the second mentioned effect is still subject of debate. Indeed, state-of-the-art hydrodynamical simulations show that baryons in

[17] The expected duration of CTA is planned for 30 years.

the host halo can largely affect its subhalo population, significantly decreasing the abundance of subhalos especially in the innermost regions of Milky-Way-size halos Kelley et al. (2019); Garrison-Kimmel et al. (2017); Grand and White (2020). Yet, these simulations do not resolve subhalos lighter than $\sim 10^6$M – the ones of interest for our work – thus it remains unclear whether or not in the presence of baryons these tiny subhalos will also be tidally stripped, see e.g. van den Bosch et al. (2017); Errani and Peñarrubia (2019).

Assuming instead that no dark subhalo is observed, we were able to compute the 95% C.L. constraints to WIMP annihilation (Figure 8.5). This was done by combining CTA sensitivity results with predictions from our repopulated N-body simulations. The EXPO scenario offers the most competitive results, followed by EGAL and DEEP. In fact, the DEEP strategy turns out to be not optimal for this kind of search, as the required exposure times to be competitive exceed the achievable ones of CTA. Nevertheless, we found interesting to include this scenario as an additional possibility a priori worth exploring. The EXPO limits are of the order of $\langle\sigma v\rangle \sim 10^{-24}$ cm$^{-3}$s$^{-1}$ for the $\tau^+\tau^-$ channel and slightly above for the $b\bar{b}$ channel. Thus, they are comparable to those obtained with dwarf satellite galaxies by current IACTs, e.g. H.E.S.S. Collaboration (2020). We placed our limits into a more general context in Figure 8.6, by showing results obtained with *Fermi*-LAT and the HAWC observatory for dark subhalos as well. This figure illustrated how nicely the three mentioned experiments are expected to complement one another.

Our study shows that, despite the fact that the chance of serendipitously observing a dark subhalo with CTA is slim (only achievable over a very wide area in the sky and by means of very large exposures), even a no subhalo detection can be used to set competitive DM limits. It is also possible that clear gravitational signatures of dark subhalos in the Galaxy will be found in the near future (see, e.g., the works by Ibata et al. (2020); Buschmann et al. (2018); Erkal et al. (2016) using gaps in stellar streams), as well as promising subhalo candidates (for instance within the pool of *Fermi*-LAT unidentified sources, as in Coronado-Blázquez, Sánchez-Conde, Mauro, Aguirre-Santaella, Ciucă, Domínguez, Kawata and Mirabal (2019)). In both cases it may be possible to obtain approximated, if not precise, sky coordinates for potential subhalos. In such scenarios, that should not be discarded, CTA would point to such candidates directly.

We underline that the obtained prospects do not require any specific pointing of the instrument to become a reality. Nonetheless, when CTA starts operating, its performance will most likely not be exactly what is stated in this paper and, thus, these forecasts may require updates. Yet, this paper is meant to already pave the way on the methodology to compute dark-subhalo based DM constraints from CTA observations. It is also possible that intermediate results in this context will be produced by CTA after 5 years and even later on, after 15 years. Over such a long exposure, changes and improvements on the instrumental side and in the description of the dark subhalo scenario may happen. However, we preferred not to speculate further on the impact of these changes. Finally, more realistic and powerful cosmological simulations, including not only DM but also hydrodynamic effects due to baryonic matter at the scale of dark subhalos, will allow us to be more precise on the characterization of the whole subhalo population in the future, this way making our limits more robust.

## 8.7 Appendix

### 8.7.1 Normal vs. divergent pointing

In the standard CTA observation mode (so-called normal or parallel), all CTA telescopes point to the same sky position. This guarantees maximum performance in terms of sensitivity. However, in this observation mode, the FoV is limited to the maximum angular acceptance of the each telescope camera.

In the *divergent* mode there is a small tilt between the lines of sight of the telescopes, that is aimed at enlarging the overall FoV. This comes at the expense of the angular and energy resolutions, as well as of the overall sensitivity. It also adds a level of complexity in the analysis (Szanecki et al.; 2015). The divergent pointing may be especially useful for large surveys, such as the EGAL or the DEEP surveys discussed in this work. Both are schematically shown in Figure 8.7, in which possible pointing strategies are highlighted.

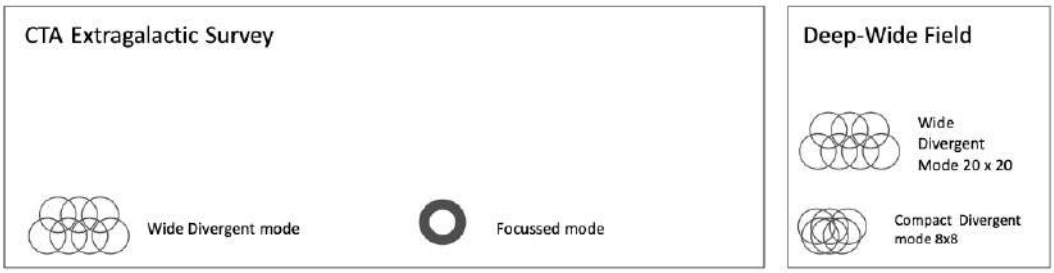


FIGURE 8.7: Schematic view of different pointing strategies, both for the EGAL and DEEP surveys, in normal and divergent mode.

According to Lucie Gérard for the CTA Consortium (2015), the divergent pointing is more optimal than the normal, focused pointing for energies above ∼5 TeV. This is because the combination of several telescopes (high multiplicity) ensures a more uniform exposure of the FoV. As the energy peaks of the DM spectra under consideration are $E^{\tau^+\tau^-}_{peak} \sim m_\chi/3$ and $E^{b\bar{b}}_{peak} \sim m_\chi/30$ (Cirelli et al.; 2010), the divergent would be better than a normal pointing for WIMP masses $\gtrsim$15 TeV for $\tau^+\tau^-$ and $\gtrsim$150 TeV for $b\bar{b}$ (which is already outside the WIMP parameter space due to the unitarity bound) (Smirnov and Beacom; 2019; Griest and Kamionkowski; 1990). As we mentioned earlier, for masses larger than $\sim$ 10 TeV, especially for the case of $\tau^+\tau^-$, the effect of electroweak corrections are unclear and therefore any results above this mass must be taken with caution.

In order to match the normal pointing mode performance by means of adopting the divergent pointing, as in the latter the sensitivity worsens by ∼25% according to Lucie Gérard for the CTA Consortium (2015), the exposure time should increase by $\geq$25% assuming that the sensitivity scales linearly with time (which may be overly optimistic for low energies, but it is expected to be the case for VHE (Charles et al.; 2016)). This means almost 4 hours per pointing in the EGAL survey, which is in the limit of feasibility given the typical area of divergent pointing and total time of the survey (1000 h). Therefore, the divergent pointing can only match, at most, the performance of the standard focused one, but not improve it.

Additionally, Lucie Gérard for the CTA Consortium (2015) assumed a number of telescopes that is more similar to the one under consideration for the CTA Southern array (99), while the Northern array is significantly smaller (19) but also participates

to the EGAL survey. Indeed, Lucie Gérard for the CTA Consortium (2015) shows that the performance decreases significantly for a CTA-North-like configuration.

As a summary, the divergent pointing may be only as good as the parallel one in the context of this work. Depending on specific assumptions on the array configuration and the scaling of the sensitivity with time, the divergent pointing performance would only worsen with respect to the parallel one.

Yet, a divergent pointing observation comes at hand useful when dealing with extended sources, such as it may happen in the case of dark subhalos, for which the brightest ones are expected to have considerably large angular extensions (Coronado-Blázquez, Sánchez-Conde, Mauro, Aguirre-Santaella, Ciucă, Domínguez, Kawata and Mirabal; 2019). Although promising thanks to the wide FoV that can be achieved, which may be able to reconstruct the annihilation profile of the source, we note that Lucie Gérard for the CTA Consortium (2015) finds a 30% average loss of angular resolution between 125 GeV and 10 TeV in the divergent pointing compared to the normal pointing.

### 8.7.2 Building up the CTA EXPO scenario from MAGIC observation records

In this Appendix, we explain the details of the extrapolation we did to build the CTA EXPO scenario starting from past MAGIC stereo operations. The latter can be completely characterized by three variables: RA, DEC and exposure time. If several pointings are done to the same (RA, DEC) sky location, we will consider their envelope.

Once the MAGIC distributions of RA, DEC and time are properly characterized, we generate mock random data following the same distributions. For CTA, we extrapolate the number of pointings assuming that they increase linearly with time. From the 250 MAGIC stereo pointings (combining multiple exposures) in 6.5 years, we generate $1.54 \times 2 \times 250 = 770$ observations. The first factor refers to the 10 years of time we assume for CTA, while the factor 2 comes from the fact of having two arrays, one in each hemisphere. In the case of DEC, we invert the DEC of half of the MAGIC pointings, as we naively assume that half of the observations will be performed by CTA South, which will be located at a latitude $-23.4^\circ$ (quite similar in absolute value to the $28.8^\circ$ of CTA North). Note that, as the distributions are drawn randomly, CTA-South pointings will not be just a mirrored image of those of CTA-North. In Figure 8.8, we plot both the actual distributions of MAGIC stereo and the resulting CTA extrapolation.

We also checked if the linear extrapolation of pointings with time is a valid approximation. In Figure 8.9 we plot the growth of the cumulative exposure area as a function of the periods of observation as done by MAGIC, where each period represents 29 days (moon cycle). The linear regime represents a good approximation, and therefore we can safely extrapolate the number of pointings linearly with time.

To compute the total observed area, we will assume the FoV of all pointings as a circular area of 6 deg of diameter. This number is motivated by the fact the observations will mostly be performed by the MSTs, the most sensitive CTA telescopes in the medium energy range. MSTs have 8 deg of FoV but the off-axis degradation is expected to be non-negligible from 6 deg outwards, thus a value of 6 deg is conservatively adopted.

Also, possible overlaps between observations must be taken into account. The area of intersection between two circles of the same radius $r$ is given by,

$$A = r^2 \cdot [q - \sin(q)] \tag{8.4}$$

where $q = 2 \cdot \mathrm{acos}\,[d/2r]$ and $d$ is the distance between centers. If $d < 6$ deg, i.e., two adjacent pointings are at a distance between their centers smaller than their diameter, there will be some overlap. This overlapping area is properly considered (i.e., removed) in the calculation of the total observed area.

Once all this is taken into account, we compute the total area and the average time of observation. To bracket the uncertainties due to the randomness of the map, we generate 2000 realizations. We obtain that the average area surveyed by CTA in 10 years will be ∼44% of the sky, almost doubling that of the EGAL survey, for an average time per pointing of 40h, i.e., a factor ∼13 larger than the one that will be adopted for the EGAL survey (3h per pointing)[18]. Figure 8.10 shows a map of the resulting mock observations.

Finally, we show the full distribution across the 2000 realizations in Figure 8.11. Both the larger area and mean observation times per pointing will make the EXPO strategy the most competitive one for dark subhalo searches.

### 8.7.3 Impact of the subhalo mass cut in the dark matter constraints

To obtain the upper limits on the annihilation cross section shown in Section 9.4, we assumed a subhalo mass cut of $10^8$M , i.e., subhalos with masses larger than this value would host a dSph and would thus be visible, while below the subhalos would be unable to host any significant baryon content and would remain completely dark. Yet, this cut is uncertain as of today (Gao et al.; 2004; Zhu et al.; 2016; Garrison-Kimmel et al.; 2017; Sawala et al.; 2017; Kelley et al.; 2019), and one may ask how dependent the derived constraints on the adopted value are. This is addressed in Figure 8.12, where we plot the EXPO constrain for different subhalo mass cuts, as well as no mass cut at all. We note that there are observed dwarf galaxies with masses as low as few times $10^7$M Simon (2019); Strigari et al. (2007); Mateo (1998). Thus, the cases of $M_{cut} = 10^9$M and no-cut shown in this figure are not realistic and are only intended to illustrate the dependence of the constraints with the subhalo cut. On the other hand, a value of $M_{cut} = 10^7$M can be overly conservative, as the precise value at which subhalos go dark is not yet settled, as mentioned above. With all these considerations in mind, we adopted an intermediate yet realistic value of $M_{cut} = 10^8$M as the default one in our limits computation.

From figure 8.12, we observe that the DM constraints only vary by a factor ∼1.5 for every order of magnitude variation in subhalo mass cut. Also, there is almost no variation for the 'no cut' case compared to the one of $10^9$ $M$ , as basically the most massive members of the subhalo population are already reached. Therefore, though we adopt a value of $10^8 M$ for the subhalo mass cut as our benchmark model, the constraints can be easily re-scaled for other mass cuts from this figure.

## Bibliography

Banik, N., Bertone, G., Bovy, J. and Bozorgnia, N. (2018). Probing the nature of dark matter particles with stellar streams, *Journal of Cosmology and Astroparticle Physics* **2018**(07): 061–061.

Baumgart, M., Cohen, T., Moulin, E., Moult, I., Rinchiuso, L., Rodd, N. L., Slatyer, T. R., Stewart, I. W. and Vaidya, V. (2019). Precision photon spectra for wino annihilation, *JHEP* **2019**(1).

[18] The total observation time is around 30000h

Belikov, A. V., Buckley, M. R. and Hooper, D. (2012). Searching for dark matter subhalos in the Fermi-LAT second source catalog, *Physical Review D* **86**(4): 043504.
**URL:** *http://adsabs.harvard.edu/abs/2012PhRvD..86d3504B*

Beneke, M., Broggio, A., Hasner, C. and Vollmann, M. (2018). Energetic $\gamma$-rays from TeV scale dark matter annihilation resummed, *Physics Letters B* **786**: 347–354.

Bergström, L. (1989). Radiative processes in dark matter photino annihilation, *Physics Letters B* **225**(4): 372–380.

Berlin, A. and Hooper, D. (2014). Stringent constraints on the dark matter annihilation cross section from subhalo searches with the Fermi Gamma-Ray Space Telescope, *Physical Review D* **89**(1): 016014.
**URL:** *http://adsabs.harvard.edu/abs/2014PhRvD..89a6014B*

Bertoni, B., Hooper, D. and Linden, T. (2015). Examining The Fermi-LAT Third Source Catalog in search of dark matter subhalos, *Journal of Cosmology and Astroparticle Physics* **12**: 035.
**URL:** *http://adsabs.harvard.edu/abs/2015JCAP...12..035B*

Bonnivard, V., Combet, C., Maurin, D., Geringer-Sameth, A., Koushiappas, S. M., Walker, M. G., Mateo, M., Olszewski, E. W. and III, J. I. B. (2015). Dark Matter Annihilation and Decay Profiles for the Reticulum II Dwarf Spheroidal Galaxy, *The Astrophysical Journal* **808**(2): L36.

Bringmann, T., Bergström, L. and Edsjö, J. (2008). New gamma-ray contributions to supersymmetric dark matter annihilation, *JHEP* **2008**(01): 049–049.

Bringmann, T., Depta, P. F., Hufnagel, M. and Schmidt-Hoberg, K. (2020). Precise dark matter relic abundance in decoupled sectors.

Bringmann, T., Galea, A. J. and Walia, P. (2016). Leading QCD corrections for indirect dark matter searches: A fresh look, *Phys. Rev. D* **93**(4).

Brun, P., Moulin, E., Diemand, J. and Glicenstein, J.-F. (2011). Searches for dark matter subhaloes with wide-field Cherenkov telescope surveys, *Phys. Rev. D* **83**(1).

Buckley, M. R., Charles, E., Gaskins, J. M., Brooks, A. M., Drlica-Wagner, A., Martin, P. and Zhao, G. (2015). Search for gamma-ray emission from dark matter annihilation in the large magellanic cloud with the fermi large area telescope, *Phys. Rev. D* **91**(10).

Buckley, M. R. and Hooper, D. (2010). Dark matter subhalos in the Fermi first source catalog, *Physical Review D* **82**(6): 063501.
**URL:** *http://adsabs.harvard.edu/abs/2010PhRvD..82f3501B*

Buschmann, M., Kopp, J., Safdi, B. R. and Wu, C.-L. (2018). Stellar Wakes from Dark Matter Subhalos, *Physical Review Letters* **120**(21).

Calore, F., De Romeri, V., Di Mauro, M., Donato, F. and Marinacci, F. (2017). Realistic estimation for the detectability of dark matter subhalos using Fermi-LAT catalogs, *Physical Review D* **96**(6): 063009.
**URL:** *http://adsabs.harvard.edu/abs/2017PhRvD..96f3009C*

Carlberg, R. G. (2009). Star Stream Folding by Dark Galactic Subhalos, *The Astrophysical Journal* **705**(2): L223–L226.

Carlberg, R. G. (2012). Dark Matter Sub-halo Counts via Star Streams Crossings, *The Astrophysical Journal* **748**(1): 20.

Cataldo, M., Pagliaroli, G., Vecchiotti, V. and Villante, F. (2019). Probing galactic cosmic ray distribution with TeV gamma-ray sky, *JCAP* **2019**(12): 050–050.

Charles, E., Sánchez-Conde, M., Anderson, B., Caputo, R., Cuoco, A., Mauro, M. D., Drlica-Wagner, A., Gomez-Vargas, G., Meyer, M., Tibaldo, L., Wood, M., Zaharijas, G., Zimmer, S., Ajello, M., Albert, A., Baldini, L., Bechtol, K., Bloom, E., Ceraudo, F., Cohen-Tanugi, J., Digel, S., Gaskins, J., Gustafsson, M., Mirabal, N. and Razzano, M. (2016). Sensitivity projections for dark matter searches with the Fermi large area telescope, *Physics Reports* **636**: 1–46.

Ciafaloni, P., Comelli, D., Riotto, A., Sala, F., Strumia, A. and Urbano, A. (2011). Weak corrections are relevant for dark matter indirect detection, *JCAP* **2011**(03): 019–019.

Cirelli, M., Corcella, G., Hektor, A., Hütsi, G., Kadastik, M., Panci, P., Raidal, M., Sala, F. and Strumia, A. (2010). PPPC 4 DM ID: A Poor Particle Physicist Cookbook for Dark Matter Indirect Detection, *JCAP* .

Conrad, J. (2015). Statistical issues in astrophysical searches for particle dark matter, *Astroparticle Physics* **62**: 165–177.

Coronado-Blázquez, J. and Sánchez-Conde, M. A. (2020). Constraints to Dark Matter Annihilation from High-Latitude HAWC Unidentified Sources, *Galaxies* **8**(1): 5.
**URL:** *https://ui.adsabs.harvard.edu/abs/2020Galax...8....5C*

Coronado-Blázquez, J., Sánchez-Conde, M. A., Domínguez, A., Aguirre-Santaella, A., Mauro, M. D., Mirabal, N., Nieto, D. and Charles, E. (2019). Unidentified gamma-ray sources as targets for indirect dark matter detection with the Fermi-Large Area Telescope, *JCAP* **2019**(07): 020–020.

Coronado-Blázquez, J., Sánchez-Conde, M. A., Mauro, M. D., Aguirre-Santaella, A., Ciucă, I., Domínguez, A., Kawata, D. and Mirabal, N. (2019). Spectral and spatial analysis of the dark matter subhalo candidates among Fermi Large Area Telescope unidentified sources, *JCAP* **2019**(11): 045–045.

Cowan, G., Cranmer, K., Gross, E. and Vitells, O. (2011). Asymptotic formulae for likelihood-based tests of new physics, *The European Physical Journal C* **71**(2).

Diemand, J., Kuhlen, M., Madau, P., Zemp, M., Moore, B., Potter, D. and Stadel, J. (2008). Clumps and streams in the local dark matter distribution, *Nature* .

Doro, M. (2014a). A decade of dark matter searches with ground-based Cherenkov telescopes, *Nuclear Instruments and Methods in Physics Research Section A: Accelerators, Spectrometers, Detectors and Associated Equipment* **742**: 99–106.

Doro, M. (2014b). A decade of dark matter searches with ground-based Cherenkov telescopes, *Nucl. Instrum. Meth. A* **742**: 99–106.

Doro, M., Conrad, J., Emmanoulopoulos, D., Sànchez-Conde, M., Barrio, J., Birsin, E., Bolmont, J., Brun, P., Colafrancesco, S., Connell, S., Contreras, J., Daniel, M., Fornasa, M., Gaug, M., Glicenstein, J., González-Muñoz, A., Hassan, T., Horns, D., Jacholkowska, A., Jahn, C., Mazini, R., Mirabal, N., Moralejo, A., Moulin, E., Nieto, D., Ripken, J., Sandaker, H., Schwanke, U., Spengler, G., Stamerra, A., Viana, A., Zechlin, H.-S. and Zimmer, S. (2013). Dark matter and fundamental physics with the Cherenkov Telescope Array, *Astroparticle Physics* **43**: 189–214.

Dubus, G., Contreras, J., Funk, S., Gallant, Y., Hassan, T., Hinton, J., Inoue, Y., Knödlseder, J., Martin, P., Mirabal, N., de Naurois, M. and Renaud, M. (2013). Surveys with the Cherenkov Telescope Array, *Astroparticle Physics* **43**: 317–330.

Erkal, D., Belokurov, V., Bovy, J. and Sanders, J. L. (2016). The number and size of subhalo-induced gaps in stellar streams, *Monthly Notices of the Royal Astronomical Society* **463**(1): 102–119.

Errani, R. and Peñarrubia, J. (2019). Can tides disrupt cold dark matter subhaloes?, *Monthly Notices of the Royal Astronomical Society* **491**(4): 4591–4601.

Facchinetti, G., Lavalle, J. and Stref, M. (2020). Statistics for dark matter subhalo searches in gamma rays from a kinematically constrained population model. I: Fermi-LAT-like telescopes.
**URL:** *https://arxiv.org/abs/2007.10392*

Fermi-LAT Collaboration (2009). The Large Area Telescope on the Fermi Gamma-ray Space Telescope Mission, *The Astrophysical Journal* **697**(2): 1071–1102.

Fermi-LAT Collaboration (2012). Search for Dark Matter Satellites Using Fermi-LAT, *The Astrophysical Journal* **747**: 121.
**URL:** *http://adsabs.harvard.edu/abs/2012ApJ...747..121A*

Fermi-LAT Collaboration and MAGIC Collaboration (2016). Limits to dark matter annihilation cross-section from a combined analysis of MAGIC and fermi-LAT observations of dwarf satellite galaxies, *Journal of Cosmology and Astroparticle Physics* **2016**(02): 039–039.

Flores, R., Olive, K. A. and Rudaz, S. (1989). Radiative processes in LSP annihilation, *Physics Letters B* **232**(3): 377–382.

Gaggero, D., Grasso, D., Marinelli, A., Taoso, M. and Urbano, A. (2017). Diffuse Cosmic Rays Shining in the Galactic Center: A Novel Interpretation of H.E.S.S. and Fermi-LAT Gamma-Ray Data, *Physical Review Letters* **119**(3).

Gaggero, D., Grasso, D., Marinelli, A., Urbano, A. and Valli, M. (2015). The Gamma-ray and Neutrino Sky: A Consistent Picture of Fermi-LAT, Milagro and IceCube Results, *The Astrophysical Journal* **815**(2): L25.

Gammaldi, V. (2019). Multimessenger Multi-TeV Dark Matter, *Frontiers in Astronomy and Space Sciences* **6**.

Gao, L., White, S. D. M., Jenkins, A., Stoehr, F. and Springel, V. (2004). The subhalo populations of ΛCDM dark haloes, *MNRAS* **355**: 819–834.
**URL:** *http://adsabs.harvard.edu/abs/2004MNRAS.355..819G*

Garrison-Kimmel, S., Wetzel, A., Bullock, J. S., Hopkins, P. F., Boylan-Kolchin, M., Faucher-Giguère, C.-A., Kereš, D., Quataert, E., Sanderson, R. E., Graus, A. S. and Kelley, T. (2017). Not so lumpy after all: modelling the depletion of dark matter subhaloes by Milky Way-like galaxies , *MNRAS* **471**(2): 1709–1727.

Grand, R. J. J. and White, S. D. M. (2020). Baryonic effects on the detectability of annihilation radiation from dark matter subhaloes around the milky way, *Monthly Notices of the Royal Astronomical Society* **501**(3): 3558–3567.
**URL:** *https://ui.adsabs.harvard.edu/abs/2021MNRAS.501.3558G*

Griest, K. and Kamionkowski, M. (1990). Unitarity limits on the mass and radius of dark-matter particles, *Physical Review Letters* **64**(6): 615–618.

HAWC Collaboration (2019). Searching for dark matter sub-structure with HAWC, *Journal of Cosmology and Astroparticle Physics* **2019**(7): 022.
**URL:** https://ui.adsabs.harvard.edu/abs/2019JCAP...07..022A

HEGRA Collaboration (2004). The Crab Nebula and Pulsar between 500 GeV and 80 TeV: Observations with the HEGRA Stereoscopic Air Cerenkov Telescopes, *ApJ* **614**(2): 897–913.

H.E.S.S. Collaboration (2020). Search for dark matter signals towards a selection of recently detected DES dwarf galaxy satellites of the Milky Way with H.E.S.S., *Physical Review D* **102**(6).

Hinton, J. (2004). The status of the H.E.S.S. project, *New Astronomy Reviews* **48**(5-6): 331–337.

Hooper, D. and Witte, S. J. (2017). Gamma rays from dark matter subhalos revisited: refining the predictions and constraints, *Journal of Cosmology and Astroparticle Physics* **4**: 018.
**URL:** http://adsabs.harvard.edu/abs/2017JCAP...04..018H

Hütten, M., Combet, C., Maier, G. and Maurin, D. (2016). Dark matter substructure modelling and sensitivity of the Cherenkov Telescope Array to Galactic dark halos, *JCAP* **2016**(09): 047–047.

Ibata, R. A., Lewis, G. F., Irwin, M. J. and Quinn, T. (2002). Uncovering cold dark matter halo substructure with tidal streams, *Monthly Notices of the Royal Astronomical Society* **332**(4): 915–920.

Ibata, R., Thomas, G., Famaey, B., Malhan, K., Martin, N. and Monari, G. (2020). Detection of Strong Epicyclic Density Spikes in the GD-1 Stellar Stream: An Absence of Evidence for the Influence of Dark Matter Subhalos?, *The Astrophysical Journal* **891**(2): 161.

Kelley, T., Bullock, J. S., Garrison-Kimmel, S., Boylan-Kolchin, M., Pawlowski, M. S. and Graus, A. S. (2019). Phat ELVIS: The inevitable effect of the Milky Way's disc on its dark matter subhaloes, *Monthly Notices of the Royal Astronomical Society* **487**(3): 4409–4423.

Knödlseder, J., Mayer, M., Deil, C., Cayrou, J.-B., Owen, E., Kelley-Hoskins, N., Lu, C.-C., Buehler, R., Forest, F., Louge, T., Siejkowski, H., Kosack, K., Gerard, L., Schulz, A., Martin, P., Sanchez, D., Ohm, S., Hassan, T. and Brau-Nogué, S. (2016). GammaLib and ctools, *A&A* **593**: A1.

Lorenz, E. (2004). Status of the 17 m MAGIC telescope, *New Astronomy Reviews* **48**(5-6): 339–344.

Lucie Gérard for the CTA Consortium (2015). Divergent pointing with the Cherenkov Telescope Array for surveys and beyond, *Proceedings of Science* .

MAGIC Collaboration (2016a). The major upgrade of the MAGIC telescopes, Part I: The hardware improvements and the commissioning of the system, *Astroparticle Physics* **72**: 61–75.

MAGIC Collaboration (2016b). The major upgrade of the MAGIC telescopes, Part II: A performance study using observations of the Crab Nebula, *Astroparticle Physics* **72**: 76–94.

Mateo, M. (1998). Dwarf Galaxies of the Local Group, *Annual Review of Astronomy and Astrophysics* **36**(1): 435–506.

Mirabal, N., Charles, E., Ferrara, E. C., Gonthier, P. L., Harding, A. K., Sánchez-Conde, M. A. and Thompson, D. J. (2016). 3FGL Demographics Outside the Galactic Plane using Supervised Machine Learning: Pulsar and Dark Matter Subhalo Interpretations, *The Astrophysical Journal* **825**: 69.
**URL:** *http://adsabs.harvard.edu/abs/2016ApJ...825...69M*

Mirabal, N., Frías-Martinez, V., Hassan, T. and Frías-Martinez, E. (2012). Fermi's SIBYL: mining the gamma-ray sky for dark matter subhaloes, *Monthly Notices of the Royal Astronomical Society* **424**: L64–L68.
**URL:** *http://adsabs.harvard.edu/abs/2012MNRAS.424L..64M*

Navarro, J. F., Frenk, C. S. and White, S. D. M. (1997). A Universal Density Profile from Hierarchical Clustering, *ApJ* **490**(2): 493–508.

Okamoto, T., Frenk, C. S., Jenkins, A. and Theuns, T. (2010). The properties of satellite galaxies in simulations of galaxy formation, *MNRAS* **406**(1): 208–222.

Sawala, T., Frenk, C. S., Fattahi, A., Navarro, J. F., Theuns, T., Bower, R. G., Crain, R. A., Furlong, M., Jenkins, A., Schaller, M. and Schaye, J. (2015). The chosen few: the low-mass haloes that host faint galaxies, *MNRAS* **456**(1): 85–97.

Sawala, T., Pihajoki, P., Johansson, P. H., Frenk, C. S., Navarro, J. F., Oman, K. A. and White, S. D. M. (2017). Shaken and stirred: the Milky Way's dark substructures, *MNRAS* **467**(4): 4383–4400.

Schoonenberg, D., Gaskins, J., Bertone, G. and Diemand, J. (2016). Dark matter subhalos and unidentified sources in the Fermi 3FGL source catalog, *Journal of Cosmology and Astroparticle Physics* **5**: 028.
**URL:** *http://adsabs.harvard.edu/abs/2016JCAP...05..028S*

Sciascio, G. D. (2016). The LHAASO experiment: from Gamma-Ray Astronomy to Cosmic Rays.
**URL:** *https://arxiv.org/abs/1602.07600*

Simon, J. D. (2019). The faintest dwarf galaxies, *Annual Review of Astronomy and Astrophysics* **57**(1): 375–415.

Smirnov, J. and Beacom, J. F. (2019). TeV-scale thermal WIMPs: Unitarity and its consequences, *Physical Review D* **100**(4).

Springel, V., Wang, J., Vogelsberger, M., Ludlow, A., Jenkins, A., Helmi, A., Navarro, J. F., Frenk, C. S. and White, S. D. M. (2008). The Aquarius Project: the subhaloes of galactic haloes, *Monthly Notices of the Royal Astronomical Society* **391**(4): 1685–1711.
**URL:** *https://ui.adsabs.harvard.edu/abs/2008MNRAS.391.1685S*

Strigari, L. E., Bullock, J. S., Kaplinghat, M., Diemand, J., Kuhlen, M. and Madau, P. (2007). Redefining the missing satellites problem, *The Astrophysical Journal* **669**(2): 676–683.

SWGO Collaboration (2019). The Southern Wide-Field Gamma-Ray Observatory (SWGO): A Next-Generation Ground-Based Survey Instrument for VHE Gamma-Ray Astronomy, *Astro2020 White Paper* .
**URL:** https://arxiv.org/abs/1907.07737

Szanecki, M., Sobczyńska, D., Niedźwiecki, A., Sitarek, J. and Bednarek, W. (2015). Monte Carlo simulations of alternative sky observation modes with the Cherenkov Telescope Array, *Astroparticle Physics* **67**: 33–46.

The Cherenkov Telescope Array Consortium (2017). *Science with the Cherenkov Telescope Array*, World Scientific.
**URL:** http://adsabs.harvard.edu/abs/2017arXiv170907997C

The Cherenkov Telescope Array Consortium (2021). Sensitivity of the Cherenkov Telescope Array to a dark matter signal from the Galactic centre, *Journal of Cosmology and Astroparticle Physics* **2021**(01): 057–057.
**URL:** http://dx.doi.org/10.1088/1475-7516/2021/01/057

van den Bosch, F. C., Ogiya, G., Hahn, O. and Burkert, A. (2017). Disruption of dark matter substructure: fact or fiction?, *Monthly Notices of the Royal Astronomical Society* **474**(3): 3043–3066.

VERITAS Collaboration (2002). VERITAS: the very energetic radiation imaging telescope array system, *Astroparticle Physics* **17**(2): 221–243.

VERITAS Collaboration (2017). Dark matter constraints from a joint analysis of dwarf spheroidal galaxy observations with VERITAS, *Physical Review D* **95**(8).

Zechlin, H.-S., Fernandes, M. V., Elsässer, D. and Horns, D. (2012). Dark matter subhaloes as gamma-ray sources and candidates in the first Fermi-LAT catalogue, *Astronomy and Astrophysics* **538**: A93.
**URL:** http://adsabs.harvard.edu/abs/2012A%26A...538A..93Z

Zechlin, H.-S. and Horns, D. (2012). Unidentified sources in the Fermi-LAT second source catalog: the case for DM subhalos, *Journal of Cosmology and Astroparticle Physics* **11**: 050.
**URL:** http://adsabs.harvard.edu/abs/2012JCAP...11..050Z

Zhu, Q., Marinacci, F., Maji, M., Li, Y., Springel, V. and Hernquist, L. (2016). Baryonic impact on the dark matter distribution in Milky Way-sized galaxies and their satellites, *MNRAS* **458**(2): 1559–1580.

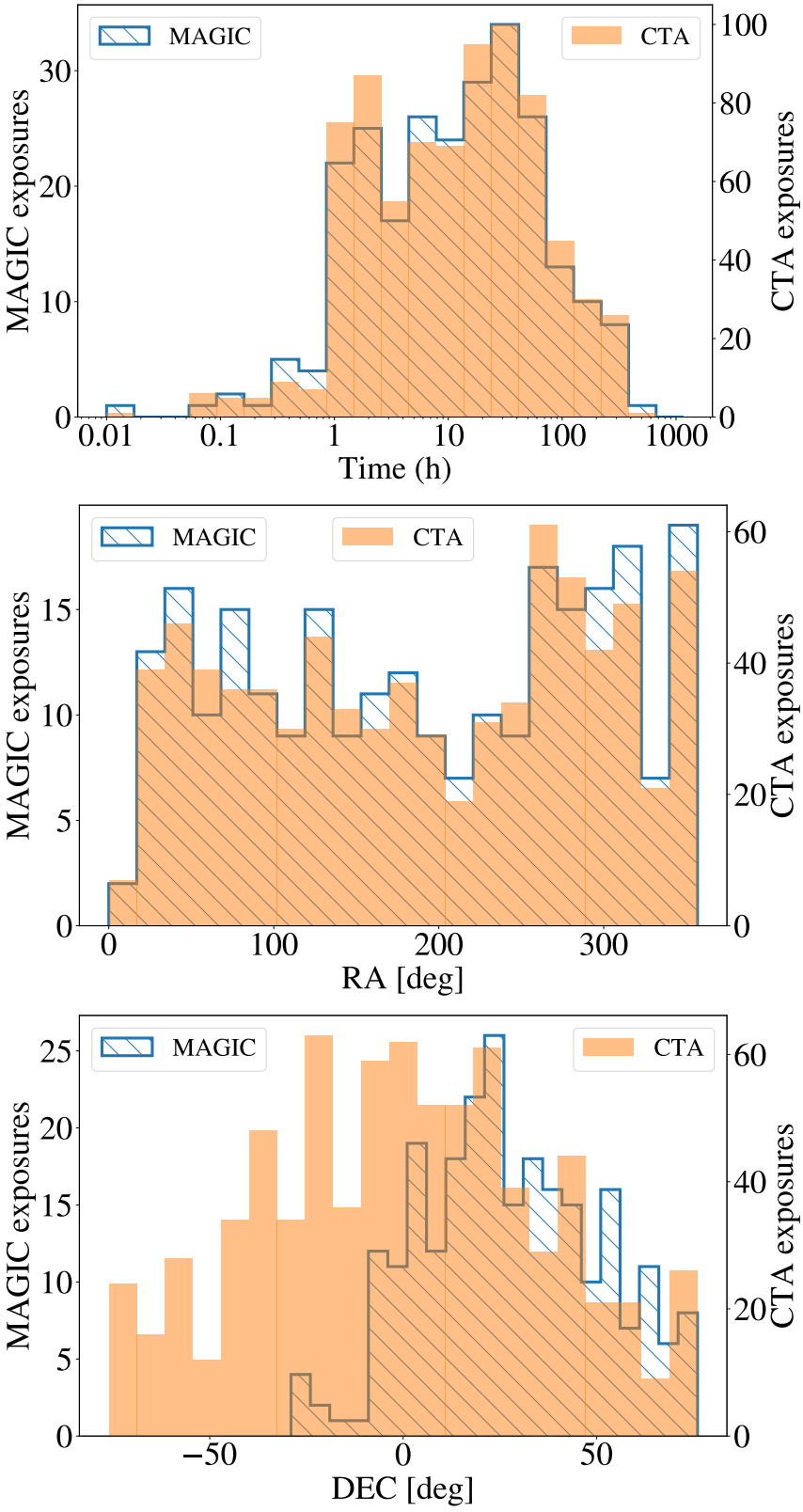


FIGURE 8.8: For a random realization, this figure shows the distribution of exposures in observation time (upper panel), RA (middle panel) and DEC (bottom panel), both for actual MAGIC stereo operations in 6.5 years and our extrapolation to 10 years of CTA observations. Note that the DEC distributions in the bottom panel must be different, as we assumed half of the observations to be performed by CTA South. See text for details.

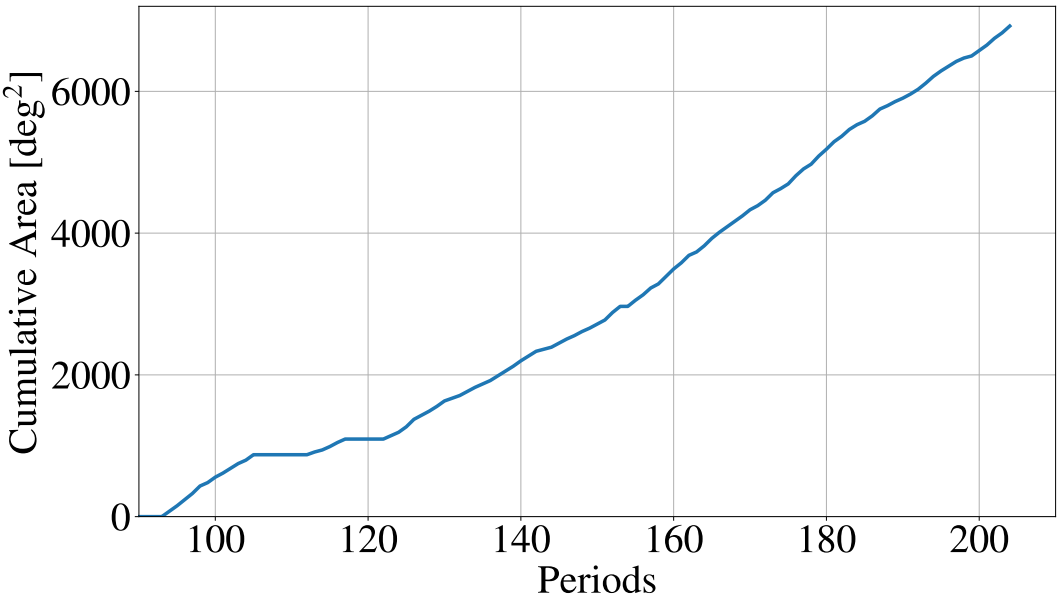


FIGURE 8.9: Growth of the cumulative exposure area as a function of period of observation (each period is equivalent to 29 days) for MAGIC stereo mode in 6.5 years. Except for some periods where no observations were made, the behavior is linear.

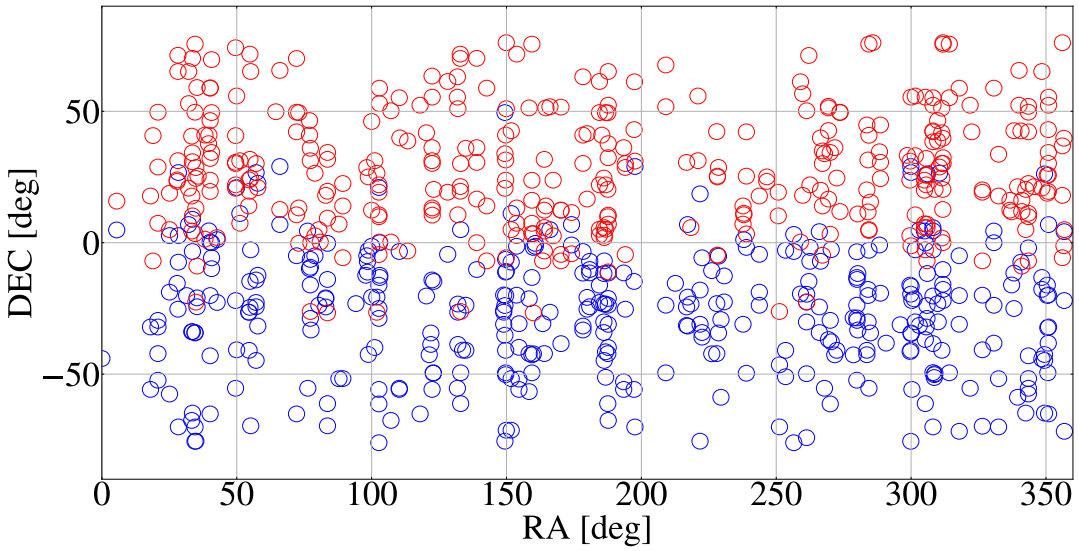


FIGURE 8.10: Map in equatorial coordinates of CTA pointings in 10 years of operation, extrapolated from 6.5 years of actual MAGIC stereo pointings, as obtained in a single random realization. Red circles are observations performed with CTA North, while blue are for CTA South. The area of each pointing is taken as a circle of 6 deg diameter. Note the overlaps between observations, which have been properly taken into account in the computation of the total effective area of exposure. See text for full details.

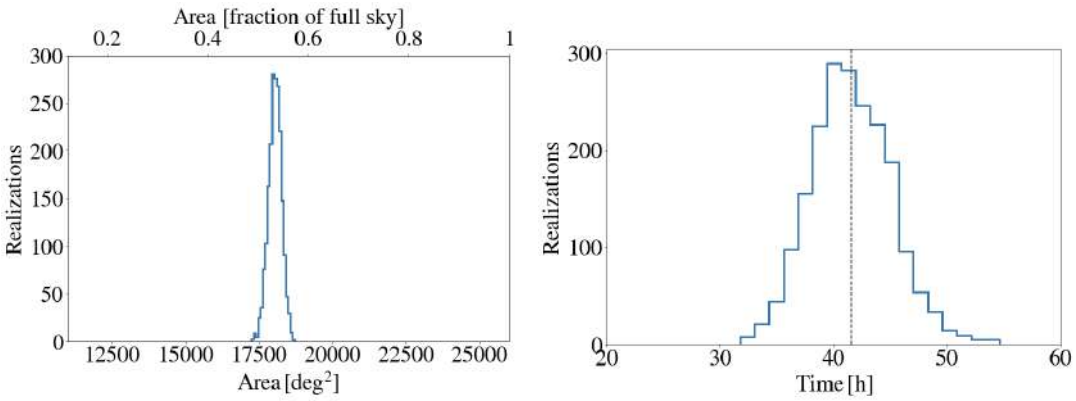


FIGURE 8.11: Distributions of the total effective area (left panel) and exposure time per pointing (right panel) in 10 years of CTA operation, extrapolated from 6.5 years of actual MAGIC stereo observations, as obtained after 2000 random realizations. The vertical line is the average values that we adopt to set constraints in Section 9.4. The corresponding 1-$\sigma$ uncertainties are below 2% in the case of the area and below 8% in the case of exposure time.

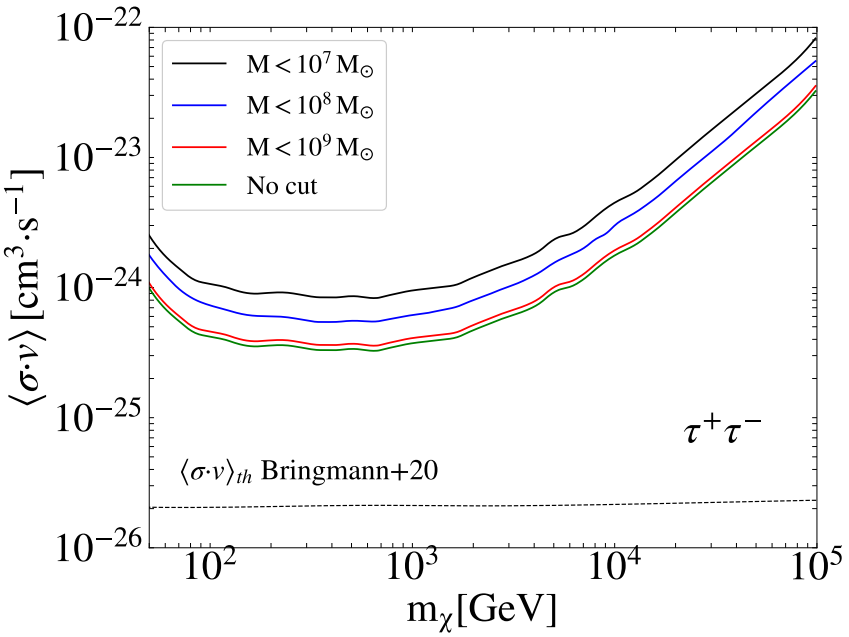


FIGURE 8.12: EXPO constraints (see Section 9.4 for the $\tau^+\tau^-$ annihilation channel, for different subhalo mass cuts. See discussion in the text for the motivation of the depicted values.

# Chapter 9

# X-ray and gamma-ray limits on the primordial black hole abundance from Hawking radiation

*Based on G. Ballesteros, J. Coronado-Blázquez and D. Gaggero, 2020, Phys. Lett. B,* ***808****, 135624*

## 9.1 Introduction

The isotropic background radiation that fills the Universe and extends over more than 16 orders of magnitude in frequency –from radio waves all the way up to high-energy gamma rays Hill et al. (2018)– carries information on the emission mechanisms of different astrophysical and cosmological sources over the history of the Universe, and can possibly shed further light on the nature of the elusive dark matter (DM) that constitutes the largest fraction of its mass.

We consider the hypothesis that the bulk of the DM is made up of (non-rotating) black holes of primordial origin (PBHs), formed from the collapse of overdense Hubble patches prior to the big-bang nucleosynthesis epoch Zel'dovich and Novikov (1966); Hawking (1971). We focus on the current PBH mass window for DM ranging from approximately $10^{17}$ g to $10^{19}$ g, revisiting the Hawking radiation constraints on their abundance from extragalactic gamma-ray data Carr et al. (2010) and showing how future gamma- and X-ray observations[1] with an increased sensitivity have the potential for discovering a population of PBHs comprising the totality of the DM.

This mass range is indeed particulary relevant for DM, given that it has been found that previously claimed femtolensing bounds Barnacka et al. (2012) were marred by an inadequate treatment of the involved optics, leaving much of that window open Katz et al. (2018). In addition, the $\sim$ 10% limit on the abundance of PBHs at $10^{19}$ g – $10^{20}$ g from the observed distribution of white dwarfs Graham et al. (2015), as well as from the disruption of neutron stars in the PBH mass range from $10^{19}$ g to $10^{23}$ g Capela et al. (2013) has been challenged Montero-Camacho et al. (2019), opening the possibility that PBHs of mass below $\sim 5 \times 10^{22}$ g –with higher masses being constrained by microlensing Niikura et al. (2019)– could explain all the DM. The lower end of the current PBH mass window for DM, at $\sim 10^{17}$ g, comes instead from Hawking evaporation limits. As we already mentioned, in this work we focus specifically on extragalactic gamma-ray bounds from evaporation Carr et al. (2010). However, there are other phenomena, related to Hawking radiation, which have been used to constrain this low mass region: the Voyager measurements of

[1] The frontier between gamma- and X-rays is not sharply defined. A reasonable distinction can be made setting it at $\sim$ 100 keV.

$e^{\pm}$ Boudaud and Cirelli (2019), the 511 keV positron-electron annihiliation line from INTEGRAL DeRocco and Graham (2019); Laha (2019); Dasgupta et al. (2020), the non-detection of a neutrino flux from PBH emission at Superkamiokande Dasgupta et al. (2020), distortions on the CMB anisotropies Poulin et al. (2017); Stocker et al. (2018), and the Galactic emission of gamma/X-rays Carr et al. (2016) (see also Laha et al. (2020)). The advantage of the bounds coming from the possible PBH extra-galatic emission is that they are free from Galactic propagation uncertainties. As we will see, making use of their full potential requires an adequate characterization of the emission from other astrophysical sources, mostly active galactic nuclei (AGNs) and blazars.

Hawking radiation Hawking (1975, 1974); Page and Hawking (1976); MacGibbon and Webber (1990); MacGibbon and Carr (1991) is an approximately thermal particle emission expected to be emitted by black holes, with temperature $T = (8\pi k_B)^{-1} c^2 \, m_P^2 / M \simeq 6 \times 10^{-8} M_\odot / M$ K, being $M$ the mass of the black hole, $M_\odot = 3 \times 10^{33}$ g the mass of the Sun and $m_P = \sqrt{\hbar \, c / G}$ the Planck Mass. In Ref. Carr et al. (2010), a conservative (but nonetheless stringent) upper bound on the cosmological PBH abundance was set for $M \lesssim 10^{17}$ g by comparing the predicted Hawking gamma-ray emission with the isotropic gamma-ray background in the approximate energy range 0.1 MeV — 10 GeV that was measured by EGRET Strong et al. (2004), Fermi-LAT Abdo et al. (2010) and COMPTEL Weidenspointner et al. (2000). This bound has recently been updated in Arbey et al. (2020) (with the data from the same experiments), finding a good agreement with Carr et al. (2010).

The main focus of our analysis is on the isotropic gamma- and X-ray background in the 10 keV – MeV domain. Using a power-law modeling of such background – motivated by the assumption that a population of unresolved extra-Galactic sources (mainly AGNs and blazars) represent the main contribution to it– we place an upper limit on the abundance of PBHs (as a function of their mass) by considering an array of datasets acquired by a variety of missions has been proposed over the latest decades. We also estimate the expected improvement in the bounds from a putative future experiment. We do so by assuming that such a (more sensitive) experiment will resolve a significantly larger number of individual AGNs and blazars and will therefore provide a lower isotropic unresolved background for energies above $\sim 200$ keV. We show that, under this assumption, a significantly better upper limit on the PBH abundance than the current one may be placed in the future. This result motivates the investment in future gamma- and X-ray experiments in this range, as well as in further theoretical studies geared towards a more precise modeling of astrophysical sources.

## 9.2 Hawking radiation from PBHs

The photon emission from a population of PBHs of mass $M$ accounting for a fraction $f = \Omega_{PBH}/\Omega_{DM}$ of the total DM density in the Universe is

$$\Phi_M = \frac{\mathrm{d}N}{\mathrm{d}E \, \mathrm{d}t} = f \frac{c \, \rho}{4\pi \, M} \int \mathrm{d}z \frac{e^{-\tau(z)}}{H(z)} \Psi_M[(1+z)E] \,, \tag{9.1}$$

where $\rho = 2.17 \times 10^{-30} \mathrm{g/cm^3}$ is the current DM density of the Universe Aghanim et al. (2020), and $H(z)$ is the Hubble rate of expansion as a function of redshift. The function $\Psi_M[E]$ denotes the differential flux emitted by a single PBH, as a function of the energy $E$, per unit of energy and time. For PBHs of masses above $10^{16}$ g is well

approximated by the primary[2] Hawking emission:

$$\Psi_M[E] = (2\pi\hbar)^{-1}\Gamma_s/(\exp(E/k_BT) - 1)\,, \tag{9.2}$$

where the so-called grey factor $\Gamma_s$ is a function of $M$ and $E$. In the high-energy limit $E \gg k_BT$, the grey factor approximately satisfies $\Gamma_s \propto (M/m_P)^2(E/m_P\,c^2)^2$; whereas for $E \ll k_BT$, $\Gamma_s \propto (M/m_P)^4(E/m_P\,c^2)^4$ MacGibbon and Webber (1990). These expressions are insufficient to render adequately the peak height and position of $\Psi_M[E]$, which is best computed numerically. To do so we use the public code BlackHawk Arbey and Auffinger (2019), which also allows to include the (subdominant) secondary emission. We find that the differential flux for BHs of mass between $10^{16}$g and $10^{20}$g can be approximated by

$$\Psi_M[E] \simeq \frac{2.5\times10^{21}\,\mathrm{GeV}^{-1}\mathrm{s}^{-1}}{(M_{18}\,E/E_0)^{-2.7} + (M_{18}\,E/E_0)^{6.7}}\,, \tag{9.3}$$

where $E_0 = 6.54\times10^{-5}$ GeV and $M_{18} \equiv M/10^{18}$g. This approximation is accurate to better than $\sim 1\%$ around the emission's peak (until $\Psi_M[E]$ decreases an order of magnitude), which is enough for our purposes. Nevertheless, we obtain the bounds on the PBH abundance from the instantaneous spectra given by BlackHawk.

The factor $(1+z)$ inside $\Psi_M[(1+z)E]$ accounts for the Doppler shift from the time of emission to the time of arrival to the detector. The optical depth $\tau(z)$ describes the attenuation due to the propagation of the signal over the relevant cosmological redshifts. Unlike for hard gamma rays, this is negligible for soft gamma-rays and $X$-rays. The integrand in Eq. 9.1 decreases very rapidly with $z$ and accurate results are obtained integrating up to $z \sim \mathcal{O}(100)$.

## 9.3 The X-ray and gamma-ray AGN background

There has been a considerable effort dedicated to interpreting the measurements of the X-ray and gamma-ray background from keV energies all the way up to $\sim$ 100 GeV in terms of a superposition of a large number of unresolved extra-Galactic sources. In particular, the data in the range $\sim$ 5–200 keV observed by *Swift*/BAT Barthelmy et al. (2005), MAXI Matsuoka et al. (2009), ASCA Tanaka et al. (1994), XMM-Newton Lumb (2012), Chandra Weisskopf et al. (2000) and ROSAT McHardy et al. (1998) are well reproduced by a population synthesis model of active galactic nuclei (AGNs) developed by Ueda et al. in Ueda et al. (2014) (see the blue dotted line in Figure 9.1). AGNs are powered by gas accretion onto a supermassive black hole and are very efficient X-ray emitters. The model of Ueda et al. (2014) is based on the extrapolation of the luminosity functions of AGNs in different redshift ranges inferred by a sample of 4039 AGNs in soft (up to 2 keV) and/or hard X-ray bands (>2 keV). The objects in the sample include both Compton-thin and Compton-thick AGNs (with the latter being heavily obscured by dust). As can be seen if Figure 9.1, this AGN modeling fails to describe adequately the SMM data.

Indeed, for energies above $\sim 50-100$ keV the contribution from blazars is expected to become progressively more important. These objects correspond to the AGNs that are detected at a small angle between the accretion disk axis and the observer line of sight Urry and Padovani (1995); together with star-forming galaxies

[2]The spectrum of BHs may feature a secondary emission component, depending on their mass, which is due to the interactions among the primary emitted particles, see e.g. Carr et al. (2010).

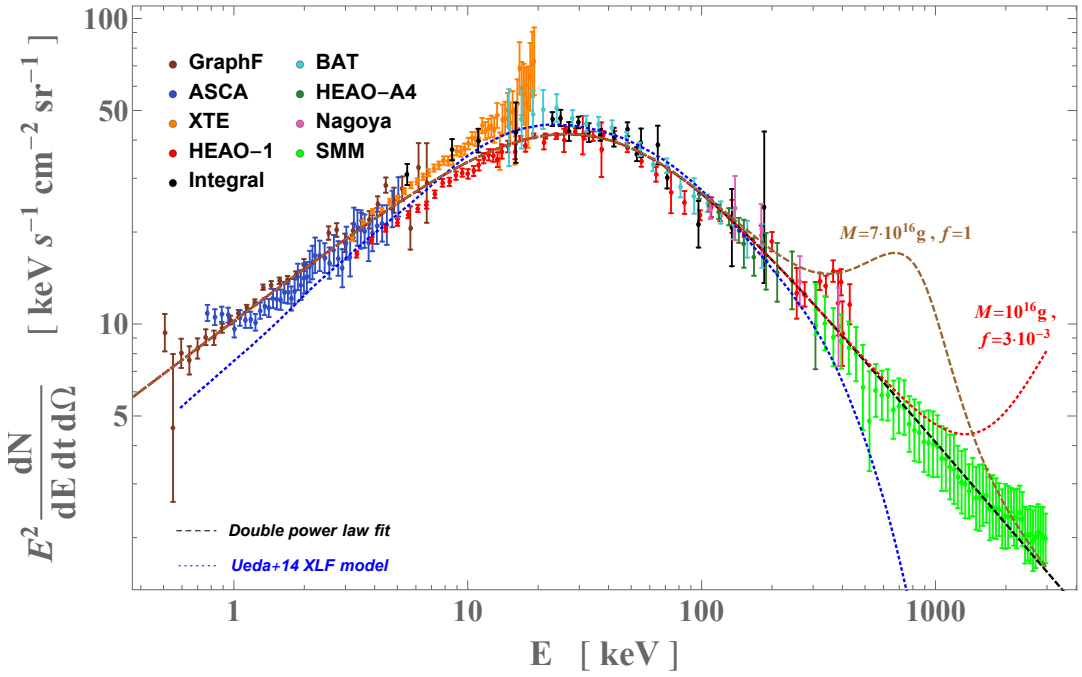


FIGURE 9.1: Cosmic X-ray background spectrum, as measured by various experiments. Overimposed are the Ueda+14 model (blue dashed line), the fit to a double power-law (black dashed line) of Eq. 9.4, and the corrections to the latter due to two hypothetical monochromatic PBH distributions with different masses $M$ and cosmological abundances $f = \Omega_{PBH}/\Omega_{DM}$.

and radio galaxies, they are thought to dominate the GeV-TeV gamma-ray isotropic background measured by Fermi-LAT (not shown in Figure 9.1).

Although the details of the intermediate MeV – GeV domain are still not clearly understood (see in particular the discussion in Tavani et al. (2018)), the previous considerations lead us to employ the working assumption that a combination of different classes of extra-Galactic emitters explain the X-ray and gamma-ray unresolved diffuse background in a wide energy range and that the emission from these populations of sources can be modeled as a superposition of featureless power-laws.

Therefore, in the approximate energy range going from 20 keV to 3000 keV, which corresponds to the region where the Hawking emission from BHs in the mass range $10^{16}$ g – $10^{19}$ g can contribute importantly to the Universe's diffuse spectrum, we model the astrophysical background as a double power-law fit to the data from the SMM Watanabe et al. (1997), Nagoya balloon Fukada et al. (1975), HEAO–1 and HEAO-A4 Gruber et al. (1999); Kinzer et al. (1997) experiments. Concretely, we use the following proxy for the combined AGN and blazar emission:

$$\Phi_{\rm AGN} = \frac{{\rm d}N}{{\rm d}E\,{\rm d}t} = \frac{A}{(E/E_b)^{n_1} + (E/E_b)^{n_2}}\,. \tag{9.4}$$

For instance, assuming zero contribution to the data from PBH evaporation, the best fit is: $E_b = 35.6966$ keV, $A = 0.0642\,{\rm keV}^{-1}{\rm s}^{-1}{\rm cm}^{-2}{\rm sr}^{-1}$, $n_1 = 1.4199$ and $n_2 = 2.8956$; see the black dashed line in Figure 9.1.

## 9.4 Constraints and prospects on $f$

We present now our results on the current upper limits on the PBH abundance $f = \Omega_{\rm PBH}/\Omega_{\rm DM}$, in the mass window of interest, and estimate the prospects for a future MeV mission. We recall that we assume a population of non-rotating PBHs. Angular momentum makes black holes evaporate faster, making the bounds on their abundance stronger Arbey et al. (2020). For PBHs formed during radiation domination –which is the most common scenario– the assumption of negligible angular momentum is the most reasonable one. Some amount of angular momentum may be expected if the PBHs form during a phase of early matter domination Harada et al. (2017). A moderate level of rotation would not change our results significantly. Only nearly extremal black holes (which is unlikely in common PBH formation models) would lead to a significant difference. In this sense, our bounds and forecast should be regarded as conservative.

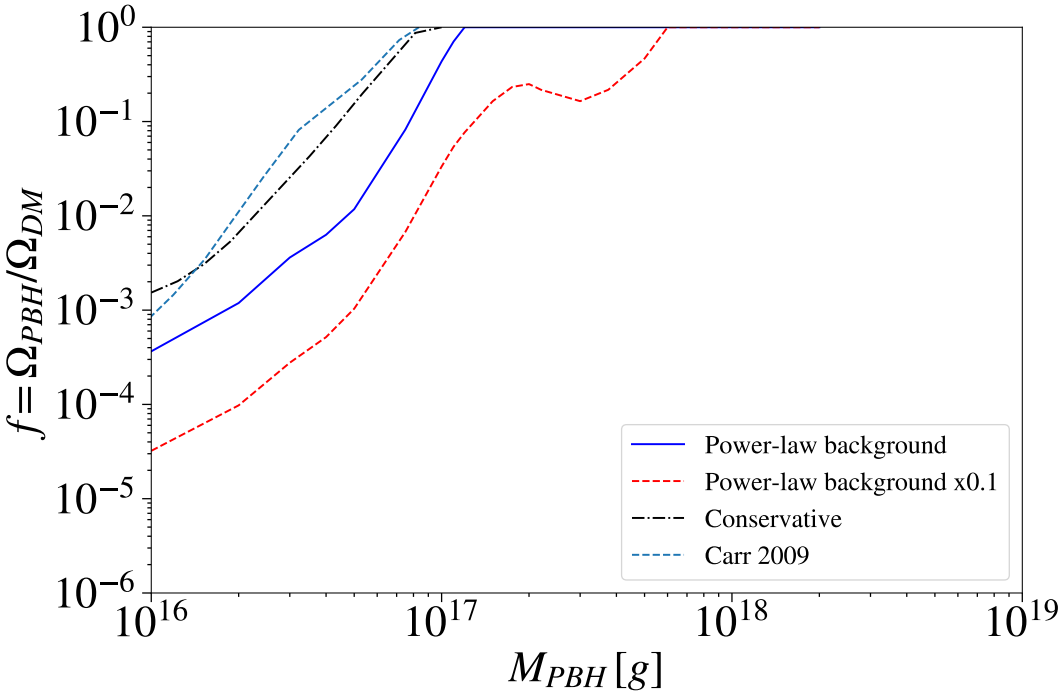


FIGURE 9.2: 95% c.l. upper limits on the PBH abundance versus the PBH mass assuming a monochromatic mass population. The black dot-dashed line is the result of the present work neglecting the background contribution from AGNs. The light blue-dotted line is the analogous result of Carr et al. (2010), see also Arbey and Auffinger (2019). The blue continuous line is the bound obtained assuming a power-law modeling of the AGN and blazar contribution to the observed spectrum. The red dashed curve indicates the sensitivity achievable with an experiment capable of reducing the astrophysical background by a factor of 10

⋆ **Current bound: Conservative approach.**

We start by deriving the present bound on $f$ under the most conservative approach, i.e. without assuming any astrophysical modeling of the data, as done in Carr et al. (2010) (see also Arbey et al. (2020)). Under the assumption that the data

are Gaussian distributed, we compute the estimator

$$\hat{\chi}^2 = \sum (D - E^2\Phi_M)^2/\Delta^2 \tag{9.5}$$

over the energy bins for which the PBH emission $\Phi_M$ is larger than the X-ray data $D$ shown in Figure 9.1 and whose errors are denoted $\Delta$ in Eq. 9.5. The allowed PBH fraction $f$ for a given PBH mass $M$ at 95% c.l. corresponds to values of $\hat{\chi}^2$ smaller than the threshold

$$\hat{\chi}^2 \leq \chi^2_{0.05}(N-1)\,, \tag{9.6}$$

where $N$ –which depends on $f$– is the number of bins in which the model overshoots the data. The threshold and the estimator are computed as functions of $f$ by adopting $N-1$ as the number of degrees of freedom for the $\chi^2$ distribution. The bound is shown in Figure 9.2 as a black dot-dashed line. Our result is in good agreement with those of Carr et al. (2010) (see blue dotted line) and Arbey et al. (2020) in the PBH mass region ($M \geq 10^{16}$g) that we consider, even though in the (relevant) region between 1 MeV and 20 MeV those works used COMPTEL data whereas we use SMM, which has a much smaller error and a broader range.

⋆ **Sensitivity reach with the current data.**

We assume now a double power-law fit of the AGN background akin to that of Eq. 9.4 and consider the following estimator, evaluated *over all energy bins* (of the data we have used to obtain the fit):

$$\hat{\chi}^2 = \sum \left(D - E^2\Phi_M - E^2\Phi_{\rm AGN}\right)^2/\Delta^2\,. \tag{9.7}$$

The upper limit on the PBH abundance is set at the value of $f$ above which $\hat{\chi}^2$ worsens beyond the threshold for the 95% c.l. with respect to the minimum: i.e. the threshold is set as

$$\hat{\chi}^2 - \hat{\chi}^2_{min} \leq \chi^2_{0.05}(1) \simeq 3.84\,. \tag{9.8}$$

Importantly, for each mass bin we obtain the best-fitting combination of AGN and blazar plus PBH emission by letting free the PBH fraction $f$ as well as the four parameters ($n_1$, $n_2$, $E_b$ and $A$) of Eq. 9.4, and then vary the parameter $f$ (recomputing the AGN and blazar contribution at each step) until the threshold above is reached.

In Figure 9.2 we show the results of both approaches (*conservative* and *sensitivity reach*) for 95% c.l. upper limits on $f$. Regarding the conservative approach (black solid line), our constraints are in good agreement with those from Carr et al. (2010) (blue dotted line), while the bound assuming the power-law AGN model (blue solid line) is a factor $\sim 10$ stronger for the same $M$ and reaches larger PBH masses (up to about $7 \times 10^{17}$g).

⋆ **Future prospects.**

In the forthcoming years, both the hard X-ray and the MeV gamma-ray sky will be probed with increasing accuracy by several planned space observatories. In the MeV range, a variety of space missions have been proposed over the last years, for instance: e-ASTROGAM Tavani et al. (2018), AMEGO Caputo et al. (2019), AdEPT Hunter et al. (2014), COSI Tomsick et al. (2019), SMILE Tanimori et al. (2015). In the

hard X-ray domain, the instrument onboard the ASTRO-H mission Matsumoto et al. (2018) will measure X-rays up to 80 keV with unprecedented accuracy.

All these instruments will detect a larger number of point sources, both AGNs and blazars. They are thus expected to characterize a lower isotropic extragalactic background due to unresolved point sources. As a consequence, a hypothetical PBH signal will be easier to detect. It is therefore important to provide a quantitative estimate of the potential of possible future experiments in either setting a stronger upper limit on the PBH abundance in the mass range under investigation, or identifying a PBH signal with sufficient significance.

A careful assessment on how the expected increase in point-source sensitivity, especially in the MeV domain, results in a lower isotropic background due to sub-threshold sources is beyond the scope of the present work[3]. Instead, we present a simple but useful calculation based on straightforward extrapolations of observed luminosity functions at low redshift. If we assume that most of the isotropic background in the MeV domain is due to blazars, and we assume a single-power law luminosity function of the form Ajello et al. (2009)

$$N(S) = N_0 (S/S_0)^{-\alpha}\,, \tag{9.9}$$

where $S$ is the source flux and $\alpha$ is a positive number, the isotropic background at redshift zero due to unresolved sources is simply given by the integral:

$$\mathcal{I}(S_a, S_b) = \int_{S_0}^{S_{th}} S\,\frac{dN}{dS}\,dS\,, \tag{9.10}$$

where $S_0$ is the minimum luminosity and $S_{th}$ is the detection threshold of the experiment. If we now consider two experiments with different thresholds $S_1$ and $S_2$, the ratio between the unresolved flux in the two cases is

$$r = \frac{\mathcal{I}(S_2, S_0)}{\mathcal{I}(S_1, S_0)}\,. \tag{9.11}$$

In the limit of $S_0 \ll S_1, S_2$ and for a exponent $0 < \alpha < 1$ (like the ones found in Ajello et al. (2009)), we get:

$$r \simeq \left(\frac{S_2}{S_1}\right)^{1-\alpha}\,. \tag{9.12}$$

Let us now consider a future experiment such as AMEGO, which is able to provide a factor of $\sim 10$ increase in point-source sensitivity with respect to COMPTEL at 1 MeV Caputo et al. (2019). Let us assume a single power-law luminosity function for a population of blazars, as in Eq. 9.9, following Ajello et al. (2009). For obtaining an order-of-magnitude estimate, we can ignore a possible (but mild) redshift dependence of the exponent $\alpha$. The above formalism implies that a background reduction by a factor of 10 is possible with a luminosity function exponent $\alpha \simeq 0.5$, which is commensurate with the values quoted in Ajello et al. (2009).

Given these considerations, we consider here two different scenarios, characterized by factors of 10 and 100 reduction in the diffuse, unresolved background, accompanied by a reduction by the same factor of its uncertainty. We generate mock data according to this prescription, and adopt the same procedure we applied to the current data in the *sensitivity reach* approach described previously. The results are

[3]Notice that such an analysis can be done only on a case-by-case basis, from the detailed specifications of the experiments (which in several cases are still being decided)

shown in Figure 9.2. The red dashed line indicates a potentially significant improvement of the current upper limits for a factor 10 reduction, together with a notable extension towards larger masses.

## 9.5 Discussion and Conclusions

In this paper we have studied the upper limits on the abundance of primordial black holes from X-ray and gamma-ray Hawking radiation, as a function of mass and assuming a monochromatic distribution in the $10^{16}$ g – $10^{19}$ g mass range. This approximate mass window is particularly interesting not only for the DM problem but also from the model-building point of view. The known examples of the conceptually simplest mechanism capable of producing PBHs from single-field inflation –based on an approximate inflection point in the potential Ivanov et al. (1994), see e.g. Garcia-Bellido and Ruiz Morales (2017); Kannike et al. (2017); Ballesteros and Taoso (2018); Cicoli et al. (2018); Dalianis et al. (2019); Ballesteros, Rey and Rompineve (2020); Ballesteros, Rey, Taoso and Urbano (2020)– tend to do so in this range, once a reasonable fit to the CMB data at cosmological scales is imposed, see e.g. the related discussion in Ballesteros and Taoso (2018). As discussed in the introduction, this mass range is within the currently most promising region for the existence of a significant contribution of PBHs to the DM.

We have first computed the upper limit with a conservative approach, by requiring that the expected signal from PBHs does not overshoot the diffuse (extragalactic) background. The bound we have obtained is mostly driven by SMM data and agrees well with the results presented in Carr et al. (2010); Arbey et al. (2020), which instead used COMPTEL data in the relevant energy range. This bound is competitive with the recently derived upper limits based on the Voyager $e^{\pm}$ data Boudaud and Cirelli (2019) and extends to larger masses.

Then, we have considered a less conservative approach, which takes into account in a simple way the expected effect of known classes of unresolved astrophysical sources –AGNs and blazars in particular– that are thought to provide the dominant contribution to the X-ray and gamma-ray diffuse isotropic background. Under the well-motivated (and common in the literature, see Ajello et al. (2008), Ueda et al. (2014)) assumption that the current data are mainly reproduced by such sources and that they can be characterized by a double power-law, we derive a stronger upper limit on the PBH abundance based on a simultaneous fit of current data to the emission of these sources and PBHs in the MeV domain. This (sensitivity reach) bound is about an order of magnitude stronger than the conservative upper limit described above.

We have also considered the potential of a future, more sensitive, experiment in the MeV domain that could resolve a larger number of individual sources, therefore providing a lower and more accurate estimate of the diffuse unresolved background. The prospects, supported by the extrapolation of currently measured AGN and blazar luminosity functions, are very promising: We remark in particular that PBH masses as large as $10^{18}$ g are within reach under the assumption of a background reduction by a factor of 10.

The exploration of the diffuse photon emission in the low-energy gamma-ray (or upper X-ray range) is therefore a promising avenue towards a possible future detection of a signal associated to a population of PBHs that may constitute a significant part –perhaps even all– of the DM in the Universe.

In order to obtain further progress in this promising PBH mass region for DM ($\gtrsim 10^{17}$g), a more sensitive experiment is needed both in the MeV domain and (particularly) in the keV one, and a more detailed understanding of the population of astrophysical sources that contribute to the bulk of the diffuse background is essential. Above 1 MeV, such modeling should potentially include not only the contributions from sources (AGNs and blazars) that are known to be dominant in the sub- and sup-Mev bands, but also possible currently subdominant sources.

For a fixed value of the PBH abundance $f$, the emission $\Phi_M$ grows if the mass $M$ of the PBHs is *decreased* –we recall that we assumed a monochromatic distribution– and, simultaneously, the location of the peak of the PBH moves towards higher energies. This can be understood qualitatively (disregarding the secondary emission) by applying the scaling discussed in Section 9.2. As the measured diffuse background has a decreasing overall tendency from $\sim 30$ keV to $\sim 10^3$ MeV (see Hill et al. (2018)), the bounds on the PBH abundance become stronger than those shown in figure 9.2 for smaller masses (below $10^{16}$ g). This low mass region is thus of no relevance for the DM problem and we have not considered it in this work. It is interesting though that the emission of a bright but sub-dominant population of PBHs of mass $\mathcal{O}(10^{15}$ g - $10^{16}$ g) would peak in the 1-10 MeV region. In this energy range, the Compton and Fermi X-ray data present a noticeable change in slope with respect to that of SMM (see e.g. figure 7 of ref. Hill et al. (2018)). This energy region of the spectrum of the Universe is still not fully characterized from a theoretical point of view. These features make it a tantalizing target for the search of potentially exotic emitters (and subdominant PBHs in particular). Indeed, the bounds on the PBH abundance from gamma-rays in this region Carr et al. (2010) necessarily use the approach that we have termed *conservative* (i.e. no astrophysical background is assumed).

Returning now to PBHs as a dark matter candidate, i.e. for masses $\sim 10^{18}$ g, the fact that $\Phi_M$ decreases as $M$ increases (and the measured diffuse background increases at the corresponding, lower, energies) a more accurate measurement and modeling of the soft X-ray diffuse background may play, as we have argued, a crucial role towards a potential discovery or, at least, to strengthen current bounds substantially. To conclude, we remark that there exist other channels for PBH detection in the mass window relevant for DM. In particular, the energy injection associated to Hawking emission around or just after recombination can be probed with CMB data Poulin et al. (2017). Also, if the effect occurs during the reionization epoch it can be potentially detectable in the 21 cm absorption line of neutral Hydrogen Clark et al. (2018). Moreover, the positron emission by PBHs of mass around $10^{17}$ g has been recently used to set a bound on $f$ using the keV line, which can improve over the gamma-ray bound, depending on the assumed Galactic density profile DeRocco and Graham (2019). All these channels are complementary and their further exploration could help to identify or rule out a significant population of PBHs in this promising mass window.

## Bibliography

Abdo, A. et al. (2010). Spectrum of the Isotropic Diffuse Gamma-Ray Emission Derived from First-Year Fermi Large Area Telescope Data, *Phys. Rev. Lett.* **104**(10): 101101.

Aghanim, N. et al. (2020). Planck 2018 results. VI. Cosmological parameters, *Astronomy & Astrophysics* **641**: A6.

Ajello, M., Costamante, L., Sambruna, R. M., Gehrels, N., Chiang, J., Rau, A., Escala, A., Greiner, J., Tueller, J., Wall, J. V. and Mushotzky, R. F. (2009). The Evolution of Swift/BAT Blazars and the Origin of the MeV Background, *APJ* **699**(1): 603–625.

Ajello, M. et al. (2008). Cosmic X-ray background and Earth albedo Spectra with Swift/BAT, *Astrophys. J.* **689**: 666.

Arbey, A. and Auffinger, J. (2019). BlackHawk: A public code for calculating the Hawking evaporation spectra of any black hole distribution, *Eur. Phys. J. C* **79**(8): 693.

Arbey, A., Auffinger, J. and Silk, J. (2020). Constraining primordial black hole masses with the isotropic gamma ray background, *Phys. Rev. D* **101**(2): 023010.

Ballesteros, G., Rey, J. and Rompineve, F. (2020). Detuning primordial black hole dark matter with early matter domination and axion monodromy, *Journal of Cosmology and Astroparticle Physics* **06**: 014.

Ballesteros, G., Rey, J., Taoso, M. and Urbano, A. (2020). Primordial black holes as dark matter and gravitational waves from single-field polynomial inflation, *Journal of Cosmology and Astroparticle Physics* **07**: 025.

Ballesteros, G. and Taoso, M. (2018). Primordial black hole dark matter from single field inflation, *Phys. Rev.* **D97**(2): 023501.

Barnacka, A., Glicenstein, J. F. and Moderski, R. (2012). New constraints on primordial black holes abundance from femtolensing of gamma-ray bursts, *Phys. Rev.* **D86**: 043001.

Barthelmy, S. D. et al. (2005). The Burst Alert Telescope (BAT) on the SWIFT Midex Mission, *Space Science Reviews* **120**(3-4): 143–164.

Boudaud, M. and Cirelli, M. (2019). Voyager 1 $e^{\pm}$ Further Constrain Primordial Black Holes as Dark Matter, *Phys. Rev. Lett.* **122**(4): 041104.

Capela, F., Pshirkov, M. and Tinyakov, P. (2013). Constraints on primordial black holes as dark matter candidates from capture by neutron stars, *Phys. Rev. D* **87**(12): 123524.

Caputo, R. et al. (2019). All-sky Medium Energy Gamma-ray Observatory: Exploring the Extreme Multimessenger Universe.

Carr, B. J., Kohri, K., Sendouda, Y. and Yokoyama, J. (2010). New cosmological constraints on primordial black holes, *Phys. Rev.* **D81**: 104019.

Carr, B., Kohri, K., Sendouda, Y. and Yokoyama, J. (2016). Constraints on primordial black holes from the Galactic gamma-ray background, *Phys. Rev. D* **94**(4): 044029.

Cicoli, M., Diaz, V. A. and Pedro, F. G. (2018). Primordial Black Holes from String Inflation, *Journal of Cosmology and Astroparticle Physics* **1806**(06): 034.

Clark, S., Dutta, B., Gao, Y., Ma, Y.-Z. and Strigari, L. E. (2018). 21 cm limits on decaying dark matter and primordial black holes, *Phys. Rev.* **D98**(4): 043006.

Dalianis, I., Kehagias, A. and Tringas, G. (2019). Primordial black holes from Î±-attractors, *Journal of Cosmology and Astroparticle Physics* **1901**: 037.

Dasgupta, B., Laha, R. and Ray, A. (2020). Neutrino and Positron Constraints on Spinning Primordial Black Hole Dark Matter, *Physical Review Letters* **125**(10).

DeRocco, W. and Graham, P. W. (2019). Constraining Primordial Black Hole Abundance with the Galactic 511 keV Line, *Phys. Rev. Lett.* **123**(25): 251102.

Fukada, Y. et al. (1975). Rocket observation of energy spectrum of diffuse hard X-rays, *Astrophysics and Space Science* **32**(1): L1–L5.

Garcia-Bellido, J. and Ruiz Morales, E. (2017). Primordial black holes from single field models of inflation, *Phys. Dark Univ.* **18**: 47–54.

Graham, P. W., Rajendran, S. and Varela, J. (2015). Dark Matter Triggers of Supernovae, *Phys. Rev.* **D92**(6): 063007.

Gruber, D. E. et al. (1999). The Spectrum of Diffuse Cosmic Hard X-Rays Measured with HEAO 1, *The Astrophysical Journal* **520**(1): 124–129.

Harada, T., Yoo, C.-M., Kohri, K. and Nakao, K.-I. (2017). Spins of primordial black holes formed in the matter-dominated phase of the Universe, *Phys. Rev. D* **96**(8): 083517. [Erratum: Phys.Rev.D 99, 069904 (2019)].

Hawking, S. W. (1971). Gravitationally collapsed objects of very low mass, *Mon. Not. Roy. Astron. Soc.* **152**: 75.

Hawking, S. W. (1974). Black hole explosions, *Nature* **248**: 30–31.

Hawking, S. W. (1975). Particle Creation by Black Holes, *Commun. Math. Phys.* **43**: 199–220.

Hill, R., Masui, K. W. and Scott, D. (2018). The Spectrum of the Universe, *The Universe* **72**: 663–688.

Hunter, S. D. et al. (2014). A Pair Production Telescope for Medium-Energy Gamma-Ray Polarimetry, *Astropart. Phys.* **59**: 18–28.

Ivanov, P., Naselsky, P. and Novikov, I. (1994). Inflation and primordial black holes as dark matter, *Phys. Rev.* **D50**: 7173–7178.

Kannike, K., Marzola, L., Raidal, M. and Veermäe, H. (2017). Single Field Double Inflation and Primordial Black Holes, *Journal of Cosmology and Astroparticle Physics* **1709**(09): 020.

Katz, A., Kopp, J., Sibiryakov, S. and Xue, W. (2018). Femtolensing by Dark Matter Revisited, *Journal of Cosmology and Astroparticle Physics* **1812**: 005.

Kinzer, R. L. et al. (1997). Diffuse Cosmic Gamma Radiation Measured HEAO 1, *The Astrophysical Journal* **475**(1): 361–372.

Laha, R. (2019). Primordial Black Holes as a Dark Matter Candidate Are Severely Constrained by the Galactic Center 511 keV $\gamma$-Ray Line, *Phys. Rev. Lett.* **123**(25): 251101.

Laha, R., Muñoz, J. B. and Slatyer, T. R. (2020). INTEGRAL constraints on primordial black holes and particle dark matter, *Physical Review D* **101**(12).

Lumb, D. H. (2012). X-ray Multi-mirror Mission (XMM-Newton) observatory, *Optical Engineering* **51**(1): 011009.

MacGibbon, J. H. and Carr, B. J. (1991). Cosmic rays from primordial black holes, *Astrophys. J.* **371**: 447–469.

MacGibbon, J. H. and Webber, B. R. (1990). Quark and gluon jet emission from primordial black holes: The instantaneous spectra, *Phys. Rev.* **D41**: 3052–3079.

Matsumoto, H. et al. (2018). Inorbit Performance of the Hard X-ray Telescope (HXT) on board the Hitomi (ASTRO-H) satellite, *J. Astron. Telesc. Instrum. Syst.* **4**(1): 011212.

Matsuoka, M. et al. (2009). The MAXI mission on the ISS: Science and instruments for monitoring all-sky x-ray images, *Publications of the Astronomical Society of Japan* **61**(5): 999–1010.

McHardy, I. M. et al. (1998). The origin of the cosmic soft x-ray background: optical identification of an extremely deep ROSAT survey, *Monthly Notices of the Royal Astronomical Society* **295**(3): 641–671.

Montero-Camacho, P., Fang, X., Vasquez, G., Silva, M. and Hirata, C. M. (2019). Revisiting constraints on asteroid-mass primordial black holes as dark matter candidates, *Journal of Cosmology and Astroparticle Physics* **2019**(08): 031–031.

Niikura, H. et al. (2019). Microlensing constraints on primordial black holes with the Subaru/HSC Andromeda observation, *Nat. Astron.* **3**(6): 524–534.

Page, D. N. and Hawking, S. W. (1976). Gamma rays from primordial black holes, *Astrophys. J.* **206**: 1–7.

Poulin, V., Lesgourgues, J. and Serpico, P. D. (2017). Cosmological constraints on exotic injection of electromagnetic energy, *Journal of Cosmology and Astroparticle Physics* **03**: 043.

Stocker, P., Kramer, M., Lesgourgues, J. and Poulin, V. (2018). Exotic energy injection with ExoCLASS: Application to the Higgs portal model and evaporating black holes, *Journal of Cosmology and Astroparticle Physics* **03**: 018.

Strong, A. W., Moskalenko, I. V. and Reimer, O. (2004). A new determination of the extragalactic diffuse gamma-ray background from egret data, *Astrophys. J.* **613**: 956–961.

Tanaka, Y., Inoue, H. and Holt, S. S. (1994). The X-ray astronomy satellite ASCA, *Publications of the Astronomical Society of Japan* **46**: L37–L41.

Tanimori, T. et al. (2015). An Electron-Tracking Compton Telescope for a Survey of the Deep Universe by MeV gamma-rays, *Astrophys. J.* **810**(1): 28.

Tavani, M. et al. (2018). Science with e-ASTROGAM: A space mission for MeV-GeV gamma-ray astrophysics, *JHEAp* **19**: 1–106.

Tomsick, J. A. et al. (2019). The Compton Spectrometer and Imager, *Astro2020 White Paper* .

Ueda, Y., Akiyama, M., Hasinger, G., Miyaji, T. and Watson, M. G. (2014). Toward the Standard Population Synthesis Model of the X-Ray Background: Evolution of X-Ray Luminosity and Absorption Functions of Active Galactic Nuclei Including Compton-Thick Populations, *Astrophys. J.* **786**: 104.

Urry, C. M. and Padovani, P. (1995). Unified schemes for radio-loud active galactic nuclei, *Publ. Astron. Soc. Pac.* **107**: 803.

Watanabe, K. et al. (1997). The cosmic gamma-ray background from supernovae, *AIP Conference Proceedings*, AIP.

Weidenspointner, G. et al. (2000). The comptel instrumental line background, *AIP Conf. Proc.* **510**(1): 581–585.

Weisskopf, M. C. et al. (2000). Chandra X-ray Observatory (CXO): overview, *in* J. E. Truemper and B. Aschenbach (eds), *X-Ray Optics, Instruments, and Missions III*, SPIE.

Zel'dovich, Y. B. and Novikov, I. D. (1966). The Hypothesis of Cores Retarded during Expansion and the Hot Cosmological Model, *Ya. Astron.Zh.* **43**: 758.

# Chapter 10

# Conclusions and future work

At this writing, dark matter (DM) ultimate nature remains a mystery. The searches for DM interactions –aside from the gravitational effects which lead to proofs of its existence– have developed in the last decades. Indeed, such searches, although have not yielded a conclusive DM signal, have gathered fields such as astrophysics, particle physics and cosmology into a common goal, with several synergies between such disciplines.

Indirect searches, aiming for the detection of by-products of DM annihilation or decay, are one of the most promising venues for the DM quest in models such as WIMPs, well motivated from the theoretical point of view. In particular, gamma rays, the most energetic radiation in the electromagnetic spectrum, are a "golden channel" for this search strategy. In order to search for possible DM signatures with gamma rays, the high-energy background, rich in diverse processes, must be well characterized and understood.

This Thesis explored such venues with the current and future generation of gamma-ray observatories, namely space-based *Fermi*-LAT, and ground-based HAWC and CTA. Our main interest was dark subhalos, structures predicted by the ΛCDM cosmological paradigm to be DM clumps not massive enough to host galaxies, therefore being invisible in all wavelengths except an eventual annihilation/decay signal in gamma rays. Thus, these subhalos would appear in the gamma-ray sky as unidentified sources (unIDs), lacking any multiwavelength counterpart or association to known astrophysical objects.

To exploit this DM scenario, first we established a general methodology to search for dark subhalos within unIDs with *Fermi*-LAT in Chapter 3. This included a repopulation of N-body simulations to account for low-mass subhalos below the resolution of the original simulation, and a source "filtering" (e.g., flux variability), based on the expected emission properties of DM annihilation processes, in order to reduce the pool of candidates. Additionally, we computed the instrumental sensitivity to DM subhalos, which differs from the assumed constant value for traditional astrophysical sources, and mainly depends both on the WIMP mass and the annihilation channel.

The unIDs filtering turned out to be very efficient, rejecting a vast majority of the unIDs (up to 99% for the 3FGL catalog), while pointed out VIP candidates. Yet, it is not possible to claim any DM origin for such sources, therefore proceeding to set constraints to the cross section vs. WIMP mass parameter space. To do so, we compare the number of surviving unIDs with the expectations from the repopulated N-body simulations. The achievable constraints are very competitive with others such as the dSphs (the most stringent and robust ones at present) –and more importantly, they are independent results. The constraints most notably depend on the number of unIDs compatible with a DM origin, with an improvement especially relevant when dealing with $\mathcal{O}(10)$ candidates or less.

Once the pool of candidates was significantly reduced, the next step was to perform a careful spectral analysis in order to enforce or reject the DM hypothesis, as assessed in Chapter 4. Using 10 years of LAT data, we reanalysed each of the remaining candidates, and computed the statistical preference of DM over an astrophysical origin with a generalized likelihood ratio test, taking into account the differences in degrees of freedom between both hypotheses. Only a few candidates showed preference for a DM explanation, yet at very low statistical significance, well below 5 sigmas. Nevertheless, many of the candidates were completely ruled out as possible dark subhalos, which enforced the previously derived constraints.

Additionally, the degeneracy between pulsars and DM was explored with the "$\beta$ plot", which translated the sources into a privileged parameter space, where more information can be obtained in order to characterize the candidates. Indeed, when drawing the spectral curvature index versus the peak energy of the spectrum, there is a clear separation between AGNs and DM, while pulsars are share part of the DM parameter space, for light WIMPs. Depending on the mass of the DM particle, such tool can be used to discriminate pulsars from DM, acting as an additional filter. This is especially interesting in the context of classification machine learning algorithms, which may shed some light on the nature of unIDs when using this parameter space.

We also searched for stellar streams with *Gaia* data at the coordinates of the best candidates, as it would possibly indicate a gamma-ray emission from a disrupted dSph or globular cluster. Only one stream was found at the position of a source, coincident with the Sagittarius stream, yet it was not possible to univocally associate the unID to the stream from this analysis alone. Finally, we also performed a spatial analysis to all the candidates, as spatial extension is expected to be a "smoking gun" for DM subhalo detection. In this work we quantitatively assess this claim by first predicting the angular extension of subhalos according to our repopulated N-body simulation. The brightest subhalos should exhibit large spatial extension, around $1-5^\circ$ when integrating their signal up to their scale radii. Interestingly, all our remaining candidates, all of them analyzed spatially, turned out to be point-like sources. Nevertheless, the predictions from N-body simulations needed to be convoluted with the instrumental response of the LAT in order to extract definitive conclusions.

This was done in a subsequent project in Chapter 5, where we used the spatial information of the subhalo. We built templates for the spatial annihilation profile of subhalos, according to their typical statistical properties in our simulations, and then performed thousands of individual realizations of extended DM subhalos with real LAT gamma-ray data. This way, we were able to quantify how well the LAT is able to resolve the spatial properties of these sources. We chose two extreme subhalo cases, which turned out to be very similar attending to their expected spatial emissions. The general conclusions from this work are that the LAT requires a factor $\sim 2$ more flux than in a point-like source scenario to detect a extended subhalo, that an unequivocal extension requires a factor $\sim 10$ more flux, and that the LAT is able to see at least hints of spatial extension from light WIMP subhalos. Above $\sim 500$ GeV, only for extreme J-factor/cross section values the LAT was able to recover spatial information. We also studied the impact of these considerations in the derived constraints, which were now degraded due to the integration of the subhalo signal up to the innermost $0.3^\circ$ (given the typical recovered values) instead of the scale radius, as done in Chapters 3 and 4.

The quantification of the spatial performance of the LAT allows to repeat the spectral and spatial analysis of Chapter 4, but with updated sources from the most

recent 4FGL catalog. By analysing the surviving candidates after our filtering procedure developed in Chapter 3, we found a handful of unIDs with preference for DM, even after having been penalized by the corresponding trials factor. Some of them also showed spatial extension (up to $3\sigma$), which matches the expectations of Chapter 5.

All the described methodology for unIDs searches can be also applied to ground-based telescopes. Indeed, these observatories, based on the Cherenkov radiation, are suitable for heavy WIMP searches, given their energy range, with a maximum sensitivity in the TeV regime. As dark subhalos would serendipitously appear in the field of view (FoV) of the telescope, large areas are required to maximize the probability of finding them. Thus, the HAWC observatory is the only suitable telescope among those currently in operation, as it daily maps 2/3 of the sky. Contrary to the LAT, HAWC data are private and only limited information, such as sources positions and detection significances, are reported.

Nevertheless, this can be used to reject unIDs according to the defined criteria. Only one of the HAWC unIDs, 2HWC J1040+308, survived the filtering. This source is promising from a DM point of view, as it exhibits a hard spectrum, it exhibits $0.5^\circ$ angular extension, and is far from the Galactic plane. This challenges astrophysical explanations, and is more data is needed to elucidate its nature given its low detection significance, near the threshold. Being agnostic to the nature of this source, we could set constraints by computing the updated sensitivity of HAWC from the Collaboration reported values, by tailoring them to the nature of our candidate. The resulting constraints were very competitive for heavy WIMPs, and complemented the H.E.S.S. GC constraints, currently the most stringent ones in the TeV WIMP mass range.

The dark subhalo scenario could also be explored with CTA, yet with simulated data, as it is currently in construction phase. Such work is performed in Chapter 8 In order to compute the expected sensitivity of CTA to dark subhalos, we distinguished three search strategies in which a DM subhalo could be serendipitously spotted; i) the planned extragalactic survey, which will map 25% of the high-latitude sky; ii) a deep dedicated observation in a narrow field; and iii) the accumulated overall exposure in 10 years of CTA operations. We computed the sensitivity to each of these three scenarios by simulating the performance of the Northern array of CTA, which will be firstly completed. In particular, we noted that, as happened with the LAT, the minimum flux required to have a $5\sigma$ detection varies more than 2 orders of magnitude depending on the assumed WIMP mass, thus this particular ingredient being very relevant to take into account.

In the case of the overall exposure method, we developed a computation of the pointing strategy of CTA in 10 years by extrapolating the actual MAGIC science operations as performed in 6.5 years. By randomly repeating this computation, we had a statistical estimation of the number of pointings, sky direction and exposure times, which were used to predict the total sky area surveyed. We also computed the expected number of subhalos above a certain J-factor in the three strategies. The brightest subhalos arose in the overall exposure method, with one at most with a J-factor larger than $10^{20}$ GeV$^2$ cm$^{-5}$. The achievable DM constraints, computed for two annihilation channels, improved prior works and complement the previous constraints we obtained for *Fermi*-LAT (Chapters 3, 4 and 5) and HAWC (Chapter 7). Through this study we assumed point-like sources, mainly due to the large FoV of the Cherenkov telescopes and their stable off-axis sensitivity up to a few degrees off the center of the camera, yet our work must should be perceived as a first attempt to be further explored and refined, especially when the actual CTA operations start.

Finally, in Chapter 9 we explored an alternative candidate for DM, primordial black holes (PBHs), which are macroscopic objects. In the context of high-energy astrophysics, light PBHs can be constrained due to the Hawking radiation emitted by those, which shifts towards higher energies for smaller masses. This is effectively as WIMP DM decay, where the PBHs have been stable "particles" up to the current age of the Universe, yet now are beginning to evaporate. Using X-ray and gamma-ray data from the high-energy isotropic background, we estimated the maximum fraction of DM made of PBHs, ruling out contributions larger than $\sim 10\%$ of the total DM content for masses between $10^{16} - 10^{17}$ g. Future experiments, which can solve part of the isotropic background as point sources, therefore reducing the background flux, should be able to enforce these constraints.

Future work would be devoted to expand the subhalo search strategy. Indeed, as *Fermi*-LAT has been in operation for more than a decade, the exposure increase will not improve much the current data; regarding ground-based observatories, only HAWC is currently suitable for dark subhalo searches. CTA will also be competitive, once it is completed and starts producing massive data, which is still years away. Thus, it seems difficult to improve the results presented in this Thesis by just increasing the amount of data – instead, it is advised to draw upon complementary probes. These include three possible approaches: i) from the simulation point of view, improving the predictions with hydrodynamical N-body simulations; ii) from the data analysis point of view, implementing machine learning techniques; and iii) from the observational point of view, exploring the synergies between stellar streams and gamma-ray astronomy.

Regarding the first point, as seen through the Thesis, the knowledge of the actual effect of baryons on DM-only simulation is currently uncertain, and, even if baryons do not play a role in shaping the inner structure of dark subhalos (as they do not host galaxies inside), are critical in the formation an evolution of the whole Galactic subhalo population. Further numerical work that includes baryon physics, together with observations from future experiments such as Euclid and LSST, will surely narrow the uncertainties involved in the subhalo structural properties and distribution.

The overwhelming amount of data from current and future experiments and probes can be exploited with machine learning techniques as well. These will be able, for example, to discriminate signals over the background in a more precise way, to find correlations in high-dimensional parameter spaces, or to better classify rare events in the data. An example of such applications, already mentioned in Chapter 4, is the $\beta$-plot. Ongoing work is currently being developed to use both linear and non-linear classifiers in this parameter space, as well as advanced algorithms including the parameter uncertainties, to shed some light on the nature of the LAT unID population.

Finally, gamma rays alone are a limited probe for DM, mainly due to the lack of crucial information such as distance, and generally large systematic uncertainties (background modeling, DM distribution, etc.). In the case of dark subhalos, with no multiwavelength counterparts, it is hard to break the degeneracies between different scenarios, e.g., large and far subhalos versus light and near ones, even when considering effects as the spatial extension. Thus, it is advisable to search for complementary probes.

One of them are stellar gaps, which can be a "smoking gun" for a dark subhalo passage through Galactic stellar streams. With enough precision data, one could reconstruct the mass and trajectory of the subhalo from the gap properties. If the overall parameters are well constrained, the position of the subhalo could also be determined, and a multiwavelength campaign could be performed in order to search

for a DM signal around the reported coordinates. A complementary approach could be to search for emission from the center of mass of the stream itself, as it should be a disrupted subhalo by itself, and thus, it should contain some DM content as well. Other probes such as gravitational lensing can also be used, yet the lens effect for low-mass subhalos is currently beyond the instrumental resolution.

# Appendix A

# List of Publications

1. *Unidentified Gamma-ray Sources as Targets for Indirect Dark Matter Detection with the Fermi-Large Area Telescope*
**J. Coronado-Blázquez**, M. A. Sánchez-Conde, A. Domínguez, A. Aguirre-Santaella, M. Di Mauro, N. Mirabal, D. Nieto and E. Charles, 2019, *Journal of Cosmology and Astroparticle Physics* 07(2019)020

2. *Spectral and spatial analysis of the dark matter subhalo candidates among Fermi Large Area Telescope unidentified sources*
**J. Coronado-Blázquez**, M. A. Sánchez-Conde, M. Di Mauro, A. Aguirre-Santaella, I. Ciuča, A. Domínguez, D. Kawata and N. Mirabal, 2019, *Journal of Cosmology and Astroparticle Physics* 11(2019)045

3. *Constraints to dark matter annihilation from high-latitude HAWC unidentified sources*
**J. Coronado-Blázquez** and M. A. Sánchez-Conde, 2020, *Galaxies* 8 (1), 5

4. *X-ray and gamma-ray limits on the primordial black hole abundance from Hawking radiation*
G. Ballesteros, **J. Coronado-Blázquez** and D. Gaggero, 2020, *Physical Letters B* 808, 135624

5. *Sensitivity of the Cherenkov Telescope Array to dark subhalos*
**J. Coronado-Blázquez**, M. Doro, M. A. Sánchez-Conde and A. Aguirre-Santaella, 2021, *Physics of the Dark Universe* **32** (2021), 100845

6. *Dark Matter search in dwarf irregular galaxies with the Fermi Large Area Telescope*
V. Gammaldi, J. Pérez-Romero, **J. Coronado-Blázquez**, M. Di Mauro, E. V. Karukes, M.A. Sánchez-Conde and P. Salucci, 2021, Submitted to *Physical Review D*

7. *Spatial extension as "smoking gun" for dark subhalo detection with Fermi-LAT and implications for WIMP constraints*
**J. Coronado-Blázquez**, M.A. Sánchez-Conde, J. Pérez-Romero and A. Aguirre-Santaella, 2021, Submitted to *Journal of Cosmology and Astroparticle Physics*

As member of the *Fermi*-LAT Collaboration:

1. *Fermi Large Area Telescope Fourth Source Catalog*
   S. Abdollahi et al. (including **J. Coronado-Blázquez**), 2020, *The Astrophysical Journal Supplementary Series* 247, 33

As member of the CTA Consortium:

1. *Sensitivity of the Cherenkov Telescope Array to a dark matter signal from the Galactic centre*
   A. Acharyya et al. (including **J. Coronado-Blázquez**), 2021, *Journal of Cosmology and Astroparticle Physics* 01(2021)057

2. *Sensitivity of the Cherenkov Telescope Array for probing cosmology and fundamental physics with gamma-ray propagation*
   H. Abdalla et al. (including **J. Coronado-Blázquez**), 2021, *Journal of Cosmology and Astroparticle Physics* 02(2021)048

# List of Figures

1.1 Composite image of the merging cluster 1E 0657–558, commonly known as the "Bullet cluster", with optical emission from the individual galaxies (orange), X-ray emission from the hot gas (pink/red) and DM halos inferred from gravitational lensing (blue) European Space Agency (2007). . . . . 6
1.2 Skymap of the temperature anisotropies of the CMB as measured by the *Planck* satellite in its third and final data release in 2018. The color scale ranges from $-300\mu$K (blue) to $+300\mu$K (red) temperature variation from the average value. Figure taken from Planck Collaboration (2020b). . . . . 11
1.3 *Planck* satellite measurements of the CMB temperature power spectrum in its final data release in 2018. The error bars come from cosmic variance (and therefore is larger for low multipoles), approximated as Gaussian. Blue, solid line is the ΛCDM best-fit. Vertical axis is the multipolar moment as defined in Eq. 1.14, and is expressed in units of $\mu K^2$. Figure taken from Planck Collaboration (2020a). . . . . 12
1.4 DES-WiggleZ survey measurements of the 2-point galaxy correlation function $\xi(s)$ times $s^2$, where $s$ is the comoving redshift-space separation. Different panels show different redshift samples. A clear peak is seen at $s \sim 100h^{-1} = 150$ Mpc, assuming *Planck* value $h = 0.67$. Figure taken from Blake et al. (2011). . . . . 14
1.5 Hubble diagram for the DES-SN3YR sample. Top panel: distance modulus $\mu$ from Type Ia Supernovæas measured by DES (red, circles) and Harvard-Smithsonian Center for Astrophysics survey Hicken et al. (2012) (orange circles). Dashed, gray line shows the best fit model, while green and blue dotted lines show models assuming no dark energy ($\Omega_\Lambda = 0$) and matter densities $\Omega_m = \{0.3, 1\}$, respectively. Bottom panel: residuals to the best fit model. Figure taken from DES Collaboration (2019a). . . . . 15
1.6 DM abundance $\Omega_\chi h^2$ as a function of $x = m_\chi/T$. Black, solid line is the abundance if DM remained in equilibrium and therefore was exponentially suppressed (see Eq. 1.22). Different colors show different values of the thermally-averaged annihilation cross section. Black, horizontal line is the inferred abundance from *Planck* CMB data, $\Omega_\chi h^2 = 0.1198$ Planck Collaboration (2020a). Figure taken from Dev et al. (2014). 18
1.7 The Large Scale Structure of the Universe, as observed by the SDSS galaxy redshift survey SDSS Collaboration (2017) up to $z \sim 0.15$ ($d_L \sim 700$ Mpc). It shows the galaxy number distribution as a function of redshift in two observational slices. Each point represents a galaxy, with hotter colors indicating larger number densities. Note the big structure in the top slice, known as the "Great Wall" Leclercq et al. (2017). . . . . 21

1.8 Large Scale Structure density maps from N-body simulations with a length of $50h^{-1}$ Mpc and a depth of $2.5h^{-1}$ Mpc. From top to bottom, different redshift snapshots are taken at $z = \{4.4, 1.1, 0\}$. From left to right, CDM, WDM ($m_\chi = 1$ keV) and WDM ($m_\chi = 0.25$ keV). WDM effects are barely discernible in the middle panels, while they are prominent in the right panels, where less substructure is present when compared to CDM Schneider et al. (2012). . . . . 22
1.9 Eight decades of N-body simulations. **Left panel:** first N-body simulation by Holmberg (1941), using 37x2 light bulbs to model the MW and Andromeda galaxies in collision. **Central panel:** first DM computer-based N-body simulation by Davis et al. (1985), with 32768 particles. **Right panel:** Uchuu N-body simulation of LSS Ishiyama et al. (2020) which comprises $2 \cdot 10^{12}$ particles. . . . . 23
1.10 Median halo (black symbols) and subhalo (colored symbols) concentration parameter $c_{200}$, as a function of $m_{200}$ as found in different N-body simulations. Different colors represent radial bins defined as $x_{sub} = r/R_{vir}$. Background dots are the individual subhalos, and the solid lines are different proposed $c(M)$ models. The $c(M)$ is flattened towards lower masses. See Moliné et al. (2017) for details. . . . . 24
1.11 Not all DM subhalos host a galaxy. **Top row:** 2 Mpc-side cube from the hydrodynamic EAGLE N-body simulation Schaye et al. (2015). Left panel is the DM density map, contrasting with the right panel, where the stellar light distribution is shown. **Bottom panel:** HOF map of one of the two main subhalos of top image, with a 400 kpc radius. Circles show three mass references, while blue (red) colors indicate a dark (luminous) halo, i.e., not hosting (hosting) a galaxy. Figures taken from Sawala et al. (2014, 2015). . . . . 26
1.12 Schematic view of DM searches based on weak interactions with SM particles. While formally this diagram would only be valid for thermally-produced DM (Section 1.2.2), it may be also applicable to some non-thermally produced particle DM candidates, such as ALPs or sterile neutrinos (Section 1.2.2). . . . . 33
1.13 Comparison of DM constraints from selected direct detection experiments at 90% CL and ATLAS LHC results at 95% CL. **Left panel:** spin-dependent WIMP-proton scattering cross-section in the vector leptophobic model. **Right panel:** spin-independent WIMP-nucleon scattering cross-section constraints in the axial-vector leptophilic model. Figure taken from Giagu (2019). . . . . 34
1.14 XENON1T recoil event excess at $1 - 7$ keV. Black error bars are the binned data, while red line is the background model. An excess is found at the lower bins, while a defect is present at 17 keV. Lower panel shows the difference in standard deviations, with green and yellow bands showing 1 and $2\sigma$ significance, respectively. Figure taken from Aprile et al. (2020). . . . . 37
1.15 Compilation of different nuclear recoil experiments 90% CL constraints on $\sigma_{SI}$ for WIMP DM. Orange, dashed line is the so-called neutrino floor, where $\nu-$nuclei interactions are indistinguishable from DM scattering. Figure taken from Lin (2019). . . . . 38
1.16 Same as Figure 1.15, but for SD scattering. **Left panel:** DM-neutron scattering. **Right panel:** DM-proton scattering. Figures taken from Schumann (2019). . . . . 38

1.17 Experimental residual rate of the scintillation events measured by the DAMA/LIBRA experiment in the 2–6 keV energy range, as function of the time. The overimposed curve is the theoretical prediction for DM modulation in the form of co-sinusoidal function $A \cdot cos[\omega(t - t_0)]$, where the period $T = 2\pi\omega$ is 1 year and the phase is $t_0 = 152.5$ days, corresponding to June 2nd. The modulation amplitude $A$ is obtained with the data best-fit. Figure taken from Bernabei et al. (2018). . 39
1.18 WIMP DM constraints set by joint observations of the GC by IceCube and ANTARES, for a variety of annihilation channels. An NFW DM density profile is assumed. Figure taken from ANTARES Collaboration and IceCube Collaboration (2020). . . . . 41
1.19 95% CL upper limits to the DM annihilation cross section with AMS-02 antiproton data, assuming annihilation into $b\bar{b}$. Dot-dashed line shows the derived limits from the *Fermi*-LAT dSphs (see Section 1.5.3). Figure taken from Cui et al. (2018). . . . . 45
1.20 Compilation of constraints on the annihilation cross section from different DM targets and search strategies, for annihilation into $b\bar{b}$. Dot-dashed gray line is the thermal relic cross section. Red line are *Fermi*-LAT dSphs Fermi-LAT Collaboration and DES Collaboration (2017), blue line antiprotons from AMS-02 Cui et al. (2018), green line dSphs observed by VERITAS VERITAS Collaboration (2017), olive line H.E.S.S. observations of the GC H.E.S.S. Collaboration (2016), orange and yellow lines IceCube and ANTARES neutrino constraints, while brown line is their combined limit ANTARES Collaboration and IceCube Collaboration (2020). The purple star is the DM best fit to the GCE, and the surrounding contour its $1\sigma$ containment region Daylan et al. (2016). Figure adapted from Petač (2019), where a typo in the units was present. . . . . 52

2.1 Schematic view of the Fermi Gamma-ray Space Telescope (left panel), and a more detailed view of the Large Area Telescope instrument, where a pair-conversion event in the tracker is shown (right panel). Taken from Fermi-LAT Collaboration (2009). . . . . 94
2.2 Examples of particle showers as generated by the `CORSIKA` software. Upper panels are the XZ plane projection, while lower panels show the XY plane. Colors refer to the particle species, being red for $e^{\pm}, \gamma$, green for $\mu^{\pm}$, and blue for hadrons. All cascades are produced at a height of 30 km, and only particles with energies higher than 0.1 MeV (0.1 GeV) are shown in the case of $e^{\pm}, \gamma$ ($\mu^{\pm}$, hadrons). **Left panels:** primary gamma ray at 100 GeV. **Central panels:** primary muon at 1 PeV. **Right panels:** primary proton at 100 GeV. Figure adapted from Schmidt and Knapp (2005). . . . . 96
2.3 Cherenkov radiation diagram from a particle (blue) traversing a polarizable medium (red). **Left panel:** the speed of the particle is $v < c/n$, and does not induce a net charge in the medium. **Right panel:** the speed of the particle is $v > c/n$, inducing a dipolar moment which results in a cone-shaped radiation emission (yellow), known as Cherenkov light. Figure taken from Mezek (2019). . . . . 97

2.4 Examples of photon (left panel) and muon (right panel) events as detected by the first H.E.S.S. telescope camera. While photons tend to leave linear traces, muon cascades show a ring-like feature. Figures taken from H.E.S.S. Collaboration (2002). . . . . 98
2.5 H.E.S.S. Galactic plane survey. Skymaps show the integral flux above 1 TeV , in units of % of the Crab Nebula flux, a standard candle in gamma-ray Astronomy. The map is only filled where the point-source sensitivity for a $5\sigma$ detection is better than 2.5% of the Crab flux. Note also the intense emission in the GC. Figure taken from H.E.S.S. Collaboration (2018b). . . . . 100
2.6 Comparison of the differential sensitivity (required flux for a $5\sigma$ detection) to a point source in current and future ground-based Cherenkov observatories, assuming diverse exposure times. Figure taken from Cherenkov Telescope Array Consortium (2020). . . . . 102
2.7 The gamma-ray sky above 1 GeV, as seen by *Fermi*-LAT in 10 years of operations. The map is shown in Galactic coordinates and a Hammer-Aitoff projection. Hotter colors indicate larger photon fluxes. Figure taken from Ciprini (2020). . . . . 103
2.8 Map of localized sources in the *Fermi*-LAT 8-year 4FGL catalog, in Hammer-Aitoff projection and Galactic coordinates (see also Figure 2.7). Blue squares are AGNs, the most numerous source type, while grey squares, mounting up to $\sim 1/3$ of the total, are unIDs. Figure taken from Fermi-LAT Collaboration (2020). . . . . 108

3.1 **Upper panel**: DM annihilation spectra with overlaid Eq. 3.4 parametric fit and interpolation for $t\bar{t}$ (left panel) and $b\bar{b}$ (right panel) for various DM masses. The points from Cirelli et al. (2011) are marked by crosses, while the fit is plotted as solid lines. Note that in the case of $t\bar{t}$ the plotted masses are larger because $m_t = 172$ GeV. **Lower panel**: Integrated DM annihilation spectra $(N_\gamma)$ for 2FHL setup (left) and 3FHL (right), for $b\bar{b}$. Both setups differ in the threshold energy. Note that $N_\gamma = 0$ if $E < 50$ GeV ($E < 10$ GeV) in the case of the 2FHL (3FHL) setup, where $E = E_{th}$. Blue crosses are the values of the integral, and orange line is the interpolation between the values of the integral, which is used to compute the DM constraints as described in Section 9.4. . . . . 123
3.2 Subhalo J-factors as a function of distance to the Earth for all subhalos in a random realization of the repopulated VL-II. The repopulation includes low-mass subhalos down to $10^3 M$ ; see text for details. The color represents the subhalo mass in $M$ . . . . . 126
3.3 Flowchart of the rejection criteria. Blue, red and green correspond to numbers in the 3FGL, 2FHL and 3FHL catalogs, respectively. The "yes" flow lists the unIDs that pass a certain filter, while the "no" flow indicates sources that do not, for each criteria. See text for details. . . . 128
3.4 Galactic latitude distribution of unIDs in the 2FHL, 3FHL, and 3FGL catalogs. Those sources between the red dashed lines are excluded from our analysis $(|b| \leq 10^\circ)$. . . . . 130

3.5 Example of "fake" variability induced by the spill over of photons due to the PSF. **Top panel**: FAVA lightcurve of 3FGL J2043.8-4801. **Low panel**: FAVA lightcurve of 3FGL J2056.2-4714 (associated with a flat-spectrum radio quasar) flare in week 55 (mission elapsed time (MET) 272519018), indicated by the dashed red line. Note the tight correlation between the variations in both curves. These two sources are 2.3° from each other in the sky. . . . . 132
3.6 TS map of 3FGL J2056.2−4714. This object shows a flare in week 55 (MET 272519018). There is still a relatively high significance ($TS = 17$) at the position of 3FGL 2043.8−4801, which lies only 2.3° away from the flaring source. Thus, we can conclude that the flare of 3FGL J2056.2−4714 is causing the variability observed for 3FGL 2043.8−4801 (the timing coincides as well, see Figure 3.5) . . . . . 133
3.7 FAVA lightcurve of 3FHL J0500.6+1903. No other source flare is temporally and spatially coincident with the flare centered on week 247 (MET 388640618), and therefore this object is rejected as DM subhalo due to its intrinsic variability. . . . . 133
3.8 LAT sensitivity to DM subhalos for $\tau^+\tau^-$ annihilation and the 3FGL setup, for $m_\chi = 10$ GeV (top) and $m_\chi = 1$ TeV (bottom). . . . . 137
3.9 LAT sensitivity to DM subhalos annihilating to $\tau^+\tau^-$ as a function of DM mass for various absolute Galactic latitudes (top panels) and as a function of absolute Galactic latitude for various DM masses (bottom panels). Left and right panels refer, respectively, to the 3FGL and 3FHL setups. A vertical red dashed line is plotted in the bottom panels to mark our latitude cut, $|b| < 10°$. . . . . 138
3.10 Distribution of the 16th (i.e. the number of remaining DM candidates in the 3FGL catalog) brightest subhalo J-factor in each of the 1000 VL-II repopulation realizations. The red (blue) distribution refers to the case without (with) a cut in both subhalo mass ($M \geq 10^7 M_\odot$) and latitude ($|b| \leq 10°$); see text for details. The dark blue vertical dashed line marks the J-factor above which 95% of the blue J-factor distribution is contained. This is the J-factor we would adopt for the computation of the 95% C.L. limits in this particular case. . . . . 139
3.11 Improvement in the DM constraints as a function of number of remaining unIDs in the catalogs. The improvement is codified in terms of a ratio of J-factors: the one to be used for the number of remaining sources after filtering, and the one corresponding to the full unID catalog (i.e. no unID rejection). Both J-factors refer to the values above which 95% of the corresponding J-factor distributions, for each number of candidates, are contained; see text and Figure 3.10 for details. The horizontal dashed line shows no improvement at all due to (lack of) unIDs filtering, and it is computed with respect to the case of having a single remaining unID (sensitivity reach of the method; see Figure 3.13). Note the exponential rise of constraining power once less than ∼20% of sources are left. . . . . 140

3.12 Limits on the DM annihilation cross section for $b\bar{b}$ (top) and $\tau^+\tau^-$ (bottom) for the three LAT catalogs used in this work, and once the unID filtering detailed in Section 3.3 has been applied to each of them. More precisely, 16, 4 and 24 unIDs remain in the 3FGL, 2FHL and 3FHL catalogs, respectively. The shaded bands refer to the 1-$\sigma$ uncertainty band coming from $F_{min}$; see text for details. The dashed line represents the thermal value of the annihilation cross section Steigman et al. (2012). The "rep" label stands for repopulated. . . . . 142
3.13 Same as Figure 3.12, but for the sensitivity reach scenario presented in Section 3.5.3, where only 1 unID is left in each corresponding catalog. We also compare our projections with the predictions for dwarfs with the Fermi LAT Charles et al. (2016) and from the Milky Way halo with CTA Lefranc and Moulin (2016). . . . . 143
3.14 Comparison of DM limits for different targets and probes. Solid line corresponds to the envelope of the three sets of limits shown in Figures 3.12 and 3.13 for the realistic scenario (Section 9.4). dot-dashed, dashed and dotted lines are, respectively, the DM constraints derived by H.E.S.S. for the Milky Way halo Lefranc et al. (2015), by the *Fermi*-LAT for dSphs Fermi-LAT Collaboration (2015c), and by Planck using the CMB DR3 latest release The Planck Collaboration (2020). Top panel is for $b\bar{b}$ and bottom panel for $\tau^+\tau^-$ annihilation channel. . . . . 146
3.15 Comparison of $\varepsilon_F$ versus $\varepsilon_J$, i.e. the relative errors associated to the $F_{min}$ (solid lines) and J-factor (dashed lines), respectively, as a function of the DM particle mass and different annihilation channels. From bottom to top, for the 3FGL, 2FHL and 3FHL catalogs. The dashed lines are, from bottom to top, the $\varepsilon_J$ of the full number of unIDs in the corresponding catalog (green), the number of unIDs in the realistic scenario detailed in Section 9.4 (blue) and the 1-source sensitivity reach of Section 3.5.3 (red). . . . . 148
3.16 Comparison of DM 95% C.L. upper limits found with and without low-mass subhalo repopulation below the resolution limit of the original VL-II simulation. Both panels are for $b\bar{b}$, in the three catalog setups. Dot-dashed lines are the constraints from the original VL-II simulation ("orig"), while the solid lines use the repopulated simulation ("rep"). Left: current number of DM subhalo candidates in the catalogs (see Figure 3.12); right: sensitivity reach of the method (see Figure 3.13). . . . . 149
3.17 Same as Figure 3.12 but for $c\bar{c}$ annihilation channel. . . . . 150
3.18 Same as Figure 3.12 but for $t\bar{t}$ annihilation channel. . . . . 150
3.19 Same as Figure 3.12 but for $W^+W^-$ annihilation channel. . . . . 151
3.20 Same as Figure 3.12 but for $Z^0Z^0$ annihilation channel. . . . . 151
3.21 Same as Figure 3.12 but for $hh$ annihilation channel. . . . . 152
3.22 Same as Figure 3.12 but for $e^+e^-$ annihilation channel. . . . . 152
3.23 Same as Figure 3.12 but for $\mu^+\mu^-$ annihilation channel. . . . . 153

4.1 Results examples of our spectral analysis, for two different types of sources in our unIDs' list: 3FGL J0336.1+7500 (left panels) and 3FHL J1440.2−2343 (right panels). The first is a bright source (detected at TS=1095) whose SED is best described by a PLE (see Eq. 4.4); while the second is a faint (TS=135) object for which a PL (Eq. 4.2) is preferred. First row is the ROI residual map leaving the unID unmodelled, so that the TS peak is clearly visible. Second row shows the model of expected counts in the ROI. The location of the source, compared with the FL8Y reported position (green circle), is shown in the third row. The fourth row features the gamma-ray SED with the best-fit spectral model and $1\sigma$ uncertainties overimposed (solid line with gray shaded regions). . . . . 166

4.2 Distribution of ΔTS values as defined in Eq. 4.6 for the comparison between astrophysical models and DM fits. The left (right) panel is for hadronic (leptonic) annihilation channels. The two vertical dashed lines mark $\Delta TS = -25$ and $\Delta TS = -9$, i.e., the best-fit astrophysical model is preferred against DM at $\sim$5 and $\sim 3\sigma$, respectively. Note that the $t\bar{t}$ channel does not appear in these plots, as no source is found to be well fitted by it. . . . . 168

4.3 SED of the seven candidates with ΔTS>0 listed in Table 4.2. Overimposed is the best-fit DM annihilation channel in each case. Note the significantly smaller model uncertainties in the case of the 3FGL sources (top panels). . . . . 169

4.4 Limits on the DM annihilation cross section for $b\bar{b}$ (top) and $\tau^+\tau^-$ (bottom) for the 3FGL, 2FHL and 3FHL LAT catalogs and the number of unIDs that are still compatible with a DM annihilation origin after our spectral analyses of Section 4.2 and Section 4.4. The wide uncertainty band in the case of the 3FGL constraint is due to false positive rates in the machine learning classification algorithms used in the unID filtering work of Ref. Coronado-Blázquez et al. (2019). The dashed line represents the thermal value of the annihilation cross section Steigman et al. (2012). . . . . 172

4.5 Comparison of DM limits from different targets and probes. Solid line corresponds to the envelope of the three sets of limits shown in Figure 8.5. Dot-dashed, dashed and dotted lines are, respectively, the DM constraints derived by H.E.S.S. for the Milky Way halo Lefranc et al. (2015), by the *Fermi*-LAT for dSphs Fermi-LAT Collaboration (2015c), and by Planck using the CMB DR3 latest release The Planck Collaboration (2020). Top panel is for $b\bar{b}$ and bottom panel for $\tau^+\tau^-$ annihilation channel. . . . . 173

4.6 Spectral curvature index ($\beta$) vs. the peak energy ($E_{peak}$) for 4FGL pulsars (psr, blue crosses), BL Lacs (bll, red crosses) and flat spectrum radio quasars (fsrq, green crosses) with TS of detection ($TS_d$) greater than 1000. Colored data symbols with error bars correspond to the ($E_{peak}$, $\beta$) with $1\sigma$ uncertainty, for different DM annihilation channels (see legend). Large gray and orange stars correspond to the best-fit annihilation channels for the two unID sources with $TS_d > 1000$ that are well fitted by a LP model out of the 44 unIDs in our list. . . . . 174

4.7 Same as Figure 4.6 but without cut in detection TS. Also shown as stars are those unIDs that are well fitted by LP (i.e., $\Delta TS \geq -25$). The color of each star refers to the best-fit DM channel in each case; see legend. . . . . 175
4.8 Spatial extension log-likelihood profiles of the seven DM candidates from Table 4.2 and one known extended source, for the case of adopting a Gaussian spatial template. The blue, vertical line is the median best-fit value, while the violet line refers to the $+1\sigma$ uncertainty of the mean (in the last source, where there is a preference for extension, this is an uncertainty band). All DM candidates appear as point-like. The use of a 2D disk spatial template instead of a Gaussian one leads to similar results. Only for illustrative purposes, we also show in the bottom right panel the source 2FHL J0648.5+4438, which is not well fitted to any DM channel but is found to have a 68% containment width of $0.5 \pm 0.1^\circ$ at $\sim 3\sigma$ significance. . . . . 177
4.9 Angular extension of subhalos following our definition in Eq. 4.9 as predicted by the N-body simulation work of Coronado-Blázquez et al. (2019). The figure shows the 100 brightest subhalos in each of the 1000 realizations of the repopulated VL-II simulation, which include subhalos with masses down to $10^3 M_\odot$, i.e. well below the resolution of the original VL-II. The typical *Fermi*-LAT PSF at $E > 1$ GeV and $E > 10$ GeV are also shown as vertical dashed lines. Most subhalos are expected to be extended for *Fermi*-LAT, especially the brightest ones. 179
4.10 A detection of a kinematical structure in the field of 3FHL J0041.7−1608. The left panel shows the data after filtering with $d > 10$ kpc. The right panel shows the results from the Gaussian Mixture Model (Holoien et al.; 2017) used to perform density estimation using the XD method (Bovy et al.; 2011) with 25 components. Ellipses represent detected Gaussian components to describe the data and the darker gray color indicates more components overlapping. The small ellipse around $(\mu_{\alpha^*}, \mu_\delta) = (-1.12, -3.15)$ mas yr$^{-1}$ is believed to be part of the Sagittarius stream in the right panel. . . . . 181

5.1 Distance to the Earth versus the subhalo mass for the 100 brightest subhalos in 1000 repopulations of the VL-II N-body cosmological simulation. The colored z-axis represents the J-factor. The vertical, dark dash-dotted line separates between dSphs and dark subhalos, and the black stars show the mass and distance of the two subhalos that were chosen as representative to perform the *Fermi*-LAT analysis in the next sections. . . . . 194
5.2 Two-dimensional templates of the DM-induced gamma-ray spatial morphology for the two representative subhalo scenarios defined in Section 5.2.1. The z axis represents the differential J-factor $\left(\frac{dJ}{d\Omega}\right)$ computed according to the DM modeling of Section 5.2.1. . . . . 199
5.3 Differential J-factor versus the radial angle for the two representative subhalo scenarios defined in Section 5.2.1. Here, we also show $\theta_{tidal}$, which represents the angle subtended by $R_{tidal}$, $\theta_s$ as defined in Eq. 5.9 and $\theta_{68}$ as defined in Eq. 5.10, all depicted with a different color in each subhalo case. The spatial distributions of the J-factor are almost identical until about $1^\circ$, emphasizing the degeneracy discussed in the main text. . . . . 199

5.4 Comparison between minimum fluxes for extended subhalos. **Left panel:** Minimum flux for detection ($TS_{det} = 25$), for the two considered annihilation channels and subhalo models. **Right panel:** The same for the case of minimum flux for extension ($TS_{ext} = 25$). The uncertainty bars come from averaging across ten realizations. Note the different flux scale in each panel. . . . . 202
5.5 Minimum fluxes for point-source $TS_{det} = 25$ detection (PS), extended subhalo $TS_{det} = 25$ detection ($F^{det}_{min}$), and extension with $TS_{ext} = 25$ ($F^{ext}_{min}$), for $b\bar{b}$ (left panel) and $\tau^+\tau^-$ (right panel) annihilation channels. Lower panels show the ratio between $F^{det}_{min}$ (green squares) and $F^{ext}_{min}$ (red circles) when compared to the PS threshold. . . . . 202
5.6 Comparison between the TS of detection ($TS_{det}$) and TS of extension ($TS_{ext}$) for the case of achieving $F^{ext}_{min}$, i.e., $TS_{ext} = 25$ (we use a tolerance of $\pm 3$). Left panel shows the results for $b\bar{b}$ and right panel for $\tau^+\tau^-$ annihilation channel. . . . . 203
5.7 Comparison of the integrated source flux with the corresponding detection ($TS_{det}$; left panel) and extension significances ($TS_{ext}$; right panel), for the two subhalo models and $b\bar{b}$ annihilation channel. Each point is averaged across the 10 different realizations of the same setup. As in Section 7.3.1, the two subhalo models that we consider turn out to be completely indistinguishable within errors, and therefore we show only one of them in each case. . . . . 205
5.8 Detection $TS_{det}$ and extension $TS_{ext}$ significances for the ($b\bar{b}$, $10^4$ M$_\odot$) and the ($\tau^+\tau^-$, $10^7$ M$_\odot$) models (left and right panels, respectively). Vertical and horizontal lines mark, respectively, $TS_{ext} = 25$ and $TS_{det} = 25$. Each point is averaged across the 10 different realizations of the same setup. . . . . 205
5.9 Normalization of the source (J-factor $\times \langle\sigma v\rangle$) versus the extension significance $TS_{ext}$, for the ($b\bar{b}$, $10^7$ M$_\odot$) and the ($\tau^+\tau^-$, $10^4$ M$_\odot$) models, in all individual realizations. Vertical, black line marks $TS_{ext} = 25$. . . . 206
5.10 Best-fit extension $R_{68}$ versus the extension ($TS_{ext}$) and detection ($TS_{det}$) significance, for the ($b\bar{b}$, $10^4$ M$_\odot$) and the ($\tau^+\tau^-$, $10^7$ M$_\odot$) models. Each $R_{68}$ is the average value of the 10 realizations, while their uncertainties are computed via a quadratic sum of the individual realization uncertainties and the $1\sigma$ spread across realizations. . . . . 207
5.11 Distribution of the brightest subhalo J-factor, across 1000 realizations of the N-body simulation (see Paper I for more details), integrating the signal either up to the scale radius (blue) or the innermost 0.3° (red). Vertical lines mark the value at which 95% of the distribution is contained, i.e., the J-factor used to set the DM constraints. . . . . 208
5.12 95% C.L. limits for DM annihilating to $\tau^+\tau^-$ (top panel) and $b\bar{b}$ (bottom panel), as a function of the number of 4FGL–DR2 unIDs compatible with DM. Black, dashed line is the constraint obtained in Paper II using the previous 3FGL catalog Fermi-LAT Collaboration (2015a) with 1 (5) compatible sources in the case of $\tau^+\tau^-$ ($b\bar{b}$) channel, starting the analysis at 100 MeV, assuming point-like sources and integrating the J-factor up to the scale radius. The horizontal dashed line is the thermal relic cross section Bringmann et al. (2021). . . . . 209

5.13 Comparison between the injected DM signal and the recovered one, in terms of recovered WIMP mass and normalization (J-factor $\times \langle \sigma v \rangle$, with units $\mathrm{GeV}^2 \cdot \mathrm{cm}^{-2} \cdot \mathrm{s}^{-1}$), for the $b\bar{b}$ annihilation channel and the $10^4$ M subhalo model. Note that, as the input mass is increased, less points are present, as the lowest normalization values do not provide detection, indeed only the largest normalizations allowing for a proper characterization of the DM spectrum. Values and error bars refer to average and standard deviation as obtained from 10 realizations. Black, dashed line marks the true values of WIMP mass and normalization (unity ratios). . . . . 212
5.14 Same as Figure 5.13, but comparing the two subhalo models considered in our work. **Upper panels:** $10^4$ M subhalo. **Bottom panels:** $10^7$ M subhalo. . . . . 213
5.15 Spatial morphology of the simulated DM subhalo for $\mathcal{N} = 5 \cdot 10^{-6}$ (top left), $10^{-5}$ (top right), $10^{-4}$ (bottom left), and $10^{-3}$ (bottom right). Green, continuous circle is the best-fit extension, while dashed green circles are the $\pm 1\sigma$ uncertainty. The color scale provides the delta log-likelihood values, being the black curves iso-contours for some particular values (note the different z-axis scale in each plot). See text for details of the analysis parameters. . . . . 214
5.16 Extension likelihood curves for $\mathcal{N} = 5 \cdot 10^{-6}$ (top left), $10^{-5}$ (top right), $10^{-4}$ (bottom left), and $10^{-3}$ (bottom right). Blue, vertical line is the extension best-fit, while the violet band is the $1\sigma$ uncertainty. See text for details of the analysis parameters. . . . . 215
5.17 Spectral energy distribution (SED) of a 100 GeV WIMP annihilating to $b\bar{b}$, for normalization values $\mathcal{N} = 5 \cdot 10^{-6}$ (top left), $10^{-5}$ (top right), $10^{-4}$ (bottom left), and $10^{-3}$ (bottom right). The black band is the best-fit DM spectrum with $1\sigma$ uncertainty. The analyses in the two first cases are performed with 4 bins per energy decade, while the two latter 8, as the signal is bright enough to allow a finer binning. See text for details of the analysis parameters. . . . . 215

6.1 SED of the two best DM subhalo candidates in Table 6.2, overimposed with the best-fit DM annihilation spectrum. **Top panel:** 4FGL J1641.3−2908, annihilating to $b\bar{b}$ with $m_\chi = 10.3 \pm 0.6$ GeV. **Bottom panel:** 4FGL 1717.5−5804, annihilating to $\tau^+\tau^-$with $m_\chi = 10.6 \pm 0.7$ GeV. . . . . 227
6.2 **Top panel:** Spatial extension likelihood profile of 4FGL J1641.3−2908, exhibiting an extension of $0.38 \pm 0.10$ degrees at $3\sigma$ level (see Table 6.2). **Bottom panel:** Based on previous work in Chapter 5, we show the position of this same source (golden star) in the expected $TS_{det}$ vs. $TS_{ext}$ parameter space for DM subhalos and the LAT. . . . . 228

7.1 VHE sources listed in the TeVCat online catalog as of November 2019, here shown in Hammer-Aitoff projection and Galactic coordinates. Background is the gamma-ray sky as seen by Fermi-LAT in 4 years of operation. Note the higher density of sources, in particular of unIDs, along the Galactic plane. The figure was generated with the TeVCat online tool Wakely and Horan (2008). . . . . 235

7.2 HAWC minimum flux, $F_{min}$, needed to reach source detection ($TS = 25$) at a sky declination equal to 30.87°. In blue, the $F_{min}$ as originally reported in The HAWC Collaboration (2017a) for the case of a point source described by a power law spectrum with index $\Gamma = 2.63$ and 507 days of exposure. The red curve shows the $F_{min}$ for our DM subhalo candidate instead (with a spatial extension of 0.5°, $\Gamma = 2.08$ and 760 days of exposure). This one is computed taking into account i) the improvement factor of $\sim 5$ derived for this unID at a pivot energy of 7 TeV The HAWC Collaboration (2017b), marked in the figure as a dashed grey vertical line; ii) the difference in exposure times, which makes the $F_{min}$ improve by a factor $\sqrt{507/760} = 0.82$; and iii) a factor $\sim$2 worsening due to the extension of the source, according to The HAWC Collaboration (2013a). See text for further details on these computations. The overall $F_{min}$ improvement is roughly an order of magnitude at low energies, while at the highest energies there is no improvement at all. . . . . 241

7.3 J-factor distributions for the brightest subhalo across 1000 realizations of the DM subhalo population as derived in Coronado-Blázquez, Sánchez-Conde, Domínguez, Aguirre-Santaella, Mauro, Mirabal, Nieto and Charles (2019) from the Via Lactea II N-body simulation. Red and blue histograms show, respectively, the values before and after applying our selection cuts on the simulated DM subhalos, namely a mass cut ($M \leq 10^7$M ) and a coordinate cut ($|b| > 30°$). The dashed, purple vertical line marks the value of the J-factor that will be used to set the 95% C.L. DM limits in Section 9.4, and it is defined as the one above which 95% of the J-factor distribution is contained. . . . . 242

7.4 95% upper limits on the DM annihilation cross section as derived from HAWC unIDs and predictions from N-body cosmological simulations. Indeed, these constraints use 2HWC J1040+308 alone, i.e., the only HAWC unID located at $|b| \geq 10°$ and surviving our selection criteria in Section 7.2.2. Left (right) panel shows the 95% C.L. upper limits for the $b\bar{b}$ ($\tau^+\tau^-$) annihilation channel. For comparison, we also show as a blue, dot-dashed line the DM constraints obtained from Fermi-LAT unIDs using the same methodology Coronado-Blázquez, Sánchez-Conde, Mauro, Aguirre-Santaella, Ciucă, Domínguez, Kawata and Mirabal (2019). Limits from the observation of the Galactic center region by H.E.S.S., i.e., the best DM constraints achieved from IACT observations at present, are included in both panels as well as a green, dashed line Lefranc et al. (2015). Finally, a dotted, orange line shows the constraints from *Fermi*-LAT observations of dSphs Fermi-LAT Collaboration (2015). We did not include in this Figure the results in The HAWC Collaboration (2019), as a one-to-one comparison would be misleading given the fact that the methodology and underlying assumptions in both works are significantly different; see discussion in Section 9.4 for details. . . . . 243

8.1 Skymap of the EGAL Survey, including also simulated sources potentially detectable by CTA. Figure adapted from Ref. (The Cherenkov Telescope Array Consortium; 2017). . . . . 256

8.2 **Upper panel**: overall 10-year exposure map for CTA in Galactic coordinates, extrapolated from 6.5 years of MAGIC stereo observations. The shown map corresponds to a random realization of our extrapolation algorithm. Color code traces the observation time per pointing. **Lower panel**: distribution of the observation time of the EXPO strategy for three bins: 0-5h, 5-50h and >50h, for the same random realization. . . . . 259
8.3 Minimum flux ($F_{min}$) to detect a dark subhalo annihilating to $b\bar{b}$ (top panel) and $\tau^+\tau^-$ (bottom panel) in the EGAL survey, assuming the Northern array and 3h of normal pointing observation with an energy threshold of 30 GeV. Gray lines are the individual 100 realizations, black solid line is the average value, and green and yellow bands are, respectively, the 68% and 95% confidence level. Right $y$ axis is expressed in units of mCrab flux. Blue dashed, horizontal line is the nominal 6 mCrab flux sensitivity of the EGAL scan. . . . . 261
8.4 Scaling of $J_{max}$ with the total observation area; see text for details. Only subhalos with M $\leq 10^8$M$_\odot$ are considered, as more massive subhalos are expected to host dSphs and thus be visible. The horizontal axes are expressed in square degrees (bottom axis) and as fraction of the full sky (top axis). We show four vertical lines, respectively, at 64 square degrees ($8 \times 8$ deg$^2$ DEEP scenario with narrow-field), 400 square degrees ($20 \times 20$ deg$^2$ DEEP with wide-field), 25% of the sky (EGAL) and 44% of the sky (EXPO). The zoom panel shows the scaling for the smallest areas, in linear scale. . . . . 265
8.5 95% C.L. upper limits to the DM annihilation cross section for $b\bar{b}$ (top) and $\tau^+\tau^-$ (bottom) assuming no unIDs are detected by CTA under any of the three observational strategies proposed in Sec. 8.2: a dedicated $10 \times 10$ deg$^2$, 100h deep-field, the EGAL survey, and the EXPO scenario. The dashed line represents the thermal value of the annihilation cross section (Bringmann et al.; 2020). See main text for details on the uncertainty bands, which, in short, come from the uncertainty in $F_{min}$ and, in the EXPO case, the uncertainty in the total sky area extrapolation. . . . . 267
8.6 Same as Figure 8.5, but showing only the EXPO constraints and the comparison with previous works, namely the *Fermi*-LAT unIDs (Coronado-Blázquez, Sánchez-Conde, Mauro, Aguirre-Santaella, Ciucă, Domínguez, Kawata and Mirabal; 2019), HAWC unIDs (Coronado-Blázquez and Sánchez-Conde; 2020), and the previous work on unIDs detection with CTA (Hütten et al.; 2016). . . . . 269
8.7 Schematic view of different pointing strategies, both for the EGAL and DEEP surveys, in normal and divergent mode. . . . . 272
8.8 For a random realization, this figure shows the distribution of exposures in observation time (upper panel), RA (middle panel) and DEC (bottom panel), both for actual MAGIC stereo operations in 6.5 years and our extrapolation to 10 years of CTA observations. Note that the DEC distributions in the bottom panel must be different, as we assumed half of the observations to be performed by CTA South. See text for details. . . . . 281

8.9 Growth of the cumulative exposure area as a function of period of observation (each period is equivalent to 29 days) for MAGIC stereo mode in 6.5 years. Except for some periods where no observations were made, the behavior is linear. . . . . 282
8.10 Map in equatorial coordinates of CTA pointings in 10 years of operation, extrapolated from 6.5 years of actual MAGIC stereo pointings, as obtained in a single random realization. Red circles are observations performed with CTA North, while blue are for CTA South. The area of each pointing is taken as a circle of 6 deg diameter. Note the overlaps between observations, which have been properly taken into account in the computation of the total effective area of exposure. See text for full details. . . . . 282
8.11 Distributions of the total effective area (left panel) and exposure time per pointing (right panel) in 10 years of CTA operation, extrapolated from 6.5 years of actual MAGIC stereo observations, as obtained after 2000 random realizations. The vertical line is the average values that we adopt to set constraints in Section 9.4. The corresponding 1-$\sigma$ uncertainties are below 2% in the case of the area and below 8% in the case of exposure time. . . . . 283
8.12 EXPO constraints (see Section 9.4 for the $\tau^+\tau^-$ annihilation channel, for different subhalo mass cuts. See discussion in the text for the motivation of the depicted values. . . . . 283

9.1 Cosmic X-ray background spectrum, as measured by various experiments. Overimposed are the Ueda+14 model (blue dashed line), the fit to a double power-law (black dashed line) of Eq. 9.4, and the corrections to the latter due to two hypothetical monochromatic PBH distributions with different masses $M$ and cosmological abundances $f = \Omega_{PBH}/\Omega_{DM}$. . . . . 288
9.2 95% c.l. upper limits on the PBH abundance versus the PBH mass assuming a monochromatic mass population. The black dot-dashed line is the result of the present work neglecting the background contribution from AGNs. The light blue-dotted line is the analogous result of Carr et al. (2010), see also Arbey and Auffinger (2019). The blue continuous line is the bound obtained assuming a power-law modeling of the AGN and blazar contribution to the observed spectrum. The red dashed curve indicates the sensitivity achievable with an experiment capable of reducing the astrophysical background by a factor of 10 . . . . . 289

# List of Tables

2.1 Summary of the current and future generation ground-based gamma-ray observatories. . . . . 102

3.1 Key properties of the *Fermi*-LAT catalogs used in this study. . . . . 127
3.2 Estimated efficiency for each of the applied filters in Section 3.3. The third column refers to the treatment adopted in each case for the remaining unIDs "beyond" the efficiency of our cuts. Note that we omit the multi-wavelength emission filter in this table given the difficulty to provide a realistic estimate as of today: among other ingredients, one would need to compute the expected source number density of each of the considered catalogs at other wavelengths, which is beyond the scope of this work. . . . . 135

4.1 Summary of the spectral analysis technical setup. See Section 4.2 for details. . . . . 164
4.2 Sources exhibiting positive $\Delta$TS values, sorted by catalog and right ascension (RA), following its definition in Eq. 4.6, i.e., in these cases DM is preferred against astrophysical models. The second column shows the DM channel(s) for which we have positive $\Delta$TS. For almost all these sources, there are different channels providing $\Delta$TS>0. The third column gives their corresponding $\Delta$TS. These values are far from being significant; see also discussion in the text. The fourth column shows best-fit DM mass with $1\sigma$ uncertainty. The last column reports the best-fit astrophysical models. . . . . 170
4.3 Summary of the number of sources from the three different catalogs which are fitted to DM annihilation channels with $\Delta\text{TS} \geq -9$. There is no overlap between catalogs, i.e., no source from a particular catalog is present in one of the other two. There is no 2FHL source or $t\bar{t}$ channel fit present in the final result. . . . . 171

5.1 Parameters needed to build the NFW DM profiles of our two subhalo scenarios, each of them representatives of the fraction of the Galactic dark subhalo population that is relevant in terms of expected annihilation flux. See Section 5.2.1 for details on the derivation of these parameters. . . . . 197
5.2 Total, integrated J-factors for the two representative subhalo scenarios, in the first column integrated up to the whole object ($R_{sub}$), and up to $r_s$ in the second. . . . . 198
5.3 Summary of the *fermipy* analysis setup. . . . . 200

6.1 Summary of the *fermipy* analysis setup. . . . . 225

6.2 Summary of the analysis of the 127 4FGL-DR2 unIDs sample, selected with the cuts detailed in Section 6.2. We only report the results for the best subhalo candidates, i.e., with the largest preferences for DM ($TS_{\mathcal{X}} > 10$). First (second) sub-table shows the candidates fitted to $b\bar{b}$ ($\tau^+\tau^-$). The $TS_{\mathcal{X}}$ values refer to the difference w.r.t the best-fit astrophysical model, corrected by the difference in d.o.f. with the Akaike criterium. The local p-value ($p_{loc}$) and corresponding local significance ($\sigma_{loc}$) are computed with the realistic TS distribution for DM annihilation from Fermi-LAT Collaboration and DES Collaboration (2017), while the global p-value ($p_{glob}$) accounts for the number of trials and is computed with Eq. 6.4. The global significance $\sigma_{glob}$ is obtained from $p_{glob}$. Note that one source, 4FGL J1204.5−5032, is well fitted to both annihilation channels and therefore is present in both sub-tables. . . . . 229

8.1 Average $F_{min}$ values with an energy threshold of 30 GeV, in ph $\cdot$ cm$^{-2}$ $\cdot$ s$^{-1}$, for the three observational strategies under discussion, and for three benchmark WIMP masses annihilating via either $b\bar{b}$ or $\tau^+\tau^-$ annihilation channels. . . . . 262

8.2 Average number of subhalos above a given $J_{min}$ in the CTA FoV for the three observation strategies of Section 8.2, across 1000 realizations of the repopulated VL-II N-body simulation as described in Section 8.3.2. . . . . 265

# List of Abbreviations

| | |
|---|---|
| **AGILE** | **A**strorivelatore **G**amma ad **I**mmagini **LE**ggero satellite |
| **AGN** | **A**ctive **G**alactic **N**uclei |
| **ALP** | **A**xion–**L**ike **P**article |
| **AMS** | **A**lpha **M**agnetic **S**pectrometer |
| **BAO** | **B**aryonic **A**coustic **O**scillation |
| **BBN** | **B**ig–**B**ang **N**ucleosynthesis |
| **BH** | **B**lack **H**ole |
| **BSM** | **B**eyond **S**tandard **M**odel |
| **CDM** | **C**old **D**ark **M**atter |
| **CL** | **C**onfidence **L**evel |
| **CMB** | **C**osmic **M**icrowave **B**ackground |
| **CR** | **C**osmic **R**ay |
| **CTA** | **C**herenkov **T**elescope **A**rray |
| **DES** | **D**ark **E**nergy **S**urvey |
| **DM** | **D**ark **M**atter |
| **dSph** | **D**warf **Sph**eroidal galaxy |
| **dIrr** | **D**warf **Irr**egular galaxy |
| **EBL** | **E**xtragalactic **B**ackground **L**ight |
| **EGRET** | **E**nergetic **G**amma-**R**ay **E**xperiment **T**elescope |
| **EM** | **E**lectro**M**agnetism |
| **EW** | **E**lectro**W**eak |
| **FGRST** | **F**ermi **G**amma–**R**ay **S**pace **T**elescope |
| **FIMP** | **F**eebly **I**nteracting **M**assive **P**article |
| **FoV** | **F**ield **o**f **V**iew |
| **FLRW** | **F**riedmann–**L**emaître–**R**obertson–**W**alker |
| **GBM** | **G**amma–ray **B**urst **M**onitor |
| **GC** | **G**alactic **C**enter |
| **GCE** | **G**alactic **C**enter **E**xcess |
| **GR** | **G**eneral **R**elativity |
| **GRB** | **G**amma–**R**ay **B**urst |
| **GUT** | **G**rand **U**nified **T**heory |
| **GLAST** | **G**amma-ray **L**arge **A**rea **S**pace **T**elescope |
| **GW** | **G**ravitational **W**ave |
| **HAWC** | **H**igh–**A**ltitude **W**ater **C**herenkov |
| **HDM** | **H**ot **D**ark **M**atter |
| **HEGRA** | **H**igh **E**nergy **G**amma–**R**ay **A**stronomy array |
| **H.E.S.S.** | **H**igh **E**nergy **S**pectroscopic **S**ystem |
| **HGPS** | **H**.E.S.S. **G**alactic **P**lane **S**urvey |
| **HST** | **H**ubble **S**pace **T**elescope |
| **IACT** | **I**maging **A**tmospheric **C**herenkov **T**elescope |
| **IC** | **I**nverse **C**ompton |
| **IE** | **I**nterstellar **E**mission |
| **ISM** | **I**nter**S**tellar **M**edium |

| | |
|---|---|
| **IGRB** | **I**sotropic **G**amma–**R**ay **B**ackground |
| **INTEGRAL** | **INTE**rnational **G**amma-**R**ay **A**strophysics **L**aboratory |
| **IR** | **I**nfra**R**ed |
| **IRF** | **I**nstrumental **R**esponse **F**unction |
| **JWST** | **J**ames **W**ebb **S**pace **T**elescope |
| **KSP** | **K**ey **S**cience **P**roject |
| **LAT** | **L**arge **A**rea **T**elescope |
| **LHC** | **L**arge **H**adron **C**ollider |
| **LIGO** | **L**aser **I**nterferometer **G**ravitational-wave **O**bservatory |
| **LMC** | **L**arge **M**agellanic **C**loud |
| **LSS** | **L**arge **S**cale **S**tructure |
| **LST** | **L**arge–**S**ized **T**elescope |
| **MACHO** | **MA**ssive **C**ompact **H**alo **O**bject |
| **MAGIC** | **M**ajor **A**tmospheric **G**amma **I**maging **C**herenkov array |
| **MOND** | **M**odification **O**f **N**ewtonian **D**ynamics |
| **ML** | **M**achine **L**earning |
| **MSP** | **M**illi**S**econd **P**ulsar |
| **MST** | **M**edium–**S**ized **T**elescope |
| **MW** | **M**ilky **W**ay |
| **NFW** | **N**avarro–**F**renk–**W**hite |
| **NS** | **N**eutron **S**tar |
| **PBH** | **P**rimordial **B**lack **H**ole |
| **QCD** | **Q**uantum **C**hromo**D**ynamics |
| **PAMELA** | **P**ayload for **A**ntimatter **M**atter **E**xploration and **L**ight–nuclei **A**strophysics |
| **PF** | **P**ositron **F**raction |
| **PMT** | **P**hoto**M**ultiplier **T**ube |
| **PSF** | **P**oint **S**pread **F**unction |
| **PSR** | **P**uls**ar** |
| **PWN** | **P**ulsar **W**ind **N**ebula |
| **ROI** | **R**egion **O**f **I**nterest |
| **SD** | **S**pin–**D**ependent |
| **SDSS** | **S**loan **D**igital **S**cale **S**urvey |
| **SHM** | **S**tandard **H**alo **M**odel |
| **SHMF** | **S**ub**H**alo **M**ass **F**unction |
| **SI** | **S**pin–**I**ndependent |
| **SM** | **S**tandard **M**odel |
| **SMBH** | **S**uper**M**assive **B**lack **H**ole |
| **SMC** | **S**mall **M**agellanic **C**loud |
| **SN** | **S**uper**N**ova |
| **SNR** | **S**uper**N**ova **R**emnant |
| **SST** | **S**mall–**S**ized **T**elescope |
| **SUSY** | **SU**per**SY**mmetry |
| **SZ** | **S**unyaev **Z**el'dovich |
| **TeVeS** | **Te**nsor–**Ve**ctor–**S**calar |
| **TS** | **T**est **S**tatistic |
| **unID** | **UnID**entified gamma-ray source |
| **UV** | **U**ltra**V**iolet |
| **VERITAS** | **V**ery **E**nergetic **R**adiation **I**maging **T**elescope **A**rray **S**ystem |
| **WDM** | **W**arm **D**ark **M**atter |
| **WIMP** | **W**eakly **I**nteracting **M**assive **P**article |